8 May 2009 | $10

Science

Plant-Microbe Interactions

AAAS

transfectionist.

Improved transfection. Unrestricted parameters. Universal protocols.

You need the best electroporation technology available, but you also want the ability to transfect primary cells with a flexible system. We understand. Bio-Rad's Gene Pulser MXcell™ electroporation system with the Shockpod™ accessory gives you the ability to quickly and seamlessly transfect primary cells like never before.

Generate reproducible data by selecting the parameters ideally suited for your specific mammalian cells. Carry out your experiment using whole or fractional plates for limited cells or use a single cuvette for scaling up primary cell numbers.

To learn more about Gene Pulser MXcell, please visit **www.bio-rad.com/ad/mxcell/** or contact your local sales representative.

Research. Together.

Eppendorf & Science Prize for

Neurobiology

$25,000 Prize

Get recognized!

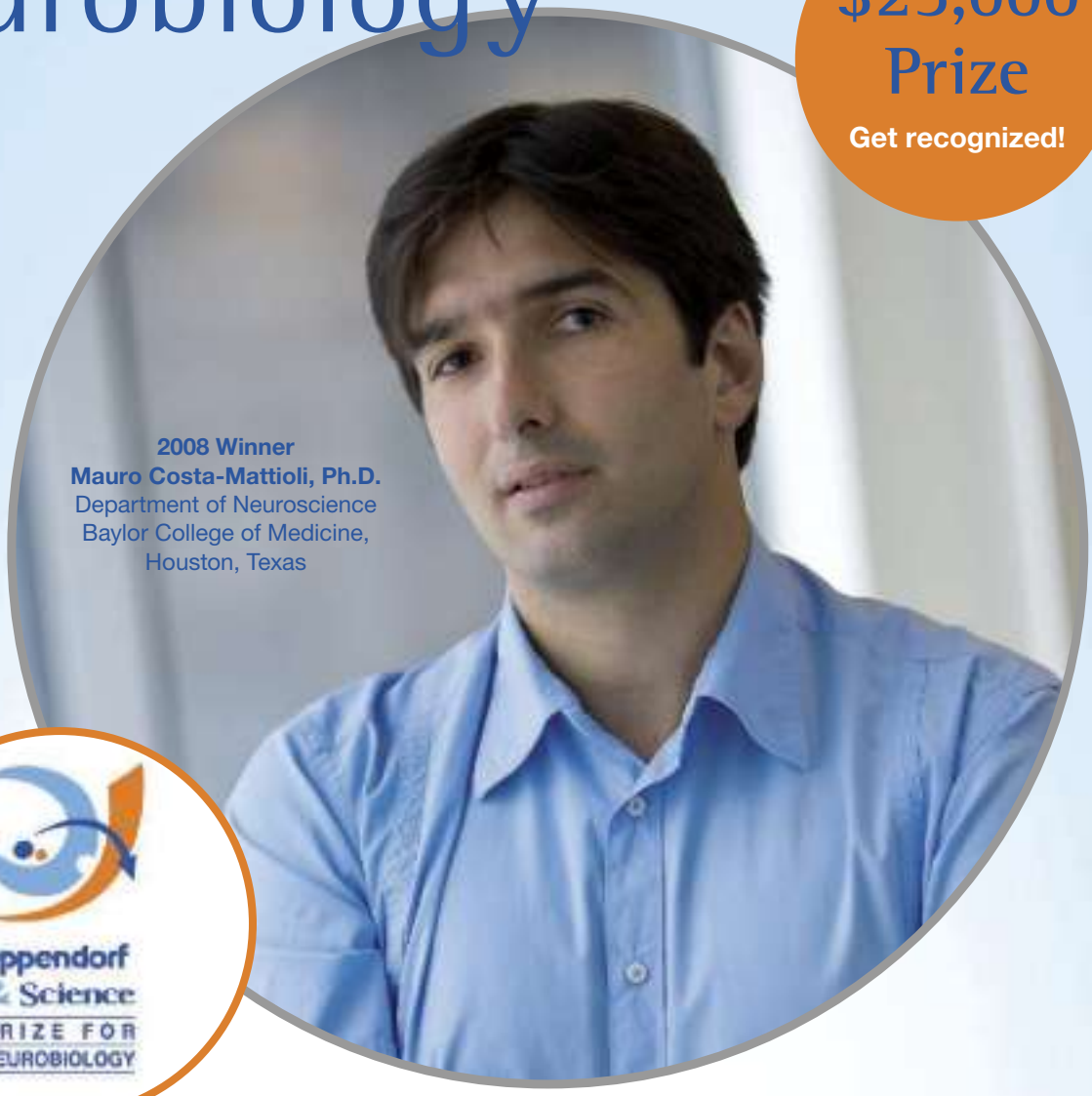

2008 Winner
Mauro Costa-Mattioli, Ph.D.
Department of Neuroscience
Baylor College of Medicine,
Houston, Texas

eppendorf & Science PRIZE FOR NEUROBIOLOGY

Deadline for entries
June 15, 2009

For more information
www.eppendorf.com/prize

This annual international research prize recognizes accomplishments in neurobiology research based on methods of molecular and cell biology. The winner and finalists are selected by a committee of independent scientists, chaired by the Editor-in-Chief of *Science*. Past winners include postdoctoral scholars and assistant professors.

To be eligible, you must be 35 years of age or younger. If you´re selected as this year´s winner, you will receive $25,000, have your work published in the prestigious journal *Science* and be invited to visit Eppendorf in Hamburg, Germany.

eppendorf
In touch with life

Science AAAS

Kurstin Roe Photography

Biacore systems

from inspiration ...to publication

Highest quality, information-rich interaction data from Biacore™ systems deepen your understanding of molecular mechanisms and interaction pathways and enable you to add function to structure.

Select the perfect solution for your application and draw conclusions with confidence – from the company that continues to set the standard for label-free protein interaction analysis.

For further information or register to have one of our scientific experts contact you, please visit **www.gelifesciences.com/biacore-science**

Biacore T100
unmatched performance

Biacore X100
ready to run research system

Biacore Flexchip
array-based comparative profiling

imagination at work

SPECIAL SECTION

Plant-Microbe Interactions

INTRODUCTION

741 What's Bugging Plants?

PERSPECTIVES

742 Innate Immunity in Plants: An Arms Race Between Pattern Recognition Receptors in Plants and Effectors in Microbial Pathogens
T. Boller and S. Y. He

744 To Nibble at Plant Resistance Proteins
F. L. W. Takken and W. I. L. Tameling

746 Plant-Microbe Interactions: Chemical Diversity in Plant Defense
P. Bednarek and A. Osbourn

748 Terrific Protein Traffic: The Mystery of Effector Protein Delivery by Filamentous Plant Pathogens
R. Panstruga and P. N. Dodds

750 Hormone (Dis)harmony Moulds Plant Health and Disease
M. R. Grant and J. D. G. Jones

753 Reprogramming Plant Cells for Endosymbiosis
G. E. D. Oldroyd et al.

755 Coevolution of Plants and Their Pathogens in Natural Habitats
J. J. Burdon and P. H. Thrall

>> See also related Editorial on p. 691

page 710

EDITORIAL

691 Next-Generation Communication
Ton Bisseling et al.
>> Plant-Microbe Interactions section p. 741

NEWS OF THE WEEK

700 Out of Mexico? Scientists Ponder Swine Flu's Origins

702 Devilish Dilemmas Surround Pandemic Flu Vaccine

703 From the *Science* Policy Blog

705 What Role for Antiviral Drugs?

706 Newsmaker Interview: Corey Goodman, Post-Pfizer, on the Allure of Enterprise

707 Army Bans Pathogen Work at Lab After Security Lapse

708 DOE Commits $777 Million to Apply Basic Science to Urgent Problems

709 Fermi Data Dim Dark-Matter Claim

709 From *Science*'s Online Daily News Site

NEWS FOCUS

710 The Famine Fighter's Last Battle

713 Wenchuan Earthquake: A Deeply Scarred Land
Some Unwelcome Questions About Big Dams

715 One Year After a Devastating Cyclone, a Bitter Harvest

717 Going the Distance to Uncover the Roots of Trade in the Near East

718 Shuttle Crew Set to Prepare Hubble for a Star-Studded Grand Finale
A Reprieve—and Risk

LETTERS

721 The Spread of Grapevine Trunk Disease
C. Bertsch et al.
Eutrophication: More Nitrogen Data Needed
D. W. Schindler and R. E. Hecky
Eutrophication: Focus on Phosphorus
C. L. Schelske
Eutrophication: Model Before Acting
A. C. Bryhn and L. Håkanson
Eutrophication: Time to Adjust Expectations
C. A. Jacoby and T. K. Frazer
Response
D. J. Conley et al.

BOOKS *ET AL.*

726 Cruelty
K. Taylor, reviewed by P. Ak

POLICY FORUM

727 A History Lesson for Stem Cells
J. M. Wilson

PERSPECTIVES

729 The Origin of Plasmaspheric Hiss
O. Santolík and J. Chum
>> Report p. 775

730 Origins of Agriculture in East Asia
M. K. Jones and X. Liu

731 The Sources of Human Volition
P. Haggard
>> Report p. 811

733 Some Like It Cold
C. H. Greene et al.
>> Report p. 791

734 An Invasive Plant Paradox
M. E. Rout and R. M. Callaway

CONTENTS continued >>

COVER

Interactions between microbes and plants can vary widely, depending upon the context and the partners of the interaction. An Editorial on page 691 and a collection of Perspectives starting on page 742 discuss recent advances in our understanding of the biochemistry, signaling, and ecosystem dynamics that reflect how microbes and plants interact.

Illustration: Chris Bickel

DEPARTMENTS

687 This Week in *Science*
693 Editors' Choice
696 *Science* Staff
699 Random Samples
818 New Products
819 *Science* Careers

Published by AAAS

Epigenetics sample and assay technologies by QIAGEN

Trust in methylation analysis

Rely on QIAGEN epigenetics sample and assay technologies for:

- **DNA purification**
- **Bisulfite conversion**
- **Whole bisulfitome amplification**
- **Methylation-specific PCR**
- **Methylation detection and quantification with Pyrosequencing**

Making improvements in life possible — www.qiagen.com

QIAGEN®

Sample & Assay Technologies

ADNAEpigenetics0309S1WW

REVIEW

736 Elemental Composition of the Martian Crust
H. Y. McSween Jr. et al.

BREVIA

758 A Gene Necessary for Reproductive Suppression in Termites
J. Korb et al.

Knocking out the *Neofem2* gene in queen termites illicits pre-reproductive behavior in workers.

RESEARCH ARTICLE

759 Representation of Confidence Associated with a Decision by Neurons in the Parietal Cortex
R. Kiani and M. N. Shadlen

Neurons in the primate parietal cortex encode information required to make a decision and also the certainty of that choice.

REPORTS

764 Characterization of Multipartite Entanglement for One Photon Shared Among Four Optical Modes
S. B. Papp et al.

Sharing a single photon between four optical modes creates entangled states that could be used in quantum information processing.

768 N-Doping of Graphene Through Electrothermal Reactions with Ammonia
X. Wang et al.

The edges of graphene nanoribbons incorporate nitrogen atoms after heating in an atmosphere of ammonia.

772 An Experimental Design Method Leading to Chemical Turing Patterns
J. Horváth et al.

Three design criteria were used to create sustained stationary patterns in the thiourea-iodate-sulfite reaction system.

775 An Observation Linking the Origin of Plasmaspheric Hiss to Discrete Chorus Emissions
J. Bortnik et al.

The radio waves that remove energetic electrons from Earth's radiation belts originate outside the plasmasphere.
>> *Perspective p. 729*

778 The Role of Aerosols in the Evolution of Tropical North Atlantic Ocean Temperature Anomalies
A. T. Evan et al.

Changes in tropical North Atlantic sea surface temperatures are caused by variability in atmospheric aerosol abundances.

781 UV Absorption Cross Sections of ClOOCl Are Consistent with Ozone Degradation Models
H.-Y. Chen et al.

Measurements of how well ClOOCl molecules absorb ultraviolet light support standard models of chlorine-induced ozone degradation.

784 Host Inhibition of a Bacterial Virulence Effector Triggers Immunity to Infection
V. Ntoukakis et al.

An enzyme in tomato targets bacterial virulence to change the outcome of infection from susceptibility to immunity.

787 Development of a Second-Generation Antiandrogen for Treatment of Advanced Prostate Cancer
C. Tran et al.

A drug that binds to the androgen receptor acts by disrupting its activity in the cell nucleus.

791 Basin-Scale Coherence in Phenology of Shrimps and Phytoplankton in the North Atlantic Ocean
P. Koeller et al.

Shrimp reproduction is primed by bottom temperature and not directly by cues from the spring phytoplankton bloom.
>> *Perspective p. 733*

794 Apicomplexan Parasites Co-Opt Host Calpains to Facilitate Their Escape from Infected Cells
R. Chandramohanadas et al.

A host protease helps newly replicated microbial parasites escape from incubator cells.

797 Human Induced Pluripotent Stem Cells Free of Vector and Transgene Sequences
J. Yu et al.

Human induced pluripotent stem cells can be generated without integration of exogenous DNA into their genomes.

801 Benzothiazinones Kill *Mycobacterium tuberculosis* by Blocking Arabinan Synthesis
V. Makarov et al.

An isomerase required for cell-wall synthesis is a target for an alternative drug lead for tuberculosis treatment.

804 Mammalian Expression of Infrared Fluorescent Proteins Engineered from a Bacterial Phytochrome
X. Shu et al.

An engineered infrared fluorescent protein derived from an extremophile bacterium gives a strong signal in mammalian cells.
>> Science *Podcast*

807 High-Throughput Sequencing of the Zebrafish Antibody Repertoire
J. A. Weinstein et al.

Sequencing of immunoglobulin messenger RNA characterizes the diversity of the antibody repertoire in individual zebrafish.

page 730

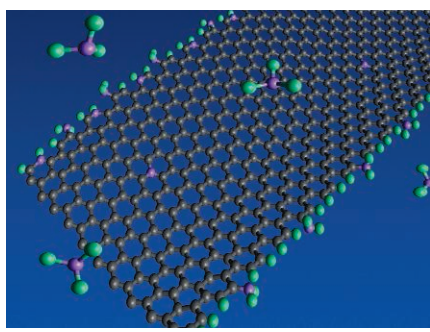

page 768

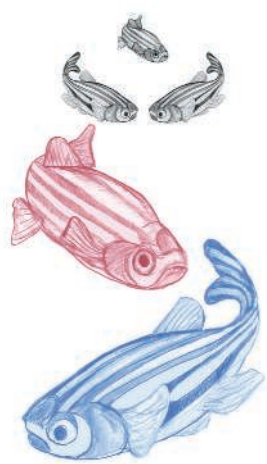

page 807

811 Movement Intention After Parietal Cortex Stimulation in Humans
M. Desmurget et al.

Stimulation of the parietal cortex causes subjects to report having moved, even in the absence of actual motor responses.
>> *Perspective p. 731*

CONTENTS continued **>>**

VILCEK PRIZE FOR CREATIVE PROMISE 2010

APPLICATION DEADLINE JULY 31, 2009

BIOMEDICAL RESEARCH

APPLICANTS MUST BE BORN ABROAD, BE NATURALIZED CITIZENS OR PERMANENT RESIDENTS OF THE UNITED STATES, AND NO MORE THAN 38 YEARS OLD.

TWO $25,000 PRIZES, ONE IN BIOMEDICAL RESEARCH, THE OTHER IN CULINARY ARTS, SHALL BE AWARDED FOR OUTSTANDING EARLY ACHIEVEMENT.

FOR MORE INFORMATION OR TO APPLY VISIT WWW.VILCEK.ORG. FOR QUESTIONS PLEASE EMAIL CREATIVEPROMISE@VILCEK.ORG OR CALL 212.472.2500.

THE VILCEK FOUNDATION

HONORING CONTRIBUTIONS OF IMMIGRANTS TO BIOMEDICAL SCIENCE AND THE ARTS

SCIENCEONLINE

SCIENCEXPRESS
www.sciencexpress.org

Greater Transportation Energy and GHG Offsets from Bioelectricity Than Ethanol
J. E. Campbell et al.

Electric vehicles powered by electricity made from biofuels are more efficient than vehicles fueled by bioethanol.
10.1126/science.1168885
>> Science *Podcast*

Large-Area Synthesis of High-Quality and Uniform Graphene Films on Copper Foils
X. Li et al.

Predominantly single-layer graphene films grow in a self-limited manner on copper and can be transferred to other substrates.
10.1126/science.1171245

IL-21 Is Required to Control Chronic Viral Infection
H. Elsaesser et al.

Interleukin-21 produced by $CD4^+$ T cells helps $CD8^+$ T cells control viral infection in a mouse model.
10.1126/science.1174182

Recruitment of an Area Involved in Eye Movements During Mental Arithmetic
A. Knops et al.

Addition and subtraction are encoded in the same part of the brain that is responsible for eye movements and spatial attention.
10.1126/science.1171599

Fluorescent False Neurotransmitters Visualize Dopamine Release from Individual Presynaptic Terminals
N. G. Gubernator et al.

Optical tracking of neurotransmitter release in the brain reveals multiple synaptic populations that depend on brain activity.
10.1126/science.1172278

SCIENCENOW
www.sciencenow.org
Highlights From Our Daily News Coverage

Running Amok in the Milky Way
Hundreds of rogue black holes could be prowling the galaxy.

Narcolepsy: A Case of the Body Attacking Itself?
New findings suggest that the sleep disorder is an autoimmune disease.

Did Mars's Magnetic Field Die With a Whimper or a Bang?
Study suggests massive asteroids could have released enough heat to shut down the Red Planet's dynamo.

SCIENCESIGNALING
www.sciencesignaling.org
The Signal Transduction Knowledge Environment

RESEARCH ARTICLE: Complexity in Transcription Control at the Activation Domain–Mediator Interface
M. A. Balamotis et al.

Transcriptional activation kinetics vary in different cell types, in part because related transcription factors make alternative mediator interactions.

PERSPECTIVE: Nitric Oxide Links Mitochondrial Fission to Alzheimer's Disease
B. Westermann

Amyloid β–induced nitrosylation of a GTPase involved in mitochondrial fission is neurotoxic.

PERSPECTIVE: Fragile Axons Forge the Path to Gene Discovery—A MAP Kinase Pathway Regulates Axon Regeneration
G. S. O'Brien and A. Sagasti

In *Caenorhabditis elegans*, a mitogen-activated protein kinase pathway is required for regenerative, but not developmental, axon outgrowth.

NETWATCH: Genes to Cognition (G2C) Online
Learn about current neuroscience research and explore the genetic and biochemical causes of neurologic and neurodevelopmental disorders; in Educator Sites.

NETWATCH: PharmGKB
A pharmacogenetics database integrates genetic, phenotypic, and pharmacological data; in Bioinformatics Resources.

SCIENCECAREERS
www.sciencecareers.org/career_magazine
Free Career Resources for Scientists

Mind Matters: Ten-Minute Tools for Managing Stress
I. S. Levine

Small chunks of dedicated time can help relieve the stress in scientific lives.

From Cells to Selling Science
A. G. Levine

Scientific training helps public relations professionals tell stories for their clients.

Funding News
GrantsNet Staff

Now published weekly, Funding News provides the latest sources of research and education funds.

SCIENCEPODCAST
www.sciencemag.org/multimedia/podcast
Free Weekly Show

Download the 8 May *Science* Podcast to hear about imaging animal cells with infrared fluorescent proteins, benefits of bioelectricity versus bioethanol, combating wheat rust, and more.

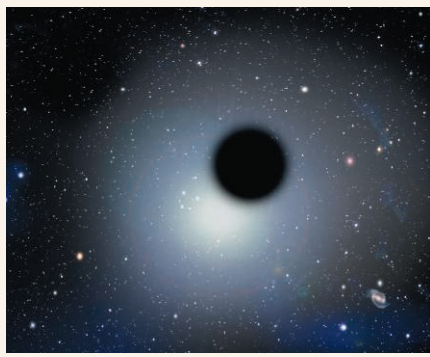

SCIENCENOW
Rogue black hole.

SCIENCESIGNALING
Controlling mitochondrial fission.

ORIGINSBLOG
blogs.sciencemag.org/origins
A History of Beginnings

SCIENCEINSIDER
blogs.sciencemag.org/scienceinsider
Science Policy News and Analysis

SCIENCE (ISSN 0036-8075) is published weekly on Friday, except the last week in December, by the American Association for the Advancement of Science, 1200 New York Avenue, NW, Washington, DC 20005. Periodicals Mail postage (publication No. 484460) paid at Washington, DC, and additional mailing offices. The title SCIENCE is a registered trademark of the AAAS. Domestic individual membership and subscription (51 issues): $146 ($74 allocated to subscription). Domestic institutional subscription (51 issues): $835; Foreign postage extra: Mexico, Caribbean (surface mail) $55; other countries (air assist delivery) $85. First class, airmail, student, and emeritus rates on request. Canadian rates with GST available upon request, GST #1254 88122. Publications Mail Agreement Number 1069624. **Printed in the U.S.A.**

Change of address: Allow 4 weeks, giving old and new addresses and 8-digit account number. **Postmaster:** Send change of address to AAAS, P.O. Box 96178, Washington, DC 20090–6178. **Single-copy sales:** $10.00 current issue, $15.00 back issue prepaid includes surface postage; bulk rates on request. **Authorization to photocopy** material for internal or personal use under circumstances not falling within the fair use provisions of the Copyright Act is granted by AAAS to libraries and other users registered with the Copyright Clearance Center (CCC) Transactional Reporting Service, provided that $20.00 per article is paid directly to CCC, 222 Rosewood Drive, Danvers, MA 01923. The identification code for *Science* is 0036-8075. *Science* is indexed in the *Reader's Guide to Periodical Literature* and in several specialized indexes.

AAAS
ADVANCING SCIENCE, SERVING SOCIETY

CREDITS: (*SCIENCE NOW*) DAVID AGUILAR/CFA; (*SCIENCE SIGNALING*) CHRIS BICKEL

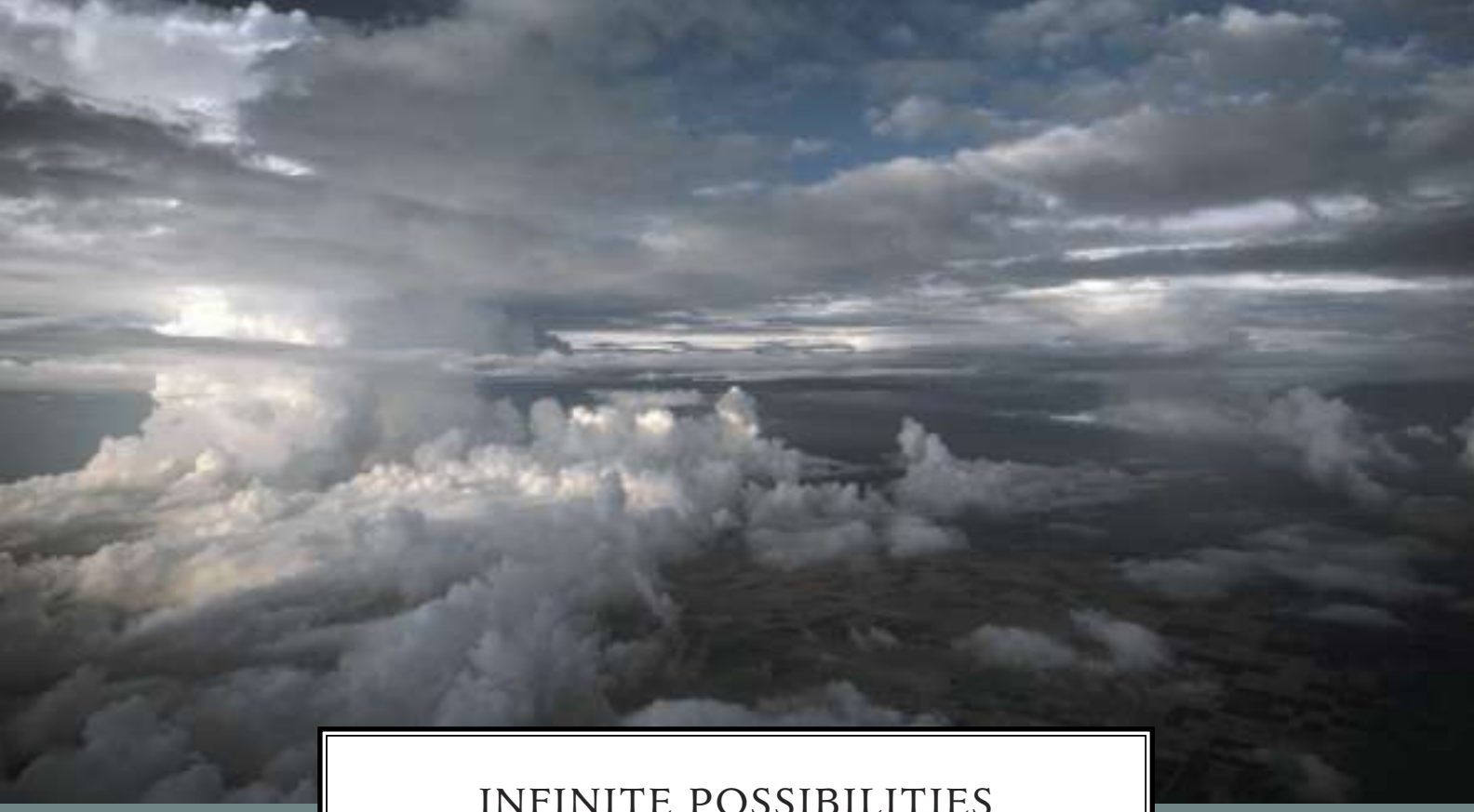

INFINITE POSSIBILITIES

Cellular Imaging & Analysis

NEB introduces SNAP-tag™ and CLIP-tag™ protein labeling systems. These innovative technologies provide simplicity and extraordinary versatility to the imaging of mammalian proteins *in vivo*, and to protein capture experiments *in vitro*. The creation of a single genetic construct generates a fusion protein which, when covalently attached to a variety of fluorophores, biotin, or beads provides a powerful tool for studying the role of proteins in living and fixed cells.

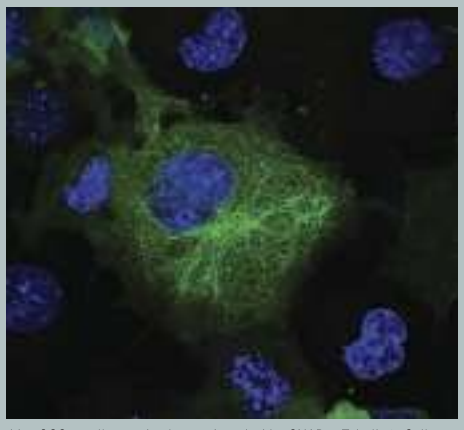

Live COS-7 cells transiently transfected with pSNAPm-Tubulinβ. Cells were labeled with SNAP-Cell TMR-Star (green pseudocolor) for 30 minutes and counterstained with Hoechst 33342 (blue) for nuclei.

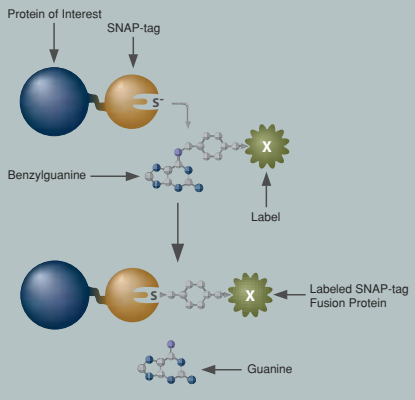

SNAP-tag Technology: *SNAP-tag (gold) fused to the protein of interest (blue) self labels releasing guanine.*

Advantages:

Versatile - Compatible systems enable dual labeling

Flexible - Multiple fluorophores allow for choice & flexibility

Innovative - A range of applications is possible with a single construct

NEW ENGLAND BioLabs® Inc.

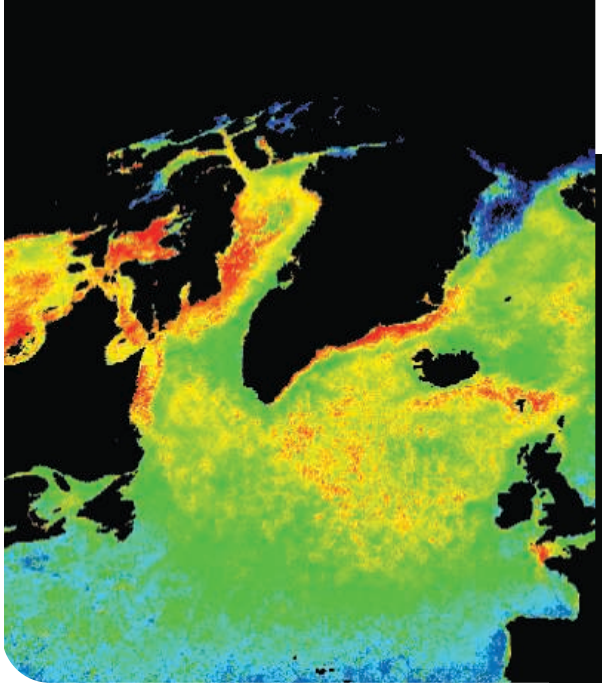

<< Fine-Tuning Fisheries

The past decade has seen a tremendous increase in our understanding of how climate anomalies affect hydrographic properties in North Atlantic Shelf ecosystems, but less about how these events impact organisms. **Koeller *et al.*** (p. 791, see the Perspective by **Greene *et al.***) measured the egg incubation and hatching times of an important fisheries resource, the pink North Atlantic shrimp, at a variety of locations and compared them to the timing of the local spring phytoplankton bloom. Shrimp reproduction was determined locally by bottom-water temperatures and was not directly coupled with the spring bloom. While the local bottom temperatures and bloom timing are well-matched in general, and match egg hatching to food availability, this evolved relationship can be decoupled by interannual variability and climate change.

Mars Matters

Several decades of exploration by orbiting and in situ spacecraft, together with analysis of martian meteorites, have resulted in a wealth of data on the chemical composition of Mars' crust. **McSween *et al.*** (p. 736) review these data, which help infer the planet's geological history, discrediting previous ideas suggesting Mars had a wet mantle—similar to that of Earth—and cautioning that martian meteorites are not representative of the planet's crust.

Negatively Doped Graphene Nanoribbons

The potential applications in electronic devices of graphene (single atom, thick layers of graphite) would be even greater if it can be accessed in both p- and n-doped forms. Graphene nanoribbons (long strips only tens of nanometers in width) are readily p-doped by adsorbates from the ambient atmosphere. **Wang *et al.*** (p. 768) show that when graphene nanoribbons are electrically heated in an ammonia atmosphere, nitrogen is incorporated mainly at the edges of the ribbon and creates an n-type material. Field-effect transistors that operate at room temperature can be made from this material.

Decisive Monkeys

Decision-making is a central theme in current research in cognitive neuroscience. Behavioral protocols have provided an entry into explorations of the neural processes that underlie decision-making. Empirical studies have provided support for a diffusion model in which information accumulates over time until a threshold is reached, with noisiness in the inputs related to decision errors. **Kiani and Shadlen** (p. 759) developed a behavioral task to study choice certainty and identified the corresponding neuronal representations in monkeys. The monkeys were allowed to choose to opt out of an uncertain, higher reward choice in favor of a certain, lower payoff. The same neurons that encoded the information used to make a choice also encoded the extent of certainty, which in humans would be described as the degree of confidence in one's decision.

Adding a Turing Pattern Reaction

Two chemical-reaction systems can form sustained stationary patterns (Turing patterns) in solution as the result of the movement of a diffusible species and the formation of negative feedback loops—the chlorite-iodide–malonic acid reaction and the ferrocyanide-iodate-sulfite reaction. **Horváth *et al.*** (p. 772) set out to find other examples based on three criteria—that the reaction can develop spatial bistability, that independent control of the negative feedback reaction can be achieved, and the activating and inhibiting processes can be decoupled by slowing down the diffusing species with a complexing agent. The thiourea-iodate-sulfite (TuIS) reaction could be developed into a system that produced different stationary patterns, including stripes and hexagonal arrays of spots. Thus, such Turing pattern–generating reactions are not necessarily uncommon.

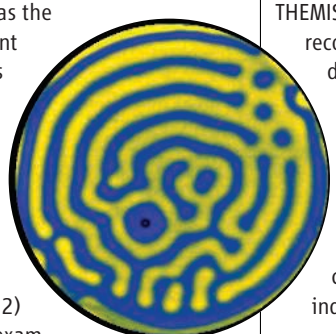

Chorus Hissing

Plasmaspheric hiss, a type of unstructured broadband, low-frequency radio emission, has long been known to exist in Earth's plasmasphere, but its origin has been uncertain. The source of hiss could be a different type of radio wave, called chorus, which originates outside the plasmasphere during geomagnetic storms. Both types of radio wave influence the behavior of energetic electrons in the near-Earth space environment, with implications for spacecraft and astronaut safety, but a correlation between the two has been difficult to establish experimentally. Recently, two of the five satellites of the THEMIS constellation were fortuitously able to record 4 minutes of electromagnetic wave data at high resolution during geomagnetically active conditions, detecting both chorus and hiss. An analysis of the data by **Bortnik *et al.*** (p. 775; see the Perspective by **Santolik and Chum**) revealed that the two sets of waves were well correlated, with hiss lagging behind chorus as expected, implying that one indeed evolved into the other.

Dust in the Wind

The temperature of North Atlantic surface waters has a major effect on climate in a variety of ways, not least because its heat content helps to control hurricane formation and strength. The North Atlantic surface has warmed considerably in recent decades, a trend generally associated

Continued on page 689

CREDITS (TOP TO BOTTOM): DEPARTMENT OF FISHERIES AND OCEANS CANADA; HORVÁTH *ET AL.*

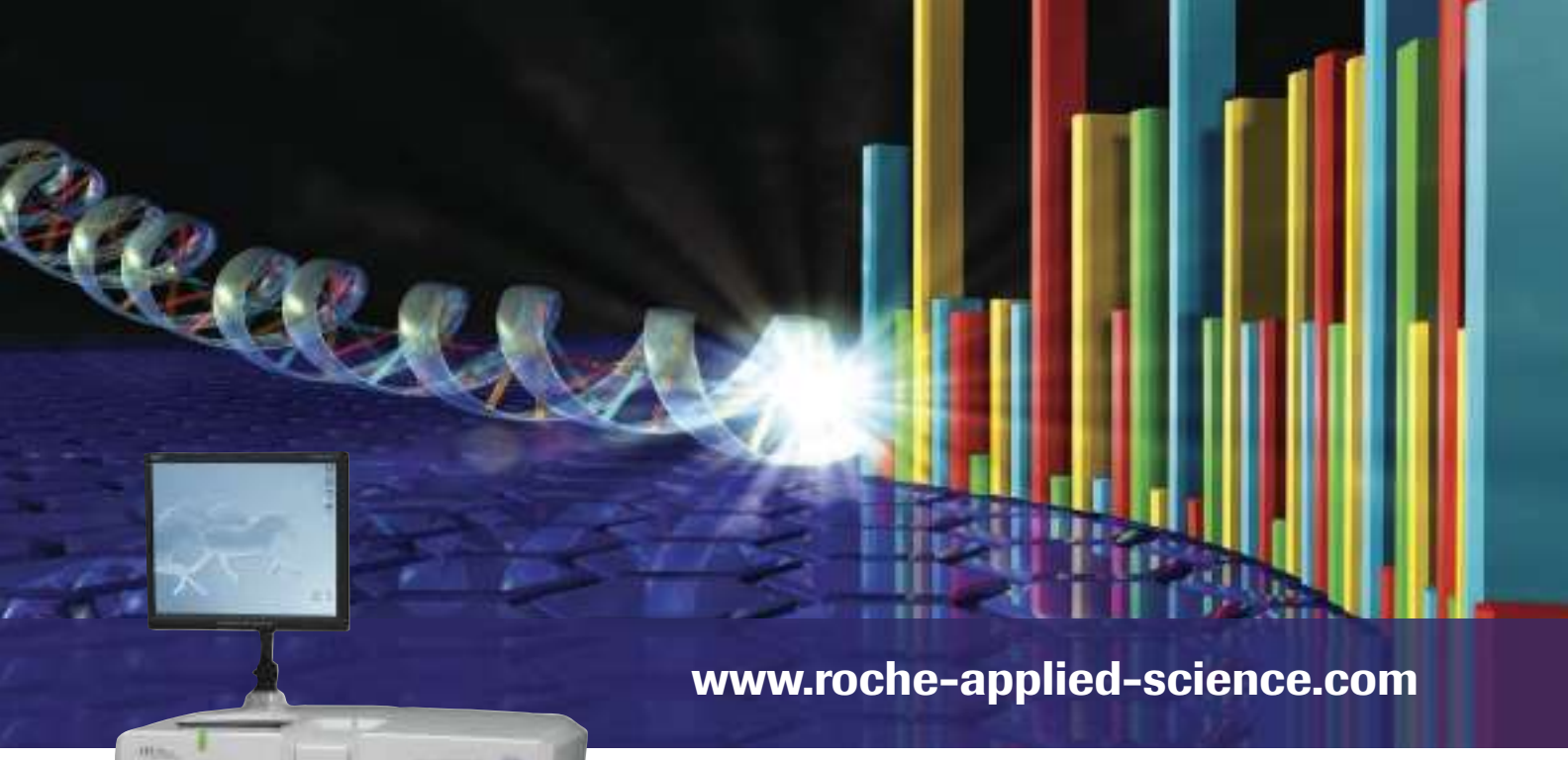

www.roche-applied-science.com

Genome Sequencer FLX System

Characterize Your Metagenomic Samples

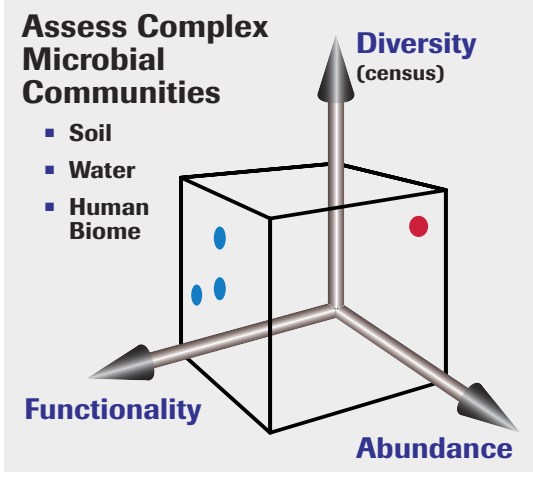

The power of metagenomic studies using the Genome Sequencer FLX. In a single instrument run, determine what microbial members of a community are present, annotate their function, and detect relative abundances. As indicated by the blue and red circles in the diagram, the combination of these variables enables the establishment of a signature profile for a specific environment, reflecting its relative health.

With more than 360 peer-reviewed publications, including more than 70 metagenomic studies, the Genome Sequencer FLX System is changing the way we view the microbial world.

Discover what microbial organisms are present.

- "*Microbial population structures in the deep marine biosphere.*" Roesch *et al.*, ISME Journal 1: 283–290 (2008).
- "*Pyrosequencing enumerates and contrasts soil microbial diversity.*" Huber *et al.*, Science 318: 97-100 (2007).

Determine the signature profile of an environment.

- "*Functional metagenomic profiling of nine biomes.*" Dinsdale *et al.*, Nature 452: 629-632 (2008).
- "*Globally distributed uncultivated oceanic N_2-fixing cyanobacteria lack oxygenic photosystem II.*" *Zehr et al.*, Science 322: 1110 (2008).

Identify viral pathogens — quickly and accurately.

- "*A new arenavirus in a cluster of fatal transplant-associated diseases.*" Palacios *et al.*, New England Journal of Medicine 358: 991-998 (2008).
- "*A metagenomic survey of microbes in honey bee colony collapse disorder.*" Cox-Foster *et al.*, Science 318: 283-287 (2007).

Visit ***www.454.com*** for more information and to view a selection of these and other published references.

454 SEQUENCING

Roche Diagnostics
Roche Applied Science
Indianapolis, Indiana

Roche

Continued from page 687

with global or regional air temperature increases, or with changes in ocean circulation. **Evan *et al.*** (p. 778, published online 26 March) use nearly 30 years of satellite data to examine another source of ocean temperature variability, the radiative effects of atmospheric aerosols. Low frequency changes in local tropical North Atlantic surface temperatures seem mostly to be caused by variability in mineral and stratospheric aerosol abundances. Thus, to provide more accurate projections of these temperatures, general circulation models will need to account for long-term changes in dust loadings.

A Second Act for Antiandrogens

Men with advanced prostate cancer are often treated with antiandrogens; drugs that inhibit the activity of male hormones, such as testosterone, that help drive tumor growth. Many of these drugs act by functionally disrupting the androgen receptor (AR), a transcriptional regulator of cell proliferation, but tumors eventually become resistant to the drugs by expressing higher levels of the AR. **Tran *et al.*** (p. 787, published online 9 April) have developed a "second-generation" antiandrogen, a thiohydantoin called MDV3100, which binds the AR with high affinity. MDV3100 retains its anticancer activity in cell culture and in mouse models even when AR levels are elevated. The drug appears to act both by inhibiting translocation of the AR into the nucleus and by reducing its transcriptional activity. MDV3100 is being tested in patients with advanced prostate cancer, the first group of which have shown a decline in blood levels of a marker of cancer growth, prostate-specific antigen.

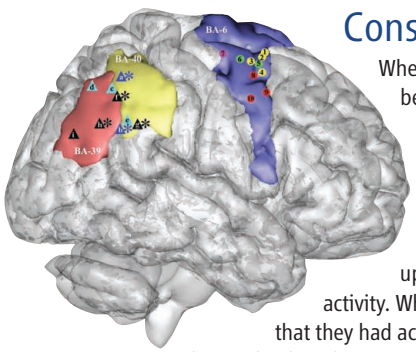

Consciousness and Intention

Where in the brain are our intentions formed and how do we become aware of these intentions? **Desmurget *et al.*** (p. 811; see the Perspective by **Haggard**) investigated the effect of direct cortical stimulation of parietal and premotor regions in patients undergoing brain surgery for tumor removal. Stimulation of the parietal lobe provoked the conscious experience of wanting to move the upper limb, lips, or tongue without any concomitant motor activity. When stimulation intensity was increased, patients believed that they had actually moved or talked, but again no muscle activity was detected. When, however, the premotor region of the frontal lobes was stimulated, real complex multijoint movements were induced. However, patients did not experience these movements as produced by a conscious internal act of will. Indeed, they were not even aware that they had moved. Increasing stimulation intensity increased the amplitude or complexity of the movement but never made it reach consciousness.

Let Me Out

Apicomplexan parasites like *Plasmodium falciparum*, which causes malaria, and *Toxoplasma gondii*, which cause toxoplasmosis, replicate inside animal host cells. In order for infections to spread successfully within the host from cell to cell, daughter parasites after replication need to be able to escape from their incubator cell. In the course of studies intended to elucidate the functions of proteases during parasite infection, **Chandramohanadas *et al.*** (p. 794, published online 2 April) noted that host cell calpain is the only protease present at the right time and place to facilitate the egress of malaria parasites from infected red blood cells. Parasite egress from infected resealed erythrocytes was prevented when calpain was removed. Moreover, *T. gondii* was unable to escape efficiently from murine fibroblast knockouts lacking a calpain regulatory subunit.

Infrared Vision

Proteins from jellyfish and corals that fluoresce in the visible wavelength range have revolutionized optical imaging of cells. However, these wavelengths are absorbed by hemoglobin, water, and lipids and the proteins are thus not appropriate for deep-tissue imaging. Now **Shu *et al.*** (p. 804) have engineered a bacteriophytochrome from *Deinococcus radiodurans* that incorporates biliverdin as the chromophore, to fluoresce with excitation and emission spectra of 648 and 708 nanometers, respectively. These infrared fluorescent proteins are expressed well in mammalian cells and mice, and can be used for whole-body imaging.

CREDIT: DESMURGET *ET AL.*

Published by AAAS

Team Spirit
What do conductors and beekeepers have in common? Leica Microsystems has mapped its corporate values. For more information, visit our website.

Mr. Hedinger, how do you integrate the user in the team?

According to Andreas Hedinger, engineer and Head of the Industry Division at Leica Microsystems, team spirit needs the strengths of the individual, open doors and ambitious joint goals. These goals can only be attained through the planned integration of users, with direct access to their ideas and needs. They therefore form part of the team and take part in developments: for day-to-day cooperation in a spirit of trust and responsibility.

www.leica-microsystems.com

Living up to Life

Leica
MICROSYSTEMS

Next-Generation Communication

Ton Bisseling is a professor in the Laboratory of Molecular Biology, Department of Plant Sciences, Wageningen University, Wageningen, Netherlands. E-mail: ton.bisseling@wur.nl

Jeffery L. Dangl is the John N. Couch Professor of Biology and associate director of the Carolina Center for Genome Science, University of North Carolina, Chapel Hill. E-mail: dangl@email.unc.edu

Paul Schulze-Lefert is the director of the Department of Plant-Microbe Interactions at the Max Planck Institute for Plant Breeding Research, Cologne, Germany, and honorary professor at the University of Cologne, Germany. E-mail: schlef@mpiz-koeln.mpg.de

IN THE PAST DECADE, THERE HAVE BEEN MAJOR ADVANCES IN OUR UNDERSTANDING OF THE molecular interplay between plants and various classes of microbial pathogens (bacteria, fungi, oomycetes, viruses, and nematodes) and microbial symbionts (rhizobia or mycorrhizal fungi). These fundamental insights, reviewed in a special section in this issue (p. 741), provide a conceptual framework for rational human intervention through the breeding or engineering of crops for durable and broad-spectrum disease resistance. However, such engineered plants will eventually be deployed into soils of varying geochemistry that harbor a staggering diversity of microbes. Many of these microbes can associate intimately with crops or other plants in natural habitats. A deeper understanding of plant-associated microbial communities is likely to offer exciting opportunities for controlling plant growth and pathogen burden in sustainable agricultural settings over the next two decades.

Genetics and molecular biology, and a focus on well-characterized model systems, uncovered the logic of an elaborate plant innate immune system. Additionally, the cellular signaling networks that determine legume nodule symbioses and mycorrhizal associations overlap, suggesting that molecular components of these "legume-specific" networks have clear non-legume counterparts. These findings revitalize prospects for the development of low-input agriculture, in which nitrogen-fixing bacteria and mycorrhizal-stimulated phosphate release are harnessed to reduce or replace the need for nitrogen- and phosphate-based fertilizers. But parasitic and symbiotic associations between plants and microbes are merely the two extreme outcomes of a continuum of interorganismal interactions affecting plant productivity. Remarkably little is understood about plant-microbe interactions that are, at first glance, symptomless. Complex communities of poorly studied plant-associated microbes are an untapped reservoir that can promote plant health and productivity.

One gram of soil typically contains ~10^{10} bacteria. Microbial DNA fingerprints from plant roots (the rhizosphere) or aerial organs (the phyllosphere) have uncovered specific microbial communities—microbiomes—thriving on the surface of or within healthy plant tissue. For instance, rhizosphere microbiomes attached to, and within the first few millimeters away from, the root surface are distinct from those in bulk soil, suggesting specific colonization events. Moreover, rhizosphere microbiomes of bacteria and fungi typically differ between plant species. The organic carbon flux from roots promotes the growth of microbial decomposers that, in turn, recycle plant nutrients for root uptake by transpiration-driven water fluxes. Seedlings exude 30 to 40%, and adult plants 20%, of photosynthetically fixed carbon into the rhizosphere in the form of poorly characterized rhizodeposits. This extrusion of nutrients outside the plant raises fundamental questions: Do plants feed and structure microbial rhizosphere communities to their advantage, and if so, how? Is the taxonomic diversity of microbiota related to the functional diversity of food webs? Can the notoriously low heritability of plant growth be accounted for by large environmental interactions with microbial assemblies in the rhizosphere, which are in turn influenced by soil types? Purified isolates of rhizosphere-derived bacteria or fungi can promote plant growth, and a subset of rhizobacteria can suppress the growth of other soil-borne pathogens. Thus, the rhizosphere microbiome is likely to tune both maximal plant growth–promoting and protective functions.

Profiling techniques currently used to assess microbial population structure discriminate genetic fingerprints only at the species level. Advanced DNA sequencing technologies applied to rhizosphere and phyllosphere samples could overcome this limitation to define interspecies community structures. Ironically, very few studies have investigated the microbial populations inhabiting either *Arabidopsis thaliana* or model legumes. These model plants, and selected major crops such as corn and rice, provide superb genetic and genomic platforms for dissecting the organization and functions of rhizosphere and phyllosphere communities, and for identifying the plant loci that contribute to their formation.

– Ton Bisseling, Jeffery L. Dangl, Paul Schulze-Lefert

10.1126/science.1174404

Published by AAAS

www.roche-applied-science.com

LightCycler® 480 Real-Time PCR System

Unleash the Potential of Real-Time PCR

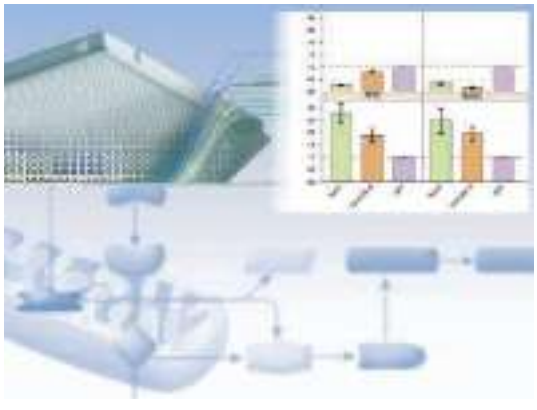

RealTime ready

RealTime ready Focus Panels make it easy to measure gene expression for targets in the apoptosis pathway.

Effortless Setup – Flexible Throughput – Precise Results

Quantify nucleic acids using outstanding data analysis algorithms, on a cycler with an easily interchangeable 96- or 384-well thermoblock.

- **Combine unsurpassed hardware with dedicated reagents, dyes and probes for pinpoint specificity and sensitivity.**
- **Discover and characterize mutations using powerful detection methods, including High Resolution Melting.**
- **Simply add cDNA and master mix to RealTime ready Focus Panels to detect genes in specific cellular pathways or gene families.**

Experience the LightCycler® 480 Real-Time PCR System's ideal combination of accuracy, versatility and speed.

Learn more at **www.lightcycler480.com** and **www.realtimeready.roche.com**

For life science research only.

Experimental data in this article are unpublished, courtesy by U.Tschulena, Ph.D., DKFZ Heidelberg, Germany.

Roche Diagnostics GmbH
Roche Applied Science
82372 Penzberg, Germany

Roche

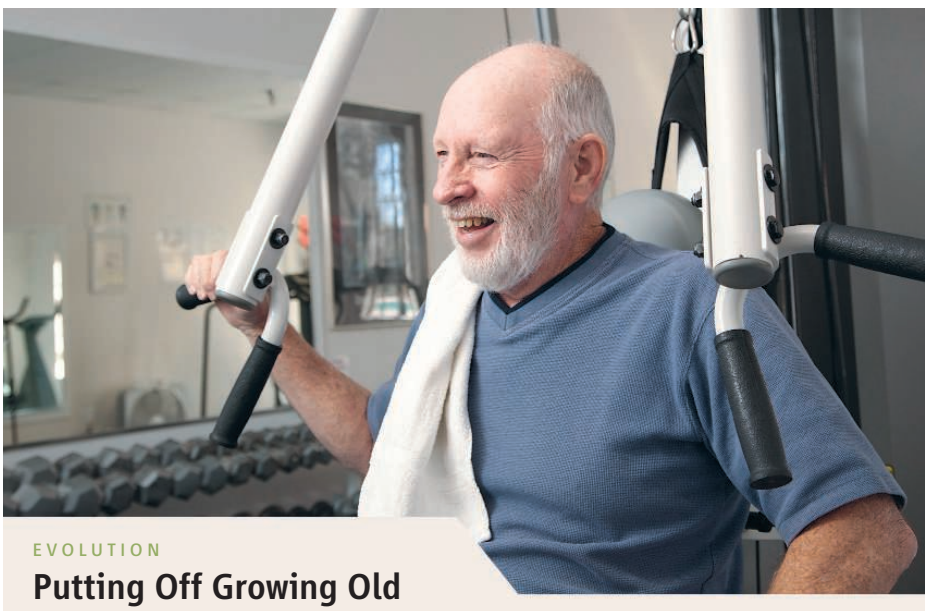

EVOLUTION

Putting Off Growing Old

In a classic 1957 paper on the evolution of senescence, Williams argued that when extrinsic mortality (death due to predation, infectious disease, or accident) is high, natural selection favors investment in early reproduction. When it is low, the increased return from allocating resources to maintain and repair the soma should lead to longer life spans. In the absence of precise information on causes of death, researchers have used hazard models to partition mortality into age-independent (interpreted as extrinsic) and age-dependent components.

Taking this approach, Gurven and Fenelon analyze mortality data from 13 remote, small-scale societies and in historical cohorts from Sweden and England over the past 250 years. They explore two statistical models (Weibull and Gompertz-Makeham) of adult mortality patterns and consider three measures of actuarial aging (mortality rate doubling time, Ricklefs's , and slope of the mortality function between ages 60 and 70). The variation in results across these two estimation procedures and three measures complicates the interpretation of the data. Nonetheless, some patterns are robust: The subsistence groups and the early Swedish cohorts exhibit similar actuarial aging, but more recent European cohorts show progressively slower aging. In the longitudinal samples, slower aging and reduced extrinsic mortality are linked. Women have lower rates of senescence than men, a difference that has increased over time. These "modest but nontrivial" changes support Williams's claims, and the authors discuss individual-level mechanisms that could underlie them. — SJS

Evolution **63**, 1017 (2009).

SIGNAL TRANSDUCTION

Adaptable Transducers

The α subunits of heterotrimeric guanine nucleotide–binding proteins (G proteins) associate with G protein–coupled receptors (GPCRs) at the cell membrane and transduce signals that affect a range of physiological processes. Yet there have been hints that Gα subunits may have other signaling roles as well. Cao *et al.* found that mouse fibroblasts lacking the $G\alpha_{i1}$ and $G\alpha_{i3}$ proteins had impaired signaling through the epidermal growth factor receptor (EGFR), a receptor with a signaling mechanism distinct from that of GPCRs. The protein Gab1 binds to activated EGFR and links it to activation of downstream proteins. The authors show that $G\alpha_{i1}$ is required for this association and that in cells stimulated with EGF, $G\alpha_{i1}$ and $G\alpha_{i3}$ are present in a complex with Gab1 and EGFR. The effects of EGF on cell survival, proliferation, and migration were all dependent on signaling through Gα proteins, suggesting that $G\alpha_i$ proteins might become the targets of therapies aimed at squelching cancer cells. — LBR

Sci. Signal. **2**, ra17 (2009).

CHEMISTRY

Put On a Platinum Face

Precious metals such as platinum are widely used in industrial catalysts. One way to reduce the amount of precious metal used—and hence the cost of the catalyst—is to create core-shell particles in which a core consisting of a cheaper, nonprecious metal is surrounded by a precious-metal shell. Methods for creating such particles, such as high-temperature treatment and chemical leaching, commonly lead to the loss of active surface area as a result of reduced particle sizes. Mayrhofer *et al.* report a method in which carbon monoxide (CO) adsorption causes surface segregation of platinum in a platinum-cobalt catalyst. The authors explored both gas-phase and electrochemical treatments, both of which lead to particles with an alloy core and a platinum shell, as evidenced by cyclic voltammetry and CO stripping measurements. The modified catalysts have higher activity than the untreated system in the oxygen reduction reaction. Particle sizes remain unaltered, without the loss of active surface area. — JFU

Angew. Chem. Int. Ed. **48**, 3529 (2009).

BIOCHEMISTRY

Burning Off a Carbon

Streptomycetes are bacterial drug designers, synthesizing a cornucopia of natural products that have found their way onto pharmacists' shelves worldwide. The precursor to one such compound, mithramycin, contains di- and trisaccharide chains (green and yellow) linked to a tetracyclic polyketide. In a subsequent downsizing reaction, dioxygen is activated by attaching it to FADH (black) at C4a (red), and the resulting peroxyflavin attacks the ketone at C1 (red) of premithramycin B (blue) in a Baeyer-Villiger oxidation. The consequences are that one of the rings can then be opened by hydrolysis of the lactone, and one of the carbon atoms can be removed via decarboxylation. Beam *et al.* describe the crystal structure of the Baeyer-

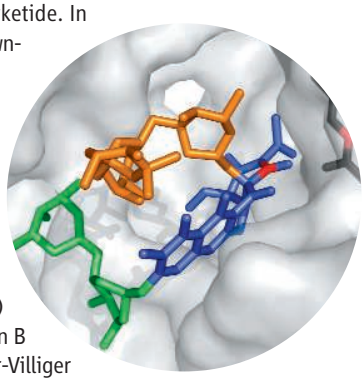

Continued on page 695

PCR Products

Switch to Superior High Fidelity PCR

PrimeSTAR®

Top Five Reasons to Switch to PrimeSTAR®:

- **Higher Accuracy:** A strong exonuclease activity results in an extremely low error rate, with only 15 errors per 480,000 bp on a GC-rich template.
- **Higher Efficiency:** Higher than *Taq* Polymerase.
- **Robust Amplifications:** A single PCR cycling protocol can be used to amplify products of varying sizes.
- **Greater Specificity:** The antibody mediated Hot Start formulation prevents false initiation events during reaction assembly.
- **Excellent with GC-Rich Targets:** Robust performance with GC-rich templates using the GC buffer formulation.

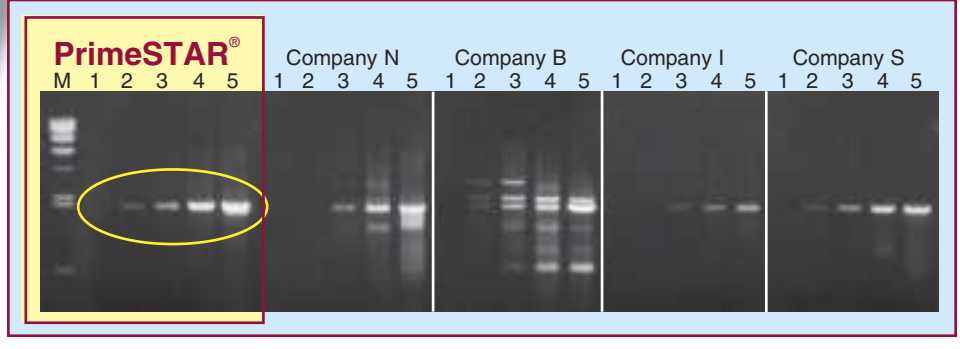

Amplification Efficiency of a 2 kb Human Genomic DNA Fragment (DCLRE1A). Excellent sensitivity and yield are observed when amplifying with PrimeSTAR®. Quantities: Lane1: 0 ng (dH_2O), Lane 2: 100 pg, Lane 3: 1 ng, Lane 4: 10 ng, Lane 5: 100 ng.

TaKaRa

For more information
www.takara-bio.com

Japan:
Takara Bio Inc.
+81 77 543 7247
www.takara-bio.com

USA:
Takara Bio USA
A Division of Clontech Laboratories, Inc
888-251-6618
www.takarabiousa.com

Europe:
Takara Bio Europe S.A.S.
+33 1 3904 6880
www.takara-bio.eu

China:
Takara Biotechnology (Dalian) Co., Ltd.
+86 411 8764 1681
www.takara.com.cn

Korea:
Takara Korea Biomedical Inc.
+82 2 2081 2525
www.takara.co.kr

Continued from page 693

Villiger monooxygenase MtmOIV (gray) and the binding of FAD and premithramycin in the active site. Of particular interest are the residues that allow the enzyme to accommodate the saccharide chains, as these are prime targets for modifications aimed at enhancing the activity of mithramycin as a DNA cross-linking agent and at decreasing its toxicity. — GJC

Biochemistry **48**, 10.1021/bi8023509 (2009).

MATERIALS SCIENCE

Shrugging Off Grime

To prevent the accumulation of unwanted microorganisms, plants, and animals on surfaces exposed to a marine environment, coatings are applied to the submerged surface. One challenge in creating such a coating is that the critical length scales involved in organism attachment range from hundreds of nanometers to centimeters. Efimenko *et al.* have developed polymer coatings that possess a hierarchical wrinkled structure. They stretched and then cross-linked the surface of poly(dimethylsiloxane), after which they applied a fluorinated silane monolayer. On gentle relaxation of the stress, a rippled surface layer formed, wherein each wrinkle had smaller-scale wrinkles on top of it that themselves bore even smaller wrinkles, proceeding over five generations. In seawater tests, flat polymer films showed fouling after a few

Flat (top) and wrinkle-protected samples.

CREDIT: EFIMENKO *ET AL.*, *ACS APPL. MATER. INTERFACES* **1**, 10.1021/AM9000562 (2009)

weeks, whereas the wrinkled polymers resisted barnacle accumulation over a period of 18 months. In tests on the adhesion of green algae zoospores, the wrinkled films performed less well, as the spores could nestle and be protected from shear flows and physical contacts within the wrinkles. However, a combination of topology and the right surface chemistry conferred improved resistance, pointing toward development of a nontoxic universal antifouling coating. — MSL

ACS Appl. Mater. Interfaces **1**, 10.1021/am9000562 (2009).

EVOLUTION

No Time for Rest

In the history of life, the Ediacaran Period is marked by an enigmatic collection of macroscopic fossils that record the appearance of animals that often took the form of discs, bags, or quilted sheets. Simultaneously, highly ornamented microfossils of an unusual size (>100 μm) appeared in the geological record. Like that of their macro brethren, the origin of these microfossils has remained something of a puzzle.

Using a process of elimination, Cohen *et al.* argue that many of these ornamented microfossils were in fact cysts—the resting stages of multicellular animals. Their large size and distinct lipid content exclude dinoflagellates as the culprits, and their size and spiny surfaces similarly argue against their being the remains of prasinophyte algae. The microfossils have complex and layered outer walls, distinct from various modern algal forms but similar to the diapause cysts of present-day brine shrimp. Encystment is a self-preservation response to an inconstant and potentially lethal environment, which may have been a chronic problem in the anoxic seas of the early- and mid-Ediacaran. This idea is reinforced by the disappearance of the microfossils roughly 560 million years ago, a period which corresponds to the oxygenation of the sea floor. So, instead of recording the loss of life, the disappearance of these microfossils would reflect a renaissance. — GR

Proc. Natl. Acad. Sci. U.S.A. **106**, 6519 (2009).

CHEMISTRY

Reaching Out to Zirconium

When alkyl chains bind to transition metals, the metal center can sometimes loosely attract electrons from the hydrogen bonds two carbons away. This attraction, termed an agostic interaction, plays an influential role in stereoselective olefin polymerizations at zirconocene centers, but it is typically too fleeting to characterize in a persistently stable complex. Forster *et al.* prepared an analog to an agostically coordinated ethyl ligand by replacing the two carbons (CH_2-CH_3) with nitrogen and boron (NH_2-BH_3). On coordinating through nitrogen to a zirconocene derivative, the ligand's boron hydride binds more stably to the metal center than the corresponding ethyl C-H. The authors characterized several such complexes in the solid state and in solution, and observed interconversion of isomers (which differed in the positions of N and B-H relative to a third substituent) on a time scale of tens of seconds. — JSY

J. Am. Chem. Soc. **131**, 10.1021/ja901460y (2009).

www.sciencemag.org

Science

1200 New York Avenue, NW
Washington, DC 20005
Editorial: 202-326-6550, FAX 202-289-7562
News: 202-326-6581, FAX 202-371-9227
Bateman House, 82-88 Hills Road
Cambridge, UK CB2 1LQ
+44 (0) 1223 326500, FAX +44 (0) 1223 326501

Subscription Services For change of address, missing issues, new orders and renewals, and payment questions: 866-434-AAAS (2227) or 202-326-6417, FAX 202-842-1065. Mailing addresses: AAAS, P.O. Box 96178, Washington, DC 20090-6178 or AAAS Member Services, 1200 New York Avenue, NW, Washington, DC 20005

Institutional Site Licenses please call 202-326-6755 for any questions or information

Reprints: Author Inquiries 800-635-7181
Commercial Inquiries 803-359-4578

Permissions 202-326-7074, FAX 202-682-0816

Member Benefits AAAS/Barnes&Noble.com bookstore www.aaas.org/bn; AAAS Online Store www.apisource.com/aaas/ code MKB6; AAAS Travels: Betchart Expeditions 800-252-4910; Apple Store www.apple/eppstore/aaas; Bank of America MasterCard 1-800-833-6262 priority code FAA3YU; Cold Spring Harbor Laboratory Press Publications www.cshlpress.com/affiliates/aaas.htm; GEICO Auto Insurance www.geico.com/landingpage/go51.htm?logo=17624; Hertz 800-654-2200 CDP#343457; Office Depot https://bsd.officedepot.com/portalLogin.do; Seabury & Smith Life Insurance 800-424-9883; Subaru VIP Program 202-326-6417; VIP Moving Services www.vipmayflower.com/domestic/index.html; Other Benefits: AAAS Member Services 202-326-6417 or www.aaasmember.org.

science_editors@aaas.org	(for general editorial queries)
science_letters@aaas.org	(for queries about letters)
science_reviews@aaas.org	(for returning manuscript reviews)
science_bookrevs@aaas.org	(for book review queries)

Published by the American Association for the Advancement of Science (AAAS), *Science* serves its readers as a forum for the presentation and discussion of important issues related to the advancement of science, including the presentation of minority or conflicting points of view, rather than by publishing only material on which a consensus has been reached. Accordingly, all articles published in *Science*—including editorials, news and comment, and book reviews—are signed and reflect the individual views of the authors and not official points of view adopted by AAAS or the institutions with which the authors are affiliated.

AAAS was founded in 1848 and incorporated in 1874. Its mission is to advance science, engineering, and innovation throughout the world for the benefit of all people. The goals of the association are to: enhance communication among scientists, engineers, and the public; promote and defend the integrity of science and its use; strengthen support for the science and technology enterprise; provide a voice for science on societal issues; promote the responsible use of science in public policy; strengthen and diversify the science and technology workforce; foster education in science and technology for everyone; increase public engagement with science and technology; and advance international cooperation in science.

Information for Authors
See pages 807 and 808 of the 6 February 2009 issue or access www.sciencemag.org/about/authors

EDITOR-IN-CHIEF **Bruce Alberts**
EXECUTIVE EDITOR **Monica M. Bradford**
NEWS EDITOR **Colin Norman**
MANAGING EDITOR, RESEARCH JOURNALS **Katrina L. Kelner**
DEPUTY EDITORS **R. Brooks Hanson, Barbara R. Jasny, Andrew M. Sugden**

Editorial senior editor/perspectives Lisa D. Chong; **senior editors** Gilbert J. Chin, Pamela J. Hines, Paula A. Kiberstis (Boston), Marc S. Lavine (Toronto), Beverly A. Purnell, L. Bryan Ray, Guy Riddihough, H. Jesse Smith, Phillip D. Szuromi (Tennessee), Valda Vinson; **associate editors** Kristen L. Mueller, Nicholas S. Wigginton, Jake S. Yeston, Laura M. Zahn; **online editor** Stewart Wills; **associate online editors** Robert Frederick, Tara S. Marathe; **web content developer** Martyn Green; **book review editor** Sherman J. Suter; **associate letters editor** Jennifer Sills; **editorial manager** Cara Tate; **senior copy editors** Jeffrey E. Cook, Cynthia Howe, Harry Jach, Barbara P. Ordway, Trista Wagoner; **copy editors** Chris Filiatreau, Lauren Kmec; **editorial coordinators** Carolyn Kyle, Beverly Shields; **publications assistants** Ramatoulaye Diop, Carlos L. Durham, Joi S. Granger, Jeffrey Hearn, Lisa Johnson, Scott Miller, Jerry Richardson, Jennifer A. Seibert, Brian White, Anita Wynn; **editorial assistants** Emily Guise, Michael Hicks, Patricia M. Moore; **executive assistant** Sylvia S. Kihara; **administrative support** Maryrose Madrid

News deputy news editors Robert Coontz, Eliot Marshall, Jeffrey Mervis, Leslie Roberts; **contributing editors** Elizabeth Culotta, Polly Shulman; **news writers** Yudhijit Bhattacharjee, Adrian Cho, Jennifer Couzin, David Grimm, Constance Holden, Jocelyn Kaiser, Richard A. Kerr, Eli Kintisch, Andrew Lawler (New England), Greg Miller, Elizabeth Pennisi, Robert F. Service (Pacific NW), Erik Stokstad; **intern** Jackie D. Grom; **contributing correspondents** Dan Charles, Jon Cohen (San Diego, CA), Daniel Ferber, Ann Gibbons, Robert Koenig, Mitch Leslie, Charles C. Mann, Virginia Morell, Evelyn Strauss, Gary Taubes; **copy editors** Linda B. Felaco, Melvin Gatling, Melissa Raimondi; **administrative support** Scherraine Mack, Fannie Groom; **bureaus** New England: 207-549-7755, San Diego, CA: 760-942-3252, FAX 760-942-4979, Pacific Northwest: 503-963-1940

Production director James Landry; **senior manager** Wendy K. Shank; **assistant manager** Rebecca Doshi; **senior specialists** Steve Forrester, Chris Redwood; **specialist** Anthony Rosen; **Preflight director** David M. Tompkins; **manager** Marcus Spiegler; **specialist** Jason Hillman

Art director Yael Kats; **associate art director** Laura Creveling; **illustrators** Chris Bickel, Katharine Sutliff; **senior art associates** Holly Bishop, Preston Huey, Nayomi Kevitiyagala; **art associate** Jessica Newfield; **photo editor** Leslie Blizard

***Science* International**

Europe (science@science-int.co.uk) **editorial: international managing editor** Andrew M. Sugden; **senior editor/perspectives** Julia Fahrenkamp-Uppenbrink; **senior editors** Caroline Ash, Stella M. Hurtley, Ian S. Osborne, Peter Stern; **associate editor** Maria Cruz; **locum editor** Helen Pickersgill; **editorial support** Deborah Dennison, Rachel Roberts, Alice Whaley; **administrative support** John Cannell, Janet Clements, Louise Moore; **news: europe news editor** John Travis; **deputy news editor** Daniel Clery; **contributing correspondents** Michael Balter (Paris), John Bohannon (Vienna), Martin Enserink (Amsterdam and Paris), Gretchen Vogel (Berlin); **intern** Claire Thomas

Asia Japan Office: Asca Corporation, Eiko Ishioka, Fusako Tamura, 1-8-13, Hirano-cho, Chuo-ku, Osaka-shi, Osaka, 541-0046 Japan; +81 (0) 6 6202 6272, FAX +81 (0) 6 6202 6271; asca@os.gulf.or.jp; **asia news editor** Richard Stone (Beijing: rstone@aaas.org); **contributing correspondents** Dennis Normile (Japan: +81 (0) 3 3391 0630, FAX +81 (0) 3 5936 3531; dnormile@gol.com); Hao Xin (China: +86 (0) 10 6307 4439 or 6307 3676, FAX +86 (0) 10 6307 4358; cindyhao@gmail.com); Pallava Bagla (South Asia: +91 (0) 11 2271 2896; pbagla@vsnl.com)

EXECUTIVE PUBLISHER **Alan I. Leshner**
PUBLISHER **Beth Rosner**

Fulfillment Systems and Operations (membership@aaas.org); **director** Waylon Butler; **senior systems analyst** Jonny Blaker; **customer service supervisor** Pat Butler; **specialists** Latoya Casteel, LaVonda Crawford, Vicki Linton, April Marshall; **data entry supervisor** Cynthia Johnson; **specialists** Eintou Bowden, Tarrika Hill, William Jones

Business Operations and Administration director Deborah Rivera-Wienhold; **assistant director, business operations** Randy Yi; **manager, business analysis** Michael LoBue; **manager, business operations** Jessica Tierney; **financial analysts** Priti Pamnani, Celeste Troxler; **rights and permissions: administrator** Emilie David; **associate** Elizabeth Sandler; **marketing director** Ian King; **marketing manager** Allison Pritchard; **marketing associates** Aimee Aponte, Alison Chandler, Mary Ellen Crowley, Julianne Wielga, Wendy Wise; **marketing executive** Jennifer Reeves; **marketing/member services executive** Linda Rusk; **director, site licensing** Tom Ryan; **director, corporate relations** Eileen Bernadette Moran; **publisher relations, eresources specialist** Kiki Forsythe; **senior publisher relations specialist** Catherine Holland; **publisher relations, east coast** Phillip Smith; **publisher relations, west coast** Philip Tsolakidis; **fulfillment supervisor** Iquo Edim; **fulfillment coordinator** Laura Clemens; **electronic media: manager** Lizabeth Harman; **project manager** Trista Snyder; **assistant manager** Lisa Stanford; **senior production specialists** Christopher Coleman, Walter Jones; **production specialists** Nichele Johnston, Kimberly Oster

Advertising director, worldwide ad sales Bill Moran

Product (science_advertising@aaas.org); **midwest/west coast/w. canada** Rick Bongiovanni: 330-405-7080, FAX 330-405-7081; **east coast/e. canada** Laurie Faraday: 508-747-9395, FAX 617-507-8189; **uk/europe/asia** Roger Goncalves: TEL/FAX +41 43 243 1358; **japan** Mashy Yoshikawa: +81 (0) 3 3235 5961, FAX +81 (0) 3 3235 5852; **senior traffic associate** Deiandra Simms

Commercial Editor Sean Sanders: 202-326-6430

Project Director, Outreach Brianna Blaser

Classified (advertise@sciencecareers.org); **u.s.: sales manager** Daryl Anderson: 202-326-6543; **inside sales representative** Tina Burks: 202-326-6577; **key account manager/midwest** Joribah Able; **east coast** Alexis Fleming: 202-326-6578; **west/south central** Nicholas Hintibidze: 202-326-6533; **sales coordinators** Rohan Edmonson, Shirley Young; **international: sales manager** Tracy Holmes: +44 (0) 1223 326525, FAX +44 (0) 1223 326532; **sales** Susanne Kharraz, Dan Pennington, Alex Palmer; **japan** Mashy Yoshikawa: +81 (0) 3 3235 5961, FAX +81 (0) 3 3235 5852; **advertising support manager** Karen Foote: 202-326-6740; **advertising production operations manager** Deborah Tompkins; **senior production specialist/graphic designer** Amy Hardcastle; **senior production specialist** Robert Buck; **senior traffic associate** Christine Hall; **publications assistant** Mary Lagnaoui

AAAS Board of Directors retiring president, chair James J. McCarthy; **president** Peter C. Agre; **president-elect** Alice Huang; **treasurer** David E. Shaw; **chief executive officer** Alan I. Leshner; **board** Alice Gast, Linda P. B. Katehi, Nancy Knowlton, Cherry A. Murray, Julia M. Phillips, Thomas D. Pollard, David S. Sabatini, Thomas A. Woolsey

AAAS
ADVANCING SCIENCE, SERVING SOCIETY

Need to assess the novelty of substances?
SciFinder is the answer.

It includes CAS REGISTRY,SM the most comprehensive substance information available, integrated with relevant journal articles and patents.

Give your research team the highest quality and most timely scientific information resource.

Make SciFinder an essential part of your research process.

For more information about SciFinder, visit www.cas.org or e-mail help@cas.org.

SciFinder®—an essential Part of the process.™

CAS | SciFinder®

www.cas.org

CAS is a division of the American Chemical Society

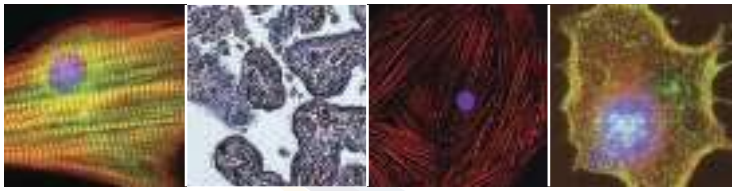

At Abcam we are dedicated to offering the best cardiovascular antibodies in the world

Your most complete cardiovascular resource

- Review articles including the new Mast Cells and Atherosclerosis
- Over 65 pathway downloads
- More than 9,000 cardiovascular-specific antibodies

www.abcam.com/cardiovascular

Protocol Library

Abcam's scientific support team has written over 60 protocols for antibody-related applications.

www.abcam.com/protocol

Our Abpromise means 100% support

Get the reassurance of expert scientific support and replacement or refund if the product does not perform as we say it should.

www.abcam.com/abpromise

Hidden Message

Researchers have cracked the fine-grained code in the Gunnison prairie dog's alarm call: It seems the animals can send information about a predator's color.

Many animals encode predator information in their calls. Ground squirrels, for example, differentiate between aerial and terrestrial threats, and black-capped chickadees can signal a predator's size.

The prairie dogs' birdlike calls are distinct for different predators, but animal behaviorist Con Slobodchikoff of Northern Arizona University in Flagstaff detected a deeper variation in their high-pitched squeaks. To see if they contained more detailed information, he and his colleagues recorded calls as three similar-sized women strolled through a prairie dog community wearing yellow, blue, or green T-shirts. Analysis of the calls' frequency patterns revealed that the chirps for blue shirts were different from those for yellow and green, which elicited the same calls. The results support the idea that the prairie dogs are incorporating colors into their alarm calls, the researchers report in the May issue of the journal *Animal Cognition*. The prairie dogs' dichromatic vision can distinguish yellow and green from blue but easily confuses yellow with green.

This is one of the finest distinctions yet to be detected in an alarm call, says James Hare, a behavioral ecologist at the University of Manitoba in Canada. "The level of sophistication in communicating subtleties is just incredible."

What a Dish

Excavations from an extensive Roman cemetery in East London, located outside the walls of the former Londinium, have yielded a rare prize: a complete millefiori dish. Made from a technique in which glass rods are fused together and sliced into multicolored patterned beads, the dish was created from hundreds of pieces stuck together.

The 23-centimeter-diameter dish was in many fragments, but they were all there, held together by the surrounding earth. It was in a grave belonging to a wealthy Roman whose cremated remains were in a casket flanked by other ceramic and glass vessels, "suggesting a rich and unusual burial," according to the Museum of London Docklands. The find, put on display at the museum last week, has yet to be dated but is likely close to 2000 years old.

No Laughing Matter

In Central Europe, homeland of psychoanalysis, psychologists have been exploring a hitherto uncodified facet of the human personality: gelotophobia, the fear of being laughed at.

In the latest of a spate of papers on the condition, published in the journal *Personality and Individual Differences*, Ilona Papousek of the University of Graz, Austria, and colleagues report that people with gelotophobia (from *gelos*, Greek for laughter) have weak control over their emotions and are hypersensitive to others' negative moods.

Co-author Willibald Ruch of the University of Zurich in Switzerland says researchers have developed a 15-item scale that can distinguish the problem from social phobias or "shame-based" neuroticism. For example, he says, gelotophobes "distrust smiling faces" and "are not able to discriminate between friendly and hostile laughter" or between teasing and ridicule. That can lead to serious consequences, says Ruch, citing two recent school shootings in Germany in which the perpetrators reportedly had a horror of being mocked. About 10% of the population has some degree of gelotophobia, he says.

In tests of the scale in 74 countries, Scandinavians ranked among the least gelotophobia-prone groups, whereas people in Muslim countries and in Africa tended to score high. The highest scores in Europe were from the United Kingdom—suggesting, Ruch says, that "maybe a well-developed sense of humor does not help [where] mock[ery] and ridicule are cultivated too."

A DIAMOND FOR CICERONE

Baseball nut Ralph Cicerone, who is also president of the National Academy of Sciences, is going to have a baseball diamond named after him. The University of California, Irvine (UCI), will rename its diamond at Anteater Park "Cicerone Field" at a pregame ceremony on 19 May, science blogger Gary Robbins reports.

The renowned climate scientist, who pitched for MIT during his undergraduate days (see photo), helped revive baseball at UCI when he was chancellor there from 1998 to 2005. "He's planning to be there and will throw out the first ball," says UCI spokesperson Tom Vasich.

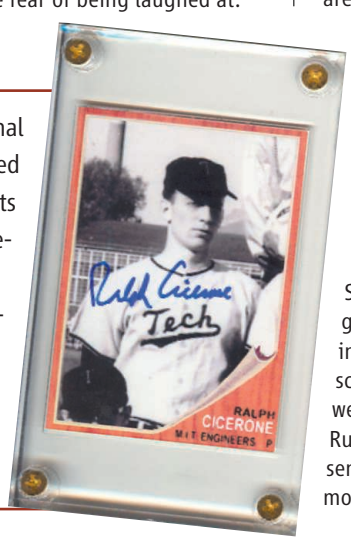

CREDITS (TOP TO BOTTOM): MUSEUM OF LONDON; CON SLOBODCHIKOFF; MIT

Published by AAAS

New energy frontiers 708

Norman Borlaug confronts an old foe 710

Breathing easier? Mexican officials believe the outbreak there has stabilized, reducing fears of widespread disease and death.

SWINE FLU OUTBREAK

Out of Mexico? Scientists Ponder Swine Flu's Origins

Each scientist at the forefront of the current swine flu outbreak remembers the day when it became clear that this was not a typical influenza season. For Celia Alpuche, that date was 7 April, more than 2 weeks before hundreds of other scientists, doctors, secretaries of health, and even presidents would also start losing sleep over a virus now officially known as 2009 A (H1N1).

Alpuche is an infectious disease microbiologist who heads the Instituto Nacional de Diagnóstico y Referencia Epidemiológicos (InDRE) in Mexico City, the country's main lab for testing influenza samples. On that Tuesday in early April, she learned that the nearby National Institute of Respiratory Diseases had severe cases of pneumonia in young adults—the age bracket that typically suffers the *least* harm from flu. "It sounded unusual," says Alpuche. "Immediately, we started to get the data around this cluster."

Alpuche and her team analyzed data on the country's influenza from this season and the one before, looking at the distributions of the virus's two strains, A and B. They noticed that this year's flu season seemed unusually long and that B cases accounted for 37% of the total, up from 15%. Surveillance data in the United States looked similar.

It turned out that the bump in influenza B had nothing to do with the swine flu outbreak, which is caused by an A strain. But it clouded Mexico's early attempts to make sense of these odd respiratory cases in young adults. "It was very confusing," says Alpuche. Nor did InDRE or other less sophisticated Mexican labs have the capability to identify a novel H1N1 strain, ultimately leading Mexico to ask Canada and the United States for assistance. "This is a new, unknown virus," she says, and those are notoriously difficult to detect. The U.S. Centers for Disease Control and Prevention (CDC) and the Public Health Agency of Canada confirmed that the novel virus was an H1N1 strain of swine flu origin on 23 April. Since then, says Alpuche, Mexico has been "working very hard" to overcome its limitations in diagnostics and surveillance.

Alpuche and her superiors reject the assertion that Mexico, where the outbreak seems to have emerged, might have contained the virus if officials had pounced on it sooner. "I don't see any way we could have acted faster," says epidemiologist Mauricio Hernández-Ávila, the vice minister of disease prevention and health promotion for Mexico's Ministry of Health.

The exact dates remain fuzzy, but Mexico's outbreak of 2009 A (H1N1) surfaced at the earliest in mid-March, and Alpuche and colleagues had their antennae wiggling by early April. "I think the Mexicans did all that was possible with a virtually impossible situation," says Ira Longini, an epidemiologist at the University of Washington, Seattle. Longini's models of influenza pandemics have shown that it's nearly impossible for a country to contain an outbreak of a new influenza virus. "You can see what happened in the United States," says Hernández-Ávila. "They even found the virus before we did, and they were not able to contain it." (The first U.S. case was confirmed on 14 April.)

Mexico is but one player under the microscope for its early actions in this outbreak:

OUTBREAK TICKTOCK

11 March: Earliest documented case (as of 5 May) from Mexico City.

30 March: A 10-year-old boy with fever, cold, and vomiting goes to Naval Medical Center San Diego in California; swab sent to the Naval Health Research Center (NHRC).

1 April: NHRC researchers determine likely infection with influenza A but cannot subtype strain.

7 April: Instituto Nacional de Diagnóstico y Referencia Epidemiológicos (InDRE) in Mexico City learns of unusual severe respiratory diseases in hospitalized young adults in the city.

10 April: The Pan American Health Organization (PAHO) receives alert, based on news stories, about outbreak of acute respiratory infections in La Gloria, Veracruz.

PAHO's Roses Periago

12 April: Mexico's director general of epidemiology confirms to PAHO existence of acute respiratory infections and says studies under way.

13 April: NHRC sends CDC sample from San Diego boy.

CREDITS (TOP TO BOTTOM): DANIEL AGUILAR/REUTERS/CORBIS; PAN AMERICAN HEALTH ORGANIZATION

Published by AAAS

Ecological aftermath of the Wenchuan quake
713

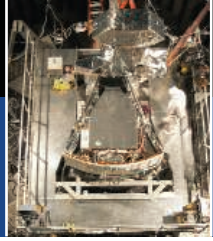

The Hubble's last fix
718

The World Health Organization (WHO) and CDC have also received close scrutiny. And the microscope has finer resolution than ever before because of Web cast press conferences, Twitter, Facebook, YouTube, Google Maps, and Skype. Yet the same Internet-fueled technologies have helped these same people do their jobs. "I'm amazed at the capacity we have with the information and communication technologies," says epidemiologist Mirta Roses Periago, head of the Pan American Health Organization. "We used to do things with our hands and smelling and looking at the patients." During the past few weeks, she notes, scientists have rapidly shared sequences of the viruses, digital images of patient x-rays, and electron micrographs of the new H1N1. "At this point in history, this is the best surveillance we've ever had," said Keiji Fukuda, one of WHO's assistant director generals. As of 4 May, that surveillance had confirmed more than 1000 cases in 21 countries, and WHO had raised the pandemic threat alert to phase 5, one shy of a full-blown pandemic. Phase 5 indicates that two countries in the same region (the United States and Mexico) had ongoing, person-to-person spread in communities. Although early this week there was some indication that the virus might not be as dangerous as first feared, many still expect that a phase 6 alert, which indicates the same high level of spread in two or more WHO regions, is inevitable.

The origin of the virus, its muscle power, and how much of a threat it presents remain mysteries. "We're not quite certain how this is going to evolve," said Fukuda at a 4 May press conference. Despite this uncertainty, health officials and companies are gearing up to rush a new vaccine into place, if it is needed (see p. 702); already, WHO and governments have released antiviral drugs from their stockpiles (see p. 705).

After Mexico, the United States has had the most cases, which on 5 May totaled 403. The almost simultaneous confirmations of the outbreak in both Mexico and the United States initially added further confusion to the outbreak's origins. But the virus itself has helped clear up matters, says Ruben Donis, CDC's chief of the molecular virology and vaccines branch.

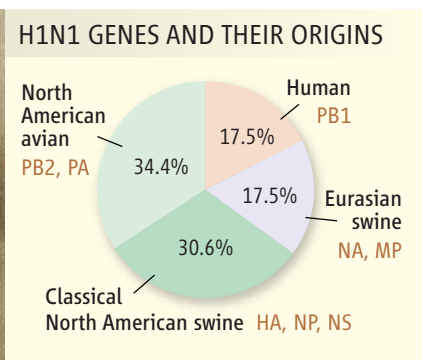

Quick picture. Within a few days of isolating the virus, shown in the electron micrograph on left, CDC had a detailed genetic phylogeny.

Donis has led a full-tilt effort to sequence viral isolates and post them in GenBank, a publicly available database that by 4 May had nearly 200 entries of H1N1 genes. The genetic information helps labs around the world develop diagnostic tests for this new virus, key to speeding the investigation; at first Mexico and many other countries had to rely on CDC or the Public Health Agency of Canada (*Science*, 1 May, p. 572) to confirm suspected cases.

Donis's group has used the gene sequences to tease out some of the virus's surprising history. A comparison to known influenza strains in different species shows that about one-third of the virus is from "classical" North American swine influenza, one-third is North American avian, and the remaining third is divided evenly between human and Eurasian swine (see pie chart). "It's almost equidistant to swine viruses from the United States and Eurasia," says Donis. "And it's a lonely branch there. It doesn't have any close relatives."

Some have speculated that the outbreak started from an infected pig in Mexico, as an early case occurred in a region in Veracruz state that has a large pig farm. But Donis says this explanation may be too pat. He suggests that the virus may have originated in a U.S. pig that traveled to Asia as part of the hog trade. The virus may have infected a human there, who then traveled back to North America, where the virus perfected human-to-human spread, maybe even moving from the United States to Mexico.

Alpuche notes that some of the earliest cases occurred in communities "well known for migration." And a scouring of older samples—which is ongoing—recently uncovered a Mexico City case from 11 March, about a week before any confirmed infections in Veracruz. As to what enabled this swine influenza for the first time to transmit easily between humans, Donis says the sequence alone can't answer that question.

On 2 May, Canada's Food Inspection Agency reported that 2009 A (H1N1) had been found in pigs for the first time. But in yet another twist, the virus seems to have come from a farm worker who recently returned from Mexico with a bout of swine flu and then infected the herd. This type of transmission, so far detected in 220 of the ▶

>>


Plummer

14 April: CDC determines sample is H1N1 virus of swine origin.

16 April: CDC notifies San Diego County Health & Human Services Agency.

17 April: Increase in cases of respiratory illness linked to death from atypical pneumonia of Oaxacan woman. Mexico issues alert to influenza monitoring units. InDRE Director Celia Alpuche asks Francis Plummer of Public Health Agency of Canada (PHAC) for help.

18 April: United States notifies WHO surveillance system of confirmed cases of H1N1 in southern California.

21 April: CDC publishes details of two California cases in *Morbidity and Mortality Weekly Report* (*MMWR*). Mexico reports to WHO atypical influenza associated with severe pneumonia in various cities. InDRE ships samples to PHAC and CDC.

23 April: PHAC and CDC confirm Mexico cases. CDC says it's producing a "seed" strain of the virus to make vaccine.

CREDITS: (TOP) SOURCE: RUBEN DONIS; (IMAGE) CDC; (BOTTOM) PUBLIC HEALTH AGENCY OF CANADA

Published by AAAS

2200 animals, may be a first, says Christopher Olsen, a swine influenza researcher at the School of Veterinary Medicine at the University of Wisconsin, Madison: "I honestly can't think of an instance where we saw a swine virus move to humans and move back in this fashion."

The greatest concern is what will this confusing virus do next? Hernández-Ávila says he believes the outbreak in Mexico has stabilized. By 4 May, fewer samples were coming into the labs and fewer patients were checking into hospitals with respiratory diseases. Earlier, the country reported a few thousand suspected cases and close to 200 deaths, but out of 2164 tested samples, labs only confirmed 727 infections and 26 fatalities.

Viral itinerary. CDC's Donis worries about H1N1's next move.

But several experts stressed that the outbreak is still young. "I don't think we're out of the woods yet," said Anne Schuchat, CDC interim deputy director for science and public health, at a 3 May press conference. "We don't know if the virus will return in the fall and come back harder than it is right now." CDC's Donis, originally from Argentina, also notes that the United States and Mexico are in the Northern Hemisphere, where flu season has peaked. "We're in a good position," he says. "The folks in Buenos Aires are in trouble. They're entering winter now."

So while scientists and health officials in the north may soon be able to get a good night's sleep, the espresso machines in labs and government ministries in the Southern Hemisphere may soon be working overtime.

–JON COHEN

SWINE FLU OUTBREAK

Devilish Dilemmas Surround Pandemic Flu Vaccine

If and when a pandemic of H1N1 swine flu hits, vaccines might be the world's best hope for softening the blow. But major uncertainties cloud the prospects for vaccines against the new strain. No pandemic vaccine yet exists, and it is unclear how much vaccine would have to be available, and by what time, to have any impact. Should manufacturers halt the production of seasonal influenza vaccine to focus on a pandemic version, and if so, when? And is there any way to ensure that people around the world have an equal chance to get the new vaccine?

These topics have been the subject of frantic, almost daily discussions among scientists, vaccine manufacturers, regulatory agencies, and the World Health Organization (WHO) over the past few weeks. But so far, there are few concrete answers, in part because no one knows just how severe a threat the new virus poses, or how difficult it will be to mass-produce a vaccine. One thing is certain, however: There won't be nearly enough vaccine to protect all the world's citizens, and the question of who has first dibs could get ugly, says David Fedson, a former pharma executive and influenza vaccine expert living in France.

Almost all seasonal flu vaccine is made using a clunky, 50-year-old process, in which companies adapt the virus to multiply in hens' eggs, grow the virus in eggs, then purify the key antigens needed to make vaccine—the hemagglutinin and neuraminidase molecules that stick out from the virus's surface. In all, the process takes more than 5 months. This is also how at least the vast majority of a pandemic vaccine will be made, because promising alternative production strategies won't be ready in time.

Bottleneck. Most flu vaccine is now produced in a process that requires growing the virus in eggs.

Immediately after isolating the new H1N1 strain, the U.S. Centers for Disease Control and Prevention and other labs began producing a "seed stock" of virus, which will be given to manufacturers in a few weeks for vaccine production. But how much pandemic vaccine will they be able to produce once they get going? A study funded by the Bill and Melinda Gates Foundation, whose main outcomes were announced in February, gives an indication. The study, carried out by Adam Sabow of the consulting company Oliver Wyman, in collaboration with WHO and the International Federation of Pharmaceutical Manufacturers & Associations, showed that all manufacturers combined can currently produce some 680 million doses of seasonal flu vaccine per year—a number that is expected to grow to at least 1.4 billion by 2014.

It's not easy to translate that figure into doses of pandemic vaccine. The number depends, among other things, on how successfully scientists can make the new virus grow in eggs, how much antigen is needed for an adequate vaccine response, and whether a so-called adjuvant can reduce the amount of antigen needed per shot. But Sabow's study concluded that in the most likely scenario, the world's vaccinemakers combined could produce almost 2.5 billion doses of pandemic vaccine in the first year.

Assuming, as many scientists do, that two shots would be needed for adequate protection—as opposed to one for seasonal vac-

<<

24 April: CDC reports six new U.S. cases, publicly links same strain of H1N1 to Mexican outbreak. WHO receives reports from Mexico of 884 suspected cases and 62 deaths. Mexican government closes schools in Mexico City.

25 April: WHO declares a public health emergency of international concern.

26 April: CDC confirms cases in five states, releases 11 million antivirals from strategic national stockpile of 50 million.

27 April: Canada and Spain report confirmed cases to WHO, which raises threat level from phase 3 to 4. Mexico suspends schools nationwide. GenBank posts first publicly available sequences of virus.

28 April: Seven countries report cases to WHO.

29 April: WHO raises threat level from phase 4 to 5. Ten countries report confirmed cases, including South Korea. First related death reported in the United States. WHO Director-General Margaret Chan holds a teleconference with vaccine manufacturers around the globe to discuss the production of pandemic vaccine.

CREDITS (TOP TO BOTTOM): JAMES GATHANY/CDC; ITAR-TASS/NIKOLAI MAROCHKIN/LANDOV

Published by AAAS

cine—that means there would be enough for 1.2 billion people, less than 20% of the world's population, that first year (see graph). The study was based on the assumption of a pandemic of H5N1 avian influenza, but the figures are not expected to be vastly different for swine flu.

Achieving that output assumes, however, that vaccine manufacturers immediately stop their production of seasonal vaccine, which they are now making for 2009–10, and go full-bore on a pandemic vaccine—a very unlikely scenario. In reality, WHO has to weigh the risk of a shortage of seasonal vaccine, and the increased risk of disease and death that would ensue, against the threat posed by the new strain. For the moment, the new virus doesn't appear to be highly virulent, but that could change over time. After a relatively mild first wave in the spring of 1918, the Spanish flu returned with a vengeance in the fall.

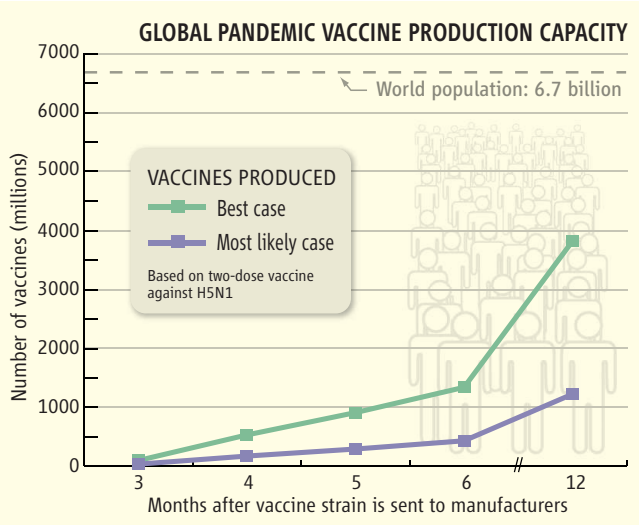

Who goes first? A study suggests global production of a pandemic vaccine will fall short.

"It's a devilish dilemma," says Jaap Venema, global project director influenza at vaccine producer Solvay in the Netherlands. At a press briefing last week, WHO vaccine expert Marie-Paule Kieny said the agency is in close contact with manufacturers; some are further along with their seasonal production than others, and those might switch first to pandemic vaccines while others do so later.

How to ensure equitable distribution of the vaccine is trickier still. Since the threat of an avian influenza pandemic became urgent 6 years ago, a few developing nations have been fighting hard to ensure they will have access to vaccines if a pandemic strikes. Indonesia even went so far as to refuse participation in WHO's system for virus sharing in an attempt to wrest hard guarantees from the agency. WHO responded with a plan to increase production capacity in the developing world, which is now home to some 13% of the global vaccine production capacity—but the plan is still in its infancy. To ensure equal access, WHO Director-General Margaret Chan has called for "international solidarity," and Kieny says WHO is already talking to donors and major global health funders about ways to buy vaccine for the world's poorest.

But there are some major obstacles. Several countries already have first dibs on any pandemic vaccine. In 2006, for instance, the Dutch government signed a contract with Solvay guaranteeing that it gets the first 16 million doses of a pandemic vaccine to protect its own population. Other governments have signed similar deals, Kieny says, so "the books of the manufacturers are already quite full."

In addition, the governments of the countries with a flu vaccine plant in their territories will be under tremendous political pressure to protect their own populations first, Fedson predicts. "You don't need a contract," he says; "all you need is an army" to prevent the vaccine from going across the border. Thus, even rich countries like Sweden and Spain that lack a vaccine plant could find ▶

1 May: Thirteen countries report cases, raising the total to 367. Between 1 and 2 billion doses of pandemic vaccine may be available within a year, says WHO's Marie-Paule Kieny.

2 May: Canada reports first isolation of virus from pigs. Signs that outbreak in Mexico is stabilizing, with 506 confirmed cases and 19 deaths. U.S. cases climb to 226 and 30 hospitalizations.

4 May: WHO reports more than 1000 cases in 21 countries. Mexico determines earliest case was 3 March but still has older samples to test.

SOURCES: Mirta Roses Periago and Daniel Epstein, PAHO; Celia Alpuche and Mauricio Hernández-Ávila, MoH, Mexico; Francis Plummer, PHAC; EMEA; WHO and CDC press conferences; *MMWR*.

SOURCE: GATES-FUNDED STUDY; (IMAGE) JUPITERIMAGES

*Science*Insider

From the *Science* Policy Blog

Since the H1N1 outbreak first surfaced 21 April, *Science*Insider has posted dozens of items as events unfolded, mixing analysis with breaking news and interviews with scientists fighting the virus around the world.

In an exclusive interview, **Celia Alpuche** of the Instituto de Diagnóstico y Referencia Epidemiológicos in Mexico City provided details of Mexico's early responses to reports of puzzling increases in respiratory illness. She described how the culprit was eventually unmasked with help from the Canadian Public Health Agency laboratory in Winnipeg and the U.S. Centers for Disease Control and Prevention (CDC). She also noted that researchers have been surviving on little sleep and a lot of coffee.

Head **CDC virologist Ruben Donis**, in another exclusive interview, discussed the genetics of the new H1N1 strain and its relationship to other flu viruses that have been circulating.

An **analysis** looked at the thorny issue of how U.S. and international health officials can balance the need to keep the public informed without causing panic. Building on the lessons of the 2003 SARS outbreak, officials have settled on a strategy of giving information early and clearly and being willing to admit that they don't know what's going to happen. "You need to announce early: People are sick, people are dying. You have to talk about that," said one expert.

Also … Writers analyzed the strange **genetics** of the new strain, how **different countries are responding**, whether travel advisories or **seasonal flu vaccine** can help, and how a **Navy lab** in San Diego first figured out that something was very wrong. An up-to-date, detailed timeline will continue to track the spread of the virus and the response.

For continuing coverage and analysis of the pandemic and of other science policy developments, go to **blogs.sciencemag.org/scienceinsider**.

Published by AAAS

Eppendorf Consumables – it's your sample

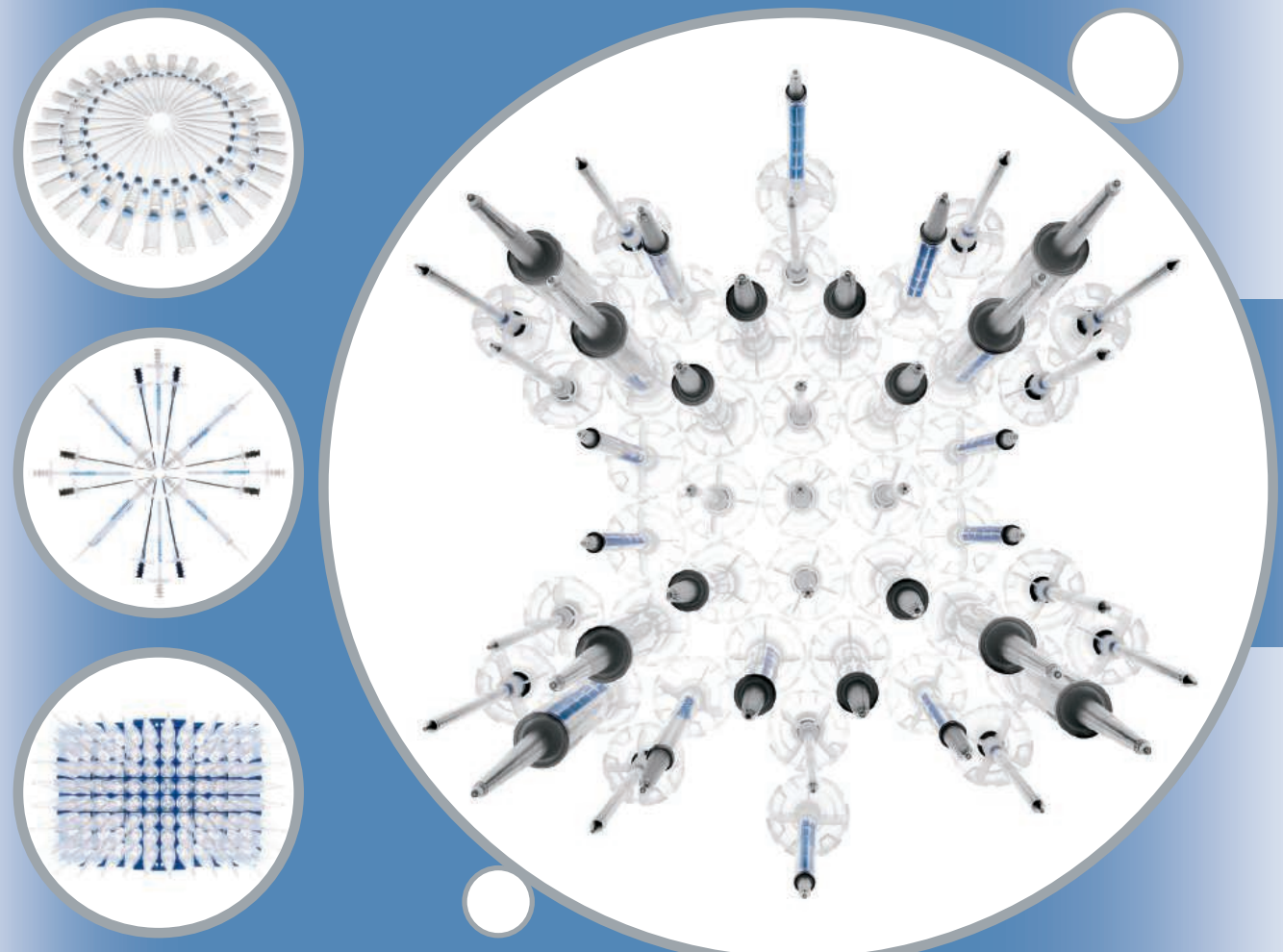

Make the best of it!

Top quality for your sample

Each of your valuable samples deserves the best treatment. See for yourself how the Eppendorf tips will save time and reduce costs.

With respect to material, fit, design and operating forces our tips set new standards. The close environment of each sample should be adapted to its specific quality and purity needs. This can involve a specific purity level or the absence of certain substances, but also stability, reliability, or geometry. The Eppendorf tips are designed to cover all of the specific needs of your samples!

Dispensing at its best! Eppendorf Combitips® plus

- Precise dispensing of liquids with high vapor pressure or higher viscosity
- Contamination-free dispensing due to positive-displacement principle
- Dispensing from 1 µl to 50 ml through 9 different sizes
- Automatic Combitip recognition with Multipette®* plus and Multipette* stream/Xstream®

Learn more about Eppendorf Combitips plus:
www.eppendorf.com/CBT

*Repeater in the U.S.

eppendorf

In touch with life

Your local distributor www.eppendorf.com/worldwide · **Application Support** E-Mail: support@eppendorf.com
Eppendorf AG · Hamburg · Germany · Tel: +49 40 538 01-0 · Eppendorf North America, Inc. · USA · Tel.: +1 800 645 3050

themselves empty-handed, he says.

Unfortunately, there are few alternatives for the moment. Most flu vaccine manufacturers are working to replace the antiquated chicken-egg technology with a cell-based method, in which the vaccine virus is grown in mammalian cells. This has several advantages: Manufacturers are less dependent on the supply of chicken eggs—which is difficult to increase quickly and can become vulnerable during bird flu outbreaks—and it could shave 10 weeks from the 22 weeks now needed to make influenza vaccine using eggs.

But although more practical and cleaner, cell-based vaccines don't promise a major boost in production capacity. Moreover, success with the technique has been slow to come, despite more than $1.5 billion in U.S. Department of Health and Human Services contracts to several companies to fund clinical trials of cell-based vaccines and scale up manufacturing. "The cell-based vaccines are coming, but we're not going to see them for this pandemic," says influenza expert Arnold Monto of the University of Michigan School of Public Health in Ann Arbor. Other recombinant vaccines that could truly lead to an explosion in production capacity are even further down the road, says John Treanor of the University of Rochester's School of Medicine and Dentistry in New York state.

That means that, at least for now, the world is still dependent on chicken eggs.

–MARTIN ENSERINK AND JOCELYN KAISER

SWINE FLU OUTBREAK

What Role for Antiviral Drugs?

When it comes to treatment, there's good news and bad news about the new H1N1 swine flu strain circling the globe. Two antiviral drugs can squelch it and are currently the best defense, given that a vaccine will not be ready for months. But stocks of Roche's Tamiflu (oseltamivir) and GlaxoSmithKline's Relenza (zanamivir) are too small to protect everyone in a worst-case scenario outbreak; health officials also worry that the virus could become resistant to the drugs.

How many doses might be needed during a pandemic depends on how severe it is and how the drugs are used; so far, countries have stockpiled roughly 250 million courses of antivirals. By comparison, the 1918–19 flu pandemic sickened at least 800 million people.

When the issue of shortages has come up at press conferences over the past 2 weeks, various health officials have pooh-poohed the role of antiviral drugs. "People get too focused on antivirals," said Angus Nicoll of the European Centre for Disease Prevention and Control last week. There are "other important medicines," he said, such as antibiotics.

But many flu experts disagree. True, severe influenza can lead to secondary infections like pneumonia, and experts believe that such infections explain many deaths in the 1918 flu pandemic, notes Anne Moscona, a pediatric infectious disease physician and virologist at Weill Cornell Medical College in New York City. But, she and others say, antivirals are critical to preventing deaths and serious illness in an outbreak. "What else do we have?" asks Arnold S. Monto, an epidemiologist at the University of Michigan, Ann Arbor.

Both Tamiflu and Relenza block the function of a viral protein, neuraminidase, thereby preventing the virus from leaving the surface of the cell and spilling out into surrounding lung tissue. The drugs are most effective when given early, before influenza spreads through the lung. If the drugs are taken 12 hours after a fever hits, the flu lasts three fewer days than if they're taken 48 hours after fever begins, says Moscona.

It's not known how effectively the drugs suppress the spread of the virus from person to person, but most flu experts believe they shorten the time course of disease and by stopping the virus from replicating. When given to healthy people, they've been shown to reduce the chance of getting sick by 70% to 80%. Flu specialists, however, disagree over whether offering the drug prophylactically now makes sense. The U.S. Centers for Disease Control and Prevention is recommending prophylaxis for only those who've had close contact with someone with H1N1 and who are at high risk themselves, such as pregnant women or young children, as well as health care workers who may have been exposed.

Will it work? Stocks of Tamiflu line a warehouse in the United Kingdom. The drug combats H1N1 swine flu, but there are worries about resistance.

CREDIT: KATIE COLLINS/PA/AP PHOTO

Supplying a drug to a large number of healthy people raises two concerns. First, because the new strain seems relatively mild, preventing its onset may not be a wise use of limited stocks—especially because they may be needed if the virus becomes more virulent later. Second, the virus could develop resistance to one or both drugs. This is a particular worry because a human H1N1 subtype—one of the seasonal flu strains—unexpectedly evolved almost complete resistance to Tamiflu in the past few years (*Science*, 27 February, p. 1162). "Giving antivirals will only force that selection" of a drug-resistant strain, says Scott Layne, an infectious disease specialist at the University of California, Los Angeles.

One pressing question is "how might you deploy" these two drugs to minimize the chance of resistance, says Ira Longini, a biostatistician at the University of Washington, Seattle. One possibility would be to treat a population with both Tamiflu and Relenza, to which H1N1 has more difficulty developing resistance. Longini believes models could help determine exactly how to distribute these drugs to minimize resistance. But because Tamiflu can be taken orally (unlike Relenza, which must be inhaled), countries have focused on amassing stocks of the former—until recently, as concern about resistance to Tamiflu spread.

For now, distributing the drugs based on the most promising model may be a pipe dream. How these drugs are used "will change as the epidemic evolves," says John Modlin, a pediatric infectious disease specialist at Dartmouth Medical School—and as the companies race to ramp up production.

–JENNIFER COUZIN-FRANKEL

Published by AAAS

NEWSMAKER INTERVIEW

Corey Goodman, Post-Pfizer, On the Allure of Enterprise

Neuroscientist Corey Goodman surprised his friends in 2001 when he took leave from a tenured professorship at the University of California, Berkeley, and gave up his post as a Howard Hughes Medical Institute investigator to dive into the world of small biotechnology companies, becoming CEO of Renovis, a company he co-founded. He surprised them again in 2007 by joining pharmaceutical behemoth Pfizer, heading up its new Biotherapeutics and Bioinnovation Center (BBC) (*Science*, 23 November 2007, p. 1223). Its goal was to put Pfizer, which, like all of big pharma, is struggling to keep its pipeline filled with ideas, on a path to developing new, more innovative therapeutics. Goodman, ever restless, left that post in April earlier than planned, after just 20 months, but says he accomplished what he set out to do. He spoke with *Science* last week; the interview has been edited for brevity.

–JENNIFER COUZIN-FRANKEL

Q: What drew you to Pfizer in the first place?

C.G.: I had been offered positions in large biotech and large pharma before and I had not gone. I always thought of myself as somewhere at the interface of biotech [and] academia, a small-company guy. Jeff Kindler [Pfizer's CEO] approached me in the summer of 2007. [He said], "What about the following opportunity? Big pharma is in trouble; the pipelines aren't deep enough; and they haven't been productive enough. Why don't you come join for a few years and build a new entrepreneurial model for how to do research?" It was very seductive.

Q: What were the goals?

C.G.: Pfizer, like much of big pharma, had its strength in small molecules, medicinal chemistry. They realized that they needed to play catch-up. [In 2006, Pfizer acquired Rinat, a small company focused on antibody technology and protein engineering.] We took what was a superb group; I essentially set them free. Then we acquired CovX [another biotechnology company], and we really let that site continue to blossom. The key in both these cases is, you let these people who are so creative continue to create and innovate. We built collaborations with academic[s]. And finally, we established a unit of regenerative medicine in Cambridge, England. So we've set up these very entrepreneurial units. The notion is to build a hybrid model: Could we get the best of the biotech model and the pharma model?

Q: All of this sounds great. Why did you leave?

C.G.: We're in the middle of the acquisition of Wyeth [Pharmaceuticals]. I was a strong proponent of that. But my unit now instead of reporting separately to the CEO [is] going to report into a larger biotherapeutics division. It's going to be more East Coast–based. It just seems to me that I had accomplished what I came in to do; now it's time for my next adventure.

CREDIT: CHRISTINE KRIEG

Q: What's happening to your Biotherapeutics and Bioinnovation Center now?

C.G.: On an interim basis, the person who is going to take it over is Rodney Lappe, [chief scientific officer] of CovX. He teases me by saying that he's been drinking the Corey Kool-Aid. He completely believes in this model. He's the perfect person to take my place.

Q: Was working in pharma what you expected?

C.G.: It has been a great education for me to see how a large corporation works. Surprises? I really enjoyed interacting with the commercial organization, with the business units. [You're] working for human health, but at the same time you have to make a profit and pay the bills.

Q: There's a lot of concern inside and outside pharma about the future of the industry. What do you make of that?

C.G.: The industry is going through a consolidation period. Companies are experimenting with new R&D models. Pfizer did what I think is a very successful experiment with our BBC model. I see variations on that going on [elsewhere]. I think over the next few years, more and more of the pharma companies will be switching to these entrepreneurial models and having more interactions with the academic and biotech communities.

Q: Are the little idea-driven companies that you've long been a proponent of surviving?

C.G.: The industry's going through a tough time right now. Capital markets have largely closed down for biotech. We will come out the other end. There will probably be a reduction in the number of biotech venture capital firms, there will probably be a reduction in the number of biotechs. [But] I think the need for innovation in biotech is as strong as ever.

Q: What about personalized medicine? Everyone talks about it, but can anyone afford it?

C.G.: It is a challenge, but it's a solvable challenge. Personalized medicine is here to stay, and it's fabulous for patients, but we have to figure out how to make it work for companies. We have to make sure that things are priced so that companies will be willing to develop all sorts of medicine. We already have evidence that it works: Genentech makes good money by selling Herceptin [a drug designed for a genetically defined subset of breast cancers]. We have to think about drugs that aren't just huge blockbusters, drugs that will still be financially successful but for a smaller group of patients.

Q: What are you up to next?

C.G.: I have ideas with friends for different companies to start, companies that want me to be in their board, going back to my roots with the biotech and venture world. I'm going to take my time. There are lots of opportunities.

Published by AAAS

BIODEFENSE

Army Bans Pathogen Work at Lab After Security Lapse

Late last year, the U.S. Army took the unprecedented step of banning one of its premier biodefense labs from conducting any work involving dangerous pathogens. The lab is part of the Armed Forces Institute of Pathology (AFIP) in Washington, D.C. The Army and AFIP decline to cite the specific reasons behind the 2 December decision, which has not been publicly announced, but it was made a few months after the Army Inspector General's (IG's) office discovered a number of security problems at the lab—a biosafety level 3 (BSL-3) facility. These include a failure to prevent potentially unreliable employees from having access to anthrax and other deadly pathogens stored there. AFIP officials say they corrected all those problems and were taken by surprise by the ban.

The decision has left some two dozen researchers in AFIP's microbiology division unable to continue high-profile research projects such as developing a vaccine against brucellosis and testing ways to rapidly detect biowarfare agents. They have been reassigned to other projects that don't involve dangerous pathogens, or select agents.

Meanwhile, a spacious new BSL-3 lab, completed in 2006 for $19 million, is no longer being used for the research for which it was built. "That's very tragic because they had only recently completed building the [BSL-3] facility," says Nobelist Sidney Altman, a Yale University biochemist who has been collaborating with AFIP on a project to inactivate biowarfare agents using RNA interference.

The entire institute, which employs 93 scientists and 75 pathologists and offers pathology services in addition to doing research and training, is slated for closure by September 2011 under a government plan to shutter dozens of military facilities. Under that plan, AFIP scientists had expected to be able to conduct select-agent research for at least two more years.

The lab's troubles began when it failed a Biological Surety Inspection that the Army IG conducted in March 2008. Officials faulted AFIP for inadequate locking systems and other physical security issues. More important, officials found that lab managers ignored information about certain employees that could have disqualified them from having access to dangerous pathogens. The redacted version of the IG's report released to *Science* does not divulge the nature of this so-called potentially disqualifying information, but it could be anything from alcoholism to mental instability.

Based on the findings, the Army ordered a temporary shutdown of the lab on 16 April 2008 until AFIP fixed the problems. Florabel Mullick, a pathologist who has directed AFIP since mid-2007, declined to speak with *Science* but responded in an e-mail that "Immediate steps were taken to ensure continued safety, security and reliability."

Tough luck. Despite AFIP Director Florabel Mullick's efforts to fix security problems, the Army decided to terminate all select-agent research at the institute's BSL-3 lab.

Among those steps, AFIP hired a new contractor to provide security. Robert Crawford, the head of the lab and director of the microbiology division since 2003, was let go. Mina Izadjoo, a microbiologist and longtime employee of the lab, succeeded him.

Other heads rolled, though it is unclear how many. "The AFIP director cleaned house after [the inspection], and there has been a complete turnover in the microbiology division leadership," Catherine With, AFIP's legal counsel, wrote in a 26 November 2008 e-mail that she sent to the Department of Defense (DOD) and the Army after learning that a permanent ban was imminent. "The … prior leaders were let go … because they could not operate in a world of rules and regulations," With wrote. "And those non-leadership personnel who did not want to follow the applicable law, rules and policies are also no longer at the AFIP." The Army won't comment on whether those steps were considered sufficient.

Another incident seems to have undermined the Army's confidence. On 24 November, four broken vials of select agents were discovered during an internal inventory of pathogens at the lab. The employee who found them did not think the incident needed to be reported because the vials were in a contained area, says Cynthia Vaughan, a spokesperson for the Army Medical Command. "Two lab workers were referred to the occupational health clinic for evaluation and follow-up," she says. Neither was infected.

On 2 December, DOD approved the Army's recommendation to "permanently disestablish" select-agent operations at the lab. One Army official told *Science* that the Army did not consider it worth the effort to resume select agent operations for just three more years. Vaughan says that while working with AFIP to correct the deficiencies discovered by the IG, Army officials realized that "maintaining experienced personnel and keeping the operations safe and secure would be a significant challenge." Mullick, on the other hand, says the decision was driven by the Army's desire to "consolidate" its biodefense labs and was unrelated to AFIP's impending closure or any safety issues.

The shutdown incensed the lab's workers, who had been assured that they would be able to resume their projects once the security problems had been addressed. Outside collaborators say the ban is unfortunate. "It was certainly a loss for us," says Steven Hinrichs, a microbiologist at the University of Nebraska Medical Center in Omaha who was working with AFIP scientists to identify genetic markers of geographic origin in *Francisella tularensis*, a microbe that causes rabbit fever. Hinrichs says that although he has access to a BSL-3 facility on his own campus, he had entered into the collaboration because Crawford and other AFIP scientists had special expertise in locating the markers. Hinrichs terminated the collaboration in January.

–YUDHIJIT BHATTACHARJEE

CREDITS: AFIP

Published by AAAS

Taking a shot. University of Notre Dame undergraduate Laura Adams works on a project to study nuclear fuels at one of DOE's new frontier research centers.

CREDIT: MATT CASHORE

ENERGY RESEARCH

DOE Commits $777 Million to Apply Basic Science to Urgent Problems

Chemist Peter Burns is grateful to the Department of Energy (DOE) for supporting his work on the behavior of actinides, a class of radioactive elements found in the waste from nuclear power plants. But he confesses that the research, although it fueled his University of Notre Dame lab for a dozen years, left him feeling less than satisfied that he was helping to solve fundamental aspects of the country's energy problems.

Last week, however, Burns won a 5-year, $18.5 million DOE grant that he says fully taps his scientific and creative juices. The funding makes Burns's team one of 46 Energy Frontier Research Centers (EFRCs) that DOE hopes will bridge the gap between basic and applied work in energy research. Eight years in the making, the $777 million program will support 1100 scientists working in interdisciplinary groups examining everything from making lighting more efficient to using photosynthesis to create new fuels derived from solar energy. Burns's new center, linking researchers from five universities and national laboratories, will have essentially free rein to design more efficient nuclear fuels and processes while dreaming up ways to make nuclear waste less harmful. "It's a whole new world," says Burns, one that he hopes will allow him "to have a much greater impact on energy."

Like many a frontier journey, the EFRC program has traveled along a bumpy road. Beginning in 2001, DOE's Office of Science sponsored a series of conferences at which energy industry officials and scientists brainstormed the fundamental breakthroughs required for new energy technologies. Drawing on that advice, DOE's Office of Basic Energy Sciences eventually sent out solicitations in solar energy, hydrogen research, nuclear energy, and instrumentation and attracted more than 700 proposals in 2007 and 2008. But a flat budget restricted DOE to only 40 small awards to individual investigators. Ever hopeful, DOE expanded the concept with a request for proposals for larger and more ambitious frontier centers. Understandably, applicants were skeptical. "We thought this might be another useless drill like the rest of the solicitations," says geochemist Donald DePaulo of DOE's Lawrence Berkeley National Laboratory (LBNL) in California, who will lead a center focusing on storing carbon dioxide underground.

But this year, DOE struck gold. The overall 2009 budget for the Office of Science, which is funding the initiative, went up 17%, to $4.8 billion. The office also gained $1.6 billion from the government-wide $787 billion stimulus package, money that must be spent by September 2010. The infusion allowed DOE to fund 50% more centers than it had planned. Each center will receive between $10 million and $25 million over 5 years, compared with typical investigator grants of $400,000 over 3 years. More time should mean more chances "to explore high-risk, high-reward research," says program manager Harriet Kung. The larger and longer awards will also make it easier to attract graduate students, Burns predicts.

Raymond Orbach, who headed the office during the Bush Administration, says the groups are intended to be large enough to encourage team building but not so big as to be unwieldy. Burns, an experimental chemist, has hooked up with theoretical and thermodynamic chemists at the University of Michigan and the University of California (UC), Davis, turning one-time competitors into collaborators. That change is likely to make for better science, says John Hemminger of UC Irvine, a member of a DOE advisory committee. "Before, you might have had two or three PIs [principal investigators] funded in a small group, in the same university. This is now saying, 'Identify an area of science that's important, and find the best people.' "

DOE officials say that the new centers have already met one program goal, namely, to attract new faces to energy research. At a meeting last week hosted by AAAS, which publishes *Science*, Energy Secretary Steven Chu said he's making progress in persuading scientists to take up the subject. "It's becoming an easier and easier sell," says Chu, a Nobelist and former director of LBNL, about his plea to colleagues "not to just write a paper and say this finding applies to energy" but to be willing to tackle a real-world problem.

Part of the reason is the field's increased visibility, including the attention it's receiving from the new Administration. "In no area will innovation be more important than in the development of new technologies to produce, use, and save energy," President Barack Obama declared last week during a speech at the annual meeting of the National Academy of Sciences (*Science*, 1 May, p. 576). Having sufficient resources also makes a difference, Chu admits. "I know that you can't herd cats," he quipped at the AAAS event, "but you can stimulate their movement by moving the cat food around."

Berend Smit, a theoretical chemist who moved from the Netherlands last year to UC Berkeley, says he was attracted by the enthusiasm of Chu and others in preaching the energy research gospel. "I wanted to be at the center of interest in energy," says Smit, who had been working on the general challenge of separating mixtures of gases. His $10 million center will be devoted to developing chemical methods to capture CO_2 from existing coal plants. "It's amazing," Smit says of the opportunity to be a pioneer on the energy frontier. "For global warming, we need to do something quickly." **–ELI KINTISCH**

Published by AAAS

ASTROPHYSICS

Fermi Data Dim Dark-Matter Claim

Data from a new satellite appear to stick a pin in a previous claim that a balloon experiment may have spotted dark matter. Last November, astrophysicists working with the balloon-borne Advanced Thin Ionization Calorimeter (ATIC) reported a dramatic excess of high-energy electrons and positrons from space, which could be a sign of dark-matter particles annihilating one another (*Science*, 21 November 2008, p. 1173). But researchers with NASA's orbiting Fermi Gamma-ray Space Telescope have measured the particles' energy spectrum with higher precision, and this week they reported that they see no such excess.

"We have much better statistics and can tell you that we do not see so extreme a feature" as ATIC observed, says Steven Ritz, a Fermi team member from NASA's Goddard Space Flight Center in Greenbelt, Maryland. The results don't disprove the existence of dark-matter particles, but they dampen hopes that researchers had already begun to see them in a clean and simple way.

Moonlighting. The Fermi Gamma-ray Space Telescope also detects electrons and other particles.

CREDITS (TOP TO BOTTOM): IRENA SCHULZ, BIRD LOVERS ONLY RESCUE INC.; NASA AND GENERAL DYNAMICS

For decades, astrophysicists have known that the average galaxy contains too little ordinary matter to keep itself from whirling apart. They assume that some form of dark matter provides the extra gravity needed to keep a galaxy whole. But physicists have never detected the stuff, which supposedly interacts with ordinary matter very weakly.

One way to spot it might be to look to the skies. Some popular theories suggest that if two dark-matter particles in space collide, they should annihilate each other to create an ordinary particle and an antiparticle, such as an electron and a positron. The electron and positron should emerge with an energy determined by the mass of the dark-matter particles, leading to a peak in their energy spectrum like the one ATIC observed as it circled the South Pole in 2000 and 2002.

But the $690 million Fermi telescope sees no peak, Fermi team members announced on 2 May at the annual April Meeting of the American Physical Society in Denver, Colorado. Launched in June to detect high-energy photons called gamma rays, Fermi is a particle detector adept at spotting electrons and positrons, too. It detected more than 4 million of them from August through January, compared with ATIC's thousands.

ATIC researchers stand by their results, however. Fermi's measurement may have far smaller statistical errors, but Fermi also has poorer energy resolution than ATIC, says John Wefel, an astrophysicist at Louisiana State University in Baton Rouge and an ATIC team leader. That would turn any peak into a broad bump, he says, noting that the Fermi spectrum does indeed show a gentle upwelling. "The difference comes down to the instrumentation," Wefel says.

Physicists may be seeing subtler signs of dark matter annihilations, says Neal Weiner, a theorist at New York University. Last year, the orbiting PAMELA cosmic-ray detector spied an odd increase in the ratio of positrons to electrons at lower energies. And the Fermi spectrum itself includes more high-energy electrons and positrons than expected. Such imbalances could be due to dark-matter particles, although stellar objects such as pulsars could also create them.

Even before the Fermi team's result, Weiner adds, theorists had realized that in the simplest annihilation scenarios, it would be difficult to produce enough electron-positron pairs to explain ATIC's big peak without also producing lots of other particles that would decay to electrons and positrons and smear the peak out. So they had begun to study more complex schemes, he says, and the new results will reinforce that trend. "I don't think it's going to dampen people's enthusiasm," Weiner says. "It's just going to change the types of models they are considering." Dark-matter annihilations aren't dead, but they may be better hidden than physicists hoped last fall.

–ADRIAN CHO

ScienceNOW.org

From *Science*'s Online Daily News Site

Beware the Planet Eaters! Like Icarus, some planets have wandered too close to their parent suns and perished. That's the conclusion of a new simulation—reported in *The Astrophysical Journal*—which helps explain why older stars tend to have few planets orbiting close to them. http://tinyurl.com/cj2mm2

That Bird Can Boogie. Snowball, the dancing sulphur-crested cockatoo, is a big hit on YouTube—and now he's also a scientific sensation. Researchers have shown that the bird, who bobs his head and lifts his legs to the Backstreet Boys' song "Everybody," is in fact listening to and following the beat. The findings—detailed in a pair of articles in *Current Biology*—challenge the notion that only humans have the neural wiring for dancing in time to music. You can see a video of Snowball getting his groove on here: http://tinyurl.com/ct3q3u

Invisibility Cloak for Almost-Visible Light. An invisibility cloak that works for visible light might soon be in sight, now that a team has made one that works for the slightly longer wavelengths of near-infrared light. The cloak, described in *Nature Materials*, is only about a micrometer in size. That makes it a little snug for Harry Potter, but experts say it's a major advance. http://tinyurl.com/csoc3w

Narcolepsy Revealed. The millions of people who suffer from narcolepsy might have their immune system to blame. Researchers have tied the disabling sleep disorder to two immune system genes, suggesting that it's an autoimmune disease. The discovery, reported in *Nature Genetics*, may eventually lead to improved narcolepsy treatments. http://tinyurl.com/d7smzn

Read the full postings, comments, and more on **sciencenow.sciencemag.org**.

Published by AAAS

The Famine Fighter's Last Battle

More than a half-century after the research that helped spark the green revolution, Norman Borlaug is again fighting a devastating fungus that threatens wheat around the world

ON A COLD, JANUARY MORNING IN 2005, A small plane landed outside the town of Njoro, Kenya, where a handful of scientists waited eagerly as the plane taxied. After the propellers stopped, an old man slowly climbed out and walked across the grassy airstrip. Norman Borlaug, then 91, had come from Nairobi to examine for himself the impact of a highly virulent race of stem rust, called Ug99, a plant pathogen that had recently crossed the border from Uganda and was now threatening wheat farmers around the world.

Few living people—scientists or farmers—had had any experience with outbreaks of stem rust. To Borlaug, however, it was a familiar enemy. After epidemics had devastated wheat fields in Mexico in the 1940s, Borlaug, who was working at an agricultural experiment station in Mexico, bred new varieties of wheat that could resist the disease. These varieties were a key component of the green revolution of the 1960s, helping to boost wheat yields in Mexico and avert famine in India, Pakistan, and elsewhere. Ever since, the world had seemed safe from stem rust. Now, the energetic, tenacious, Nobel Peace Prize–winner is trying once more to defeat the threat.

Persistent. Norman Borlaug surveying research fields.

CREDIT: E. STOKSTAD/*SCIENCE*

At the airstrip, researchers from the Kenya Agricultural Research Institute (KARI) hustled Borlaug into a car and drove him 50 kilometers to the experimental plots they had planted in the village of Mau Narok. These small fields contained more than 100 varieties of wheat that had been sent to KARI from around the world to see how they would fare against Ug99.

The situation looked bad. As Borlaug combed every inch of the field, bent over in the chilling wind, his alarm grew. Almost all of the varieties were infected, their stems covered with a rash of red, spore-filled pustules of *Puccinia graminis*. Finally, Borlaug found a few varieties that showed some resistance, but he remained pensive. The world was ill-prepared to fight this reemerging threat, he thought.

Back in his office at the International Maize and Wheat Improvement Center (CIMMYT) in El Batan, Mexico, Borlaug kicked into high gear. With his characteristic passion and impatience with bureaucracy, he wrote a blunt memo to CIMMYT's director general calling for more funding and threatening to sever his ties with the institution if it didn't happen immediately. Soon the Rockefeller Foundation, which had supported Borlaug's early work on stem rust, contributed as well. Borlaug and others formed the Global Rust Initiative (GRI) to coordinate international activities, key among them testing more wheat varieties and breeding resistance. Relentless, Borlaug has kept using his connections and reputation to highlight the danger of Ug99 and extract more funding from governments.

Since then, CIMMYT has created 15 varieties of high-yielding Ug99-resistant wheat. Seed is being grown to send to countries infected with, or in the path of, Ug99. The fungus is already endemic in Kenya and Ethiopia, it has been found as far east as Iran, and it is threatening the breadbaskets of South Asia. Meanwhile, three new, dangerous

Published by AAAS

variants have appeared in South Africa and Kenya. "There is no room for complacency," Borlaug exhorted more than 300 wheat breeders and pathologists at a March conference in Ciudad Obregón, Mexico. "So let's get on with the job."

Hunger pangs

Born and raised on a farm near Cresco, Iowa, Borlaug initially wanted to be a high school science teacher. When he enrolled at the University of Minnesota in 1933, at the height of the Great Depression, he was sickened by the number of homeless people he encountered camped out in parks, hungry and begging for food—a sight he never forgot. In the fall of 1937, Borlaug heard a lecture by Elvin Stakman, a renowned plant pathologist who studied stem rust, a poorly understood disease that periodically decimated wheat production around the world. "Rust is a shifty, changing, constantly evolving enemy," Stakman said in his lecture. "We can never lower our guard." Inspired by Stakman's weaving together of microbial evolution and human hunger, Borlaug switched to plant pathology and earned his Ph.D. with Stakman in 1942.

Borlaug took a wartime job with DuPont, working on fungicides and bactericides. At that time, the Rockefeller Foundation was starting to work with Mexico to improve its agriculture. The foundation hired Stakman, and Borlaug joined the team in 1944. It was a rude awakening coming from the laboratories of DuPont. When Borlaug arrived at the fields donated by the Mexican government 30 kilometers outside of Mexico City, there wasn't much to work with: one adobe shed and no equipment.

Once again, Borlaug was shocked by poverty and hunger; on top of other problems, 3 years of stem rust had slashed wheat yields in half. "I've seen the misery that comes from rust epidemics," he says. Borlaug began to train Mexican technicians and made thousands of crosses of wheat varieties from around the world, trying to improve resistance to stem rust, boost production, and adapt varieties to local conditions. Counter to the culture of the time, Borlaug insisted that scientists work alongside technicians in the fields. Yields began to improve.

But the progress wasn't fast enough for Borlaug. When he learned about an abandoned experiment station 2000 kilometers to the north in the Yaqui Valley of Sonora, he decided to visit. Stem rust had caused massive problems for wheat farmers there as well, but apparently one variety was somewhat resistant. It took 2 days to fly there in an old Fokker Tri-Motor.

The station was in shambles, Borlaug recalls. "There was nothing except a few goats running around." But Borlaug saw an opportunity and had a crucial—if unorthodox—insight: He realized that because of the difference in climate between the two stations, his team could grow two generations of wheat a year. First, they could plant summer wheat in the cooler highlands near Mexico City, then harvest that seed and plant it in the warmer fall weather in Sonora, which was only 40 meters above sea level.

His idea instantly met with opposition. At the time, most agronomists thought that seeds required a dormant phase after harvest. Another dogma was that breeders should plant their varieties and make selections in the same place that farmers were planting. His boss, who vetoed the idea, also balked at the cost of renovating a second experiment station, as well as the time involved in transporting researchers and seed across the country. Borlaug threatened to resign. Finally, Stakman intervened, and Borlaug got the green light.

This new approach, called shuttle breeding, cut breeding time in half; it also allowed Borlaug's team to produce more adaptable varieties that could grow in a range of latitudes, climates, and soils. By 1956, the team had introduced 40 varieties that could resist stem rust, and Mexico no longer needed to import wheat. Breeders at CIMMYT are still shuttling seeds between Mexico City and Ciudad Obregón.

Starting in 1953, they bred varieties with even greater yield potential, crossing their resistant wheat with short-stemmed wheat from Japan that produced more grain. Their short, sturdy stems prevented them from blowing over, which damages the plant. With these dwarf Mexican wheat varieties, first introduced in 1961, yield potential doubled to 9 metric tons per hectare.

In action. Borlaug evaluating wheat in Mexico in the early 1960s. He assessed damage from Ug99 in Kenya in 2005.

CREDITS (LEFT TO RIGHT): CIMMYT; USDA/KAY SIMMONS

Worldwide impact

Impressed with the success in Mexico, the Rockefeller Foundation decided to take it global. Working with the United Nations' Food and Agriculture Organization, Borlaug helped create a network of about 15 testing nurseries around the world to test the disease-fighting, yield-boosting potential of these new varieties. These data proved crucial for helping deal with famines in South Asia in the mid-1960s. After some head-butting with bureaucrats to get the seed introduced, wheat yields rose by 60% in India and Pakistan by 1970. Pakistan became self-sufficient in 1968, and India 6 years later.

When CIMMYT was founded in 1966, Borlaug became director of the wheat-breeding program. On 20 October 1970, he had already left for the fields when his wife, Margaret, received a call at 4 a.m. announcing that Borlaug had won the Nobel Peace Prize. The citation noted that "more than any other single person of this age, he has helped to provide bread for a

Online
sciencemag.org
Slideshow narrated by author Erik Stokstad.

Published by AAAS

hungry world. We have made this choice in the hope that providing bread will also give the world peace."

The green revolution has been criticized for its reliance on synthetic fertilizers, irrigation that led to salinization of soils, and other problems; Borlaug acknowledges some of these shortcomings but says they pale in comparison to starvation and political unrest. Moving forward, he says, scientists will have to find a way to boost global grain production by 50% in 2 decades "in environmentally more sustainable ways."

After he officially retired from CIMMYT in 1979, Borlaug turned to Africa, co-leading the Sasakawa-Global 2000 Programme to bring relatively simple technology—fertilizer, improved irrigation techniques, and crop management—to poor farmers. By the 1990s, Borlaug was also teaching fall semester courses at Texas A&M University. He spent the rest of the year mainly in Mexico, where he consulted at CIMMYT, starting his workday, as usual, before 6 a.m. His family saw him for just a few months a year, at most, as had been the case since he first began fighting stem rust in the 1940s.

Test bed. Wheat varieties are being bred in many countries, including Ethiopia (*top*), for resistance to stem rust (*bottom*).

Stem rust returns

Borlaug's resistant varieties protected the world's wheat against stem rust for decades. So it was a surprise to Ravi Singh, the chief bread wheat breeder for CIMMYT, when he heard about an infestation of stem rust at a research station in Uganda in 1998. "My first thought was it's a mistake. It can't be possible," Singh recalls. Wheat in Uganda had typically been afflicted with yellow rust, not stem rust.

But Borlaug says he was not surprised by the return of stem rust. "I used to tell the new people, 'Don't think this isn't a problem,'" he recounted to *Science* in a 2007 interview.

At first, the severity of the threat was hard to gauge, Singh says. After surfacing in 1998, the new race, dubbed Ug99, did not reappear at the Uganda research station's monitoring plots for several years. But in 2002, the fungus showed up at the research station in Njoro, Kenya. Initially, some 30% of the varieties tested at KARI appeared vulnerable. The wind-borne spores were clearly spreading.

"This is a time bomb," Borlaug told his colleagues at CIMMYT, recalls Christopher Doswell of the Consultative Group on International Agricultural Research (CGIAR), a longtime associate. Even if conditions are not wet enough for an outbreak, stem rust can lie in wait on alternative hosts, such as a shrub called barberry. Ug99 is "going to lie there, and then all of the sudden it's going to go boom," Borlaug warned colleagues.

In 2003, Ug99 was detected in Ethiopia, where it became established in the damp wheat fields of the highlands. Borlaug thought nations should start growing, or "multiplying," seed from the few known resistant varieties from Kenya. But agriculture departments in various nations that hadn't seen stem rust in decades underestimated it, thinking their own varieties would be resistant. Hit with a budget crisis, CIMMYT couldn't do the work alone.

Borlaug started a quiet campaign, requesting a private meeting in 2004 with then–U.S. Department of Agriculture Secretary Michael Johanns, who steered an initial $35,000 of emergency funds to testing efforts by scientists in Kenya and Ethiopia. Borlaug and Doswell also went to the U.S. Agency for International Development, which later provided $400,000.

Borlaug was even more alarmed when he returned from his visit to Kenya in January 2005. He railed against the bureaucracy and the shortage of funds at CGIAR, which hampered a rapid response. He was also mad at what he saw as the low priority national agricultural departments were giving to monitoring for rust.

Again, he appealed to the Rockefeller Foundation, which provided $80,000 to CIMMYT. It was enough to fund an expert panel to further assess the threat. Then CIMMYT and the International Center for Agricultural Research in the Dry Areas hosted an international meeting in Nairobi. Borlaug and Singh had urged breeders from 18 countries to send samples of commercially grown wheat to be planted by KARI. That way, they could see how they fared when infected with Ug99. During the field trip to the experimental plots, the visiting breeders were shocked at how many wheat varieties were stricken. "It was a mixture of embarrassment and desperation," says Miriam Kinyua, a wheat breeder who was head of KARI's Njoro station at the time.

Ug99 continued its march. The next year, it turned up in Yemen, continuing a global track predicted to take it across the fertile crescent and into Southern Asia (*Science*, 30 March 2007, p. 1786). By 2007, the fungus had been found in the main wheat-growing area of western Iran, where for now it has stalled due to drought.

Borlaug, too, has slowed down a bit after being diagnosed with lymphoma in 2006. But he still helped garner a 5-year, $27 million grant from the Gates Foundation that's being used to fund basic research, surveillance, and breeding.

The cancer is under control now, and Borlaug was full of vigor at a March meeting of the renamed Borlaug Global Rust Initiative in Ciudad Obregón. After visiting his old research plots, he says he's pleased with progress but insists much more needs to be done. "It has to be an international effort," he says, thumping his finger on the arm of his wheelchair. "So you can move the multiplication [of seed] and the replacement of the susceptible varieties before disaster strikes."

Ronnie Coffman of Cornell University, BGRI's vice chairperson, says that bringing researchers together to work on stem rust has become a second calling for Borlaug. "He's almost an evangelist now," he says. And the missionary work continues. When Coffman and Borlaug visited Washington, D.C., last year, Borlaug insisted on renewing his passport.

–ERIK STOKSTAD

CREDITS (TOP TO BOTTOM): JENNY NELSON, DRRW PROJECT, CORNELL UNIVERSITY; USDA/CEREAL DISEASE LAB

Sanctuary or survival test? Scientists can only guess how pandas are faring in Baishuihe reserve, beyond the collapsed Xiao Yu Dong Bridge.

WENCHUAN EARTHQUAKE

A Deeply Scarred Land

Rock and mudslides in Sichuan have buried vast forested areas, ruined farmland, and disrupted the habitats of pandas and golden monkeys; the recovery will take decades

LONGMENSHAN, CHINA—In the morning of 12 May 2008, Ren Diandong gave a talk on landslide modeling at the Institute of Atmospheric Physics of the Chinese Academy of Sciences (CAS) in Beijing. A few hours later, Ren's model was put to the supreme test: a magnitude-7.9 earthquake in Sichuan Province's Longmenshan range (*Science*, 20 June 2008, p. 1578). As early reports came in that afternoon of a disaster that would leave nearly 90,000 people dead or missing, Ren, a climatologist at the University of Texas, Austin, knew the quake had struck in landslide country—and with the rainy season about to begin, the fractured land would soon be thick with mudslides.

In the weeks that followed, Ren and colleagues pored over satellite images of landslides, rock falls, and debris flows in an earthquake-ravaged area the size of Belgium. Their model suggests that slides buried about 235 million tons of carbon in vegetation from Longmenshan's forest ecosystem. As it rots in the coming decades, it should release more than 100 million tons of carbon dioxide (CO_2), according to the model—roughly equivalent to 2% of current annual global emissions from fossil fuel combustion. Soil in many landslide zones will also be nitrogen-poor for decades to come.

As China mourns the first anniversary of the Wenchuan earthquake, the ecological toll is just coming to light. Besides unleashing greenhouse gases, landslides caused widespread habitat fragmentation—threatening the region's unique assemblage of species, including its dwindling wild population of giant pandas. Landslides destroyed 122,000 hectares of vegetation, including 98,000 hectares of forest, says Bao Weikai, a plant ecologist at Maoxian Mountain Ecosystem Research Station of CAS's Chengdu Institute of Biology (CIB). It will take years of survey work, he and others say, to understand how Sichuan's biodiversity hot spot will respond.

Damaged habitats

On a misty late April day, schoolchildren on bicycles race home along a highway leading to the Longmenshan mountains. They blur past four elderly men playing mahjong outside a prefabricated shelter, past a group of women practicing tai chi moves in sync, past bustling construction sites in Tongji, where duplexes and townhouses will replace homes reduced to rubble by the Wenchuan earthquake. Most of the town's houses were destroyed, but by good fortune only a few dozen residents died. "When the earthquake struck, farmers were in their fields, and it was 3 minutes before the next class, so a lot of children were outside the school," says CIB ethnobotanist Luo Peng.

End of the line. The road to Baishuihe disappears just past this wrecked hotel in Longmenshan town.

In neighboring Longmenshan town, on the other side of the collapsed Xiao Yu Dong Bridge, the semblance of normality evaporates. Sheared-off slabs of highway lie in ravines, and landslides with patchy new grass entomb other sections. In a narrowing valley, just past a ruined hotel—ecotourism was Longmenshan's main source of revenue before the quake—the road leading to Baishuihe National Nature Reserve was wiped off the map.

That makes Zang Xuan's job difficult. Before the earthquake, the ranger lived in a field station deep inside the reserve. Zang and his fellow rangers escaped with minor injuries when their outposts collapsed. Nowadays, getting into Baishuihe is an arduous hike. "We can't carry out regular monitoring," Zang says. But from what they've seen in limited excursions, the damage is enormous: Landslides caused extensive forest fragmentation up to an altitude of about 2500 meters. "The earthquake damaged half of the giant panda's habitat in Baishuihe," says CIB forest ecology Pan Kaiwen. Rangers have no idea how the reserve's star attraction is faring, nor how other animals such as golden monkeys are coping. "With the road gone and no more tourists, maybe the pandas are happier. Or maybe they are struggling to find food," says Zang. "We just don't know."

Although the impact on the panda's food supply is still unclear, many farmers suffered real losses. "Landslides destroyed a lot of cultivated land," Pan says. One priority of the reconstruction effort is to identify new cropland—no easy task in the rugged earthquake zone. A failure to replace farmland could further harm the region's ecosystems, says Pan, if desperate former farmers were to start foraging in nature reserves for lucrative medicinal plants.

Slow recovery

Since the first days after the earthquake last May, a team led by geomorphologist Cui Peng of CAS's Institute of

CREDITS (TOP TO BOTTOM): R. STONE/*SCIENCE*; R. STONE/*SCIENCE*

Some Unwelcome Questions About Big Dams

CHENGDU, CHINA—Soon after the magnitude-7.9 Wenchuan earthquake struck last May, geologist Fan Xiao uttered publicly what many anxious scientists were discussing privately: Could a large dam near the fault have triggered the devastating quake?

The 156-meter-high Zipingpu Dam began to fill in December 2004, and within 2 years the water level had risen to 120 meters. Following normal operation, the reservoir's level dropped as water was released downstream during the winter and early spring 2008 and was at a low level when the Wenchuan earthquake occurred. Removing the pressure of several hundred million tons of water on a slip thrust fault like Longmenshan may have destabilized it, increasing the risk of a rupture, argues Fan, a senior engineer at the Sichuan Bureau of Geology and Mineral Resources in Chengdu. Reservoir-induced seismicity is an accepted phenomenon, but Wenchuan's magnitude was much higher than that of the biggest earthquake previously linked to a dam, a magnitude-6.5 temblor in India in 1967 that killed nearly 200 people.

Dam or no, the Wenchuan earthquake was inevitable, Fan says. But he asserts that Zipingpu, just 5.5 kilometers from the quake's epicenter, may have caused the Longmenshan fault to fail decades or even centuries earlier than it might have without added stress. Fan's outspokenness—and *Science*'s coverage (*Science*, 16 January, p. 322)—has provoked the wrath of hydropower proponents and scientists who rule out a Zipingpu-Wenchuan link. *Science* spoke with Fan about his views. **–R.S.**

Q: What further evidence would support a Zipingpu-Wenchuan link?
X.F.: According to the State Council, every dam higher than 100 meters and with a capacity of more than 50 million cubic meters of water must have a special monitoring system to detect slight tremors. Zipingpu has such a system. A reservoir-triggered earthquake should have more foreshocks than a natural earthquake. Last fall, a paper in *Geology and Seismology* reported that before the Wenchuan earthquake, there were many small foreshocks around the dam. And this activity correlated to changes in the reservoir's water levels.

Q: You mean the earthquake swarm near Dujiangyan [a town near the epicenter badly damaged in the quake] in February 2008?
X.F.: Yes, it was spectacular. There were about 200 small earthquakes, including five bigger than magnitude 3 during the evening on 14 February. Many people in Dujiangyan ran out of their homes. Then there was another swarm at the end of February and early March between Dujiangyan and Pengzhou. All these earthquakes happened when the water level in Zipingpu reservoir was low.

SSB [Sichuan Seismological Bureau] has data that would let us examine this more closely. Last October, SSB's director promised to release the data. I hope this happens soon.

Sticking his neck out. Fan Xiao.

Q: There are many dams planned or under construction in seismic areas in western China. Are there any you are especially worried about?
X.F.: Jinping on the Yalong River. When it's finished, it will be one of the highest dams on Earth—305 meters high—and it will accumulate four times as much water as Zipingpu. It's in an earthquake-prone area [of southwestern Sichuan]. Last year, SSB found that the dam's developers hadn't yet established the required monitoring system.

Q: What should be done about this?
X.F.: There's no possibility to delay or stop building dams, even in high-risk areas. What we can do is raise building standards and improve monitoring of foreshocks. Early warning might give people a chance to escape.

Q: Have you come under pressure for expressing your views?
X.F.: Scientific issues are open to discussion. But hydropower companies—it is fair to say they are not happy with me.

Mountain Hazards and Environment in Chengdu has made a few dozen expeditions into the disaster area to chart the extensive scarring of the slopes. Because landslide scars tend to be midway up slopes, the loss of shearing resistance makes slides at higher elevations more likely. The dramatic loss of stability "is a huge change" that could last 5 years or more, says Cui.

Ren's group took stock using a model that he calls "a unified approach for a disparate set of poorly understood geophysical phenomena," from landslides to glacier movements. The team cut its teeth on southern California's wildfires in 2007, successfully predicting which burn scars would be most unstable and prone to slides. Applied to the Wenchuan quake, the model produced staggering figures for how much carbon and nitrogen will seep into the atmosphere, the team reported in March in *Geophysical Research Letters*. And those releases could become chronic: "If a warming climate causes more frequent storms of greater intensity, it's likely that the affected ecosystem will become a net CO_2 source," Ren says.

CIB researchers are eager to ground-truth Ren's predictions, which they feel may be an overestimate. Data in Ren's paper are "coarse," says Bao. On many Longmenshan slopes the soil is "very thin," he says, and could not support the amount of vegetation Ren's group says was uprooted or smothered. The CIB team also notes that satellite-based estimates of landslide-degraded land are imprecise. "Monitoring should give us a more exact understanding," says plant ecologist Wu Ning, CIB's director. According to Bao, CIB plans to assess carbon loss at as many as 200 landslide sites in various ecosystems and climate regimes.

Another wildcard is how fast vegetation will recover—and that will not be uniform across the Longmenshan range. Areas to the south and east "are very moist and should recover more easily," says Pan. Grasses and shrubs are already gaining footholds on landslides in those areas. But it could take much longer for more arid land to the west, where the soil is thinner and nutrient-impoverished, to regain its pre-earthquake vitality, he says. Even 30 years after the magnitude-7.2 Songpan earthquake rattled the northern Longmenshan, some steeper slopes are still mostly bare. It could take a century or longer for forests to return on similar dry slopes destabilized by last year's earthquake, says Bao.

For most slopes, CIB researchers will be content to watch natural restoration unfold. But they are planning to restore destroyed sections near towns and along highways, mainly by planting indigenous shrubs. When they are able to lay hands on seedlings, that is: No organization has been responsible for breeding these species, says Wu. CIB also hopes to minimize the impact of a major reconstruction project, a new railway line that will connect Chengdu and Lanzhou. The tracks will run through several reserves and could further degrade habitats, CIB researchers say. Bisecting the reserves could be a particular problem for pandas, which range widely for food.

In the meantime, some researchers could spend the rest of their careers measuring the earthquake's ruinous environmental footprint. "We'll need at least 30 to 50 years to get a true picture of how the region recovers its ecological function," says Wu.

–RICHARD STONE

CREDIT: R. STONE/*SCIENCE*

Published by AAAS

MYANMAR

One Year After a Devastating Cyclone, a Bitter Harvest

Myanmar weathered Cyclone Nargis better than expected, but the global financial crisis has jeopardized the country's fragile food security

During the night of 2 May 2008, Cyclone Nargis barreled across Myanmar's Ayeyarwady delta, flattening homes and sweeping away people, draft animals, and stores of rice. On a visit to the region 4 months later, plant physiologist Abdelbagi Ismail saw vestiges of the storm's fury, including tidal-surge watermarks more than 2.5 meters high on the few trees left standing. He witnessed the lingering anguish of survivors who lost entire families among the 140,000 people dead or missing. "The scene was shocking, and the stories we heard from farmers were horrific," says Ismail, who with four colleagues from the International Rice Research Institute (IRRI) in Los Baños, Philippines, went to Myanmar (formerly Burma) to advise local scientists on how to restore rice yields after the cyclone.

A year after one of the deadliest cyclones in modern history, Myanmar's food security teeters on a knife's edge. Emergency food relief averted starvation among the 2.4 million survivors in the delta, and rice production countrywide has largely rebounded thanks to favorable weather and the use of high-yield varieties. But Nargis paved the way for another crisis—the global financial meltdown—to push Myanmar to the brink of catastrophe. Credit has evaporated, paddy farmers are going broke, and household rice stores are dwindling. "The country's rural economy has virtually collapsed," an official with International Development Enterprises, a nonprofit operating in Myanmar, said to a gathering of food security experts in Yangon in March. "The current conditions are unprecedented in living memory."

To help Myanmar cope, the European Commission, Australia, the U.K.'s Department for International Development (DFID), and other donors are establishing LIFT, a $100 million, 5-year fund for livelihoods and food security. Priorities of the U.N.-managed fund are expected to include microcredit schemes, agricultural policy reform, small business development, and R&D to boost agricultural productivity.

Nargis meted out a major blow to fragile farm communities. With gusts topping 200 kilometers an hour, the cyclone cut a swath of devastation 150 kilometers wide as it churned northeast across the Ayeyarwady delta and over Yangon (formerly Rangoon), Myanmar's capital and biggest city. The tidal surge swamped an estimated 783,000 hectares of paddy fields, destroying a third of the crop in the delta, the country's rice bowl. Local rice varieties are tall and blow down easily, says Ismail, and they succumb readily when fields are flooded or salty. Nargis also ruined much of the delta's rice seeds, which had been stored in bamboo containers that were easily waterlogged. "Nargis made a bad food-security situation worse," says Zoe Hensby, livelihoods adviser at DFID.

Resilience. Nargis survivors transplanting rice last August in the Ayeyarwady delta.

CREDIT: DAVID JOHNSON/IRRI

At first, Burmese scientists feared that delta paddies would remain too saline to grow rice for months. "From the beginning, our advice was not to worry about it," says Ismail. According to observations after the December 2004 tsunami and Cyclone Sidr, which slammed Bangladesh in November 2007, salt intrusions were washed out the following rainy season. Nargis came at the end of Myanmar's dry season, just before cleansing rains. By the time the IRRI team arrived in the middle of the monsoon season in August, salinity was back to normal in fields they inspected and farmers had managed to replant 80% of disaster-hit paddies. "They bounced back and had a crop in the ground," says IRRI's Grant Singleton. "They showed tremendous resilience."

Such perseverance helped Myanmar last year to export nearly half a million tons of rice, according to a report last January for the United Nations Food and Agriculture Organization (FAO) and the U.N. World Food Programme. "The paddies are recovering," says Cheng Fang, an economist at FAO's Global Information and Early Warning System on Food and Agriculture in Rome. His team had rare permission from Myanmar authorities to travel to all areas of the tightly controlled country for a month last autumn.

Robust rice yields were about the only piece of good news that Fang's team uncovered. In addition to the appalling human toll, Nargis drowned 122,000 water buffalo and robbed survivors of farm implements and fishing boats and gear. "Many families lost everything: their homes, property, and job opportunities," says Fang.

The U.N. team also noted that Nargis coincided with a grave pest infestation in Chin, Myanmar's poorest state. In a phenomenon that recurs every half-century or so, bamboo flowered en masse in Chin in 2007. The sudden fecundity fueled an explosion in the rat population. "When this happens, it is invariably a major traumatic event," says Singleton, a zoologist who specializes in rodents. Last year, rats decimated Chin's corn and rice harvests, "leading to acute food insecurity in many villages," according to the U.N. report, which forecasts that the situation will remain critical until July.

In the meantime, the global financial downturn has exposed and aggravated the frailties of Myanmar's agricultural system. "Many households are facing unprecedented levels of hardship," says Hensby.

To mitigate the impact of future cyclones, IRRI has sent submergence and salt-tolerant rice varieties to Myanmar for testing. IRRI's Irrigated Rice Research Consortium is also working with Burmese universities to incorporate cutting-edge technologies and knowledge into curricula to better train future agricultural scientists and extension officers. Myanmar may have weathered Nargis better than expected, but the country's food security is more vulnerable than ever.

–RICHARD STONE

Published by AAAS

Meet your new lab partner.

The new Thermo Scientific NanoDrop 2000 and 2000c Spectrophotometers offer true micro-sample analysis, with sample size capability as low as 0.5 µl and a measurement time of less than five seconds. Either of these is the perfect instrument for all your quantitation needs—DNA, RNA, proteins and more. Providing full spectrum UV-Vis results, both instruments can analyze samples with concentrations greater than 15,000 ng/µl (dsDNA) without dilutions. Innovative software makes it easy to build your own methods, design reports and export data. And with both pedestal and cuvette capability, the NanoDrop™ 2000c is the one spectrophotometer that does it all.

Test-drive the NanoDrop 2000 or 2000c in your own lab!*
Visit **www.nanodrop.com** to schedule your test-drive. Try out an instrument and run your own samples. It's completely free.

* Available only in US and Canada

Thermo Scientific NanoDrop 2000c
The only spectrophotometer that combines micro-volume pedestal technology and cuvette capability

Moving science forward

Thermo SCIENTIFIC
Part of Thermo Fisher Scientific

ARCHAEOLOGY

Going the Distance to Uncover The Roots of Trade in the Near East

Archaeologists are revealing the "invisible exports" of the world's first civilizations: textiles, silk, and stone shipped to ordinary people rather than elites

As long as there have been humans, there has been trade. Long before animals were domesticated and agriculture took hold, people moved prized objects over long distances. But trade in gemstones and other prized goods has generally been seen as playing only a minor part in the emergence of civilization.

Now archaeologists are finding a more important role for trade at the start of the 2nd millennium B.C.E., when the first complex societies took hold across the Old World. "Most of our focus on trade in the Bronze Age has been on exotic, high-value goods," says archaeologist Monica Smith of the University of California, Los Angeles. There is growing evidence that more ordinary goods—ranging from textiles to food—were transported over long distances, Smith and others said at the recent Society for American Archaeology (SAA) meeting, held in Atlanta, Georgia, from 22 to 26 April. That network, connected in part by mobile pastoralists or nomads, may have played an important role in encouraging the growth of the world's first cities, as well as mercantile classes, standardized measures, and other aspects of life we take for granted in our globalized economy.

During the start of the 2nd millennium B.C.E., the market for precious goods such as lapis lazuli boomed from Central Asia in the north to the Persian Gulf in the south, and from Mesopotamia in the west to the Indus in the east (see map). Such durable goods were often passed on or buried, and so are visible to archaeologists.

Until recently, however, there has been little data on trade in more ordinary and degradable objects, such as textiles. But scholars who examine Mesopotamian cuneiform texts have long puzzled over hints of widespread trade in common goods as far back as 2500 B.C.E. Using new methods of analysis, researchers are now picking up traces of what they once called "invisible exports." In recent years they have found evidence, for example, that linen, wool, and hemp were shipped from the Indus civilization in today's Pakistan and India to Shahr-i Sokhta, a former city in eastern Iran. In a recent issue of *Archaeometry*, Harvard University archaeologist Irene Good demonstrated that silk made in the Indus (centuries before there is evidence for it in China) made its way as far north as Afghanistan and as far east as the Deccan plateau. Fabric impressions, knives likely used for cutting carpet fibers, and images showing sophisticated patterns in clothes point to textiles as an important export of the Indus civilization until it began to dissolve around 1800 B.C.E. And to the north, in today's Afghanistan and Turkmenistan, large settlements that were part of the Oxus civilization, which flourished from roughly 2000 to 1700 B.C.E., imported a host of goods. "It is hard to imagine the immense amount of raw stone, metal, and other production materials which had to be brought into the desert oases," says archaeologist Fredrik Hiebert of the National Geographic Society in Washington, D.C., who presented at the SAA meeting. "It represents interregional exchange to a level not previously seen."

Nomad man. Michael Frachetti examines ancient pastoralist evidence in Kazakhstan.

How were these goods moved? In Mesopotamia, Assyrian traders left behind texts detailing their business. But some archaeologists are also turning their attention to the shadowy role of nomads.

Nomads were once thought to have grown numerous only with widespread domestication of the horse across Eurasia, well into the 2nd millennium B.C.E. But Michael Frachetti of Washington University in St. Louis, Missouri, has found evidence that mobile pastoralists thrived as early as 2460 B.C.E. in eastern Kazakhstan—800 years earlier than once thought. In an SAA presentation, he asserted that such sheep and goat herders played a key role in transmitting innovations during the Bronze Age.

Nomads could carry large quantities of light goods such as textiles over long distances as part of their regular movements. Rather than an organized system controlled by a powerful king or merchant class, trade in this period may have depended in large part on such pastoralists who left little behind in the archaeological record. "They are the agents of the networks—the Web brokers of their world," says Frachetti. Solid evidence of this has yet to come to light and may be hard to come by. But Hiebert agrees that pastoralists likely played a critical role in connecting urban societies like the Oxus; he found evidence that the Oxus people turned to the growing pastoral populations as both a market and source of goods after the Indus civilization collapsed.

And where there were few pastoralists or independent merchants, there may have been little trade. During the early 2nd millennium B.C.E., few pastoralists roamed between Mesopotamia and Egypt, and the civilizations apparently had virtually no interaction, says Smith. Meanwhile, trade between Mesopotamia and the Indus was steady despite the longer distances involved.

Smith further suggests that ancient peoples may have seen goods such as ceramics and flints as throwaway items and viewed "perishable" textiles as both valuable and durable. Viewed from that perspective, the Mesopotamian rug may have entranced an Anatolian homemaker—and spurred civilization at the same time.

–ANDREW LAWLER

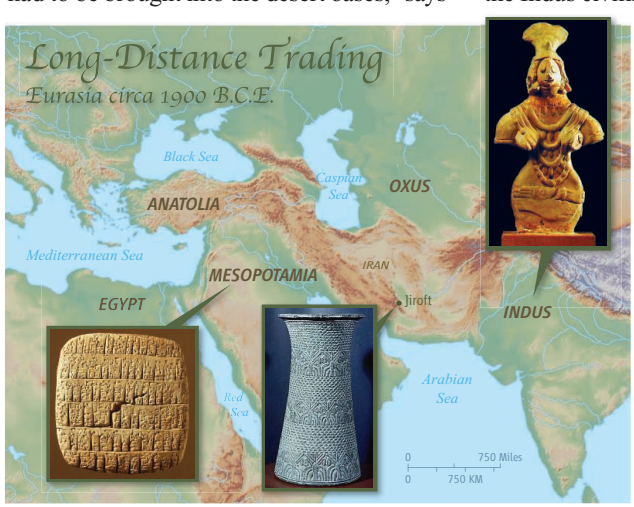

Global market. Ancient objects such as this chlorite vase from Iran traveled thousands of kilometers, while Mesopotamian tablets detail trade in textiles, perhaps hinted at in the elaborate clothing of an Indus statue.

CREDITS (TOP TO BOTTOM): TAYLOR HERMES; (MAP INSETS, LEFT TO RIGHT) ARALDO DE LUCA/CORBIS; FRANCIS G. MAYER/CORBIS; COURTESY OF EXOTIC INDIA, WWW.EXOTICINDIAART.COM

ASTRONOMY

Shuttle Crew Set to Prepare Hubble For a Star-Studded Grand Finale

New instruments and crucial repairs will make the Hubble Space Telescope's last years an astronomical feast, if a NASA mission this month goes as planned

Five years ago, after NASA canceled its fifth and final servicing mission to the Hubble Space Telescope in the aftermath of the Columbia shuttle disaster, the glory days of the astronomical workhorse seemed to be drawing to a close. Unless NASA changed its mind, astronomers predicted, the end of the decade could be the time to write the telescope's epitaph.

This month, however, a mission to fix and upgrade the Hubble will blast skyward in hopes of giving the orbiting observatory a fresh lease on life and another shot at glory. Astronauts are scheduled to install a new camera and a spectrograph many times more powerful than previous instruments, swap out all six of the telescope's gyroscopes, replace its batteries, install a new backup computer, and attempt to repair an existing spectrograph and camera that are not functioning. The mission—expected to be the final maintenance visit to the Hubble—is aimed at keeping the telescope in operation until 2014.

If all goes well, NASA officials and researchers outside the agency say the upgraded Hubble will send home images of the near and distant universe far more detailed than anything seen before. In doing so, the telescope should enable astronomers to gain new insights into fundamental questions such as the structure of the universe and the nature of dark matter. Observations made by the new instruments should also provide researchers with a better understanding of the evolution of galaxies, the birth of stars, and the composition of intergalactic gases.

Astronomers expect the results from the next chapter to match the luster of Hubble's legendary discoveries such as the age of the universe and the existence of dark energy. In its 18 years of operations, "Hubble has changed the way the world looks at the universe," says Eric Smith, NASA program manager for both Hubble and the James Webb Space Telescope—an infrared telescope scheduled for launch in 2013. The coming 5 years of observations "will push Hubble to its limits," he says. "The questions that arise from these observations will point the way to telescopes in the future."

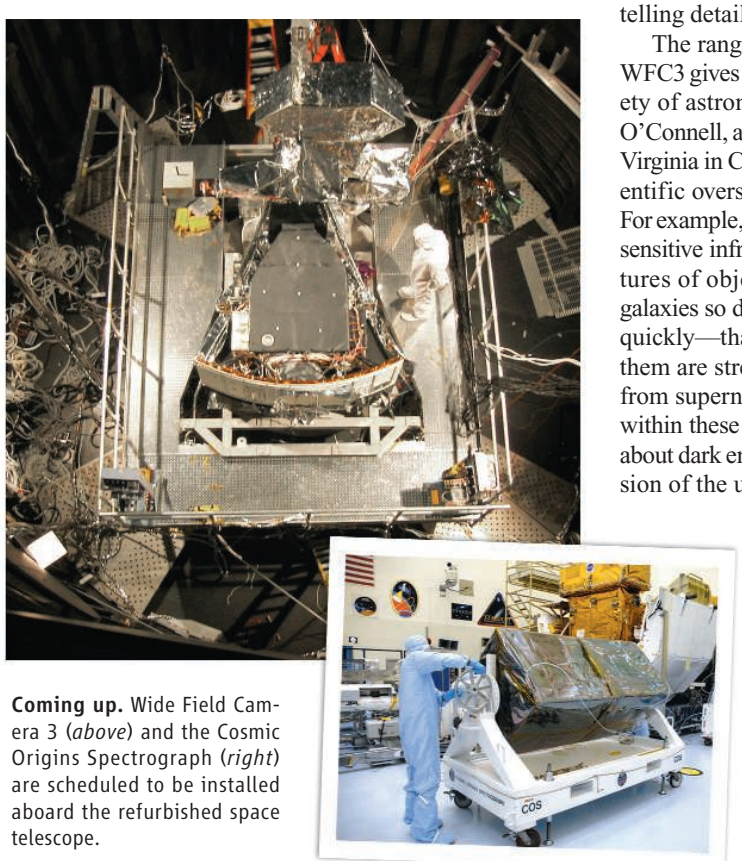

Coming up. Wide Field Camera 3 (*above*) and the Cosmic Origins Spectrograph (*right*) are scheduled to be installed aboard the refurbished space telescope.

Fainter, farther, sharper

The two new instruments being flown to the Hubble are the Wide Field Camera 3 (WFC3), which will replace the existing Wide Field Planetary Camera 2 (WFPC2), and the Cosmic Origins Spectrograph (COS). They will join two instruments on board that astronauts will maneuver to fix after they have installed the new ones. The first is the Advanced Camera for Surveys (ACS), which gave researchers the deepest glimpses yet of the distant universe before an electronics failure put it out of commission in January 2007. The second is the Space Telescope Imaging Spectrograph, which enabled astronomers to find supermassive black holes at the centers of galaxies and fathom the atmosphere of an extrasolar planet until a 5-volt power supply failure froze it in August 2004.

WFC3 is designed to take pictures in wavelengths stretching from the ultraviolet (UV) to the near-infrared region of the electromagnetic spectrum. That will allow it to observe young, hot stars, which glow in the ultraviolet, as well as older and cooler stars, which glow in the infrared. With a wider field of view than the ACS and more-efficient detectors, the camera should be 10 to 30 times more sensitive than previous instruments were: It will see fainter and more distant objects and image nearby galaxies in more telling detail.

The range of observations possible with WFC3 gives it the capability to address a variety of astronomical questions, says Robert O'Connell, an astronomer at the University of Virginia in Charlottesville who chairs the scientific oversight committee for the camera. For example, researchers will be able to use its sensitive infrared channel to get detailed pictures of objects with a very high redshift: galaxies so distant—and receding from us so quickly—that the light waves coming from them are stretched along the way. The light from supernovae or exploding stars spotted within these galaxies should lead to insights about dark energy, whose effect on the expansion of the universe is discernible from the brightness of such supernovae. WFC3's unprecedented sensitivity in the UV region will provide for high-resolution images of stellar populations nearby, which researchers will be able to mine "to learn about the star-formation history" of those galaxies, O'Connell says.

COS is an instrument the size of a snack vending machine, built to observe how UV light from a variety of sources is modified as it passes through the material between galaxies. The most sensitive UV spectrograph ever built for space, it should be able to observe objects 20 times fainter than what was possible with previous Hubble instruments, says J. Michael Shull of the University of Colorado, Boulder, where the instrument was designed. As a result, researchers will now be able to look at light from many more background sources than before, in effect expanding the cosmic vistas that can be probed.

One of COS's goals is to help understand the structure and composition of the cosmic

CREDITS (TOP TO BOTTOM): NASA; NASA/JACK PFALLER

Published by AAAS

Dry run. Astronaut in a neutral-buoyancy tank train to repair the Advanced Camera for Surveys.

A REPRIEVE—AND RISK

It's the ultimate house call. Orbiting 500 kilometers above Earth, astronauts should soon begin the laborious and dangerous task of repairing and renovating the world's most famous telescope. Juggling 60 new tools, wrestling with more than 100 pesky screws, and dodging countless micrometeoroids, the crew of the Atlantis orbiter aims to refurbish the Hubble Space Telescope during five feverish days. "This is no piece of cake," says Edward Weiler, NASA's space science chief. "But there's a huge payoff."

The astronauts' task in orbit, however, is just the tail end of a long and bitter battle. The fight began in 2004, in the wake of the Columbia disaster, when NASA officials decided that returning to the $1.5 billion Hubble posed an unacceptable risk to astronauts and the space shuttle. "That threw the [astronomy] community into a frenzy," recalls Eric Smith, NASA's program scientist for the Hubble. Researchers, he adds, were eager to keep Hubble going until the James Webb Space Telescope (JWST) goes into orbit in the next decade. But without a fifth servicing mission, Hubble was likely to go on the blink by 2007 or 2008.

Scientists were not the only people flummoxed and infuriated by the decision. "The public had a great sense of ownership," Smith recalls. Angry editorials appeared, congressional hearings were called, and then–NASA Administrator Sean O'Keefe was put on the defensive. Efforts to send a robotic mission to upgrade the telescope fell through when high cost and technical risk made it an unrealistic option. O'Keefe eventually resigned, in part, NASA insiders say, because the White House lost faith in him because of the controversy. At the prodding of Congress, his successor, Michael Griffin, reversed the decision in October 2006.

A second shuttle will be poised on the launch pad when Atlantis roars into space, in case a space rescue is necessary. And the crew is experienced: John Grunsfeld flew twice on earlier repair missions to the telescope. The astronauts have been undergoing years of grueling training sessions at Johnson Space Center in Houston, Texas. Along with installing two new instruments (see main text), the crew will replace failed and failing batteries and gyroscopes with new ones designed to allow Hubble to function at least until 2014—a year after JWST is slated to take to the stars. They will also replace Hubble's data formatter, which failed just weeks before a planned October 2008 launch of the Atlantis mission, forcing NASA engineers to postpone the flight by several months while they readied replacement hardware and trained the crew to install it.

The sheer complexity of the task, which will require two more days of spacewalks than previous repairs did, is not the only concern. Hubble flies higher than the space station and is exposed to a greater amount of rocket and satellite debris as well as to micrometeoroids that burn up at lower altitudes. To avoid that space junk, which could puncture the shuttle, the pilot will turn the craft's rugged main engines in the direction most likely to encounter oncoming debris.

If the complex effort proves successful, NASA officials say that it will demonstrate conclusively that humans can play an important role in future robotic missions—what Smith calls "the beautiful dance between man and machine."

–ANDREW LAWLER

web—the cross-linked arrangement of narrow filaments containing the matter that galaxies and planets are made of. Much of this matter—comprising protons, neutrons, and other subatomic particles—is invisible and resides in the gigantic voids between galaxies. Using COS to trace the spectral signature of ionized hydrogen and oxygen in the intergalactic medium, "we are going to map out the filaments of the web to billions of light-years away," says Shull. He adds that the instrument will also enable researchers to study questions such as the chemical composition of some of the earliest stars to form after the big bang and the nature of intergalactic dust clouds.

Pushing the envelope

It's not just the upgrades to the Hubble that astronomers are looking forward to. Many are just as keenly hoping that the scheduled repairs go as planned. Brian Chaboyer, a professor at Dartmouth College, is counting on the replacement of the gyroscopes for his studies of some of the oldest stars in the universe.

Originally designed to operate using three gyros, instruments that help the telescope point and stabilize in space, the Hubble has been using only two since February 2005. Chaboyer says that has been a limitation in accurately determining the distances of old stars. With three gyros working again, he expects to be able to "push the envelope on accuracy," going down from a 10% margin of error to within 3% to 4%. It makes a big difference: "The current error can mean plus or minus 2 billion years for the age of the star," he says. The improved accuracy can help better address questions related to the formation of early galaxies, for instance, "if there was a window of 2 [billion] to 3 billion years when stars were forming all over the place," Chaboyer says.

François Schweizer, an astronomer at the Carnegie Observatories in Pasadena, California, is keeping his fingers crossed about the repairs to ACS. He needs that camera to resume studying NGC 7252, the remnant of a merger between two galaxies. On the basis of earlier observations with the WFPC2, the camera scheduled to be taken off the Hubble during this mission, Schweizer and colleagues reported in 2003 that NGC 7252 had some extraordinarily massive young star clusters. High-resolution imaging of the clusters with ACS, they hoped, would help them understand how clusters form and evolve in the merger of galaxies. But ACS failed before the researchers could get their chance.

Schweizer and his colleagues have again been granted observing time with ACS, whose spatial resolution—unmatched even by WFC3—is essential for the planned study. "The catch is that it's the very last scheduled repair. Every planned fix will have to be carried out successfully before it happens," he says. "As you can imagine, all members of our team are keeping their fingers crossed."

NASA officials are optimistic. "The fully restored instruments, along with the new ones, will give the astronomical community a marvelous machine to exploit its creativity," says Smith. "The science we expect to get will be great, but the science we didn't forecast will change the way we think about the universe forever."

–YUDHIJIT BHATTACHARJEE

CREDITS (TOP TO BOTTOM): NASA; NASA

Published by AAAS

Dive In!

With MISSION® esiRNA genome-wide libraries

SIGMA Life Science

NEW! MISSION esiRNA (Endoribonuclease-prepared siRNA) provides RNAi researchers with a proven, cost-effective, and simple way to perform RNAi screens. MISSION esiRNA are available for genome-wide libraries, custom libraries, and individual genes.

- **Value** – Dive in today with affordable genome-wide libraries
- **Proven** – esiRNA have been successfully used in a variety of published RNAi screens
- **Confidence** – Highly specific and reduced off-target effects
- **Simplify** – Rapid genome-wide primary screens

Dive into screening and leave the rest to us. Visit ***sigma.com/esirna***

Our Innovation, Your Research — Shaping the Future of Life Science

Why so cruel? 726

Rice and millet domestication 730

Invasion strategies 734

LETTERS | BOOKS | POLICY FORUM | EDUCATION FORUM | PERSPECTIVES

LETTERS

edited by Jennifer Sills

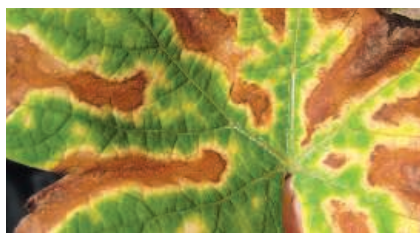

Vines at risk. Symptoms of grapevine trunk disease.

The Spread of Grapevine Trunk Disease

THE GRAPEVINE DIEBACK DISEASES, ALSO CALLED GRAPEVINE TRUNK diseases, are the consequences of a complex of fungi that was described as early as the end of the 20th century. They attack the perennial organs of a vine and ultimately lead to the death of the plant. Over the past decade, the frequency of symptoms due to these fungi has considerably increased worldwide. For example, cumulated disease incidence values estimated for Italian vineyards may reach up to 50% (*1*). The lack of resources to fight the diseases and favorable environmental conditions worsen the situation. Sodium arsenic is the only treatment that has a potential effect against dieback diseases, but it has been prohibited in some countries. Some vineyards that have never been treated with sodium arsenic now present an exponential development of symptoms. Why are these symptoms emerging today? Are they due to changes in the vine behavior, in the climate, or in the microbial equilibrium, or are they due to undiagnosed pathogens? Despite all the studies on the fungi associated with the disease, on the host-pathogen interactions, and on the symptoms, the actual causes for their development are still elusive.

CHRISTOPHE BERTSCH,[1]* PHILIPPE LARIGNON,[2] SIBYLLE FARINE,[1] CHRISTOPHE CLÉMENT,[3] FLORENCE FONTAINE[3]

[1]Laboratoire Vigne Biotechnologie et Environnement, Université de Haute-Alsace, UFR Pluridisciplinaire Enseignement Professionnalisant Supérieur, 68000 Colmar, France. [2]Institut Français de la Vigne et du Vin (ENTAV-ITV France) Pôle Rhône-Méditerranée, France, Domaine de Donadille, 30230 Rodilhan, France. [3]Laboratoire de Stress, Défenses et Reproduction de Plantes URVVC EA 2069, Université de Reims Champagne-Ardenne, UFR Sciences Moulin de la Housse, 51687 Reims cedex 2, France.

*To whom correspondence should be addressed. E-mail: christophe.bertsch@uha.fr

Reference

1. G. Surico, L. Mugnai, G. Marchi, *Phytopathol. Mediterr*. **45**, S68 (2006).

Eutrophication: More Nitrogen Data Needed

WE AGREE WITH D. J. CONLEY *ET AL*. ("CONtrolling eutrophication: Nitrogen and phosphorus," Policy Forum, 20 February, p. 1014) that there are many compelling reasons for controlling agricultural and industrial sources of nitrogen. In many areas, nitrate and ammonium are now the main pollutants causing damage by acidification and base cation depletion in forests and freshwaters (*1*). In some areas, nitrate concentrations in drinking water have increased enough to exceed health standards (*2*). However, at this time, we cannot agree that reducing nitrogen is essential for controlling eutrophication, because there are insufficient whole ecosystem-scale data to show that removing nitrogen will reduce eutrophication.

Phosphorus control alone has succeeded in reducing eutrophication in many lakes [reviewed by (*3*)] and in at least one low-salinity estuary (*4*). In contrast, not a single ecosystem-scale study in any aquatic system has shown that reducing inputs of nitrogen decreases eutrophication.

The authors state that reducing phosphorus inputs has not reduced eutrophication in some lakes and many estuaries. In most cases, the reason is high "internal loading" of phosphorus from anoxic sediments. High concentrations of phosphorus and anoxia in surface sediments are the result of decades of high phosphorus loading causing increased settling and decomposition of organic matter. However, long-term studies of lakes in Europe (*5*, *6*) have shown that internal loading decreases slowly after external sources of phosphorus are controlled, so that ecosystems recover over a period of years to decades.

Many of the arguments put forward by Conley *et al*. are based on physiological or short-term indices of nitrogen limitation, which we have found to be spurious in our long-term, whole-lake manipulations. Simply put, over time algal and bacterial communities change to include species that fix nitrogen when fixed nitrogen limits the growth of other species. Small but long-term inputs of nitrogen through fixation and subsequent return from sediments eventually correct nitrogen deficits in ecosystems (*7*, *8*). The importance of these long-term, adaptive processes cannot be evaluated by short-term incubations or dissolved nutrient concentration ratios (*9*).

Conley *et al*. state that the nitrogen-fixing cyanobacteria that are capable of correcting ecosystem-scale nitrogen deficiencies in lakes are absent in saline estuaries. However, recent measurements of N_2/Ar ratios indicate that there is considerable N fixation by bacteria and phytobenthos in shallow, saline estuaries (*10*, *11*). Rates of fixation are similar to those that we have observed in lakes (*8*), and we anticipate similar results in overcoming N deficiencies. In fact, in whole systems, N removal accomplished at great expense in wastewater treatment may be offset by N fixation in natural open systems (*8*).

Globally, reducing inputs of nitrogen from sewage as well as phosphorus would require

Letters to the Editor

Letters (~300 words) discuss material published in *Science* in the previous 3 months or issues of general interest. They can be submitted through the Web (www.submit2science.org) or by regular mail (1200 New York Ave., NW, Washington, DC 20005, USA). Letters are not acknowledged upon receipt, nor are authors generally consulted before publication. Whether published in full or in part, letters are subject to editing for clarity and space.

CREDIT: CHRISTOPHE BERTSCH, UNIVERSITÉ DE HAUTE ALSACE

spending many billions of dollars. The costs of removing both nutrients may even discourage any treatment in developing countries, particularly in the current economic depression. We believe that before the additional expense of nitrogen removal from sewage is to be imposed on society, it should first be demonstrated at ecosystem scales to effectively reduce eutrophication.

D. W. SCHINDLER[1]* AND R. E. HECKY[2]

[1]Department of Biological Sciences, University of Alberta, Edmonton, AB T6G 2E9, Canada. [2]Department of Biology, University of Minnesota-Duluth, Duluth, MN 55812, USA.

*To whom correspondence should be addressed. E-mail: d.schindler@ualberta.ca

References

1. S. A. Watmough, P. J. Dillon, *For. Ecol. Manage.* **177**, 155 (2003).
2. B. T. Nolan, K. J. Hitt, B. C. Ruddy, *Environ. Sci. Technol.* **36**, 2138 (2002).
3. D. W. Schindler, J. R. Vallentyne, *The Algal Bowl: Overfertilization of the World's Freshwaters and Estuaries* (Univ. of Alberta Press, Edmonton, AB, 2008).
4. G. Brattberg, *Vatten* **42**, 141 (1986).
5. I. Ahlgren, *Verh. Internat. Verein Limnol*. **20**, 846 (1978).
6. E. Søndergaard, E. Jeppesen, J. P. Jensen, T. Lauridsen, *Lakes Reservoir Res. Manage.* **5**, 151 (2000).
7. D. W. Schindler, R. H. Hesslein, M. A. Turner, *Can. J. Fish. Aquat. Sci.* **44** (suppl. 1), 26 (1987).
8. D. W. Schindler *et al.*, *Proc. Natl. Acad. Sci. U.S.A.* **105**, 11254 (2008).
9. R. E. Hecky, P. Kilham, *Limnol. Oceanogr.* **33**, 796 (1988).
10. R. W. Fulweiler, S. W. Nixon, B. A. Buckley, S. L. Granger, *Nature* **448,** 180 (2007).
11. W. S. Gardner *et al*., *Limnol. Oceanogr.* **51**, 558 (2006).

Eutrophication: Focus on Phosphorus

THE POLICY FORUM BY D. J. CONLEY *ET AL*. ("Controlling eutrophication: Nitrogen and phosphorus," 20 February, p. 1014) advocates expensive and unnecessary nitrogen (N) control in lakes.

Many demonstrations of successful phosphorus (P)–only control in lakes are found in the literature (*1*). In the 1970s, P control was implemented in the Laurentian Great Lakes, an important North American freshwater source (*2*). Total P (TP) in Lake Ontario decreased to half the maximum in response to P management and by half again after zebra mussel invasion, reducing phytoplankton standing crop and shoreline nuisance blooms of Cladophora. The lower phytoplankton N demand alleviated nitrate shortages. Thus, Lake Ontario was a real-time experiment to validate P control as a means to manage eutrophication.

I take exception to Conley *et al*.'s prediction that P-only reduction strategies will fail in Lake Apopka. Sediments deposited since 1947 provide the basis for estimating whole-lake historic TP sedimentation (*3*). The sediment inventory shows average annual deposition of 0.367 g TP m^{-2} $year^{-1}$ (1947 to 1996). Some TP, however, was in a form that is not readily recycled (*4*, *5*). External loading averaged 0.55 g TP m^{-2} $year^{-1}$ in the 1990s when water-column TP was 0.320 g TP m^{-2} (*6*). The large TP sediment sink and short TP residence time in the water column indicate that sediment recycling is low (*6*). Therefore, strategies that control external P loading will control eutrophication over time.

CLAIRE L. SCHELSKE

Department of Geological Sciences, Land Use and Environmental Change Institute, University of Florida, Gainesville, FL 32611–2120, USA. E-mail: schelsk@ufl.edu

References

1. E. Jeppesen *et al*., *Freshw. Biol*. **50**, 1747 (2005).
2. C. L. Schelske, E. F. Stoermer, W. F. Kenney, *Limnol. Oceanogr*. **51**, 748 (2006).
3. C. L. Schelske, *Limnol. Oceanogr*. **51**, 2472 (2006).
4. W. F. Kenney, C. L. Schelske, A. D. Chapman, *Can. J. Fish. Aquat. Sci.* **58**, 879 (2001).
5. K. E. Havens, C. L. Schelske, *Environ. Pollut.* **113**, 1 (2001).
6. M. F. Coveney, E. F. Lowe, L. E. Battoe, E. R. Marzolf, R. Conrow, *Freshw. Biol*. **50**, 1718 (2005).

Eutrophication: Model Before Acting

IN A RECENT POLICY FORUM ("CONTROLLING eutrophication: Nitrogen and phosphorus," 20 February, p. 1014), D. J. Conley *et al*. made a controversial case for a dual nutrient-reduction strategy to address eutrophication in lakes, estuaries, and coastal areas.

We believe that all asserted beneficial effects must be robustly predictable to ensure that society actually gets something in return for this effort, given the high cost of nutrient reductions. For instance, Swedish nitrogen (N) reductions in a very ambitious abatement plan for the Baltic Sea may not be possible to fulfill unless a large part of Swedish agriculture is permanently shut down, according to recent calculations by the Swedish Department of Agriculture (*1*).

Unfortunately, there are no general, validated mass-balance models for nitrogen that have been tested for independent coastal systems and been demonstrated to yield good predictive power. Any N model can be tuned, using different calibration constant sets for different systems, to give perfect descriptive power. However, such tuning may obscure the true aspects of a natural system (*2*). In addition, the effects of N abatement on many coastal areas have been quite disappointing (*3*).

There is one general dynamic phosphorus (P) model (thus far) that has yielded good predictions of phosphorus and chlorophyll in all Baltic Sea basins without basin-specific tuning and without taking N concentrations into account. The abatement strategy for the Baltic Sea should therefore focus on cost-effective P reductions, such as urban sewage treatment (*2*). Strategies designed for other estuaries, coastal areas, and lakes should also be based on methods with documented cross-systems predictive power.

ANDREAS C. BRYHN* AND LARS HÅKANSON

Department of Earth Sciences, Uppsala University, Uppsala SE-752 36, Sweden.

*To whom correspondence should be addressed. E-mail: andreas.bryhn@geo.uu.se

References

1. Swedish EPA, Report 5830 (Stockholm, 2008).
2. L. Håkanson, A. C. Bryhn, *Eutrophication in the Baltic Sea* (Springer, Berlin, 2008).
3. C. M. Duarte *et al*., *Estuaries Coasts* **32**, 29 (2009).

Eutrophication: Time to Adjust Expectations

D. J. CONLEY *ET AL*. ("CONTROLLING EUTROphication: Nitrogen and phosphorus," Policy Forum, 20 February, p. 1014) advocate a shift in strategies to control eutrophication of aquatic systems. We agree that the best hope for success rests with strategies couched in a systems perspective and founded on an understanding of interactions among biogeochemical cycles.

Current efforts to control eutrophication focus on repairing past damage, with systems expected to return to a desired state after obvious stressors are reduced. One approach is to restrict nutrient inputs to waterbodies that are declared impaired by limiting total maximum daily loads. Although costly, managing anthropogenic loads of macronutrients represents an essential, sensible, and feasible strategy for controlling eutrophication and reversing its effects. Increased loads of nutrients drive, support, or enable eutrophication.

Reducing loads of macronutrients, including simultaneous reductions for nitrogen and

phosphorus, may not yield desired responses. Beyond lags due to "legacy loads," systems may not return to undamaged states along desired trajectories if they have entered alternative stable states or baseline conditions have shifted (*1*–*3*). For example, ocean acidification may prevent corals from regaining ascendancy on reefs, and impacts from overfishing may cascade through trophic webs to create stable but undesirable assemblages of consumers and producers. In such cases, reversing eutrophication may require restoration of habitats, repair of trophic webs, or relatively drastic projects that remove accumulated effects and thus shift systems toward previous states. In some cases, our best efforts may not produce systems that are structurally identical to a previous, desired state, so we will have to settle for restoring dynamic functions that consistently yield desired services (*1*, *2*).

Sustainable control of eutrophication in aquatic systems requires all stakeholders to acknowledge our inability to predict the exact trajectory followed by any particular ecosystem in response to management interventions, including reduced loads of nitrogen and phosphorus. Stakeholders can foster success by embracing an adaptive approach supported by monitoring that evaluates alternative actions and endpoints, promotes continual learning, and fosters progressive improvement (*4*).

CHARLES A. JACOBY* AND THOMAS K. FRAZER

School of Forest Resources and Conservation, University of Florida, Gainesville, FL 32653, USA.

*To whom correspondence should be addressed. E-mail: cajacoby@ufl.edu

References

1. C. S. Holling, *Ann. Rev. Ecol. Sys*. **4**, 1 (1973).
2. C. M. Duarte, D. J. Conley, J. Carstensen, M. Sánchez-Camacho, *Estuaries Coasts* **32**, 29 (2009).
3. A. V. Norström, M. Nyström, J. Lokrantz, C. Folke, *Mar. Ecol. Prog. Ser*. **376**, 295 (2009).
4. C. S. Holling, *Adaptive Environmental Assessment and Management* (Wiley, New York, 1978).

Response

WE ARE GRATIFIED THAT OUR POLICY FORUM has stimulated numerous responses on effective strategies for controlling phosphorus (P) and nitrogen (N) to reduce eutrophication in freshwater and coastal marine ecosystems.

Rigid application of P control—the only paradigm proffered by Schindler and Hecky—has been increasingly called into question even for lakes (*1*, *2*) and was rejected long ago for estuarine and coastal waters for the reasons discussed in our Policy Forum. The paradigm depends on sufficient N_2 fixation by cyanobacteria to meet the demands of algal growth that could be supported by the available P. While this is not always reached even in lakes (*1*, *2*), quantitatively significant N_2 fixation simply does not occur in the water columns of coastal ecosystems except, as we pointed out, under low-salinity conditions found in the more freshwater portions of estuaries and the Baltic Sea. The evidence cited by Schindler and Hecky for estuaries is for N_2 fixation in bottom sediments, which is seldom important in the N economy of estuarine ecosystems.

Although demonstration at the whole-ecosystem scale advocated by Schindler and Hecky is powerful, it is not usually possible to intentionally make whole-ecosystem experiments in marine systems. Nonetheless, there is substantial evidence of N limitation in coastal marine ecosystems at the whole-ecosystem and large-mesocosm scale (*3*). In fact, the example by Schindler and Hecky of P control alone succeeding in reducing eutroph-

Published by AAAS

ication in a low-salinity estuary, the Stockholm Archipelago, is only half of the story. Phytoplankton chlorophyll levels further declined after the waste treatment facilities substantially removed N (*4*).

Schelske's basic points are similar to those of Schindler and Hecky, namely, that N_2 fixation can alleviate N shortages for phytoplankton and that there have been many demonstrations of successful P-only control in lakes, such as in some of the Laurentian Great Lakes. Unfortunately, such P-only control has not been universally effective. In fact, the very reference Schelske provides to support the success of P-only control noted that it is important to consider not only P but also N loading (*5*). Shallow hyper-eutrophic lakes such as Lake Apopka frequently have blooms of cyanobacteria that do not fix N_2 and have not responded to P-load reduction, probably because of the large internal recycling of P from sediments. Schelske's calculations consider only external P loading and ignore P remobilization from sediments.

We agree with Bryhn and Håkanson that P reductions are required for improvements to be observed in the Baltic Sea; however, we differ in the need for N reductions. Their model is only for P because they believe that it is not possible to construct adequate models for nitrogen mass-balances, despite the fact that N models are common. Their model parameterization for P cycling is unusual—the boundary conditions are very different from other models used in the Baltic Sea, and their conclusions differ substantially as well (*6*–*8*), bringing into question their validity.

Jacoby and Frazer agree with us that both P and N controls should be considered, but stress that this might not yield desired responses because the damaged ecosystems may have shifted to alternative stable states. This issue fell beyond the scope of our short Policy Forum, but we have addressed it elsewhere (*9*). We certainly agree that this makes the exact recovery trajectory somewhat unpredictable and requires an adaptive approach, the first step of which is aggressive control of nutrient loads based on a rational and context-specific two-nutrient strategy.

DANIEL J. CONLEY,[1]* HANS W. PAERL,[2] ROBERT W. HOWARTH,[3] DONALD F. BOESCH,[4] SYBIL P. SEITZINGER,[5] KARL E. HAVENS,[6] CHRISTIANE LANCELOT,[7] GENE E. LIKENS[8]

[1]GeoBiosphere Science Centre, Department of Geology, Lund University, Sölvegatan 12, SE-223 62 Lund, Sweden. [2]Institute of Marine Sciences, University of North Carolina at Chapel Hill, Morehead City, NC 28557, USA. [3]Department of Ecology and Evolutionary Biology, Cornell University, Ithaca, NY 14853, USA. [4]University of Maryland Center for Environmental Science, Cambridge, MD 21613, USA. [5]International Geosphere-Biosphere Programme, Royal Swedish Academy of Sciences, SE-104 05 Stockholm, Sweden. [6]Florida Sea Grant, University of Florida, Gainesville, FL 32611, USA. [7]Ecologie des Systèmes Aquatiques, Université Libre de Bruxelles, B1050 Brussels, Belgium. [8]Cary Institute of Ecosystem Studies, Millbrook, NY 12545, USA.

*To whom correspondence should be addressed. E-mail: daniel.conley@geol.lu.se

References

1. W. M. Lewis Jr., W. A. Wurtsbaugh, *Int. Rev. Hydrobiol.* **93**, 446 (2008).
2. R. W. Sterner, *Int. Rev. Hydrobiol.* **93**, 433 (2008).
3. R. W. Howarth, R. Marino, *Limnol. Oceanogr.* **51**, 364 (2006).
4. D. Boesch, R. Hecky, C. O'Melia, D. Schindler, S. Seitzinger, *Eutrophication of Swedish Seas* (Rep. 5509, Naturvårdverket, Stockholm, 2006).
5. E. Jeppesen *et al.*, *Freshw. Biol.* **50**, 1747 (2005).
6. G. Schernewski, T. Neumann, *J. Mar. Syst.* **53**, 109 (2005).
7. H. Pitkänen *et al.*, *Ambio* **36**, 272 (2007).
8. F. Wulff *et al.*, *Ambio* **36**, 243 (2007).
9. C. M. Duarte, D. J. Conley, J. Carstensen, M. Sánchez, *Estuaries Coasts* **32**, 29 (2009).

Published by AAAS

PSYCHOLOGY

Human Inhumanity

Prashanth Ak

As Amnesty International's annual reports testify, the historical connection of cruelty to the exercise of political power persists. Despite its ubiquity and unparalleled contribution to human and animal misery, cruelty has not received the scholarly attention it deserves (*1*). One reason for this state of affairs is the difficulty of defining cruelty in an objective sense, easy though it is to spot. Like pornography, one more or less knows it when one sees it. But letting the beholder subjectively decide what counts as cruel is quite unsatisfactory—Bertrand Russell found himself "incapable of believing that all that is wrong with wanton cruelty is that I don't like it" (*2*).

In *Cruelty*, Kathleen Taylor aims to examine the topic comprehensively. She purports to address weighty questions, with chapter titles such as "What is cruelty?" "Why does cruelty exist?" "Why are we callous?" "Can we stop being cruel?"

Taylor formulates cruelty as "unjustified behaviour which intentionally causes undeserved suffering." She sets the demand for precision aside for a "more-or-less" conception, commenting in an endnote that "[f]uzzy blobs rather than tidy packets is certainly what our understanding of neuroscience, with its emphasis on probability, suggests we should expect." Unfortunately, this confusing start is not an anomaly, and the chapters (except for that on sadism) don't offer particularly insightful or comprehensive explorations of their titular questions.

The author attempts to parse cruelty into components (beliefs, emotions, and actions) and mechanisms such as threat responses and "otherization" (her term for people's spiraling hostility toward the "inferior outgroup"). Taylor considers these aspects using neuroscience and psychology. However, the neuroscience she presents is only vaguely relevant and not detailed enough to provide a scientific grip on cruelty's various manifestations; rather, it remains at a popular science level. Also contributing to a sense of cursory treatment are a few too many parenthetical asides and a breezy journalistic tone (e.g., "To get a deeper view of cruelty, therefore, means plunging our attention into a sea of neurons, the soggy, fatty mass from which cruelty is born").

Addressing cruelty from multiple perspectives, including moral and evolutionary ones, the book does accord a complex subject its due. A good, quick read, it successfully outlines the topic. But given the book's ambitious scope and extensive references—ranging from Aeschylus to Zimbardo (of "Stanford prison experiment" fame)—a more serious treatment would have provided a valuable multidisciplinary reference for scholars addressing cruelty from a range of fields. A few examples notwithstanding, a body of empirical work on cruelty doesn't currently exist. A more comprehensive account could have contributed usefully to setting a research agenda.

Nonetheless, simply by its existence, the book should help raise cruelty as a topic worthy of serious research interest. It should be possible to begin scientific examination of at least some types of cruelty in terms of their underlying mechanisms. For example, certain facets of cruelty share features with addictive behavior. The wide range of dopamine-driven behaviors related to addiction means these could include cruel actions. From such general facts, we can speculate on possible neural bases of why and how particular forms of cruelty are triggered or how they fulfill their perpetrators, and these hypotheses could serve as starting points for neuroscience research.

As with other complex human behaviors, the composite meanings and varying cultural, sociological, and moral values layered on cruelty make it likely that empirical findings regarding the mechanisms will only be part of the story. Even so, such findings will contribute knowledge that could help societies and individuals deal with cruelty. Then, however, a sobering lot would depend on how that knowledge might be used or who will apply that knowledge to control whom.

Before delving into the neuroscientific basis of cruelty (or anything else, for that matter) and its mechanisms, one wants to have a clear, rigorous intellectual framework that will allow the formulation of precise, experimentally tractable questions. No such framework currently exists for cruelty. As political scientist Judith Shklar pointed out in her classic essay "Putting Cruelty First" (*3*), philosophers have generally avoided the topic—as, surprisingly, have political theorists. In general, academic (especially American) discourse, which holds dear enlightenment notions of an inexorable march to perfection, has not focused on the darker recesses of the human condition, other than to treat them as (regrettable) anomalies. The typical approach has been to pathologize problematic behaviors, removing them from the ambit of normalcy. Surprisingly few citations to cruelty occur in scholarly literature; many that do are with reference to sadism. In older anthropology literature, cruelty was often discussed in connection with "savages," who were supposed to possess an abundance of it.

Cruelty
Human Evil and the Human Brain
by Kathleen Taylor
Oxford University Press, New York, 2009.
349 pp. $34.95, £16.99.
ISBN 9780199552627.

Outside the academy, cruelty continues to exert its powerful hold on popular and intellectual imagination, as glances at contemporary fiction, film, video games, and the Web will attest. In premodern societies, public occasions or festivals routinely included displays of torture, an execution or two, or other spectacles of cruelty—one of the oldest festive joys of mankind, as Nietzsche labeled it. Today, "cruelty-free" has entered our vernacular, if only in reference to consumer products. Hopefully, *Cruelty*, with Taylor's timely highlighting of the topic, will encourage fresh thought on an issue that continues to be central to human existence.

References and Notes

1. An exception is work by Lucien Febvre [e.g., (*4*)].
2. B. Russell, *Russell on Ethics*, C. R. Pigden, Ed. (Routledge, London, 1999).
3. J. N. Shklar, *Daedalus* **111** (3), 17 (1982).
4. L. Febvre, *Ann. Hist. Soc.* **3**, 5 (1941).

The reviewer is at the Center for Systems Biology, Institute for Advanced Study, 1 Einstein Drive, Princeton, NJ 08540, USA. E-mail: prashanth@ias.edu

10.1126/science.1173430

MEDICINE

A History Lesson for Stem Cells

Factors that led to the decline of gene therapy at the turn of the century should be considered by the stem cell community to avoid a similar outcome.

James M. Wilson

When President Barack Obama signed an Executive Order on 9 March 2009 rolling back the previous administration's restrictions on federal funding of human embryonic stem cell (hESC) research, he took pains to temper Americans' hopes for quick fixes. "At this moment, the full promise of stem cell research remains unknown and it should not be overstated," the president said. "I cannot guarantee that we will find the treatments and cures we seek" (*1*). Unfortunately, some stakeholders in hESC research have failed to exhibit the same restraint, effectively promising cures for Parkinson's disease, Alzheimer's disease, spinal cord injuries, diabetes, cancer, heart disease, multiple sclerosis, muscular dystrophy, macular degeneration, and hearing loss, to name a few.

Studies of hESCs and their non–embryo-derived counterparts, induced pluripotent stem (iPS) cells, will likely deepen our understanding of cell differentiation, human development, and birth defects. Hopefully they will also lead to novel therapeutics for some diseases, and I applaud President Obama for giving scientists longer leashes as they explore this exciting field. But in today's clamor of stem cell enthusiasm it is possible to detect haunting echoes of the early and ultimately troubled days of gene therapy.

The field of gene therapy began with laboratory studies in the mid- to late-1980s and grew linearly during the 1990s (see figure, right). Very early in this evolution, clinical trials were initiated, and their number and overall patient recruitment figures grew in step with the science. During that period, gene therapy was touted as a potential cure for a huge array of ailments. By 2000, researchers had launched more than 400 clinical trials, testing the approach against a wide spectrum of illnesses. Yet the Food and Drug Administration concluded in a September 2000 review, "the hyperbole has exceeded the results" and "little has worked" (*2*). Although the field has improved since then, with notable successes against inherited blindness (*3*–*5*) and immune deficiency (*6*), those successes are shadowed by several tragic adverse events, including treatment-induced cancers in some volunteers (*7*) and, in 1999, the death of an 18-year-old, Jesse Gelsinger, in a gene therapy clinical trial that I led (*8*). Gelsinger's death initiated a chain of events that seriously derailed the field.

It would be unfortunate if the field of hESC research missed this lesson from history and took a similar trajectory. Yet many of the social and economic forces that drove gene therapy's burst of clinical activity also exist today in the stem cell arena. Without passing judgment on the scientific merits of any individual clinical study or plan, I am concerned that expectations for the timeline and scope of clinical utility of hESCs have outpaced the field's actual state of development and threaten to undermine its success.

The hyperaccelerated translation to the clinic that occurred in the field of gene therapy in the 1990s was driven by multiple factors, including: (i) a straightforward, if ultimately simplistic, theoretical model indicating that the approach "ought to" work; (ii) a large population of patients with disabling or lethal diseases and their affiliated foundations harboring fervent hopes that this novel therapy could help them; (iii) unbridled enthusiasm of some scientists in the field, fueled by uncritical media coverage; and (iv) commercial development by the biotechnology industry during an era in which value and liquidity could be achieved almost entirely on promise, irrespective of actual results.

In response to growing concerns that the field was getting ahead of itself, Harold Varmus, then director of the National Institutes of Health (NIH), convened a panel in 1995 chaired by Stuart Orkin and Arno Motulsky to "assess the NIH investment in research on gene therapy" (*9*). Prime among the committee's conclusions was that scientists' basic understandings of gene-transfer vectors and host-vector interactions were inadequate to support successful clinical development of the field and that stakeholders had oversold their results. Indeed, the panel concluded that "only a minority" of clinical studies had been designed in ways likely to yield "useful basic information." The report recommended that researchers get back to basics and develop a

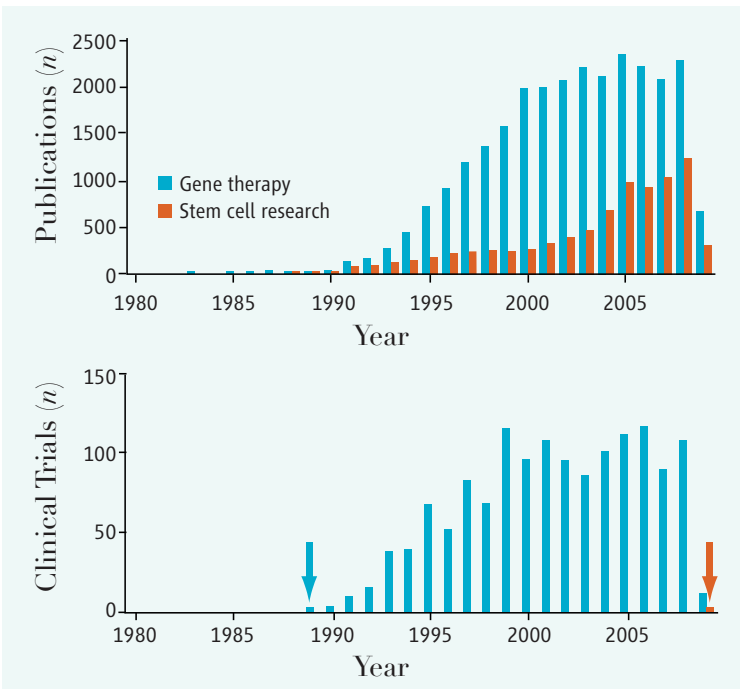

Publications and clinical trials (1980–2009) related to gene therapy and hESCs. (Top) Publication data were retrieved from ISI Web of Knowledge (www.isiknowledge.com). Gene therapy publications include English language articles or reviews retrieved by using the search terms "gene therapy." ESC publications include English language articles or reviews found by using the search terms "embryonic stem cell," "ES cells," or "ESC." (Bottom) Gene therapy clinical trial data was extracted from Gene Therapy Clinical Trials Worldwide (*15*). ESC clinical trial projected start date taken from (*16*). Data for 2009 are incomplete. Arrows indicate the point when clinical trials started for gene therapy and are projected to begin for hESC.

University of Pennsylvania, Philadelphia, PA 19104, USA; e-mail: wilsonjm@mail.med.upenn.edu

more robust understanding of gene transfer in animals.

The researchers continued to pursue clinical trials aggressively. And the hype continued until the turn of the century when a confluence of events—the tragic and widely publicized death of Jesse Gelsinger, questions regarding regulatory oversight of gene therapy, bursting of the overall biotech bubble, and stakeholder impatience due to unmet expectations—led to a precipitous decline in financial and public support.

The central concern of the Orkin-Motulsky panel, a lack of scientific understanding about vectors and vector-host interactions, proved to be on the mark. Virtually every major unexpected toxicity encountered in gene therapy clinical trials can be attributed to complex interactions between vector and host that were not predicted by, or understood at the time of, preclinical studies. Learning from these travails, the gene therapy community eventually adopted a more sober approach to clinical trials and bolstered its commitment to basic vector biology and disease pathogenesis.

Many of the factors that fueled gene therapy's premature expansion are major drivers of the hESC and iPS research agenda today. A large and vocal population of patients suffering from a wide variety of ailments is pressing for stem cell–based therapies. Disease-specific stem cell research groups are more politically sophisticated than ever, in some cases employing congressional lobbyists. Unrealistic expectations have been fueled by relentless media coverage, driven in part by a factor not present in the gene therapy roll-out: a debate over the ethics of research on human embryos and embryo cells, which has served as a "news hook" that brings media attention to even the most incremental of advances.

It is difficult to avoid getting caught up in the unabashed enthusiasm that attends the emergence of a novel, but untested, therapeutic technology platform, as I myself experienced. Still, January's media coverage of the first U.S. Food and Drug Administration (FDA) approval of a hESC-related clinical trial—an experiment sponsored by Geron Corporation of Menlo Park, California, aimed at spinal cord injuries—was surprising for its lack of restraint. News reports characterized Geron's mere gaining of federal permission to test the cells in patients as a "breakthrough" (*10*). And in a highly questionable move, *Good Morning America* accompanied its news report with faux video footage depicting the paralyzed actor Christopher Reeve getting out of his wheel chair and walking again (*10*).

Proponents of clinical trials can argue that by some measures, at least, the stem cell field is further along than gene therapy was when clinical studies began in 1990. More papers have been published on the basic biology of hESCs than were published on gene therapy before that field's first clinical trials (see figure on page 727). Furthermore, we have witnessed during the last 2 years a multitude of discoveries in the basic cell biology of stem cells.

Despite advances, our understanding of the biology of hESCs and iPS cells remains thin with regard to clinical safety and utility. Controlled incorporation of transplanted stem cells into host tissues and organs remains a major challenge. Questions about engraftment, rejection, and toxicity abound. Steps involved in transformation of hESCs, iPS cells, or their derivatives into tumor cells (and strategies to ablate any tumors that might arise) need further investigation. In February, researchers in Israel reported that a 13-year-old boy with ataxia telangiectasia who had received injections of human fetal neural stem cells into his brain as part of an experimental treatment performed in a Russian clinic developed brain tumors apparently derived from the injected stem cells (*11*).

The purpose of raising these issues is not to undermine policy changes now under way at the National Institutes of Health that aim to increase support for basic stem cell studies. Such basic studies are exactly the kind that must be done if embryonic or iPS cells are to move responsibly into the clinical arena. The key question is how can stem cell therapeutics avoid the pitfalls encountered in clinical gene therapy research?

Excellent preclinical regulatory review is key, of course, and, for example, Geron's cells are different from those used in the Russian study and have withstood rigorous FDA analysis. Professional societies, such as the recently established International Society for Stem Cell Research (ISSCR), can also play an important role in steering this young discipline in the right direction. Leadership of the society must steadfastly discourage overselling the clinical reality of stem cell therapeutics (*12*) and must effectively communicate how long it takes to go from laboratory bench to bedside. To get ahead of the impending avalanche of clinical trial proposals using hESC- and iPS-derived cells, the society has promulgated thoughtful and comprehensive guidelines for clinical translation (*13*). However, adherence to these guidelines is voluntary because the society does not have regulatory authority.

A high degree of transparency is also necessary to secure the public's trust and support. This was accomplished in gene therapy through the Recombinant DNA Advisory Committee (RAC) of the NIH, to which adverse events had to be reported and whose deliberations, though nonbinding, were open to the public. After the reports of Jesse Gelsinger's death, gene therapy's public image suffered further when news stories revealed that a number of researchers had failed to report adverse events to the RAC as required. The NIH should consider the potential value of a RAC-like board for the early generations of stem cell–related clinical trials (*14*)—not to add an extra layer of pre-clinical review to that already done by FDA, but to oversee a public registry of clinical trials and to serve as an open forum for addressing novel trial-related issues. The board should also consider whether some of the ISSCR's recommendations on clinical trials should be codified in NIH guidelines.

It is gratifying that through its current crafting of new funding guidelines and the launching of new initiatives (*17*), the NIH is making basic stem cell research a high priority. But, I encourage hESC and iPS researchers to remember the Orkin-Motulsky report's central theme: that no one is served by bypassing the hard work of basic research and experiments in animal models.

References and Notes

1. B. H. Obama, memorandum, www.whitehouse.gov/the_press_office/Remarks-of-the-President-As-Prepared-for-Delivery-Signing-of-Stem-Cell-Executive-Order-and-Scientific-Integrity-Presidential-Memorandum/.
2. L. Thompson, *FDA Consum.* **34**(5), 19 (2000); www.fda.gov/Fdac/features/2000/500_gene.html.
3. W. W. Hauswirth *et al.*, *Hum. Gene Ther.* **19**, 979 (2008).
4. J. W. Bainbridge *et al.*, *N. Engl. J. Med.* **358**, 2231 (2008).
5. A. M. Maguire *et al.*, *N. Engl. J. Med.* **358**, 2240 (2008).
6. A. Aiuti *et al.*, *N. Engl. J. Med.* **360**, 447 (2009).
7. S. Hacein-Bey-Abina *et al.*, *J. Clin. Invest.* **118**, 3132 (2008).
8. J. M. Wilson, *Mol. Genet. Metab.* **96**, 151 (2009).
9. S. H. Orkin, A. G. Motulsky, *Report and Recommendations of the Panel to Assess the NIH Investment in Research on Gene Therapy* (NIH, Bethesda, MD, 1995); www.nih.gov/news/panelrep.html.
10. "Stem cell study breakthrough," *ABC News*, 23 January 2009; http://abcnews.go.com/Video/playerIndex?id=6714904.
11. N. Amariglio, *PLoS Med.* **6**, e1000029 (2009).
12. I. Hyun *et al.*, *Cell Stem Cell* **3**, 607 (2008).
13. ISSCR, www.ISSCR.org.
14. T. Friedmann, *Perspect. Biol. Med.* **48**, 585 (2005).
15. Gene Therapy Clinical Trials Worldwide, provided by *Journal of Gene Medicine* (Wiley Publishers) www.wiley.co.uk/genetherapy/clinical/.
16. Geron Corp., news release, 23 January 2009, www.geron.com/media/pressview.aspx?id=1148.
17. See, for example, http://grants.nih.gov/grants/guide/rfa-files/RFA-HL-09-004.html.

10.1126/science.1174935

PLANETARY SCIENCE

The Origin of Plasmaspheric Hiss

Observations by the THEMIS spacecraft are providing a better picture of the electromagnetic environment surrounding Earth.

Ondřej Santolík[1,2] and Jaroslav Chum[1]

The role of electromagnetic waves in shaping the space environment around our planet has been studied since the early 1960s (*1*, *2*). Initial analysis of these waves at audible frequencies consisted of playing the recorded data through a loudspeaker. The historical terminology in this field thus resembles an experimental musical score where we can encounter whistlers, noise, hiss, and chorus. On page 775 of this issue, Bortnik *et al.* (*3*) invite us to this world of "space sound." On the basis of measurements by NASA's THEMIS (Time History of Events and Macroscale Interactions during Substorms) spacecraft mission, the authors describe two types of natural electromagnetic waves: chorus and plasmaspheric hiss. They show that plasmaspheric hiss can be interpreted as arising from transformed chorus waves, thus providing important clues as to its origin.

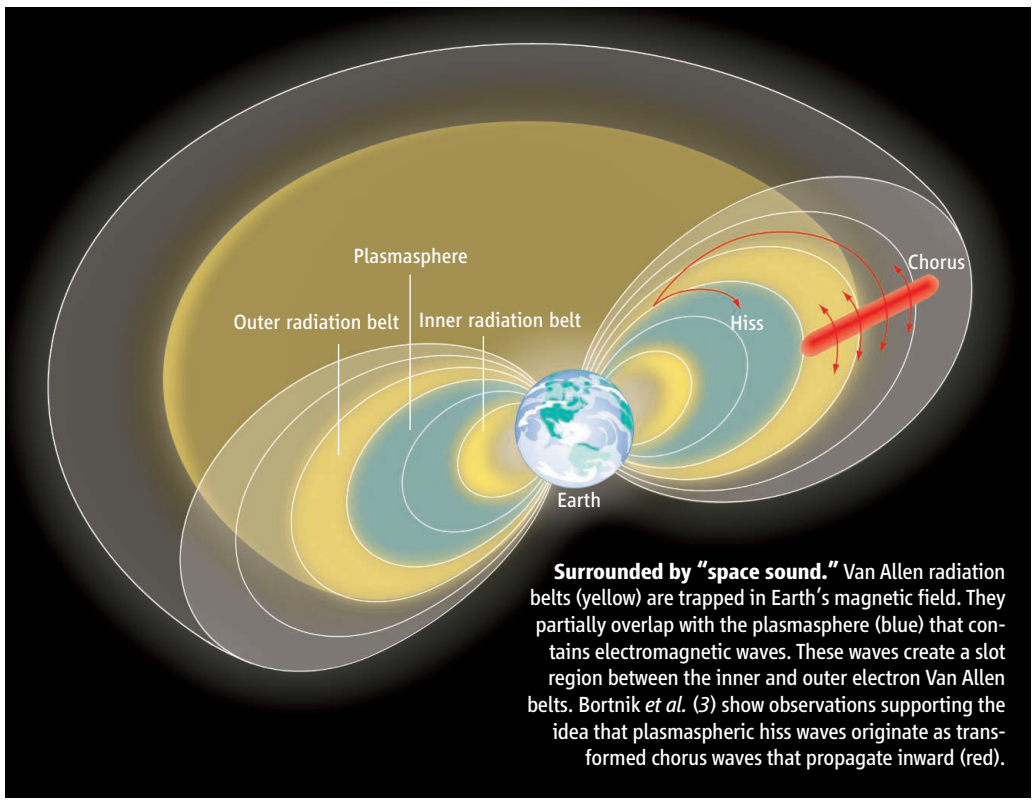

Surrounded by "space sound." Van Allen radiation belts (yellow) are trapped in Earth's magnetic field. They partially overlap with the plasmasphere (blue) that contains electromagnetic waves. These waves create a slot region between the inner and outer electron Van Allen belts. Bortnik *et al.* (*3*) show observations supporting the idea that plasmaspheric hiss waves originate as transformed chorus waves that propagate inward (red).

Both chorus and plasmaspheric hiss are attracting attention as key ingredients in modeling the Van Allen radiation belts—regions that contain high-energy particles trapped in Earth's magnetic field (*4*). The Van Allen belts partially overlap with the plasmasphere where co-rotating low-energy plasma is confined (see the figure). This medium creates a bubble of higher refractive index for electromagnetic waves at audible frequencies. These waves are believed to release energetic electrons in the Van Allen belts from the magnetic trap down to Earth's atmosphere (*5*, *6*). As a result, a slot region is created in the area where this interaction takes place, between the inner and outer electron Van Allen radiation belts.

The origin of plasmaspheric hiss has been a puzzle for a long time, with three basic hypotheses having been put forward. The first proposes that hiss is spontaneously amplified from preexisting weak waves, arising thus from free energy of unstable electron populations. However, waves cannot grow to the observed intensities from weak background turbulence under typical conditions—this mechanism requires an unknown "embryonic" source of sufficiently intense waves to initiate the growth (*7*). The second mechanism consists of an accumulation of whistlers (*8*), waves coming from lightning discharges in the atmosphere (*9*). This hypothesis has recently been favored by a statistical study (*10*), but the results and data interpretation have led to a lively discussion (*11*).

The third proposed mechanism (*12*, *13*) explains plasmaspheric hiss as coming from the inward propagation of chorus into the plasmasphere from an outside source located close to the geomagnetic equatorial plane. The problem here is that chorus can sound very different from hiss, being composed of short chirplike tones lasting for a fraction of a second and resembling a sound "of a rookery heard from a distance" (*9*). However, these tones can superpose and merge during their propagation and transform themselves into hiss (see supporting online material).

Bortnik *et al.* use measurements of two THEMIS satellites, fortuitously located at two different positions—one outside the plasmasphere and the other inside. They show a good correlation of enhancements of average chorus intensity with enhancements of plasmaspheric hiss at time scales from several seconds to tens of seconds. The correlation is maximum at a time delay that corresponds to the expected propagation time. This is exciting evidence in favor of the inward propagation of chorus scenario. In fact, chorus appears in a double role in this story. First, intense chorus is considered to act as local accelerator of energetic electrons to high energies (*14*) in the outer Van Allen belt. Then, after it propagates inward and transforms itself into plasmaspheric hiss, it can act as a destroyer of energetic electrons in the slot region.

The story would thus seem to be concluded, with no mysteries left. But controversies around the origin of plasmaspheric hiss will probably not disappear. Technical problems remain to be solved by adding a third dimension to the ray-tracing simulation; the simulated waves also need to propagate azimuthally

[1]Institute of Atmospheric Physics, Prague, Czech Republic. [2]Charles University, Faculty of Mathematics and Physics, Prague, Czech Republic. E-mail: ondrej.santolik@mff.cuni.cz

Published by AAAS

toward the local evening to explain the observations. But the most important source of controversy could be that Bortnik *et al.* analyze a single data interval, and although the results are convincing in this case, other mechanisms may also be operating at different times. An open question is what percentage of plasmaspheric hiss is generated by each of the different mechanisms. It may well turn out that chorus is a dominant source, but it will take further measurements to determine the relative contributions of the other "voices" to the cacophony of plasmaspheric hiss.

References and Notes

1. C. F. Kennel, H. E. Petschek, *J. Geophys. Res.* **71**, 1 (1966).
2. A. A. Andronov, V. Y. Trakhtengerts, *Geomagn. Aeron.* **4**, 233 (1964).
3. J. Bortnik *et al.*, *Science* **324**, 775 (2009).
4. J. Van Allen, *J. Geophys. Res.* **64**, 1683 (1959).
5. B. Abel, R. M. Thorne, *J. Geophys. Res.* **103**, 2385 (1998).
6. J. Bortnik, U. S. Inan, T. F. Bell, *J. Geophys. Res.* **108**, 1199 (2003).
7. S. R. Church, R. M. Thorne, *J. Geophys. Res.* **88**, 7941 (1983).
8. A. B. Draganov *et al.*, *Geophys. Res. Lett.* **19**, 233 (1992).
9. L. R. O. Storey, *Philos. Trans. R. Soc. London A* **246**, 113 (1953).
10. J. L. Green *et al.*, *J. Geophys. Res.* **110**, A03201 (2005).
11. N. P. Meredith *et al.*, *J. Geophys. Res.* **111**, A09217 (2006).
12. J. Chum, O. Santolik, *Ann. Geophys.* **23**, 3727 (2005).
13. J. Bortnik, R. M. Thorne, N. P. Meredith, *Nature* **452**, 62 (2008).
14. R. B. Horne *et al.*, *Nature* **437**, 227 (2005).

15. The authors acknowledge support from grants GACR-205/09/1253 and GAAV-IAA301120601.

Supporting Online Material

www.sciencemag.org/cgi/content/full/324/5928/729/DC1
SOM Text
Audio S1 to S4

10.1126/science.1172878

ARCHAEOLOGY

Origins of Agriculture in East Asia

During the initial phase of cereal cultivation in East Asia, domesticated traits emerged only slowly.

Martin K. Jones and Xinyi Liu

Some of the world's most important crops, including rice and soybean, originate from eastern Asia. This region is also the original home of several minor crops, such as buckwheat and certain types of millet. In their search for the earliest farms, archaeologists have been drawn to China's two major river valleys: the Yellow River in the north and the Yangtze River in the south. Grains of broomcorn and foxtail millet have been found in Neolithic farmsteads in the Yellow River region (*1*, *2*), and sites in the Yangtze River region have yielded the world's earliest evidence of harvested rice grains (*3*).

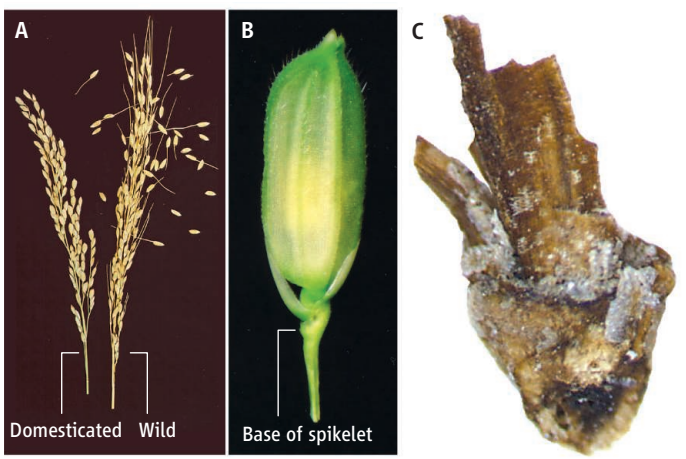

Toward rice domestication. (**A**) In wild rice (right), the grain head breaks up as soon as the grains within it are fully formed, whereas in domesticated rice (left), grains enclosed in their husks remain attached to the stem. In the latter case, detachment and propagation depend fully on the farmer. (**B**) The natural point of breakage in the grain head is at the base of the spikelet (the dispersal unit of grains enclosed in their husks). The shape of the spikelet base provides direct morphological evidence for domestication. (**C**) This rice spikelet base from the Neolithic site of Tianluoshan in the Lower Yangtze River Valley is of the domesticated type.

These discoveries contribute to a growing picture of the greatest revolution in human ecological history: the transition from gathering foods from the wild to producing them in farms. The remains of wheat and barley chart a similar story in southwest Asia, as does maize in Central America. It is easy to imagine how momentous this revolutionary transition must have been, to envisage the shockwaves it dispatched through communities. Yet recent research is changing our understanding of the geography and timing of the transition. It may have started out so gradually that individuals immersed in it may have hardly noticed the change.

Improvements in methods for recovering archaeological plant remains have pushed the earliest records for a number of crops back in time (*2*, *4*). Charred rice remains have been found embedded in 10,000-year-old pottery from the Lower Yangtze River region (*5*). Even older are phytoliths (microscopic fragments of intracellular silica) of rice recovered from caves in the Middle Yangtze River region, for example, at Diaotonghuan in levels dated to 12,000 years ago (*3*). However, the morphological traits associated with domesticated rice did not become fixed for another five millennia (*6*). (Fixation refers to a genetic trait that has replaced all others across a population.)

Evidence for the timing of fixation comes from archaeological fragments of the stem and chaff that surrounded the grain (see the first figure). These features provide direct morphological evidence for the genetic changes associated with domestication—in particular, the change from a form that freely disperses in the wild to one whose reproduction depends on the farmer.

In the case of rice, this transformation can be effected by a substitution in a single transcription factor (*7*, *8*). In terms of genetic change, this is a very small step. Yet archaeological rice chaff recovered from the Lower Yangtze indicates that fixation of the resulting trait in rice populations was slow (*6*). Many generations of early farmers were cultivating plots of land by preparing soil and removing weeds long before most plants harvested from those plots showed the morphological traits of domestication. The proportions of harvested plants with or without the domesticated stem trait changed by just a few percent in each human lifetime. What was happening in the rice fields during that long period of predomestication cultivation?

Between 9000 and 4500 years ago, in the heartlands of its domestication, rice appears to have been harvested but was not the only plant food; people were also gathering fruits, nuts, and acorns (*6*, *9*). Genetic evidence suggests that the rice they exploited was interbreeding

McDonald Institute of Archaeological Research, University of Cambridge, Cambridge CB2 3ER, UK. E-mail: mkj12@cam.ac.uk

CREDIT: PANELS A AND B FROM (*8*), PANEL C FROM (*6*)

Millet then and now. Foxtail millet is still harvested near Xinglonggou, Inner Mongolia, the location of some of the earliest Neolithic records of foxtail and broomcorn millet.

CREDIT: M. K. JONES

with wild stands: The comparative levels of diversity in the domesticated and wild forms today can best be explained by a substantial exchange of genes (*10*). Crops from the other major old world center, the West Asian "Fertile Crescent," show a similar very gradual shift in the fragmentation patterns of the grain-bearing stem (*11*). In both regions, the weed species in the early assemblages are indicative of soil preparation (*6*, *9*, *12*).

Rather than a revolutionary shift from hunter-gatherers to farmers in a few human generations, the evidence now suggests that many generations of "affluent foragers" combined the gathering of wild fruits and nuts with the gathering of cultivated cereals (*13*). Incremental shifts to a different form of rice stem indicate that some rice was sown. Beyond that, we have to imagine harvested plots that were quite different from modern agricultural fields, and in which gene flow between plots was freer than it is today (*14*). The domesticated stem trait may have become fixed within the harvested plots only when such plots became sufficiently isolated from the wild stands. In other words, the fixation of the domesticated trait marks not the beginning of farming, but an early stage in its geographical spread (*15*).

Remains of millet chaff are rare before 7000 years ago, and it is thus not yet possible to chart domestication stem traits through time. The archaeological evidence for millet is, however, much more informative about another aspect of the crop's history: its long-distance spread. One of the earliest sites of millet cultivation is near Xinglonggou in Inner Mongolia, on a low foothill more than 600 km to the north of the Yellow River (*2*, *16*, *17*) (see the second figure), where 8000-year-old millet has been recovered. Just 1000 years later, broomcorn millet had spread widely, with more than 20 published occurrences west of the Black Sea (*16*)—much wider than rice around the same time (*1*). By 4000 to 5000 years ago, cereals were spreading in the opposite direction to millet, with finds of the Fertile Crescent crops wheat and barley in several regions in China (*18*, *19*).

The growing convergence between archaeological and genetic research has elucidated a series of episodes that can be followed in East Asia, just as they can in the more intensively studied Fertile Crescent. At various stages between 12,000 and 7000 years ago, key locations between the valleys and the foothills were chosen to cultivate the soil and optimize the seasonal use of water (*17*). The plants grown in these plots continued to exchange genes with wild stands for millennia before core morphological traits such as the change in stem form were fixed.

But the story does not end there. In East Asian crops, as in crops around the world, the change in stem fragmentation that linked the fate of these plants intimately with their human consumers is only one step in the evolutionary history of the relation between people and plants. Later steps include major changes to structure, ecology, and culinary chemistry (*20*). In the 12,000 years since rice phytoliths were deposited in Diaotonghuan Cave (*3*), the domestication of plants has been a continuing process, made up of episodes of both rapid and gradual change. It is a process that continues apace today.

References

1. G. W. Crawford, X. Chen, J. Wang, *Dongfang Kaogu (East Asia Archaeology)* **3**, 247 (2007).
2. Z. Zhao, *Kaogu (Archaeology)* **454**, 522 (2005).
3. Z. Zhao, *Antiquity* **72**, 885 (1998).
4. G.-A. Lee, G. W. Crawford, L. Liu, X. Chen, *Proc. Natl. Acad. Sci. U.S.A.* **104**, 1087 (2007).
5. L. Jiang, L. Liu, *Antiquity* **80**, 355 (2006).
6. D. Q. Fuller *et al.*, *Science* **323**, 1607 (2009).
7. C. Li, A. Zhou, T. Sang, *Science* **311**, 1936 (2006); published online 8 March 2006 (10.1126/science.1123604).
8. S. Konishi *et al.*, *Science* **312**, 1392 (2006); published online 12 April 2006 (10.1126/science.1126410).
9. D. Q. Fuller, E. Harvey, L. Qin, *Antiquity* **81**, 316 (2007).
10. A. J. Garris *et al.*, *Genetics* **74**, 21 (2005).
11. K.-I. Tanno, G. Willcox, *Science* **311**, 1886 (2006).
12. G. Willcox, S. Fornite, L. Herveux, *Veg. Hist. Archaeobot.* **17**, 313 (2008).
13. L. Liu, G.-A. Lee, L. Jiang, J. Zhang, *Holocene* **17**, 1059 (2007).
14. M. J. Kovach, M. T. Sweeney, S. R. McCouch, *Trends Genet.* **23**, 578 (2007).
15. R. G. Allaby, D. Q. Fuller, T. A. Brown, *Proc. Natl. Acad. Sci. U.S.A.* **105**, 13982 (2008).
16. H. V. Hunt *et al.*, *Veg. Hist. Archaeobot.* **17**, 5 (2008).
17. X. Liu, H. V. Hunt, M. K. Jones, *Antiquity* **83**, 82 (2009).
18. G. Jin, *Nongye Kaogu (Agricultural Archaeology)* **92**, 11 (2007).
19. X. Li *et al.*, *Sci. China Ser. D* **50**, 1707 (2007).
20. T. A. Brown, M. K. Jones, W. Powell, R. G. Allaby, *Trends Ecol. Evol.* **24**, 103 (2009).

10.1126/science.1172082

NEUROSCIENCE

The Sources of Human Volition

Patrick Haggard

Two regions of the brain contribute to the conscious experience of carrying out an action.

Every day we make actions that seem to depend on our "free will" rather than on any obvious external stimulus. This capacity not only differentiates humans from other animals, but also gives us the clear sense of controlling our bodies and lives. It therefore forms a key element of our personal identity. However, such voluntary actions are a puzzle for modern neuroscience. Where do they come from? A study by Desmurget *et al.* (*1*) on page 811 of this issue reveals how the brain may produce our experience of initiating voluntary action.

Neuroscientists have long recognized that instructions for all voluntary body movements pass through the final staging post in the primary motor cortex (see the figure). This area of the brain receives two important inputs. One, from the premotor cortex, is involved when animals move in response to visual signals (*2*). But when animals make the same movements spontaneously, without any specific external trigger, a different area—the presupplementary motor area—instead supplies the major input to the primary motor cortex (*3*). The presupplementary motor area is also a likely source of "readiness potential," a buildup of electrical activity in the brain during the period just before voluntary action.

However, most neuroscientific studies of voluntary action in humans face a methodological and a conceptual problem. The for-

Institute of Cognitive Neuroscience, University College London, London WC1N 3AR, UK. E-mail: p.haggard@ucl.ac.uk

mer is that voluntary action seems to vanish in laboratory experiments designed to investigate it. Volunteers can be asked to choose what action to make, when to make it, or even whether to make it at all (*4*). But these instructions—which amount to "Have free will now!"—have something unsatisfactory, even paradoxical, about them. Scientists typically investigate systems by delivering controlled inputs and measuring outputs, but in volition, the experimenter cannot control the input, almost by definition. The conceptual problem is consciousness. Voluntary actions appear to start with a kind of thought—a "conscious intention." As the philosopher Ludwig Wittgenstein asked, "What is left over if I subtract the fact that my arm goes up from the fact that I raise my arm?" (*5*). Conscious intention is one partial answer to his question (although not one that he himself would have welcomed). But how does conscious intention relate to the intended movement? Neurosurgeons sometimes directly stimulate the awake patient's brain during clinical exploration before surgery. This situation partly resolves both of these problems: The neurosurgeon's electrode delivers a precisely known input to the motor system; when applied to the presupplementary motor area, this electrical stimulation can produce a distinct conscious experience of an "urge to move" (*6*). Desmurget *et al.* now report that stimulation of another area, the inferior part of the posterior parietal cortex, also generates experiences of intention. The parietal cortex has traditionally been considered a sensorimotor association area—linking visual stimuli to appropriate responses, for example—and quite distinct from the frontal lobe areas responsible for voluntary action.

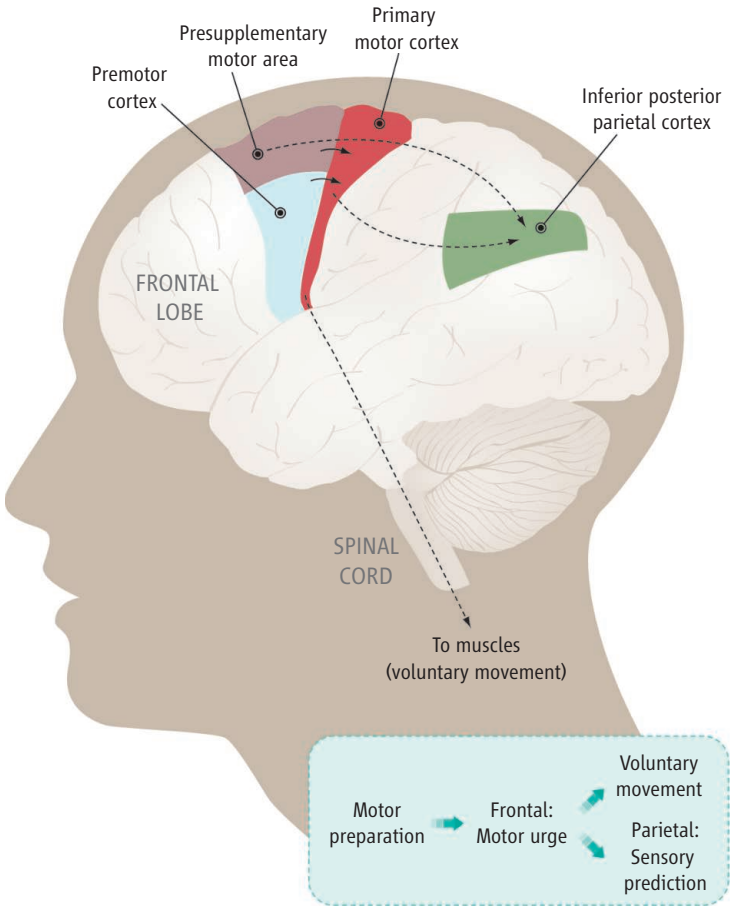

Voluntary action. (**Top**) The premotor cortex prepares commands for voluntary actions triggered by external stimuli, whereas the presupplementary motor area prepares commands for internally generated "intentional" actions, which are then executed by the primary motor cortex. Signals containing copies of prepared motor commands are also sent to the parietal cortex, where they are used to predict sensory consequences of movement. (**Bottom**) The preparation of motor commands for voluntary movement by the presupplementary motor area causes a sense of urge. The inferior part of the posterior parietal cortex generates sensory representations of the predicted consequences of the movement.

The study by Desmurget *et al.* investigates the experience that a patient has during electrical stimulation of specific brain areas. Experimental subjects were patients undergoing brain surgery; thus, stimulation took place with the patient awake but immobilized in a stereotactic frame, with the parietal cortex exposed—not an ideal setting for considering the nature of consciousness. However, stimulating this part of the brain led to experiences of intention that were clearly linked to specific body parts (patients reported wanting to move their arm, lips, or even chest). Moreover, experience of intention was a direct result of the electrical stimulation, not just of experimenter suggestion: When the neurosurgeon did not actually apply any current, patients did not report an urge to move.

The results of Desmurget *et al.* suggest that the parietal cortex, and not just the frontal cortex, may be involved in the experience of conscious intention. Other studies confirm that the parietal cortex contributes to the sense of controlling our actions (*7*), and also to conscious intention before movement. However, stimulation at one site may have remote effects elsewhere (*8*). Thus, stimulation of the presupplementary motor area could evoke urges indirectly, by remotely activating the parietal cortex, or vice versa. But if stimulation at the two sites produces qualitatively different effects, this would suggest that the two areas house distinct components of the experience of voluntary action.

In fact, there are important differences between frontal and parietal stimulation. Stimulation of the presupplementary motor area at low current caused an experience of urge, whereas stronger stimulation caused actual movement (*6*). By contrast, Desmurget *et al.* found that parietal stimulation, even at high intensities, never caused movements, though it could produce the illusion that a movement had occurred. This difference suggests that there may be two distinct aspects to conscious intention (see the figure). One would be a conscious correlate of preparing motor commands in the presupplementary motor area. Another would be a sensory prediction, in the parietal cortex, of the consequences of those commands. Sensory predictions could help to establish a sense of authorship over one's own voluntary movements (*9*). This view predicts that parietal cortex lesions should make one's actions feel involuntary, perhaps like delusions of control in psychosis (*10*). Low-level sensorimotor measures, such as the perceived time of intention, fit this prediction (*11*). But when patients with parietal lesions explicitly judged whether visual feedback reflected their own action or another person's action, they overattributed observed actions to themselves, contrary to the prediction (*12*). It remains unclear why stimulation of the parietal cortex causes conscious intention, yet damage to the same areas causes an excessive, rather than a reduced, sense of control over voluntary movement.

Could the conscious experience that patients call "urge" really be a sensory feedback from slight muscle contraction? Desmurget *et al.* exclude this long-standing alternative explanation by demonstrating that parietal stimulation does not produce any muscle activity (yet patients clearly experienced a desire to move). By contrast,

stimulation of the premotor cortex produced large limb movements, yet the patients never reported any sense of urge, nor awareness of such movement. Therefore, conscious intention—or at least the parietally generated aspect of it—seems to be a specific class of experience generated within the brain, rather than a sensation of slight tension in the muscles. Thus, Desmurget *et al*. confirm that the parietal cortex contributes to conscious experience of volition. Just how the frontal, motor aspect of this experience differs from the parietal, sensory aspect is the next question.

References

1. M. Desmurget *et al*., *Science* **324**, 811 (2009).
2. M. Weinrich, S. P. Wise, K. H. Mauritz, *Brain* **107**, 385 (1984).
3. J. Tanji, H. Mushiake, *Brain Res. Cognit. Brain Res.* **3**, 143 (1996).
4. M. Brass, P. Haggard, *Neuroscientist* **14**, 319 (2008).
5. L. Wittgenstein, *Philosophical Investigations* (Blackwell, Oxford, 1953).
6. I. Fried *et al*., *J. Neurosci.* **11**, 3656 (1991).
7. C. Farrer *et al*., *Cereb. Cortex* **18**, 254 (1991).
8. S. Bestmann *et al*., *Eur. J. Neurosci.* **19**, 1950 (2004).
9. D. M. Wegner, *The Illusion of Conscious Will* (MIT Press, Cambridge, MA, 2003).
10. S.-J. Blakemore, D. Wolpert, C. Frith, *Trends Cognit. Sci.* **6**, 237 (2002).
11. A. Sirigu *et al*., *Nat. Neurosci.* **7**, 80 (2004).
12. A. Sirigu *et al*., *Brain* **122**, 1867 (1999).

10.1126/science.1173827

ECOLOGY

Some Like It Cold

Northern shrimp stocks thrive when climatic conditions lead to cold bottom waters.

Charles H. Greene,* Bruce C. Monger, Louise P. McGarry

The northern shrimp, *Pandalus borealis*, makes up ~70% of the 500,000 tons of cold-water shrimp harvested annually from the world's oceans. Commonly captured in shelf waters deeper than 100 meters, it supports major fisheries throughout the North Atlantic. On page 791 of this issue, Koeller *et al*. (*1*) report that the reproductive cycles of most northern shrimp stocks are finely tuned to match the timing of egg hatching with that of the local spring phytoplankton bloom (see the figure). This remarkable degree of local adaptation on a basin scale is achieved by females regulating the initiation date of their temperature-dependent egg incubation period so that eggs hatch on average within a week of the expected spring bloom. Thus, in typical years, eggs hatch at the time of maximum food availability. The potential downside of this reproductive strategy is its sensitivity to climate-associated changes in the ocean environment.

A species' sensitivity to the vagaries of climate is often most evident at the limits of its distributional range. In the Gulf of Maine, the northern shrimp's southern limit in the northwest Atlantic, the temporal match between egg hatching and the spring bloom is relatively poor (*1*). Here, the deeper offshore waters are warmer than in other parts of the species' range because they are partially derived from the relatively warm and salty slope waters entering the gulf from the North Atlantic (*2*). Because northern shrimp are bottom dwelling and eggs develop faster at higher temperatures, eggs hatch earlier in the gulf stock than in any other stock investigated, and well before the spring bloom. Egg hatching would occur even earlier if gulf females did not exhibit a behavior seen nowhere else in the species' range. During winter, egg-bearing females migrate from offshore into the colder, shallower nearshore waters, a behavior that Koeller *et al*. suggest is an adaptation to delay egg development and improve the match between egg hatching and the spring bloom.

Bottom temperatures in the northwest Atlantic's shelf waters often respond to climate-associated changes in ocean circulation, and such responses can impact the population biology of northern shrimp. The North Atlantic

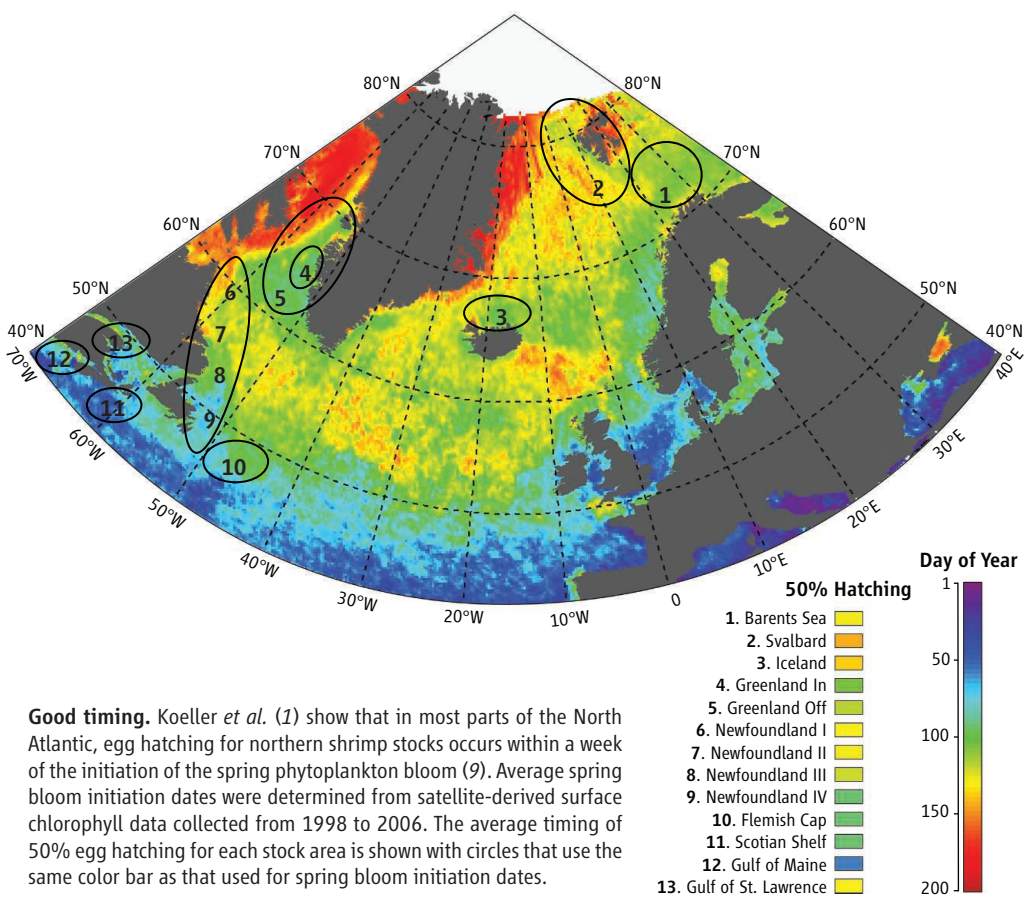

Good timing. Koeller *et al.* (*1*) show that in most parts of the North Atlantic, egg hatching for northern shrimp stocks occurs within a week of the initiation of the spring phytoplankton bloom (*9*). Average spring bloom initiation dates were determined from satellite-derived surface chlorophyll data collected from 1998 to 2006. The average timing of 50% egg hatching for each stock area is shown with circles that use the same color bar as that used for spring bloom initiation dates.

Ocean Resources and Ecosystems Program, Department of Earth and Atmospheric Sciences, Cornell University, Ithaca, NY 14853, USA.

*To whom correspondence should be addressed. E-mail: chg2@cornell.edu

Oscillation (NAO) is the main mode of interannual to interdecadal climate variability in the North Atlantic. By altering circulation patterns in the northwest Atlantic, the NAO can affect the bottom temperatures throughout the region. During positive NAO conditions, volume transport in the Labrador Current increases, resulting in colder bottom temperatures and lower salinities in the shelf waters north of the tail of Newfoundland's Grand Banks (*3*). The reverse occurs during negative NAO conditions. Paradoxically, because of a bifurcation in the Labrador Current near the tail of the Grand Banks, responses to the NAO downstream of this point are reversed, with bottom waters tending to be warmer and saltier during positive NAO conditions and colder and fresher during negative NAO conditions.

During the 1960s, negative NAO conditions predominated, and the Gulf of Maine stock of northern shrimp thrived in the colder bottom temperatures. During the 1970s, the NAO shifted into a predominantly positive phase and the stock collapsed. Although overfishing cannot be excluded as a contributing factor to this collapse (*1*), environmental conditions in the gulf were certainly more favorable physiologically for northern shrimp in the 1960s than the 1970s.

The NAO has remained in a predominantly positive phase since the 1970s, yet northern shrimp stocks throughout the northwest Atlantic increased to relatively high abundances during the early 1990s (*1*). This increase has been attributed to two factors. First, the abundance of groundfish predators (especially cod) that feed on northern shrimp declined, mostly as a result of overfishing (*4*). This release of predation pressure must have boosted shrimp survivorship dramatically. Second, atmospheric changes in the Arctic resulted in two large salinity anomalies—pulses of anomalously cold, low-salinity water—entering the northwest Atlantic's shelf circulation (*5*). Throughout the region, surface waters freshened and became more stratified, enhancing phytoplankton production during autumn and winter. Favorable feeding conditions during these seasons may have contributed to the reproductive success and larval survival of northern shrimp.

The future distributional range of northern shrimp will reflect the interplay between climate-associated changes in the ocean and the demographic responses of a stock-structured population. It is commonly assumed that more northerly species will contract their ranges in response to climate warming, but just the opposite has been seen during recent decades in at least one part of the northwest Atlantic (*5*). In shelf ecosystems upstream of the tail of the Grand Banks, the predominantly positive NAO conditions since the 1970s have led to colder bottom waters that are physiologically favorable for boreal species like the northern shrimp. Episodic large salinity anomalies have reinforced this bottom-water cooling for several years in each decade since the 1970s (*6*).

Colder bottom temperatures not only offer physiological advantages for northern shrimp; they also provide an ecological advantage by slowing the growth and reproductive rates of cod, its principal predator (*7*). The recovery of cod stocks from overfishing has been suppressed by the same cold temperatures that have enabled stocks of northern shrimp and snow crab to flourish. The expanded shrimp and snow crab fisheries have been more lucrative than the cod fishery ever was. The sustainability of marine fisheries will depend on scientific advances that enable managers to better anticipate the responses of stock-structured populations to an ever-changing climate (*8*).

References and Notes

1. P. Koeller *et al.*, *Science* **324**, 791 (2009).
2. Marine Ecosystem Responses to Climate in the North Atlantic Working Group, *Oceanography* **14**, 76 (2001).
3. J. W. Loder *et al.*, *Deep-Sea Res. II* **48**, 3 (2001).
4. B. Worm, R. A. Myers, *Ecology* **84**, 162 (2003).
5. C. H. Greene *et al.*, *Ecology* **89** (suppl.), S24 (2008).
6. I. M. Belkin, *Geophys. Res. Lett.* **31**, L08306; 10.1029/2003GL019334 (2004).
7. G. A. Rose, B. deYoung, D. W. Kulka, S. V. Goddard, G. L. Fletcher, *Can. J. Fish. Aquat. Sci.* **57**, 644 (2000).
8. C. H. Greene *et al.*, *Oceanography* **22**, 210 (2009).
9. R. Ueyama, B. C. Monger, *Limnol. Oceanogr.* **50**, 1820 (2005).

10. This Perspective was developed during the synthesis phase of the U.S. Global Ocean Ecosystem Dynamics Northwest Atlantic/Georges Bank Program. We thank I. Belkin, P. Koeller, D. Mountain, and G. Rose for their comments.

10.1126/science.1173951

PLANT SCIENCE

An Invasive Plant Paradox

One reason that invasive plants may thrive in new environments is their interactions with soil microbes that increase nitrogen cycling.

Marnie E. Rout and Ragan M. Callaway

Division of Biological Sciences, University of Montana, Missoula, MT 59812, USA. E-mail: marnie.rout@mso.umt.edu

Why some plants attain extremely high densities in communities where they are exotic, yet remain at low densities in their native ranges is a mystery. The pattern has been called a "paradox" because it conflicts with long-held ideas about the importance of local adaptation for the ecological performance of organisms (*1*). This biogeographical shift may be connected to other apparent ecological paradoxes that occur with plant invasions involving processes mediated by soil microbes. Invasions can decrease plant species diversity but also increase plant productivity. Rather than depleting soil resources as productivity increases, invasions often increase soil stocks, pools, and fluxes of nitrogen through processes regulated by microbial communities.

Plant species richness and functional diversity can increase local net primary productivity (see the figure), predominantly through more complete use of resources, or "niche complementarity" (*2*). Exotic plant invasions locally reduce native plant diversity, often to the point of becoming the only plant species present (*3*). However, contrary to what diversity-productivity experiments would predict, net primary productivity typically increases with exotic invasions (*4*–*6*). In a recent meta-analysis of 94 studies, the average increase in annual net primary productivity was over 80% in invaded ecosystems (*6*). This "invasion-diversity-productivity" paradox cannot be explained by niche complementarity, but differences in plant-soil-microbe interactions in the invaded and native ranges could perhaps provide part of the answer. Soil microbes can have strong density-dependent effects on plants, often called plant-soil-microbe feedbacks (*7*). These feedbacks are usually neutral or negative for plants in soils from their native ranges, but can be positive for invasive plants in soils from invaded ranges (*8*, *9*). This directional shift is likely due to the absence of evolved species-specific plant-pathogen relations for the invasive plants (*9*). This absence likely enhances the competitive dominance of plant species in new ranges and increases their productivity.

Nitrogen is the primary factor limiting net primary productivity in most ecosystems (*10*),

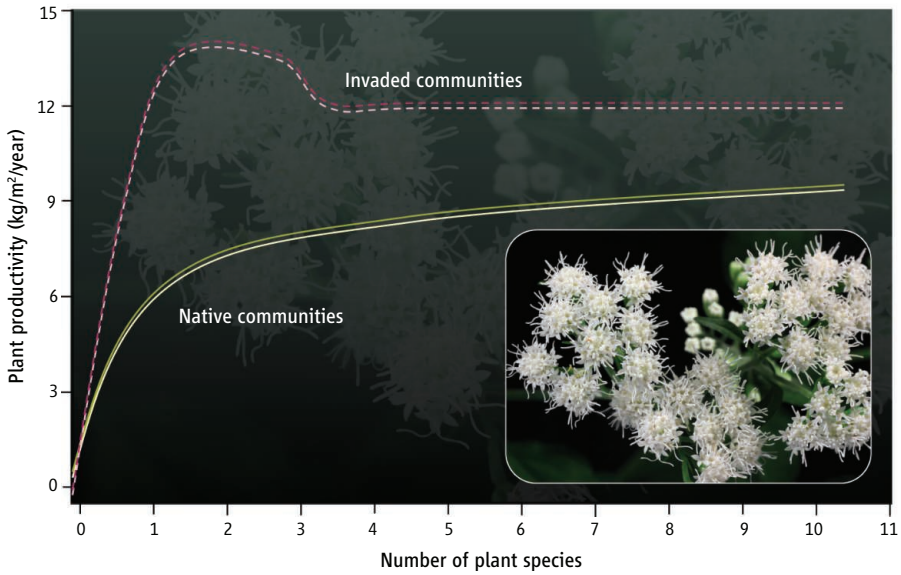

Diversity and productivity. Plant productivity increases to an asymptote as plant diversity increases [solid line; derived from (*2*) with permission from the Ecological Society of America]. Higher productivity correlates with losses in native species richness, and invasives dominate [dashed line; estimated from (*6*); see (*17*)]. The asymptote remains higher due to invader presence in the system at lower relative densities. (**Inset**) The photo shows *A. adenophora.*

and short-term increases in this productivity (for example, as a result of agricultural practices) typically deplete nitrogen and other soil resources. By contrast, plant invasions increase soil nitrogen pools and total ecosystem nitrogen stocks (*6*, *11*, *12*). Soil nitrogen is regulated by the activity of soil-dwelling and mutualistic microbes. On average, invaders double litter decomposition rates, and increase both soil nitrogen mineralization and nitrification by over 50% (*6*). For example, the invasive trees *Acer platanoides* and *Ailanthus altissima* increase net nitrogen mineralization, net nitrification, and soil nitrogen availability compared to native tree species, including the congener *Acer saccharum* (*13*).

How do invasive plants decrease species diversity but increase soil nitrogen and net primary productivity? Invaders might possess morphological or biochemical traits that differ from those of native species in ways that increase nitrogen cycling in the soil. For example, thinner chlorophyll-enriched leaves that are also lower in structural carbon (characteristics that promote rapid growth) could be important traits for invasive success. Such characteristics would allow more rapid leaf decomposition, creating litter that contains a higher concentration of nitrogen (higher litter quality). Increased litter deposition rates or litter quality (*14*) could then explain increased nitrogen pools, stocks, and fluxes in soil. However, leaf traits may not provide all of the answers. Invaders vary widely in leaf traits, and invasive plant species do not appear to initiate the same chain of ecosystem changes in their home ranges. For example, *Spartina alterniflora* is native to eastern North America but is an aggressive invader in China where it has a greater leaf area index [(LAI), the ratio of leaf surface areas to ground surface area]. A higher LAI indicates that a plant produces a denser canopy (larger sized and greater quantity of leaves) in the invaded range (*5*). Reciprocally, *Phragmites australis* is native to China but is a highly successful invader in North America where it has greater net primary productivity (*5*). If invasive species enhance net primary productivity and nitrogen cycling in invaded ranges but not in their native ranges, then the inherent traits of plants are unlikely to drive these processes as these alterations should also be occurring in the native ranges. Alternatively, invasive plants may undergo rapid natural selection for such key leaf traits only in invaded ranges. For example, the invasive aster *Ageratina adenophora* (see the figure), which is native to Mexico, is an invader throughout the subtropics and appears to have evolved increased nitrogen allocation to photosynthesis and reduced allocation to cell walls in the absence of specialist herbivores (*15*). This would make leaves easier to decompose and suggests a potential mechanism by which invaders might possess leaves with traits that enhance nitrogen cycling in the soil of invaded ecosystems.

Soil microbes might simply be passengers in the process of increasing nitrogen pools and fluxes. However, invaders and soil microbes might interact in a biogeographically explicit way, as is often seen for plant-soil-microbe feedbacks (*9*), allowing the microbial community to drive changes in the nitrogen cycle that occur with plant invasions. Such shifts in plant-soil-microbe feedbacks would indicate that communities of soil microbes and plants have regional evolutionary trajectories in different parts of the world, and that mixing plants and soil microbes from different evolutionary trajectories might alter ecosystem functions. If microbial communities responsible for various ecosystem processes (including nitrogen fixation, nitrification, ammonification, and organic matter decomposition) interact with invasive plants in ways determined by evolution and biogeography, then this may help to explain the apparent paradox of increased nitrogen pools and fluxes with plant invasions.

What is needed are biogeographical comparisons of soil microbial communities and of the processes by which they drive plant invasions, specifically in native and invaded ranges. For example, invasion by some exotic grasses corresponds with increased soil nitrification rates and higher abundance and diversity of ammonia-oxidizing bacteria in invaded ranges (*16*). Additionally, nitrification rates positively correlate with changes in the bacterial community, suggesting a mechanism for increased nitrogen cycling in these invaded soils. As our understanding of microbial biogeography and associated functional differences expands, we may learn much about regional evolutionary relationships among plants and soil microbes and how this affects ecosystem functioning.

References and Notes

1. D. Sax, J. H. Brown, *Global Ecol. Biogeogr.* **9**, 363 (2000).
2. D. U. Hooper *et al.*, *Ecol. Monogr.* **75**, 3 (2005).
3. W. M. Ridenour, R. M. Callaway, *Oecologia* **126**, 444 (2001).
4. S. Vanderhoeven *et al.*, *Plant Soil* **275**, 169 (2005).
5. C. Liao *et al.*, *Ecosystems* **10**, 1351 (2007).
6. C. Liao *et al.*, *New Phytol.* **177**, 706 (2008).
7. W. H. van der Putten, C. van Dijk, B. A. M. Peters, *Nature* **362**, 53 (1993).
8. R. M. Callaway *et al.*, *Nature* **427**, 731 (2004).
9. K. O. Reinhart, R. M. Callaway, *New Phytol.* **170**, 445 (2006).
10. P. M. Vitousek, R. W. Howarth, *Biogeochemistry* **13**, 87 (1991).
11. J. G. Ehrenfeld, *Ecosystems* **6**, 503 (2003).
12. M. E. Rout, T. H. Chrzanowski, *Plant Soil* **315**, 163 (2009).
13. L. Gomez-Aparicio, C. D. Canham, *Ecol. Monogr.* **78**, 69 (2008).
14. R. R. Blank, *Invasive Plant Sci. Manage.* **1**, 226 (2008).
15. Y.-L. Feng *et al.*, *Proc. Natl. Acad. Science U.S.A.* **106**, 1853 (2009).
16. C. V. Hawkes *et al.*, *Ecol. Lett.* **8**, 976 (2005).
17. Data from table 1 and figure 3 (flow chart) of (*6*) were used to generate the dashed line in the figure. The data used were the mean increase of 83% net primary productivity (NPP, also called ANPP in table 1) in invaded systems.

10.1126/science.1173651

Elemental Composition of the Martian Crust

Harry Y. McSween Jr.,[1]* G. Jeffrey Taylor,[2] Michael B. Wyatt[3]

The composition of Mars' crust records the planet's integrated geologic history and provides clues to its differentiation. Spacecraft and meteorite data now provide a global view of the chemistry of the igneous crust that can be used to assess this history. Surface rocks on Mars are dominantly tholeiitic basalts formed by extensive partial melting and are not highly weathered. Siliceous or calc-alkaline rocks produced by melting and/or fractional crystallization of hydrated, recycled mantle sources, and silica-poor rocks produced by limited melting of alkali-rich mantle sources, are uncommon or absent. Spacecraft data suggest that martian meteorites are not representative of older, more voluminous crust and prompt questions about their use in defining diagnostic geochemical characteristics and in constraining mantle compositional models for Mars.

Over the past decade, instruments on orbiting spacecraft, landers, and rovers have measured the abundances of elements present in martian rocks and soils. Some analyses are incomplete, and the scales of analyzed areas range from centimeters to hundreds of kilometers in diameter, complicating comparisons. Martian meteorites [shergottite, nakhlite, and chassignite (SNC)] constitute another important source of geochemical data. Although the meteorites come from as-yet undetermined locations on Mars, laboratory analyses permit complete chemical characterizations that cannot be obtained by remote sensing techniques.

Based on these data, Mars has been viewed as a basalt-covered world (*1*). Although basalts are ubiquitous on rocky planets, the apparent lack of other rock compositions suggests that the geologic evolution of Mars has been distinct from Earth. Rocks at the Mars Pathfinder landing site previously identified as andesite (*2*) may be coated with alteration rinds, and martian spectral signatures formerly interpreted as andesitic (*3*) are now attributed to the effects of chemical weathering (*4*, *5*). Only a few occurrences of evolved siliceous rocks have been discovered in global spectral surveys (*6*), supporting the view that magmatic differentiation has been very limited. Although much of the surface is covered by sediments, these materials largely retain the chemical compositions of their basaltic precursors.

Sufficient geochemical data now exist to better characterize the crust and the igneous processes that produced it. Here, we compare and critically evaluate geochemical data from all these sources to constrain the composition of the crust and consider how martian magmatism may have differed from that on Earth.

Geochemical Data Sets

The Gamma-Ray Spectrometer (GRS) on the Mars Odyssey orbiter has provided elemental abundance data and global distribution maps for H, Si, Ca, K, Cl, Fe, and Th (*7*). A global map will be available for Al, but at present we use only the global Al mean value. We used data collected from June 2002 to January 2006. Reduced elemental concentrations were originally binned at 0.5° by 0.5° and smoothed using mean filters over radii of 5° (K), 10° (H, Fe, and Th), or 15° (Si and Ca). For our analysis, we rebinned data to 5° by 5° grid points, resulting in large spatial resolution. We used only points in regions where H contents are low enough not

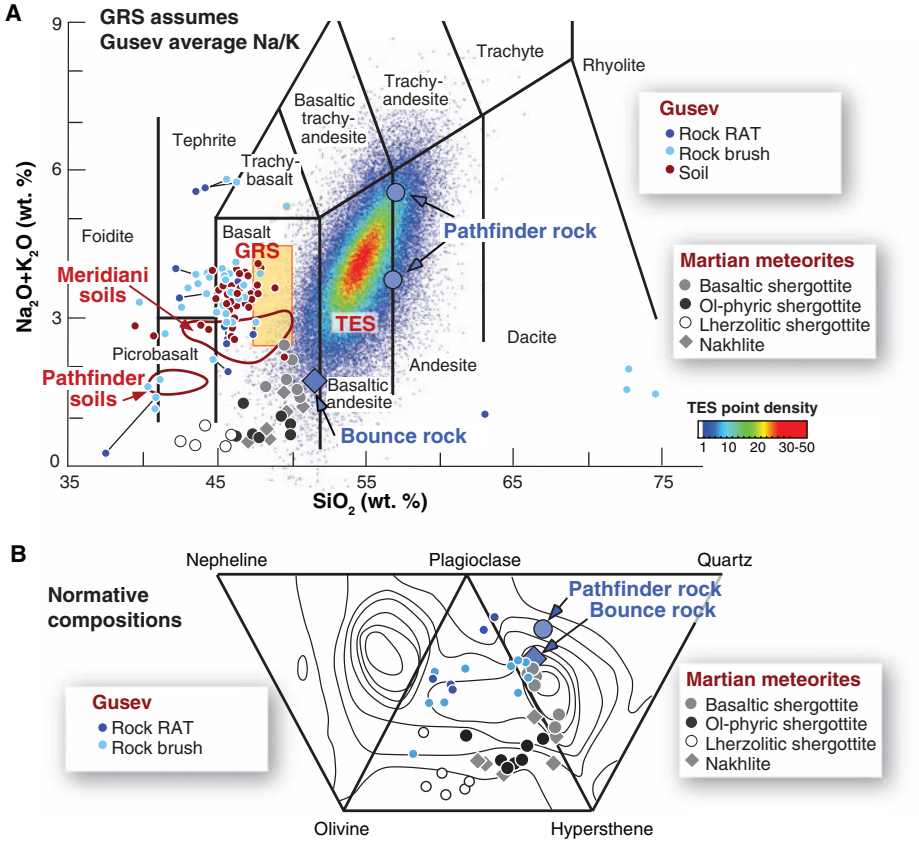

Fig. 1. (**A**) Total alkalis-silica diagram used for classification of volcanic rocks. Gusev RAT-ground and RAT-brushed compositions for the same rocks are connected by tie-lines. Analyses of Gusev rocks and soils, martian meteorites, and global GRS data (calculated on a volatile-free basis) indicate a crust dominated by basalts. TES-derived data and possibly the Mars Pathfinder rock composition may reflect alteration. Data sources in this and other figures are discussed in the text. (**B**) Calculated normative minerals in the martian crust. The three triangles correspond (from left to right) to alkaline basalts, olivine tholeiites, and quartz tholeiites. The critical plane of silica undersaturation separates alkaline basalts and olivine tholeiites; fractionating liquids to the left of this plane form silica-deficient compositions, whereas those to the right evolve to silica-enriched compositions. Contours indicate the relative abundances of terrestrial basaltic rocks (*37*). Martian meteorites and Gusev rocks plot mostly in the fields of olivine tholeiites and quartz tholeiites; nepheline-normative rocks have not been encountered.

[1]Planetary Geosciences Institute and Department of Earth and Planetary Sciences, University of Tennessee, Knoxville, TN 37996–1410, USA. [2]Hawai'i Institute for Geophysics and Planetology, University of Hawai'i at Manoa, Honolulu, HI, 96822, USA. [3]Department of Geological Sciences, Brown University, Providence, RI 02912–1846, USA.

*To whom correspondence should be addressed. E-mail: mcsween@utk.edu

to interfere in the determination of Si, Fe, and Ca concentrations. Hydrogen has a high cross-section for capturing thermal neutrons, substantially affecting the neutron flux in the upper ~30 cm of the martian surface. We corrected the data for this effect (*7*) by a process that uses measured fluxes of γ-rays from H, Fe, Si, and Ca, and the fluxes calculated from a neutron transport γ-ray production model. This approach produces reasonable values at equatorial latitudes but uncertain values at higher polar latitudes where H dominates elemental signatures. Accordingly, we constrained our results using a mask based on H concentration, corresponding to roughly ±45° of latitude from the equator. The concentration of H does not affect K and Th data because their γ-rays result from radioactive decay. To compare igneous rock compositions, we further adjusted the data to a volatile-free basis by removing H_2O, Cl, and SO_2, the quantities of which were calculated from the S/Cl ratio of ~5 found at rover landing sites. We represent GRS element abundances as boxes defined by global averages and standard deviations (1σ).

Measurements of the Thermal Emission Spectrometer (TES) onboard the Mars Global Surveyor orbiter are sensitive to the chemistry and structure of silicates (*8*). Complex mixtures can be deconvolved into mineral abundances using a spectral library of known minerals (*9*). The major oxide concentrations can be estimated from TES data to within ±5 weight percent (wt %) using known mineral chemistries and deconvolved mineral abundances from thermal emission studies (*10*, *11*). We modeled the spectra (*12*) over 233 to 508 cm^{-1} and 825 to 1301 cm^{-1} using an end-member set consisting of primary (e.g., plagioclase, pyroxene, and olivine) and secondary (e.g., phyllosilicates, sulfates, and oxides) phases with known chemistries. Finally, we calculated major oxide concentrations on a H_2O-free and CO_2-free basis. The data clouds in our graphs represent derived chemical compositions from global TES data binned at 4 pixels per degree.

In comparing GRS analyses and TES-derived compositions, it is necessary to realize that γ-rays can penetrate to depths of 20 to 30 cm and thus analyze a much greater volume of material, relative to thermal emission spectra that sample only the outermost 10 to 100 μm. Thus, surface alteration processes may have a profound effect on geochemical classifications based on TES data.

Sediments potentially sample broad areas of the crust, although fractionation of heavy minerals is likely during their transport. X-Ray Fluorescence (XRF) instruments on the Viking landers obtained six soil analyses from two landing sites (*13*). Another five soils were analyzed by the Alpha-Proton-X-ray Spectrometer (APXS) on the Mars Pathfinder rover. APXS (*14*) on the Mars Exploration Rovers (MER), Spirit and Opportunity, analyzed nearly 100 soils at two different sites (*15*, *16*). We plot Gusev crater soil

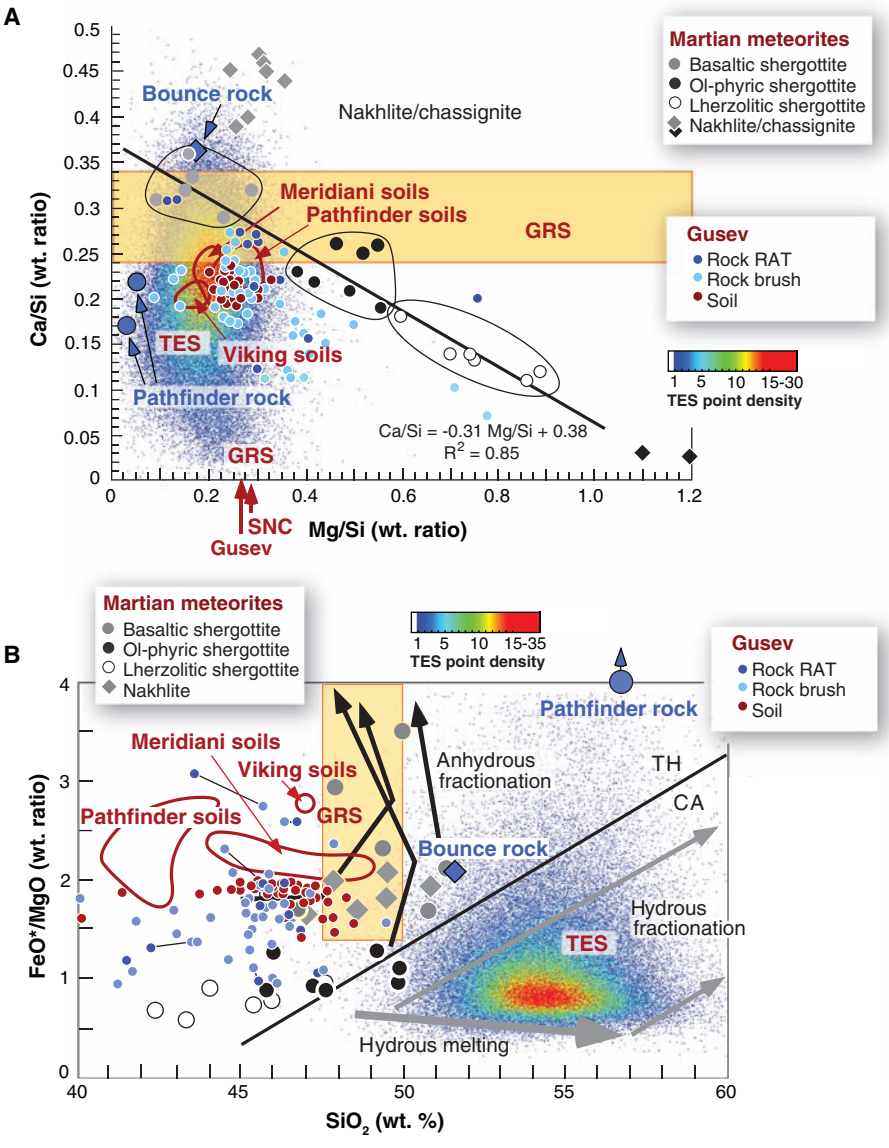

Fig. 2. (**A**) Ca/Si-Mg/Si diagram used for classification of martian meteorites. The GRS-measured Ca/Si ratio and standard deviation is represented by a horizontal band. Global Mg/Si can be estimated from the intersection of that band with the regression line for shergottites or from the average Mg/Si value for Gusev rocks and soils (red arrows). (**B**) FeO*/MgO-silica diagram used for distinguishing dry tholeiitic (TH) and wet calc-alkaline (CA) rocks. All martian samples are tholeiitic. TES-derived compositions result from alteration. Arrows represent melting and fractionation trends in terrestrial magmas.

compositions measured by Spirit, but Viking, Pathfinder, and Opportunity soils are illustrated by ovoids enclosing the data, to minimize complexity in our diagrams.

Two different calibrations of five rock analyses by the Mars Pathfinder APXS have been published (*17*, *18*). The true compositions of the Pathfinder rocks are unknown, because the APXS analyzed only the outermost few micrometers. The dust-free rock composition has been estimated by plotting abundances of various oxides versus sulfur and extrapolating trends to zero sulfur, in effect removing the sulfur-rich dust coatings. There remains, however, a concern that alteration rinds might have been present on these rocks.

The MER have performed analyses of more than 250 rocks with their APXS (*15*, *16*). Rock Abrasion Tools (RAT) brushed away surface dust and ground into rock interiors. Detailed observations of RAT holes and comparison of brushed and abraded rock compositions reveal that rocks at both sites commonly have alteration rinds (*19*). In compiling MER rock analyses, we used only data from RAT-ground or RAT-brushed rocks. Rocks at the Opportunity landing site in Meridiani Planum are altered basaltic sandstones cemented by salts (*20*). Meridiani has a distinctive TES spectrum (*21*) produced by lag deposits of hematite concretions; this spectrum is not representative of the martian surface. Consequently, these evaporitic sediments are not

likely to be a major crustal component. However, one sample from Meridiani, Bounce Rock (*22*), has a chemical and mineralogical composition similar to martian meteorites (shergottites) and was included in our compilation. Unlike Meridiani, Spirit's Gusev landing site spectrally resembles most of the martian surface, and thus its igneous rocks are more likely to represent other parts of the crust. Here, we focus especially on Gusev samples, estimated to have formed at ~3.7 billion years ago (*23*).

Martian meteorites (*24*) include three types of shergottites (basaltic, olivine-phyric, and lherzolitic), nakhlites, chassignites, and ALH84001—all igneous rocks. We focus on shergottites and nakhlites, because they are the most abundant and well characterized. Moreover, their petrographic characteristics are consistent with near-surface rocks. With the exception of ALH84001, the radiometric ages of all these meteorites indicate that they crystallized since ~1.4 billion years ago (*25*). Thus, they are considerably younger than Gusev rocks. The times of ejection of these meteorites from Mars, estimated from cosmogenic nuclide measurements (*26*), define four clusters with several outliers, each containing a single meteorite type and likely representing a distinct launch site. Although crystallization ages suggest that these meteorites constitute a chronologically biased sampling of the martian crust, they represent more sampling locations than those visited so far by landers and rovers. Bulk-rock geochemical data for shergottites and nakhlites from various sources were compiled by (*27*). Here, we consider major and minor elemental abundances that can be compared with remote sensing data.

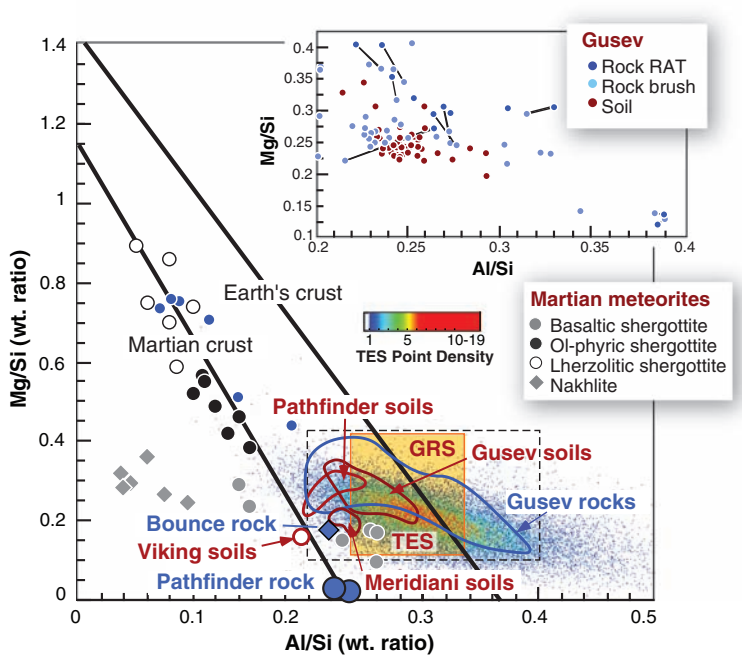

Fig. 3. Mg/Si-Al/Si diagram previously thought to discriminate between Mars and Earth rocks. Gusev and GRS data do not show the Al depletion seen in martian meteorites. GRS Al data represent the global mean ± 1 SD analytical uncertainty.

Geochemical Classification of Crustal Rocks

The total alkalis-silica diagram (Fig. 1A) is commonly used for geochemical classification of volcanic rocks. Martian meteorites plot within the basalt field, as does compositionally similar Bounce Rock. Gusev rocks also are concentrated within the basalt field, but they have higher Na_2O+K_2O values. Their compositions are scattered (some are tephrites or picrobasalts), possibly resulting from fractional crystallization at varying depths (*28*). Gusev rocks are clearly more alkali-rich than other martian compositions. The Mars Pathfinder dust-free rock composition is andesite, although this composition may reflect surficial silica enrichment during weathering.

Gusev soils plot in the basalt field, superimposed on compositions of the local basaltic rocks. Meridiani soils are basaltic, but with slightly lower alkalis than Gusev soils. Pathfinder soils have lower silica and alkalis and are distinct from the composition of the local rocks. Viking soils are not plotted because Na was not analyzed.

The globally averaged GRS-measured silica abundance (Fig. 1A) corresponds to basalt, and the standard deviation indicates that few analyses lie outside the basalt range. The GRS analyzed K but not Na, so the average Na_2O/K_2O weight ratio for Gusev rocks and soils (8.9) was assumed in constructing the GRS box. Martian meteorites have very low K_2O abundances and thus a high average Na_2O/K_2O ratio (12.5); using this ratio gives unreasonable results when combined with GRS measurements of K.

TES-derived compositions are clearly distinct from other data sets (Fig. 1A). We interpret this difference to result from surface chemical weathering. Global variations in silica abundances are modest, and, at the course scale of GRS data, no areas dominated by siliceous rocks are apparent in a GRS silica distribution map (*7*).

Additional information about basaltic compositions is revealed by calculated norms (Fig. 1B), which recast bulk chemistry into minerals. The normative mineral abundances for martian meteorites, Bounce Rock, the Mars Pathfinder dust-free rock, and the least altered Gusev rocks (*29*) plot within the field of olivine tholeiites or in the quartz tholeiite field close to the plagioclase-hypersthene join. The absence of nepheline-normative rocks suggests that melts from alkali-rich mantle sources are uncommon, despite GRS observations and models that suggest Mars is enriched in alkalis relative to Earth (*30*, *31*). Terrestrial alkaline magmas typically form by melting altered mantle sources, and their absence on Mars points to limited fluid-assisted metasomatism at depth.

We use the Ca/Si-Mg/Si diagram for geochemical classification of martian meteorites (Fig. 2A). Our version uses weight ratios, although the original diagram (*32*) used molar ratios. Basaltic, olivine-phyric, and lherzolitic shergottites are enclosed by ovals, and increasing Mg/Si reflects increasing proportions of olivine. Nakhlites have higher Ca/Si ratios, reflecting abundant augite. Gusev rocks and soils have lower Ca/Si, and Gusev, Meridiani, Pathfinder, and Viking soils all nearly overlap.

The GRS-measured average Ca/Si value and standard deviation are indicated by a horizontal bar (Fig. 2A). The GRS cannot measure Mg, but we estimated a global Mg/Si value of 0.29 (range 0.11 to 0.42) from the intersection of the average GRS Ca/Si value with the Ca/Si-Mg/Si regression line for shergottites (Fig. 2A). The value agrees closely with the average Mg/Si ratio for Gusev rocks and soils (0.27 ± 0.10), so it is immaterial whether we derive this value from martian meteorites or Gusev analyses. The Mg/Si ratio corresponds to ~11.0 wt % MgO, which will be used as the global GRS value in other diagrams. TES-derived Mg/Si and Ca/Si ratios partly overlap with those of Gusev samples.

Tholeiitic or Calc-Alkaline Magmas?

Magmatic trends are markers for plate tectonics on Earth, reflecting melting of dry or wet mantle sources at spreading centers or subduction zones, respectively. The compositions of martian meteorites, Bounce Rock, Gusev rocks, and the soils from all sites are tholeiitic (Fig. 2B). The GRS average FeO*/MgO ratio (FeO* is total Fe, expressed as FeO; MgO was estimated from Fig. 2A) is likewise tholeiitic. However, TES-derived compositions plot in the calc-alkaline field.

Tholeiitic magmas, which are relatively dry, show Fe enrichment during fractionation, as illustrated by the nearly vertical black arrows. Different degrees of hydrous partial melting produce magmas distributed along the thick gray arrow at the bottom of the figure, and fractionation of those hydrous magmas produces silica-enriched (calc-alkaline) liquids that follow the smaller diagonal gray arrows. It has been speculated (*1*) that the ancient Mars mantle was wet, accounting for the TES-derived compositions of older

geologic units. In this model, early melting events dehydrated the mantle, so that magmas derived by later melting (martian meteorites having young radiometric ages) were tholeiitic. However, this model must be incorrect, because chemically weathered surface compositions, as measured by TES spectra, cannot be interpreted in terms of igneous processes. Instead, TES-derived calc-alkaline compositions are artifacts of alteration, and they provide no evidence for crustal recycling.

Mars Geochemical Discriminants

Several distinctive geochemical characteristics of martian meteorites are commonly assumed to be fingerprints of Mars, although it has been noted that some unusual terrestrial rocks (ferropicrites) share their compositions (*33*). Martian meteorites are depleted in Al relative to terrestrial rocks (*30*) (Fig. 3). This distinguishing characteristic might result from depletion of Al during early melting of mantle source regions (*34*) and, indeed, ancient Gusev rocks are not as depleted in Al as are the younger meteorites. The GRS global average data also support the higher Al/Si ratios for Gusev rocks. This brings into question the validity of Al depletion as a geochemical discriminant for all Mars samples. The Gusev RAT-ground rock compositions have consistently higher Mg/Si ratios than RAT-brushed compositions (inset in Fig. 3). This difference can be explained by preferential leaching of olivine in alteration rinds during acidic weathering (*35*).

The Fe/Mn ratio is another geochemical characteristic thought to be diagnostic for Mars. Fe/Mn ratios of pyroxene and olivine in martian meteorites are distinct from those of lunar and terrestrial minerals (*36*), and the average bulk Fe/Mn in meteorites was used to constrain the martian mantle composition (*31*). The Fe/Mn weight ratio in the martian mantle, based on martian meteorites, is ~41, lower than that of Earth's mantle (~62). However, Fe/Mn ratios for Gusev rocks and soils are significantly different (Fig. 4A). It is unclear which ratio provides a more accurate assessment of the Mars mantle composition.

Ni/Mg ratios are distinctive for martian meteorites (Fig. 4B) and have been used to estimate a Ni abundance for Mars that is considerably lower than for Earth (*31*). However, RAT-ground Gusev basalts plot along the terrestrial trend, clearly distinct from the meteorites (Fig. 4B). RAT-brushed rocks and soils generally fall to the Mg-poor side of this trend. This diagram suggests that Ni/Mg may not be a valid discriminant for Earth and Mars rocks. The global Mg abundance estimated for GRS data is shown by a vertical bar, but Ni data are unavailable.

Conclusions

A critical review of element abundance data for Mars from available sources supports the conclusion that the crust is basaltic, with very limited siliceous rocks and no rocks critically undersaturated in silica. The basalts are tholeiites, and a previous hypothesis that older crustal rocks are calc-alkaline is incorrect. Thus, important roles for crustal differentiation or melting of recycled, hydrous, or alkali-rich mantle sources are not supported by the data, pointing to distinct magmatic processes in producing the crusts of Mars and Earth. The abundance of basalts indicates that chemical weathering has been limited over much of the planet's history. The spacecraft data also suggest that young martian basaltic meteorites are not representative of the older crust and cast doubt on the validity of geochemical fingerprints for Mars that are based on martian meteorite data alone. Although martian meteorites remain a critically important data set, element abundances in the crust derived from spacecraft measurements suggest that magma source regions are heterogeneous and constraints on mantle compositional models from the meteorites may not apply to the entire mantle.

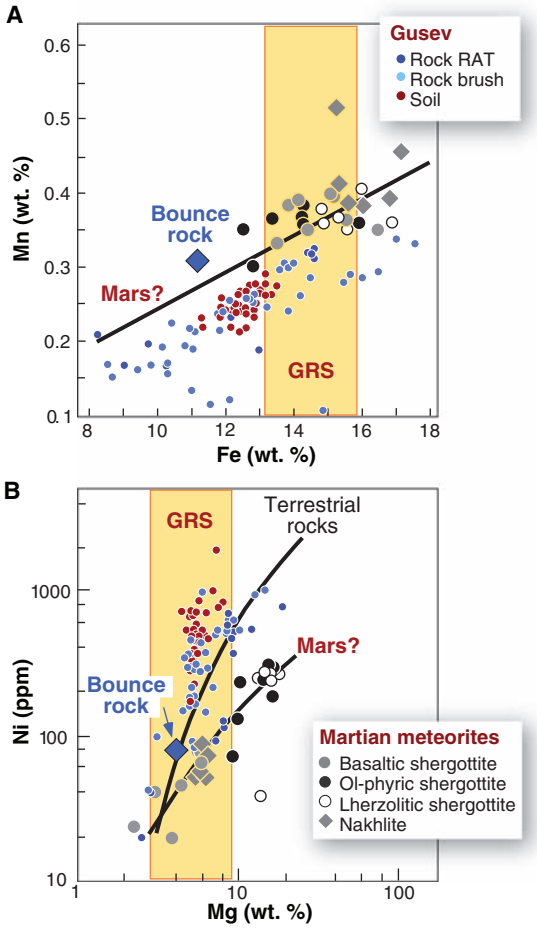

Fig. 4. (**A**) Mn-Fe diagram suggests that the commonly accepted Fe/Mn ratio for the martian mantle, based on martian meteorites, may not apply to all mantle sources, such as that for Gusev rocks. (**B**) Ni-Mg diagram thought to distinguish Mars and Earth samples. Gusev rocks and soils plot along a trend defined by terrestrial basalts rather than martian meteorites.

References and Notes

1. H. Y. McSween, T. L. Grove, M. B. Wyatt, *J. Geophys. Res.* **108**, (E12), 5135 10.1029/2003JE002175 (2003).
2. H. Y. McSween *et al.*, *J. Geophys. Res.* **104**, 8679 (1999).
3. J. L. Bandfield, V. E. Hamilton, P. R. Christensen, *Science* **287**, 1626 (2000).
4. M. B. Wyatt, H. Y. McSween, K. L. Tanaka, J. Head, *Geology* **32**, 645 (2004).
5. J. R. Michalski *et al.*, *Icarus* **174**, 161 (2005).
6. P. R. Christensen *et al.*, *Nature* **436**, 504 (2005).
7. W. V. Boynton *et al.*, *J. Geophys. Res.* **112**, E12S99 10.1029/2007JE002887 (2007).
8. P. R. Christensen *et al.*, *J. Geophys. Res.* **97** (E5), 7719 (1992).
9. M. S. Ramsey, P. R. Christensen, *J. Geophys. Res.* **103**, 577 (1998).
10. M. B. Wyatt *et al.*, *J. Geophys. Res.* **106**, 14711 (2001).
11. V. E. Hamilton *et al.*, *J. Geophys. Res.* **106**, 14733 (2001).
12. TES spectra are limited from the mapping orbit data set up to 5317 and are constrained by surface temperatures >250 K, lambert albedo <0.15, dust extinctions of <0.18 (1075 cm^{-1} opacity of ~0.3), water ice extinctions of <0.1 (800 cm^{-1} opacity of ~0.15), and emission angles of <30°.
13. B. C. Clark *et al.*, *J. Geophys. Res.* **87**, 10059 (1982).
14. The APXS on Mars Pathfinder was an Alpha Proton X-ray Spectrometer; the same abbreviation on MER stands for Alpha Particle X-ray Spectrometer.
15. R. Gellert *et al.*, *J. Geophys. Res.* **111**, E02S05 10.1029/2005JE002555 (2006).
16. D. W. Ming *et al.*, *J. Geophys. Res.* **113**, E12S39 10.1029/2008JE003195 (2008).
17. H. Wanke, J. Bruckner, G. Dreibus, R. Rieder, I. Ryabchikov, *Space Sci. Rev.* **96**, 317 (2001).
18. C. N. Foley, T. E. Economou, R. N. Clayton, *J. Geophys. Res.* **108** (E12), ROV 37-1 (2003).
19. L. A. Haskin *et al.*, *Nature* **436**, 66 (2005).
20. S. W. Squyres, A. H. Knoll, *Earth Planet. Sci. Lett.* **240**, 1 (2005).
21. P. R. Christensen *et al.*, *J. Geophys. Res.* **106**, 23873 (2001).
22. J. Zipfel *et al.*, *Meteorit. Planet. Sci.* **39** (Suppl.), A118 (2004).
23. R. Greeley *et al.*, *J. Geophys. Res.* **110**, E05008 (2005).
24. H. Y. McSween, A. H. Treiman, *Rev. Mineral.* **36**, 6-1 (1998).
25. L. E. Nyquist *et al.*, *Space Sci. Rev.* **96**, 105 (2001).
26. R. Christen, O. Eugster, H. Busemann, *Antarc. Met. Res.* **18**, 117 (2005).
27. C. Meyer Jr., The Mars Meteorite Compendium (JSC #27672 Revision, NASA Johnson Space Center, Houston, TX); http://curator.jsc.nasa.gov/antmet/mmc/index.cfm (2006).
28. H. Y. McSween *et al.*, *J. Geophys. Res.* **111**, E09S91 10.1029/2006JE002698 (2006).
29. H. McSween *et al.*, *J. Geophys. Res.* **113**, E06S03 10.1029/2007JE002970 (2008).
30. H. Wanke, G. Dreibus, *Philos. Trans. R. Soc. Lond. Ser. A* **325**, 545 (1988).
31. A. N. Halliday, H. Wanke, J.-L. Birck, R. N. Clayton, *Space Sci. Rev.* **96**, 197 (2001).
32. Y. Ouri, N. Shirari, M. Ebihara, *Antarc. Met. Res.* **16**, 80 (2003).
33. J. Filiberto, *Icarus* **197**, 52 (2008).
34. J. Longhi, *Proc. Lunar Planet. Sci. Conf.* **21**, 695 (1991).
35. J. Hurowitz *et al.*, *J. Geophys. Res.* **111**, E02S19 10.1029/2005JE002515 (2006).
36. J. J. Papike, *Rev. Mineral.* **36**, 7-1 (1998).
37. A. R. McBirney, *Igneous Petrology, 3rd ed.* (Jones & Bartlett, Sudbury, MA, 2007).

38. This work was partly supported by NASA Cosmochemistry grant NNG06GG36G to H.Y.M.

10.1126/science.1165871

WE DISCOVERED STEM CELLS.
IT'S TIME TO DISCOVER US.

Ontario has been home to one breakthrough discovery after another. In 1961, Lasker Award-winning scientists James Edgar Till and Ernest Armstrong McCulloch proved the existence of stem cells. Earlier this year in Ontario, Dr. Andras Nagy and his team discovered a novel way to generate safer stem cells from somatic cells, bringing us closer to treating or curing a multitude of diseases, including Parkinson's, Alzheimer's, macular degeneration and autism using the patients' own cells. Other Ontario scientists have found novel ways to treat cancer with viruses and have made advances in many additional fields, including regenerative medicine and neuroscience. Dr. Tony Pawson won the 2008 Kyoto Prize for Basic Sciences for his work in cell signaling, becoming the first Canadian awarded this honour. We're committed to even greater achievements in the future. Isn't it time you made a major discovery of your own? Ontario. **The world works here.**

ONTARIO
CANADA

investinontario.com/research
1-800-819-8701

Discover us at BIO Atlanta
Booth #3311

Ontario Paid for by the Government of Ontario.

INTRODUCTION

What's Bugging Plants?

PLANTS, LIKE OTHER ORGANISMS, INCLUDING ANIMALS, LIVE IMMERSED IN A THRIVING community of microbes. The diversity of fungi, oomycetes, and bacteria with which plants interact brings both plague and benefit. The more we understand how plants tame, thwart, and succumb to their bugs, the more likely we will be able to extract new resources for antimicrobial treatments and manage agricultural challenges (Editorial, p. 691).

Microbial pathogens on the attack give the host plant several opportunities to respond. The very molecules of the microbe provide a means by which plants can identify the specific threat and take action. And the signal molecule(s) that the microbe exudes in its pathogenic actions can provide other targets. Boller and He (p. 742) discuss how innate immunity represents the first line of inducible defense against infection in both plants and animals. Takken and Tameling (p. 744) look at the biochemistry of the resistance (R) proteins as they detect microbial signals and activate plant defenses.

Phytochemicals that function primarily in warding off microbial pests warrant much more diverse analysis, as detailed by Bednarek and Osbourn (p. 746), who discuss interwoven networks of function for plant secondary metabolites. Pathogens must also get past various physical barriers at the plant surface. Some of the means by which fungi deliver their effector proteins into the plant cell are highlighted by Panstruga and Dodds (p. 748). When the various defenses fail and the pathogen gains access to the plant, both plant and pathogen make use of complex signaling networks of hormones, including jasmonate, auxin, abscisic acid, and gibberellin, as discussed by Grant and Jones (p. 750).

Microbes tend to get our most immediate attention when things go wrong in ways that affect us—when the fruit is blemished or the wheatfield destroyed. But not all microbial interactions are detrimental. Some plants benefit from interactions with their microbial community. The root nodules on soybeans, where bacteria bask in symbiotic comfort, provide the host plant with important nutrition. Oldroyd *et al.* (p. 753) survey our current understanding of how plants form and maintain mutually beneficial interactions with fungi and bacteria. Over time, microbial partnerships may shift between parasitism, pathogenesis, commensalism, and mutualism, as the balance of changes between partners. Burdon and Thrall (p. 755) take an organismal view of plant-microbe interactions, examining the importance of ecological factors and the need for realistic models of coevolution.

The interactions between plants and their bugs reflect an extremely complex system. This special collection of articles highlights some of the recent research progress made in understanding microbes and what they bring to the plant world.

– Pamela J. Hines and Laura M. Zahn

Plant-Microbe Interactions

CONTENTS

Perspectives

742 Innate Immunity in Plants: An Arms Race Between Pattern Recognition Receptors in Plants and Effectors in Microbial Pathogens
T. Boller and S. Y. He

744 To Nibble at Plant Resistance Proteins
F. L. W. Takken and W. I. L. Tameling

746 Plant-Microbe Interactions: Chemical Diversity in Plant Defense
P. Bednarek and A. Osbourn

748 Terrific Protein Traffic: The Mystery of Efector Protein Delivery by Filamentous Plant Pathogens
R. Panstruga and P. N. Dodds

750 Hormone (Dis)harmony Moulds Plant Health and Disease
M. R. Grant and J. D. G. Jones

753 Reprogramming Plant Cells for Endosymbiosis
G. E. D. Oldroyd et al.

755 Coevolution of Plants and Their Pathogens in Natural Habitats
J. J. Burdon and P. H. Thrall

See also related Editorial on p. 691

Science

Published by AAAS

PERSPECTIVE

Innate Immunity in Plants: An Arms Race Between Pattern Recognition Receptors in Plants and Effectors in Microbial Pathogens

Thomas Boller[1]* and Sheng Yang He[2]*

For many years, research on a suite of plant defense responses that begin when plants are exposed to general microbial elicitors was underappreciated, for a good reason: There has been no critical experimental demonstration of their importance in mediating plant resistance during pathogen infection. Today, these microbial elicitors are named pathogen- or microbe-associated molecular patterns (PAMPs or MAMPs) and the plant responses are known as PAMP-triggered immunity (PTI). Recent studies provide an elegant explanation for the difficulty of demonstrating the role of PTI in plant disease resistance. It turns out that the important contribution of PTI to disease resistance is masked by pathogen virulence effectors that have evolved to suppress it.

Plants are exposed to myriads of potential microbial pathogens, but the world is still green. Why? Plants possess an innate immune system that efficiently detects and wards off potentially dangerous microbes (*1*–*3*). A first layer of this system is based on the amazingly sensitive perception of pathogen- or microbe-associated molecular patterns (PAMPs or MAMPs) through pattern recognition receptors (PRRs) at the plant's cell surface (Fig. 1). For example, plants perceive bacterial flagellin through a PRR known as FLS2 (flagellin sensitive 2), a leucine-rich repeat receptor kinase (LRR-RK) located in the plasma membrane. Similarly, mammals use the Toll-like receptor TLR5 to perceive bacterial flagellin and mount multifaceted downstream immune responses (*1*, *4*). The responses to flagellin and other MAMPs have been called PAMP-triggered immunity (PTI). Successful pathogens produce effectors to inhibit PTI, but plants, in turn, can perceive such effectors through additional receptors—typically nucleotide-binding leucine-rich repeat (NB-LRR) proteins—to mount a second layer of defense called effector-triggered immunity (ETI). Although the importance of ETI (formerly known as gene-for-gene resistance) in plant immunity is well established, only recently have we begun to appreciate a fundamental role of PTI in mediating plant-microbe interactions. Here, we highlight recent literature on PRR signaling and the ability of microbial pathogens to suppress PTI as a key virulence strategy.

Perception of Microbes Through Pattern Recognition Receptors

A hallmark of PRRs is their sensitivity and specificity: Plants possessing the appropriate PRRs perceive a specific MAMP at subnanomolar concentrations, whereas plants lacking the PRRs are completely blind to it. A given MAMP is recognized through a specific conserved epitope, such as the stretch of 22 amino acids (flg22) in the N terminus of flagellin. Can pathogens avoid perception by the PRRs? It appears they can, but at a cost. Introduction of mutations into flagellin that make the molecule unrecognizable by FLS2 also render the microbe motionless and reduce its virulence (*5*). Thus, the specificity of the PRR appears to be focused exactly on a highly conserved domain of the MAMP that is functionally important to the microbe.

FLS2 homologs exist in all higher plants for which genomic information is available (*1*), and the rice homolog is functionally active as a flagellin receptor (*6*). Hence, flagellin perception through FLS2 homologs is evolutionarily old and conserved. Another well-characterized PRR of *Arabidopsis*, EFR (EF-Tu receptor), perceives bacterial EF-Tu (elongation factor Tu). Perception of this MAMP seems to be confined to the Brassicaceae and is not found in other dicots or monocots, which suggests that EF-Tu perception is evolutionarily young. However, all plant genomes so far sequenced contain homologs of the EFR-encoding gene with a comparable LRR structure. The rice genome encodes about 40 such homologs (*1*). One of them, found in some rice cultivars, is the disease resistance gene *Xa21*, the protein product of which appears to recognize a quorum-sensing molecule of the rice pathogen *Xanthomonas oryzae*; thus, although the EFR-type PRRs show elements of conserved sequences among plants, they appear to recognize different MAMPs in different plant families (*1*).

One of the first steps in signaling of the FLS2 receptor is its interaction with BRI1-associated kinase (BAK1), an LRR-RK (*7*, *8*). This comes as a surprise, because BAK1 has previously been known as a co-receptor of the plant hormone brassinosteroid receptor BRI1, as its name indicates (*9*). How can the same co-receptor function both in defense signaling and hormonal signaling? BRI1 and BAK1 are phosphorylated upon activation in hormonal signaling (*9*). Does this also occur in the FLS2-BAK1 interaction, and does differential phosphorylation contribute to the specificity of downstream responses? Is there competition between PTI and the brassinosteroid response for the co-receptor? What is the function of the four BAK1 homologs, the somatic embryogenesis-related kinases (SERKs), in *Arabidopsis*? Dysfunction of two of these, bak1 and serk4, sends *Arabidopsis* seedlings to death with symptoms of the hypersensitive response, a hallmark immune response of ETI (*7*, *9*, *10*).

Despite the specificity and sensitivity of MAMP perception by PRRs, it has taken the scientific community a long time to accept that such systems could support plant disease resistance during pathogen infection. Opinion began to shift with the discovery that mutations in the fls2 receptor left *Arabidopsis* plants unusually susceptible to the bacterial pathogen *Pseudomonas syringae* (*11*). Even more convincing were observations that pathogens actively deploy virulence factors as a virulence strategy to suppress PTI.

Suppression of PTI by Pathogen Effectors

A variety of bacterial virulence factors, including the phytotoxin coronatine, extracellular polysaccharides, and proteinaceous effectors secreted through the type III secretion system (TTSS), suppress PTI (*1*–*3*). Most spectacularly, two secreted effectors, AvrPto and AvrPtoB (from *P. syringae* strain DC3000), physically interact with the kinase domains of FLS2, EFR, or BAK1 (*12*–*14*). Such physical interactions inhibit the kinase activity of PRRs (*12*) or interfere with the formation of FLS2-BAK1 complexes (*13*). Whereas AvrPto seems to be a novel protein, AvrPtoB contains a C-terminal domain that resembles E3 ubiquitin ligase; ubiquitination by this domain initiates degradation of a tomato kinase (Fen) that is part of a unique and presumably ancient ETI pathway (*15*). The same domain also initiates degradation of PRRs, and thus its more important role may be in defeating PTI (*14*, *16*). The ability of AvrPto and AvrPtoB to derail PRRs provides a satisfying explanation for previous discoveries that these effectors could suppress a variety of responses of PTI, including callose deposition, activation of kinase cascades, and expression of MAMP-responsive proteins and small RNAs (*17*–*19*). Not all bacteria—indeed, not even all strains of *P. syringae*—express AvrPto and AvrPtoB, which suggests that other strategies exist to inhibit PRR signaling. Indeed, the effector HopAI1, present in many but not all *P. syringae* strains, is a phosphothreonine lyase that dephosphorylates mitogen-activated protein kinases (MAPKs) MPK3 and MPK6 to terminate

[1]Zurich-Basel Plant Science Center, Botanical Institute, University of Basel, Hebelstrasse 1, 4056 Basel, Switzerland. [2]Department of Energy Plant Research Laboratory, Department of Plant Biology, Michigan State University, East Lansing, MI 48824, USA.

*To whom correspondence should be addressed. E-mail: thomas.boller@unibas.ch (T.B.); hes@msu.edu (S.H.E.)

PRR signaling (*20*). Interestingly, another member of this effector family dephosphorylates kinases involved in mammalian innate immunity (*21*), showing that pathogens can apply the same mechanism of host immune modulation to both plants and mammals.

Pathogen effectors target more than PRRs or the MAPK cascade to suppress PTI. These effectors also attack processes directly downstream of PRR signaling and other consequent events (Fig. 1) (*22*). For example, the *P. syringae* effector HopU1 modifies several *Arabidopsis* RNA-binding proteins, including GRP7, by adenosine diphosphate ribosylation. HopM1, another *P. syringae* effector, triggers degradation of the *Arabidopsis* MIN7 protein, which is a member of the ARF family of guanine nucleotide exchange factors involved in vesicle trafficking. Plants lacking either *grp7* or *min7* are abnormally susceptible to bacterial infection, implicating RNA metabolism and vesicle trafficking as part of the plant's immune response to pathogens (*22*). The *P. syringae* effector HopI1 resides in the chloroplast, where its action (presumably through interaction with Hsp70 chaperones) suppresses accumulation of salicylic acid, a plant hormone key to defense responses; three other *P. syringae* effectors—AvrRpm1, AvrB, and AvrRpt2—interact with or modify proteins such as RIN4 and RAR1 that regulate pathogen- and effector-triggered immunity (*22*).

The many examples of physical associations between pathogen effectors and regulators of host immune responses have spurred a notion that pathogen effectors can be used as molecular probes to identify unknown components of the plant innate immune system, including those involved in PTI. This is an exciting time for researchers in this area, especially because recent functional genomics studies suggest that bacteria, fungi, oomycetes, and nematodes that are pathogenic to plants could collectively deliver hundreds of virulence effectors into host cells. Identification of the plant targets of this vast repertoire of pathogen effectors will likely yield many new discoveries that could have a great impact on our understanding of plant immunity, pathogenesis, and plant biology for years to come.

Concluding Remarks

The past few years have witnessed paradigm-shifting advances in the field of plant-microbe interactions. Contributing to these advances are experimental demonstrations of a functional role of PRRs in plant disease resistance and the discovery that many bacterial virulence factors are involved in suppressing PRR signaling and PTI-associated immune responses. Nonetheless, current research is limited by heavy reliance on information derived from essentially a single pathosystem: the interaction between the plant *Arabidopsis* and the bacterium *P. syringae* (Fig. 1). Thus, our current understanding of plant-pathogen interactions is of a pioneering but preliminary nature. It remains to be seen whether the conceptual framework emerging from the study of this pathosystem will translate to other plant-microbe interactions. The incredibly diverse interactions between plants and microbes suggest that other systems will involve many novel mechanisms, which are likely to refine or even challenge the current models. However, because all pathogens carry MAMPs that may be recognized by plants, yet all plants are still susceptible to virulent pathogens, it is certain that activation and suppression of PTI is a general principle underpinning plant-microbe interactions.

References and Notes

1. T. Boller, G. Felix, *Annu. Rev. Plant Biol.* **60**, 379 (2009).
2. S. T. Chisholm, G. Coaker, B. Day, B. J. Staskawicz, *Cell* **124**, 803 (2006).
3. J. D. G. Jones, J. L. Dangl, *Nature* **444**, 323 (2006).
4. N. K. Clay, A. M. Adio, C. Denoux, G. Jander, F. M. Ausubel, *Science* **323**, 95 (2009); published online 18 December 2008 (10.1126/science.1164627).
5. K. Naito *et al.*, *Mol. Plant Microbe Interact.* **21**, 1165 (2008).
6. R. Takai *et al.*, *Mol. Plant Microbe Interact.* **21**, 1635 (2008).
7. D. Chinchilla *et al.*, *Nature* **448**, 497 (2007).
8. A. Heese *et al.*, *Proc. Natl. Acad. Sci. U.S.A.* **104**, 12217 (2007).
9. X. Wang *et al.*, *Dev. Cell* **15**, 220 (2008).
10. K. He *et al.*, *Curr. Biol.* **17**, 1109 (2007).
11. C. Zipfel *et al.*, *Nature* **428**, 764 (2004).

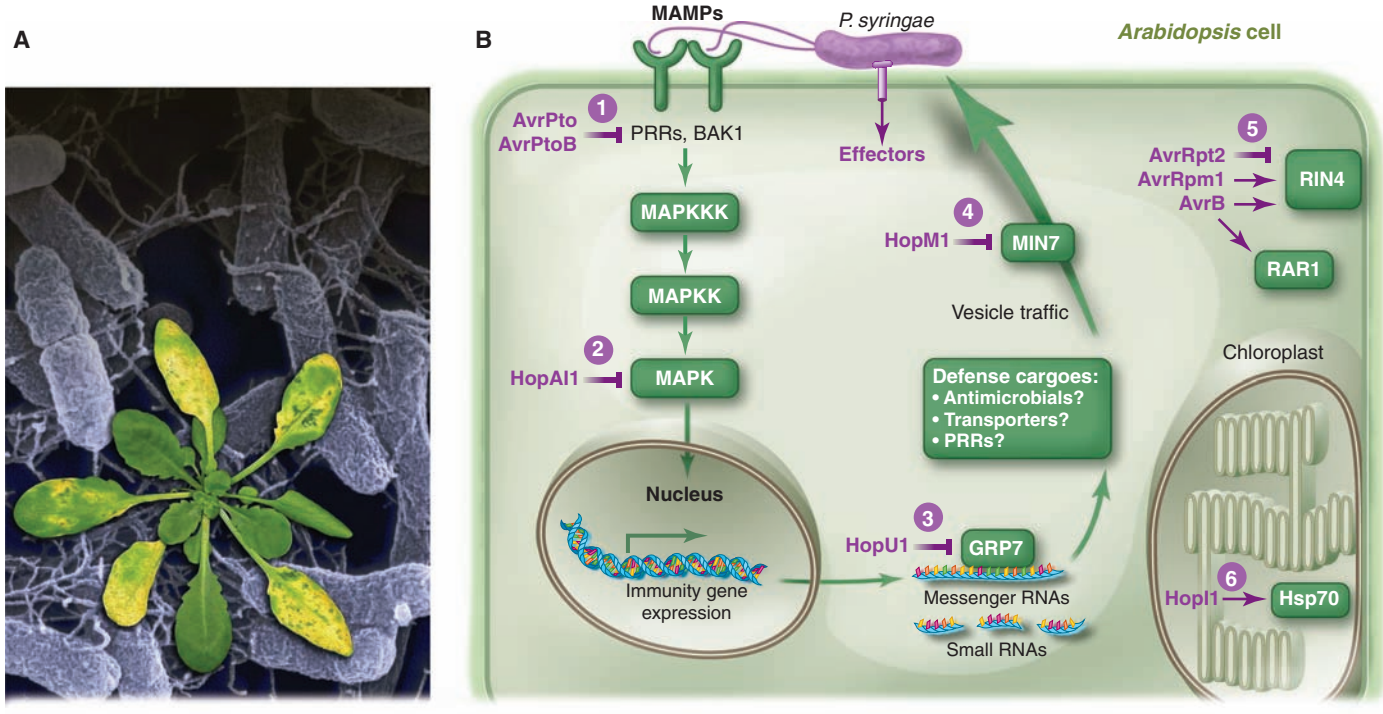

Fig. 1. Concept of activation and suppression of PTI during pathogen infection. (**A**) An *Arabidopsis* plant showing disease symptoms (in the foreground; natural size) after infection by *P. syringae* bacteria (electron microscopy image in the background; magnification, 10,000×). (**B**) A conceptual diagram of PRR signaling and action of several *P. syringae* effectors for which the plant targets and immune suppression function have been characterized. Green and purple colors indicate plant targets and *P. syringae* effectors, respectively. Numbers in circles denote six steps targeted by effectors: MAMP perception (PRRs), the MAPK cascade (MPK3 and MPK6), RNA metabolism (GRP7), vesicle traffic (MIN7), regulators of PTI (RIN4 and RAR1), and chloroplast function (Hsp70) (*22*).

12. T. Xiang *et al.*, *Curr. Biol.* **18**, 74 (2008).
13. L. Shan *et al.*, *Cell Host Microbe* **4**, 17 (2008).
14. V. Göhre *et al.*, *Curr. Biol.* **23**, 1824 (2008).
15. T. R. Rosebrock *et al.*, *Nature* **448**, 370 (2007).
16. S. Gimenez-Ibanez, *Curr. Biol.* **19**, 423 (2009).
17. P. Hauck, R. Thilmony, S. Y. He, *Proc. Natl. Acad. Sci. U.S.A.* **100**, 8577 (2003).
18. P. He *et al.*, *Cell* **125**, 563 (2006).
19. L. Navarro, F. Jay, K. Nomura, S. Y. He, O. Voinnet, *Science* **321**, 964 (2008).
20. J. Zhang *et al.*, *Cell Host Microbe* **1**, 175 (2007).
21. H. Li *et al.*, *Science* **315**, 1000 (2007).
22. A. Block, G. Li, Z. Q. Fu, J. R. Alfano, *Curr. Opin. Plant Biol.* **11**, 396 (2008).

23. Supported by Swiss National Science Foundation grant 31003A-105852 (T.B.) and by NIH grant R01AI060761, U.S. Department of Energy grant DE-FG02-91ER20021, and NSF grant IOB0444915 (S.Y.H.).

10.1126/science.1171647

PERSPECTIVE

To Nibble at Plant Resistance Proteins

F. L. W. Takken[1]* and W. I. L. Tameling[2]*

To intercept invading microbes that threaten growth and reproduction, plants evolved a sophisticated innate immune system. Recognition of specialized pathogens is mediated by resistance proteins that function as molecular switches. Pathogen perception by these multidomain proteins seems to trigger a series of conformational changes dependent on nucleotide exchange. The activated resistance protein switches on host defenses, often culminating in the death of infected cells. Given their control over life and death, activity of these proteins requires tight regulation that involves intramolecular interactions between the various domains.

Discrimination between self and non-self is a fundamental ability of immune systems. Vertebrates rely on both an innate and an adaptive immune system of which the last is based on immunological memory. In contrast, plants primarily rely on their innate immune system in which each individual plant cell can autonomously mount a defense response (*1*). Two layers can be distinguished in the plant immune system. One is based on extracellular trans-membrane receptors that recognize conserved microbe-associated molecules and induce a relatively weak immune response that, nevertheless, effectively halts colonization by most microbes. The second layer is effective against specialized pathogens that can successfully break through the first layer and is based on highly polymorphic resistance (R) proteins. R proteins act mainly (but not exclusively) intracellularly and confer protection against (hemi-) biotrophic pathogens that need living host tissues for their proliferation. During infection, these pathogens (which include many viruses, bacteria, fungi, oomycetes, and nematodes) produce virulence factors (effectors), of which several suppress the first layer of the plant's immune system (*1*), clearing the way for infection. Some effectors, or the perturbations they cause in the plant, are perceived by R proteins, which consequently set off strong defense responses in the plant that often leads to suicide of the infected cells (*1*).

Most R proteins are multidomain NB-LRRs ("nibblers"), named after their central nucleotide-binding (NB) and leucine-rich repeat (LRR) domains. The NB domain is part of a larger domain, the so-called NB-ARC domain, which consists of three subdomains: NB, ARC1, and ARC2 (*2*). The N termini of these R proteins are structurally diverse; some have homology to the Toll and human interleukin 1 receptor (TIR) and are called TIR-NB-LRRs. Others are commonly referred to as CC-NB-LRRs, because most carry predicted coiled-coil (CC) regions (*1*, *2*). Plant NB-LRRs, together with the metazoan cell death regulators Apaf-1 and CED-4, form the NB-ARC family within the class of STAND [signal transduction adenosine triphosphatases (ATPases) with numerous domains] proteins (*3*). The NACHT sister family within this class encompasses the animal NLR (NACHT-LRR/NOD-LRR) innate immune receptors, where the NB domain is also fused to an LRR domain (*4*). STAND proteins are proposed to function as molecular switches, regulating cellular responses through nucleotide-dependent conformational changes (*2*, *3*). Here, we discuss and evaluate the R protein–switch model in the context of other STAND proteins.

Because R proteins have the potential to trigger host cell death, their activity needs to be tightly regulated. They should be strongly inhibited in the absence of a pathogen, but rapidly activated upon attack. How is this process controlled? It appears that inappropriate activation is prevented by autoinhibition, which seems to be mainly accomplished by intramolecular interactions between the various domains. Interaction and mutagenesis studies with various NB-ARC and NLR proteins, including R proteins, identified both the N-terminal part of the repeat domain and the ARC2 subdomain to be essential for this autoinhibition (*5*, *6*) (Fig. 1). Disturbance of the interaction between these two subdomains, by mutations or domain swaps, diminishes autoinhibition and results in constitutive R protein activation (*5*, *7*).

The LRR domain is not only involved in negative regulation, but provides positive control as well. Expression of truncated R proteins that lack the LRR domain and carry autoactivating mutations in the NB-ARC domain generally does not induce full host defenses unless the corresponding LRR domain is coexpressed (*7*). Furthermore, various studies have shown that the C-terminal part of the LRR domain provides pathogen recognition specificity (*2*, *7*). Hence, the LRR domain has a dual function; it provides autoinhibition and it translates pathogen recognition into activation. How exactly the LRR recognizes a pathogen is unclear. Whereas some R proteins bind effectors directly, others require an intermediary host factor. This factor often interacts with the N-terminal domain of the R protein and could represent either the virulence target (thereby acting as a guardee) or a target mimic (thereby acting as a decoy) (*8*, *9*). In this situation, the LRR is likely involved in sensing the effector-induced perturbations of the target. Either way, effector recognition evokes R-protein activation, a process that, as with other STAND proteins, requires the R protein to bind nucleotides [adenosine diphosphate or adenosine triphosphate (ADP/ATP)] (*2*, *10*–*15*).

Biochemical studies on the tomato R protein I-2 revealed that it tightly binds ADP in vitro and that mutations reducing its ATP-hydrolysis rate result in constitutive defense activation. On the basis of these data, it was proposed that R proteins function as nucleotide-controlled molecular switches (*10*). In this model, the ADP-bound state represents the "OFF" state and the ATP-bound state the "ON" state of the protein (Fig. 1). Recognition of an effector triggers a conformational change that results in an "intermediate" open state, which enables ADP to be exchanged for ATP. Upon ATP-binding, the R protein adopts its active conformation ("ON" state) that subsequently unchains, in a still unknown way, host defenses. ATP hydrolysis eventually returns the protein to its autoinhibited "OFF" state.

Recently, this model gained support by the observation that related STAND proteins also tightly bind ADP in their autoinhibited state (*16*–*18*). Furthermore, the hypothesis that effector-binding sets the stage for nucleotide-exchange was substantiated by data on two STAND proteins: the *Escherichia coli* transcriptional regu-

[1]Plant Pathology, Swammerdam Institute for Life Sciences (SILS), University of Amsterdam, Post Office Box 94215, 1090 GE Amsterdam, the Netherlands. [2]Laboratory of Phytopathology, Wageningen University, Post Office Box 8025, 6700 EE Wageningen, the Netherlands.

*To whom correspondence should be addressed. E-mail: F.L.W.Takken@uva.nl (F.L.W.T.); wladimir.tameling@wur.nl (W.I.L.T.)

lator MalT and the human NLR protein NALP1 (NLRP1). Binding of the inducer, maltotriose or muramyl dipeptide, respectively, to these STAND proteins is an absolute requirement for their nucleotide exchange, as exogenously applied ATP was not bound in absence of the inducer (*12*, *18*). Moreover, addition of the inducer in the absence of ATP led to a conformational change that likely corresponds to the "intermediate" open state proposed for R proteins upon effector recognition (*10*, *12*) (Fig. 1). Analogous to the R protein I-2 (*10*), MalT became constitutively active after mutation of its catalytic residue, which abolished ATP hydrolysis and locked the protein in its ATP-bound state (*18*) (fig. S1). Naturally occurring mutations of the corresponding putative catalytic residue in the NLR proteins NOD2 and PYPAF1 (NLRP3) also resulted in constitutive activity and, as a consequence, autoinflammation (*19*, *20*) (fig. S1). Finally, recent biochemical analysis showed that the active, oligomeric conformation of Apaf-1 harbors either deoxyadenosine triphosphate (dATP) or ATP [for simplicity, both are referred to as (d)ATP]. However, it remains to be resolved whether the monomeric autoinhibited form of Apaf-1 is bound to (d)ADP or to (d)ATP, and whether nucleotide-exchange has to be preceded by hydrolysis of prebound (d)ATP (*16*, *21*). Taken together, these data link the "ON" and "OFF" state of STAND proteins to an ATP- and ADP-bound state, respectively, and support the hypothesis that effector recognition induces nucleotide exchange in R proteins (Fig. 1).

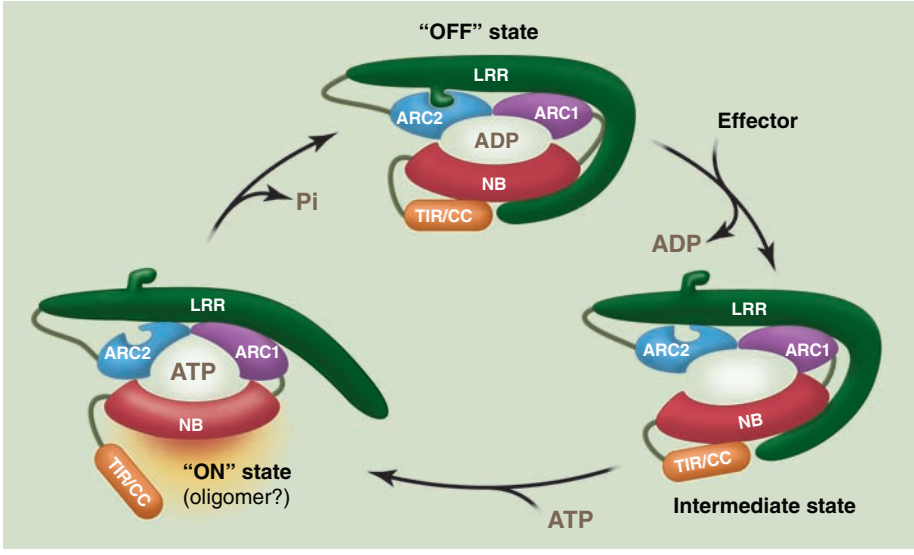

Fig. 1. Model for R-protein activation. In the absence of a pathogen, NB-LRR R proteins reside in an autoinhibited, ADP-bound "OFF" state that is stabilized by the LRR domain. Effector-perception by the C-terminal part of the LRR domain changes the interface between its N-terminal part and the ARC2 subdomain, thereby creating a more open conformation of the R protein that is prone to nucleotide exchange. ADP/ATP exchange triggers a second conformational change, altering the interactions between the central NB-ARC, the N-terminal TIR/CC and C-terminal LRR domains resulting in the "ON" state. In the activated state, the NB subdomain becomes exposed to initiate defense signaling. ATP hydrolysis resets the protein into its ADP-bound autoinhibited "OFF" state. The model is a refined version of that presented in (*2*).

To date, it remains unclear how activated R proteins trigger defense signaling. STAND proteins such as Apaf-1 and CED-4 oligomerize and form ring-like structures that provide an activation platform for signaling components (*11*). For plant R proteins, effector-induced oligomerization has been described for only one R protein so far (*22*). Although some R proteins depend on other NB-LRR proteins for their function (*23*, *24*), it remains an open question whether (hetero-) oligomerization is a common feature for R proteins. For a number of NB-ARC and NLR proteins, the N-terminal domain has been shown to interact with downstream signaling partners (*25*). However, no such partners have been identified to interact with the N-terminal domains of R proteins, and evidence for a signaling function of this domain remains slim (*9*). It now seems that the N terminus, together with the LRR domain, is actually involved in recognition rather than signaling, as suggested by its interactions with putative effector targets or target mimics (*8*, *9*, *26*).

If both the N- and C-terminal domains of R proteins are indeed involved in recognition rather than signaling, that leaves the NB domain, perhaps surprisingly, as a candidate to serve as an interaction platform for downstream signaling components. The observation that expression of only the NB subdomain of the potato R protein Rx triggers constitutive defenses in the absence of the pathogen lends support to this idea (*26*). A mechanism in which the NB domain itself is responsible for downstream signaling would be a unique property of R proteins, not shared with other members of the NB-ARC and NLR families. Direct signaling by the NB domain instead would resemble the molecular switch function of regulatory guanosine triphosphatases (GTPases) of the Ras superfamily (*27*). In these GTPases, different nucleotide-dependent conformations of two effector loops within the core nucleotide binding fold regulate downstream events. Nucleotide binding and hydrolysis—and, thereby, the activation state of these GTPases—are regulated by accessory proteins. It is tempting to speculate that in R proteins these functions are embedded in its multidomain structure.

In recent years, nibbling at NB-LRR protein function has shed some light on the molecular mechanistic basis of their activation and the role of nucleotide binding. To gain a deeper understanding of how these proteins regulate plant defenses, we now need to investigate their biochemical properties in more detail and to further analyze the dynamics and subcellular localization of NB-LRR signaling complexes in vivo. Identification of partners interacting with the NB domain should eventually reveal how R proteins activate host defenses. Another major challenge will be the elucidation of the three-dimensional structure of R proteins, preferably in the different conformational states, as this is the key for a full understanding of the molecular mechanisms underlying the choice between life and death.

References and Notes

1. J. D. G. Jones, J. L. Dangl, *Nature* **444**, 323 (2006).
2. F. L. W. Takken, M. Albrecht, W. I. L. Tameling, *Curr. Opin. Plant Biol.* **9**, 383 (2006).
3. D. D. Leipe, E. V. Koonin, L. Aravind, *J. Mol. Biol.* **343**, 1 (2004).
4. S. Mariathasan, D. M. Monack, *Nat. Rev. Immunol.* **7**, 31 (2007).
5. G. J. Rairdan, P. Moffett, *Plant Cell* **18**, 2082 (2006).
6. T. Tanabe *et al.*, *EMBO J.* **23**, 1587 (2004).
7. G. Rairdan, P. Moffett, *Microbes Infect.* **9**, 677 (2007).
8. R. A. L. van der Hoorn, S. Kamoun, *Plant Cell* **20**, 2009 (2008).
9. E. Lukasik, F. L. W. Takken, *Curr. Opin. Plant Biol.*, in press; 10.1016/j.pbi.2009.03.001.
10. W. I. L. Tameling *et al.*, *Plant Physiol.* **140**, 1233 (2006).
11. S. J. Riedl, G. S. Salvesen, *Nat. Rev. Mol. Cell Biol.* **8**, 405 (2007).
12. B. Faustin *et al.*, *Mol. Cell* **25**, 713 (2007).
13. J. A. Duncan *et al.*, *Proc. Natl. Acad. Sci. U.S.A.* **104**, 8041 (2007).
14. W. I. L. Tameling *et al.*, *Plant Cell* **14**, 2929 (2002).
15. C. Lu *et al.*, *Biochem. Biophys. Res. Commun.* **331**, 1114 (2005).
16. Q. Bao, W. Lu, J. D. Rabinowitz, Y. Shi, *Mol. Cell* **25**, 181 (2007).
17. S. J. Riedl, W. Li, Y. Chao, R. Schwarzenbacher, Y. Shi, *Nature* **434**, 926 (2005).
18. E. Marquenet, E. Richet, *Mol. Cell* **28**, 187 (2007).
19. N. Kanazawa *et al.*, *Blood* **105**, 1195 (2005).
20. T. A. Dowds, J. Masumoto, L. Zhu, N. Inohara, G. Nunez, *J. Biol. Chem.* **279**, 21924 (2004).
21. H. E. Kim, F. Du, M. Fang, X. Wang, *Proc. Natl. Acad. Sci. U.S.A.* **102**, 17545 (2005).
22. P. Mestre, D. C. Baulcombe, *Plant Cell* **18**, 491 (2006).
23. J. R. Peart, P. Mestre, R. Lu, I. Malcuit, D. C. Baulcombe, *Curr. Biol.* **15**, 968 (2005).
24. S. H. E. J. Gabriëls *et al.*, *Plant J.* **50**, 14 (2007).

25. Z. Ye, J. P. Ting, *Curr. Opin. Immunol.* **20**, 3 (2008).
26. G. J. Rairdan *et al.*, *Plant Cell* **20**, 739 (2008).
27. S. R. Sprang, *Sci. STKE* **2000**, pe1 (2000).
28. We thank M. Rep, C. Testerink, and M. Joosten for critical review. We apologize to the many colleagues whose work could not be discussed due to size restriction. W.I.L.T. is supported by a VENI grant from the Netherlands Organization for Scientific Research (NWO). Research in the Takken lab is supported by the Centre for BioSystems Genomics (Netherlands Genomics Initiative/NWO) and by the European Union Integrated Project BIOEXPLOIT CT-2005-513959.

Supporting Online Material
www.sciencemag.org/cgi/content/full/324/5928/744/DC1
Fig. S1
References

10.1126/science.1171666

PERSPECTIVE

Plant-Microbe Interactions: Chemical Diversity in Plant Defense

Paweł Bednarek[1]* and Anne Osbourn[2]*

The chemical diversity within the plant kingdom is likely to be a consequence of niche colonization and adaptive evolution. Plant-derived natural products have important functions in defense. They also have broader ecological roles and may in addition participate in plant growth and development. Recent data suggest that some antimicrobial phytochemicals may not serve simply as chemical barriers but could also have functions in defense-related signaling processes. It is important, therefore, that we should not to be too reductionist in our thinking when endeavoring to understand the forces and mechanisms that drive chemical diversification in plants.

Collectively, plants are a tremendous resource of structurally diverse metabolites. Examples of the structures of some of these are shown in Fig. 1. It is widely accepted that these compounds have important functions in influencing interactions between plants and other organisms. Deciphering the chemical signaling processes that mediate these interactions represents a substantial challenge for plant science.

The importance of synthesis and accumulation of antimicrobial metabolites for plant defense has intrigued researchers for the best part of a century (*1*). Antimicrobial compounds can be produced as part of normal plant growth and development and are usually stored in specialized organs or tissues (e.g., trichomes, oil glands, or epidermal cell layers). These constitutive or preformed antimicrobial chemicals are sometimes also referred to as phytoanticipins (*2*). In addition, antimicrobial compounds can be synthesized de novo in response to microbial attack by transcriptional activation of genes for biosynthetic pathways. Such compounds are known as phytoalexins.

Our understanding of the role of phytochemicals in plant defense is still incomplete. Knowledge and interpretation of chemical diversity in plants depends very much on the ability to detect, analyze, and measure compounds, as well as their metabolic precursors and derivatives in plant tissues. Despite recent progress in the development of higher-resolution multidimensional separation/detection systems, many compounds are likely to be present in trace amounts that are below the current levels of detection, at least in wild-type plants (*3*). A shortage of reference standards makes comprehensive analysis of phytochemicals in plant extracts even more challenging. Use of mutant, RNA interference, and overexpression lines in which the expression of genes encoding regulatory and biosynthetic components of metabolic pathways has been altered can greatly facilitate both identification of new metabolites and pathway discovery (*4*–*6*).

There is evidence to indicate that preformed antimicrobial chemicals confer protection against disease. For example, oat roots produce an antimicrobial triterpene glycoside known as avenacin (*1*). Genetic analysis of a fungal pathogen of oat, *Gaeumannomyces graminis* var. *avenae*, has shown that infection of oat roots depends on production of a fungal avenacin hydrolase (*1*). Complementary experiments involving isolation and characterization of avenacin-deficient mutants of diploid oat have provided further evidence that this compound confers broad-spectrum disease resistance (*7*). Another class of constitutively produced secondary metabolites is the steroidal glycoalkaloids. The tomato steroidal glycoalkaloid α-tomatine has long been implicated in plant defense (*1*). The ability to degrade this compound contributes to the pathogenicity of various microbes to tomato (*1*, *8*, *9*). Superficially, these degradation processes represent simple detoxification events. However, α-tomatine hydrolysis products are able to suppress induced plant defenses (*10*, *11*). The aglycone of α-tomatine, tomatidine, has recently been shown to inhibit sterol biosynthesis in yeast (*12*). It is not yet known whether suppression of induced defenses in tomato by steroidal alkaloid hydrolysis products is due to interference with plant sterol metabolism.

Induced defense responses in plants usually involve cell polarization, reorganization of the actin cytoskeleton, directed movement of particular organelles, targeted secretion, and deposition of the glucan polymer callose at the site of pathogen contact (*13*). This may also include trafficking and secretion of antimicrobial compounds to the infection site (*14*). Visualization of delivery of vesicles containing red-pigmented flavonoids to pathogen challenge sites in sorghum leaves provides a clear demonstration of such trafficking (*15*). Recent evidence suggests that glucosinolates, amino acid–derived thioglucosides that are commonly synthesized and stored in cells of healthy crucifer plants, may also be mobilized to pathogen challenge sites (*16*, *17*). Upon tissue disruption, glucosinolates are converted to biologically active compounds by myrosinases (plant glycosyl hydrolases). Although best known as insect deterrents, glucosinolate breakdown products have potent antimicrobial activity (*1*).

Research drawing on the extensive array of mutants and tools available for the model crucifer *Arabidopsis thaliana* has recently implicated indole glucosinolates and their breakdown products (compounds distinct from those considered as insect deterrents) in induced broad-spectrum disease resistance to microbial challenge (*16*, *17*). Unlike the passive mode of glycoside activation proposed for other phytoanticipins, pathogen-triggered glucosinolate metabolism is an active process involving directed movement and the concentration of a hydrolase to the cell periphery at fungal penetration sites (*18*), which likely generates high local concentrations of end product(s). Of note, the same genetic and metabolic components are required for the extracellular accumulation of callose in response to treatment with a microbe-associated molecular pattern derived from bacterial flagellin (*16*). Localized accumulation of glucosinolate metabolism products may serve as the signal for this deposition, or alternatively may trigger callose deposition directly as a consequence of phytotoxicity. Accumulation of late avenacin pathway intermediates in oat roots also results in callose accumulation (*19*), raising the question of whether this is a straightforward response to localized accumulation of a toxic compound or part of a more sophisticated defense response. More broadly, the contribution of phytoalexins to disease resistance has been the subject of intensive investigation in a range of different plant species [e.g., for camalexin in *Arabidopsis* and pisatin in pea

[1]Department of Plant Microbe Interactions, Max-Planck-Institut für Züchtungsforschung, Köln, Germany. [2]Department of Metabolic Biology, John Innes Centre, Norwich, UK.

*To whom correspondence should be addressed. E-mail: bednarek@mpiz-koeln.mpg.de (P.D.); anne.osbourn@bbsrc.ac.uk (A.O.)

(*1*, *20*, *21*)]. These compounds have, in at least some cases, been shown to contribute to disease resistance, possibly by serving as disinfectants that assist in isolating infected cells from healthy tissue.

Some phytochemicals are known to have multiple functions in ecological interactions. For example, glucosinolates serve as antimicrobial defense compounds and as attractants and repellents for insects and predators of feeding insects. They are also important in determining palatability of brassicas for animals and humans (*1*, *22*). These multiple roles present challenges when considering how to distil knowledge of the biological functions of particular phytochemicals into a framework that will enable the importance of these chemicals for survival in nature to be understood, particularly given temporal and spatial environmental heterogeneity.

Phytochemicals can also have functions in plant growth and development, for example in auxin transport and in regulation of seed longevity and dormancy (*14*). Strigolactones, terpenoid lactones produced by many plants, are not known to be involved in defense against microbes but nevertheless merit attention here because they provide an excellent example of the multiple roles that phytochemicals can serve. Strigolactones stimulate seed germination of parasitic plants such as *Striga* (*23*). More recently, they have also been implicated as signals for the establishment of mycorrhizal symbioses (*24*, *25*), which suggests that parasitic plants have learned to eavesdrop on a signal that plants normally produce to favor the establishment of beneficial interactions. A further twist to this story is the finding that strigolactones serve as plant growth hormones and can suppress subapical shoot outgrowth (*26*, *27*).

Genes functioning in secondary metabolism are generally more divergent than those coding for proteins involved in primary metabolism. Investigations of chemical diversification in plants will therefore benefit from focusing on genes and regions of genomes that are divergent when related producing and nonproducing species are compared, rather than those that are conserved. Although genes for most metabolic pathways in plants are generally thought to be unclustered, an increasing number of operon-like gene clusters have been identified that are required for synthesis of plant defense compounds (*5*, *28*–*30*). It is not clear why genes for some metabolic pathways are clustered and others are not. There may be epistatic selection for the maintenance of a gene cluster because the pathway end-product confers a selective advantage and, in at least some cases, because disruption of the pathway can lead to the accumulation of toxic intermediates (*5*, *19*). Clustering may in addition facilitate coordinated regulation at the level of nuclear organization/chromatin. It may be that these gene clusters, which tend to be in subtelomeric regions, are of recent origin and have not yet been fully integrated into the genome.

Clustered or not, natural product pathways serve as read-outs for adaptive evolution and offer a means of understanding the mechanisms that drive metabolic diversification. Computational biology and genomics provide new and powerful tools with which to understand the molecular basis of complex traits and to integrate these with knowledge of the natural products that plants produce (*31*, *32*). Connecting the catalytic landscape of secondary metabolism to fitness landscapes of organisms represents a major challenge, particularly as it is becoming increasingly evident that secondary metabolites are likely to have multiple functions both in plant development (in at least some cases) and chemical ecology (*33*). Real progress will require a shift from reductionism to more comprehensive analyses of natural and agronomic systems (*34*), and the development of sophisticated ecological and evolutionary models that integrate plant metabolism and biotic interactions.

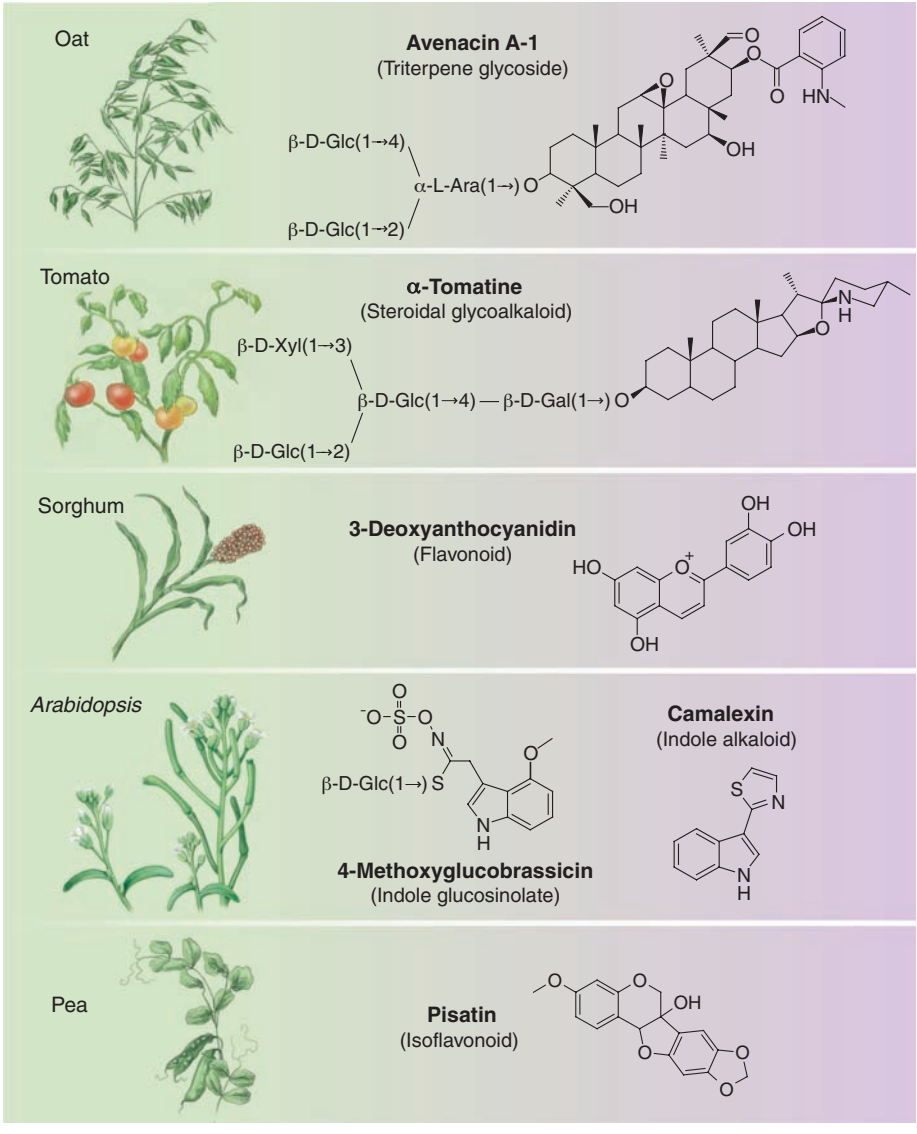

Fig. 1. Examples of phytochemicals with roles in plant-microbe interactions.

References and Notes

1. J. P. Morrissey, A. E. Osbourn, *Microbiol. Mol. Biol. Rev.* **63**, 708 (1999).
2. H. D. VanEtten, J. W. Mansfield, J. A. Bailey, E. E. Farmer, *Plant Cell* **6**, 1191 (1994).
3. J. W. Allwood, D. I. Ellis, R. Goodacre, *Physiol. Plant.* **132**, 117 (2008).
4. J. O. Borevitz, Y. Xia, R. A. Dixon, C. Lamb, *Plant Cell* **12**, 2383 (2000).
5. B. Field, A. E. Osbourn, *Science* **320**, 543 (2008).
6. K. Yonekura-Sakakibara *et al.*, *Plant Cell* **20**, 2160 (2008).
7. K. Papadopoulou, R. E. Melton, M. Leggett, M. J. Daniels, A. E. Osbourn, *Proc. Natl. Acad. Sci. U.S.A.* **96**, 12923 (1999).
8. R. W. Sandrock, H. D. Vanetten, *Physiol. Mol. Plant Pathol.* **58**, 159 (2001).
9. Y. Pareja-Jaime, M. I. G. Roncero, M. C. Ruiz-Roldan, *Mol. Plant Microbe Interact.* **21**, 728 (2008).
10. K. Bouarab, R. Melton, J. Peart, D. Baulcombe, A. Osbourn, *Nature* **418**, 889 (2002).
11. S. Ito *et al.*, *FEBS Lett.* **571**, 31 (2004).
12. V. Simons *et al.*, *Antimicrob. Agents Chemother.* **50**, 2732 (2006).

13. C. Kwon, P. Bednarek, P. Schulze-Lefert, *Plant Physiol.* **147**, 1575 (2008).
14. B. Field, F. Jordán, A. Osbourn, *New Phytol.* **172**, 193 (2006).
15. B. A. Snyder, R. L. Nicholson, *Science* **248**, 1637 (1990).
16. N. K. Clay, A. M. Adio, C. Denoux, G. Jander, F. M. Ausubel, *Science* **323**, 95 (2009).
17. P. Bednarek *et al.*, *Science* **323**, 101 (2009).
18. V. Lipka *et al.*, *Science* **310**, 1180 (2005).
19. P. Mylona *et al.*, *Plant Cell* **20**, 201 (2008).
20. E. Glawischnig, *Phytochemistry* **68**, 401 (2007).
21. L. A. Hadwiger, *Phytopathology* **98**, 372 (2008).
22. F. Geu-Flores, C. E. Olsen, B. A. Halkier, *Planta* **229**, 261 (2009).
23. H. J. Bouwmeester, C. Roux, J. A. Lopez-Raez, G. Becard, *Trends Plant Sci.* **12**, 224 (2007).
24. K. Akiyama, K. Matsuzaki, H. Hayashi, *Nature* **435**, 824 (2005).
25. A. Besserer *et al.*, *PLoS Biol.* **4**, 1239 (2006).
26. V. Gomez-Roldan *et al.*, *Nature* **455**, 189 (2008).
27. M. Umehara *et al.*, *Nature* **455**, 195 (2008).
28. M. Frey *et al.*, *Science* **277**, 696 (1997).
29. X. Qi *et al.*, *Proc. Natl. Acad. Sci. U.S.A.* **101**, 8233 (2004).
30. K. Shimura *et al.*, *J. Biol. Chem.* **282**, 34013 (2007).
31. J. J. B. Keurentjes *et al.*, *Nat. Genet.* **38**, 842 (2006).
32. H. C. Rowe, B. G. Hansen, B. A. Halkier, D. J. Kliebenstein, *Plant Cell* **20**, 1199 (2008).
33. P. E. O'Maille *et al.*, *Nat. Chem. Biol.* **4**, 617 (2008).
34. M. R. Kant, I. T. Baldwin, *Curr. Opin. Genet. Dev.* **17**, 519 (2007).
35. The authors acknowledge their sources of funding (A.O., Biotechnology and Biological Sciences Research Council UK; P.B., Max Planck Chemical Genomics Center) and thank their colleagues for helpful discussions in the preparation of this article. A.O. has the following patents awarded/pending: A.O. and K. Haralampidis (2000), Plant gene PCT/GB00/04908 (WO 01/46391); U.S. patent awarded 6 March 2007 (US7,186,884,B2); Mexico 25 July 2008 (259077); Canada pending (2,392,435); Australia issued (783739); Europe pending (EP1240312). X. Qi and A.O. (2004), Enzymes involved in triterpene synthesis (WO/06044508); U.S. pending (11/248,986); Canada pending (CA2581099); Australia pending (AU5295733); Europe pending (EP18709752). A.O., K. Haralampidis, R. Melton, S. Bakht, and X. Qi (2006), Root-specific promoters (U.S. patent application no. 11/940,638, pending). A. O. and X. Qi (2007), Enzymes involved in triterpene synthesis (WO/2009/041932, pending).

10.1126/science.1171661

PERSPECTIVE

Terrific Protein Traffic: The Mystery of Effector Protein Delivery by Filamentous Plant Pathogens

Ralph Panstruga[1]* and Peter N. Dodds[2]*

Many biotrophic fungal and oomycete plant pathogens deliver effector proteins directly into host cells during infection. Recent advances are revealing the extensive effector repertoires of these pathogens and are beginning to shed light on how they manipulate host cells to establish a parasitic relationship. Surprisingly, oomycete effectors seem to share a common uptake system with those from the human malaria pathogen. The current explosion of information is opening new research avenues in molecular plant pathology and is providing new opportunities to limit the impact of plant disease on food production.

A new fungal strain causing stem rust disease of wheat emerged recently in East Africa and is now spreading through the Near East, causing worldwide concern (www.globalrust.org/) (*1*). This highly virulent Ug99 strain of the wheat stem rust fungus *Puccinia graminis tritici* overcomes wheat lines that are widely used and have heretofore shown durable resistance to fungal infection. Ug99 is already well established in Kenya, where it causes losses of up to 80% of the wheat in farmers' fields. *P. graminis* represents a class of destructive plant pathogens that share a biotrophic lifestyle; that is, they rely entirely on living host tissue for the completion of their life cycle (*2*). Elaborate parasitic relationships allow these biotrophic fungi to feed from their host plants. During infection, they establish their lifeline through the formation of specialized infection structures (haustoria) that penetrate the plant cell wall and allow nutrient uptake (Fig. 1). These structures are shared with some of the equally destructive oomycete pathogens, which resemble fungi but are more related to brown algae. For instance, the pathogen responsible for the Irish potato famine, the oomycete *Phytophthora infestans*, forms haustoria during its initial biotrophic stage of infection.

Plant strains that are able to fend off these attacks do so in part by means of molecular recognition of proteins (effectors) delivered from haustoria into host cells during infection (*3*). However, haustoria are separated from the host cells by three distinct physical barriers: the pathogen plasma membrane, the cell wall, and the extrahaustorial membrane, which is derived from the plant plasma membrane but is molecularly distinct (Fig. 1). Exciting new research is now shedding light on the intriguing and as-yet unanswered question of how molecules are shuttled between the host and the invader.

Effector Delivery

Many bacterial pathogens of animals and plants possess a syringe-like apparatus, such as the one produced by prokaryotic (type III) secretion systems, which injects pathogenicity effector proteins into host cells. Effector proteins from fungal and oomycete parasites, on the other hand, seem to travel by way of the eukaryotic (type II) secretory pathway, which involves exocytosis of Golgi-derived secretory vesicles. Most known effectors from these parasites harbor a canonical N-terminal type II secretion signal (*2*, *4*–*7*), which suffices to get the effectors past the first two barriers. However, although some effectors function in the extracellular environment, many others clearly do actually get into the plant cell because they are recognized by intracellular plant proteins [the resistance (R) proteins] that are part of the plant innate immune system (*5*, *7*–*9*). Direct evidence of the transfer of effector proteins during infection came from the immunocytological detection of a rust effector (*10*) and the detection of a tagged oomycete effector (*11*) inside infected host cells.

Many oomycete effectors harbor a bipartite amino acid motif [RXLR–(D)EER], located downstream of the signal peptide, that is dispensable for exocytosis but required for plant access (*11*, *12*). The RXLR domain is necessary and sufficient to mediate entry of effectors or reporter proteins into host cells in the absence of the oomycete, which indicates that the uptake occurs independently of any pathogen-derived machinery (*12*). The identification of a number of plant proteins that also contain the RXLR motif, several of them associated with membrane trafficking (*13*), suggests that oomycetes may exploit the plant endocytic pathway for host cell entry. Some fungal effectors can also enter plant cells in the absence of the pathogen, although they lack an RXLR domain and do not share other conserved peptide motifs (*8*, *14*). Indeed, in plant-rust interactions, ultrastructural studies have visualized tubular extensions of the extrahaustorial membrane with associated budding vesicles that reach into the host cell cytoplasm and can form close contact with host endoplasmic reticulum and dictyosomes (*15*). In an alternative scenario, effector uptake could be mediated by a parasite-derived protein channel (*16*). The oomycete RXLR sequence motif is

[1]Max-Planck Institute for Plant Breeding Research, Department of Plant-Microbe Interactions, Carl-von-Linné-Weg 10, D-50829 Köln, Germany. [2]Commonwealth Scientific and Industrial Research Organization Plant Industry, General Post Office Box 1600, Canberra ACT 2601, Australia.

*To whom correspondence should be addressed. E-mail: panstrug@mpiz-koeln.mpg.de (R.P.); peter.dodds@csiro.au (P.N.D.)

reminiscent of a similar domain in effectors of the protist *Plasmodium falciparum*, the malaria parasite that invades mammalian erythrocytes (*17*). The oomycete and *Plasmodium* delivery motifs appear to function interchangeably in either pathogen and in either host, which suggests that they target the same host admission route (*18*, *19*). Because oomycetes and *Plasmodium* are members of the Chromalveolata, this peptide domain may have a common origin in these plant and animal pathogens, although convergent evolution is another possibility.

Biotroph effectors were initially identified based on their function as avirulence proteins that are recognized by plant immune receptors (*7*, *8*). However, with the use of sequence signatures from the conserved N-terminal secretion signal and, for oomycetes, the RXLR motif, a more extensive suite of effectors can now be predicted from genome and transcriptome analyses (*11*, *20*–*23*). Through these biocomputational means, the genomes of several fungal and oomycete phytopathogens unexpectedly were found each to encode several hundred effector candidates. In the case of *Phytophthora* species, many of these probably evolved from a common ancestor through rapid duplication and divergence (*23*). Nevertheless, only a few RXLR-type effectors are known to be detected by the plant defense machinery. However, this biocomputational approach may still overlook effectors that engage alternative trafficking routes, such those currently known from powdery mildew fungi, which lack canonical eukaryotic secretion tags (*24*).

Toward Effector Functions

The next challenge is to understand how these effector proteins turn the host cell to their own purposes. Although the biocomputational approach promises riches of new proteins to work with, the sheer number of effector candidates renders functional analysis a formidable task. Most candidates lack informative homologies other than the signal domain. Functional studies are hindered by the inaccessible genetics of many of these pathogens. Alternate means are thus being explored for the expression of candidate effector proteins inside plant cells or the heterologous delivery of effectors. The bacterial type III secretion system can be engineered to deliver these proteins (*25*), and certain hemibiotrophic phytopathogens that are more amenable to genetic manipulation may be useful transfer vehicles as well. Some effectors have been shown to heighten pathogen virulence (*24*, *25*) or suppress host immune responses (*25*–*27*). Mutational analysis of *Ustilago maydis* suggests a high degree of redundancy in effector functions (*22*), and there is also considerable redundancy in oomycete effector repertoires, with the suppression of plant cell death processes being a common function of many effectors (*26*). The actual biochemical functions and host targets of identified effectors also need to be characterized. Protein x-ray crystallography has revealed that the structure of some bacterial effectors resembles known host proteins despite the absence of any sequence homology (*28*). However, the intensive analysis of protein crystallography is difficult to scale up to encompass whole-genome effector repertoires. Bioassays are therefore needed to probe the functions of numerous effector candidates simultaneously. Conceivable possibilities include the search for cellular targets on the basis of protein-protein interactions or experimental settings that explore the capacity of effectors to interfere with host defense or cell death. Alternatively, activity-based enzyme profiling might be employed to test the interference of effectors with host enzyme activities (*29*).

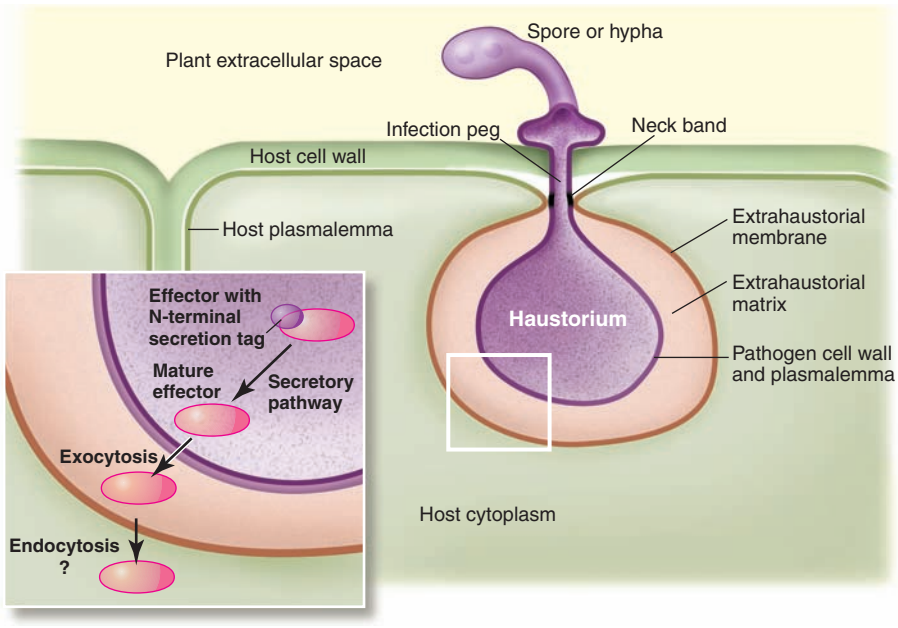

Fig. 1. Organization of haustoria and the presumed route of effector delivery. Haustoria emerge from extracellular pathogen infection structures (such as spores or hyphae) and enter plant cells through the infection peg by invaginating the host plasma membrane. Haustoria are surrounded by the pathogen plasmalemma and cell wall as well as the modified host plasma membrane (extrahaustorial membrane). These membranes enclose the extrahaustorial matrix, an interface zone that is sealed by the neck band. The inset illustrates the delivery of a pathogen effector (red) with an N-terminal secretion tag (purple) through the secretory pathway and into the host cell.

Most effectors seem to be specific to individual pathogen species, and even closely related pathogens reveal little overlap in their effector complements (*21*). This probably reflects a very rapid evolution of these proteins, which is driven by both the proteins' need to target divergent host proteins and to escape recognition by host immune receptors. It will be intriguing to learn whether the effector suites from different parasites are of similar size and targeted to similar biochemical host functions. So far, few effectors with nuclear localization have been described (*10*), although the transcriptional reprogramming of host cells is a plausible effector task. Other effectors localizing to defined host compartments have not been identified yet and possibly await discovery.

Given that pathogenesis of obligate biotrophs is a multistep process that is characterized by a series of morphogenetic changes, it seems unlikely that all effectors are released simultaneously and from the same location into host cells. It is rather conceivable that sets of effectors are delivered in a coordinated manner as pathogenesis progresses, perhaps first from extracellular infection structures and then from haustoria or intracellular infection hyphae. It will be informative in this respect to find out whether the spatially linked effector genes in the genome of *U. maydis* (*22*) are transcriptionally co-regulated. Unravelling the spatial and temporal order of effector delivery as well as untangling the regulatory networks governing this proposed hierarchical process will surely be prominent topics in future research.

Although recent experimental efforts have mainly been focused on proteinaceous effectors, biotrophic pathogens also use nonproteinaceous metabolites to manipulate their host's cells. In the phytopathogenic bacterium *Pseudomonas syringae*, the low–molecular-weight compounds coronatine (a mimic of the plant defense–signaling molecule jasmonic acid) and syringolin (a proteasome inhibitor) help to divert plant defense responses. Secondary metabolites may also be

revealed as powerful nonproteinaceous effectors of fungal and oomycete biotrophs (*30*). It seems, however, that this effector category would be even more difficult to analyze than their proteinaceous cousins.

Future Perspectives

Secreted effectors are emerging as the prime weapons of plant parasites and also as targets for host recognition and immunity. As such, the current focus on pathogen effectors promises to reveal fascinating insights into the molecular basis of the biotrophic life-style and plant-microbe coevolution and probably will lead to innovative disease-control measures. It will be intriguing to learn whether biotroph effectors actively divert host metabolism or whether nutrient flow to the pathogen is an indirect consequence of disarmed host cells. It will also be fascinating to compare the effector suites of closely related pathogen species to find out whether and how effector diversity contributes to host range restriction and parasite speciation. Molecular fingerprinting of pathogen isolates on the basis of the natural variation in their effector repertoires has the potential to serve as a valuable diagnostic tool in epidemiological surveys and will shed light on how new pathogen strains, such as the wheat stem rust strain Ug99, evolve to overcome host resistance.

Plant resistance genes that recognize effectors with important and nonredundant virulence functions are more likely to prove durable in the field because this will constrain the evolution of the pathogen. New resistance genes may be found in wild relatives of crop plants, a strategy that has already proven successful in defending against the Irish potato famine pathogen *P. infestans* (*31*).

Several biotechnological resistance strategies can now be envisaged, including the blocking of the effector delivery mechanism, the modifying of host targets in order to elude effector function, and the rational design of synthetic plant immune receptors in order to detect as-yet unrecognized parasite effectors. The pathogens' effectors may be the source of their own undoing if research into their biochemical activity generates tools to selectively manipulate plant cellular functions. The current devastating impact of Ug99 stem rust on wheat production in Africa highlights the critical importance of developing durable and effective strategies to protect agricultural production from disease threats.

References and Notes

1. R. P. Singh *et al.*, *Adv. Agron.* **98**, 271 (2008).
2. R. J. O'Connell, R. Panstruga, *New Phytol.* **171**, 699 (2006).
3. J. G. Ellis, P. N. Dodds, G. J. Lawrence, *Curr. Opin. Microbiol.* **10**, 326 (2007).
4. A. M. Catanzariti, P. N. Dodds, J. G. Ellis, *FEMS Microbiol. Lett.* **269**, 181 (2007).
5. A. P. Rehmany *et al.*, *Plant Cell* **17**, 1839 (2005).
6. R. L. Allen *et al.*, *Science* **306**, 1957 (2004).
7. P. N. Dodds, G. J. Lawrence, A. M. Catanzariti, M. A. Ayliffe, J. G. Ellis, *Plant Cell* **16**, 755 (2004).
8. A. M. Catanzariti, P. N. Dodds, G. J. Lawrence, M. A. Ayliffe, J. G. Ellis, *Plant Cell* **18**, 243 (2006).
9. M. R. Armstrong *et al.*, *Proc. Natl. Acad. Sci. U.S.A.* **102**, 7766 (2005).
10. E. Kemen *et al.*, *Mol. Plant Microbe Interact.* **18**, 1130 (2005).
11. S. C. Whisson *et al.*, *Nature* **450**, 115 (2007).
12. D. L. Dou *et al.*, *Plant Cell* **20**, 1930 (2008).
13. P. R. J. Birch *et al.*, *Curr. Opin. Plant Biol.* **11**, 373 (2008).
14. V. A. Manning, L. M. Ciufetti, *Plant Cell* **17**, 3203 (2005).
15. C. W. Mims, C. Rodriguez-Lother, E. A. Richardson, *Protoplasma* **219**, 221 (2002).
16. W. Morgan, S. Kamoun, *Curr. Opin. Microbiol.* **10**, 332 (2007).
17. M. Marti, R. T. Good, M. Rug, E. Knuepfer, A. F. Cowman, *Science* **306**, 1930 (2004).
18. S. Bhattacharjee *et al.*, *PLoS Pathog.* **2**, 453 (2006).
19. S. Grouffaud, P. van West, A. O. Avrova, P. R. J. Birch, S. C. Whisson, *Microbiology* **154**, 3743 (2008).
20. R. A. Dean *et al.*, *Nature* **434**, 980 (2005).
21. B. M. Tyler *et al.*, *Science* **313**, 1261 (2006).
22. J. Kämper *et al.*, *Nature* **444**, 97 (2006).
23. R. H. Y. Jiang, S. Tripathy, F. Govers, B. M. Tyler, *Proc. Natl. Acad. Sci. U.S.A.* **105**, 4874 (2008).
24. C. J. Ridout *et al.*, *Plant Cell* **18**, 2402 (2006).
25. K. H. Sohn, R. Lei, A. Nemri, J. D. G. Jones, *Plant Cell* **19**, 4077 (2007).
26. D. L. Dou *et al.*, *Plant Cell* **20**, 1118 (2008).
27. J. I. B. Bos *et al.*, *Plant J.* **48**, 165 (2006).
28. R. Janjusevic, R. B. Abramovitch, G. B. Martin, C. E. Stebbins, *Science* **311**, 222 (2006).
29. R. A. L. van der Hoorn, M. A. Leeuwenburgh, M. Bogyo, M. Joosten, S. C. Peck, *Plant Physiol.* **135**, 1170 (2004).
30. H. U. Bohnert *et al.*, *Plant Cell* **16**, 2499 (2004).
31. V. G. A. A. Vleeshouwers *et al.*, *PLoS One* **3**, e2875 (2008).

32. We thank S. Kamoun, J. Ellis, and S. Schmidt for inspiring discussions. Work in the lab of R.P. is supported by funds of the Max-Planck Society and the Deutsche Forschungsgemeinschaft (DFG; SFB670). Work in the lab of P.D. is supported by funding from the Australian Research Council, the Australian Grains Research and Development Corporation, and NIH (grant GM074265-01A2).

10.1126/science.1171652

PERSPECTIVE

Hormone (Dis)harmony Moulds Plant Health and Disease

Murray R. Grant[1] and Jonathan D. G. Jones[2]*

Diseased plants often display phenotypes consistent with hormone perturbations. We review recent data that have revealed roles in plant-microbe interactions for cellular components and signaling molecules that previously were associated only with hormone signaling. A better understanding of cross-talk between hormonal and defense signaling pathways should reveal new potential targets for microbial effectors that attenuate host resistance mechanisms.

Plant pathogens can trigger a rich diversity of symptoms that indicate hormonal disorders, from galls and cankers of trees and shrubs, to "foolish seedling" disease of rice, and to premature senescence (or its converse, "green islands") in many plants (Fig. 1). These hormonal aspects of pathogenesis were relatively neglected until recently, with the spotlight more on gene-specific interactions between host and pathogen. Integrated models now include activation of defense by pathogen-associated molecular patterns (PAMPs), suppression of defense by effectors, and recognition of particular effectors by specific resistance proteins (*1*, *2*). Recent work is now revealing how pathogens enhance host susceptibility by manipulation of hormone signaling, and how hosts attenuate this manipulation. Here we assess current knowledge of hormonal signaling in plant-microbe interactions and highlight areas for future scrutiny, with a particular focus on the hormones jasmonate (JA), auxin, abscisic acid (ABA), and gibberellin (GA).

[1]School of Biosciences, University of Exeter, Exeter EX4 4QD, UK. [2]The Sainsbury Laboratory, Norwich Research Park, Colney, Norwich NR4 7UH, UK.

*To whom correspondence should be addressed. E-mail: jonathan.jones@tsl.ac.uk

Antagonism of Salicyclic Acid Signaling as a Key Pathogen Virulence Mechanism

Salicylic acid (SA) and JA are signaling molecules in plant defense against biotrophic and necrotrophic pathogens, respectively (*3*). JA alone activates responses to wounding and herbivory, but in the presence of ethylene (Et), it activates defense against necrotrophs. JA signaling and SA signaling can compromise one another (*4*, *5*). The result is that plant tissues usually can activate either SA or JA signaling, but not both.

Because the balance between JA and SA can determine whether the plant succumbs to infection, selection favors pathogens that can influence this balance in their favor. Pathogen modulation of other hormones, whether at the level of biosynthesis, bioactivity, or signaling, might also influence this balance. We propose that successful defense likely requires that the plant attenuate any microbe-induced hormonal perturbations.

Although the SA receptor remains elusive, the mechanism of JA, auxin, and GA signaling via targeted proteasome-mediated degradation through their respective Skp1-cullin-F box protein (SCF) E3 ubiquitin ligase complexes (*6*) is now better understood.

Jasmonates. Multiple JA derivatives exist, though knowledge of their bioactivity remains scarce. Many, but not all, jasmonate responses are mediated through the activity of the SCF^{COI1} E3 ligase complex containing the coronatine-insensitive 1 (COI1) F-box protein (*7*). SCF^{COI1} degrades a class of jasmonate signaling repressor (JAZ) proteins in the presence of jasmonoyl-L-isoleucine (JA-Ile) (*8*, *9*). Many strains of the phytopathogenic bacterium *Pseudomonas syringae* (*Pst*) make coronatine (COR), a JA-Ile mimic. Activation of JA signaling by COR suppresses SA signaling, thus enhancing host susceptibility (*10*). COR binds with high affinity to a JAZ/SCF^{COI1} complex, promoting degradation of JAZ proteins and thus providing a mechanistic link between COR action and virulence (*11*). The 12 *Arabidopsis* JAZ proteins form homo- and heterodimers, creating combinatorial diversity that could fine-tune responses during JA signaling (*12*). Additional receptors likely exist for JA relatives and other oxylipin signals because the JA-Ile–forming JAR1 mutant (*13*) fails to recapitulate all *coi1* phenotypes and JA application induces *coi1*-independent JA responses (*14*, *15*).

Auxin. Auxin promotes virulence during biotrophic interactions (*16*–*18*). During defense triggered by flg22 (a peptide derived from the bacterial PAMP flagellin), mRNA expression of many auxin-signaling related genes is suppressed by the microRNA (miR393) that targets the auxin receptor F-box protein TIR1 and its paralogs AFB2 and AFB3. Plants that overexpress miR393 are more resistant to *Pst*, whereas plants that overexpress AFB1 (which is less sensitive to miR393 due to a nucleotide substitution) are more sensitive (*17*). PAMPs trigger SA accumulation (*19*), and SA can counteract auxin-induced virulence through generalized repression of auxin-related genes (including *TIR1*), which in turn stabilizes transcriptional repressors such as AXR2, thus inhibiting auxin responses (*18*).

GA. GA activates the $SCF^{SLY1/GID2}$ complex to initiate degradation of the DELLA family of GRAS transcriptional repressors. A loss-of-function mutant lacking four of the five *Arabidopsis* DELLA-encoding genes exhibits enhanced resistance to *Pst* and, conversely, hypersusceptibility to the necrotrophic fungal pathogen *Alternaria brassicicola*. Infection by *Pst* results in elevated induction of the SA signaling marker *PR1* and reduced and delayed expression of the JA/Et-induced *PDF1.2* gene (*20*). DELLAs may potentiate JA signaling, suggesting that the rice "foolish seedling" disease pathogen *Gibberella fujikoroi* makes GA to eliminate DELLAs and compromise JA-mediated defense. Stress-induced DELLA accumulation increases the expression of genes encoding reactive oxygen species (ROS)–detoxification enzymes, thus reducing ROS levels (*21*). ROS may potentiate SA signaling, suggesting a mechanism whereby GA acts synergistically with SA by removing DELLAs, allowing more ROS accumulation because of reduced levels of ROS detoxification enzymes.

Fig. 1. Examples of plant growth distortions likely associated with disease-induced hormone perturbations. (**A**) Rust (*Atelocauda digitata*) on *Acacia koa* leaf, Hawaii. (**B**) Wheat infected with leaf rust (*Puccinia striiformis*) showing "green islands" in some interactions. (**C**) Wool sower gall maker (*Callirhytis seminator*) on oak. (**D**) Crown gall caused by *Agrobacterium tumefaciens*. (**E**) Witches broom in silver birch caused by *Taphrina* sp. (**F**) *Gymnosporangium cornutum* rust on European mountain-ash.

ABA. ABA influences many plant-pathogen interactions depending on pathogen life-style; *Arabidopsis* ABA-deficient mutants are hypersensitive to the oomycete *Pythium irregulare* (*22*) and fungus *Leptosphaeria maculans* (*23*) but more resistant to *Botrytis cinerea* (*24*). ABA positively regulates defense to *Pst* through regulation of pre-invasive stomata-based responses (*25*). However, at later stages, bacterial effectors activate ABA biosynthesis to overcome plant basal defenses (*26*). *Botrytis* and *Cercospora* species can themselves make ABA (*27*, *28*). Because these pathogens are generally thought of as necrotrophs, this suggests a role for ABA during an early biotrophic phase before the pathogens switch to necrotrophy. ABA (and also methyl JA) can suppress callose deposition in response to flg22 (*26*, *29*).

A Central Role for DELLA Proteins?

An unexpected interaction between ABA, Et, and DELLA proteins has emerged. Both ABA and Et stabilize DELLA proteins (*30*, *31*), which could potentiate JA signaling and attenuate SA signaling. Conceivably, Et switches JA signaling from wound responses to defense through its effect on DELLA stability. If DELLAs promote ROS detoxification and ABA stabilizes DELLAs, then ABA may promote susceptibility by reducing ROS levels, attenuating SA signaling. Auxin also promotes Et biosynthesis, and the resulting Et could stabilize DELLA proteins, thus promoting JA/Et signaling and attenuating SA signaling (*32*, *33*). DELLA proteins upregulate expression of *XERICO*, a putative E3 ligase that promotes ABA accumulation (*34*), thus establishing a potential positive-feedback loop to maintain ABA concentrations and ROS detoxification. ABA may also act at another node in the signaling network that promotes virulence. *Pst* infection of the *aao3* mutant, which lacks the pathogen-inducible *Arabidopsis* aldehyde oxidase 3, leads to rapid accumulation of SA in the early stages of infection and failure to suppress PAMP-inducible genes (*35*). Notably, salt stress stabilizes DELLAs (*36*), and salt stress or exogenous ABA application suppresses chemically induced systemic immunity in *Arabidopsis* (*37*). In Fig. 2, we propose a model whereby DELLA proteins fine-tune the defenses mounted through the JA, Et, or SA pathways.

Multiple Mechanisms of Control

In addition to these complicated signaling pathways, new insight is needed into other ways in which hormone and pathogen signaling intersect.

The role of conjugation. The *Arabidopsis GH3* family of adenylate-forming enzymes, which includes JAR1, can adenylate a variety of plant hormones including JA, auxins, and SA (*38*). Inactivation of auxin via specific GH3s in *Arabidopsis* (*39*) or rice (*40*) conferred enhanced defense responses. However, GH3 variants also affect SA signaling (*41*, *42*) or, in the case of GH3.5, both SA and auxin (*39*). PBS3, a GH3, acts not on SA but rather on 4-substituted benzoates, perhaps by priming or inducing SA biosynthesis (*43*). JAR1 conjugates isoleucine to JA, making active JA-Ile. Thus, GH3s can both activate and attenuate plant defense responses. SA can be conjugated to glucose and sequestered in the vacuole. The role of such conjugations in regulating signaling pathways is still not fully defined.

Regulation of de novo synthesis. We need more knowledge of hormone biosynthesis during the infection response. Although plant-pathogen interactions are usually studied in the leaf, many analyses of hormone biology are conducted on roots or seedlings, and the results might not be relevant to leaf processes. JA signaling can be modulated by SA that comes either from de novo synthesis or from large pools of glycosylated SA. Knowledge of how SA biosynthesis is regulated, in particular the signaling mechanism that activates *isochorismate synthase* (*ICS1*) (*44*), is still required.

Precursors for JA, SA, ABA, and GA are made in the chloroplast, then exported to the cytosol for the final synthetic steps. Infection with virulent *Pst* suppresses a range of nuclear-encoded chloroplast-associated genes (*45*, *46*), though in contrast, stress-associated transcripts encoding components of ABA biosynthesis are up-regulated (*46*). Some bacterial type III effectors act in the chloroplast to suppress defense (*47*), indicating the importance of signaling between chloroplast and nucleus to modulate hormonal responses to pathogens.

The necessity for detailed temporal analysis. Exogenous hormone application reveals hormonal cross-talk on a gross scale but seldom mimics the temporal and spatial deployment of endogenous phytohormones. Exogenously applied ABA does not exert the same physiological effects as endogenous ABA (*48*). Pretreatment with GA enhanced susceptibility to *Pst*, suggesting GA may affect signaling of other hormones via destabilization of DELLAs (*20*). Similarly, when using mutants compromised in hormone biosynthesis or signaling, it is important to distinguish direct effects of a pathogen or defense modulation of specific hormones, from indirect effects arising from modification of the endogenous phytohormone balance.

We need studies that examine hormonal dynamics in detail through the course of an infection. Hormone endpoint measurements are inadequate. Microarray experiments on various pathogen infections over various time courses often suggest the involvement of hormone signaling, and temporally separated transient increases in hormone concentrations are likely to play an important role in configuring plant responses to microbial infection (*49*, *50*). Challenges and opportunities remain in exploring the mechanisms underpinning the complex interactions between hormones and defense in whole plants.

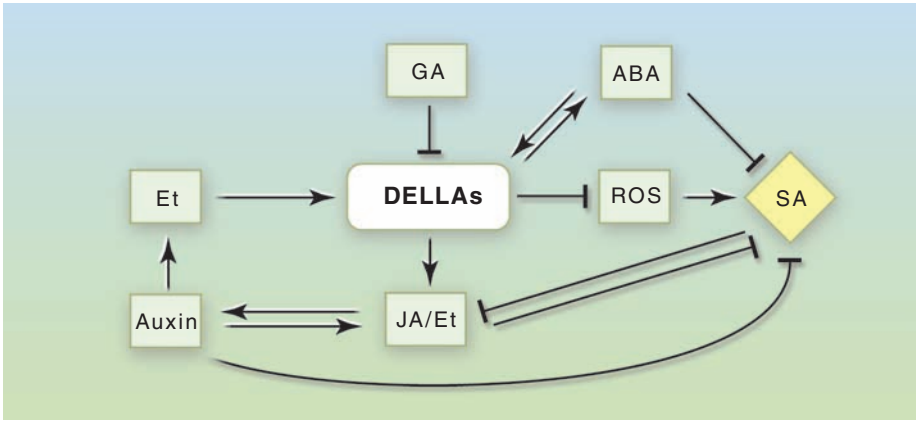

Fig. 2. Possible interactions between hormone signaling pathways are shown. JA/Et and SA signaling mutually interfere with each other. ABA and Et could strengthen JA/Et signaling and attenuate SA signaling via DELLA stabilization. Because auxin promotes Et biosynthesis, it might also interfere with SA signaling via DELLA stabilization. DELLAs increase expression of ROS detoxification mechanisms, attenuating redox stress and thus conceivably attenuating SA signaling.

References and Notes

1. J. L. Dangl, J. D. Jones, *Nature* **411**, 826 (2001).
2. J. D. Jones, J. L. Dangl, *Nature* **444**, 323 (2006).
3. J. Glazebrook, *Annu. Rev. Phytopathol.* **43**, 205 (2005).
4. K. Kazan, J. M. Manners, *Plant Physiol.* **146**, 1459 (2008).
5. A. Koornneef, C. M. Pieterse, *Plant Physiol.* **146**, 839 (2008).
6. E. Lechner, P. Achard, A. Vansiri, T. Potuschak, P. Genschik, *Curr. Opin. Plant Biol.* **9**, 631 (2006).
7. A. Devoto *et al.*, *Plant J.* **32**, 457 (2002).
8. A. Chini *et al.*, *Nature* **448**, 666 (2007).
9. B. Thines *et al.*, *Nature* **448**, 661 (2007).
10. D. M. Brooks, C. L. Bender, B. N. Kunkel, *Mol. Plant Pathol.* **6**, 629 (2005).
11. L. Katsir, A. L. Schilmiller, P. E. Staswick, S. Y. He, G. A. Howe, *Proc. Natl. Acad. Sci. U.S.A.* **105**, 7100 (2008).
12. H. Chung, G. Howe, *Plant Cell* **21**, 131 (2009).
13. P. E. Staswick, I. Tiryaki, *Plant Cell* **16**, 2117 (2004).
14. A. Devoto *et al.*, *Plant Mol. Biol.* **58**, 497 (2005).
15. N. Taki *et al.*, *Plant Physiol.* **139**, 1268 (2005).
16. Z. Chen *et al.*, *Proc. Natl. Acad. Sci. U.S.A.* **104**, 20131 (2007).
17. L. Navarro *et al.*, *Science* **312**, 436 (2006).
18. D. Wang, K. Pajerowska-Mukhtar, A. H. Culler, X. Dong, *Curr. Biol.* **17**, 1784 (2007).
19. K. Tsuda, M. Sato, J. Glazebrook, J. D. Cohen, F. Katagiri, *Plant J.* **53**, 763 (2008).
20. L. Navarro *et al.*, *Curr. Biol.* **18**, 650 (2008).
21. P. Achard, J. P. Renou, R. Berthome, N. P. Harberd, P. Genschik, *Curr. Biol.* **18**, 656 (2008).
22. B. A. Adie *et al.*, *Plant Cell* **19**, 1665 (2007).
23. M. Kaliff, J. Staal, M. Myrenas, C. Dixelius, *Mol. Plant Microbe Interact.* **20**, 335 (2007).
24. K. Audenaert, G. B. De Meyer, M. M. Hofte, *Plant Physiol.* **128**, 491 (2002).
25. M. Melotto, W. Underwood, J. Koczan, K. Nomura, S. Y. He, *Cell* **126**, 969 (2006).
26. M. de Torres-Zabala *et al.*, *EMBO J.* **26**, 1434 (2007).
27. M. Inomata, N. Hirai, R. Yoshida, H. Ohigashi, *Phytochemistry* **65**, 2667 (2004).
28. V. Siewers, J. Smedsgaard, P. Tudzynski, *Appl. Environ. Microbiol.* **70**, 3868 (2004).
29. N. K. Clay *et al.*, *Science* **323**, 95 (2009).
30. P. Achard *et al.*, *Proc. Natl. Acad. Sci. U.S.A.* **104**, 6484 (2007).
31. P. Achard *et al.*, *Plant Physiol.* **143**, 1163 (2007).
32. A. N. Stepanova *et al.*, *Cell* **133**, 177 (2008).
33. S. Abel, M. D. Nguyen, W. Chow, A. Theologis, *J. Biol. Chem.* **270**, 19093 (1995).
34. R. Zentella *et al.*, *Plant Cell* **19**, 3037 (2007).
35. M. de Torres Zabala, M. H. Bennett, W. Truman, M. Grant, *Plant J.* 10.1111/j.1365-313X.2009.03875.x.
36. P. Achard *et al.*, *Science* **311**, 91 (2006).
37. M. Yasuda *et al.*, *Plant Cell* **20**, 1678 (2008).
38. I. Tiryaki, P. E. Staswick, *Plant Physiol.* **130**, 887 (2002).
39. Z. Zhang *et al.*, *Plant Physiol.* **145**, 450 (2007).
40. X. Ding *et al.*, *Plant Cell* **20**, 228 (2008).
41. G. Jagadeeswaran *et al.*, *Plant J.* **51**, 234 (2007).
42. K. Nobuta *et al.*, *Plant Physiol.* **144**, 1144 (2007).
43. R. A. Okrent, M. D. Brooks, M. C. Wildermuth, *J. Biol. Chem.* **284**, 9742 (2009).
44. M. A. Strawn *et al.*, *J. Biol. Chem.* **282**, 5919 (2007).
45. R. Thilmony, W. Underwood, S. Y. He, *Plant J.* **46**, 34 (2006).
46. W. Truman, M. T. de Zabala, M. Grant, *Plant J.* **46**, 14 (2006).
47. J. Jelenska *et al.*, *Curr. Biol.* **17**, 499 (2007).
48. A. Christmann, T. Hoffmann, I. Teplova, E. Grill, A. Muller, *Plant Physiol.* **137**, 209 (2005).
49. S. H. Spoel, J. S. Johnson, X. Dong, *Proc. Natl. Acad. Sci. U.S.A.* **104**, 18842 (2007).
50. W. Truman, M. H. Bennett, I. Kubigsteltig, C. Turnbull, M. Grant, *Proc. Natl. Acad. Sci. U.S.A.* **104**, 1075 (2007).

51. J.D.G.J. acknowledges support from the Gatsby Foundation and the Biotechnology and Biological Sciences Research Council (BBSRC), and helpful discussion with A.-R. Seilaniantz and R. Bari. M.R.G. acknowledges support from BBSRC.

10.1126/science.1173771

PERSPECTIVE

Reprogramming Plant Cells for Endosymbiosis

Giles E. D. Oldroyd,[1] Maria J. Harrison,[2]* Uta Paszkowski[3]

The establishment of arbuscular mycorrhizal (AM) symbioses, formed by most flowering plants in association with glomeromycotan fungi, and the root-nodule (RN) symbiosis, formed by legume plants and rhizobial bacteria, requires an ongoing molecular dialogue that underpins the reprogramming of root cells for compatibility. In both endosymbioses, there are distinct phases to the interaction, including a presymbiotic anticipation phase and, subsequently, an intraradical accommodation of the microsymbiont. Maintenance of the endosymbiosis then depends on reciprocal nutrient exchange with the microsymbiont-obtaining plant photosynthates in exchange for mineral nutrients: enhanced phosphate and nitrogen uptake from AM fungi and fixed nitrogen from rhizobia. Despite the taxonomically distinct groups of symbionts, commonalities are observed in the signaling components and the modulation of host cell responses in both AM and RN symbioses, reflecting common mechanisms for plant cell reprogramming during endosymbiosis.

The establishment of either arbuscular mycorrhizal (AM) or root-nodule (RN) endosymbiosis starts with a chemical signal exchange between root and microsymbiont, priming both partners for the subsequent association (Fig. 1). Plant root exudates contain biological molecules, including flavonoids and strigolactones, that are perceived by rhizobial bacteria [reference S1 in the supporting online material] and AM fungi (references S2 and S3), respectively. In RN symbiosis, flavonoids from the plant root activate the NodD transcription factor, which results in the bacteria producing lipochitooligosaccharide Nod factors (reference S4). Nod factors, in turn, are perceived by the plant and induce the development of root nodules, specialized organs required for accommodation of the rhizobia. Strigolactones stimulate AM fungi to switch from asymbiotic to presymbiotic growth, which is marked by induced hyphal branching (reference S2) and elevated energy metabolism (*1*). A hypothesized diffusible compound (called Myc factor) of unknown chemical structure that activates gene expression changes in the plant (reference S5) is also elicited from AM fungi.

Nod factors are recognized by receptor-like kinases that contain sugar binding LysM domains (*2*) (references S6 to S8). Analogous AM-specific receptors most likely also exist (reference S9). When Nod and Myc factors are perceived, they induce calcium oscillations in the plant associated with the nucleus, and these oscillations act as a secondary messenger linking Nod-factor perception at the plasma membrane to gene expression changes in the nucleus. The genetic components required for Nod- and Myc-factor–induced signaling are conserved and commonly referred to as the symbiotic (Sym) pathway (*3*) (reference S10). This pathway contains a receptor-like kinase, nuclear pore proteins, and nuclear-localized potassium channels required for the induction of the calcium oscillations (*4*, *5*). Results from diverse Angiosperms suggest that recognition of the calcium oscillations requires a calcium/calmodulin-dependent protein kinase (CaMK) and has been associated with a protein of unknown function (Cyclops) (*5*, *6*). Once ongoing oscillations are recognized by the plant, Nod-factor–specific transcriptional regulators are required, including a complex of two GRAS proteins and ERF transcription factors that directly associate with the promoters of Nod-factor–inducible genes (*7*, *8*). Despite the fact that the mechanisms of signaling are the same for different symbionts, specific Nod- or Myc-factor recognition is maintained. This may be through unequal calcium oscillations with differing structures induced, respectively, by Nod and Myc factors (*3*). Thus, we hypothesize that CaMK may be differentially activated in response to Nod and Myc factors and subsequently may drive the signal toward the differential induction of rhizobial (and AM)–specific transcription factors.

Considering that AM interactions evolved over 300 million years before the hypothesized origin of rhizobial associations (references S11 and S12), it seems likely that the RN symbiosis originated with the use of a preexisting signaling pathway. Components of the Sym pathway in rice are conserved for AM symbiosis (*6*, *9*, *10*) (reference S13). Gene expression analyses in *Lotus japonicus* show additional common Sym pathway signaling events independent of the seven defined genetic components of the common Sym pathway (reference S14). Likewise, AM-specific signaling pathways that either operate in parallel or diverge from the common Sym pathway were observed in rice (*10*). Therefore, signaling networks involved in root endosymbiosis may be multifaceted and, in scale, reminiscent of complex signaling that occurs during plant defense (reference S15). Components of the Sym pathway have also been recruited in *Causarina glauca* (a nodulating species outside the legumes, in the so called actinorhizal group) to recognize nitrogen fixing *Frankia* bacteria (*11*, *12*) and in *Lotus japonicus* to recognize a diffusible signal from parasitic nematodes (reference S16), suggesting that the recognition machinery of signals is promiscuous and has originated in multiple taxonomically different organisms. This, in turn, suggests that mutualism and parasitism represent ends of an uninterrupted continuum.

Conservation in the AM and RN symbioses extends beyond early signaling and includes common cellular structures associated with intracellular microbial colonization. The rhizobial invasion of root cells requires Nod-factor and rhizobial surface polysaccharides that act as signals, inducing an invagination of the plant cell membrane to create a tube-like infection thread (IT) that delivers rhizobia to the inner root tissue (reference S17). Cortical cells in front of the growing IT form specific cytoplasmic alterations, known as preinfection threads (PiT), and these predict the path of the IT (reference S18). An analogous process has been observed during AM symbiosis. AM fungal infection is initiated with the formation of a swollen hyphal infection structure (hyphopodium) on the root surface and is accompanied by the assembly of a pre-penetration apparatus (PPA) in the underlying cell. The PPA is an intracellular structure composed of endoplasmic reticulum and cytoskeletal material that outlines the route for the subsequent hyphal growth across the cell lumen (reference S19). The development of PiTs and PPAs indicates that the plant cell is actively preparing for invasion by microsymbionts. This preparation is believed to be restricted to symbiosis, because analogous structures have not been observed during the compatible interaction of *M. truncatula* with a pathogenic fungus or upon mechanical stimulation of cells (*13*).

After entry into the root, the microbial symbionts establish specialized biotrophic interfaces for nutrient exchange with their plant hosts. Rhizobial bacteria are accommodated in specialized structures, known as nodules, that require the plant hormones auxin and cytokinin for their development (references S20 to S22). Although most rhizobia activate legume cell reprogramming through the release of Nod factors, some species of rhizobia are capable of inducing nodule formation without producing Nod factor (reference S23). Genetic studies suggest that these rhizobia may use cytokinins to induce nodulation in their host plant. The same rhizobial strain is a natural

[1]Department of Disease and Stress Biology, John Innes Centre, Norwich NR4 7UH, UK. [2]Boyce Thompson Institute for Plant Research, Tower Road, Ithaca, NY 14853, USA. [3]Department of Plant Molecular Biology, University of Lausanne, 1015 Lausanne, Switzerland.

*To whom correspondence should be addressed. E-mail: mjh78@cornell.edu

endophyte of wetland wild rice (*Oryza breviligulata*), and it markedly increases shoot biomass and grain yield, possibly owing to the bacterial nitrogen fixing capacity (reference S24) and demonstrating the benefits to the plant of such associations. Inside root nodule cells, bacteria are released from the IT into membrane-bound compartments, symbiosomes, where nutrient exchange with the host cell occurs. The bacteria then differentiate into nitrogen-fixing bacteroids, a process that may be actively controlled by the plant. Appropriate nutrient exchange is required to ensure a sustained interaction: If rhizobia unable to fix nitrogen are present, their nodules developmentally arrest prematurely and rapidly senesce (reference S25), suggesting that the plant can measure nitrogen levels released from the bacteria. This measurement by the host plant may function via amino acid cycling between the plant and bacterial cells (reference S26).

In AM symbiosis, the fungus colonizes the root cortex and develops extensively branched hyphae (arbuscules) within the inner cortical cells. As each arbuscule develops, the plant cell envelops it in the peri-arbuscular membrane (PAM). Phosphate (P_i) transport proteins essential for symbiotic P_i transfer to the plant cell reside within the PAM (*14*) (reference S27), and in solanaceous species, lysophosphatidylcholine induces their expression (reference S28). P_i transporter mutants showed that symbiotic P_i transport is essential for maintenance of the arbuscule and, subsequently, symbiosis (references S29 and S30). Whereas the underlying mechanisms remain to be determined, P_i may signal the establishment of cellular conditions to support the arbuscule. The coupling of symbiotic P_i transfer to maintenance of the arbuscule may provide a functional checkpoint in AM symbiosis.

In contrast to plant/symbiont interactions where it appears that the plant controls the interaction, in plant/pathogen interactions the invading microbe releases effectors that control plant cell function. Some rhizobia contain type III and type IV secretion systems that deliver effectors that can define host range into the plant cell (*15*) (reference S31). However, some rhizobial species lack the mechanisms for delivering effectors (*16*), indicating that effector release is not essential for symbiosis. The plant derived reprogramming for compatibility that follows recognition of symbiont signals most likely explains the observed suppression of plant defenses during symbioses (*17*) (reference S32). Here, compatibility between plants and microbes is guided by sustained plant/microbe communication. The symbioses are carefully monitored by the plant, and symbionts that fail to provide benefit to the plant (in the form of nutrients) are not maintained. In this regard, the plant represents the dominant partner in this interaction, in marked contrast to pathogenic interactions where the pathogen engineers the plant response. However, this polar view of symbiosis and pathogenesis is likely to be an oversimplification, and the boundaries between symbiosis and pathogenesis are probably more fluent than is currently apparent.

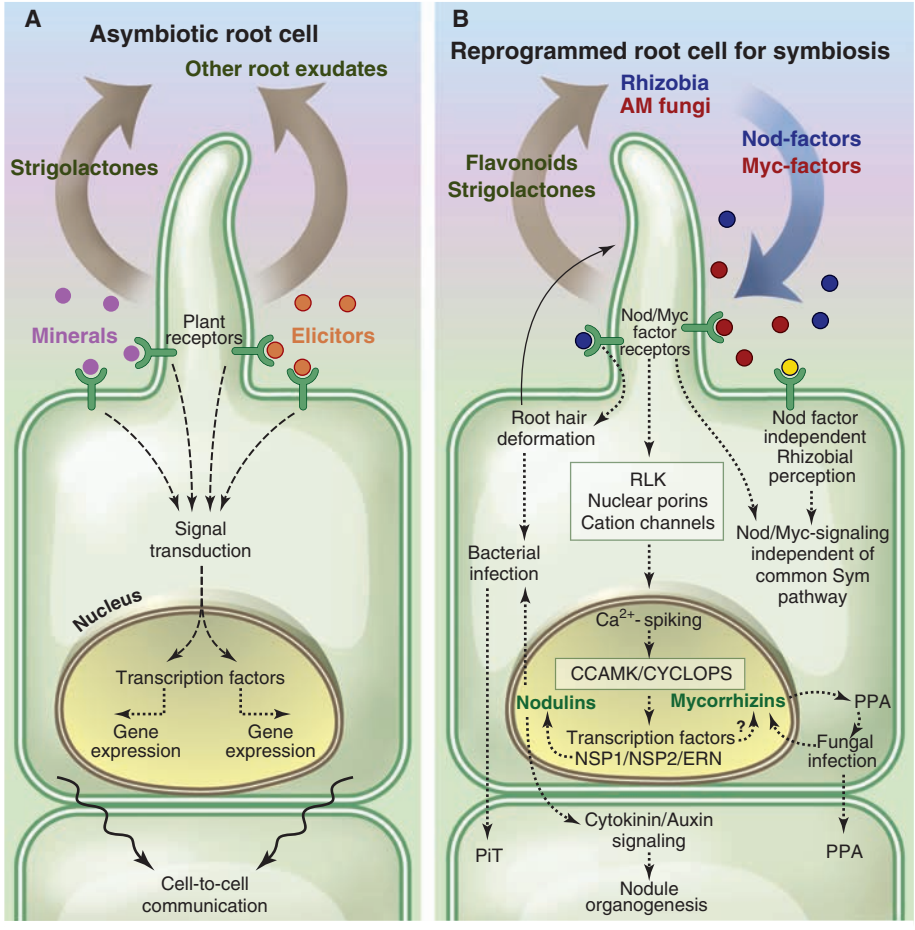

Fig. 1. Signal exchange during symbiosis. (**A**) An asymbiotic cell consitutively releases root exudates, including strigolactones. The root cell monitors the concentration of minerals and microbial organisms in the soil and transduces the respective signals. Integration of the signals occurs at the cellular and organismic levels and includes cell-to-cell communication. (**B**) A root-hair cell primed for interaction with rhizobia or AM fungi, respectively. Plant roots release flavanoids and strigolactones that prime the rhizobia and AM fungi. Nod and Myc factors act as signals from the symbionts to plant root cells that activate calcium spiking via the Sym pathway (boxed). The potential differential activation of CaMK/Cyclops leads to differential induction of nodulation-specific transcription factors (NSP1, NSP2, and ERN) and unknown mycorrhizal-specific transcription factors. Rhizobial and mycorrhizal infection require the common Sym pathway but also exhibit recognition and signaling independent of this pathway. The path for fungal infection and the IT is predicted by the PiT and the PPA, respectively, indicating directed signaling to neighboring cells. Nodule organogenesis is induced in inner cortical cells after Nod-factor perception by epidermal cells. This requires cytokinin signaling and is associated with changes in auxin levels.

References and Notes

1. A. Besserer, G. Becard, A. Jauneau, C. Roux, N. Sejalon-Delmas, *Plant Physiol.* **148**, 402 (2008).
2. S. Radutoiu *et al.*, *EMBO J.* **26**, 3923 (2007).
3. S. Kosuta *et al.*, *Proc. Natl. Acad. Sci. U.S.A.* **105**, 9823 (2008).
4. M. Charpentier *et al.*, *Plant Cell* **20**, 3467 (2008).
5. G. E. D. Oldroyd, J. M. Downie, *Annu. Rev. Plant Biol.* **59**, 519 (2008).
6. K. Yano *et al.*, *Proc. Natl. Acad. Sci. U.S.A.* **105**, 20540 (2008).
7. A. Andriankaja *et al.*, *Plant Cell* **19**, 2866 (2007).
8. S. Hirsch *et al.*, *Plant Cell* **21**, 545 (2009).
9. M. Banba *et al.*, *Plant Cell Physiol.* **49**, 1659 (2008).
10. C. Gutjahr *et al.*, *Plant Cell* **20**, 2989 (2008).
11. H. Gherbi *et al.*, *Proc. Natl. Acad. Sci. U.S.A.* **105**, 4928 (2008).
12. K. Markmann, G. Giczey, M. Parniske, *PLoS Biol.* **6**, e68 (2008).
13. A. Genre, G. Ortu, C. Bertoldo, E. Martino, P. Bonfante, *Plant Physiol.* **149**, 1424 (2009).
14. M. Parniske, *Nat. Rev. Microbiol.* **6**, 763 (2008).
15. K. Kambara *et al.*, *Mol. Microbiol.* **71**, 92 (2009).
16. M. Krehenbrink, J. A. Downie, *BMC Genomics* **9**, 55 (2008).
17. V. A. Benedito *et al.*, *Plant J.* **55**, 504 (2008).

18. G.E.D.O. was supported by the Biotechnology and Biological Sciences Research Council through grant BB/E003850/1; M.J.H. was supported by NSF (Integrative Organismal Systems # 0343975) and the U.S. Department of Agriculture (2008-35301-19039); and U.P. was supported by the Swiss National Science Foundation grant PP00A–110874.

Supporting Online Material

www.sciencemag.org/cgi/content/full/324/5928/753/DC1
References

10.1126/science.1171644

PERSPECTIVE

Coevolution of Plants and Their Pathogens in Natural Habitats

Jeremy J. Burdon* and Peter H. Thrall

Understanding of plant-pathogen coevolution in natural systems continues to develop as new theories at the population and species level are increasingly informed by studies unraveling the molecular basis of interactions between individual plants and their pathogens. The next challenge lies in further integration of these approaches to develop a comprehensive picture of how life history traits of both players interact with the environment to shape evolutionary trajectories.

Advances in understanding host-pathogen coevolutionary interactions requires integrating knowledge of the molecular basis of host resistance and pathogen virulence with studies of how polymorphism in genes controlling these characteristics affects disease in nature. This must be coupled with quantification of the roles of life history and environmental heterogeneity in the maintenance of such polymorphisms (*1*). Aspects of this broad challenge have been articulated in recent years (*2*, *3*), but major empirical and theoretical gaps remain. These include the impact of sexual recombination and short-term selection on variability in avirulence (*Avr*) gene sequences and pathogen virulence phenotypes, how sequence divergence and specific amino acid differences in Avr or resistance (R) proteins affect host recognition, and the extent to which population and regional variation in host resistance influences the maintenance of pathogen population diversity. Answers to these questions may also help to resolve ongoing debate regarding the role of coevolutionary arms races versus balancing selection in shaping patterns of polymorphism in host resistance and pathogen virulence (*4*).

Here, we briefly highlight recent studies of wild plant-pathogen associations and illustrate their value as model coevolutionary systems. Notably, at a molecular level, plant defense systems have similarity to mammalian innate cellular immunity and utilize analogous components to recognize pathogen-derived signals and to induce defense responses (*5*–*7*). The evolutionary commonalities of animal and plant disease, as well as the scientific promise of this conceptual realization, have been previously highlighted (*8*, *9*). These characteristics, combined with the lack of ethical issues that constrain experimental manipulations in animal populations, make plant-based systems powerful models for quantifying the epidemiological impacts of genetic variation in host disease resistance.

Plant pathogens are ubiquitous—their demographic impacts are well recognized in agriculture and acknowledged in natural communities through the effects of iconic invasive diseases (e.g., sudden oak death or *Phytophthora* die-back). However, the epidemiology of wild plant–pathogen interactions is significantly understudied relative to the dynamics of infectious disease in animal and human populations. Perhaps more critically, in both plant and animal systems, direct investigation of causal links between population genetic structure and disease dynamics has received scant attention, although studies involving agricultural pathogens provide insight into how disease pressure and host diversity may interact to determine rates of pathogen evolution (*10*, *11*). The lack of empirical evidence is surprising, given the potential for genetic variation to affect not only disease dynamics and prevalence, but also when or where new diseases emerge. Characterization of ecological and evolutionary processes at spatiotemporal scales, ranging from genes to populations to species, is critical in this context.

Coevolutionary biology has advanced beyond ecological and population genetics approaches that, on one hand, assumed detailed investigation of single populations could provide surrogate assessments for all populations and, on the other, that deterministic global models were adequate representations of real-world host-pathogen associations. The formal development of metapopulation theory (*12*, *13*) and the geographic mosaic theory of coevolution (*14*) has given added impetus to the articulation of a new paradigm arising from the idea that understanding the forces driving coevolutionary trajectories requires accounting for both within- and among-population processes in space and time. In keeping with this perspective, spatial structure is increasingly viewed as integral to empirical studies of natural plant-pathogen interactions (*15*, *16*).

Simulation models further illustrate the importance of integrating studies across multiple, inter-

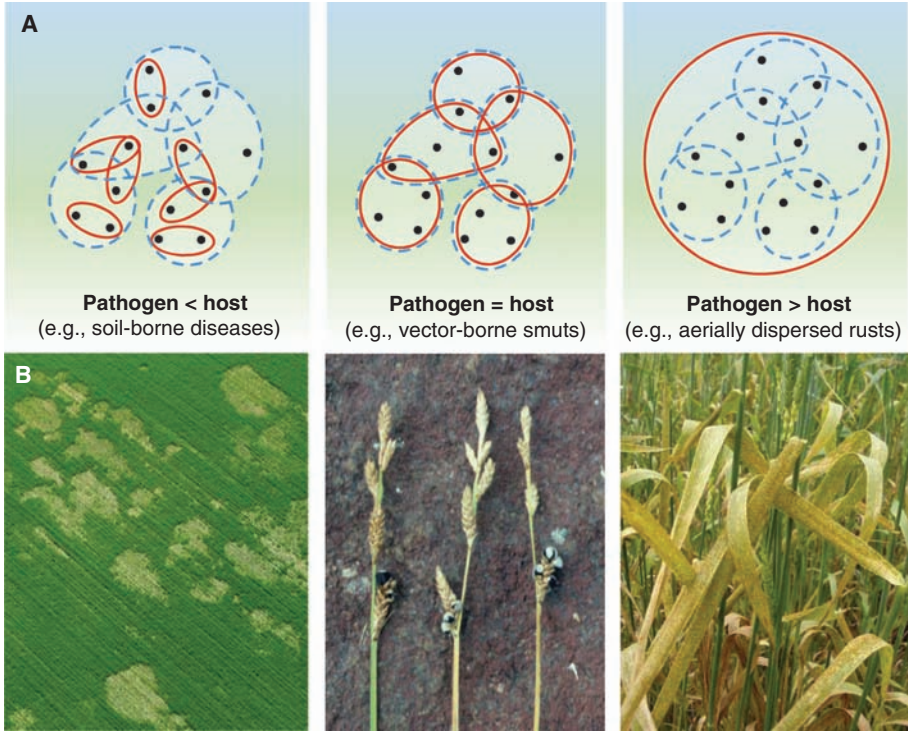

Fig. 1. (**A**) Examples of different host and pathogen dispersal strategies [redrawn from (*32*)] that determine spatial interactions (dashed and solid lines represent the relative scale of host and pathogen movement, respectively). (**B**) Specific host-pathogen associations that fit these dispersal scenarios while simultaneously representing pathogens that (left to right): kill hosts outright (Rhizoctonia on *Triticum aestivum*), castrate hosts (*Anthracoidea fischeri* on *Carex mackenziei*), and debilitate hosts (*Puccinia striformiis* on *Triticum aestivum*).

Commonwealth Scientific and Industrial Research Organization (CSIRO)–Plant Industry, Post Office Box 1600, Canberra, ACT 2601, Australia.

*To whom correspondence should be addressed. E-mail: Jeremy.Burdon@csiro.au

connected populations and undermine many premises underlying earlier thinking (e.g., the assumption of fitness costs associated with resistance) (*17*). Although empirical studies are limited, available evidence is consistent with the idea that evolutionary trajectories of natural host-pathogen systems do not reflect the dynamics of ephemeral local populations, where the evolutionary consequences of random drift, extinction, and recolonization are magnified and where selection can favor distinct resistance and virulence patterns even in adjacent populations (*18*). Indeed, environmental differences may create local variation in pathogen severity and lead to hot and cold spots (*14*) of selection pressure. Intriguingly, recent evidence that infection may stimulate host recombination rates in subsequent generations suggests a mechanism whereby disease-prone populations may respond more rapidly than otherwise possible (*19*, *20*).

A major unanswered question regarding the evolution of wild plant–pathogen associations is the extent to which resistance and virulence depend on specific interactions between single genes (qualitative resistance) versus those in which resistance is determined by many genes, individually of minor effect (quantitative resistance). Although in reality, most host-pathogen systems involve genes of both major and minor effect, the conceptual distinction between these has provided a powerful stimulus to theoretical models of host-pathogen interactions (*21*, *22*). Whether qualitative or quantitative resistance is more likely to provide hosts with the greatest selective advantages against disease organisms over time is unknown—does resistance confer high short-term fitness but a high probability of ultimate failure (gene-for-gene), or are fitness impacts more constantly present but largely restricted in magnitude? Resolution of this question depends on understanding the interaction between host and pathogen life history characters that affect reproduction, survival, and dispersal and how they are mediated by environmental factors.

More generally, the role of life history (e.g., reproductive system, host range, and pathogen-dispersal mechanisms) in influencing the timing, severity, and selective impact of disease has received little concerted focus in natural plant-pathogen interactions, despite demonstration that comparative analysis of such data can provide valuable insights into the evolution of animal-parasite systems (*23*) and a means of assessing the durability of resistance in crops (i.e., following commercial adoption of a resistant cultivar, the period of time before the evolution of new pathotypes that can parasitize the resistant cultivar) (*24*). In plant-pathogen associations, even characters as simple as mode of pathogen impact or dispersal distance suggest a rich repertoire of possible interactions. Thus, pathogen dispersal envelopes may be substantially smaller than, may equate with, or may exceed that of their host (Fig. 1). Variation in such traits is likely to result in different evolutionary trajectories as direct effects on contact patterns and disease incidence lead to longer-term impacts on the maintenance of genetic variation (*25*) and patterns of local adaptation (*26*).

Environmental variation generates further complexity in life-history interactions. Heuristic models suggest that particular combinations of environmental conditions impose a series of selective sieves, the nature and intensity of which may be determined by specific plant and pathogen life-history features (*27*). For example, harsh environments that promote plant survival via seed or dormant rootstock impose selective pressure on foliar pathogens, the intensity of which depends on particular traits. Pathogens that can survive saprophytically or have specialized resting stages or have refugia on other hosts are subject to much smaller population fluctuations than those without such adaptations. These contrasting situations may generate marked differences in the relative importance of drift, migration, extinction, and recolonization and thus may promote distinctly different evolutionary trajectories. To understand the evolutionary drivers of resistance and virulence, we therefore need a theoretical framework for investigating the interplay between physical environment and host and pathogen life histories.

In summary, progress in understanding host-pathogen evolutionary dynamics in nature needs characterization of processes occurring at many spatiotemporal scales, including genes and cells, within host individuals, and within and among host and pathogen populations. To achieve this requires integration of molecular approaches currently being focused on agricultural pathogens, with population- and species-level studies. For example, cloning and sequencing of specific *Avr* genes in *Melampsora lini* found evidence for functional changes in the coding regions of targeted *Avr* genes that occurred almost exclusively via nonsynonymous mutations (*28*). These observations provide strong independent evidence for the operation of selection on these genes. These results, coupled with population-level studies of *Linum marginale* resistance structure, are generating a picture of the evolutionary dynamics of selection on specific *Avr* genes.

Insights provided by the *Linum* system will be greatly strengthened by application of approaches developed to investigate interactions between *Arabidopsis* and its pathogens, where, for example, molecular studies have demonstrated significant resistance costs (*29*). However, the need now is to place this work into a real-world ecological genetics context involving studies of interacting suites of host and pathogen populations.

The scientific rewards from comprehensive research programs such as described above include greater fundamental understanding of the natural world, as well as immediate practical benefits. For weed biocontrol, population models incorporating parasitic mode and host longevity have been used to predict pathogen characteristics most likely to lead to initial rapid host population declines, as well as relative effectiveness in preventing subsequent population recovery (*30*). Similar approaches could estimate threats posed by specific pathogens to conservation and population restoration, or the dangers of deliberate translocation of species to new habitats where they may serve as inoculum reservoirs for vulnerable host species. Finally, in forestry and agricultural situations where plant genetic diversity is still significant, deeper understanding of the complex array of factors affecting host-pathogen coevolution could ensure efficient targeting of control methods.

These examples underscore the need for a more generally predictive science of coevolutionary biology (*14*, *31*) that can account for human impacts on all levels of biological organization (e.g., fragmentation of natural systems and exotic introductions) and in novel ways (genetically modified organisms, introduction of new resistance genes into crops, and antibiotics). Integrated investigations of coevolution in host-microbe interactions will ultimately increase our ability to predict the long-term consequences of different types of human intervention on disease.

References and Notes

1. L. G. Barrett *et al.*, *Trends Ecol. Evol.* **23**, 678 (2008).
2. M. Tibayrenc, *Int. J. Parasitol.* **28**, 85 (1998).
3. L. A. Real *et al.*, *Proc. Natl. Acad. Sci. U.S.A.* **102**, 12107 (2005).
4. G. Wichmann *et al.*, *Appl. Environ. Microbiol.* **71**, 2418 (2005).
5. J. L. Dangl, J. D. G. Jones, *Nature* **411**, 826 (2001).
6. B. J. Staskawicz *et al.*, *Science* **292**, 2285 (2001).
7. B. F. Holt, D. A. Hubert, J. L. Dangl, *Curr. Opin. Immunol.* **15**, 20 (2003).
8. L. G. Rahme *et al.*, *Proc. Natl. Acad. Sci. U.S.A.* **97**, 8815 (2000).
9. N. Keen *et al.*, *Proc. Natl. Acad. Sci. U.S.A.* **97**, 8752 (2000).
10. K. M. Chin, M. S. Wolfe, *Plant Pathol.* **33**, 535 (1984).
11. C. Lannou *et al.*, *Plant Pathol.* **54**, 699 (2005).
12. M. Gilpin, I. Hanski, Eds., *Metapopulation Dynamics: Empirical and Theoretical Investigations* (Harcourt Brace Jovanovich, London, 1991).
13. I. Hanski, *Metapopulation Ecology* (Oxford Univ. Press, Oxford, 1999).
14. J. N. Thompson, *The Geographic Mosaic of Coevolution* (Chicago Univ. Press, Chicago, 2005).
15. P. H. Thrall, J. J. Burdon, *Science* **299**, 1735 (2003).
16. A. L. Laine, *J. Ecol.* **92**, 990 (2004).
17. C. Damgaard, *J. Theor. Biol.* **201**, 1 (1999).
18. P. H. Thrall, J. J. Burdon, A. Young, *J. Ecol.* **89**, 736 (2001).
19. A. Boyko *et al.*, *Nucleic Acids Res.* **35**, 1714 (2007).
20. J. Molinier *et al.*, *Nature* **442**, 1046 (2006).
21. A. Agrawal, C. M. Lively, *Evol. Ecol. Res.* **4**, 79 (2002).
22. S. L. Nuismer, *Evolution* **60**, 24 (2006).
23. A. B. Lockhart, P. H. Thrall, J. Antonovics, *Biol. Rev. Camb. Philos. Soc.* **71**, 415 (1996).
24. B. A. McDonald, C. Linde, *Euphytica* **124**, 163 (2002).
25. P. H. Thrall, J. J. Burdon, *Plant Pathol.* **51**, 169 (2002).
26. S. Gandon *et al.*, *Proc. R. Soc. Lond. B. Biol. Sci.* **263**, 1003 (1996).
27. J. J. Burdon *et al.*, *Oikos* **76**, 411 (1996).
28. P. N. Dodds *et al.*, *Proc. Natl. Acad. Sci. U.S.A* **103**, 8888 (2006).
29. D. Tian *et al.*, *Nature* **423**, 74 (2003).
30. P. H. Thrall, J. J. Burdon, *Weed Technol.* **18**, 1269 (2004).
31. P. H. Thrall *et al.*, *Trends Ecol. Evol.* **22**, 120 (2007).
32. P. H. Thrall, J. J. Burdon, *J. Ecol.* **85**, 743 (1997).

33. This work was supported by CSIRO and NIH grant 5R01GM074265-01A2.

10.1126/science.1171663

A Gene Necessary for Reproductive Suppression in Termites

Judith Korb,[1,2]* Tobias Weil,[2,3]* Katharina Hoffmann,[1] Kevin R. Foster,[4] Michael Rehli[3]

A major transition in evolution is the origin of a division between reproduction and work among individuals. Nowhere is this divide more striking than in social insects, where workers rarely produce offspring even though they are often capable of reproduction should the queen or king die. The molecular mechanisms that control worker reproduction remain largely unknown (*1*). We used a combination of behavioral assays and RNA interference (RNAi) (*2*) to identify a gene required for the reproductive division of labor between the queen and the workers.

With use of cDNA representational difference analysis (cDNA-RDA), we previously identified genes that are specifically overexpressed in queens but not kings and workers of the lower termite *Cryptotermes secundus* (Fig. 1A) (*3*). One of these, *Neofem2*, is a homolog of a gene involved in communication in the Maderian cockroach, *Leucophaea maderae* (*3*, *4*). Thus, we hypothesized that *Neofem2* plays a critical role in queen-worker communication.

In lower termites, workers are totipotent and can develop into reproductives (Fig. 1) but only when the queen or king dies. Because it is not possible to induce a worker to molt into a new queen within the short functional period of RNAi (preliminary experiments revealed a decline of gene knockdown after 48 hours), we developed a behavioral assay to function as a proxy for the absence of queens. Removing queens from colonies resulted in a single observable effect: an increase in butting behavior among workers (Wilcoxon paired rank test: $Z = -2.43$, $n = 9$ pairs, $P = 0.015$) (Fig. 1B, fig. S1, table S1, and movie S1). Butting is associated with reproductive dominance, and workers that go on to replace the king or queen display more butting than workers that do not change caste (figs. S2 and S3). These observations are consistent with those of bees, ants, and wasps, where aggressive interactions among workers increase before, or associated with, worker reproduction (*5*). Therefore, we used the frequency of butting interactions received by a focal worker as an indicator of the queen's absence and the eventual succession of the queen.

We silenced *Neofem2* in queens with RNAi in eight queenright colonies (figs. S4 and S5) and recorded the behavioral repertoire 1 day before and 1 day after silencing. Although silencing had no observable effect on the behavior of the queen herself (Wilcoxon paired rank tests: always $P > 0.200$) (fig. S6 and table S2), workers showed a significant increase in butting behavior (Wilcoxon paired rank test: $Z = -2.52$, $n = 8$ pairs, $P = 0.012$) (Fig. 1C, fig. S7, and table S3) that was not observed in our 24 control colonies (table S4). Thus, we conclude that inhibiting *Neofem2* makes workers behave as though the colony is queenless and that *Neofem2* is necessary for the queen to suppress worker reproduction. *Neofem2*'s putative 532–amino acid gene product suggest that it is a β-glycosidase, a member of the glycosyl hydrolase family 1 (*3*). These enzymes are found among all taxa—including bacteria, fungi, plants, and animals (*6*)—and have a major function in breaking down polysaccharides like cellulose. The closest homolog of *Neofem2* plays a role in wood consumption in the termite *Neotermes koshuensis* (table S5). β-glycosidases also can release volatiles from substrates composed of sugars and a small chemical group (*7*) and may play a role in egg pheromones in *Reticulitermes speratus* and cockroach species (*8*) and in sex-specific signaling in the Maderian cockroach (*4*). All together, these results suggest that *Neofem2* may have evolved from an ancestral role of wood digestion to one of queen-worker pheromonal communication in modern termites. If confirmed, *Neofem2* provides insight into the chemistry of queen pheromone production, something that has been described in honeybees (*9*).

The evolution and maintenance of a reproductive division of labor is predicted to occur only under restricted ecological conditions (*5*). Our data suggest that this major step in social evolution can be achieved through relatively minor changes to preexisting biochemistry. The finding that termite social organization can be influenced by single genes also suggests a novel strategy for insect control: chemical genetic inhibitors that cause anarchy within their societies.

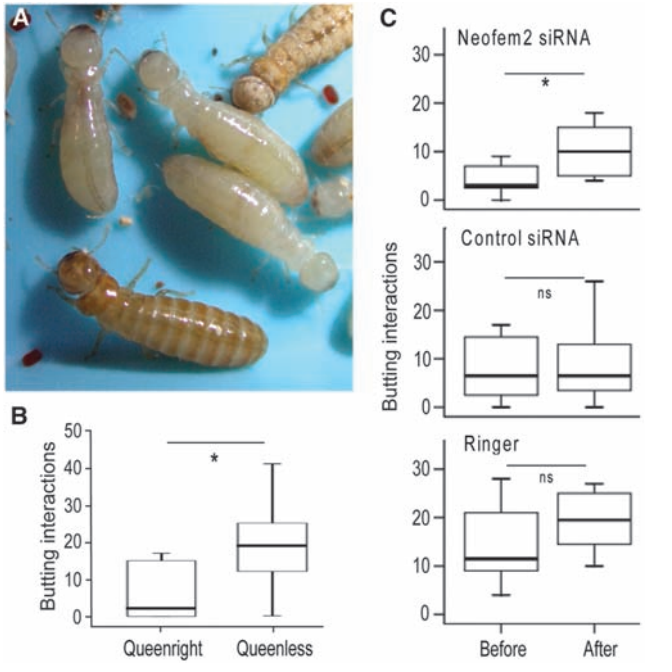

Fig. 1. (**A**) *Cryptotermes secundus* queen (bottom left) together with the king (top right) and workers. (**B**) Frequency of butting interactions among workers in queenright and queenless colonies. (**C**) Frequency of butting interactions before and after treatment of the queen with *Neofem2* small interfering RNA (siRNA), control siRNA, and Ringer's solution. Shown are boxplots with median, quartiles, and minimal and maximal values. Outliers are not shown but were analyzed (tables S1, S3, and S4). *Significant increase in the frequency of butting by workers.

References and Notes

1. C. R. Smith, A. L. Toth, A. V. Suarez, G. E. Robinson, *Nat. Rev. Genet.* **9**, 735 (2008).
2. Materials and methods are available as supporting material on *Science* Online.
3. T. Weil, M. Rehli, J. Korb, *BMC Genomics* **8**, 198 (2007).
4. R. Cornette, J. P. Farine, D. Abed-Viellard, B. Quennedey, R. Brossut, *Biochem. J.* **372**, 535 (2003).
5. A. F. G. Bourke, N. R. Franks, *Social Evolution in Ants* (Princeton Univ. Press, Princeton, NJ, 1995).
6. W. R. Terra, C. Ferreira, B. P. Jordao, R. J. Dillon, in *Biology of the Insect Midgut*, M. J. Lehane, P. F. Billingsley, Eds. (Chapman & Hall, London, 1996), pp. 153–194.
7. L. Mattiacci, M. Dicke, M. A. Posthumus, *Proc. Natl. Acad. Sci. U.S.A.* **92**, 2036 (1995).
8. K. Matsuura, T. Yashiro, K. Shimizu, S. Tatsumi, T. Tamura, *Curr. Biol.* **19**, 30 (2009).
9. E. Plettner, K. N. Slessor, M. L. Winston, J. E. Oliver, *Science* **271**, 1851 (1996).

10. The authors thank S. Schneuwly and J. Landskron for micromanipulator help and K. Merches and K. Borner for laboratory support. Supported by a Deutsche Forschungsgemeinschaft (DFG) grant to J.K. and M.R. (KO1895/6).

Supporting Online Material

www.sciencemag.org/cgi/content/full/324/5928/758/DC1
Materials and Methods
Figs. S1 to S7
Tables S1 to S6
Movie S1

8 January 2009; accepted 12 March 2009
10.1126/science.1170660

[1]Behavioral Biology, University of Osnabrueck, Barbarastrasse 11, D-49076 Osnabrueck, Germany. [2]Biologie I, University of Regensburg, Universitätsstrasse, D-93040 Regensburg, Germany. [3]Department of Hematology, University Hospital Regensburg, D-93042 Regensburg, Germany. [4]Center for Systems Biology, Harvard University, Bauer Laboratory, 52 Oxford Street, Cambridge, MA 02138, USA.

*To whom correspondence should be addressed. E-mail: judith.korb@biologie.uni-osnabrueck.de (J.K.); weil.tobias@web.de (T.W.)

Representation of Confidence Associated with a Decision by Neurons in the Parietal Cortex

Roozbeh Kiani and Michael N. Shadlen

The degree of confidence in a decision provides a graded and probabilistic assessment of expected outcome. Although neural mechanisms of perceptual decisions have been studied extensively in primates, little is known about the mechanisms underlying choice certainty. We have shown that the same neurons that represent formation of a decision encode certainty about the decision. Rhesus monkeys made decisions about the direction of moving random dots, spanning a range of difficulties. They were rewarded for correct decisions. On some trials, after viewing the stimulus, the monkeys could opt out of the direction decision for a small but certain reward. Monkeys exercised this option in a manner that revealed their degree of certainty. Neurons in parietal cortex represented formation of the direction decision and the degree of certainty underlying the decision to opt out.

Choice certainty—the degree to which a decision-maker believes a choice is likely to be correct—affects a variety of cognitive functions: how we plan subsequent actions, how we react and learn from mistakes, and how we justify our choices to others. Choice certainty is pivotal for planning actions in a complex environment in which subsequent decisions depend on pending outcomes of previous decisions (*1*–*3*). For example, a decision to undergo a risky operation depends, among other factors, on the degree of certainty that the diagnosis is correct. Psychologists have long proposed that choice certainty serves as a link between the physical world and belief: It provides a graded scale that allows us to translate our convictions into suitable actions (*4*, *5*).

Despite the importance of choice certainty, its neural mechanisms are poorly understood. It is well established that choice certainty is closely correlated with both decision accuracy and reaction time (*6*–*11*). This close relationship suggests that the same mechanism that underlies the decision-making process might underlie certainty judgments (*1*, *10*, *12*, *13*). It has been suggested that neurons in orbitofrontal cortex and cingulate cortex, which are known to represent reward expectation or conflict, represent reward expectations associated with decision uncertainty (*14*–*16*). However, these neurons do not give rise to a representation of decision uncertainty but presumably receive this information from neurons that compute this quantity in the decision-making process.

The neural mechanism of decision-making has been investigated using simple perceptual tasks in which a monkey makes a categorical choice between two or more discrete options based on a sensory stimulus (*17*). When the monkey is required to report the perceived direction of motion by a saccadic eye movement, neurons in lateral intraparietal cortex (LIP) represent the accumulation of evidence, termed a decision variable, that supports the target in their response fields (RFs) (*17*–*19*). Furthermore, these neurons signal the termination of the decision process when their firing rates reach a critical level or bound (*19*–*21*). Theoretical and experimental studies raise the possibility that the neural computations approximate a form of probabilistic reasoning about the alternatives (*22*–*24*). We hypothesize that the graded, time-dependent firing rates of LIP neurons also represent choice certainty. Our hypothesis, therefore, unifies the representation of the three components of decisions—choice, reaction time, and certainty—in a single neural population.

Two monkeys made perceptual decisions about the net direction of motion in a dynamic random-dot display (Fig. 1A) (*25*). Task difficulty was controlled by varying both the percentage of coherently moving dots and the viewing duration. After a delay period, the fixation point was extinguished, which instructed the monkey to indicate its direction choice by making an eye movement to one of the direction-choice targets. On a random half of the trials, the monkey was given the option to abort the direction discrimination and to choose instead a small but certain reward associated with a third saccade target. This "sure target" was shown during the delay period, at least 500 ms after the random-dot motion was extinguished. During motion viewing, the monkey did not know whether the sure-bet option would arise. The task design, a form of postdecision wagering (*26*–*28*), ensured that the monkey made a decision about motion direction on each trial. We hoped that the monkey would choose the sure target when less certain of the high-stakes direction choice, allowing us to study neural responses associated with choice certainty.

We first describe behavioral observations, which demonstrate that the postdecision wager reflects choice certainty. We then demonstrate a neural correlate of this certainty in the LIP firing rate. Together, these observations support a mechanism in which the same decision variable, represented by LIP neurons, underlies both the choice and the degree of certainty in that choice.

The monkeys opted for the sure target when the chance of making a correct decision about motion direction was small. They exercised this option more frequently for the weaker motion strengths and for the shorter stimulus durations ($P < 10^{-8}$) [equation 1 (*25*) and Fig. 1B], that is, when the probability of making an error was higher ($P < 10^{-8}$) [equation 2 (*25*) and Fig. 1C]. More interestingly, when the monkeys waived this option, the choice accuracy was better than on the trials when they were not offered the postdecision wager ($P < 10^{-3}$) [equation 3 (*25*) and Fig. 1C]. This improvement was apparent at almost all motion strengths and stimulus durations. It implies that the monkeys did not choose the sure target on the basis of stimulus difficulty but instead based on a sense of uncertainty on each trial. This same pattern was observed on a subset of trials in which identical random-dot patterns were repeated ($P < 0.025$) (fig. S1), which suggests that the source of information about difficulty is not governed solely by properties of the stimulus but also by internal variability that renders the evidence more or less reliable to the decision-maker.

We recorded extracellularly from 70 LIP neurons while the monkeys performed this task. These neurons exhibited spatially selective persistent activity that predicted whether an eye movement was planned into the RF of the neuron on a memory-guided saccade task (*29*–*31*). For the main motion task, we placed one of the direction targets (T_{in}) in the RF of the recorded neuron, the other direction target (T_{opp}) on the opposite side of the screen, and the sure target (T_s) orthogonal to the axis that connected the two direction targets.

Figure 2A shows responses of an example neuron for trials without the sure target. The neural activity after motion onset underwent a brief dip and then diverged to indicate the monkey's decision for T_{in} or T_{opp}. The activity persisted through the delay period until the eye movement (*18*). For simplicity, the graph combines all motion strengths and stimulus durations (*25*), but, as shown previously (*18*–*21*), the buildup of firing rate reflected the stimulus strength ($P = 0.01$) [equation 10 (*25*) and fig. S2], compatible with the representation of accumulated evidence in favor of T_{in}. We observed a similar divergence and persistence of activity for

Howard Hughes Medical Institute, National Primate Research Center, and Department of Physiology and Biophysics, University of Washington, Seattle, WA 98195, USA. E-mail: roozbeh@u.washington.edu (R. K.); shadlen@u.washington.edu (M.N.S.)

T_{in} and T_{opp} choices on the trials in which T_s was presented but was waived by the monkey (Fig. 2B, solid traces).

In contrast, when the monkey chose T_s, the activity after the motion changed more gradually and achieved intermediate values compared with the T_{in} and T_{opp} choices. This pattern persisted into the delay period until T_s appeared ($P < 10^{-8}$, t test). Before T_s appeared, the monkey did not know whether the sure bet would be offered. After the onset of T_s, there was a dip in activity, followed by a return to the level of activity preceding the onset of T_s. When the monkey chose T_s, the response gradually converged to the T_{opp} level. The profile of activity suggests that even before the onset of T_s, the neuron was informative about whether the monkey would choose or waive this option should it be offered.

We observed a similar pattern of activity across the population of 70 LIP neurons (*32*). Intermediate firing rates during motion viewing and the early delay were associated with choosing the sure target later in the trial, as shown by the population average firing rates (Fig. 2D). To quantify this effect in single neurons, we compared activity in the 200-ms period before T_s onset (Fig. 2D, hatched box) for trials in which the monkey selected or waived the sure-bet option. For motion toward T_{in}, the neural activity across the population was significantly smaller for T_s choices than for T_{in} choices [$P = 0.007$, analysis of variance (ANOVA)] (Fig. 2E). For motion toward T_{opp}, the activity was significantly larger for T_s choices than for T_{opp} choices ($P = 0.001$) (Fig. 2F).

These observations demonstrate that the monkey is more likely to opt for T_s when the LIP activity achieves an intermediate level of firing rate. However, a possible concern is that the intermediate level of activity represented by the mean firing rates from many trials is an unfair representation of the activity on single trials. According to this argument, the intermediate means might represent a mixture of the high and low firing rates that would have corresponded to T_{in} and T_{opp} choices, had the monkey indicated a direction choice on these trials. This "mixture of states" alternative makes a clear prediction, which is not supported by the data. If the intermediate means were solely mixtures of the responses associated with T_{in} and T_{opp} choices, then the variance should reflect the dispersion of values associated with these extremes. This idea is rejected: The variance associated with T_s choices was significantly smaller than the variance associated with the mixtures of T_{in} and T_{opp} choices ($P = 4.7 \times 10^{-5}$, F-test). We conclude that these intermediate levels of activity are not artifactual but represent a low state of certainty.

This conclusion is supported further by comparing the activity from neurons on single trials with the monkey's decision to choose or waive the T_s option (Fig. 3A). For each trial, from each neuron, we calculated the deviation of firing rate, in the epoch just preceding T_s onset, from an intermediate level. The magnitude of this deviation was inversely related to the probability that the monkey chose the sure-bet option ($P = 2.3 \times 10^{-5}$) [equation 11 (*25*) and Fig. 3A]. The influence of a single neuron on the probability of a postdecision wager is expected to be small because it is but one member of a large population of neurons that govern the behavior, presumably (*33*–*35*). Nonetheless, the significance of the effect is a strong indication that LIP responses represent the choice certainty.

This single-trial analysis addresses another possible concern. Because stimulus difficulty (i.e., motion coherence and duration) affects both LIP responses and confidence judgments, it seems possible that the correlation between LIP activity and the postdecision wager is merely accidental, that is, totally explained by the stimulus difficulty. Alternatively, if T_s choices are based on LIP activity, they should be influenced by both the stimulus and the noisy fluctuations of LIP firing rates. To address this, we performed a variant of the single-trial analysis described in the previous paragraph. We calculated the trial-to-trial fluctuation of LIP responses relative to the mean response dictated by each motion strength and direction. These residual fluctuations before the sure-target onset had significant leverage on the probability of choosing the sure target ($P = 4.0 \times 10^{-5}$) [equation 12 (*25*)]. This finding also held for the subset of trials in which we used identical random-dot motion stimuli ($P = 0.015$). Therefore, the linkage of neural responses with sure-target choices is not explained merely by their shared covariation with the stimulus. We conclude from these analyses that the variable discharge of LIP activity was related to the monkey's choice certainty, whether these variations were caused by experimental manipulations (i.e., motion strength and duration) or random effects (i.e., neural noise).

The single-trial analyses have focused thus far on neural activity in the delay period, immediately preceding the onset of T_s. Is the LIP activity during decision formation also related to choice certainty? The evolution of neural activity accompanying motion viewing suggests an affirmative answer. The rate of change of LIP activity after motion onset, termed the buildup rate (*36*), was related to the probability of choosing

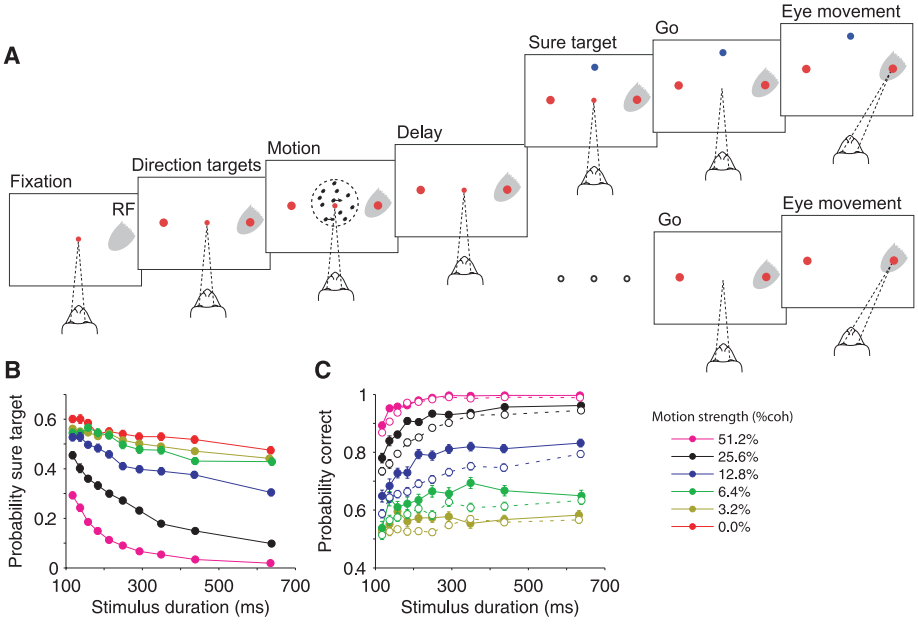

Fig. 1. Postdecision wagering behavior in monkeys is indicative of choice certainty. (**A**) The sequence of events in the task. After acquiring a central fixation point (small red circle), two direction targets (large red circles) appeared on the screen, one inside the neural RF (gray shading), the other on the opposite side of the screen. The motion stimulus appeared after a short delay, remained visible for 100 to 900 ms, and was followed by another delay (1200 to 1800 ms). On half of the trials (lower branch) the delay persisted until the fixation point was turned off, which served as a "go" signal that instructed the monkey to indicate the perceived direction of motion by a saccadic eye movement to one of the direction targets. A correct response led to a liquid reward; a wrong response led to no reward and a brief time-out. On the other half of the trials (upper branch), a third target was presented 500 to 750 ms after extinction of the motion. Choosing this sure target (T_s, blue circle) led to a smaller reward (~80% of correct reward). On these trials, the monkey could choose T_s or a direction choice. The two trial types were randomly interleaved. (**B**) The frequency of choosing T_s was greater when the motion strength (% coherence) was weak or the duration brief. The points are data, grouped in duration quantiles (deciles). Error bars (SE) are smaller than the symbols. (**C**) Decision accuracy when the T_s option was waived. The graph compares performance on trials in which T_s was not shown (open circles, dashed curves) with trials in which T_s was offered but waived (filled circles, solid curves).

T_s later in the trial. For stronger stimuli, the buildup was steeper ($P < 10^{-8}$) [equation 10 (*25*)], consistent with the accumulation of stronger evidence, shorter decision times, and ultimately more accurate decisions (*13*, *17*). According to our hypothesis, the buildup rates should tend toward intermediate values when the monkey chose T_s. To test this, we performed a logistic regression analysis using buildup rates estimated from single trials. Deviation of the buildup rate from intermediate values was associated with a lower probability of choosing the sure target ($P = 0.017$) [equation 11 (*25*) and Fig. 3B]. Moreover, this link was not simply due to covariation of buildup rates and choice certainty with motion strength ($P = 0.0018$) [equation 12 (*25*)].

It is also interesting to note that, although the fluctuations in buildup rate and delay period activity were weakly correlated ($r = 0.10$, $P < 10^{-8}$), each exerted independent leverage on the likelihood that the monkey would opt for the T_s wager ($P < 0.03$) [equation 13 (*25*)]. In other words, both the evolution of decision-related activity and the sustained activity in the delay period carry information about choice certainty. Although both quantities reflect the state of evidence, variation in the buildup rate also affects the amount of time it takes to reach a decision (*19*–*21*, *37*, *38*), consistent with the long-held view that decision time contributes to choice certainty (*8*, *9*, *12*).

Indeed, a Bayesian framework that incorporates both evidence and decision time explains several aspects of the data. As previously shown, the left-right choices on this task are governed by the accumulation of evidence favoring one or the other option (*17*). This accumulation, which we call a decision variable, $v(t)$, is represented by the firing rates of LIP neurons. It begins at a neutral value and undergoes a random walk with drift (also termed drift diffusion) as evidence accumulates for and against the two direction alternatives. The decision terminates naturally when there is no more evidence (e.g., when the stimulus duration is short) or when v reaches a critical level or bound. In both cases, the choice is determined by the sign of v. As previously shown, this simple model explains the monkey's accuracy as a function of stimulus strength and viewing time. It explains both the diminishing returns associated with prolonged viewing in our experiment (fig. S3) (*20*) and the trade-off between speed and accuracy in reaction-time experiments (*13*, *39*, *40*). It also explains the saturating firing rate curves in Fig. 2.

A simple extension of this bounded evidence accumulation model also explains the postdecision wagering. The key insight is that both v and t convey information about certainty. Figure 4A shows the distribution of $v(t)$, combined across all stimulus strengths when the rewarded direction is, for example, rightward. Application of the decision rule described in the previous paragraph to $v(t)$ would lead to different proportions of correct and incorrect choices, depending on the motion strength. This transformation is shown in Fig. 4B, which replaces the probability distribution of $v(t)$ with the log odds of a correct decision. This is the log-posterior odds based solely on $v(t)$. For example, if a rightward stimulus is shown, the log odds of a

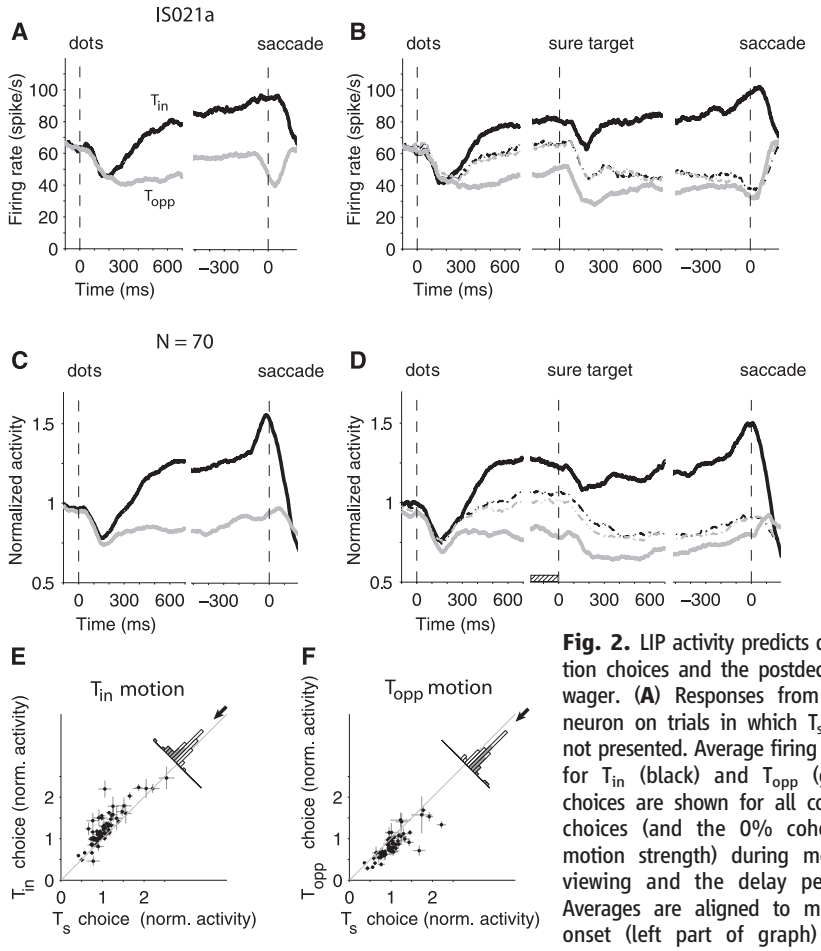

Fig. 2. LIP activity predicts direction choices and the postdecision wager. (**A**) Responses from one neuron on trials in which T_s was not presented. Average firing rates for T_{in} (black) and T_{opp} (gray) choices are shown for all correct choices (and the 0% coherent motion strength) during motion viewing and the delay period. Averages are aligned to motion onset (left part of graph) and saccade initiation (right). (**B**) Responses from the same neuron on trials in which T_s was presented. The dashed lines show neural activity on trials in which T_s was chosen (black and gray, motion toward T_{in} and T_{opp}, respectively). The middle portion of the graph shows activity in the delay period, aligned to onset of T_s. (**C** and **D**) Population average responses of 70 LIP neurons from two monkeys. Same conventions as in (A) and (B). Firing rates from each neuron were normalized to the mean level before onset of the motion stimulus. (**E**) The activity before T_s presentation was smaller for T_s choices than for T_{in} choices. Each data point represents the mean activity of an LIP neuron in the 200 ms before T_s presentation [hatched rectangle in (D)]. Error bars, mean ± SEM. Shading in the histogram shows significant cases ($P < 0.05$). The arrow shows the mean difference of normalized activity across the population (mean ± SEM, −0.20 ± 0.03). (**F**) The activity before T_s presentation was larger for T_s choices than for T_{opp} choices. Same conventions as in (E) (mean difference = 0.18 ± 0.02).

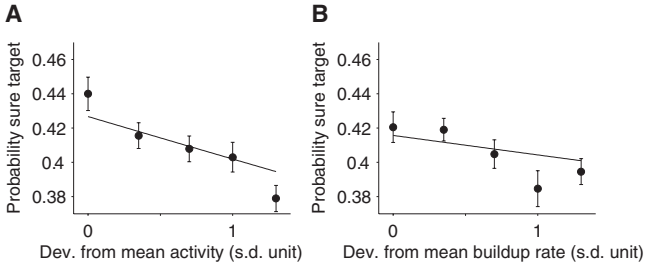

Fig. 3. T_s choices were correlated with trial-to-trial variation of neural activity. Responses from single trials were represented as the absolute deviation, in units of standard deviation, from the mean value using all the trials from a neuron (z score). (**A**) The frequency of choosing T_s as a function of deviation from mean in the activity before T_s presentation. Curves are fits of equation 11 (*25*) to individual trials. The points illustrated on the graph were formed by grouping trials into five bins. (**B**) The frequency of choosing T_s as a function of deviations from the mean buildup rate of activity after motion onset. Same conventions as in (A).

correct choice is simply the log posterior odds that the stimulus is to the right

$$\underbrace{Log\frac{p(S_1|v(t))}{p(S_2|v(t))}}_{\text{log posterior odds}} = \underbrace{Log\frac{\sum_i p(v(t)|S_1, C_i)p(C_i|S_1)}{\sum_i p(v(t)|S_2, C_i)p(C_i|S_2)}}_{\text{log likelihood ratio}} + \underbrace{Log\frac{p(S_1)}{p(S_2)}}_{\text{log prior odds}}$$

where C is motion coherence, and S_1 and S_2 represent the rightward and leftward motion direction, respectively. The last term vanishes, because the prior probability that motion is left or right is equal. The summation terms implement marginalization over motion strength. The left side of the equation formalizes belief in the proposition $S = S_1$.

From the depiction in Fig. 4B, it is easy to imagine that opting out of the direction decision might happen when the expected chance of success based on $v(t)$ at decision time is less than a criterion level (Fig. 4C). This simple model explains the observed behavior and successfully predicts the amount of improvement in the probability of being correct for trials in which the monkey waives T_s. The model has only three free parameters (table S1), which were set by fitting the proportion of T_s choices and the probability of being correct for trials without T_s [dashed curves in Fig. 4D ($R^2 = 0.97$) and Fig. 4E ($R^2 = 0.98$)]. This establishes a prediction (not a fit) for the probability of being correct on the trials in which T_s was shown but waived (Fig. 4E, solid curves) ($R^2 = 0.95$). The agreement between this simple model and the data affirms the plausibility of the Bayesian sequential sampling framework (*41*).

Moreover, the evolution of $v(t)$ predicted by the model resembles qualitatively the responses of LIP neurons (Fig. 4F and fig. S4). For stronger motion, the decision variable associated with T_s choices follows less intermediate trajectories (note the separation of dashed curves), and the decision variable associated with direction choices rises (or falls) faster toward its plateau level. Both of these features are evident in the neural responses. The agreement is only approximate, presumably because neurons other than the ones we recorded contribute to the estimation of certainty (*1*, *22*). These neurons might represent evidence for other directions of motion, but they are unlikely to represent the T_s choice option directly, as shown next.

To gain a better understanding of the representation of choice certainty across the population of LIP neurons, we recorded from 19 cells using the task configuration shown in Fig. 5. T_s was in the RF, whereas the direction-choice targets were not. Although T_s was not displayed until late in the delay period and only on half of the trials, its position was fixed throughout the course of the experiment. Nevertheless, these neurons did not show a significant modulation of activity during the motion stimulus or in the ensuing delay period (*42*). Moreover, the weak activity that was present was uninformative about the choice to forego or choose the T_s option (Fig. 5B) ($P > 0.1$ for both directions of motion). Unlike the neurons with a direction choice target in the RF, the neurons that encode the location of T_s do not appear to represent choice certainty.

This observation argues against an alternative explanation of our finding based on allocation of attention to the T_s location. More generally, it provides additional evidence that the monkey made a decision about the motion direction in the period preceding the onset of T_s, even on trials when it opted out of the direction task. There is no indication that the monkey approached the task as a choice between three alternatives, T_{in}, T_{opp}, and T_s. However, after the appearance of T_s, these neurons with a sure target in their RF became predictive of the postdecision wager. Although it is not obvious from the traces, the visual response in the first 200 ms was slightly larger when the monkey would choose T_s ($P < 0.01$, ANOVA), suggesting that T_s was more salient when there

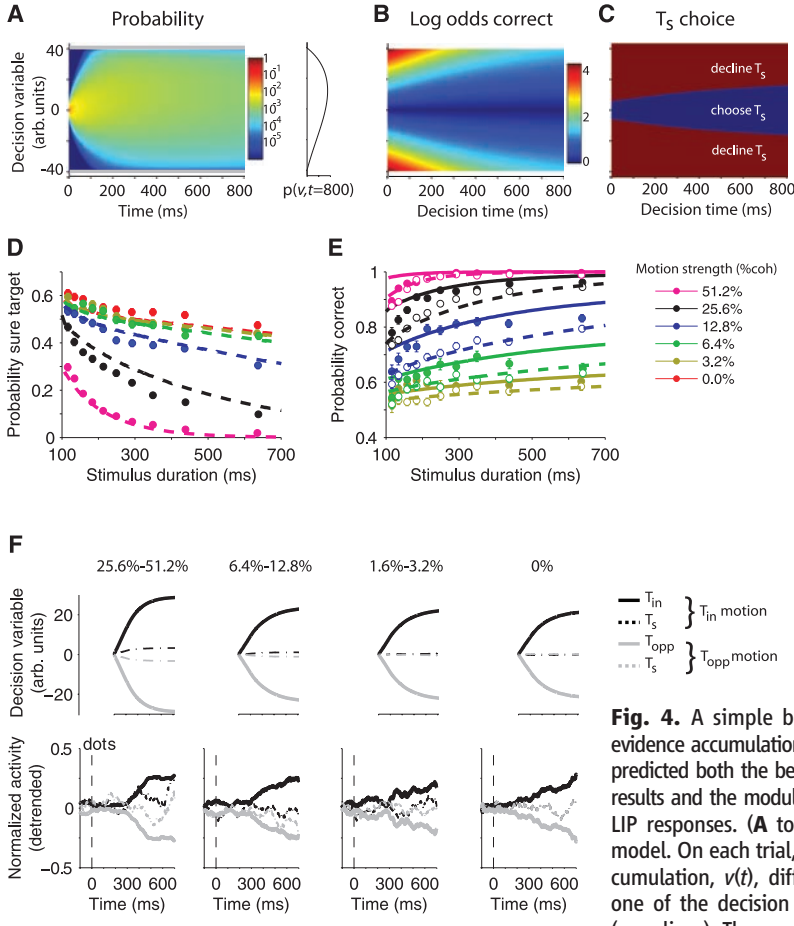

Fig. 4. A simple bounded evidence accumulation model predicted both the behavioral results and the modulation of LIP responses. (**A** to **C**) The model. On each trial, the accumulation, $v(t)$, diffuses to one of the decision bounds (gray lines). The process terminates when $v(t)$ reaches a bound or the stream of motion evidence ceases. (**A**) Representation of $v(t)$ as a propagating probability density, for all motion strengths, when the rewarded direction is rightward. Positive values for $v(t)$ represent accumulated evidence in favor of rightward. At time zero, the distribution is a delta function at $v = 0$. As time elapses, the range of $v(t)$ expands to fill the space between the two bounds, and there is a drift toward positive values, as shown by the probability density of v at $t = 800$ ms (inset to the right of color map). The distribution associated with leftward motion (not shown) is the mirror symmetric graph reflected about $v = 0$. (**B**) The log odds of a correct response based on the value of $v(t)$ at decision time. Correct responses are associated with larger v, but the relationship between v and probability correct changes with decision time. (**C**) T_s is chosen when the probability of a correct response is less than a criterion level. (**D** and **E**) Model fits and predictions. The three model parameters (table S1) were fit to the observed frequency of correct responses on trials in which T_s was not shown and the observed frequency of T_s choices on trials in which T_s was shown. These parameters predict the probability of a correct response on trials in which T_s was waived [solid curves in (E)]. (**F**) Comparison of model predictions and neural data. The average trajectory of $v(t)$ in the model was calculated for different coherence levels using the fit parameters. The calculation is based on the stimulus durations used in the experiment and assumes that v is fixed from termination of the accumulation process. The calculated trajectories (top) resemble the LIP responses (bottom). Neural responses were detrended by subtracting the mean response at each moment. Predictions are shifted by the neural latency (200 ms).

was greater choice uncertainty (*43*). The effect was weak (median difference = 7.7%), but as time elapsed during the remainder of the delay period the firing rates gave a clear indication of whether the monkey would choose the T_s.

Discussion. A connection between signal reliability, choice accuracy, and confidence has been proposed previously (*1*, *13*, *14*, *44*, *45*), but until now this connection has not been observed directly in the same neurons. Neurons in a variety of brain structures represent the size, preference, and probability of obtaining a reward (*15*, *46*–*54*), but it is not known how these representations arise. The present results show that the same neurons that participate in decision formation (*20*, *55*) carry the relevant signals for assigning the probability of obtaining a reward. It therefore seems likely that the computation of choice certainty is passed from LIP to brain structures that anticipate reward, and it is likely that feedback from these structures affects LIP in the epoch after the appearance of T_s to mediate the decision to choose or forgo the T_s option.

The mechanism underlying the representation of certainty in LIP is linked to the same evidence accumulation that underlies choice and decision time (*17*, *20*). This accumulation is encoded in the firing rates of LIP neurons with RFs aligned to the choice targets representing the direction alternatives (*18*, *55*–*57*). This is the decision variable, $v(t)$, that governs the choice of direction, having either attained a critical level—a decision termination bound—or by comparison to a criterion if the evidence stream ceases. This mechanism can be viewed as a merging of decision models based on sequential analysis (*58*–*60*) and signal detection theory (*61*). The magnitude of this decision variable, combined with knowledge of elapsed time, maps directly to the probability of obtaining a reward. An associative-learning process based on LIP responses can therefore underlie the monkey's choice of T_s. The ability to explain the rich pattern of behavioral results and the qualitative agreement between model and physiology favors the simple conceptual model. It is probably also consistent with other models that exploit a broader population of LIP neurons to encode posterior probability (*22*, *41*).

This simple mechanism brings certainty, which is commonly conceived as a subjective aspect of decision-making, under the same rubric as choice and reaction time (*1*, *62*) and removes the need to resort to metacognitive explanations for certainty monitoring (*45*). Our findings support a low-level explanation of postdecision wagering in our task, but they do not preclude the possibility that an animal that experiences subjective awareness of degree of certainty might base such impressions on neural signals like the ones exposed here.

LIP neurons are hypothesized to encode the attentional salience or expected value of a visual saccade target (*52*, *53*, *63*), but these concepts cannot explain the pattern of LIP activity in our experiment. For example, a diversion of attention away from T_{in} to the potential location of T_s should have led to a reduction in firing rate for both T_{in} and T_{opp} directions during motion viewing and in the delay period before T_s appeared. Attention (or motor planning) might explain the activity just preceding saccades, but it does not explain the intermediate firing rates, particularly for T_{opp} directions, in the key epochs of interest.

A second alternative, expected reward, seems more plausible, at least to the extent that it mimics the belief that a choice will be correct. However, the expected value of T_{in}, in the objective sense (from economics), changes as a function of motion strength (psychometric function) (Fig. 1C), whereas the firing rate before T_s onset is minimally affected by motion strength when the monkey waives T_s (Fig. 4F and fig. S4). Even subjective expected value, which is synonymous with certainty, fails to capture fully the deeper insight our experiment reveals about mechanism: The evolution of decision-related activity that gives rise to a choice also underlies certainty and a wager based upon it.

A famous controversy in the history of probability theory concerned whether it is meaningful to embrace the truth of a hypothesis as a graded quantity expressed as a probability or whether, instead, hypotheses are simply true or false. The latter approach led frequentists to reject the Bayesian concept of degree of belief, relegating probability to the analysis of error rates in assertions of truth (*64*, *65*). Our finding suggests that when the brain embraces a truth, it does so in a graded way so that even a binary choice leaves in its wake a quantity that represents degree of belief. From this perspective, our neural recordings support the idea of a "Bayesian brain" (*66*) and a neural mechanism of decision-making that does not flip into a fixed point or attractor state but instead approximates the formation of a probability distribution (*41*, *67*). Accordingly, the intermediate levels of activity associated with less certain choices might be a sign of a more homogeneous level of activity across the population of neurons. Fundamentally, our results advance understanding of the neural mechanisms that underlie decision-making by coupling for the first time the mechanisms leading to decision formation and the establishment of a degree of confidence.

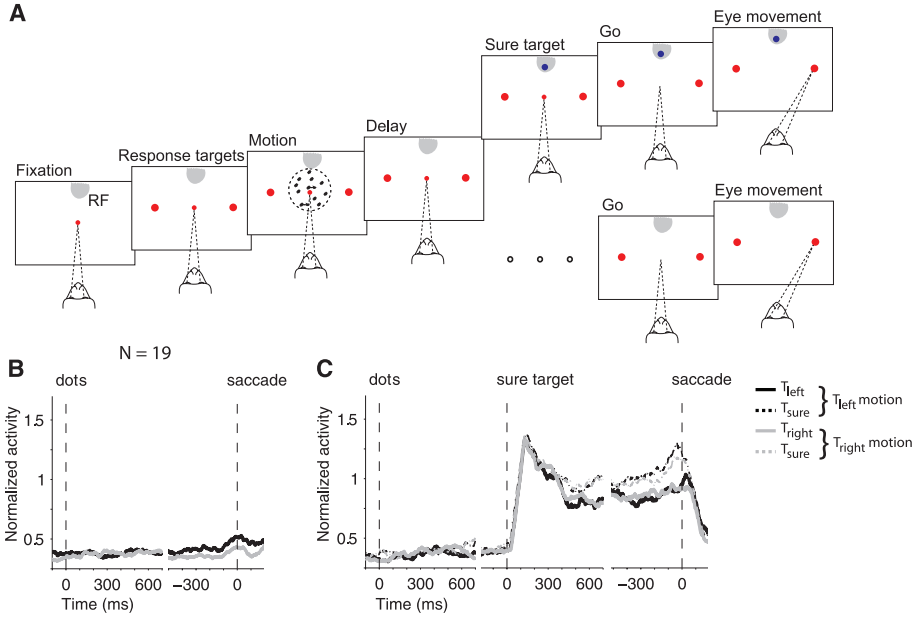

Fig. 5. Activity of LIP neurons when the location of T_s was in the RF. (**A**) Task design. For 19 neurons from two monkeys, we placed T_s in the RF. The high-stakes direction targets were outside the RF. Task sequence was otherwise unchanged. (**B**) Responses on trials in which T_s was not offered. (**C**) Responses on trials in which T_s was presented. Firing rates were normalized to the visual activity in the 300-ms epoch after onset of T_s.

References and Notes

1. D. Vickers, *Decision Processes in Visual Perception* (Academic Press, New York, 1979).
2. N. D. Daw, Y. Niv, P. Dayan, *Nat. Neurosci.* **8**, 1704 (2005).
3. P. Dayan, N. D. Daw, *Cogn. Affect. Behav. Neurosci.* **8**, 429 (2008).
4. F. B. Sumner, *Psychol. Rev.* **5**, 616 (1898).
5. W. McDougall, *Psychol. Rev.* **28**, 315 (1921).
6. V. C. A. Henmon, *Psychol. Rev.* **18**, 186 (1911).
7. C. S. Pierce, J. Jastrow, *Proc. Natl. Acad. Sci. U.S.A.* **3**, 75 (1884).
8. J. Volkmann, *Psychol. Bull.* **31**, 672 (1934).
9. D. M. Johnson, *Arch. Psychol.* **34**, 1 (1939).
10. W. M. Petrusic, J. V. Baranski, *Psychon. Bull. Rev.* **10**, 177 (2003).
11. D. Vickers, P. Smith, *Perception* **14**, 471 (1985).
12. R. J. Audley, *Br. Med. Bull.* **20**, 27 (1964).
13. S. W. Link, *The Wave Theory of Difference and Similarity*, Scientific Psychology Series (Erlbaum, Hillsdale, NJ, 1992).
14. A. Kepecs, N. Uchida, H. A. Zariwala, Z. F. Mainen, *Nature* **455**, 227 (2008).
15. C. Padoa-Schioppa, J. A. Assad, *Nature* **441**, 223 (2006).
16. B. Y. Hayden, A. C. Nair, A. N. McCoy, M. L. Platt, *Neuron* **60**, 19 (2008).
17. J. I. Gold, M. N. Shadlen, *Annu. Rev. Neurosci.* **30**, 535 (2007).

18. M. N. Shadlen, W. T. Newsome, *J. Neurophysiol.* **86**, 1916 (2001).
19. J. D. Roitman, M. N. Shadlen, *J. Neurosci.* **22**, 9475 (2002).
20. R. Kiani, T. D. Hanks, M. N. Shadlen, *J. Neurosci.* **28**, 3017 (2008).
21. A. K. Churchland, R. Kiani, M. N. Shadlen, *Nat. Neurosci.* **11**, 693 (2008).
22. J. M. Beck *et al.*, *Neuron* **60**, 1142 (2008).
23. J. I. Gold, M. N. Shadlen, *Trends Cogn. Sci.* **5**, 10 (2001).
24. T. Yang, M. N. Shadlen, *Nature* **447**, 1075 (2007).
25. Materials and methods are available as supporting material on *Science* Online.
26. N. Persaud, P. McLeod, A. Cowey, *Nat. Neurosci.* **10**, 257 (2007).
27. W. E. Shields, J. D. Smith, D. A. Washburn, *J. Exp. Psychol. Gen.* **126**, 147 (1997).
28. N. Kornell, L. K. Son, H. S. Terrace, *Psychol. Sci.* **18**, 64 (2007).
29. C. L. Colby, M. E. Goldberg, *Annu. Rev. Neurosci.* **22**, 319 (1999).
30. J. W. Gnadt, R. A. Andersen, *Exp. Brain Res.* **70**, 216 (1988).
31. M. L. Platt, P. W. Glimcher, *J. Neurophysiol.* **78**, 1574 (1997).
32. The activity of each neuron was normalized to the average response in the 300 ms preceding the motion, that is, the period after the appearance of the direction choice targets in the RF.
33. A. J. Parker, W. T. Newsome, *Annu. Rev. Neurosci.* **21**, 227 (1998).
34. E. Zohary, M. N. Shadlen, W. T. Newsome, *Nature* **370**, 140 (1994).
35. M. N. Shadlen, K. H. Britten, W. T. Newsome, J. A. Movshon, *J. Neurosci.* **16**, 1486 (1996).
36. The buildup rate on each trial was calculated by fitting a line to the neural activity in a ~300-ms window starting at the dip of activity after motion onset (*25*).
37. E. P. Cook, J. H. Maunsell, *Nat. Neurosci.* **5**, 985 (2002).
38. D. P. Hanes, J. D. Schall, *Science* **274**, 427 (1996).
39. J. Palmer, A. C. Huk, M. N. Shadlen, *J. Vis.* **5**, 376 (2005).
40. D. Vickers, J. Packer, *Acta Psychol. (Amst.)* **50**, 179 (1982).
41. W. J. Ma, J. M. Beck, P. E. Latham, A. Pouget, *Nat. Neurosci.* **9**, 1432 (2006).
42. The activity of each neuron was normalized by its (visual) response in the 300 ms after T_s onset.
43. J. W. Bisley, M. E. Goldberg, *Science* **299**, 81 (2003).
44. J. N. Kim, M. N. Shadlen, *Nat. Neurosci.* **2**, 176 (1999).
45. J. D. Smith, M. J. Beran, J. J. Couchman, M. V. Coutinho, *Psychon. Bull. Rev.* **15**, 679 (2008).
46. M. Watanabe, *Nature* **382**, 629 (1996).
47. A. Izquierdo, R. K. Suda, E. A. Murray, *J. Neurosci.* **24**, 7540 (2004).
48. R. Kawagoe, Y. Takikawa, O. Hikosaka, *Nat. Neurosci.* **1**, 411 (1998).
49. M. I. Leon, M. N. Shadlen, *Neuron* **24**, 415 (1999).
50. L. Tremblay, W. Schultz, *Nature* **398**, 704 (1999).
51. J. D. Wallis, E. K. Miller, *Eur. J. Neurosci.* **18**, 2069 (2003).
52. L. P. Sugrue, G. S. Corrado, W. T. Newsome, *Science* **304**, 1782 (2004).
53. M. L. Platt, P. W. Glimcher, *Nature* **400**, 233 (1999).
54. M. A. Belova, J. J. Paton, C. D. Salzman, *J. Neurosci.* **28**, 10023 (2008).
55. T. D. Hanks, J. Ditterich, M. N. Shadlen, *Nat. Neurosci.* **9**, 682 (2006).
56. A. C. Huk, M. N. Shadlen, *J. Neurosci.* **25**, 10420 (2005).
57. C. T. Law, J. I. Gold, *Nat. Neurosci.* **11**, 505 (2008).
58. A. Wald, *Sequential Analysis* (Wiley, New York, 1947).
59. D. R. J. Laming, *Information Theory of Choice Reaction Time* (Wiley, New York, 1968).
60. R. D. Luce, *Response Times: Their Role in Inferring Elementary Mental Organization* (Oxford University Press, Belfast, 1986).
61. D. M. Green, J. A. Swets, *Signal Detection Theory and Psychophysics* (Wiley, New York, 1966).
62. P. L. Smith, *J. Math. Psychol.* **32**, 135 (1988).
63. J. Gottlieb, *Neuron* **53**, 9 (2007).
64. E. T. Jaynes, *Probability Theory: The Logic of Science*, G. L. Bretthorst, Ed. (Cambridge University Press, Cambridge, 2003).
65. D. Howie, *Interpreting Probability: Controversies and Developments in the Early Twentieth Century* (Cambridge University Press, Cambridge, 2007).
66. D. C. Knill, A. Pouget, *Trends Neurosci.* **27**, 712 (2004).
67. R. S. Zemel, P. Dayan, A. Pouget, *Neural Comput.* **10**, 403 (1998).
68. This work was supported by the Howard Hughes Medical Institute, National Eye Institute grant EY11378, and National Center for Research Resources grant RR00166. We thank T. Hanks, A. Pouget, A. Churchland, D. Lee, P. Phillips, J. Palmer, and C. D. Salzman for helpful discussions and comments and A. Boulet and K. Ahl for technical assistance.

Supporting Online Material

www.sciencemag.org/cgi/content/full/324/5928/759/DC1
Materials and Methods
Figs. S1 to S4
Table S1
References

5 December 2008; accepted 11 March 2009
10.1126/science.1169405

REPORTS

Characterization of Multipartite Entanglement for One Photon Shared Among Four Optical Modes

Scott B. Papp,[1]* Kyung Soo Choi,[1]* Hui Deng,[2] Pavel Lougovski,[3] S. J. van Enk,[3] H. J. Kimble[1]†

Access to genuine multipartite entanglement of quantum states enables advances in quantum information science and also contributes to the understanding of strongly correlated quantum systems. We report the detection and characterization of heralded entanglement in a multipartite quantum state composed of four spatially distinct optical modes that share one photon, a so-called *W* state. By randomizing the relative phase between bipartite components of the *W* state, we observed the transitions from four- to three- to two-mode entanglement with increasing phase noise. These observations are possible for our system because our entanglement verification protocol makes use of quantum uncertainty relations to detect the entangled states that span the Hilbert space of interest.

Investigations of entanglement for two quantum systems have answered many fundamental questions in quantum physics (*1*, *2*) and revealed powerful new capabilities of quantum mechanics within the field of quantum information science (*3*–*5*). Many of these advances have used well-tested methods for the characterization of quantum entanglement in bipartite (two-component) systems (*6*, *7*). Entangled states of more than two systems enhance our knowledge of quantum theory, because new classes of states are available (*7*–*9*). Beyond applications to conventional quantum computation (*3*), exotic multipartite states have emerged as crucial resources for new directions in quantum information processing such as measurement-based quantum computation (*10*, *11*), quantum secret sharing (*12*), and quantum simulation (*13*). Despite the extraordinary promise that they offer, unambiguously detecting multipartite entangled states is still a major challenge from both an experimental and a theoretical standpoint.

Genuine N-partite entanglement is realized only with the simultaneous participation of all N of the constituent systems. The exponential increase with N in the amount of information required to describe the overall quantum system, although exceedingly beneficial for large-scale quantum information protocols (*3*), makes the task of classifying (*8*, *9*) and detecting such entangled states extremely difficult (*7*). Still, there are prescribed methods to detect entanglement in select classes of multipartite states that generally rely on reconstructing the density matrix $\hat{\rho}$. Linear entanglement witnesses supplemented by tomography of $\hat{\rho}$ have been used to detect entanglement in six (*14*) and eight (*15*) atomic ions, as well as for hyperentangled photons (*16*). A serious drawback of quantum-state tomography is the prohibitive number of measurements and their accuracies that are required with increasing N.

Our work focuses on a specific class of quantum states in which exactly one photon is coherently shared among N distinct optical modes in the form of

$$|W\rangle = \frac{1}{2}[(|1000\rangle + e^{i\phi_1}|0100\rangle) + e^{i\phi}(|0010\rangle + e^{i\phi_2}|0001\rangle)] \quad (1)$$

shown here for $N = 4$ and with the relative phases ϕ, ϕ_1, ϕ_2 of the modes. This is a so-called W state,

[1]Norman Bridge Laboratory of Physics 12-33, California Institute of Technology, Pasadena, CA 91125, USA. [2]Department of Physics, University of Michigan, Ann Arbor, MI 48109, USA. [3]Department of Physics, University of Oregon, Eugene, OR 97403, USA.

*These authors contributed equally to this work.
†To whom correspondence should be addressed. E-mail: hjkimble@caltech.edu

which plays an important role in quantum information protocols with photonic and matter qubits, because its entanglement is known to be robust against losses (for example, tracing over a set of modes $K \leq N-2$).

To detect entanglement for pure states in the form of Eq. 1 and their mixed-state counterparts $\hat{\rho}_W$, we introduce the use of fundamental quantum uncertainty relations. It has long been known for continuous variable systems that the uncertainty principle for noncommuting observables defines a boundary of measurement precision that can be crossed only by entangled states (*17*, *18*). This observation has formed the basis of numerous Einstein-Podolsky-Rosen–type experiments (*19*). For discrete variable systems as in Eq. 1, the uncertainty principle can be recast as a sum of uncertainties in certain physical observables that must always be greater than some minimum bound Δ_b for all unentangled states, whether pure or mixed (*20*).

As a first test of this concept, we created a bipartite entangled state analogous to $|W\rangle$. We verified the entanglement both by violation of an uncertainty relation (*21*) and by the well-established method of concurrence (*22*, *23*). The precise agreement of these two measurements over a wide range of parameter space attests to the reliability of uncertainty-based verification for the entanglement of discrete variables (Figs. 1B and 2). We then extended our setup to create multipartite entangled states that coherently share a single photon among four optical modes and applied our verification protocol to them. Varying the phase coherence and the photon statistics of a candidate state $\hat{\rho}_W$ allowed us to explore the boundary between separable and entangled states, including those that separate fourfold, threefold, and twofold entanglement.

Our verification protocol is based on an exclusion principle for which N-mode entanglement can be unambiguously detected by simultaneously measuring physical observables $\{\hat{M}_i\}$ (projectors) with $i \in \{1,\ldots,N\}$ more precisely than is possible with only $(N-1)$–mode entangled states and their mixtures (*20*, *21*). Specifically, we consider a sum uncertainty relation $\Delta = \sum_{i=1}^{N} \langle \hat{M}_i^2 \rangle - \langle \hat{M}_i \rangle^2 = 1 - \sum_{i=1}^{N} \langle \hat{M}_i \rangle^2$ and its lower boundary $\Delta_b^{(K)}$, which represents the smallest sum uncertainty obtained by any state with at most $K < N$–mode entanglement. For all K-mode entangled states, the inequality $\Delta \geq \Delta_b^{(K)}$ holds; therefore, a violation of this inequality serves as a sufficient condition for genuine N-mode entanglement. The projective operators are $\{\hat{M}_i\} = \{|W_i\rangle\langle W_i|\}$ with

$$
\begin{aligned}
|W_1\rangle &= \frac{1}{2}(|1000\rangle + e^{i\beta_1}|0100\rangle + \\
&\quad e^{i\beta_2}|0010\rangle + e^{i\beta_3}|0001\rangle) \\
|W_2\rangle &= \frac{1}{2}(|1000\rangle - e^{i\beta_1}|0100\rangle - \\
&\quad e^{i\beta_2}|0010\rangle + e^{i\beta_3}|0001\rangle) \\
|W_3\rangle &= \frac{1}{2}(|1000\rangle - e^{i\beta_1}|0100\rangle + \\
&\quad e^{i\beta_2}|0010\rangle - e^{i\beta_3}|0001\rangle) \\
|W_4\rangle &= \frac{1}{2}(|1000\rangle + e^{i\beta_1}|0100\rangle - \\
&\quad e^{i\beta_2}|0010\rangle - e^{i\beta_3}|0001\rangle) \qquad (2)
\end{aligned}
$$

for the case of $N = 4$, and with phases $\{\beta_j\}$ where $j \in \{1,2,3\}$. They are optimally sensitive to entanglement, for particular settings of β_j, because the entangled state $|W\rangle$ in Eq. 1 is the only simultaneous eigenstate of all projective operators $\hat{M}_i$ (*21*).

In our work, the purported N-mode entangled state $\hat{\rho}_W$ analogous to $|W\rangle$ is generated via the operation $\hat{\rho}_{in} \xrightarrow{\hat{U}_{gen}} \hat{\rho}_W$ (Fig. 1A) on an input state $\hat{\rho}_{in}$. Similarly, entanglement is verified with

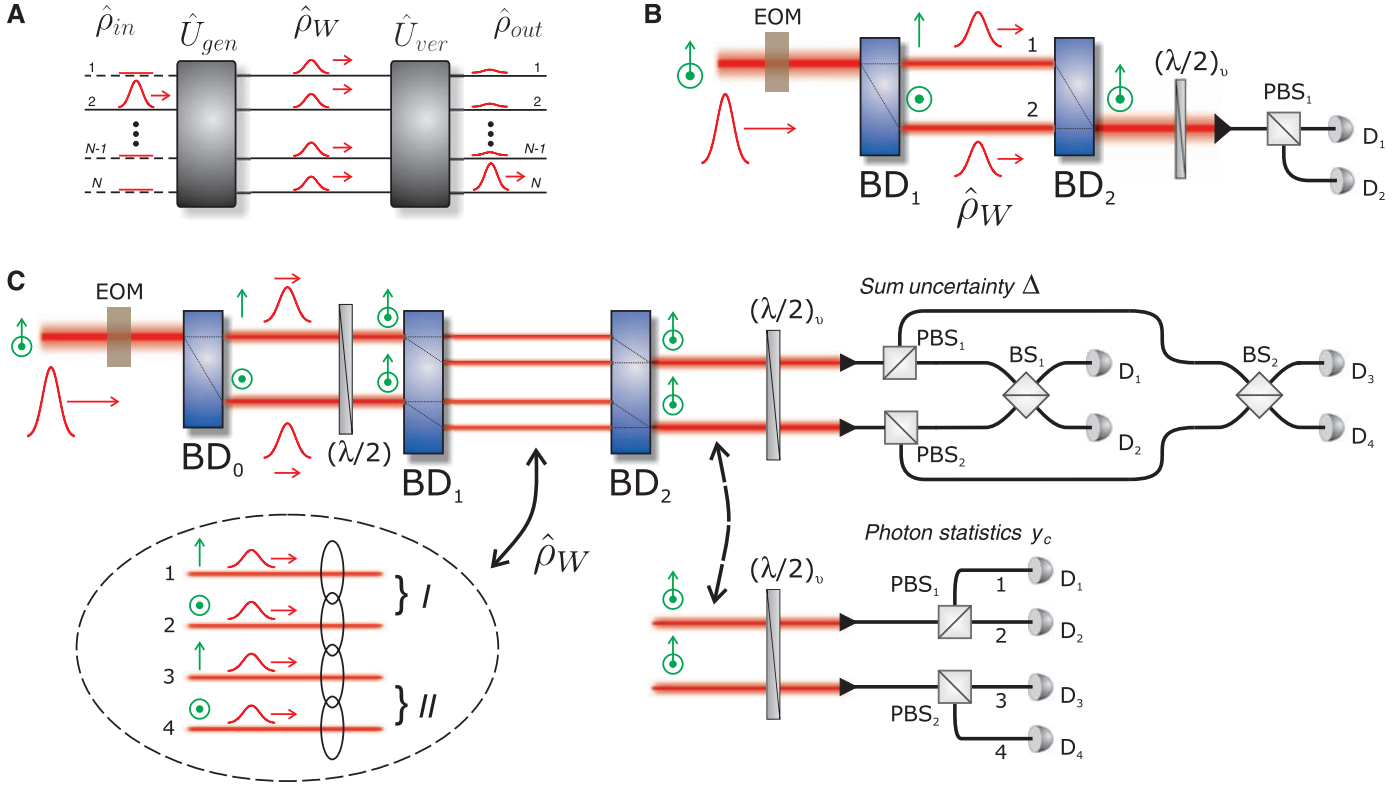

Fig. 1. Diagram of our entanglement generation and verification setups. (**A**) A single-photon pulse is transformed from a single input into an N-mode entangled state by $\hat{U}_{gen}$, and entanglement is verified with the operation $\hat{U}_{ver}$. (**B**) Details of the setup for bipartite entanglement. Single photons are coherently split to occupy the two modes defined by the interferometer BD_1-BD_2 with the relative phase ϕ of $\hat{\rho}_W$ controlled by the EOM. By setting the waveplate $(\lambda/2)_v$ at 0°, the occupation of the individual modes is detected at D_1 and D_2, and we obtain the two-photon components of $\hat{\rho}_W$. With a setting of $(\lambda/2)_v$ at 22.5°, single-photon interference occurs at PBS_1, from which we obtain Δ; see also Fig. 2. (**C**) Details of the setup to create and verify quadripartite entanglement. The sequences of beamsplitters BD_0 and BD_1 generate the optical modes 1 to 4, which share a single photon. To measure Δ, we jointly optimized the relative phases in the verification interferometers for interferences at $PBS_{1,2}$ [$(\lambda/2)_v$ at 22.5°] and $BS_{1,2}$ to minimize the photon probability of all but one output mode. Here, switching between measurements of Δ and y_c requires the indicated reconfiguration of fiber-optic components.

$\hat{\rho}_W \xrightarrow{\hat{U}_{\mathrm{var}}} \hat{\rho}_{\mathrm{out}}$. We implemented $\hat{M}_i$ for the case of two (Fig. 1B) and four (Fig. 1C) optical modes using beamsplitters (*24*) and photodetectors. The limit $\Delta \to 0$ indicates a significant overlap of the state $\hat{\rho}_W$ with only one of the projectors $\hat{M}_i$. In particular, for any choices of ϕ, ϕ_1, ϕ_2 that define Eq. 1 and the three corresponding orthonormal states, our measurements of $\hat{M}_i$ would yield $\Delta = 0$ for optimal settings of the phases β_j. A small Δ corresponds to a large statistical imbalance in the event distribution of the output optical modes, with one mode strongly preferred over the others. Conversely, if the generated state contains a photon that occupies one mode (e.g., $|1000\rangle$), our measurements would yield $\Delta = 0.75$. Because of the presence of transmission losses and beamsplitter imbalances in our setups, the projectors $|W_i\rangle\langle W_i|$ evolve into mixed states with significant vacuum components, but genuine multipartite entanglement can still be robustly detected for $\hat{\rho}_W$ (*21*, *25*).

To theoretically determine the boundaries $\Delta_b^{(K)}$ for N-mode entanglement, we calculated Δ for all possible admixtures of states containing at most $K = N - 1$–mode entanglement. The presence of more than one excitation in $\hat{\rho}_W$ may allow significant overlap of its one-photon subspace with $|W\rangle$, leading to a spurious detection of entanglement. Therefore it is necessary to determine the contamination of the state $\hat{\rho}_W$ caused by multiple excitations. By invoking local filtering operations, we are justified in confining our analysis to the reduced-density matrix $\hat{\rho}_W^{(r)} = p_0\hat{\rho}_0 + p_1\hat{\rho}_1 + p_{\geq 2}\hat{\rho}_{\geq 2}$, which contains no more than one photon per mode, while still being guaranteed a lower bound of entanglement (*6*, *23*). In our experiments, we measured the photon probabilities p_0, p_1, and $p_{\geq 2}$ that characterize the occupation of the vacuum subspace $\hat{\rho}_0$, the single-photon subspace $\hat{\rho}_1$, and the subspace containing multiple excitations $\hat{\rho}_{\geq 2}$. The degree of contamination due to more than one excitation is quantified by the parameter $y_c = 2\left(\frac{N}{N-1}\right)\frac{p_2 p_0}{p_1^2}$, which is normalized to the case of independent and balanced coherent states for which $y_c = 1$. The observation of measurement uncertainty Δ below the threshold $\Delta_b^{(K)}$ together with a determination of y_c, then, manifestly confirms the presence of genuine $(K + 1)$–mode entanglement.

Our experimental starting point was the generation of heralded single photons via Raman transitions in an optically dense atomic ensemble of Cs atoms (*25*, *26*). Two-mode entangled states were created by coherently splitting a single photon into parallel modes with beam displacer BD_1 (Fig. 1B); the modes' relative phase, analogous to ϕ in Eq. 1, was controlled by an electro-optic modulator (EOM). The spatially separated modes were recombined at BD_2 and coupled into a single-mode optical fiber, with each mode encoded in the polarization bases $|H\rangle$ and $|V\rangle$. Achieving entanglement requires a constant relative phase of the optical modes. In the absence of any fluctuating drive voltage on the EOM, the beam displacer pair BD_1-BD_2 forms a passively stable interferometer (*27*). By driving the EOM with a randomly oscillating voltage, the phase coherence of the modes is destroyed, and any entanglement between them is lost. This setup provides a calibrated tool to explore the boundary between separable and entangled states.

After the generation of bipartite states, we searched for the signatures of entanglement, using our verification protocol. To measure Δ, we rotated the polarizations of both modes by 45° and interfered them with a polarizing beamsplitter (PBS_1). We recorded the photoelectric detection events at single-photon counters D_1 and D_2, and converted them to the normalized joint photon probabilities P_{ij} (i.e., i photons for mode 1 and j for mode 2). Varying the relative phase of the modes after they exit BD_2 produces the interference fringes shown in Fig. 2A′ (corresponding to P_{10} and P_{01}), which allow us to identify the minimum value of Δ supported by the modes for a given y_c. In particular, the sum uncertainty Δ is related to the fringe visibility V by $\Delta = \frac{1}{2}(1 - V^2)$. When the relative phase β between modes 1,2 is either 0° or 180°, we obtain a value of Δ as small as 0.006, which corresponds to a visibility of 99.4% (*25*). To measure the two-photon suppression of $\hat{\rho}_W$, we detected the individual modes and recorded the time series of all relevant coincidence events (i.e., P_{ij} with $\{i,j\} \in \{0, 1\}$). Based on a calibration of the transmission from the face of BD_2 to the detectors, we inferred the photon probabilities that determine y_c (*25*). We controlled y_c via the pump intensity for Raman transitions in the source ensemble (*25*).

We have explored bipartite entanglement verification in our system by varying both the phase coherence and the two-photon suppression of $\hat{\rho}_W$. Figure 2A shows the dependence of Δ on the amplitude $\delta\phi$ of phase noise produced by the EOM. These results were obtained with two-photon contamination $y_c = 0.063 \pm 0.011$, so that entanglement is detected when $\Delta \lesssim 0.46$. With $\delta\phi = 360°$, we expect the fringe visibility to be minimized, and therefore $\Delta = 0.5$. As $\delta\phi$ decreases below 270°, the statistics of our measurements become sufficiently imbalanced that the presence of entanglement is manifest. Without any phase noise in the state generated at BD_1 (i.e., $\delta\phi = 0$), we obtain $\Delta \leq 0.03$ over a wide range of y_c as shown in Fig. 2B. The first-order coherence of our single-photon source and the phase stability of our apparatus guarantee $\Delta \approx 0$. The boundary in Δ between fully separable states and those that contain entanglement, $\Delta_b^{(1)}$, depends primarily on y_c through the rela-

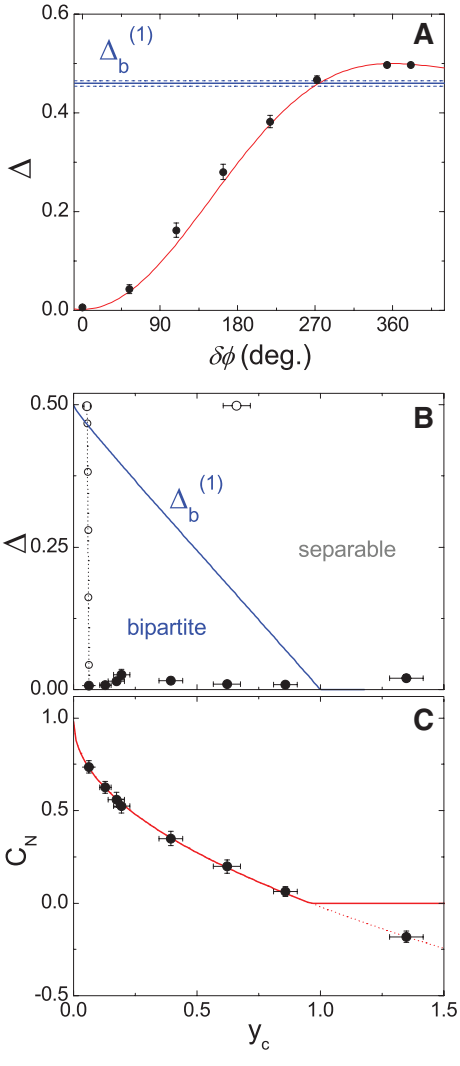

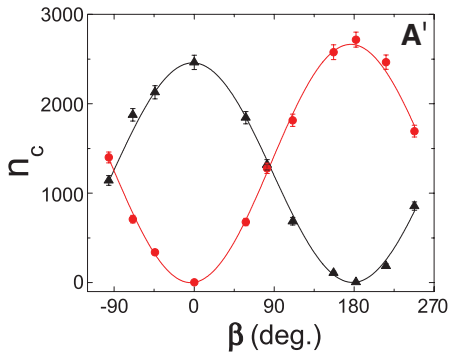

Fig. 2. Detection of entanglement between two optical modes using uncertainty relations. (**A**) The sum uncertainty Δ as a function of peak-to-peak phase noise $\delta\phi$ in the generated state $\hat{\rho}_W$. The solid blue line gives the boundary, $\Delta_b^{(1)}$, between entangled and separable states. The dotted blue lines indicate the range of $\Delta_b^{(1)}$ values that result from the uncertainty in our measurements of y_c. The red line is a fit to the data, based on a uniform distribution of phase noise. (**A′**) Number of photons detected n_c in the output modes for a measurement time of 250 s as the relative phase β of the verification interferometer is varied. At minima and maxima of n_c, we obtain $\Delta = 0.01$. (**B**) Measured sum uncertainty with $\delta\phi = 0$ (solid circles) and boundary $\Delta_b^{(1)}$ (blue line) as a function of two-photon suppression. Data with $y_c < 1.0$ demonstrate entanglement of the two modes. By variation of $\delta\phi$ from 0° to 360° (open circles), the modes' phase coherence is reduced, resulting in a loss of entanglement for $\delta\phi \gtrsim 270°$. (**C**) Concurrence C_N (filled circles) inferred from measurements of Δ and the boundary $\Delta_b^{(1)}$. The solid line shows a theoretical prediction of concurrence $[\max(C_N,0)]$ based on an independent measurement of V and $p_1 = 0.22 \pm 0.02$. All the error bars in this figure represent standard deviations.

tion $\Delta_b^{(1)} = \frac{1}{2}(1 - y_c)$. Given the uncertainty of our measurements, of which the largest contribution is counting fluctuations in y_c, all of the states created with $y_c \leq 0.86$ verifiably contain entanglement.

A rigorous correspondence exists between our uncertainty verification protocol (for two modes) and concurrence, a measure of bipartite entanglement (*22*, *25*). As a tool to understand the dependencies of the sum uncertainty and as a secondary confirmation of two-mode entanglement, we inferred the (normalized) concurrence $C_N = V - \sqrt{y_c}$ from our measurements of Δ. Using previously introduced relations, we can reformulate it as $C_N = \sqrt{1 - 2\Delta} - \sqrt{1 - 2\Delta_b^{(1)}}$. The inferred concurrence data shown in Fig. 2C demonstrate an increasing C_N, therefore a larger degree of entanglement, as we decrease y_c. This behavior is in excellent quantitative agreement with our theoretical expectation for concurrence based on quantum-state tomography (*23*, *25*); this validates the use of uncertainty relations for entanglement verification.

We now describe our investigation of multipartite entanglement with a single photon shared among four optical modes (Figs. 3 and 4). To generate four-mode entangled states, we used the setup shown in Fig. 1C. A third beam displacer (BD_0) was added to the two-mode setup immediately before BD_1; it coherently splits a single photon polarized at 45° into two modes. In this case, the space between BD_1 and BD_2 supports four independent modes of $\hat{\rho}_W$ (composed of pairs *I* and *II*) that share a single photon. The EOM influences only the relative phase of the two pairs *I*, *II*, labeled ϕ in Eq. 1, leaving intact their individual phase coherence; and it provides a means to induce dephasing between the *I*, *II* pairs. The four spatially separated modes in the state $\hat{\rho}_W$ are combined into two separated spatial modes (each carrying two modes encoded via the polarizations $|H\rangle$ and $|V\rangle$) that exit BD_2 and are coupled into single-mode fibers.

Measurements of Δ were performed by rotating the polarizations of all the modes by 45° and pairwise interfering them with the network of four cascaded beamsplitters shown in Fig. 1C. We recorded all photoelectric events from detectors $\{D_1,...,D_4\}$, but employed only events with a single photodetection for the determination of Δ (*25*). In this case, Δ depends jointly on the fringe visibilities of all four interferometric outputs. BD_1 and BD_2 still guarantee long-term interferometric stability for the two pairs of modes *I* and *II*, and the relative phases between other pairs are actively stabilized with respect to a laser that shares the same path. With the stabilization laser off, we applied calibrated feed-forward signals to the servo electronics, that transiently optimized the setup for measurements of various phase dependencies of Δ, including its global minimum (*25*). To extract y_c for the separated modes 1 to 4, we inserted the "photon statistics" setup at the location indicated in Fig. 1C, and we ensured that no interference occurred at PBS_1 and PBS_2 by setting the polarizations to the eigenaxes of the respective PBS. We obtained a record of the 16 photon probabilities P_{ijkl} that determine y_c, with indices $i, j, k, l \in \{0, 1\}$ (*25*).

Using sum uncertainty relations (*20*, *21*), we have unambiguously detected the presence of full four-mode entanglement in a photonic *W* state. Because $N > 2$, entanglement may be found not only among the full set of modes, but bipartite- and tripartite-entangled states exist within a subset of them. A crucial feature of our verification protocol is that it clearly defines boundaries that distinguish between states with $\{N, N-1,..., 2\}$–mode entanglement. As in the case with $N = 2$, the boundaries for $N = 4$ exist within the parameter space defined by Δ and y_c. To understand how the multipartite entanglement is affected by the phase coherence of $\hat{\rho}_W$, we introduced phase noise δϕ over the range from 0° to 360° between the two pairs of modes. Figure 3 shows Δ as a function of δϕ and the theoretical boundaries for two-, three-, and four-mode entanglement. For $\delta\phi \leq 225°$, our verification protocol confirmed the presence of genuine multipartite entanglement for three and four modes. Owing to the fact that dephasing was induced among only two pairs, the measured sum uncertainties do not exceed the threshold ($\Delta_b^{(1)} = 0.7$) defined by fully separable states. A primary feature of multipartite *W* states is their resilience against phase noise, evidenced by the

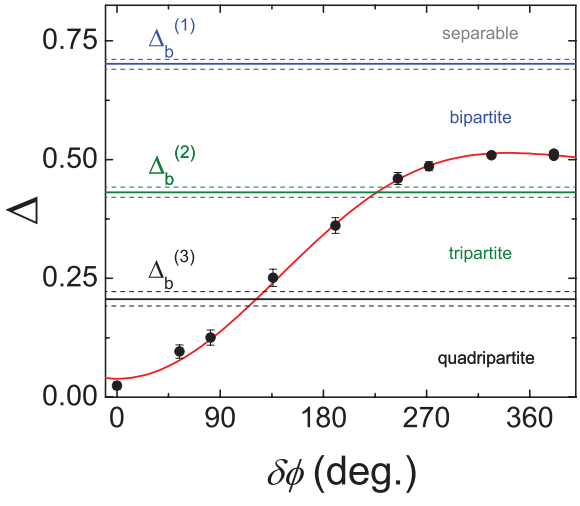

Fig. 3. Dependence of the sum uncertainty Δ on the amplitude of phase noise δϕ in the state $\hat{\rho}_W$. These data were acquired with an approximately constant y_c in the range from 0.06 to 0.08; under these conditions, $\Delta \lesssim 0.2$ demonstrates genuine four-mode entanglement. The horizontal lines indicate the boundaries $\Delta_b^{(K)}$ for entanglement. Here the uncertainty of each boundary $\Delta_b^{(K)}$ (dashed lines) corresponds to the observed fluctuations in y_c. The red line is a fit to the data, based on a model including a uniform distribution of phase noise.

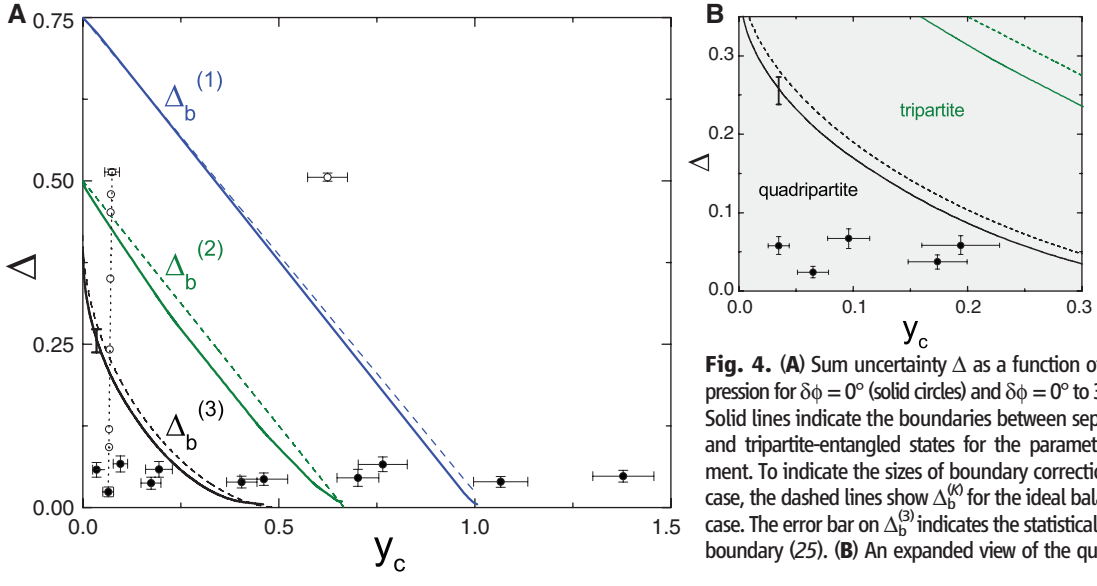

Fig. 4. (**A**) Sum uncertainty Δ as a function of two-photon suppression for $\delta\phi = 0°$ (solid circles) and $\delta\phi = 0°$ to 360° (open circles). Solid lines indicate the boundaries between separable, bipartite-, and tripartite-entangled states for the parameters of our experiment. To indicate the sizes of boundary corrections from the ideal case, the dashed lines show $\Delta_b^{(K)}$ for the ideal balanced and lossless case. The error bar on $\Delta_b^{(3)}$ indicates the statistical uncertainty in the boundary (*25*). (**B**) An expanded view of the quadripartite sector.

fact that the state that results from tracing over two modes in Eq. 1 still remains two-mode entangled (*28*). This property of $|W\rangle$ explains our observation of entanglement even in the face of complete dephasing between pairs *I* and *II* with 360° of phase noise.

We have also explored the transitions from fully separable to bipartite ($K = 1$), tripartite ($K = 2$), and quadripartite ($K = 3$) entangled W states by measuring the sum uncertainty as a function of two-photon suppression y_c, with our results presented in Fig. 4. With $\delta\phi = 0$, we obtained a uniformly low $\Delta \leq 0.08$ over a range in y_c from 0.035 to 1.37. These values of Δ are larger than in the two-mode case (Fig. 2B) and are explained by a small imbalance in $\hat{\rho}_W$ and by imperfections in the entanglement verification interferometers. Furthermore, these imperfections play an important role in the determination of the boundaries $\Delta_b^{(K)}$ for entanglement. As detailed in (*25*), small imbalances in the beamsplitter ratios of $PBS_{1,2}$ and $BS_{1,2}$ in Fig. 1C, and nonbalanced transmission losses lead to displacements of the boundaries toward smaller Δ, y_c. To reduce these boundary corrections, the beamsplitter ratios were all matched to 50%/50% to less than 3%, and the difference in losses of corresponding free-space and in-fiber optical paths were always held to less than 4%. Figure 4 shows the sizes of the corrections by displaying the boundaries $\Delta_b^{(K)}$ for the ideal lossless and balanced case as dashed lines.

In comparison to quantum-state tomography, our multipartite verification protocol features an exponential reduction in the number of measurements required to unambiguously detect entanglement. Specifically, our protocol requires us to determine 2^4 elements of $\hat{\rho}_W^{(r)}$ for y_c and 4 elements of $\hat{U}_{ver}^{\dagger}\hat{\rho}_W^{(r)}\hat{U}_{ver}$ for Δ, a total of 20 elements out of the $4^4 = 256$ that make up the reduced-density matrix $\hat{\rho}_W^{(r)}$. Our protocol inherently features the use of nonlocal measurements $\hat{M}_i$, thereby requiring only two experimental steps to measure all necessary elements and unambiguously detect entanglement in $\hat{\rho}_W$. Furthermore, the nonlinear structure of Δ allows the simultaneous detection of all possible realizations of Eq. 1 (*7*, *21*). These features alleviate the need for any complicated mechanism to control the measurement basis, which can be a challenge in tomography experiments (*16*) and other local measurement–based verification protocols for $\hat{\rho}_W$. Although linear witnesses might also enable entanglement detection with less than full knowledge of $\hat{\rho}_W$ obtained from a few experimental steps (*29*), the unambiguous verification of entanglement requires robustness in the face of experimental imperfections, including multiple excitations and losses (*25*).

Our study has introduced a new technique for the unambiguous verification of multipartite W states. Specifically, we examined entanglement in heralded quantum states specified by $\hat{\rho}_W$ with $N = 2,4$. Entanglement detected with our protocol refers to that of the complete density matrix $\hat{\rho}_W$ presented to our verification system, and not to fictitious components deduced via post selection (*6*). An extension of our protocol to different states (requiring increased experimental resources) is discussed in (*21*). Photonic entanglement, such as generated here, can be coherently mapped into atomic memories by way of electromagnetically induced transparency (*30*) for scalable quantum networks.

References and Notes

1. J. F. Clauser, A. Shimony, *Rep. Prog. Phys.* **41**, 1881 (1978).
2. A. Aspect, P. Grangier, G. Roger, *Phys. Rev. Lett.* **47**, 460 (1981).
3. M. A. Nielsen, I. L. Chuang, *Quantum Computation and Quantum Information* (Cambridge Univ. Press, Cambridge, 2000).
4. P. Zoller *et al.*, *Eur. Phys. J. D* **36**, 203 (2005).
5. H. J. Kimble, *Nature* **453**, 1023 (2008).
6. S. J. van Enk, N. Lütkenhaus, H. J. Kimble, *Phys. Rev. A* **75**, 052318 (2007).
7. O. Gühne, G. Toth, preprint available at http://arxiv.org/abs/0811.2803v2 (2008).
8. W. Dur, G. Vidal, J. I. Cirac, *Phys. Rev. A* **62**, 062314 (2000).
9. F. Verstraete, J. Dehaene, B. De Moor, H. Verschelde, *Phys. Rev. A* **65**, 052112 (2002).
10. R. Raussendorf, H. J. Briegel, *Phys. Rev. Lett.* **86**, 5188 (2001).
11. E. Knill, R. Laflamme, G. J. Milburn, *Nature* **409**, 46 (2001).
12. M. Hillery, V. Buźek, A. Berthiaume, *Phys. Rev. A* **59**, 1829 (1999).
13. S. Lloyd, *Science* **273**, 1073 (1996).
14. D. Leibfried *et al.*, *Nature* **438**, 639 (2005).
15. H. Haffner *et al.*, *Nature* **438**, 643 (2005).
16. W.-B. Gao *et al.*, preprint available at http://arxiv.org/abs/0809.4277v1 (2008).
17. L.-M. Duan, G. Giedke, J. I. Cirac, P. Zoller, *Phys. Rev. Lett.* **84**, 2722 (2000).
18. R. Simon, *Phys. Rev. Lett.* **84**, 2726 (2000).
19. S. L. Braunstein, P. van Loock, *Rev. Mod. Phys.* **77**, 513 (2005).
20. H. F. Hofmann, S. Takeuchi, *Phys. Rev. A* **68**, 032103 (2003).
21. P. Lougovski *et al.*, preprint available at http://arxiv.org/abs/0903.0851v1 (2009).
22. W. K. Wootters, *Phys. Rev. Lett.* **80**, 2245 (1998).
23. C. W. Chou *et al.*, *Nature* **438**, 828 (2005).
24. M. Reck, A. Zeilinger, H. J. Bernstein, P. Bertani, *Phys. Rev. Lett.* **73**, 58 (1994).
25. See the supporting material on *Science* Online.
26. L.-M. Duan, M. D. Lukin, J. I. Cirac, P. Zoller, *Nature* **414**, 413 (2001).
27. C.-W. Chou *et al.*, *Science* **316**, 1316 (2007).
28. C. F. Roos *et al.*, *Science* **304**, 1478 (2004).
29. H. Nha, *Phys. Rev. A* **77**, 062328 (2008).
30. K. S. Choi, H. Deng, J. Laurat, H. J. Kimble, *Nature* **452**, 67 (2008).

31. We gratefully acknowledge critical discussions with J. Laurat, P. Zoller, and J. Ye. This research is supported by IARPA, by NSF, and by NGST. S.P. and H.D. acknowledge support as Fellows of the Center for the Physics of Information at Caltech.

Supporting Online Material

www.sciencemag.org/cgi/content/full/324/5928/764/DC1
Methods
SOM Text
Figs. S1 to S5
Table S1
References

13 February 2009; accepted 18 March 2009
10.1126/science.1172260

N-Doping of Graphene Through Electrothermal Reactions with Ammonia

Xinran Wang,[1] Xiaolin Li,[1] Li Zhang,[1] Youngki Yoon,[2] Peter K. Weber,[3] Hailiang Wang,[1] Jing Guo,[2] Hongjie Dai[1]*

Graphene is readily p-doped by adsorbates, but for device applications, it would be useful to access the n-doped material. Individual graphene nanoribbons were covalently functionalized by nitrogen species through high-power electrical joule heating in ammonia gas, leading to n-type electronic doping consistent with theory. The formation of the carbon-nitrogen bond should occur mostly at the edges of graphene where chemical reactivity is high. X-ray photoelectron spectroscopy and nanometer-scale secondary ion mass spectroscopy confirm the carbon-nitrogen species in graphene thermally annealed in ammonia. We fabricated an n-type graphene field-effect transistor that operates at room temperature.

Recently, graphene has been made into semiconductors in the form of nanoribbons, leading to room temperature p-type graphene field-effect transistors (FETs) (*1*, *2*). However, a fundamental problem has been that the edge structures and chemical terminations of graphene synthesized by various methods are unknown and uncontrolled, whereas their effects to the physical properties have been widely predicted (*3*–*9*). In particular, graphene nanoribbons (GNRs) edge-terminated by nitrogen species were shown to be electron-rich, leading to n-type transistor behavior (*8*). Therefore, it is essential to precisely control the edge structures and chemical terminations to obtain desirable device characteristics. Edge doping could present a new means of doping for nanoscale graphene.

We now report that GNRs can be functionalized by nitrogen species by high-power electrical annealing (e-annealing) in NH_3 and exhibit n-type electronic doping. GNRs were synthesized chemically (*1*) or were lithographically patterned from pristine peel-off graphene (*10*–*12*); the

[1]Department of Chemistry and Laboratory for Advanced Materials, Stanford University, Stanford, CA 94305, USA. [2]Department of Electrical and Computer Engineering, University of Florida, Gainesville, FL 32611, USA. [3]Chemical Sciences Division, Lawrence Livermore National Laboratory (LLNL), Livermore, CA 94550, USA.

*To whom correspondence should be addressed. E-mail: hdai@stanford.edu

width ranged from below 10 nm up to ~150 nm. Chemically derived GNRs were dispersed on a 300-nm SiO_2/Si chip, located and imaged by scanning electron microscopy (SEM) with 1-kV acceleration voltage (*13*) and by atomic force microscopy (AFM) [Fig. 1, B and C, and fig. S1; see also supporting online material (SOM) (*14*)]. We then fabricated FET-like devices on selected ribbons with palladium (Pd) metal source/drain (S-D) and highly doped Si backgate (Fig. 1, A and D).

We first focused on GNRs wider than ~20 nm. Under ambient conditions, the edges of these as-made GNRs were probably terminated by hydrogen, oxygen, hydroxyl groups, and carboxylic groups (*15*) and exhibited p-doping with the Dirac point at gate voltage $V_{gs} > 40$ V in current-gate voltage I_{ds}-V_{gs} curves [fig. S3 (*14*)] (*1*, *2*). The p-doping was partly attributed to the oxygen edge groups (*6*, *7*), physisorbed oxygen molecules, and noncovalent poly(m-phenylenevinylene-co-2,5-dioctoxy-p-phenylenevinylene) (PmPV) coatings used in the synthesis process that are known to p-dope carbon nanotubes (*16*, *17*). Pumping in a vacuum reduced the conductance of GNRs slightly [fig. S3 (*14*)], corresponding to a decrease in p-doping by partial desorption of oxygen, either from the GNRs or GNR-metal contacts (*16*).

We then e-annealed the devices in high vacuum (~10^{-6} torr) by double sweeping the S-D bias V_{ds} (Fig. 2A). As V_{ds} was increased to high biases, the slope of I_{ds}-V_{ds} curve decreased or even became negative, with a noticeable hysteresis between back-and-forth sweeps that indicated the removal of the p-doping sources (*18*). We recorded I_{ds}-V_{gs} curves immediately after each e-annealing sweep and observed that the Dirac point gradually moved toward zero V_{gs} [fig. S2 (*14*)]. We continued to increase V_{ds} during I_{ds}-V_{ds} sweeps until no hysteresis occurred, which indicated that most of the *p*-doping was removed (Fig. 2A and fig. S2). After e-annealing, the I_{ds}-V_{gs} curve of GNR devices always showed the Dirac point at finite positive V_{gs} (typically 5 to 20 V) and slightly asymmetric hole and electron conduction (Fig. 2B). The residual p-doping was probably caused by oxygen species remaining on the edges (Fig. 3C) (*6*, *7*), as well as the doping

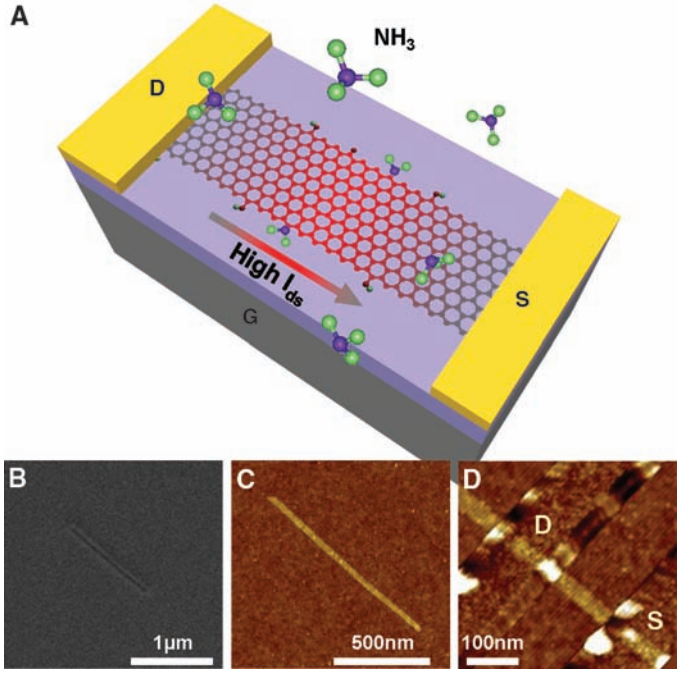

Fig. 1. Electrothermal reaction of individual GNRs in NH_3. (**A**) Schematics of a GNR device e-annealed under high current in NH_3. The devices have metal S-D, highly doped Si backgate and 300-nm SiO_2 gate dielectrics. The color gradient along the GNR represents the temperature profile: higher in the center region and lower near the contacts (*18*, *25*). Atomic colors are as follows: H, green; O, red; N, purple; C, gray. The GNR shown here is assumed to have ideal zigzag edges, which may not correspond to the GNRs in experiments. D, drain; S, source; G, gate. (**B**) SEM (acceleration voltage = 1 kV) and (**C**) AFM images of a ~30-nm-wide GNR. (**D**) AFM image of the device fabricated on the GNR shown in (B) and (C).

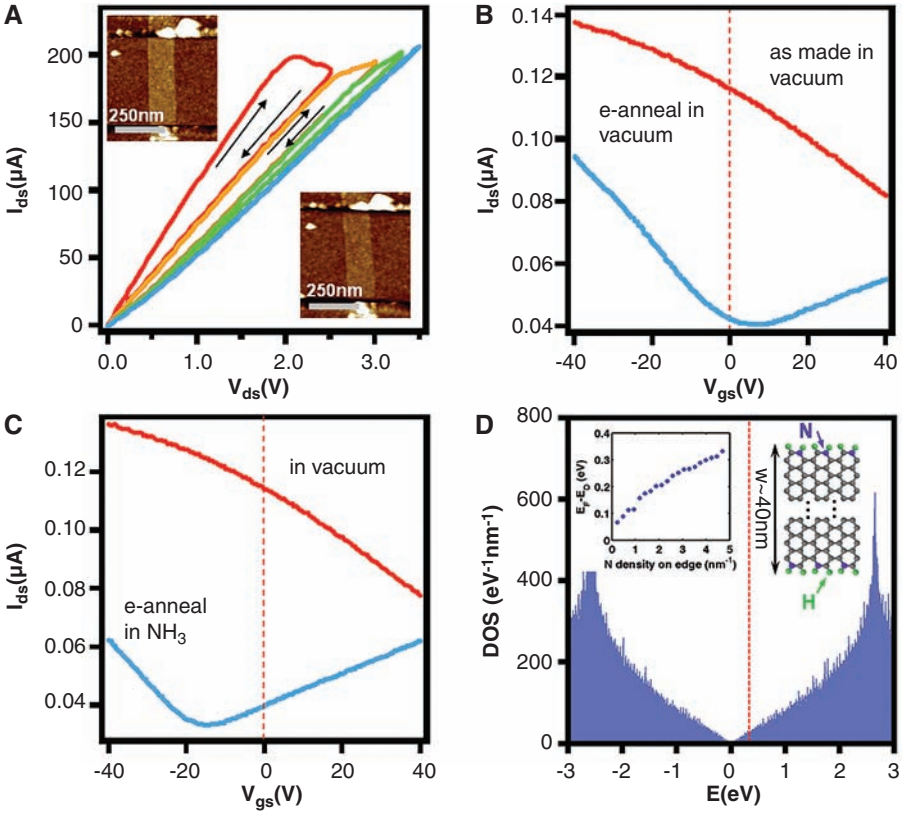

Fig. 2. E-annealing of individual GNRs in vacuum and NH_3. (**A**) Typical e-annealing process in vacuum for a w ~ 125-nm GNR. The process consisted of several double I_{ds}-V_{ds} sweeps (direction pointed by the arrows) with gradually increasing V_{ds}. We stopped when no hysteresis existed between back and forth sweeps (blue curve). (Upper and lower insets) AFM images of the same device as-made and after e-annealing in vacuum, respectively. The height was reduced from ~1.5 to ~1.0 nm because of removal of PmPV coatings by e-annealing. (**B**) I_{ds}-V_{gs} curves of the same GNR device as-made (red) and after e-annealing in vacuum (blue). The Dirac point moved from beyond 40 to ~8 V. (**C**) I_{ds}-V_{gs} curves of the same GNR device in vacuum before (red) and after e-annealing in NH_3 (blue). After e-annealing in NH_3, we pumped the device to base pressure for overnight before taking the blue curve. The Dirac point moved from beyond 40 to ~−14 V. $V_{ds} = 1$ mV in (B) and (C). (**D**) Calculated DOS of a w ~ 40-nm armchair GNR terminated partly by nitrogen species (*14*). The red dashed line denotes the Fermi level. (Left inset) The dependence of doping level (the position of the Fermi level from the Dirac point) on the density of substitutional N on the edges. (Right inset) Three unit cells of the simulated structure. There are two NH groups in the unit cell of the simulated structure. These edge groups are likely to coexist in real GNRs.

from the contact metal caused by the high work function of Pd (*19*).

During e-annealing, hundreds of microwatts of power were injected into a single GNR, which caused electrothermal self-heating of the GNR. We probed the temperature of GNRs under high-power input by measuring the red shift of the Raman G band of a single GNR (*14*, *20*). For a typical GNR under V_{ds} = 2 V (356-μW input power), a G-band shift of ~4.4 cm^{-1} was observed [fig. S5 (*14*)], corresponding to an average temperature of ~300°C along the GNR (*20*). Thus, electrical annealing of GNRs to hundreds of degrees led to the removal of physisorbed oxygen and PmPV molecules and reduced p-doping, consistent with the GNR height decrease by ~0.3 to 0.6 nm after e-annealing removal of the coating on GNRs (Fig. 2A, insets).

To chemically modify GNRs, we e-annealed the GNR devices in a ~1-torr NH_3/Ar environment with carefully designed sequences and control experiments [fig. S3 (*14*)]. In NH_3, we applied similar e-annealing sequences as in vacuum. After e-annealing, we pumped the chamber to base pressure for overnight (~8 hours) to fully remove physisorbed NH_3 molecules (*14*). Comparing the Dirac point positions of the devices in vacuum before and after e-annealing in NH_3, we observed a large ~−20-V shift (Fig. 2C and fig. S3B) that stayed stable and constant in vacuum. The shift caused by physisorbed NH_3 molecules (*21*) was usually smaller in magnitude [typically –5 V; fig. S3B (*14*)], and control experiments showed that physisorbed NH_3 molecules were unstable and removed in vacuum after overnight (~8 hours) pumping [fig. S3C (*14*)]. Considering the high temperature of GNRs during e-annealing in NH_3, we propose chemical reactions between GNRs and NH_3 leading to nitrogen functionalization, most likely at the more reactive edge carbon atoms (*15*). As a result, n-doping was introduced by the electron-rich nitrogen species (*8*). We cannot rule out the possibility of C–N bond formation at defect sites within the GNR plane; however, defect density in our chemically derived GNRs was low, based on their comparable electrical properties (including mobility, estimated to be a few hundred to ~1000 cm^2/Vs for GNRs wider than 20 nm) to similar-width lithographically patterned ribbons from pristine graphene (*2*). Furthermore, we carried out e-annealing of lithographically patterned GNRs from pristine peel-off graphene in NH_3 and qualitatively observed the same behavior as that of chemically derived GNRs [fig. S4 (*14*)]. These results suggest C–N formation most likely at the edge sites. Unlike the potassium doping approach (*22*), our doping approach introduced no appreciable charged impurities to degrade carrier mobility in GNR devices, as evidenced by similar p- and n-channel slopes in I_{ds}-V_{gs} curves before and after e-annealing in NH_3 (Fig. 2, B and C).

We theoretically investigated the effect of edge functionalization by calculating the band structure of GNRs terminated by oxygen- and nitrogen-containing species (*14*). Calculations showed that GNRs with edge functionalization by oxygen and nitrogen species were p- and n-doped, respectively (Figs. 2D and 3, C and D), which agrees with the Dirac point shifts observed in experiments. P-doping was originated from a sub-band introduced near the Fermi level by edge C=O double bonds (Fig. 3C). A nitrogen atom bonded to two C atoms at the edges (that is, a N atom substituting a C atom at the edges, Figs. 2D and 3D) was the most effective in n-doping (*8*), whereas NH_2 groups terminating a GNR with perfect zigzag or armchair edges did not introduce n-doping (*7*). In real GNRs, however, the edges could be imperfect. N and NH substitution and NH_2 termination could all be possible after e-annealing, which leads to an n-doping effect (Fig. 3D). The n-doping level was approximately proportional to the density of edge substitutional N atoms in GNRs (Fig. 2D, inset). Under the same density of edge substitutional N atoms, the calculated doping concentration per unit area was found to scale inversely with the GNR width, which results in the Fermi level closer to the Dirac point for wider ribbons. Although the calculated structures were not the same as GNRs in our experiments, our calculations did confirm the possibility of "bulk" p- and n-doping of

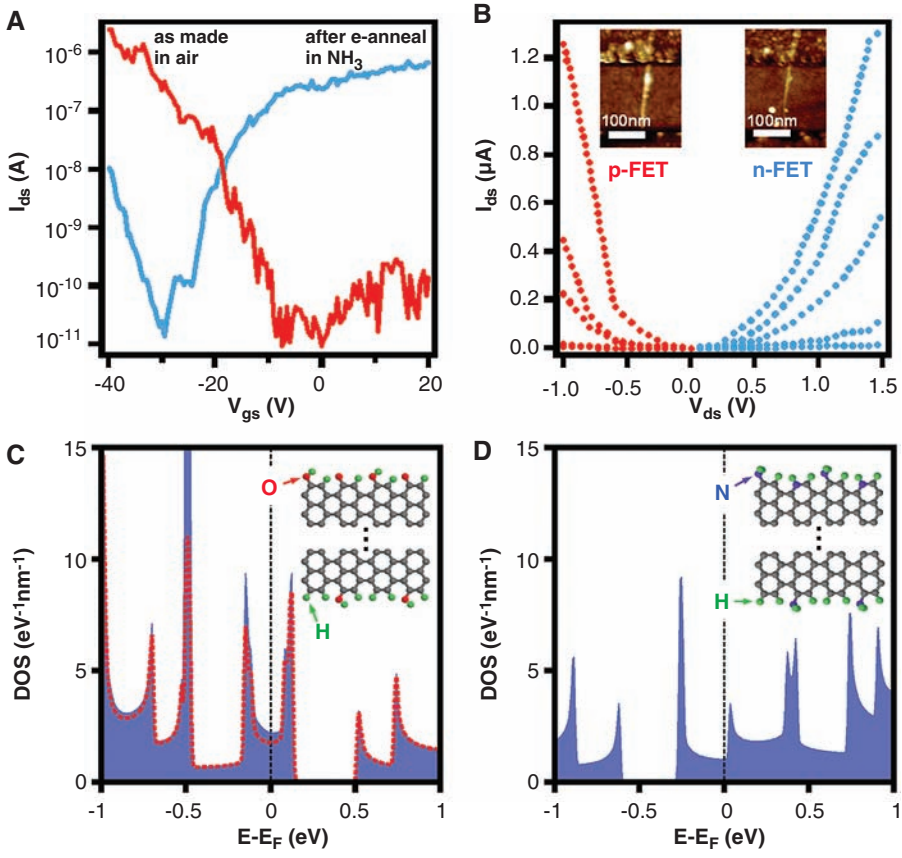

Fig. 3. Room temperature n-type graphene FETs. (**A**) I_{ds}-V_{gs} curves of the as-made GNRFET in vacuum (p-type, red) and after e-annealing in NH_3 (n-type, blue). V_{ds} = 1 V for both curves. (**B**) I_{ds}-V_{ds} curves of the same device. Red curves were taken on an as-made device: V_{gs} = −40 V, −37 V, −34 V, −31 V, and −28 V from top to bottom. Blue curves were taken on e-annealed device: V_{gs} = 40 V, 35 V, 30 V, 25 V, and 20 V from top to bottom. The nonlinear characteristics for both p- and n-type transistors near zero bias were due to finite SB for both electrons and holes by Ti contact used for this part of the work (*24*). Higher performance devices can be made by using higher (lower) work-function metals for p- (n-) type transistors and by heavily doping the contact regions, respectively. (Insets) AFM images of the device before and after e-annealing. Height was reduced by ~0.4 nm after e-annealing due to removal of PmPV coatings. (**C**) Calculated DOS of a semiconducting 21-armchair GNR (w ~ 2.5 nm) terminated by oxygen-containing groups (*14*). The red dashed line is the projected DOS (PDOS) on the carbon backbone, which clearly shows a p-type doping effect. (Inset) Two unit cells of the simulated GNR. There are one C=O and two C–OH groups in each unit cell. These edge groups are likely to coexist in real GNRs. E, energy; E_F, Fermi energy. (**D**) Calculated DOS of a 21-armchair GNR with nitrogen-containing groups on the edge sites, which is an n-type semiconductor (*14*). The DOS in the range of interest is mainly from the carbon atoms, and the PDOS on the carbon backbone has negligible difference with the total DOS within the energy range of interest. (Inset) Two unit cells of the edge structures of the simulated GNR. There are one NH and two C–NH_2 groups in each unit cell. These edge groups are likely to coexist in real GNRs.

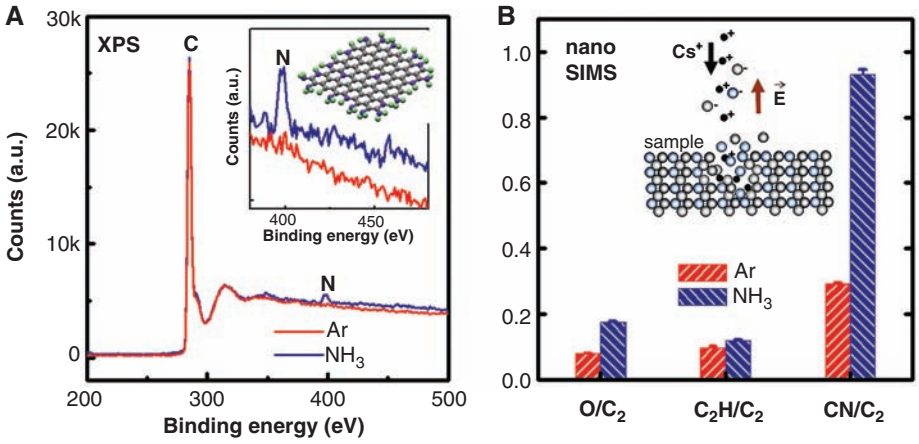

Fig. 4. Spectroscopy of GS films thermally annealed in NH_3 and Ar. (**A**) XPS on GS film thermally annealed in NH_3 (blue) and Ar (red, control sample). The peaks around 285 and 399 eV are assigned as C and N peaks, respectively. (Inset) Zoom-in view of the XPS data near the N peak. The sample annealed in NH_3 shows a clear N signal, whereas the control sample does not. (Sub-inset) Schematics of GSs thermally annealed in NH_3. a.u., arbitrary units. (**B**) Relative ionic O/C_2, CH_2/C_2, and CN/C_2 ratios detected by nanoSIMS (*14*). The sample annealed in NH_3 has a much higher CN/C_2 ratio than the control sample, indicating C–N bonds formed during thermal annealing in NH_3. The intensities and error bars are means and SEs from different regions of interest in the collection area. The finite N signal of control sample came from residual intercalant (tributyl ammonium hydroxide) used for making GSs (*23*). (Inset) Schematics of nanoSIMS experiment.

GNRs (up to width $w \sim 40$ nm) by edge chemical groups.

Direct spectroscopy of individual GNRs is difficult given the small quantity of the material and the limited spatial resolution of most spectroscopic tools, so we carried out x-ray photoelectron spectroscopy (XPS) and nanometer-scale secondary ion mass spectroscopy (nanoSIMS) studies on graphene sheet (GS) films (*23*) thermally annealed in NH_3 (*14*). Thermal reactions should give similar products as electrothermal reactions on graphene under similar reaction conditions. We thermally annealed a GS film under NH_3 to 1100°C and, as control, a similar film sample under Ar to 800°C. XPS data (Fig. 4A) revealed that both samples showed similar C signals, indicating a similar amount of carbon material measured. We observed a clear N signal on the sample annealed in NH_3, whereas we detected no N signal on the control sample (Fig. 4A, inset). From nanoSIMS (Fig. 4B), the sample annealed in NH_3 showed similar O/C_2 and C_2H/C_2 but greater CN/C_2 ratio than the control sample, suggesting C–N bond formation in GSs by thermal annealing. Both XPS and nanoSIMS data provided spectroscopic evidence of N atoms incorporated into graphene during thermal annealing in NH_3. Similar reactions were expected during electrothermal annealing of graphene. C–N bond formation should occur predominantly on the edges and defect sites in the plane, where the C atoms are much more chemically reactive than in the plane of perfect graphene (*15*). The observation of similar carrier mobilities after N-doping in our GNRs suggested no substantial bulk modification. However, the precise degree of bulk N substitution in graphene undergone reactions with NH_3 at various temperatures should be investigated systematically.

Tuning the electronic properties of graphene by chemistry of the edges and/or defects will have a large impact on graphene properties and applications. Previously, we demonstrated p-type sub–10-nm GNRFETs with as-made GNRs (*1*, *2*). In this experiment, we used the e-annealing approach in NH_3 to demonstrate n-type sub–10-nm GNRFETs operating at room temperature (Fig. 3). We used lower work-function metal Ti as the contact metal with a 5-nm Pd buffer layer to enhance electron conduction in the devices. As-made $W <$ ~5 nm GNRFETs were p-type with I_{on}/I_{off} ratio ~ 10^5 (Fig. 3A), because of the aforementioned p-doping sources. We first e-annealed the GNRFETs in vacuum, after which the devices became ambipolar [fig. S6 (*14*)]. We then exposed the devices in NH_3, followed by e-annealing in NH_3. After e-annealing in NH_3, the GNRFET turned largely to n-type, with $I_{on} \sim 1$ μA, I_{on}/I_{off} ratio ~ 10^5, and similar subthreshold slope as the as-made p-type GNRFETs. Physisorption of NH_3 alone had only weak effect on transistor characteristics with small difference between I_{ds}-V_{gs} curves in vacuum and NH_3 [fig. S6 (*14*)]. We never succeeded in making n-GNRFETs by simple NH_3 physisorption. The nonlinearity near zero bias in I_{ds}-V_{ds} curves for both n- and p-type transistors was due to finite Schottky barriers (SB) for both electrons and holes at Ti contacts (*24*). Ti contacts were used to observe a clear p- to n-FET evolution through the electrothermal reaction. For optimal device performances, one should use the highest and lowest possible work-function metal contacts for p- and n-type transistors respectively. Heavy doping at the contacts could also be invoked to improve performance. Ultra thin high-κ dielectrics could greatly improve the switching characteristics of p- and n-GNRFETs.

We calculated the density of states (DOS) of a semiconducting 21-armchair GNR (~2.5 nm wide) terminated by oxygen- and nitrogen-containing groups and observed p- and n-doping, respectively (Fig. 3, C and D), again confirming the edge chemical effects to the bulk properties of GNRs in the narrow-width regime. Taken together, the ability to control graphene chemistry is an important step toward controlled graphene electronics. Our results suggest that edge doping represents a new approach to dope graphene ribbons and affect its bulk properties, an interesting feature not likely in edge-free seamless carbon nanotubes. This technique, combined with precise control of edge shape (i.e., zigzag or armchair), may lead to precise determination of GNR device characteristics in the future. The current work also opens new possibilities of doing further chemistry on graphene.

References and Notes

1. X. Li, X. Wang, L. Zhang, S. Lee, H. Dai, *Science* **319**, 1229 (2008); published online 23 January 2008 (10.1126/science.1150878).
2. X. Wang *et al.*, *Phys. Rev. Lett.* **100**, 206803 (2008).
3. K. Nakada *et al.*, *Phys. Rev. B* **54**, 17954 (1996).
4. Y.-W. Son, M. L. Cohen, S. G. Louie, *Phys. Rev. Lett.* **97**, 216803 (2006).
5. D. Gunlycke, D. A. Areshkin, C. T. White, *Appl. Phys. Lett.* **90**, 142104 (2007).
6. D. Gunlycke *et al.*, *Appl. Phys. Lett.* **91**, 112108 (2007).
7. F. Cervantes-Sodi *et al.*, *Phys. Rev. B* **77**, 165427 (2008).
8. Q. Yan *et al.*, *Nano Lett.* **7**, 1469 (2007).
9. P. Zhao *et al.*, *Nano Res.* **1**, 395 (2008).
10. K. S. Novoselov *et al.*, *Science* **306**, 666 (2004).
11. Y. Zhang, T. Chen, H. L. Stormer, P. Kim, *Nature* **438**, 201 (2005).
12. K. S. Novoselov *et al.*, *Nature* **438**, 197 (2005).
13. T. Brintlinger *et al.*, *Appl. Phys. Lett.* **81**, 2454 (2002).
14. Experimental details and supporting data are available as supporting material on *Science* Online.
15. X. Wang, S. M. Tabakman, H. Dai, *J. Am. Chem. Soc.* **130**, 8152 (2008).
16. P. Avouris, *Acc. Chem. Res.* **35**, 1026 (2002).
17. H. S. Woo *et al.*, *Appl. Phys. Lett.* **77**, 1393 (2000).
18. J. Moser, A. Barreiro, A. Bachtold, *Appl. Phys. Lett.* **91**, 163513 (2007).
19. A. Javey *et al.*, *Naure* **424**, 654 (2003).
20. I. Calizo *et al.*, *Nano Lett.* **7**, 2645 (2007).
21. F. Schedin *et al.*, *Nat. Mater.* **6**, 652 (2007).
22. J.-H. Chen *et al.*, *Nature Physics* **4**, 377 (2008).
23. X. Li *et al.*, *Nat. Nanotechnol.* **3**, 538 (2008).
24. R. Martel *et al.*, *Phys. Rev. Lett.* **87**, 256805 (2001).
25. E. Pop *et al.*, *J. Appl. Phys.* **101**, 093710 (2007).

26. This work was supported in part by the Microelectronics Advanced Research Corporation Materials, Structures, and Devices Focus Center; Intel; and Office of Naval Research (ONR). The work done at the University of Florida was supported in part by NSF and ONR. The work at LLNL was performed under the auspices of the U.S. Department of Energy, contract DE-AC52-07NA27344.

Supporting Online Material

www.sciencemag.org/cgi/content/full/324/5928/768/DC1
Materials and Methods
SOM Text
Figs. S1 to S6
References

29 December 2008; accepted 13 March 2009
10.1126/science.1170335

An Experimental Design Method Leading to Chemical Turing Patterns

Judit Horváth,[1] István Szalai,[2] Patrick De Kepper[1]*

Chemical reaction-diffusion patterns often serve as prototypes for pattern formation in living systems, but only two isothermal single-phase reaction systems have produced sustained stationary reaction-diffusion patterns so far. We designed an experimental method to search for additional systems on the basis of three steps: (i) generate spatial bistability by operating autoactivated reactions in open spatial reactors; (ii) use an independent negative-feedback species to produce spatiotemporal oscillations; and (iii) induce a space-scale separation of the activatory and inhibitory processes with a low-mobility complexing agent. We successfully applied this method to a hydrogen-ion autoactivated reaction, the thiourea-iodate-sulfite (TuIS) reaction, and noticeably produced stationary hexagonal arrays of spots and parallel stripes of pH patterns attributed to a Turing bifurcation. This method could be extended to biochemical reactions.

Chemical reaction-diffusion systems have been intensively studied during the past decades (*1*), especially because of their potential relevance in the understanding of biological rhythms and patterns (*2*, *3*). However, stationary patterns have been observed in only two different single-phase chemical systems (*4*). The chemical mechanisms required for the development of stationary patterns are analogous to those for chemical oscillating reactions; that is, the systems must evolve far from thermodynamic equilibrium and involve competing positive and negative kinetic feedback processes. In the 1980s, hundreds of variants of oscillatory reactions were discovered by operating autoactivatory reactions in well-stirred open reactors, reactors that exchange matter and energy with their environment, and the use of a systematic design method (*5*). This method subdivided the problem in more tractable elements: the search for steady-state bistability and subsequently for a suitable negative-feedback species. Although sustained stationary patterns were discovered in other physicochemical systems (*6*), the observation of such patterns in solution chemistry remained limited to the chlorite–iodide–malonic acid (CIMA) and ferrocyanide-iodate-sulfite (FIS) reactions for lack of an effective design method. These pioneer observations were the result of targeted research but not of a comprehensive design (*7*, *8*). Full comprehension came sometimes much later (*9*, *10*).

Taking advantage of the wealth of available oscillatory reactions, we proposed a systematic approach to stationary reaction-diffusion patterns that has led us to the second example of sustained Turing patterns (*11*) in a single-phase reaction system. The method relies on well-established theoretical analyses (*3*, *9*, *12*, *13*) and on many former experimental observations (*10*, *14*–*18*). It is based on three features: (i) reactions that exhibit steady-state bistability and sustained temporal oscillations when operated in a continuously fed stirred tank reactor (CSTR) generally lead to so-called spatial bistability (*14*) and spatiotemporal oscillations or waves when operated in a one-side-fed unstirred spatial reactor (OSFR) (*19*); (ii) reactions where the major negative feedback process is achieved by a species not involved in the activatory pathway are more flexible to control, therefore optimal for our purpose; and (iii) the space scale and time scale over which a process extends can be controlled by an appropriate complexing agent (*9*, *12*, *13*).

The spatial bistability phenomenon has been observed for an increasing number of reactions (*8*, *10*, *14*–*18*). In most cases, the spatially bistable systems also display oscillatory spatiotemporal dynamics, even when the activatory and inhibitory processes rely on the same major reactants (*17*, *18*). Symmetry-breaking patterns, whether they are stationary or unstationary, require appropriate differences between the diffusion coefficients of some species. In case of a competition between one activatory and one inhibitory species, the activator must have a lower diffusion coefficient (*1*–*3*, *9*, *12*, *13*) and is referred to as short-range activation and, correl-

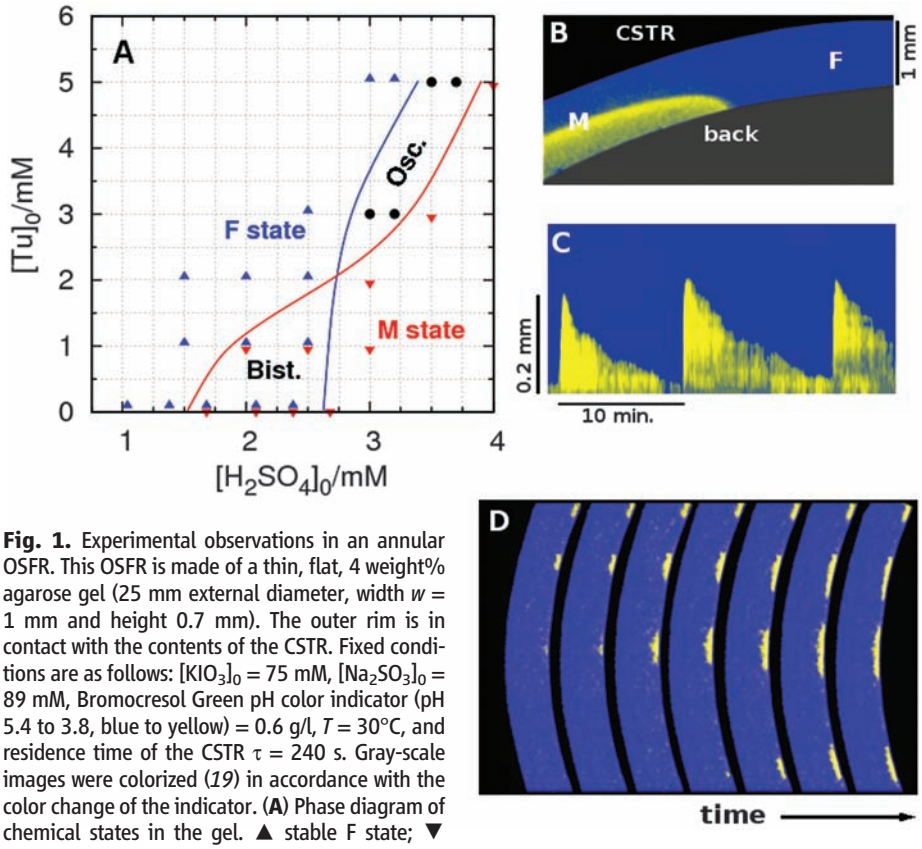

Fig. 1. Experimental observations in an annular OSFR. This OSFR is made of a thin, flat, 4 weight% agarose gel (25 mm external diameter, width w = 1 mm and height 0.7 mm). The outer rim is in contact with the contents of the CSTR. Fixed conditions are as follows: $[KIO_3]_0$ = 75 mM, $[Na_2SO_3]_0$ = 89 mM, Bromocresol Green pH color indicator (pH 5.4 to 3.8, blue to yellow) = 0.6 g/l, T = 30°C, and residence time of the CSTR τ = 240 s. Gray-scale images were colorized (*19*) in accordance with the color change of the indicator. (**A**) Phase diagram of chemical states in the gel. ▲ stable F state; ▼ stable M state; • oscillatory (Osc.) state. Blue and red curves indicate the limits of existence of the steady F and M states, respectively. Bist. indicates bistability domain. (**B**) A sector of the annular gel (colored part) with an interface between the M and F states in the spatial bistability domain. On the left, the sharp color switch (pH drop) from blue to yellow characterizes the M state. On the right, the quasi-uniformly blue part corresponds to the F state. Feed conditions are $[Tu]_0$ = 1.0 mM and $[H_2SO_4]_0$ = 2.0 mM. (**C**) Time-space plot illustrating the spatiotemporal oscillatory state at $[Tu]_0$ = 3.0 mM and $[H_2SO_4]_0$ = 3.0 mM. The pH color indicator switching position moves periodically back and forth with a period of about 10 min. (**D**) Sequence of snapshots showing the development of a stationary low-pH pulse pattern when NaPAA is added. Time interval between snapshots is 200 s. Feed conditions are $[Tu]_0$ = 4.0 mM, $[H_2SO_4]_0$ = 3.70 mM, and $[NaPAA]_0$ = 6 mM (carboxylic function units).

[1]Centre de Recherche Paul Pascal, CNRS, University of Bordeaux, 115, Avenue Schweitzer, F-33600 Pessac, France. [2]Institute of Chemistry, Eötvös Loránd University, Laboratory of Nonlinear Chemical Dynamics, Post Office Box 32, H-1518 Budapest 112, Hungary.

*To whom correspondence should be addressed. E-mail: dekepper@crpp-bordeaux.cnrs.fr

atively, as long-range inhibition. When there are more than two independent variables, as in real chemical systems, short-range activation is still required, but the slow-diffusing species is not necessarily the major activator. The low-mobility requirement can be transferred to a species acting on the rate of the activatory process. Still, most oscillatory chemical reactions involve small-molecular-weight species with similar or inappropriately differing (e.g., protons) diffusion coefficients. Short-range activation can be induced by adding a large-molecular-weight complexing agent that reversibly binds the activator, like starch or poly(vinyl alcohol) for triiodide or long-chain polycarboxylates for protons. Stationary patterns in the CIMA and FIS reactions, respectively, rely on the above agents (*9*, *10*, *20*).

Theoretical models that use pool chemical approximation (i.e., fixed uniform reactant concentration) (*1*, *3*) or arrays of coupled flow-through reactors (*21*) predict that chemical patterns can develop in simple bistable systems with appropriate short-range activation properties (*21*, *22*). However, our observations on quite different reactions operated in real open spatial reactors show that the slowing down of the activatory process and of the activator in a simple spatially bistable system is not enough to produce stationary patterns in an OSFR. These patterns were obtained only when a major negative feedback was provided by a substrate not involved in the activatory pathway, for example, malonic acid in the CIMA reaction family (*7*, *16*, *20*) and ferrocyanide ions in the FIS reaction (*8*, *10*). This second requirement in our method serves as a convenient way to considerably broaden the experimentally accessible parameter space and helps to uncover conditions where stationary patterns develop. Analogously, the addition of independent feedback species to an autoactivated reaction operated in a CSTR had induced oscillations or greatly broadened their range in systems where the reactants of the positive feedback process were also driving a negative feedback (*1*). In an OSFR, we anticipate a more profound reason for the use of systems with an independently controlled inhibitory process: Lower effective diffusion coefficient of the activator means a slower in- and outflux of this species at the feed boundary of the gel reactor while the influxes of the major feed reactants remain basically unchanged. This favors the accumulation of the activator even if its rate of production is slower. This conflicts with the targeted stabilization of a standing pulse of this species. The addition of a reactant, providing an independently tunable source or sink for the activator that acts in opposition, enables one to compensate for the increased activation and helps to stabilize localized concentration patterns of the activator (*23*). The present empirical requirement is supported by numerical results obtained with different realistic kinetic models (*24*, *25*).

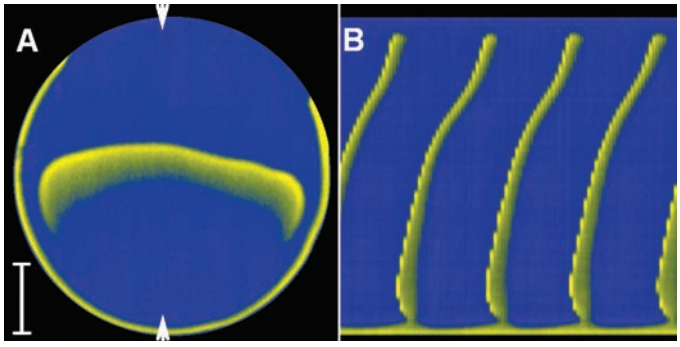

Fig. 2. pH wave propagation in the disc OSFR. The disc (4 weight % agarose gel) has a thickness of 0.75 mm. Temperature and feed conditions are the same as in Fig. 1, except for $[Tu]_0$ = 5.0 mM and $[H_2SO_4]_0$ = 3.39 mM. Colors are set to follow the pH color indicator changes opposite to the feed surface. Scale bar corresponds to 4.0 mm. (**A**) Snapshot of a traveling low-pH wave. The wave spontaneously starts at a pacemaker region close to the bottom of the image and steadily propagates in all directions. However, the wave stops and fades away at a finite distance (≈2 mm) from the rim of the mask. (**B**) Time-space plot of pH changes across a narrow vertical section of the disc, following the direction of the white arrows on the snapshot. The wave period is 8.0 min; the time span of the image is 28 min.

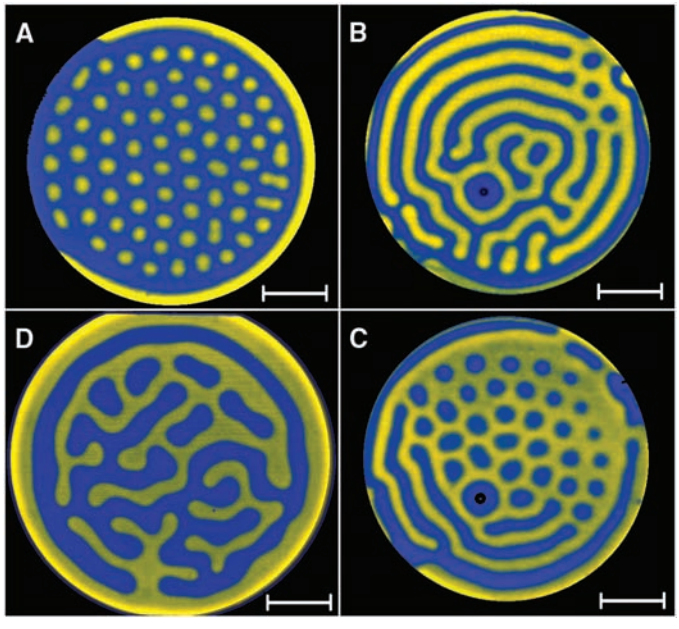

Fig. 3. Stationary patterns observed in the disc OSFR. Experimental conditions and color code of pictures are as for Fig. 2. Scale bars equal 4.0 mm. (**A**) Hexagonal array of low-pH spots at $[Tu]_0$ = 5.0 mM, $[H_2SO_4]_0$ = 3.57 mM, and $[NaPAA]_0$ = 6 mM (carboxylic function units). The wavelength is $\lambda = 1.9 \pm 0.1$ mm. (**B**) Stripe pattern at $[Tu]_0$ = 4.5 mM, $[H_2SO_4]_0$ = 3.60 mM, and $[NaPAA]_0$ = 6 mM. The wavelength is $\lambda = 1.6 \pm 0.07$ mm. (**C**) Coexistence of spots and stripes at $[Tu]_0$ = 4.5 mM, $[H_2SO_4]_0$ = 3.63 mM, and $[NaPAA]_0$ = 6 mM. The wavelength is $\lambda = 1.9 \pm 0.1$ mm. (**D**) Irregular branch pattern at $[Tu]_0$ = 3.0 mM, $[H_2SO_4]_0$ = 3.36 mM, and $[NaPAA]_0$ = 12 mM. The wavelength is $\lambda = 1.6 \pm 0.07$ mm.

Below, we detail our systematic approach to the discovery of stationary patterns in the TuIS reaction (*26*). When this reaction was operated in a CSTR, large-amplitude pH oscillations and bistability were observed between a high pH (7.0 to 6.0), low extent of reaction steady-state branch and a low pH (≈ 3.0), high extent of reaction steady-state branch (*19*). This oscillator has its basis in the proton autoactivated oxidation of sulfite ions by iodate (Eq. 1). The thiourea [Tu ≡ $SC(NH_2)_2$] introduces a negative feedback on this proton production through its oxidation to formamidine disulfide (Tu_2^{2+}) (Eq. 2).

$$IO_3^- + 3HSO_3^- \rightarrow 3SO_4^{2-} + I^- + 3H^+ \quad (1)$$

$$IO_3^- + 6H^+ + 6Tu \rightarrow I^- + 3Tu_2^{2+} + 3H_2O \quad (2)$$

We made use of two different geometries of gel OSFRs (*19*), either a flat annular or a thin disc-shaped inert piece of gel, respectively, in contact with the contents of a CSTR through the external rim or one circular face. The pieces of gels, which are inert porous media where any collective fluid motion is quenched, allow the undisturbed development of reaction-diffusion patterns in their core. All of the chemicals, that is, reagents and products, are diffusively exchanged at the contact area with the CSTR. The spatial studies were performed with CSTR contents belonging to the low extent of reaction steady-state branch, (the stable high pH branch), which insured far-from-equilibrium conditions at the feed boundary of the OSFRs. A pH color indicator was also supplied with the feed solutions. The two reactors provide complementary orthogonal views of the patterns and enable one to understand their three-dimensional (3D) structure. The annular OSFR allows a direct view of the concentration profiles that develop between the feed boundary and the opposite impermeable side, whereas in the disc OSFR we can see the integrated color changes across the disc (*19*).

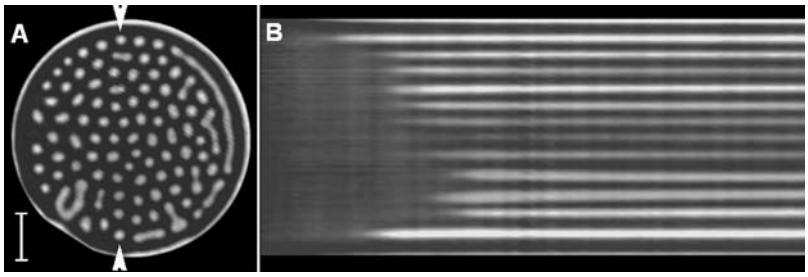

Fig. 4. Dynamics of pattern development in the Turing domain. Conditions are $[Tu]_0 = 5.0$ mM, $[H_2SO_4]_0 = 3.54$ mM, and $[NaPAA]_0 = 12$ mM (carboxylic function units). (**A**) Hexagonal-type planform array of low-pH spots; picture taken 2 hours after a supercritical change of $[H_2SO_4]_0$. The wavelength is $\lambda = 1.5 \pm 0.07$ mm. The scale bar is 4.0 mm. (**B**) Time-space plot along the vertical section of the disc indicated by arrows in (**A**). For technical reasons (*19*), the patterns preferentially start to develop at the circumference of the disc and gradually invade the entire disc. The time span of the image is 100 min.

We began by searching for spatial bistability, the simplest nonlinear phenomenon expected from an autoactivated reaction, using the annular OSFR (*19*). For the sake of simplicity, the dynamics of the system were first explored in the absence of the feedback species, here thiourea. The remaining iodate-sulfite subsystem was already known to produce spatial bistability (*16*). However, the iodate and sulfite feed concentrations and also their ratios are higher than in the previous work to keep the pH changes large enough even when the Tu is added. The sulfuric acid feed concentration, a parameter which controls the pH of the input solution and thereby the induction time (*1*, *17*) of the reaction, was used as an expandable parameter (Fig. 1A). Two very different steady acid concentration profiles can develop orthogonally between the feed boundary and the opposite side. One, at low $[H_2SO_4]_0$ (*27*), is characterized by the quasi-uniform blue color of the pH indicator (hereafter the F state). The other, at high $[H_2SO_4]_0$, is characterized by a steep color change from blue to yellow parallel to the rim of the annulus (hereafter the M state). These are illustrated by the right and left parts of Fig. 1B, respectively. The stability domains of these two states overlap for $1.5 \text{ mM} \leq [H_2SO_4]_0 \leq 2.5$ mM, which is the required spatial bistability phenomenon.

We then introduced Tu into the feed and noted that the extent of the spatial bistability domain, as a function of $[H_2SO_4]_0$, decreased and eventually vanished at $[Tu]_0 \geq 2$ mM (Fig. 1A). Above this critical $[Tu]_0$, the F and M steady-state domains were separated by a domain of oscillatory spatial states (Fig. 1C) that manifested as periodic rapid expansions of the pH indicator color switch position followed by its slow decay. Under similar conditions, oscillations in the disc OSFR organized in periodic low pH traveling waves (Fig. 2). The cross-shaped topology of the phase diagram is a checkpoint in the method. The onset of the oscillatory dynamics is the sign attesting that the feedback process reached an appropriate amplitude in the gel reactor.

In the final stage, we added sodium polyacrylate (NaPAA) in the feed solution, the low-mobility complexing agent that reversibly binds the activator, the proton. Its carboxylate functional groups have pK_a (where K_a is the acid dissociation constant) values in the range of 5 that is above the typical pH of the acid part of the M state and can efficiently bind protons. The most rewarding observations were uncovered for parameter conditions corresponding, in the absence of NaPAA, to the domain of spatiotemporal oscillations, in the vicinity of the crosspoint of the stability limits of the F and M states (Fig. 1A). The addition of sufficient concentrations of NaPAA quenched the oscillations, and, eventually, stationary patterns emerged spontaneously (Fig. 1D). Stationary patterns were often preceded by precursor signs such as the slowing down and the repulsion of colliding fronts when NaPAA was introduced.

We next used the disc OSFR to observe the pattern arrangement in a 2D extended reactor (*19*). We obtained stationary patterns for $[NaPAA]_0 \geq 6$ mM and $[Tu]_0 \geq 3$ mM (Fig. 3). Noticeably, for $[Tu]_0 \geq 4.5$ mM, we observed patterns that present planforms (Fig. 3, A to C) and dynamics of development typical of a Turing bifurcation. Starting from the uniform F state, a supercritical increase of $[H_2SO_4]_0$ first led to the spread of low-pH spots that tended to organize in a hexagonal array (Fig. 3A). On further gradual increase of $[H_2SO_4]_0$, the array of spots changed into parallel stripes (Fig. 3B) and, ultimately, to a hexagonal array of high-pH spots in a low-pH background (Fig. 3C) before the system turned into the uniform M state. The above patterns are the three standard 2D planforms expected from a Turing bifurcation (*3*, *6*).

The reverse changes in $[H_2SO_4]_0$ reversed the pattern sequence. The range of $[H_2SO_4]_0$ over which these patterns develop was narrow and shifted to higher values with increasing $[Tu]_0$ or the use of thinner discs (*19*). Within the accuracy of our experimental steps (changes of ≈0.02 mM), no hysteresis was observed at the onset of both hexagonal array of spots. At the minimal step increment, the spot array started to grow at locations near the circumference of the disc, where, for technical reasons, the boundary conditions differed from the rest of the disc (*19*). The theoretically (*3*, *6*) expected subcritical domain of hexagon patterns is often very narrow and beyond experimental accuracy (*20*). Yet, as expected for a system close to or in the subcritical Turing region, patterns developed through the emergence of spots in the vicinity of existing ones at a well-defined distance and position to produce a hexagonal planform. This well-organized pattern growth is illustrated in the time-space plot (Fig. 4).

Besides the Turing-type bifurcation to stationary patterns, other scenarios were also observed. Especially at feed compositions near the crosspoint in Fig. 1A, irregular highly branched patterns (Fig. 3D) formed through a complex mixture of coalescence of patches and finger growth mechanism, reminiscent of Ising and Bloch front instabilities (*22*). No stationary patterns were observed for $[Tu]_0 \geq 6$ mM nor for $[Tu]_0 \leq 2.5$ mM.

The present design method can be used to explore the pattern-forming capacity of other known oscillatory reactions. It may require technical adjustments in specific systems, for example, down-scaling the thickness (w) of the reactor and the use of more elaborated optical monitoring techniques, but we believe that we have identified the major steps for the design of stationary patterns in a large number of oscillatory reactions. The approach is mostly phenomenological. Apart from the identification of two appropriate species governing, respectively, the positive and negative feedback processes of the oscillatory reaction, the method requires no detailed knowledge of the reaction mechanism. The appropriateness of the negative feedback level is guided by the topology (i.e., cross-shaped) of the OSFR phase diagram, and the efficiency of the requested short-range activatory process is tested by the growing repulsions between colliding fronts when an appropriate low-mobility player is introduced. The most limiting factor to our method is the ability to find low-mobility complexing agents that would selectively, or at least preferentially, bind a species controlling the positive feedback mechanism. In addition, to quench the oscillations the complexed form of the activator has to be kinetically less active than the free form in order to decrease its effective evolution time to or below that of the species controlling the inhibitory process. For protons, hydroxide ions, polyiodide ions, and diiodine, many complexing agents are available. For other activatory species, such as BrO_2 or $HBrO_2$ in the Belousov-Zhabotinsky reaction (*28*), it can be a nontrivial problem to solve. Note that, if one starts with a system in which the inhibitory process already evolves faster than the activation, there would be no oscillations and the complexed form of the activator could be as active as its free form. Although some stationary patterns might also be obtained (*22*) in such systems, a general theoretical analysis predicts that, when using complexing agents to generate appropriate effective diffusion differences, a Turing bifurcation is only obtained if the system undergoes a Hopf bifurcation to oscillations when the complexing agent is decreased (*13*). Our observations are consistent with this prediction.

Our method, with separated well-defined checkpoints, should allow for extensions into biochemical reactions, such as the glycolytic path-

way, where adenosine diphosphate and adenosine triphosphate play the role of an activator and an inhibitor, respectively. Recent model studies (*12*) have shown that the presence of low-mobility enzymes such as phosphofructokinase can induce a short-range activation process suitable for the development of Turing patterns even when the complex is not inert.

References and Notes

1. I. R. Epstein, J. Pojman, *An Introduction to Nonlinear Chemical Dynamics* (Oxford Univ. Press, New York, 1998).
2. H. Meinhardt, *Models of Biological Pattern Formation* (Academic Press, London, 1982).
3. J. D. Murray, *Mathematical Biology* (Springer-Verlag, Berlin, 2003).
4. We do not consider the one example of transient symmetry-breaking patterns observed in a complex water-in-oil medium, which are made possible by the peculiar batch kinetic properties of the Belousov-Zhabotinsky reaction (*29*).
5. J. Boissonade, P. De Kepper, *J. Phys. Chem.* **84**, 501 (1980).
6. A. De Wit, *Adv. Chem. Phys.* **109**, 435 (1999).
7. V. Castets, E. Dulos, J. Boissonade, P. De Kepper, *Phys. Rev. Lett.* **64**, 2953 (1990).
8. K. J. Lee, W. D. McCormick, Q. Ouyang, H. L. Swinney, *Science* **261**, 192 (1993).
9. I. Lengyel, I. R. Epstein, *Proc. Natl. Acad. Sci. U.S.A.* **89**, 3977 (1992).
10. I. Szalai, P. De Kepper, *Chaos* **18**, 026105 (2008).
11. A. Turing, *Philos. Trans. R. Soc.* **237**, 37 (1952).
12. D. E. Strier, S. Ponce Dawson, *PLoS One* **2**, e1053 (2007).
13. J. E. Pearson, W. J. Bruno, *Chaos* **2**, 513 (1992).
14. P. Blanchedeau, J. Boissonade, P. De Kepper, *Physica D* **147**, 283 (2000).
15. J. Boissonade, E. Dulos, F. Gauffre, M. N. Kuperman, P. De Kepper, *Faraday Discuss. Chem. Soc.* **120**, 353 (2002).
16. I. Szalai, P. De Kepper, *J. Phys. Chem. A* **108**, 5315 (2004).
17. I. Szalai, P. De Kepper, *Phys. Chem. Chem. Phys.* **8**, 1105 (2006).
18. Z. Virányi, I. Szalai, J. Boissonade, P. De Kepper, *J. Phys. Chem. A* **111**, 8090 (2007).
19. Materials and methods are available as supporting material on *Science* Online.
20. B. Rudovics *et al.*, *J. Phys. Chem. A* **103**, 1790 (1999).
21. D. Horváth, Á. Tóth, *J. Chem. Soc. Faraday Trans.* **93**, 4301 (1997).
22. A. Hagberg, E. Meron, *Chaos* **4**, 477 (1994).
23. No stationary patterns could be obtained in the chlorite-tetrathionate (*15*) and chlorine dioxide–iodide (*16*) reactions, which do not have such an independent source or sink for the respective activatory species. Large amounts of polyacrylate or poly(vinyl alcohol) eventually induce morphological traveling front instabilities, but they have never led to a stationary pattern.
24. D. E. Strier, P. De Kepper, J. Boissonade, *J. Phys. Chem. A* **109**, 1357 (2005).
25. K. Benyaich, thesis, Université Libre de Bruxelles, Bruxelles, Belgique (2005).
26. G. Rábai, Z. V. Nagy, M. T. Beck, *React. Kinet. Catal. Lett.* **33**, 23 (1987).
27. The $[]_0$ notation denotes the concentration that the input species would have in the input flow after mixing and before any reaction.
28. R. J. Field, E. Kőrös, R. M. Noyes, *J. Am. Chem. Soc.* **94**, 8649 (1972).
29. V. Vanag, I. R. Epstein, *Chaos* **15**, 047510 (2005).

30. We acknowledge the support from the French Agence National de la Recherche, the French-Hungarian Centre Nationale de la Recherche Scientifique–Magyar Tudományos Akadémia collaboration program (21420), and the Hungarian funds Országos Tudományos Kutatási Alapprogram (49666 and 67701). I.S. thanks the support of the Bolyai Fellowship. We thank J. Boissonade and P. Borckmans for fruitful discussions.

Supporting Online Material

www.sciencemag.org/cgi/content/full/324/5928/772/DC1
Materials and Methods
Figs. S1 and S2
References

18 December 2008; accepted 16 March 2009
10.1126/science.1169973

An Observation Linking the Origin of Plasmaspheric Hiss to Discrete Chorus Emissions

J. Bortnik,[1]* W. Li,[1] R. M. Thorne,[1] V. Angelopoulos,[2] C. Cully,[3] J. Bonnell,[4] O. Le Contel,[5] A. Roux[5]

A long-standing problem in the field of space physics has been the origin of plasmaspheric hiss, a naturally occurring electromagnetic wave in the high-density plasmasphere (roughly within 20,000 kilometers of Earth) that is known to remove the high-energy Van Allen Belt electrons that pose a threat to satellites and astronauts. A recent theory tied the origin of plasmaspheric hiss to a seemingly different wave in the outer magnetosphere, but this theory was difficult to test because of a challenging set of observational requirements. Here we report on the experimental verification of the theory, made with a five-satellite NASA mission. This confirmation will allow modeling of plasmaspheric hiss and its effects on the high-energy radiation environment.

Naturally occurring electromagnetic waves are known to play a dominant role in the dynamics of Earth's radiation belts, a zone of high-energy electrons that are trapped by Earth's magnetic field (*1*–*5*). One important class of such waves is plasmaspheric hiss (*6*, *7*), which is responsible for creating a relatively empty zone, called the slot region, between the inner and outer belts, thus shaping the large-scale structure of the radiation belts (*3*, *4*). This incoherent band of waves was discovered in the late 1960s (*8*–*11*), spans from ~200 Hz to 2 kHz, and was named plasmaspheric hiss because of its confinement within the high-density plasmasphere, and its unstructured "hissy" nature. Despite the recognized importance of plasmaspheric hiss, its origin has proven remarkably difficult to identify. Here we describe an experimental observation that unambiguously links plasmaspheric hiss to a different and seemingly unrelated wave type, called chorus, occurring in distant regions of the magnetosphere.

Unlike plasmaspheric hiss, chorus occurs outside the plasmasphere as short (~0.1-s) coherent pulses in the frequency range from 0.1 f_{ce} to 0.6 f_{ce} (where f_{ce} is the frequency with which electrons gyrate about Earth's magnetic field line and is proportional to the magnetic field intensity) (*12*–*15*). Recent modeling shows that a fraction of chorus energy can propagate from its equatorial source region to high latitudes, avoid Landau damping, and refract into the plasmasphere, where it merges into the incoherent band of hiss (*7*). To do so, the chorus waves must originate from a spatial region between $L \sim 4$ and 7 (where the L value roughly tags a certain magnetic field line by the radial distance in Earth radii of its equatorial crossing), in the lower range of frequencies (~0.1 f_{ce} to 0.3 f_{ce}), with wave normals pointed toward lower L ($\psi_0 \sim -30°$ to $-60°$, where ψ_0 is the angle formed between the wave vector **k**, normal to the plane of the wave, and Earth's magnetic field). The predictions of this model are consistent with previously reported statistical observations of hiss, but a direct experimental test is challenging, because it requires simultaneous observations with at least two satellites equipped with high-resolution wave instruments capable of unambiguously detecting chorus and hiss: one located near the equatorial source region of chorus and the other in the plasmasphere, at approximately the same local time (which should coincide with the local time in which chorus and hiss both occur) and in the same frequency band, during geomagnetically active conditions. Such an experimental situation was serendipitously achieved with NASA's five-satellite THEMIS (Time History of Events and Macroscale Interactions during Substorms) mission (*16*).

At ~04:00 UT on 4 October 2008, THEMIS E was located on the day side, in the low-density region outside the plasmasphere (Fig. 1C), and was observing waves with both electric and magnetic components (Fig. 1, A and B), which were in the range from ~0.1 f_{ce} to 0.6 f_{ce} and thus consistent with chorus. Simultaneously, THEMIS D

[1]Department of Atmospheric and Oceanic Sciences, University of California, Los Angeles, CA 90095, USA. [2]Institute of Geophysics and Planetary Physics/Earth and Space Sciences, University of California, Los Angeles, CA 90095, USA. [3]Swedish Institute of Space Physics, Box 537, SE-751 21, Uppsala, Sweden. [4]Space Science Laboratory, University of California, Berkeley, CA 94720, USA. [5]Centre d'Etude des Environnements Terrestre et Planétaires, Velizy, France.

*To whom correspondence should be addressed. E-mail: jbortnik@gmail.com

was located on the day side in the high-density plasmasphere and was observing electromagnetic waves (Fig. 1, D and E) in the frequency range from ~100 Hz to 1 kHz, which were not scaled to the gyrofrequency and are consistent with hiss.

Using low-resolution data, it is not possible to determine whether there exists a correlation between chorus and hiss (Fig. 1). However, in the time interval from 03:54 to 04:00 UT (gray block in Fig. 1, C and F), both satellites switched into a high-resolution burst-collection mode (*16*), revealing that the waves recorded on THEMIS E (Fig. 2A) are discrete chorus elements, in the frequency range from ~700 Hz to 2 kHz (~0.17 to 0.5 f_{ce}), with predominantly oblique wave normal angles (Fig. 2B). THEMIS D was simultaneously observing waves between a few 100 Hz and ~2 kHz, exhibiting the typical structureless *f-t* (frequency-time) signature indicative of plasmaspheric hiss (Fig. 2C).

In the most intense portion of the chorus spectrum (~0.3 f_{ce}), there is a clear correspondence between the chorus (THEMIS E) and hiss (THEMIS D) wave power (Fig. 2D), even though the two satellites are separated radially by ~3.2 R_E (R_E, Earth radius) (~20,400 km) and by ~2.9 hours in local time. Almost every chorus element (Fig. 2D, red trace) results in an increase in hiss power (blue trace), which decays away with a time constant of ~10 s. The correspondence is most evident near the beginning of the period (03:54 UT), possibly because the longitudinal separation is at a minimum [magnetic local time (MLT) difference, ~2.78 hours] and diminishes toward the end of the period, when the longitudinal separation increases (MLT difference, ~3.05). It is possible that the ~3-hour MLT longitudinal separation between spacecraft is the maximum separation at which a correspondence between chorus and hiss can be observed, and as such this coincidental measurement is even more fortuitous. Alternatively, it is possible that the high chorus wave normals ($\psi \sim -60°$ to $-40°$) near the beginning of the period (Fig. 2B) are more conducive to producing hiss than are the lower wave normals ($\psi \sim -50°$ to $-10°$) in the later part. The average power levels of chorus and hiss are comparable (especially in the earlier part of the observation), but the hiss intensity is weaker than that of the individual chorus elements by a factor of ~100. The results of a frequency-resolved cross-covariance analysis (Fig. 3) indicate that the correlation is strongest [correlation coefficient (r) ~ 0.7] in the most intense spectral portion of the chorus (~1200 to 1650 Hz) and occurs when the hiss waveform lags behind the chorus waveform by ~1 to 7 s. The intense hiss spectrum at ~100 to 700 Hz (Fig. 2C) is expected to be generated by chorus at $L > 6$ (that is, regions of lower f_{ce}), as suggested in Fig. 1.

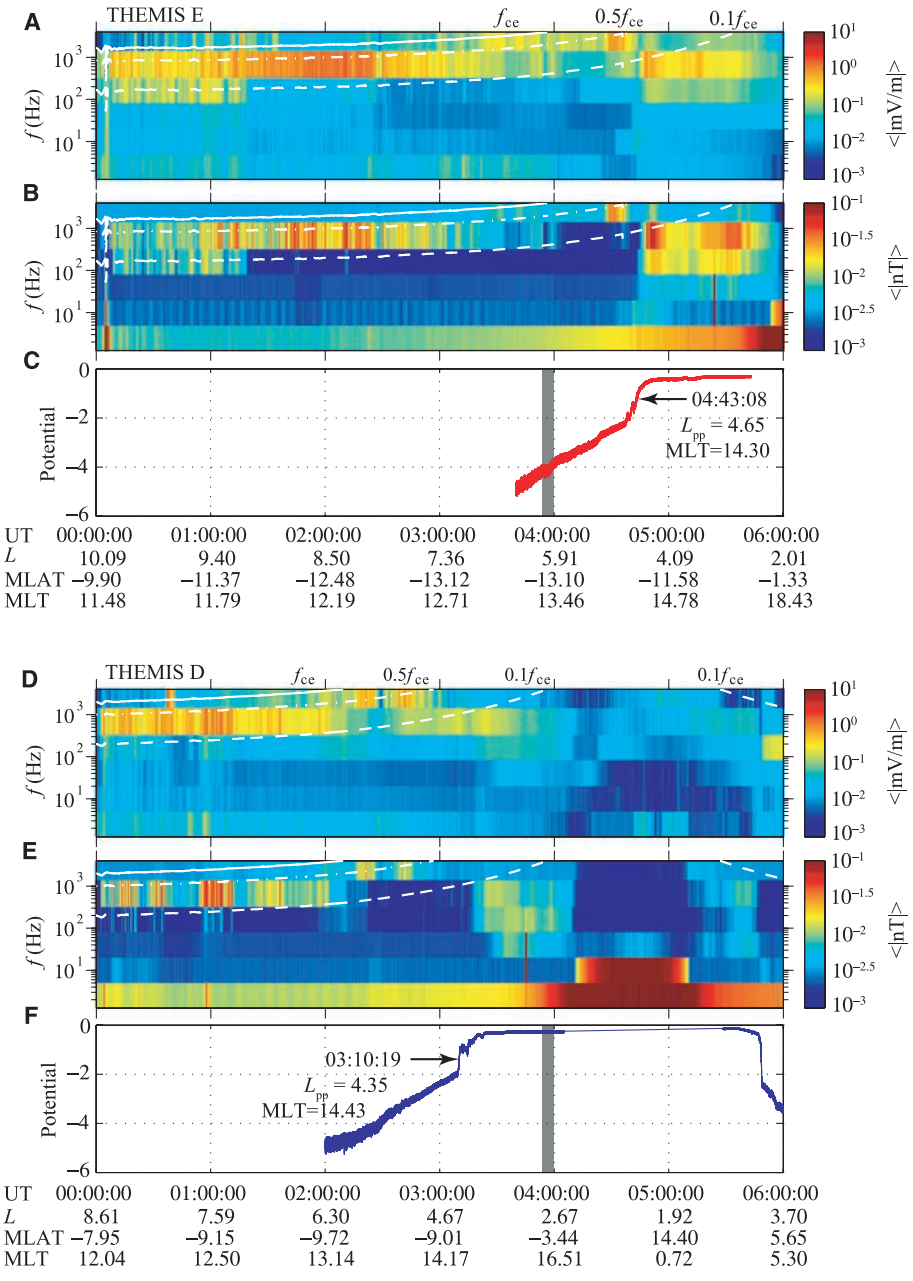

Fig. 1. A 6-hour overview plot of simultaneous data recorded by THEMIS E [(A) to (C)] and THEMIS D [(D) to (F)] on 4 October 2008. (**A** and **D**) The wave electric field intensity and (**B** and **E**) the wave magnetic field intensity in six frequency bins from 2 Hz to 4 kHz. (**C** and **F**) The spacecraft electric potential, which acts as a proxy for the electron density. The *x* axis labels indicate each satellite's universal time (UT) local *L* value; the magnetic latitude (MLAT), which is the latitude of each spacecraft relative to the geomagnetic equator; and MLT, which is the local time of the equatorial crossing of the magnetic field line passing through the satellite and can be slightly different from the actual local time. The white lines in (A) and (B) and (D) and (E) represent fractions of the equatorial gyrofrequency (f_{ce}) corresponding to 1, 0.5, and 0.1, represented by solid, dash-dotted, and dashed lines, respectively. The inferred plasmapause crossing based on spacecraft potential is shown in (C) and (F). The magnetic signal <20 Hz [(B) and (E)] at low *L* is due to contamination from Earth's geomagnetic field.

Theoretical analysis similar to that of (*7*) showed that a group of rays representing chorus, initiated near the location of THEMIS E ($L = 6$), was able to propagate into the plasmasphere and be observed near the location of THEMIS D ($L = 2.8$) (Fig. 4). The key angular range of rays that entered the plasmasphere and evolved into plasmaspheric hiss was $\psi_0 \sim -49.5°$ to $-46.5°$ (similar to the measured angles in Fig. 2B), with waves at $\psi_0 < -50°$ becoming Landau-damped before reaching the plasmasphere, and waves with $\psi_0 > -46°$ being unable to refract into the plasmasphere and instead propagating to the ground (Fig. 4A, green and yellow rays) or refracting toward higher *L* shells (red rays) and possibly forming a different emission called extremely low-frequency (ELF) hiss (*17*).

To further quantify the approximate time scale of chorus entry into the plasmasphere, we traced a single ray for its entire lifetime (Fig. 4B), from initiation at $t = 0$ s to termination at $t = 20$ s. Using

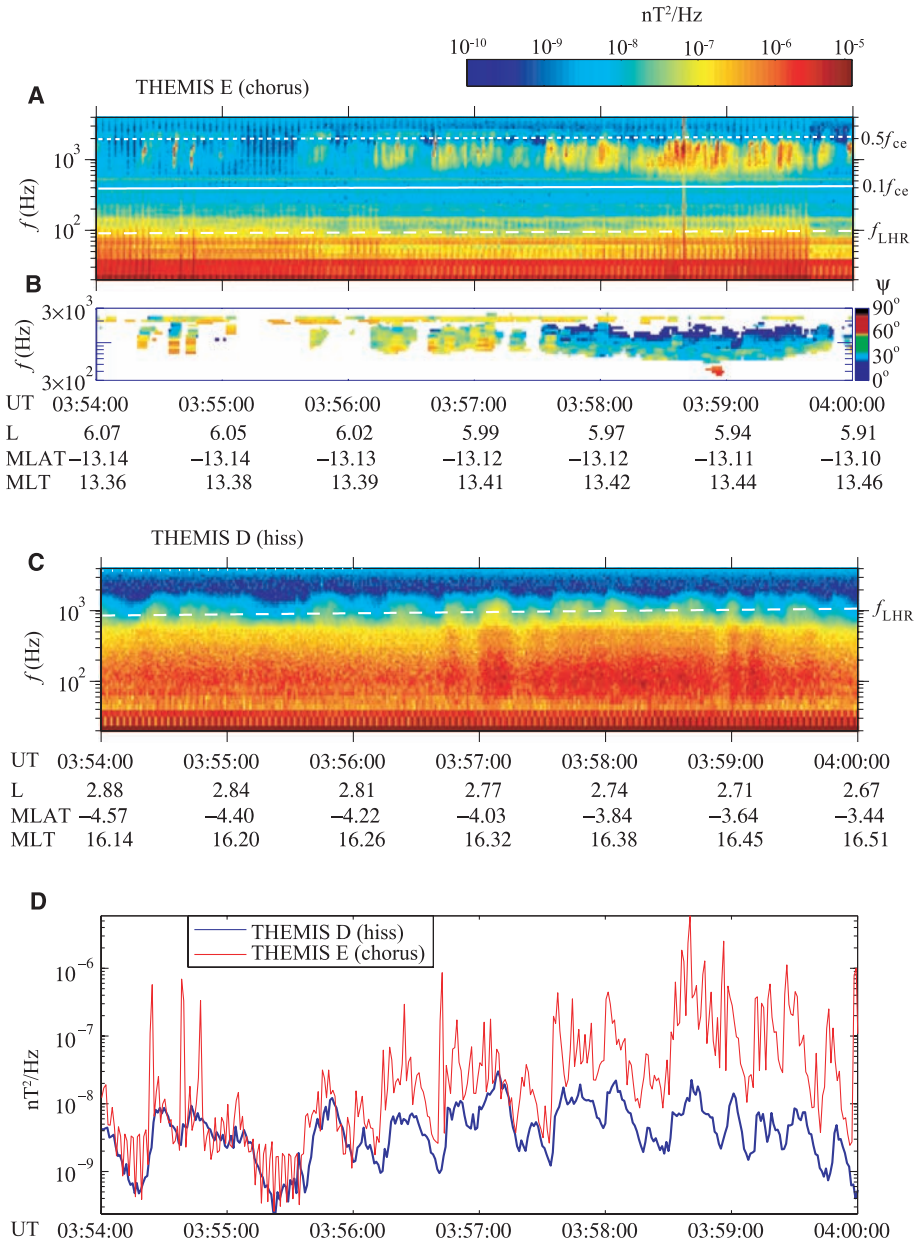

Fig. 2. High-resolution data from the two THEMIS spacecraft from 03:54 to 04:00 UT, corresponding to Fig. 1. (**A**) Wave magnetic field data recorded by THEMIS E, in the range from 20 Hz to 4 kHz. (**B**) Corresponding wave normal angle estimates of the intense chorus elements in the range from 300 Hz to 3 kHz, calculated using (*19*). (**C**) THEMIS D data shown as in (A). (**D**) Frequency-averaged magnetic field intensity in the frequency band from 1200 to 1650 Hz, for THEMIS E (red trace) and D (blue trace). The ephemeris of each spacecraft is shown on the *x* axes of (A) and (C) in the same format as Fig. 1. The white dashed line in (A) and (C) corresponds to the local lower hybrid resonance frequency (f_{LHR}); the white solid and dotted lines in (A) are 0.1 and 0.5 f_{ce}, respectively; and signals below ~200 Hz suffer from instrumental noise. High-resolution wave electric field data corresponding to (A) and (B) were also recorded by THEMIS E and D and look similar to the magnetic field data (not shown in the figure).

this representative ray, we found that the ray entered the plasmasphere at approximately $t = 1$ s and crossed the geomagnetic equator at $t = 2$ s, near $L = 3$. This is in agreement with observations by THEMIS D (Fig. 2), which was located at $L \sim 2.8$ during the period of hiss observation and according to our model would have recorded the first entry of the chorus wave power at roughly $t \sim 2$ s after chorus was excited. The ray then continued to propagate and filled the entire plasmasphere (Fig. 4B, solid gray oval). It experienced a magnetospheric reflection at $t \sim 3$ s, reflected off the plasmapause at $t \sim 4.5$ s, and recirculated back to lower L. At $t \sim 7.5$ s, the ray returned again to the geomagnetic equator, at $L \sim 2.5$, and would have been sensed again by a satellite at that location. Thereafter, the ray continued to propagate and was completely damped at $t = 20$ s. The relevant time scales for observing chorus wave power appearing inside

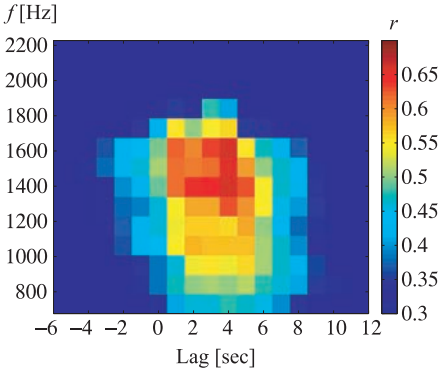

Fig. 3. Cross-covariance analysis between THEMIS E and D data. A frequency-resolved cross-covariance analysis in 16 frequency channels between 700 Hz and 2.2 kHz is shown as a function of time lag, positive values indicating that THEMIS D data (hiss) lags behind THEMIS E data (chorus). The time-series data are taken from the first 3 min (03:54 to 03:57 UT) of the wave magnetic intensity in Fig. 2, A and B, because this gives slightly more resolved time lags than would using the entire 6-min interval. The time series in each frequency band is normalized so that the autocovariance is 1 at zero lag.

the plasmasphere and propagating multiple times across the equator in the vicinity of $L \sim 2.8$ is $t \sim 2$ to 7 s for the entire group of rays shown in Fig. 4A. Comparing Fig. 4B to Fig. 3, the peak correlation between the hiss and chorus waveforms occurs with a ~2- to 7-s lag, in direct agreement with the theory.

The high-resolution observation made by the THEMIS satellites directly supports the theory of the origin of plasmaspheric hiss, which involves

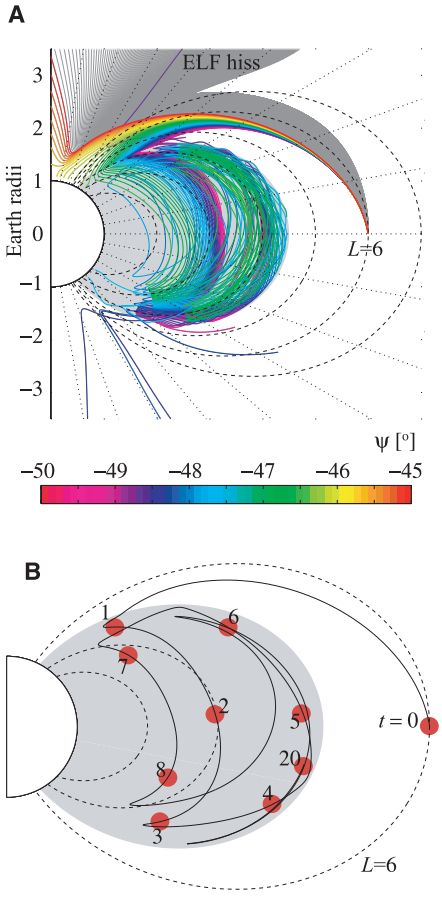

Fig. 4. Ray-tracing model of chorus and hiss. (**A**) Ray paths representing chorus are initiated at the equator, at $L = 6$, $f = 0.21\ f_{ce}$ (~855 Hz), in the range $\psi_0 = -50°$ to 0° (gray ray paths), plotted at every 0.1°, with the key wave normal range $\psi_0 = -50°$ to −45° that enters the plasmasphere shown in color. The corresponding color scale indicates the initial wave normal angle of each ray in degrees. (**B**) A single ray from the group shown in (A) is displayed, with $\psi_0 = -48°$. The red circles indicate group time in seconds, from the time of ray initiation $t = 0$ s. The day-side cold plasma density is modeled according to (*20*), with the plasmapause located at $L = 4.5$, for consistency with the THEMIS observations; and the L-dependent suprathermal flux model was used as in (*7*, *21*) for active conditions. Each ray in (A) and (B) is plotted only while its power is above 1% of its initial value, so that in the case of (B), the ray duration is ~20 s.

the propagation and evolution of discrete chorus elements from their source region outside the plasmasphere into the incoherent noise band that characterizes plasmaspheric hiss, inside the plasmasphere. Understanding the origin of hiss will enable space physicists to calculate spatial maps of hiss characteristics and in turn predict the effect of hiss on the radiation belt electrons that are a known hazard to astronauts and to a variety of technological systems in space (*18*).

References and Notes

1. C. F. Kennel, H. E. Petschek, *J. Geophys. Res.* **71**, 1 (1966).
2. L. R. Lyons, R. M. Thorne, C. F. Kennel, *J. Geophys. Res.* **77**, 3455 (1972).
3. R. W. Abel, R. M. Thorne, *J. Geophys. Res.* **103**, 2385 (1998).
4. L. R. Lyons, R. M. Thorne, *J. Geophys. Res.* **78**, 2142 (1973).
5. R. B. Horne *et al.*, *J. Geophys. Res.* **111**, A03225 (2005).
6. R. M. Thorne, E. J. Smith, R. K. Burton, R. E. Holzer, *J. Geophys. Res.* **78**, 1581 (1973).
7. J. Bortnik, R. M. Thorne, N. P. Meredith, *Nature* **452**, 62 (2008).
8. N. Dunckel, R. A. Helliwell, *J. Geophys. Res.* **74**, 6371 (1969).
9. C. T. Russell, R. E. Holzer, E. J. Smith, *J. Geophys. Res.* **74**, 755 (1969).
10. W. W. L. Taylor, D. A. Gurnett, *J. Geophys. Res.* **73**, 5615 (1968).
11. M. Hayakawa, S. S. Sazhin, *Planet. Space Sci.* **40**, 1325 (1992).
12. R. K. Burton, R. E. Holzer, *J. Geophys. Res.* **79**, 1014 (1974).
13. W. J. Burtis, R. A. Helliwell, *Planet. Space Sci.* **24**, 1007 (1976).
14. S. S. Sazhin, M. Hayakawa, *Planet. Space Sci.* **40**, 681 (1992).
15. O. Santolik, *Nonlinear Process. Geophys.* **15**, 621 (2008).
16. V. Angelopoulos, *Space Sci. Rev.* **141**, 5 (2008).
17. O. Santolik *et al.*, *J. Geophys. Res.* **111**, A10208 (2006).
18. D. N. Baker, *Science* **297**, 1487 (2002).
19. D. Lengyel-Frey *et al.*, *J. Geophys. Res.* **99**, 13325 (1994).
20. D. L. Carpenter, R. R. Anderson, *J. Geophys. Res.* **97**, 1097 (1992).
21. J. Bortnik, R. M. Thorne, N. P. Meredith, *J. Geophys. Res.* **112**, A08204 (2007).

22. The authors gratefully acknowledge support from NASA grant NNX08A1135G and contract NAS5-02099.

22 January 2009; accepted 31 March 2009
10.1126/science.1171273

The Role of Aerosols in the Evolution of Tropical North Atlantic Ocean Temperature Anomalies

Amato T. Evan,[1,2]* Daniel J. Vimont,[2] Andrew K. Heidinger,[3] James P. Kossin,[4] Ralf Bennartz[2]

Observations and models show that northern tropical Atlantic surface temperatures are sensitive to regional changes in stratospheric volcanic and tropospheric mineral aerosols. However, it is unknown whether the temporal variability of these aerosols is a key factor in the evolution of ocean temperature anomalies. We used a simple physical model, incorporating 26 years of satellite data, to estimate the temperature response of the ocean mixed layer to changes in aerosol loadings. Our results suggest that the mixed layer's response to regional variability in aerosols accounts for 69% of the recent upward trend, and 67% of the detrended and 5-year low pass–filtered variance, in northern tropical Atlantic Ocean temperatures.

Since 1980, tropical North Atlantic Ocean temperatures have been rising at a rate of nearly 0.25°C per decade (*1*). Studies have attributed this increase, explicitly and implicitly, to global warming (*2*, *3*), mean Northern Hemisphere temperature variations (*4*), changes in the thermohaline circulation (*5*, *6*), or some combination of these factors (*7*). However, many of these studies fail to provide either a mechanism for or direct evidence of how these variables control tropical North Atlantic Ocean temperatures. At the same time, models (*8*) and observations (*1*, *9*) demonstrate that local changes in aerosol cover should have a non-negligible impact on Atlantic Ocean temperature via the scattering of sunlight and reduction in surface solar insolation.

The tropical North Atlantic is unique among tropical ocean basins because of its oftentimes extensive and heavy aerosol cover (*10*), a consequence of being downwind of West Africa, the world's largest dust source (*11*). Annual North African dust emission and deposition to the North Atlantic have been estimated to be 240 to 1600 Tg and 140 to 259 Tg, respectively (*12*), with the peak in West African dust production occurring during the boreal summer months (*13*). A smoothed time series of northern tropical Atlantic dust cover (Fig. 1) shows a maximum and minimum in dust activity that occurred in 1985 and 2005, respectively, and a downward trend in dust optical depth over the record. It has been shown that during both the summer (*14*) and winter seasons (*15*) these year-to-year changes

[1]Cooperative Institute for Meteorological Satellite Studies, University of Wisconsin, Madison, WI 53706, USA. [2]Department of Atmospheric and Oceanic Sciences, University of Wisconsin, Madison, WI 53706, USA. [3]National Oceanic and Atmospheric Administration (NOAA)/National Environmental Satellite, Data, and Information Service (NESDIS)/Center for Satellite Applications and Research (STAR), 1225 West Dayton Street, Madison, WI 53706, USA. [4]NOAA/NESDIS/National Climatic Data Center, Madison, WI 53706, USA.

*To whom correspondence should be addressed. E-mail: atevan@wisc.edu

in dust cover are related to variations in previous-year Sahelian precipitation. Additionally, wintertime dust production is strongly related to the strength of the North Atlantic Oscillation (*16*) and, to a lesser extent, the El Niño–Southern Oscillation (*15*).

Evan *et al.* (*9*) used satellite retrievals of aerosol optical thickness (AOT) from the Advanced Very High Resolution Radiometer (*17*) as the input to a shortwave radiative transfer model that estimated the change in surface solar radiation and the associated instantaneous cooling of sea surface temperatures (SSTs) by dust. Here, we update those methods by also estimating the longwave surface forcing by dust, including the radiative impact of stratospheric aerosols in our analysis (*18*), and using a stochastic ocean temperature model with a variable mixed layer depth (*19*), to calculate the response of local SSTs to radiative forcing by dust and volcanic aerosols (*20*). We force our model with satellite observations of aerosols over the 1982–2007 period to estimate how the temperature of the ocean mixed layer responds to month-to-month changes in tropospheric mineral dust and stratospheric volcanic aerosols (*21*).

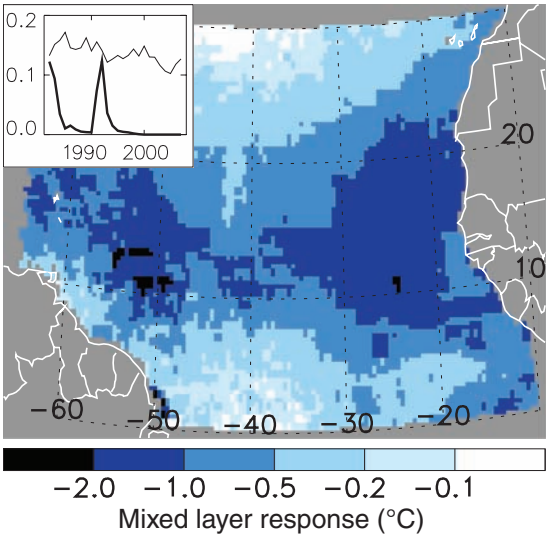

Fig. 1. Map of the mixed layer response to the presence of dust and volcanic aerosols and time series of aerosol optical depth. Estimations of mixed layer temperature response to surface radiative forcing by mineral dust and stratospheric volcanic aerosols are averaged over the 1982–2007 period and have a spatial resolution of 0.5°. The inset plot is a time series of annual mean monthly dust optical depth (thin black line) and stratospheric aerosol optical depth (thick black line), both averaged over the northern tropical Atlantic (0° to 30°N, 15° to 65°W).

From the model output, the spatial pattern of the mixed layer response to aerosol surface forcing (Fig. 1) is strongly indicative of the distribution of dust (fig. S1) and cloud cover (fig. S5), and of ocean mixed layer depth (fig. S6) (*20*). Aerosols exert their strongest influence on ocean temperatures along the coast of West Africa and extending westward between roughly 10° and 20°N; across the tropical North Atlantic, climatological cooling of the ocean mixed layer by aerosols ranges from –0.1° to –2.0°C (Fig. 1).

An annual time series of the mixed layer temperature response to local changes in dust and stratospheric aerosols, averaged over the tropical North Atlantic (0° to 30°N and 15° to 65°W), shows that mean cooling can range from –1.1° to –0.4°C, with the maximum and minimum in the magnitude of cooling occurring in 1983 and

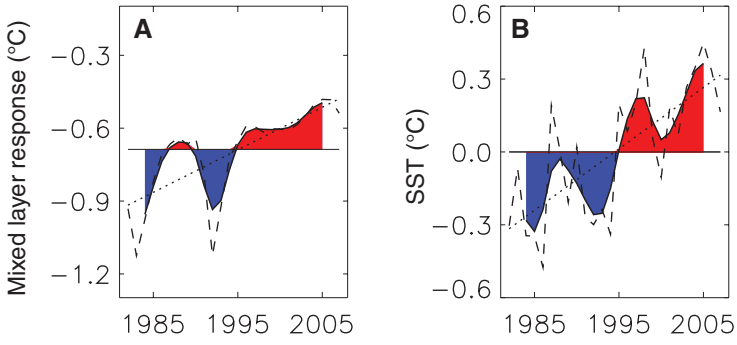

Fig. 2. Time series of mixed layer response to dust and stratospheric aerosol forcing (**A**) and observed SST anomalies (**B**). Data for both are averaged over the tropical North Atlantic (0° to 30°N, 15° to 65°W). In each panel the dashed line represents the annual mean values, the thin solid line is the climatological mean, the dotted line is the linear least-squares trend, and the thick black line is the annual mean time series processed with a 1-4-6-4-1 filter. The red and blue regions correspond to periods that are above and below the climatological mean, respectively.

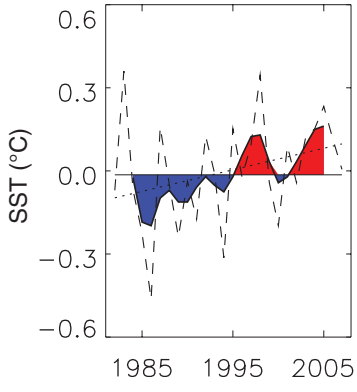

Fig. 3. Anomaly time series of observed SST (Fig. 2B) minus the aerosol forced component (Fig. 2A). Description is otherwise the same as for Fig. 2.

Table 1. Sensitivities in estimating aerosol forcing of tropical North Atlantic Ocean temperatures. The first row gives the mean SST forcing by dust and stratospheric aerosols estimated by (from left to right) the standard model without any modifications, increasing and decreasing cloud cover by 5%, decreasing and increasing AOT by 0.1, deepening and shoaling the mixed layer depth (MLD) by 5 m, and using an upper and lower limit on the so-called feedback parameter (λ) in the stochastic temperature model (*20*). The remaining rows report the percent of the variance in the detrended and smoothed SST time series that is due to stratospheric aerosols, the percent reduction in the SST trend when effects from stratospheric aerosols are removed, and the SST trend when effects from stratospheric aerosols are removed (the residual SST); the values in parentheses take into account both dust and stratospheric aerosols. All values are from time series averaged over the northern tropical Atlantic (0° to 30°N and 15° to 65°W). Note that the trend in observed SST over this region is 0.25°C per decade (Fig. 2B).

	Standard case	Clouds (+5%)	Clouds (–5%)	AOT (–0.1)	AOT (+0.1)	MLD (+5 m)	MLD (–5 m)	λ (upper)	λ (lower)
Mean forcing (°C)	–0.70	–0.62	–0.78	–0.31	–1.31	–0.56	–0.95	–0.62	–0.79
Reduction in variance (%)	55 (67)	56 (66)	52 (66)	54 (64)	56 (68)	56 (65)	43 (60)	56 (66)	52 (67)
Reduction in SST trend (%)	46 (69)	41 (61)	52 (77)	48 (69)	44 (64)	37 (56)	61 (93)	42 (63)	52 (77)
Residual SST trend (°C/decade)	0.14* (0.08)	0.15* (0.10)	0.12* (0.06)	0.13* (0.08)	0.14* (0.09)	0.16* (0.11*)	0.10 (0.02)	0.14* (0.09)	0.12* (0.06)

*Trends statistically significant at the 95% level (*23*).

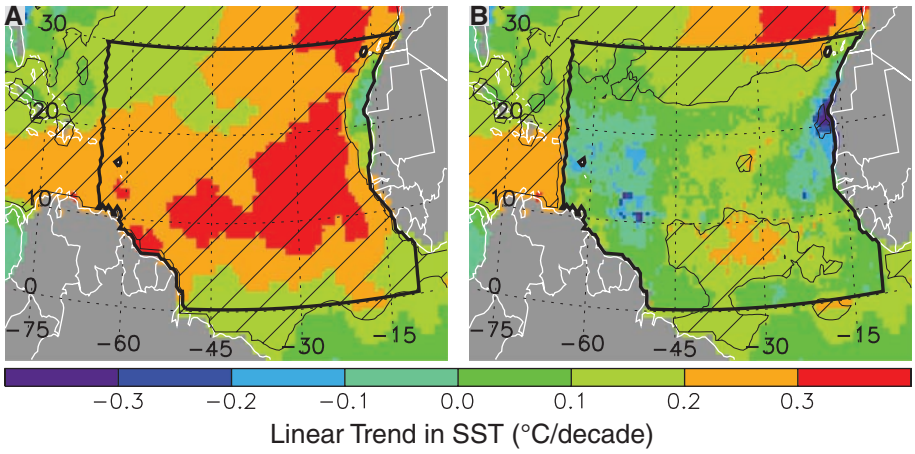

Fig. 4. Map of linear trends in observed SST (**A**) and the residual SST (**B**). Trends are calculated from the annual mean time series at each 0.5° grid cell over the 1982–2007 period. Hatched areas represent regions with linear trends that are statistically significant at the 95% level (*23*). The area enclosed by thick black lines (i.e., the oceanic regions of 0° to 30°N and 15° to 65°W) represents the region over which mean time series are calculated (Figs. 2 and 3), and in (B) is the area where the aerosol direct effect and its impact on ocean temperatures have been estimated.

2005, respectively (Fig. 2A). Cooling in 1992 was slightly less than that in 1983, both reflecting increases in stratospheric aerosols after volcanic eruptions of El Chichón and Mount Pinatubo, respectively (Fig. 1). The anomalously weak cooling of 2005 is caused by the minimum in dust cover observed for that year (Fig. 1). A 5-year smoothed (using a 1-4-6-4-1 filter) version of the annual mean time series highlights the two similar periods of anomalous cooling and the anomalous warming at the end of the record (Fig. 2A). A trend based on the linear least-squares fit of the annual time series gives a weakening in the magnitude of aerosol cooling of 0.18°C per decade (Fig. 2A).

To contrast our estimation of the ocean mixed layer response to changes in aerosol loadings with observed SSTs, we plotted the time series of the northern tropical Atlantic SST anomaly using the Hadley Centre HadSST data set (*22*) (Fig. 2B). Over the past 26 years, the range of SST anomalies is 1.0°C, from –0.5°C in 1986 to 0.5°C in 2005, with a linear trend of 0.25°C per decade, significant at the 99.9% level (*23*). The 5-year smoothed SST series shows periods of anomalous cooling and warming that are separated at 1995, a point thought to represent the transition from negative to positive phase of the Atlantic Multidecadal Oscillation (*6*).

The smoothed versions of the modeled mixed layer temperature response to aerosols (Fig. 2A) and the observed SST anomalies (Fig. 2B) are very similar; both show local minimums in the early 1980s and early 1990s, in addition to a maximum in temperature in 2005. The plot of the temperature response to aerosols also exhibits a transition from generally negative to positive anomalies around 1995 but does not exhibit the local maximum around 1997, and the maximum in 2005 is about 0.1°C cooler than is that from the Hadley Centre SST observations.

To better determine the extent to which aerosols have contributed to the evolution of this tropical North Atlantic temperature anomaly, we subtracted our monthly estimates of the oceanic cooling by dust and stratospheric aerosols from the observed tropical North Atlantic SST and plotted the anomaly of the residual (Fig. 3). This is our estimation of variability in northern tropical Atlantic SST that is not directly driven by local changes in aerosols, which we term the residual SST. The trend in the residual SST time series is 0.08°C per decade (Table 1 and Fig. 3), weaker than the trend in observed SST by 0.17°C per decade (Fig. 2B) and not statistically significant (*23*). These calculations suggest that 69% of the recent upward trend in northern tropical Atlantic SST is due to changes in aerosols. Separating by aerosol type, 46% of the trend in SST here is driven by changes in stratospheric volcanic aerosols, and 23% of the trend is driven by changes in tropospheric mineral aerosols (Table 1). The 5-year smoothed residual SST exhibits a less pronounced transition than is seen in the observations from anomalously cool to warm temperatures in 1995 (Fig. 2B). In the residual SST, the anomalous warming of 2005 has a magnitude that is roughly half of what is seen in the observations, consistent with previous studies suggesting that changes in surface solar insolation played a role in the warming during those summer months (*9*, *24*).

To quantify the overall importance of changes in aerosols to the evolution of the SST time series, in addition to the percent reduction in the trend, we also report the percent variance attributable to aerosol variability in the detrended, 5-year smoothed ocean temperature time series. This is defined as 1 – [(detrended residual low-frequency variance)/(detrended observed low-frequency variance)] × 100% (*20*). In the case of Fig. 3, the variance in the smoothed and detrended residual time series is 33% of that for the detrended measured SST series, which suggests that 67% of the detrended low-frequency variability in northern tropical Atlantic temperatures is driven by local variations in aerosol loadings (Table 1). Separating by aerosol type, 55% of the smoothed detrended temperature variance is due to changes in volcanic stratospheric aerosols, and 12% of the variance is due to changes in tropospheric mineral aerosols (Table 1). When we repeated this analysis for only the boreal summer months (July to September), we found that 75% of the variance in observed SST (after detrending and smoothing) can be attributed to changes in aerosol loadings, and the 0.23°C per decade trend in summertime SST—which is statistically significant at the 99% level (*23*)—is nearly an order of magnitude stronger than the 0.03°C per decade residual summertime trend, which is not statistically significant (*20*).

A map of the linear trends in observed annual mean SST for the 1982–2007 period shows that recent warming is not uniform across the tropical Atlantic basin (Fig. 4A). Although the trends in SST are statistically significant throughout the area we are interested in, the warming is most pronounced between 10° and 20°N and east of 60°W, with values here exceeding 0.3°C per decade. This pattern of northern tropical Atlantic SST trends (Fig. 4A) is similar to that of annual mean dust loadings (fig. S1) and the climatological mixed layer temperature response to surface aerosol forcing (Fig. 1). Linear trends in the residual SST, also based on annual means for the 1982–2007 period, are weaker and more uniform across our region of interest. For example, the warming in the region of 10° to 20°N and east of 60°W is neither strongly positive nor statistically significant. North of roughly 25°N there are statistically significant upward trends in the residual SST, which seem to be a continuation of the warming pattern north of 30°N.

Because there are uncertainties associated with our methodology for estimating the impact of aerosol loadings on ocean temperature, we also ran our model with modifications to parameters to which the output is sensitive (Table 1). This includes increasing and decreasing cloud cover by 5%, deepening and shoaling the mixed layer depth by 5 m, increasing and decreasing AOT by 0.1, and applying an upper and lower limit to the so-called feedback parameter (*20*). Although the results from the sensitivity study show that our estimation of the magnitude of aerosol cooling of ocean temperatures is sensitive to our model parameters (mean cooling values range from –1.31° to –0.31°C), estimations of the detrended and smoothed SST variance attributed to aerosols are more robust (values range from 60 to 68%), as are estimations of the percent reduction in the residual SST trend (values from 56 to 93%) and the magnitude of the residual SST trends (0.02° to 0.11°C per decade). Additionally, for each case in the sensitivity study except increasing the mixed layer depth, none

of the residual SST trends are statistically significant at the 95% level (*23*). Note that our analysis does not show that aerosols explain year-to-year changes in SST, but that their effect is realized when considering variability on longer time scales because year-to-year changes in tropical Atlantic SST are more strongly modulated by wind-induced latent heat fluxes (*24*, *25*).

The present analysis is an estimate of the direct effect of dust radiative forcing on the upper-ocean heat budget. Our analysis does not exclude other sources of variability in the northern tropical Atlantic (*24*), nor does it account for reductions in atmospheric water vapor (*20*, *26*) or possible increases in cloudiness (*20*, *27*) associated with dust outbreaks. Nor does it include dynamical feedbacks from an atmospheric response to aerosol forcing and associated SST changes, including changes in the latent and sensible heat fluxes (*28*–*30*). Therefore, further analysis of coupled and dynamical feedbacks to aerosol forcing of tropical ocean temperatures is warranted.

Over the past 30 years, temperatures in other tropical ocean basins have been rising steadily, but at a slower rate than in the Atlantic (*31*). At the same time, projections of surface temperature increases under a doubled carbon dioxide climate suggest that the Atlantic should be warming at a rate slower than the other observations (*32*). We suggest that this apparent disconnect between observations and models may be due to the influence of Atlantic dust cover. Our results imply that because dust plays a role in modulating tropical North Atlantic temperature, projections of these temperatures under various global warming scenarios by general circulation models should account for long-term changes in dust loadings. This is especially critical because studies have estimated a reduction in Atlantic dust cover of 40 to 60% under a doubled carbon dioxide climate (*33*), which, on the basis of model runs with an equivalent reduction of the mean dust forcing, could result in an additional 0.3° to 0.4°C warming of the northern tropical Atlantic.

References and Notes

1. G. R. Foltz, M. J. McPhaden, *Geophys. Res. Lett.* **35**, L20706 (2008).
2. T. P. Barnett *et al*., *Science* **309**, 284 (2005); published online 2 June 2005 (10.1126/science.1112418).
3. B. D. Santer *et al*., *Proc. Natl. Acad. Sci. U.S.A.* **103**, 13905 (2006).
4. M. E. Mann, K. A. Emanuel, *Eos* **87**, 233 (2006).
5. T. L. Delworth, M. E. Mann, *Clim. Dyn.* **16**, 661 (2000).
6. S. B. Goldenberg, C. W. Landsea, A. M. Mestas-Nuñez, W. M. Gray, *Science* **293**, 474 (2001).
7. K. E. Trenberth, D. J. Shea, *Geophys. Res. Lett.* **33**, L12704 (2006).
8. M. Yoshioka *et al*., *J. Clim.* **20**, 1445 (2007).
9. A. T. Evan *et al*., *Geochem. Geophys. Geosyst.* **9**, Q05V04 (2008).
10. R. B. Husar, J. M. Prospero, L. L. Stowe, *J. Geophys. Res.* **102**, 16889 (1997).
11. A. S. Goudie, N. J. Middleton, *Earth Sci. Rev.* **56**, 179 (2001).
12. S. Engelstaedter, I. Tegen, R. Washington, *Earth Sci. Rev.* **79**, 73 (2006).
13. S. Engelstaedter, R. Washington, *Geophys. Res. Lett.* **34**, L15805 (2007).
14. J. M. Prospero, P. J. Lamb, *Science* **302**, 1024 (2003).
15. A. T. Evan, A. K. Heidinger, P. Knippertz, *J. Geophys. Res.* **111**, D12210 (2006).
16. C. Moulin, C. E. Lambert, F. Dulac, U. Dayan, *Nature* **387**, 691 (1997).
17. L. L. Stowe, A. M. Ignatov, R. R. Singh, *J. Geophys. Res.* **102**, 16923 (1997).
18. M. Sato, J. E. Hansen, M. P. Mccormick, J. B. Pollack, *J. Geophys. Res.* **98**, 22987 (1993).
19. C. Deser, M. A. Alexander, M. S. Timlin, *J. Clim.* **16**, 57 (2003).
20. See supporting material on *Science* Online.
21. PATMOS-x data are available at http://cimss.ssec.wisc.edu/patmosx.
22. N. A. Rayner *et al*., *J. Geophys. Res.* **108**, 4407 (2003).
23. All reported significance levels are based on the two-tailed *t* score for the correlation coefficients.
24. G. R. Foltz, M. J. McPhaden, *Geophys. Res. Lett.* **33**, L19703 (2006).
25. G. R. Foltz, M. J. McPhaden, *J. Clim.* **21**, 5048 (2008).
26. J. P. Dunion, C. S. Marron, *J. Clim.* **21**, 5242 (2008).
27. Y. J. Kaufman, I. Koren, L. A. Remer, D. Rosenfeld, Y. Rudich, *Proc. Natl. Acad. Sci. U.S.A.* **102**, 11207 (2005).
28. P. Chang, R. Saravanan, L. Ji, G. C. Hegerl, *J. Clim.* **13**, 2195 (2000).
29. G. R. Foltz, M. J. McPhaden, *J. Clim.* **19**, 6122 (2006).
30. S. Wong, A. E. Dessler, N. M. Mahowald, P. R. Colarco, A. da Silva, *Geophys. Res. Lett.* **35**, L07812 (2008).
31. G. J. Holland, P. J. Webster, *Philos. Trans. R. Soc. London Ser. A* **365**, 2695 (2007).
32. G. A. Vecchi, B. J. Soden, *Nature* **450**, 1066 (2007).
33. N. M. Mahowald, C. Luo, *Geophys. Res. Lett.* **30**, 1903 (2003).

34. We thank three anonymous reviewers for their constructive comments. Supported by grants from NOAA/NESDIS/STAR and Risk Prediction Initiative. The views, opinions, and findings contained in this report are those of the authors and should not be construed as an official NOAA or U.S. government position, policy, or decision.

Supporting Online Material

www.sciencemag.org/cgi/content/full/1167404/DC1
Materials and Methods
Figs. S1 to S8
References

20 October 2008; accepted 11 March 2009
Published online 26 March 2009;
10.1126/science.1167404
Include this information when citing this paper.

UV Absorption Cross Sections of ClOOCl Are Consistent with Ozone Degradation Models

Hsueh-Ying Chen,[1]* Chien-Yu Lien,[1]* Wei-Yen Lin,[1,2] Yuan T. Lee,[1,2] Jim J. Lin[1,3]†

Recently, discrepancies in laboratory measurements of chlorine peroxide (ClOOCl) absorption cross sections have cast doubt on the validity of current photochemical models for stratospheric ozone degradation. Whereas previous ClOOCl absorption measurements all suffered from uncertainties due to absorption by impurities, we demonstrate here a method that uses mass-selected detection to circumvent such interference. The cross sections of ClOOCl were determined at two critical wavelengths (351 and 308 nanometers). Our results are sufficient to resolve the controversial issue originating from the ClOOCl laboratory cross sections and suggest that the highest laboratory estimates for atmospheric photolysis rates of ClOOCl, which best explain the field measurements via current chemical models, are reasonable.

After the discovery of the Antarctic ozone hole (*1*), scientists directed great effort toward studying the underlying chemical and photochemical processes. Until recently, the consensus was that the chemical processes that are responsible for the formation of the ozone hole were reasonably well understood (*2*). However, laboratory data on the ultraviolet absorption spectrum of chlorine peroxide (ClOOCl) published in 2007 by Pope *et al*. (*3*) cast doubt (*4*–*6*) on that understanding. The absorption cross sections measured by Pope *et al*. (*3*) at wavelengths longer than 300 nm ($\lambda > 300$ nm) are much smaller than previously accepted values (*7*). If these recent data are correct, the atmospheric photolysis rates of ClOOCl are much smaller than originally thought, and it would be impossible to produce enough Cl atoms to explain the observed ozone loss via any known chemical mechanisms. Moreover, atmospheric measurements of constituents such as ClO/ClOOCl could not be reconciled with the Pope *et al*. data (*3*), which raises questions (*4*–*6*) about the validity of either the laboratory measurements or model calculations, thus heightening the need for new laboratory studies to either confirm or refute those findings.

Among the major factors controlling ozone loss in the polar stratospheric vortices is the kinetics of the ClOOCl catalytic cycle, in which the photolysis rate of ClOOCl plays a key role (*2*, *5*, *8*). The ultraviolet absorption spectrum of ClOOCl shows a relatively strong and broad feature with a peak at ~245 nm and a long tail extending to 300 nm and longer wavelengths (*3*, *8*–*11*). Because ozone strongly absorbs and therefore depletes sunlight of $\lambda < 300$ nm, it is the

[1]Institute of Atomic and Molecular Sciences, Academia Sinica, Taipei 10617, Taiwan. [2]Department of Chemistry, National Taiwan University, Taipei 10617, Taiwan. [3]Department of Applied Chemistry, National Chiao Tung University, Hsinchu 30010, Taiwan.

*These authors contributed equally to this work.
†To whom correspondence should be addressed. E-mail: jimlin@gate.sinica.edu.tw

weak absorption of ClOOCl at $\lambda > 300$ nm that is responsible for its photodecomposition to Cl atoms. The Cl atoms react with O_3 to form O_2 + ClO; ClO can then dimerize to form ClOOCl again (*12*), thus catalytically converting O_3 to O_2. In this atmospherically relevant region of $\lambda > 300$ nm, however, it is difficult to accurately determine the small absorption cross sections of ClOOCl, and there are substantial discrepancies between different laboratory studies. These discrepancies in turn result in large uncertainties in the partitioning of Cl, ClO, and ClOOCl in the resulting ozone loss rate, and therefore in our basic understanding of ozone degradation chemistry.

A review of the literature on both ClOOCl synthesis (*12*–*17*) and its ultraviolet absorption spectrum (*3*, *8*–*11*) reveals that it is extremely difficult to prepare a pure ClOOCl sample at a high enough concentration for an absorption measurement in the gas phase. Except for the latest work by Pope *et al.* (*3*), all other spectroscopic studies (*8*–*11*) largely relied on mass balance to estimate the concentrations of absorbing species. The use of mass balance was based on spectral measurements of the reactants, products, and side products in the synthesis/absorption cell. Accurately estimating the concentrations of absorbing species is further hindered by spectral overlaps, uncertainties in reaction rate constants, and possible unknown side reactions.

Pope *et al.* (*3*) tried to go beyond the method of mass balance by purifying their sample with low-temperature trapping and evaporation. Unfortunately, a pure ClOOCl sample was still unobtainable. The authors then employed a functional fitting method to remove the absorbance of the impurity. They posited that the impurity in their experiments was exclusively Cl_2 and that two Gaussian-like functions could represent the ClOOCl spectrum. The relative weighting between the concentrations of Cl_2 and ClOOCl was obtained by means of least-squares fitting. This method would work best if the ClOOCl spectrum were very different from the Cl_2 spectrum; it becomes unreliable, however, if ClOOCl has a spectral component that is similar to Cl_2. Both the mass balance and functional fitting methods are quite complicated, and both have potential weaknesses. Such problems become worse for the long-wavelength region, in which the absorption cross sections of ClOOCl become diminishingly small.

Aware of the impurity problem, we designed an experimental approach in which instead of measuring the attenuation of a photon beam after an absorption cell, we formed a ClOOCl molecular beam and determined the photodissociation probability by measuring the decrease in beam intensity after laser irradiation. Under the condition that the number of photons greatly exceeds the number of molecules, an alternative form of Beer's law can be written as

$$\ln \frac{N_0}{N} = I\sigma\phi \qquad (1)$$

where N_0 and N are the numbers of the molecules before and after the laser irradiation, respectively; I is the laser fluence in number of photons per unit area; σ is the absorption cross section; and ϕ is the dissociation quantum yield. By precisely measuring the ratio of the molecules before and after laser irradiation, we can quantify the absorption cross section without knowing the absolute concentration. We used a mass spectrometer to detect the ClOOCl molecules with high selectivity. In general, this is a powerful method for measuring photodissociation cross sections of species that cannot be prepared in a pure form because the mass selection eliminates interference from most impurities.

Figure 1 shows the schematic setup. The ClOOCl sample is prepared in a pulsed effusive molecular beam and detected downstream with a mass detector at its parent mass. The mass detector (*18*) is equipped with an electron impact ionizer, a quadrupole mass filter, and a Daly-type ion counter. Before the mass detector, the molecular beam is intersected by a pulsed laser beam that photodissociates and thus depletes the ClOOCl molecules with a probability that is proportional to their absorption cross section. Equation 1 could be used to analyze the photodepletion signals and quantify the absorption cross section, but to do so would require knowledge of the absolute fluence distribution of the laser beam, which is difficult to measure precisely. In contrast, comparing the photodepletion signal of ClOOCl to that of a reference molecule only requires the ratio of the laser fluences (which can be more easily measured) to obtain the cross section ratio

$$\frac{[\sigma\phi]_{\mathrm{ClOOCl}}}{[\sigma\phi]_{\mathrm{ref}}} = \frac{I_{\mathrm{ref}}}{I_{\mathrm{ClOOCl}}} \frac{\ln(N/N_0)_{\mathrm{ClOOCl}}}{\ln(N/N_0)_{\mathrm{ref}}} \qquad (2)$$

With a known cross section of the reference molecule, the absolute cross section of ClOOCl can then be obtained.

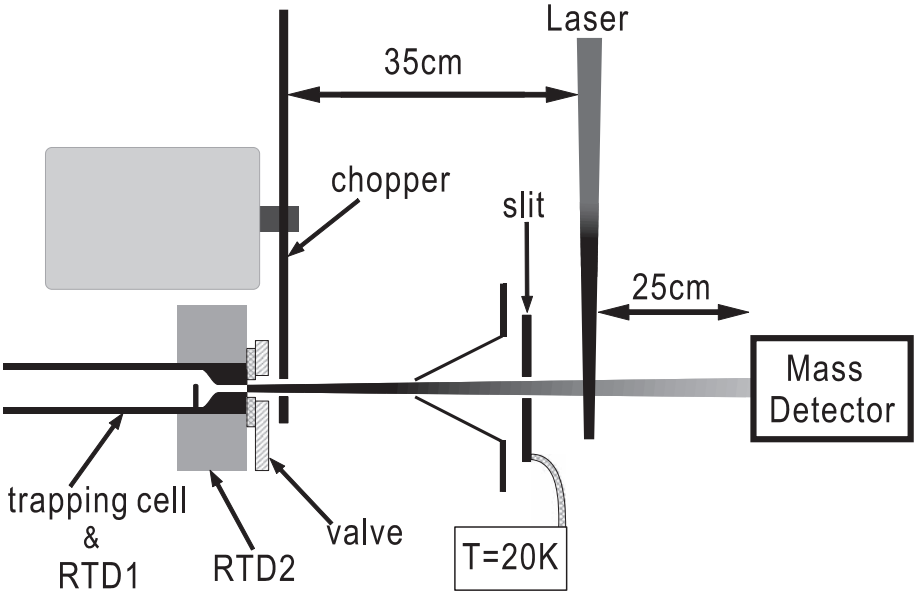

Fig. 1. Schematic of the experimental setup (not to scale). The exit of the trapping cell (fused silica) connects to a capillary array (fused silica) that serves as the nozzle of an effusive molecular beam. The temperatures are monitored with resistance temperature detectors (RTD1 and RTD2). The valve (stainless steel and Teflon) isolates the trapping cell from the vacuum chamber during the high pressure period of the ClOOCl condensation.

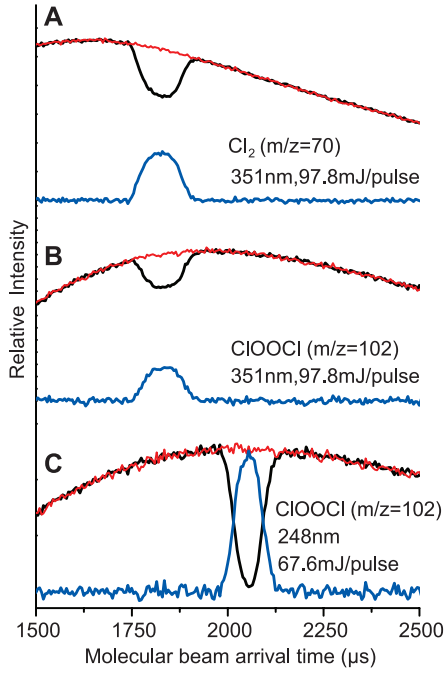

Fig. 2. Time profiles of the molecular beams showing the photodepletion of molecules. Black and red lines represent the molecular beam signals with and without laser irradiation, respectively; the blue line is the difference. The laser spot size and delay time are the same in (**A**) and (**B**) but different in (**C**). Therefore, the photo-depletion signal in (C) appears at a different time.

ClOOCl was synthesized by following the method 1 of Pope *et al.* (*3*) ($Cl_2 + h\nu \rightarrow 2Cl$; $Cl + O_3 \rightarrow ClO + O_2$; and $2ClO + M \rightarrow ClOOCl + M$) and trapped in a trapping cell at 150 K. Upon slowly warming up the trap, ClOOCl evaporated and flowed through a temperature-controlled capillary array to form an effusive molecular beam. The thermal velocity distribution of the molecules results in a broad distribution of arrival times for a given species in the molecular beam (Fig. 2).

The mass spectra of the ClOOCl sample in the molecular beam were fully consistent with those previously reported (*14*, *16*). The major impurities were Cl_2 and O_2; Cl_2O was observed in small amounts. Higher chlorine oxides such as Cl_2O_3 were not observed in the mass scans. Additional evidence regarding the ClOOCl sample purity can be found in a very recent work (*19*) that used the same synthesis method and confirmed the purity of the sample by means of both infrared and Raman spectroscopy.

Figure 2, A and B, shows the photodepletion signals of Cl_2 and ClOOCl upon 351 nm irradiation at the same laser fluence. At 351 nm, ClOOCl has a photodepletion signal smaller than Cl_2, indicating a smaller but still appreciable photodissociation cross section. Figure 2C shows the photodepletion signal of ClOOCl at 248 nm. Because the absorption cross section of ClOOCl at 248 nm is quite large, almost all molecules in the interaction volume have dissociated. For the cross section measurements, saturation effects were carefully checked at various laser fluences. The photodepletion signals of ClOOCl were not affected by different impurity levels at all, even for very large variations (>100 times) of the impurity concentrations.

To determine the absolute cross sections of ClOOCl, we chose Cl_2 as the reference molecule at 351 nm and both Cl_2O and Cl_2 at 308 nm. The absorption cross sections of these two reference molecules have been well measured (*7*, *20*). It is well known that the excited states of Cl_2 are all rapidly dissociative, leading to 100% dissociation ($\phi_{Cl_2} = 1$). A similar argument can be applied to ClOOCl, because ab initio calculations (*21*–*23*) and molecular beam experiments (*24*) all suggest a fast dissociation. The near-ultraviolet photodissociation of Cl_2O has been investigated in a molecular beam (*25*, *26*) and in a gas cell (*27*); the results also indicate a unity dissociation yield under low pressure conditions.

A summary of the cross section measurements is shown in Table 1. A check of consistency was possible at 308 nm because two reference molecules were available. The good agreement of the ClOOCl cross sections determined with two different reference molecules demonstrates the accuracy of this method (*28*). Furthermore, the photodissociation cross section ($\sigma\phi$) is in fact a more relevant quantity than the absorption cross section when estimating the atmospheric photolysis rate (*J* value).

Our results together with previously measured spectra are plotted in Fig. 3. At 308 nm, the value of DeMore *et al.* (*11*) and that recommended by the Jet Propulsion Laboratory (JPL) (*7*) are consistent with ours; Burkholder's value (*9*) is only slightly larger. Because the solar flux of $\lambda < 308$ nm is weak in the stratosphere, the cross section at 351 nm is a much more important factor in the atmospheric photolysis rates of ClOOCl, but previous laboratory data do not agree with each other in this region, as shown in Fig. 3. At 351 nm, the Burkholder cross section is consistent with ours at 200 K but slightly lower than our value at 250 K. Burkholder *et al.* noted only that their data were recorded over the temperature range of 205 to 250 K without mentioning any temperature dependence. Our data show that the temperature dependence of the ClOOCl cross sections at 351 nm is significant. Such temperature dependence may be attributed to the contributions of vibrational hot bands. Because ClOOCl has low-frequency vibrational modes, of which the lowest one is about 127 cm^{-1} (*29*), the populations of vibrational excited states are substantial even at temperatures around 200 K.

Von Hobe *et al.* (*5*, *6*) and others (*2*, *30*) have investigated the effects of using different laboratory values for ClOOCl absorption cross sections in the atmospheric modeling of ozone degradation, and they compared the numerical results with field measurements. Their conclusion is that most observations of ClO, ClOOCl, and ozone loss are best explained by the Burkholder 1990 cross sections (*9*) and that ClOOCl cross sections smaller than the JPL 2006 recommended values (*7*) cannot explain the field observations. Our results clearly indicate that, indeed, those smaller cross sections cannot be correct for $\lambda >$ 300 nm and that even the JPL 2006 recommendation slightly underestimates the cross sections at about 350 nm. The Burkholder cross sections are quite close to our results, suggesting that modeling using those cross sections at wavelengths in the atmospheric window ($\lambda > 300$ nm) should be realistic. The Burkholder cross sections and ours are the largest in the atmospheric window, leading to higher atmospheric photolysis rates of ClOOCl and suggesting the ClOOCl catalytic

Table 1. Summary of the measured photodissociation cross sections of ClOOCl.

Wavelength	Temperature*	Reference molecule (temperature)	$\frac{[\sigma\phi]_{ClOOCl}}{[\sigma\phi]_{ref}}$	σ_{ref} (10^{-20} cm^2)	$[\sigma\phi]_{ClOOCl}$ (10^{-20} cm^2)
351 nm	200 K	Cl_2 (200 K)	0.608 ± 0.027†	18.45	11.21‡
	250 K	Cl_2 (250 K)	0.687 ± 0.030	18.35	12.61
308 nm	200 K	Cl_2O (296 K)	1.116 ± 0.054	44.00	49.11
	200 K	Cl_2 (250 K)	2.829 ± 0.132	17.30	48.95
	250 K	Cl_2O (296 K)	1.154 ± 0.060	44.00	50.77
	250 K	Cl_2 (250 K)	2.953 ± 0.147	17.30	51.09

*Nozzle temperature of the ClOOCl effusive beam. †See the supporting online material for error analysis. ‡Assuming $\phi_{ref} = 1$.

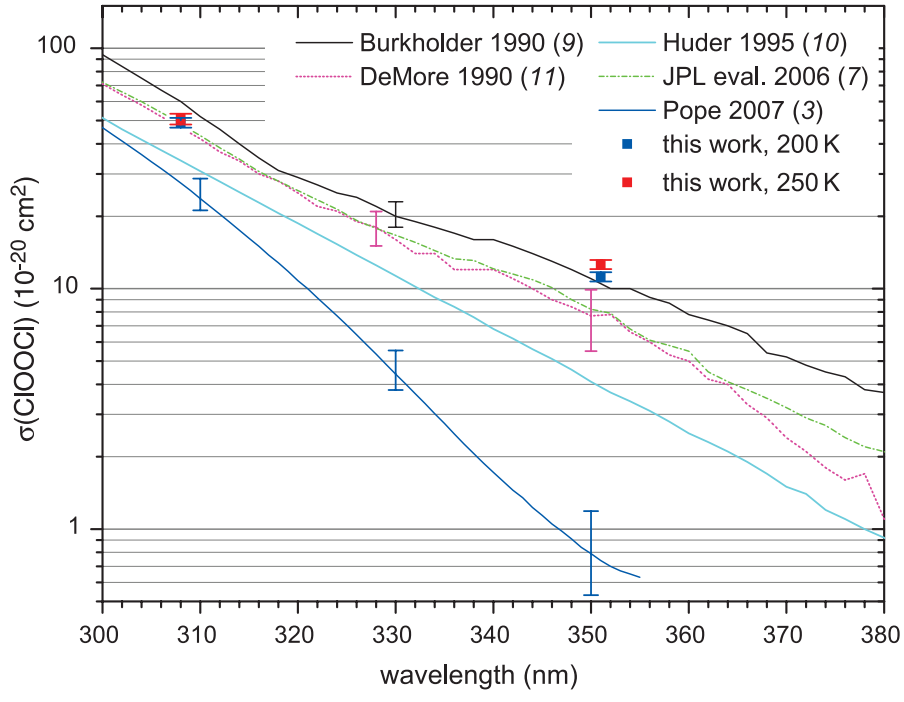

Fig. 3. Comparison of different laboratory measurements of absorption cross sections of ClOOCl. Error bars (if available) are also shown at selected wavelengths. The error bars of this work are about the size of the symbols.

cycle is an even more efficient process for polar ozone loss than previously thought (*2*). As for the Pope 2007 cross sections (*3*), it is likely that the authors' functional fitting method may overcorrect for the Cl_2 absorbance, resulting in cross sections that are too small in the wavelength region at which Cl_2 absorbs significantly (>300 nm).

Although at this point we can only report the cross sections of ClOOCl at two wavelengths because of our requirement of high-intensity lasers, these measurements are surely sufficient to resolve the discrepancies in the photolysis rates of ClOOCl and to restore confidence in standard photochemical models for ozone degradation. We have also demonstrated a promising method for measuring reliable laboratory cross sections of important species in atmospheric chemistry, free from interference by impurities.

References and Notes

1. J. C. Farman, B. G. Gardiner, J. D. Shanklin, *Nature* **315**, 207 (1985).
2. World Meteorological Organization (WMO), *Scientific Assessment of Ozone Depletion: 2006* (WMO, Geneva, Switzerland, 2007); http://ozone.unep.org/Assessment_Panels/SAP/Scientific_Assessment_2006.
3. F. D. Pope, J. C. Hansen, K. D. Bayes, R. R. Friedl, S. P. Sander, *J. Phys. Chem. A* **111**, 4322 (2007).
4. Q. Schiermeier, *Nature* **449**, 382 (2007).
5. M. von Hobe *et al*., *Atmos. Chem. Phys.* **7**, 3055 (2007).
6. M. von Hobe, *Science* **318**, 1878 (2007).
7. S. P. Sander *et al*., *Chemical Kinetics and Photochemical Data for Use in Atmospheric Studies 06-2* (Jet Propulsion Laboratory, Pasadena, CA, 2006).
8. R. A. Cox, G. D. Hayman, *Nature* **332**, 796 (1988).
9. J. B. Burkholder, J. J. Orlando, C. J. Howard, *J. Phys. Chem.* **94**, 687 (1990).
10. K. J. Huder, W. B. DeMore, *J. Phys. Chem.* **99**, 3905 (1995).
11. W. B. DeMore, E. Tschuikow-Roux, *J. Phys. Chem.* **94**, 5856 (1990).
12. L. T. Molina, M. J. Molina, *J. Phys. Chem.* **91**, 433 (1987).
13. W. J. Bloss, S. L. Nickolaisen, R. J. Salawitch, R. R. Friedl, S. P. Sander, *J. Phys. Chem. A* **105**, 11226 (2001).
14. J. R. McKeachie, M. F. Appel, U. Kirchner, R. N. Schindler, Th. Benter, *J. Phys. Chem. B* **108**, 16786 (2004).
15. J. Plenge *et al*., *J. Phys. Chem. A* **109**, 6730 (2005).
16. T. Ingham, S. P. Sander, R. R. Friedl, *Faraday Discuss.* **130**, 89 (2005).
17. R. Broske, F. Zabel, *J. Phys. Chem. A* **110**, 3280 (2006).
18. J. J. Lin, D. W. Hwang, S. Harich, Y. T. Lee, X. Yang, *Rev. Sci. Instrum.* **69**, 1642 (1998).
19. M. von Hobe, F. Stroh, H. Beckers, T. Benter, H. Willner, *Phys. Chem. Chem. Phys.* **11**, 1571 (2009).
20. C. L. Lin, *J. Chem. Eng. Data* **21**, 411 (1976).
21. A. L. Kaledin, K. Morokuma, *J. Chem. Phys.* **113**, 5750 (2000).
22. A. Toniolo, G. Granucci, S. Inglese, M. Persico, *Phys. Chem. Chem. Phys.* **3**, 4266 (2001).
23. K. A. Peterson, J. S. Francisco, *J. Chem. Phys.* **121**, 2611 (2004).
24. T. A. Moore, M. Okumura, J. W. Seale, T. K. Minton, *J. Phys. Chem. A* **103**, 1691 (1999).
25. R. Aures *et al*., *J. Chem. Phys.* **117**, 2141 (2002).
26. T. A. Moore, M. Okumura, T. K. Minton, *J. Chem. Phys.* **107**, 3337 (1997).
27. S. L. Nickolaisen *et al*., *J. Chem. Phys.* **104**, 2857 (1996).
28. Materials and methods are available as supporting material on *Science* Online.
29. M. Birk *et al*., *J. Chem. Phys.* **91**, 6588 (1989).
30. R. M. Stimpfle, D. M. Wilmouth, R. J. Salawitch, J. G. Anderson, *J. Geophys. Res.* **109**, D03301 (2004).

31. This work is supported by Academia Sinica and National Science Council (NSC 95-2113-M-001-041-MY3), Taiwan. We thank M.-C. Liang for bringing our attention to the ClOOCl issue and K. A. Boering and Y.-P. Lee for valuable comments.

Supporting Online Material

www.sciencemag.org/cgi/content/full/324/5928/781/DC1
Materials and Methods
Figs. S1 to S3
Table S1
References

23 January 2009; accepted 17 March 2009
10.1126/science.1171305

Host Inhibition of a Bacterial Virulence Effector Triggers Immunity to Infection

Vardis Ntoukakis, Tatiana S. Mucyn, Selena Gimenez-Ibanez, Helen C. Chapman, Jose R. Gutierrez, Alexi L. Balmuth, Alexandra M. E. Jones, John P. Rathjen*

Plant pathogenic bacteria secrete effector proteins that attack the host signaling machinery to suppress immunity. Effectors can be recognized by hosts leading to immunity. One such effector is AvrPtoB of *Pseudomonas syringae*, which degrades host protein kinases, such as tomato Fen, through an E3 ligase domain. Pto kinase, which is highly related to Fen, recognizes AvrPtoB in conjunction with the resistance protein Prf. Here we show that Pto is resistant to AvrPtoB-mediated degradation because it inactivates the E3 ligase domain. AvrPtoB ubiquitinated Fen within the catalytic cleft, leading to its breakdown and loss of the associated Prf protein. Pto avoids this by phosphorylating and inactivating the AvrPtoB E3 domain. Thus, inactivation of a pathogen virulence molecule is one mechanism by which plants resist disease.

The effector proteins of bacterial, fungal, and oomycete plant pathogens collectively determine pathogenicity on susceptible host species. However, resistance (R) proteins of the plant immune system can recognize these effectors and restrict pathogen growth. The largest class of R proteins is the nucleotide-binding site–plus–leucine-rich repeat (NB-LRR) class (*1*). Recognition of pathogen effectors by R proteins not only protects crops from pathogen attack, but also controls important immune responses in animals (*2*). Despite their importance, R proteins are poorly understood at a mechanistic level. *Pseudomonas syringae* pv. *tomato* DC3000 (*Pst* DC3000) is a pathogen of tomato and *Arabidopsis*, and it injects ~30 effectors into host cells (*3*). One of these effectors, AvrPtoB, degrades host protein kinases through ubiquitination and proteasomal degradation mediated by a C-terminal E3 ubiquitin ligase domain (*4*–*6*). AvrPtoB is widely conserved among diverse bacterial pathogens, including *Xanthomonas*, *Erwinia*, and many strains of *Pseudomonas* (*7*). One target of AvrPtoB is the tomato kinase Fen (*4*), which signals together with the NB-LRR resistance protein Prf. AvrPtoB mutants lacking ubiquitin ligase activity elicit a host immune response mediated by Fen/Prf, leading to defense gene induction and localized cell death known as the hypersensitive response. In resistant cultivars, AvrPtoB is recognized by a protein complex composed of Prf and the Pto kinase, which is highly related (80% identity) to Fen (*8*–*10*). The inability of AvrPtoB to degrade Pto underlies its recognition, but its molecular mechanism is not yet understood.

The Sainsbury Laboratory, Colney, Norwich NR4 7UH, UK.
*To whom correspondence should be addressed. E-mail: john.rathjen@tsl.ac.uk

One important difference between Pto and Fen is their relative kinase activities. Pto autophosphorylation activity in vitro was substantially higher than that of Fen (Fig. 1A), and Pto (but not Fen) was phosphorylated in vivo after transient expression in *Nicotiana benthamiana* leaves (fig. S1) (*11*). Fen was substantially less active than Pto in phosphorylating the in vitro substrate Pti1 (*12*) (fig. S2). While studying interactions between effector protein AvrPtoB and the host kinases, we found that both Pto and Fen were able to phosphorylate AvrPtoB (Fig. 1A). Again Pto was more active, with a Michaelis-Menton constant (K_m) of 2.2 μM compared with 10 μM for Fen. A kinase mutant, PtoD164N (*13*), did not autophosphorylate or transphosphorylate AvrPtoB in these assays. We mapped the phosphorylation site on AvrPtoB to Thr^{450} using mass spectrometry analysis, based on the series of y and b ions (Fig. 1B and fig. S3). This residue lies in the E3 ligase domain and is conserved among AvrPtoB homologs from different *P. syringae* strains (*14*).

Protein phosphorylation is important in the regulation of E3 ligases (*15*–*18*). To test the effect of phosphorylation on AvrPtoB E3 ligase activity, we analyzed autoubiquitination in the presence of Pto with the use of recombinant proteins. Increasing amounts of Pto decreased the levels of polyubiquitinated AvrPtoB (Fig. 2A). Similarly, Pto inhibited the trans-ubiquitination of Fen by AvrPtoB in vitro, in a dose-dependent manner (Fig. 2B). Conversely, Fen inhibited its own ubiquitination only when it was allowed to prephosphorylate AvrPtoB (fig. S4), consistent with its weaker kinase activity. Thus, the in vitro data suggest that ubiquitination and phosphorylation are competitive processes that determine the outcome of the AvrPtoB-Pto interaction. Substitution

mutants of Thr^{450} could not be phosphorylated by Pto or Fen (fig. S5) and displayed no E3 ligase activity in vitro (Fig. 2C and fig. S6). The phosphomimetic mutant, AvrPtoBT450D, caused cell death upon transient expression in *N. benthamiana* leaves, as described for other AvrPtoB E3 ligase mutants (*19*) (fig. S7). We next investigated whether AvrPtoBT450D was able to trigger immunity on susceptible tomatoes, like other E3 ligase mutants such as AvrPtoBF479A (*4*). In these experiments, we used the Rio Grande tomato line, which is resistant to *Pst* DC3000 infection, containing both *Pto* and *Prf* genes (RG-pto11) and two isogenic susceptible lines containing the *prf-3* (RG-prf3) or *pto-11* (RG *pto-11*) mutations (*20*). All lines carried the *Fen* gene. These plants were infected with a *Pst* DC3000 strain containing deletions in the *avrPto* and *avrPtoB* genes (*21*) expressing an empty vector control, *AvrPtoB*, or the E3 ligase mutants *AvrPtoBT450D* and *AvrPtoBF479A* (Fig. 2D). Whereas all bacterial strains grew to similar levels on the line lacking *Prf*, only the vector control grew on the resistant line, indicating that the Pto/Prf complex recognized AvrPtoB and its mutant forms. Growth of bacteria expressing *AvrPtoBT450D* or *AvrPtoBF479A*, but not wild-type (WT) AvrPtoB, was severely restricted on the line containing the *pto-11* mutation, indicating that the mutants were recognized by Fen (*4*). Thus, the host kinase Pto probably abrogates the ubiquitination activity of AvrPtoB by phosphorylating it within the E3 ligase domain.

To further investigate this, we mapped AvrPtoB-dependent ubiquitination sites on Fen generated in vitro. We identified one ubiquitinated peptide, DVK164CTNILLDENFVPK (*22*) (fig. S8). A Lys^{164} substitution mutant, FenK164R, was not polyubiquitinated by AvrPtoB, either in vitro or in vivo, in the presence of the proteasome inhibitor MG132 (Fig. 3, A and B). This residue is invariant in protein kinases and contributes to the mechanism of catalytic phosphotransfer (*23*); thus, AvrPtoB may target this residue generally to inactivate host protein kinases. The greater kinase activity of Pto relative to Fen may explain its ability to resist ubiquitination by AvrPtoB. To test this possibility, we examined the ubiquitination of the kinase mutant PtoD164N. Whereas both Fen (*4*) and PtoD164N were polyubiquitinated by AvrPtoB in vitro, WT Pto was not (Fig. 3A). Similarly in *N. benthamiana*, Fen and PtoD164N, but not WT Pto, were polyubiquitinated by AvrPtoB in the presence of MG132 (Fig. 3B) and degraded in its absence (fig. S9). These data suggest a mechanism in which Fen is polyubiquitinated by AvrPtoB within the catalytic cleft of the kinase, leading to its proteasomal degradation, whereas Pto avoids this by phosphorylating and inhibiting the E3 ligase domain of AvrPtoB.

Pto resides in a constitutive molecular complex with the resistance protein Prf (*9*), and Prf was unstable in the absence of Pto homologs because of proteasomal degradation (fig. S10). We tested to determine whether Fen degradation induced by AvrPtoB diminished Prf levels. Resistant tomatoes expressing *Pto*, *Fen*, and *Prf* or an isogenic susceptible line containing the *pto-11* mutation were infected with *Pst* DC3000 or a deletion mutant lacking the *avrPtoB* gene (*21*). No loss of Prf was visible in the tomato line containing *Pto*. In contrast, there was a severe decrease of Prf levels in the line lacking *Pto*, in the presence but not absence of *AvrPtoB* (Fig. 4A). To further test if AvrPtoB degrades Prf in a proteasome-dependent manner, we used stable transgenic *N. benthamiana* lines expressing the tomato *Prf* and/or *Pto* genes (*24*). Transient expression of *AvrPtoB* resulted in Prf degradation,

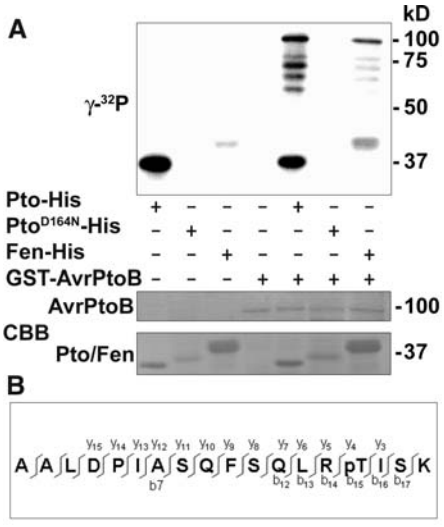

Fig. 1. Pto phosphorylates AvrPtoB within the E3 ligase domain. (**A**) Kinase activity assay showing Pto and Fen autophosphorylation and transphosphorylation of AvrPtoB. The assays were conducted as described previously (*26*) on purified proteins, as indicated. Proteins were fractionated on SDS–polyacrylamide gel electrophoresis before transfer to polyvinylidene difluoride membranes for autoradiography. (**B**). Liquid chromatography–mass spectrometry analysis of phosphorylated AvrPtoB identified peptide A436ALDPIASQFSQLRTISK. The fragmentation pattern is presented, possible cleavages are indicated by vertical bars, and observed b and y ions are numbered. Full spectra are presented in fig. S3.

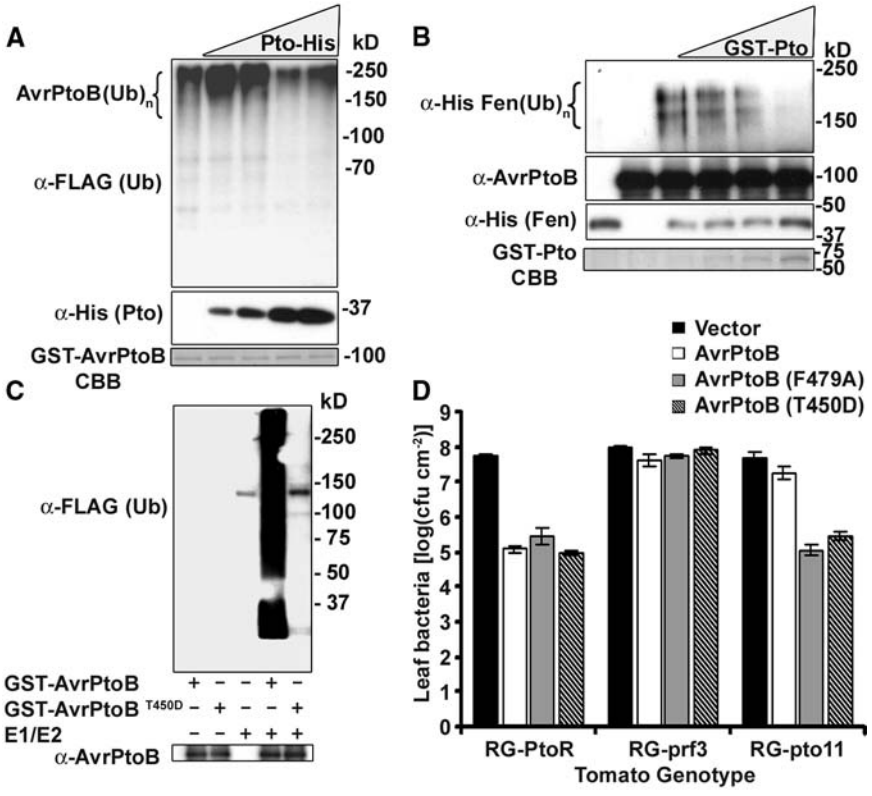

Fig. 2. Phosphorylation of AvrPtoB by Pto inhibits its E3 ligase activity. (**A**) Effector protein AvrPtoB autoubiquitination assay with increasing amounts of host kinase Pto, analyzed by immunoblot. (**B**) Ubiquitination assay of Fen kinase by AvrPtoB with increasing amounts of Pto, analyzed by immunoblot. (**C**) In vitro ubiquitination assay consisting of ubiquitination reaction mixture with FLAG-Ub, containing glutathione *S*-transferase (GST)–AvrPtoB or GST-AvrPtoBT450D as indicated. Proteins were analyzed by immunoblot. (**D**) Bacterial growth on tomato leaves infected with a *Pst* DC3000 strain containing deletions in the *avrPto* and *avrPtoB* genes, expressing an empty vector control, *AvrPtoB*, the phosphomimetic mutant *AvrPtoBT450D*, or the E2-binding mutant *AvrPtoBF479A*. The bars represent bacterial growth after three days of infection. At 0 days, the bacterial leaf titer was uniformly ~3.0 log [colony-forming units (cfu) cm^{-2}] for all treatments. Data represent two independent replicate experiments and error bars ± SE (n = 4 samples).

dependent on proteasome function and the E3 ligase activity of AvrPtoB (Fig. 4B). Similar to the tomato experiments, Pto protected Prf from AvrPtoB-mediated degradation. Both Prf and PtoD164N were degraded in the presence of AvrPtoB (fig. S11). Thus, Prf loss was attributable to instability of the associated kinase, and as such, Prf is an indirect target of the effector protein. We have not found evidence of direct interaction between Prf and AvrPtoB. The data suggest an indirect mechanism of degradation where the fate of the Prf complex depends on the activity of the specific kinase within the complex. The results above show a clear role for Pto kinase activity in AvrPtoB inactivation. Signaling by Pto is believed to be kinase-independent downstream of Pto activation (*13*, *25*). To test a role for Pto kinase activity beyond phosphorylation of AvrPtoB, we examined elicitation of immunity by an AvrPtoB E3 ligase mutant. In these experiments, AvrPtoBF479A was delivered by *P. syringae* pv. *tabaci* or *Agrobacterium* on transgenic *N. benthamiana* plants expressing both *PtoD164N* and *Prf*. The Pto kinase mutant was able to recognize the AvrPtoB E3 ligase mutant, leading to functional disease resistance and induction of cell death (Fig. 4C and fig. S12). Thus, in these experiments, Pto kinase activity was important only for inactivation of AvrPtoB E3 ligase activity.

Plant immunity against bacteria relies on recognition of bacterial effectors by R proteins. In many cases, R proteins are organized into protein complexes capable of recognizing the effectors and activating signal transduction (*1*). Our results demonstrate a mechanism in which the bacteria inject an effector into the plant cell to target the stability of a resistance complex, among other known targets (*5*, *6*). The outcome of the interaction depends on competition between the phosphorylation and ubiquitination events mediated by the host kinase and bacterial effector, respectively. Pto represents a host variant molecule with higher kinase activity and, hence, the ability to fight back against the effector. Phosphorylation of AvrPtoB restores the normal function of effector recognition. Overall, this study describes host enzymatic inactivation of a bacterial virulence effector to confer immunity.

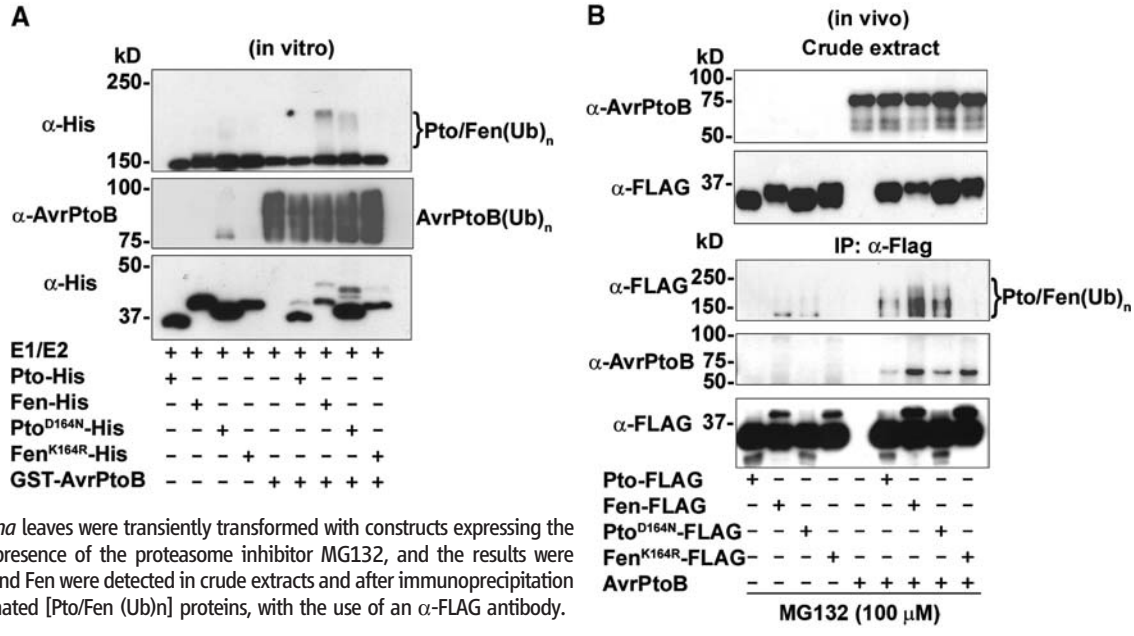

Fig. 3. Ubiquitination of Fen and Pto by AvrPtoB. (**A**) In vitro assays performed with ubiquitination reaction mixture and the indicated His-tagged fusions proteins. Pto and Fen were detected as polyubiquitinated [Pto/Fen (Ub)n], oligoubiquitinated, or unmodified proteins, with an α-His antibody. PtoD164N is a kinase-deficient mutant; FenK164R contains a substitution in an in vitro ubiquitinated residue. Polyubiquitinated forms of AvrPtoB [AvrPtoB (Ub)n] were detected with α-AvrPtoB antisera. (**B**) Ubiquitination of Fen and PtoD164N by AvrPtoB in vivo. *N. benthamiana* leaves were transiently transformed with constructs expressing the proteins as indicated, in the presence of the proteasome inhibitor MG132, and the results were analyzed by immunoblot. Pto and Fen were detected in crude extracts and after immunoprecipitation as unmodified or polyubiquitinated [Pto/Fen (Ub)n] proteins, with the use of an α-FLAG antibody.

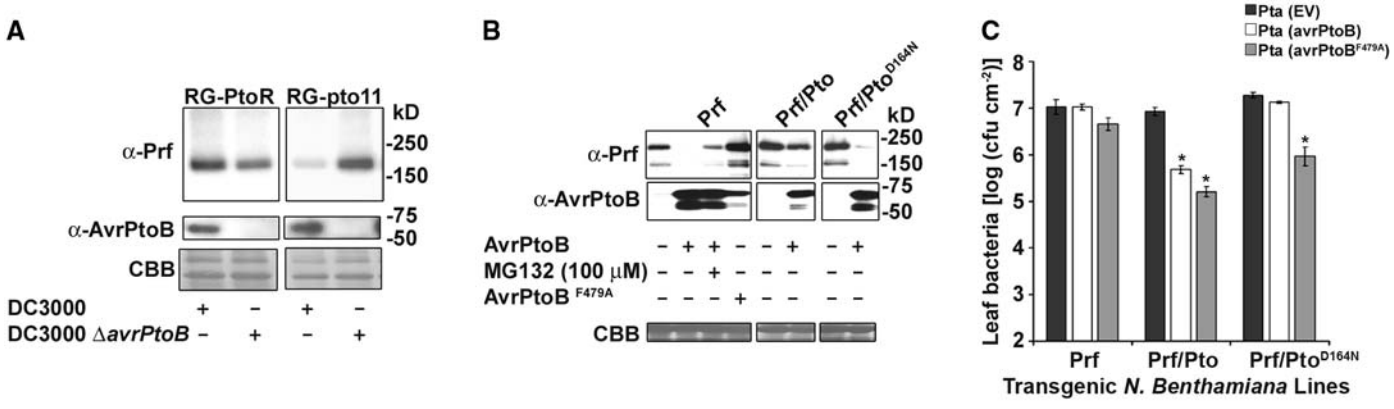

Fig. 4. AvrPtoB targets the Prf signaling complex for degradation. (**A**) Immunoblot of Prf levels in tomato leaves containing *Pto* (RG-PtoR) or lacking *Pto* (RG-pto11) after bacterial infection with *Pst* DC3000 or a deletion mutant Pst DC3000*ΔavrPtoB* lacking the *AvrPtoB* gene. Coomassie brilliant blue (CBB) staining of the membrane confirmed equal gel loading. (**B**) Prf degradation by AvrPtoB is proteasome-mediated and suppressed by the kinase activity of Pto. Stable transgenic *N. benthamiana* lines expressing tomato *Prf* only, *Prf* and *Pto*, or *Prf* and *PtoD164N* genes were transiently transformed with 35S:*AvrPtoB* or 35S:*AvrPtoBF479A* as indicated, in the presence or absence of the proteasome inhibitor MG132, and they were analyzed by immunoblot. CBB staining of the membrane confirmed equal gel loading. (**C**) Bar chart of bacterial growth of *P. syringae* pv. *tabaci* (*Pta*) 11528 bacteria expressing either empty vector (EV), *AvrPtoB*, or *AvrPtoBF479A* after 6 days of infection on the stable transgenic lines from (B). At 0 days, the bacterial leaf titer was uniformly ~1.0 log (cfu cm^{-2}) for all treatments. Data represent two independent replicate experiments. Asterisks indicate significant ($P < 0.01$) reduction in bacterial growth and error bars ± SE ($n = 4$).

References and Notes

1. J. L. Dangl, J. D. G. Jones, *Nature* **411**, 826 (2001).
2. W. Strober, P. J. Murray, A. Kitani, T. Watanabe, *Nat. Rev. Immunol.* **6**, 9 (2006).
3. L. M. Schechter *et al.*, *Mol. Plant-Microbe Interact.* **19**, 1180 (2006).
4. T. R. Rosebrock *et al.*, *Nature* **448**, 370 (2007).
5. V. Gohre *et al.*, *Curr. Biol.* **18**, 1824 (2008).
6. S. Gimenez-Ibanez *et al.*, *Curr. Biol.* **19**, 423 (2009).
7. R. B. Abramovitch, Y.-J. Kim, S. Chen, M. B. Dickman, G. B. Martin, *EMBO J.* **22**, 60 (2003).
8. R. B. Abramovitch, G. B. Martin, *FEMS Microbiol. Lett.* **245**, 1 (2005).
9. T. S. Mucyn *et al.*, *Plant Cell* **18**, 2792 (2006).
10. R. Janjusevic, R. B. Abramovitch, G. B. Martin, C. E. Stebbins, *Science* **311**, 222 (2006); 21 December 2005 (10.1126/science.1120131).
11. Materials and methods are available as supporting material on *Science* Online.
12. J. Zhou, Y.-T. Loh, R. A. Bressan, G. B. Martin, *Cell* **83**, 925 (1995).
13. A.-J. Wu, V. M. E. Andriotis, M. C. Durrant, J. P. Rathjen, *Plant Cell* **16**, 2809 (2004).
14. N. C. Lin, R. B. Abramovitch, Y. J. Kim, G. B. Martin, *Appl. Environ. Microbiol.* **72**, 702 (2006).
15. R. Kulikov, K. A. Boehme, C. Blattner, *Mol. Cell. Biol.* **25**, 7170 (2005).
16. C. Yang *et al.*, *Mol. Cell* **21**, 135 (2006).
17. M. Gao *et al.*, *Science* **306**, 271 (2004); published online 9 September 2004 (10.1126/science.1099414).
18. K. Tatematsu, N. Yoshimoto, T. Okajima, K. Tanizawa, S. Kuroda, *J. Biol. Chem.* **283**, 11575 (2008).
19. R. B. Abramovitch, R. Janjusevic, C. E. Stebbins, G. B. Martin, *Proc. Natl. Acad. Sci. U.S.A.* **103**, 2851 (2006).
20. J. M. Salmeron, S. J. Barker, F. M. Carland, A. Y. Mehta, B. J. Staskawicz, *Plant Cell* **6**, 511 (1994).
21. N. C. Lin, G. B. Martin, *Mol. Plant-Microbe Interact.* **18**, 43 (2005).
22. Single-letter abbreviations for the amino acid residues are as follows: A, Ala; C, Cys; D, Asp; E, Glu; F, Phe; G, Gly; H, His; I, Ile; K, Lys; L, Leu; M, Met; N, Asn; P, Pro; Q, Gln; R, Arg; S, Ser; T, Thr; V, Val; W, Trp; and Y, Tyr.
23. M. Huse, J. Kuriyan, *Cell* **109**, 275 (2002).
24. A. Balmuth, J. P. Rathjen, *Plant J.* **51**, 978 (2007).
25. W. Xing *et al.*, *Nature* **449**, 243 (2007).
26. V. M. Andriotis, J. P. Rathjen, *J. Biol. Chem.* **281**, 26578 (2006).

27. We thank L. Serazetdinova for help with mass spectroscopy and G. Martin (Cornell University) for bacterial strains and RG-pto11 mutant seeds. Part of this work was funded by a Biotechnology and Biological Science Research Council grant BB/D00456X/1 to J.P.R. We gratefully acknowledge the support of the Gatsby Charitable foundation.

Supporting Online Material

www.sciencemag.org/cgi/content/full/324/5928/784/DC1
Materials and Methods
Figs. S1 to S12
References

5 December 2008; accepted 24 February 2009
10.1126/science.1169430

Development of a Second-Generation Antiandrogen for Treatment of Advanced Prostate Cancer

Chris Tran,[1*] Samedy Ouk,[5*] Nicola J. Clegg,[1] Yu Chen,[1,3] Philip A. Watson,[1] Vivek Arora,[1] John Wongvipat,[1] Peter M. Smith-Jones,[2] Dongwon Yoo,[5] Andrew Kwon,[1] Teresa Wasielewska,[1] Derek Welsbie,[6] Charlie Degui Chen,[6]† Celestia S. Higano,[7] Tomasz M. Beer,[8] David T. Hung,[9] Howard I. Scher,[3] Michael E. Jung,[5]‡ Charles L. Sawyers[1,4]‡

Metastatic prostate cancer is treated with drugs that antagonize androgen action, but most patients progress to a more aggressive form of the disease called castration-resistant prostate cancer, driven by elevated expression of the androgen receptor. Here we characterize the diarylthiohydantoins RD162 and MDV3100, two compounds optimized from a screen for nonsteroidal antiandrogens that retain activity in the setting of increased androgen receptor expression. Both compounds bind to the androgen receptor with greater relative affinity than the clinically used antiandrogen bicalutamide, reduce the efficiency of its nuclear translocation, and impair both DNA binding to androgen response elements and recruitment of coactivators. RD162 and MDV3100 are orally available and induce tumor regression in mouse models of castration-resistant human prostate cancer. Of the first 30 patients treated with MDV3100 in a Phase I/II clinical trial, 13 of 30 (43%) showed sustained declines (by >50%) in serum concentrations of prostate-specific antigen, a biomarker of prostate cancer. These compounds thus appear to be promising candidates for treatment of advanced prostate cancer.

Treatment of advanced prostate cancer is limited by the development of resistance to antiandrogen therapy. Castration-resistant prostate cancer (CRPC) is commonly associated with increased androgen receptor (AR) gene expression, which can occur through AR gene amplification or other mechanisms (*1*, *2*). Elevated AR expression is necessary and sufficient to confer resistance to antiandrogen therapy in mouse xenograft models (*3*). In addition, first-generation AR antagonists such as bicalutamide (also called Casodex) or flutamide demonstrate agonist properties in cells engineered to express higher AR amounts. The partial agonism of these compounds is a potential liability, best illustrated clinically by the antiandrogen withdrawal response in which serum concentrations of prostate-specific antigen (PSA) decline in patients after discontinuation of either of these AR antagonists (*4*). Collectively, these findings implicate increased AR expression as a molecular cause of drug resistance and suggest that second-generation antiandrogens might be identified by their ability to retain antagonism in cells expressing excess AR.

Our earlier mutagenesis studies revealed that increased AR expression conferred resistance to antiandrogens in model systems only when the receptor contains a functional ligand binding domain (LBD) (*3*). Second-generation antiandrogens could, in theory, be optimized to exploit this well-characterized LBD. Co-crystal structures of wild-type AR bound to antagonists have not been solved, but a co-crystal of bicalutamide with mutant AR (in an agonist conformation), together with structural knowledge of estrogen receptor–α (ER-α) antagonists (*5*), suggests a steric clash mechanism in which the bulky phenyl ring on bicalutamide leads to a partial unfolding of AR (*6*). However, bicalutamide has relatively low affinity for AR [at least 30-fold reduced relative to the natural ligand dihydrotestosterone (DHT)] (*7*), suggesting that antagonism could be optimized by improved binding characteristics.

To search for improved antiandrogens, we selected the nonsteroidal agonist RU59063 as a starting chemical scaffold on the basis of its relatively high affinity for AR (only threefold reduced compared to testosterone) and selectivity for AR over other nuclear hormone receptors (*8*, *9*). Through an iterative process to be described in detail separately (see also U.S. Patent Application 20070004753), we evaluated nearly 200 thiohydantoin derivatives of RU59063 for AR agonism and antagonism in human prostate cancer cells engineered to express increased amounts of AR. On the basis of these structure-activity relationships and further chemical modifications to improve serum

[1]Human Oncology and Pathogenesis Program, Memorial Sloan-Kettering Cancer Center, New York, NY 10065, USA. [2]Department of Radiology, Memorial Sloan-Kettering Cancer Center, New York, NY 10065, USA. [3]Genitourinary Oncology Service, Division of Solid Tumor Oncology and Sidney Kimmel Center for Prostate and Urologic Cancers, Memorial Sloan-Kettering Cancer Center, New York, NY 10065, USA. [4]Howard Hughes Medical Institute, Memorial Sloan-Kettering Cancer Center, New York, NY 10065, USA. [5]Department of Chemistry and Biochemistry, University of California Los Angeles, Los Angeles, CA 90095, USA. [6]Molecular Biology Institute, University of California Los Angeles, Los Angeles, CA 90095, USA. [7]Division of Oncology, Departments of Medicine and Urology, University of Washington, Fred Hutchinson Cancer Center, Seattle, WA 98109, USA. [8]OHSU Knight Cancer Institute, Oregon Health and Science University, Portland, OR 97239, USA. [9]Medivation, Inc., 201 Spear Street, San Francisco, CA 94105, USA.

*These authors contributed equally to this work.
†Present address: State Key Laboratory of Molecular Biology, Institute of Biochemistry and Cell Biology, Shanghai Institutes for Biological Sciences, Chinese Academy of Sciences, Shanghai 200031, China.
‡To whom correspondence should be addressed. E-mail: sawyersc@mskcc.org; jung@chem.ucla.edu

half-life and oral bioavailability, the diarylthiohydantoins RD162 and MDV3100 were selected as the lead compounds for further biological studies (Fig. 1A). In a competition assay with 16β-[^{18}F]fluoro-5α-DHT (18-FDHT) to measure relative AR binding affinity (*10*), both RD162 and MDV3100 bound AR in castration-resistant LNCaP/AR human prostate cancer cells (engineered to express higher amounts of wild-type AR to mimic the clinical scenario) with five- to eightfold greater affinity than bicalutamide and only two- to threefold reduced affinity relative to the derivative of the native ligand FDHT (Fig. 1B). RD162 binding to AR was specific, as there was little to no binding to the progesterone, estrogen, or glucocorticoid receptors in an in vitro fluorescence polarization assay (table S1). We next compared the effects of RD162 and MDV3100 versus bicalutamide on androgen-dependent gene expression in LNCaP/AR cells. Expression of the AR target genes PSA and transmembrane serine protease 2 (TMPRSS2) was induced by bicalutamide but not by RD162 or MDV3100 (Fig. 1C), indicating that RD162 and MDV3100 do not have agonist activity in a castration-resistant setting. Both RD162 and MDV3100 antagonized induction of PSA and TMPRSS2 by the synthetic androgen R1881 in parental LNCaP cells (fig. S1). In the human prostate cancer cell line VCaP, which has endogenous AR gene amplification (*11*), RD162 and MDV3100 suppressed growth and induced apoptosis, whereas bicalutamide did not (Fig. 1, D and E). This growth suppression was reversed by cotreatment with the synthetic androgen R1881, which competes for AR binding (fig. S2A) and was not observed in the AR-negative DU145 human prostate cancer cells (fig. S2B). In addition, RD162 and MDV3100 inhibited the transcriptional activity of a mutant AR protein (W741C, mutation of Trp^{741} to Cys) isolated from a patient with acquired resistance to bicalutamide (fig. S3). The W741C substitution in the AR LBD causes bicalutamide to act as a pure agonist (*12*).

To evaluate the activity of RD162 in vivo, we first determined its pharmacokinetic properties in mice. RD162 was ~50% bioavailable after oral delivery with a serum half-life of about 30 hours (Fig. 2A and table S2A). Trough concentrations observed 24 hours after a single 20 mg/kg oral dose (~23 μM) exceeded concentrations expected to block AR activity based on the in vitro studies (~1 to 10 μM). We evaluated the pharmacodynamic effects of RD162 on AR function in vivo by measuring luciferase activity of human LNCaP/AR xenografts grown in castrated male mice. These tumors coexpressed exogenous AR and the AR-dependent reporter construct ARR2-Pb-Luc (*13*). Luciferase activity was consistently reduced relative to vehicle control in mice treated for 5 days with 10 mg/kg RD162 daily by oral gavage (Fig. 2B), whereas lower doses of 0.1 and 1.0 mg/kg daily had minimal effect (fig. S4A). Commensurate with reduced AR transcriptional function, cellular proliferation of LNCaP/AR xenografts as measured by KI-67 staining was substantially reduced after 5 days of RD162 treatment (fig. S4B).

To assess the therapeutic activity of RD162 in CRPC, we measured the effect of daily 10 mg/kg oral RD162 treatment on established LNCaP/AR tumors growing in castrate male mice. After 28 days of treatment, 11 of 12 tumors in vehicle-treated mice increased in size by ~2- to 20-fold (Fig. 2C, yellow bars). Bicalutamide retains some activity in this model as one tumor regressed by 50% and four tumors did not change substantially in size (stable disease), but the remaining seven tumors progressed on treatment with an increase in tumor volume up to fivefold (Fig. 2C, red bars). Plasma concentrations of bicalutamide in all mice exceeded 25 μM (Fig. 2C, see *y* axis on right), which is well above concentrations typically achieved in patients (*14*). In contrast, all 12 tumors in the RD162-treated mice regressed: 9 tumors by more than 50% and three tumors that were no longer palpable

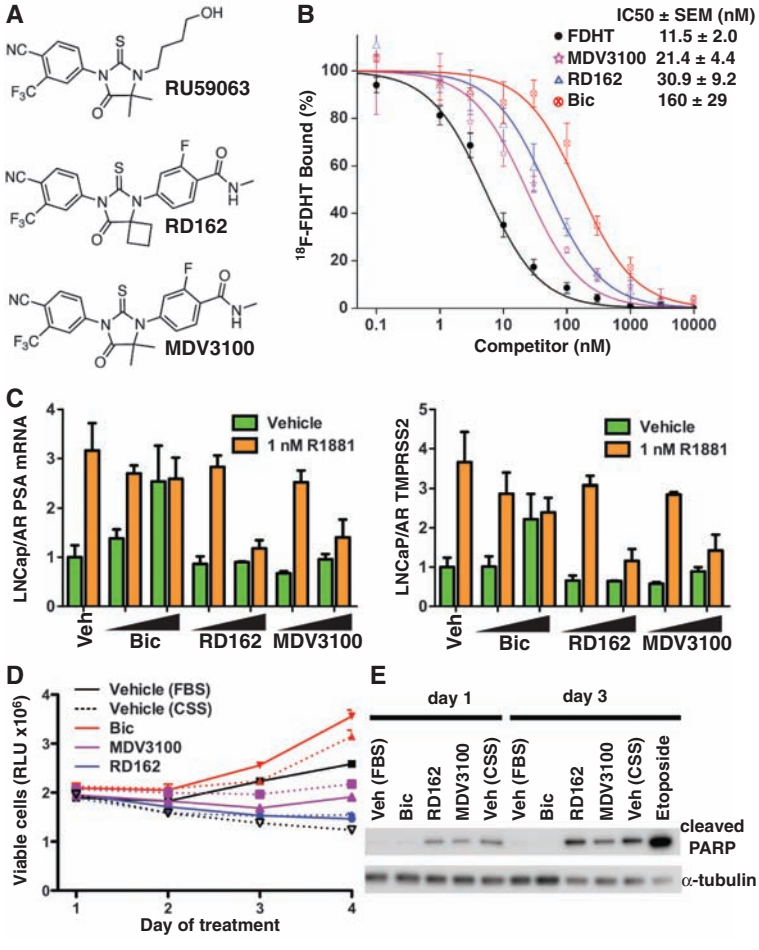

Fig. 1. Effect of RD162 and MDV3100 in human prostate cancer cells in vitro. (**A**) Chemical structures of the parent arylthiohydantoin scaffold compound RU59063 and the AR antagonists RD162 and MDV3100. (**B**) Representative competition binding curve showing inhibition of ^{18}F-FDHT equilibrium binding to AR by FDHT, RD162, MDV3100, and bicalutamide (Bic) in LNCaP/AR cells. The median inhibitory concentration (IC_{50}) values from this experiment were 5.1 nM (FDHT), 36 nM (MDV3100), 50 nM (RD162), and 159 nM (Bic) (error bars represent the SD of triplicate measurements). The inset shows the mean IC_{50} values (± SEM) from five replicate experiments. (**C**) Quantitative reverse transcription–polymerase chain reaction (qRT-PCR) analysis of the AR-dependent genes *PSA* and *TMPRSS2* in LNCaP/AR cells cultured in androgen-depleted media with 5% charcoal-stripped serum (CSS). Cells were treated for 8 hours with or without 1 nM of the synthetic androgen R1881 combined with dimethyl sulfoxide (DMSO) (Veh), bicalutamide (Bic, 1 and 10 μM), RD162 (1 and 10 μM), and MDV3100 (1 and 10 μM) (normalized to actin mRNA, mean ± SD, $n = 3$). (**D**) Effect of bicalutamide, RD162, or MDV3100 on cell proliferation. VCaP cells were treated with the indicated antiandrogen and concentration (dashed line: 1 μM; solid line: 10 μM) in media containing fetal bovine serum (FBS). Vehicle-treated cells were in media containing either FBS or CSS. The viable cell fraction was determined by CellTiter-GLO (n = 3, error is SEM). (**E**) Effect of bicalutamide, RD162, or MDV3100 on cleavage of poly(ADP-ribose) polymerase (PARP). VCaP cells were treated for 1 or 3 days with 10 μM antiandrogen in media containing FBS. Vehicle-treated cells were in media containing either FBS or CSS. Cells treated with 10 μM etoposide for 1 day served as a positive control for apoptosis. Whole-cell lysates were analyzed by Western blot.

(Fig. 2C, cyan bars). Median time to tumor progression in the RD162-treated group was 186 days versus 35 days in bicalutamide-treated mice (Fig. 2D). The superiority of RD162 over bicalutamide in this model is unlikely explained by pharmacokinetic properties because plasma concentrations of RD162 were somewhat lower (mean 24 μM) than those of bicalutamide (mean 40 μM) (Fig. 2C, see *y* axis on right). Furthermore, in vitro protein-binding studies revealed a modest increase in protein-bound RD162 and MDV3100 relative to bicalutamide (table S2B). Tumor responses were also observed with MDV3100 (fig. S5) and in castration-resistant LNCaP/HR xenografts derived by serial passage in castrate male mice (rather than by forced AR overexpression) as well as in a distinct castration-resistant xenograft model LAPC4/AR (fig. S6).

Two lines of evidence suggest that the activity of RD162 in these mice is mediated through AR inhibition rather than through off-target effects. First, antitumor activity in the LNCaP/AR model is dose-dependent, with some slowing of tumor growth at 0.1 mg/kg RD162 and a few tumor regressions at 1 mg/kg (fig. S7), correlating closely with the effect of these same doses on AR transcriptional activity in the luciferase imaging experiment (fig. S4A). Second, neither bicalutamide nor RD162 impaired the growth of AR-negative DU145 prostate cancer xenografts (fig. S8).

In considering mechanisms for the superiority of RD162 and MDV3100 over bicalutamide in these models, we examined potential effects on AR protein expression in vitro and found no obvious changes (fig. S9). Bicalutamide impairs AR transcriptional activity by promoting the assembly of transcription complexes that incorporate co-repressors such as NCoR and SMRT rather than coactivators such as SRC1 at the promoters of AR target genes (*15*, *16*). The partial agonism of bicalutamide revealed in the setting of increased AR expression is associated with AR recruitment to enhancer regions and aberrant recruitment of coactivators to these transcription complexes, leading to target gene activation rather than repression (*3*). Because RD162 and MDV3100 do not display agonism in AR-overexpressing cells (Fig. 1C), we explored whether they exert different effects on AR transcription complex assembly. In chromatin immunoprecipitation experiments, both R1881 and bicalutamide promoted AR recruitment to the PSA enhancer and TMPRSS2 enhancer in LNCaP/AR cells, whereas only R1881 promoted recruitment in parental LNCaP cells. Neither RD162 nor MDV3100 recruited AR to enhancer regions in either cell line (Fig. 3A and fig. S10). To test whether altered AR localization in RD162- or MDV3100-treated cells might explain this result, we visualized transfected AR-EYFP (enhanced yellow fluorescent protein) by confocal microscopy in live LNCaP cells. AR-EYFP was predominantly cytoplasmic in the absence of androgen but largely nuclear after treatment with R1881 or bicalutamide (Fig. 3B). The ratio of nuclear versus cytoplasmic AR in RD162- or MDV3100-treated cells was about fivefold reduced relative to bicalutamide. To determine whether the nuclear AR in RD162- or MDV3100-treated cells is competent for DNA binding, we used a VP16-AR fusion protein that activates an AR-dependent luciferase reporter. Due to the strong transactivation and nuclear localization properties provided by the VP16 domain, this AR construct is not dependent on ligand-induced conformational changes for nuclear localization or coactivator recruitment (*17*). As expected, wild-type AR was activated only by R1881 and not by the antiandrogens, whereas both R1881 and bicalutamide activated VP16-AR (Fig. 3C). In contrast, neither RD162 nor MDV3100 activated VP16-AR (Fig. 3C), providing further evidence that these compounds impair AR DNA binding.

First-generation nonsteroidal antiandrogens induce a conformational change in AR that, though distinct from that conferred by the natural ligands testosterone and DHT, remains competent to bind certain LxxLL or FxxLF motif–containing coactivator proteins. The interaction induced by this conformational change can be modeled in vitro and quantified by fluorescence resonance energy transfer (FRET) (*18*). DHT and bicalutamide both promoted dose-dependent interaction of the AR LBD with an FxxLF-containing peptide, whereas RD162 and MDV3100 did not (Fig. 3D). On the basis of the AR localization, DNA binding, and FxxLF peptide interaction studies, we hypothesize that RD162 and MDV3100 induce a conformational change in AR distinct from that induced by bicalutamide. Future crystallographic studies could provide further insight into its mechanism of action and guide efforts to develop additional antiandrogens.

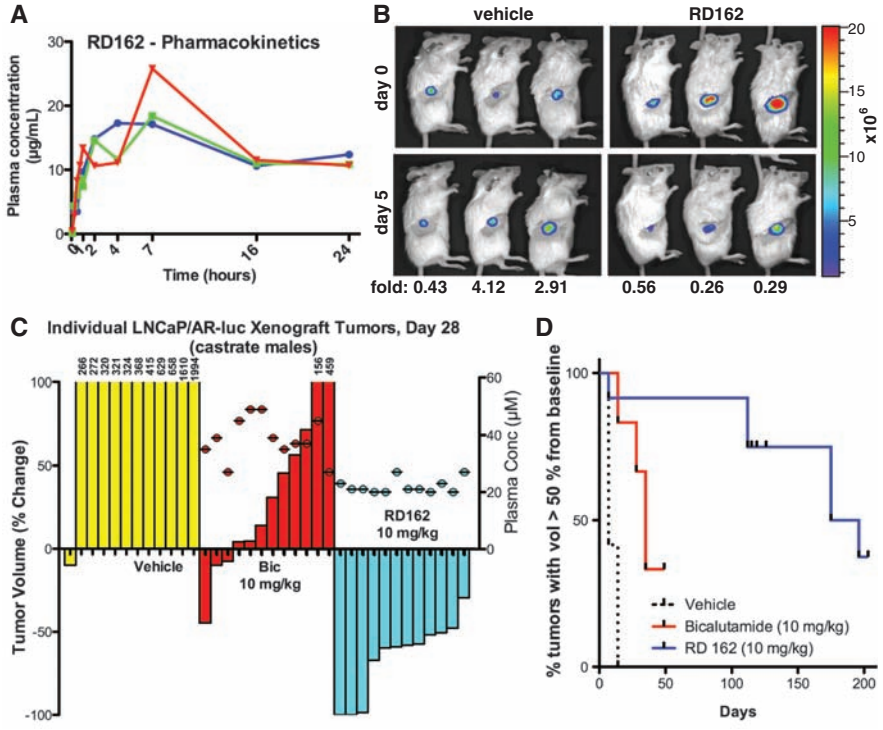

Fig. 2. Activity of RD162 in mice. (**A**) Pharmacokinetic analysis of RD162 in male mice (n = 3 per time point) dosed by oral gavage as a slurry of 20 mg/kg in 0.5% hydroxy-methyl-propyl-cellulose. (**B**) Pharmacodynamics of AR antagonism in castrate male mice after 5 days of treatment with daily oral RD162 (10 mg/kg) or vehicle control (n = 3 mice per treatment group). Antagonism was measured by luciferase imaging of LNCaP/AR xenograft tumors expressing a luciferase reporter construct driven by the promoter of the probasin gene, which is androgen regulated. Light emission at day 5 (2 hours after final dose) was quantified from a region of interest drawn over the tumors and normalized for each animal to light emission at day 0. Luciferase activity was quantified at day 5 (normalized for each animal to day 0 luciferase activity) and expressed as fold-change, as indicated for the individual mouse. Means ± SD: 2.5 ± 1.9 (vehicle), 0.4 ± 0.2 (RD162). (**C**) Effects of RD162 and bicalutamide in a xenograft model of CRPC. Castrate male mice bearing LNCaP/AR tumors > 100 mm^3 in size were treated by oral daily gavage with vehicle, bicalutamide (10 mg/kg), or RD162 (10 mg/kg). The percent change in volume for each tumor (12 tumors per treatment group) after 28 days is shown as a waterfall plot (*y* axis, left). Plasma concentrations of bicalutamide and RD162 for each mouse were measured 20 hours after the final dose on day 28 (filled circles above the waterfall plot; *y* axis, right). (**D**) Time to progression in mice continually treated as in (C). The percent change in volume for each tumor (12 tumors per treatment group) was assessed weekly. Events (tumor volume > 50% of baseline) were plotted on a Kaplan-Meier curve. Differences between all three groups were statistically significant: Bic versus R162 (P = 0.04), Bic versus Veh (P < 0.0001), RD162 versus Veh (P < 0.0001) by log-rank (Mantel-Cox) test.

Because of its activity in CRPC xenograft models and its favorable druglike properties, MDV3100 was selected for clinical development. In an ongoing Phase I/II clinical trial, 30 men with CRPC who have progressed on first-line antiandrogens, 12 of whom had also failed taxane-based chemotherapy (table S3, A and B), received either 30 mg (n = 3) or 60 mg (n = 27) of daily oral MDV3100. Twenty-two patients had a sustained decline in serum PSA concentrations for at least 12 weeks, which in 13 of these patients represented a PSA decrease of more than 50% (Fig. 4 and table S3C). MDV3100 was well tolerated, with 11 patients remaining on study longer than 25 weeks. All discontinuations at these doses were due to disease progression. Results from 110 additional patients who received MDV3100 at higher doses will be reported separately. Although preliminary, these clinical data appear promising and validate the persistent role of AR in driving castration-resistant disease.

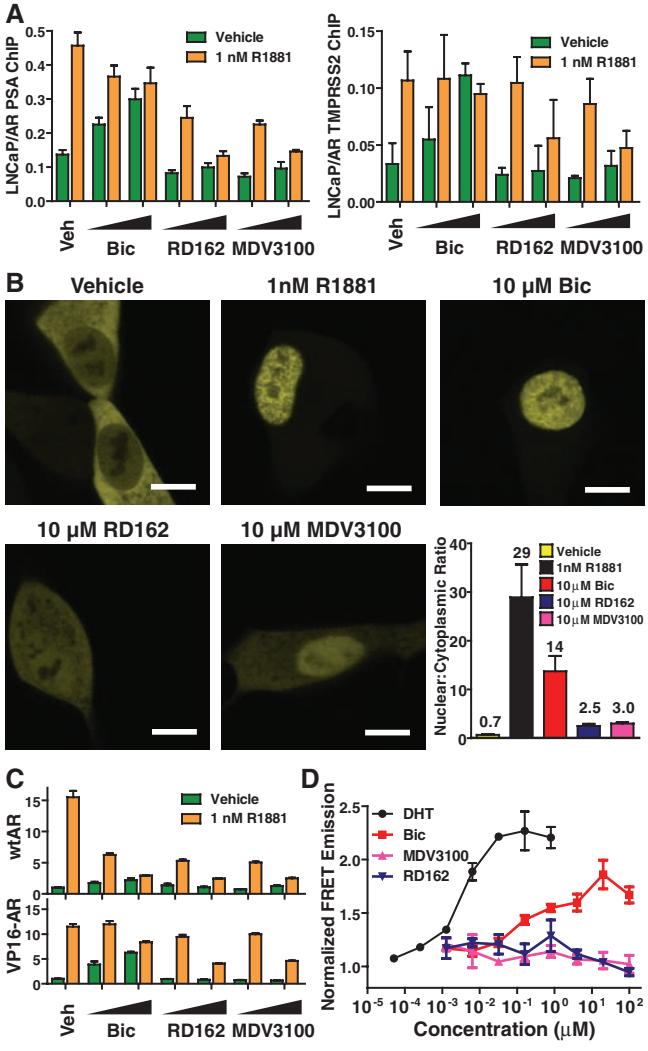

Fig. 3. RD162 and MDV3100 impair AR nuclear translocation, DNA binding, and coactivator peptide recruitment. (**A**) Chromatin immunoprecipitation analysis of AR in LNCaP cells. The cells were cultured in androgen-depleted media with 5% CSS and treated for 8 hours with or without 1 nM R1881 combined with DMSO (Veh), bicalutamide (Bic, 1 and 10 μM), RD162 (1 and 10 μM), and MDV3100 (1 and 10 μM). Real-time PCR quantification of immunoprecipitated *PSA* enhancer and *TMPRSS2* enhancer is shown (percent input mean ± SD, n = 3). (**B**) Representative confocal microscopic images (scale bars, 10 μm) of LNCaP cells transfected with AR-EYFP in androgen-depleted media with 5% CSS and treated with DMSO, 1 nM R1881, 10 μM bicalutamide, 10 μM RD162, or 10 μM MDV3100. The ratio of nuclear to cytoplasmic fluorescence intensity of individual cells was calculated (n = 3, mean ± SEM). (**C**) Activation of an androgen-regulated reporter gene by VP16-AR. Cos-7 cells were cotransfected with ARE(4x)-luciferase plasmid and either wild-type AR or VP16-AR fusion protein. Cells were treated for 24 hours with or without 1 nM R1881 combined with DMSO (Veh), bicalutamide (Bic, 1 and 10 μM), RD162 (1 and 10 μM), and MDV3100 (1 and 10 μM) for 24 hours. A luciferase assay was conducted with cell lysates, and relative light units shown (n = 3, mean ± SEM). (**D**) In vitro FRET analysis of the interaction between AR LBD and FxxLF coactivator peptide. Increasing concentrations of DHT, bicalutamide, RD162, or MDV3100 were incubated with purified AR LBD, terbium-labeled AR-specific antibody, and fluorescein-labeled AR FxxLF coactivator peptide (four replicates). FRET between terbium and fluorescein, indicative of binding of FxxLF peptide to AR-LBD, was measured by ratio of fluorescence emission at 525 nm (fluorescein emission) to 488 nm (terbium emission) after excitation at 322 nm (terbium excitation). Normalized ratio is plotted (mean of two experiments ±SEM).

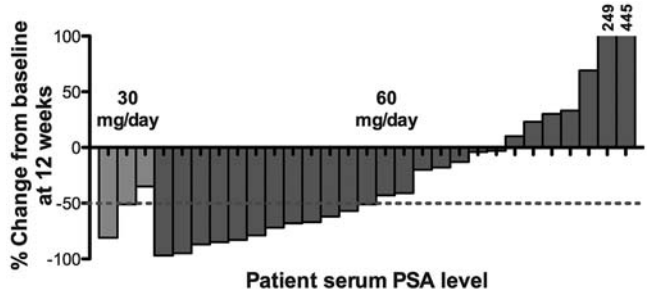

Fig. 4. PSA response data in the first 30 patients receiving MDV3100 in Phase I/II trial. Thirty men with CRPC were treated with oral daily MDV3100 at doses of 30 mg/day (n = 3) or 60 mg/day (n = 27). The percent change in serum PSA concentration for each patient after 12 weeks is shown as a waterfall plot. Patient 30's participation in the study ended before 12 weeks due to disease progression and is therefore not shown.

References and Notes

1. H. I. Scher, C. L. Sawyers, *J. Clin. Oncol.* **23**, 8253 (2005).
2. M. E. Taplin, S. P. Balk, *J. Cell. Biochem.* **91**, 483 (2004).
3. C. D. Chen *et al.*, *Nat. Med.* **10**, 33 (2004).
4. W. K. Kelly, S. Slovin, H. I. Scher, *Urol. Clin. North Am.* **24**, 421 (1997).
5. A. K. Shiau *et al.*, *Cell* **95**, 927 (1998).
6. C. E. Bohl, W. Gao, D. D. Miller, C. E. Bell, J. T. Dalton, *Proc. Natl. Acad. Sci. U.S.A.* **102**, 6201 (2005).
7. G. J. Kolvenbag, B. J. Furr, G. R. Blackledge, *Prostate Cancer Prostatic Dis.* **1**, 307 (1998).
8. G. Teutsch *et al.*, *J. Steroid Biochem. Mol. Biol.* **48**, 111 (1994).
9. M. E. Van Dort, D. M. Robins, B. Wayburn, *J. Med. Chem.* **43**, 3344 (2000).
10. S. M. Larson *et al.*, *J. Nucl. Med.* **45**, 366 (2004).
11. W. Liu *et al.*, *Neoplasia* **10**, 897 (2008).
12. T. Yoshida *et al.*, *Cancer Res.* **65**, 9611 (2005).
13. K. Ellwood-Yen, J. Wongvipat, C. Sawyers, *Cancer Res.* **66**, 10513 (2006).
14. I. D. Cockshott, K. J. Cooper, D. S. Sweetmore, N. J. Blacklock, L. Denis, *Eur. Urol.* **18** (suppl. 3), 10 (1990).
15. M. C. Hodgson *et al.*, *J. Biol. Chem.* **280**, 6511 (2005).
16. S. H. Baek *et al.*, *Proc. Natl. Acad. Sci. U.S.A.* **103**, 3100 (2006).
17. D. Masiello, S. Cheng, G. J. Bubley, M. L. Lu, S. P. Balk, *J. Biol. Chem.* **277**, 26321 (2002).
18. M. S. Ozers *et al.*, *Biochemistry* **46**, 683 (2007).

19. We thank S. Balk and M. Diamond for plasmids; E. De Stanchina, N. Wu, Q. Weige, and C. Wa for assistance with pharmacokinetic and serum protein binding studies; O. Ouerfelli, A. Dilhas, H. Zhao, and G. Yang for chemistry support; the Memorial Sloan-Kettering Cancer Center (MSKCC) molecular cytology core for immunohistochemistry; S. Cai, E. Burnazi, and the MSKCC Radiochemistry Core for ^{18}F-FDHT production; the MSKCC Small-Animal Imaging Core Facility; D. Liang for technical support; and D. Danila for helpful discussions. Funded in part by the Prostate Cancer Foundation, the National Cancer Institute, and U.S. Department of Defense PC051382 Prostate Cancer Research Program Clinical Consortium Award. N.J.C. is supported by the Charles H. Revson Foundation. Y.C. is supported by an American Society of Clinical Oncology Young Investigator Award and American Association for Cancer Research–Bristol-Myers Squibb Fellowship. C.L.S. is a Doris Duke Distinguished Clinical Scientist. C.T., S.O., J.W., D.Y., D.W., C.C., M.E.J., and C.L.S. are co-inventors on patent applications covering RD162, MDV3100, and related compounds. C.L.S. and M.J. have been paid consultants for and have stock options in Medivation, Inc. D.T.H. is an employee of Medivation, Inc.

Supporting Online Material

www.sciencemag.org/cgi/content/full/1168175/DC1
Materials and Methods
Figs. S1 to S10
Tables S1 to S3
References

6 November 2008; accepted 13 March 2009
Published online 9 April 2009;
10.1126/science.1168175
Include this information when citing this paper.

Basin-Scale Coherence in Phenology of Shrimps and Phytoplankton in the North Atlantic Ocean

P. Koeller,[1]* C. Fuentes-Yaco,[1,2] T. Platt,[1,3] S. Sathyendranath,[1,2,3] A. Richards,[4] P. Ouellet,[5] D. Orr,[6] U. Skúladóttir,[7] K. Wieland,[8] L. Savard,[5] M. Aschan[9]

Climate change could lead to mismatches between the reproductive cycles of marine organisms and their planktonic food. We tested this hypothesis by comparing shrimp (*Pandalus borealis*) egg hatching times and satellite-derived phytoplankton bloom dynamics throughout the North Atlantic. At large spatial and long temporal (10 years or longer) scales, hatching was correlated with the timing of the spring phytoplankton bloom. Annual egg development and hatching times were determined locally by bottom water temperature. We conclude that different populations of *P. borealis* have adapted to local temperatures and bloom timing, matching egg hatching to food availability under average conditions. This strategy is vulnerable to interannual oceanographic variability and long-term climatic changes.

During the early 1990s, populations of the northern shrimp (*Pandalus borealis*) increased to levels previously unobserved in the North Atlantic, resulting in the expansion of existing fisheries and the establishment of new ones (fig. S1). The shrimp population increases have been attributed to concurrent decreases in groundfish predators and to large-scale climatic changes (*1*–*8*). A link between spring sea surface temperatures (SSTs) and shrimp larval survival has been reported in the Gulf of St. Lawrence and the Gulf of Maine (*4*, *9*). Because SSTs also influence the onset and intensity of the spring phytoplankton bloom (*10*), the success of the shrimp hatch may be linked to the spring bloom. Until recently, we lacked the tools necessary to study the matter on a globally significant scale (*11*, *12*). We tested Cushing's hypothesis (*13*), that variability in year-class strength is at least partly due to matches or mismatches in the timings of larval release and the spring phytoplankton bloom, by comparing shrimp hatch dates and spring bloom timing at the scale of the North Atlantic basin. Specifically, we asked whether there is evidence that *P. borealis* has adapted its reproductive cycle to match hatching times with seasonal phytoplankton dynamics in different ecological regimes throughout its wide latitudinal range (42° to 80°N).

Characteristics of the spring bloom, particularly its timing, vary with latitude (*14*). It follows that if shrimp are to match hatch and bloom timing over a broad latitudinal band, there must be some local genetic or behavioral adaptation of their annual reproductive cycles. Furthermore, shrimp must adapt to local differences in bottom water temperatures, which are known to determine the duration of the summer-to-spring egg-bearing (development) period (*6*, *15*–*17*), and hence egg hatching times. Short-term oceanographic variability or long-term climatic changes might degrade the relationship between hatch and bloom (fig. S2).

We found average bottom temperatures correlated with the length of the egg development period throughout the North Atlantic Ocean (Fig. 1) (*18*). Two southern stocks (Gulf of Maine and Gulf of St. Lawrence) experienced the warmest temperatures (~6° and 5°C, respectively) and had the shortest egg development periods (~6 and 7 months), whereas two northern stocks (Northern Iceland and Svalbard) living at the coldest temperatures (~1° and 1.5°C) had the longest development periods (~10 and 19 months). Despite development times ranging between 6 and 10 months and spawning times differing by ≤3 months, in 6 of the 13 areas the mean times for 50% hatching and maximum chlorophyll concentrations differed by only a few days (Fig. 2A). Mean hatch and bloom initiation times for all stocks in the North Atlantic differed by less than a week. The timing of phytoplankton bloom and hatch north of 60°N are earlier than would be predicted by latitude alone, probably in part because of the strong influence of the annual melting of sea ice (*19*).

When hatching, bloom maximum, and spawning times were regressed separately against latitude, the third-order polynomial fits for hatching and bloom times were both significant and identical in shape (Fig. 2B). However, the regression between spawning times and latitude did not show a latitudinal pattern (fig. S3). Because the duration of the egg development period is dependent on bottom temperature, which has little influence on the timing of phytoplankton blooms, spawning times must have evolved according to local temperatures to make hatch and bloom times coincide.

Data from the Newfoundland shelf confirm that later hatchings are a direct result of longer egg development times (Fig. 3A). Because water temperatures determine the duration of the egg development period (Fig. 1), they also determine hatching times (Fig. 3B). During the early 1990s, when water temperatures were colder, egg hatching was later (Fig. 3C) and the Newfoundland stock increased markedly, as shown by the catch per unit of effort from commercial trawlers (Fig. 3D).

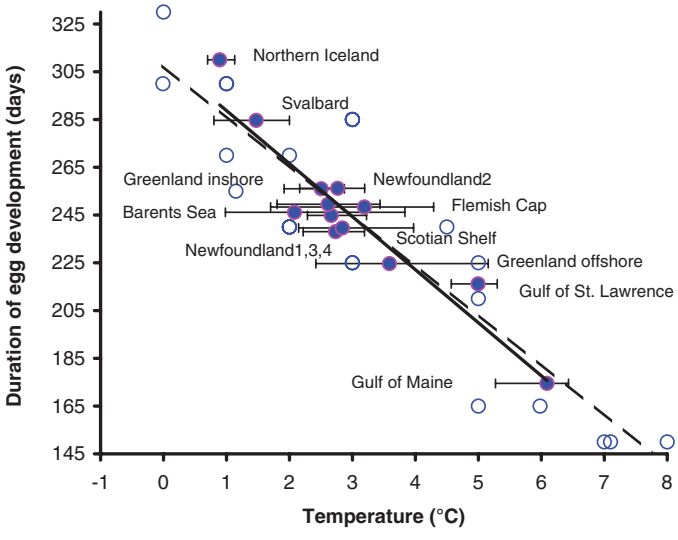

Fig. 1. Mean length of the egg-bearing (development) period versus ambient bottom temperatures in different areas. Solid circles and the solid regression line indicate data from this study; areas are identified. Bars show the range of annual mean temperatures for each shrimp survey data series. Open circles and dashed regression line indicate published data (*6*). Both regression lines from these independent studies are significant ($P < 0.01$), but they are not significantly different from each other.

[1]Department of Fisheries and Oceans, Bedford Institute of Oceanography, Post Office Box 1006, Dartmouth, B2Y 4A2 Nova Scotia, Canada. [2]Dalhousie University, Halifax, B3H 4R2 Nova Scotia, Canada. [3]Plymouth Marine Laboratory, Prospect Place, PL1 3 Plymouth, UK. [4]Northeast Fisheries Science Center, National Marine Fisheries Service, 166 Water Street, Woods Hole, MA 02543-1026, USA. [5]Pêches et Océans Canada, Institut Maurice-Lamontagne, 850 Route de la Mer, Caisse Postale 1000, Mont-Joli, G5H 3Z4 Québec, Canada. [6]Department of Fisheries and Oceans, Northwest Atlantic Fisheries Centre, Post Office Box 5667, St. John's, A1C 5X1 Newfoundland, Canada. [7]Marine Research Institute, Post Office Box 1390, Skúlagata 4, 121 Reykjavik, Iceland. [8]National Institute of Aquatic Resources, Technical University of Denmark, Post Office Box 101, DK-9850 Hirtshals, Denmark. [9]Norwegian College of Fisheries Science, University of Tromsø, N-9037 Tromsø, Norway.

*To whom correspondence should be addressed. E-mail: koellerp@mar.dfo-mpo.gc.ca

These results argue for the evolution of *P. borealis* egg hatch timing to accommodate to long-term average bottom temperatures and bloom times in each area, rather than for a direct link between egg hatching and spring blooms mediated by, for example, a chemical cue from senescent bloom material arriving at the ocean bottom. They also indicate that the population increases observed throughout much of the northwest Atlantic in the early 1990s were partly a result of later egg hatching times due to the widespread colder bottom water temperatures during this period, caused by changes in Arctic climate that resulted in the propagation of anomalously cold low-salinity waters down the western North Atlantic (fig. S1) (*8*, *20*). In following years, bottom water temperature increases triggered earlier hatching relative to

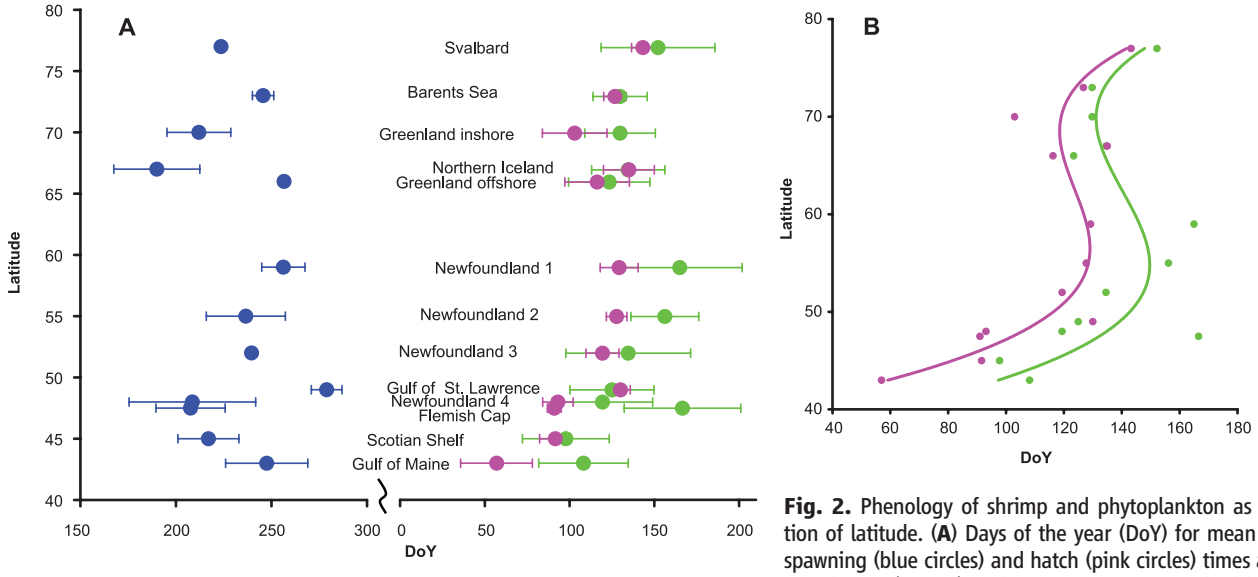

Fig. 2. Phenology of shrimp and phytoplankton as a function of latitude. (**A**) Days of the year (DoY) for mean shrimp spawning (blue circles) and hatch (pink circles) times at 50% completion (±1 SD) and mean timing of peak chlorophyll concentration (green circles). Bars indicate mean bloom initiation and completion times for each of the stock areas or subareas. Eggs are spawned in the summer/fall and are carried while they develop on the abdomen for 6 to 10 months until they hatch in the spring. (**B**) Third-order polynomial fits of 50% hatch DoY (pink line, R^2 = 0.81, P < 0.01) and phytoplankton bloom maximum (green line, R^2 = 0.47, P < 0.05) regressed against latitude as the independent variable. The fit between latitude and spawn timing (R^2 = 0.04) is not significant (fig. S3). A linear regression between hatch and bloom timing is significant at P < 0.01.

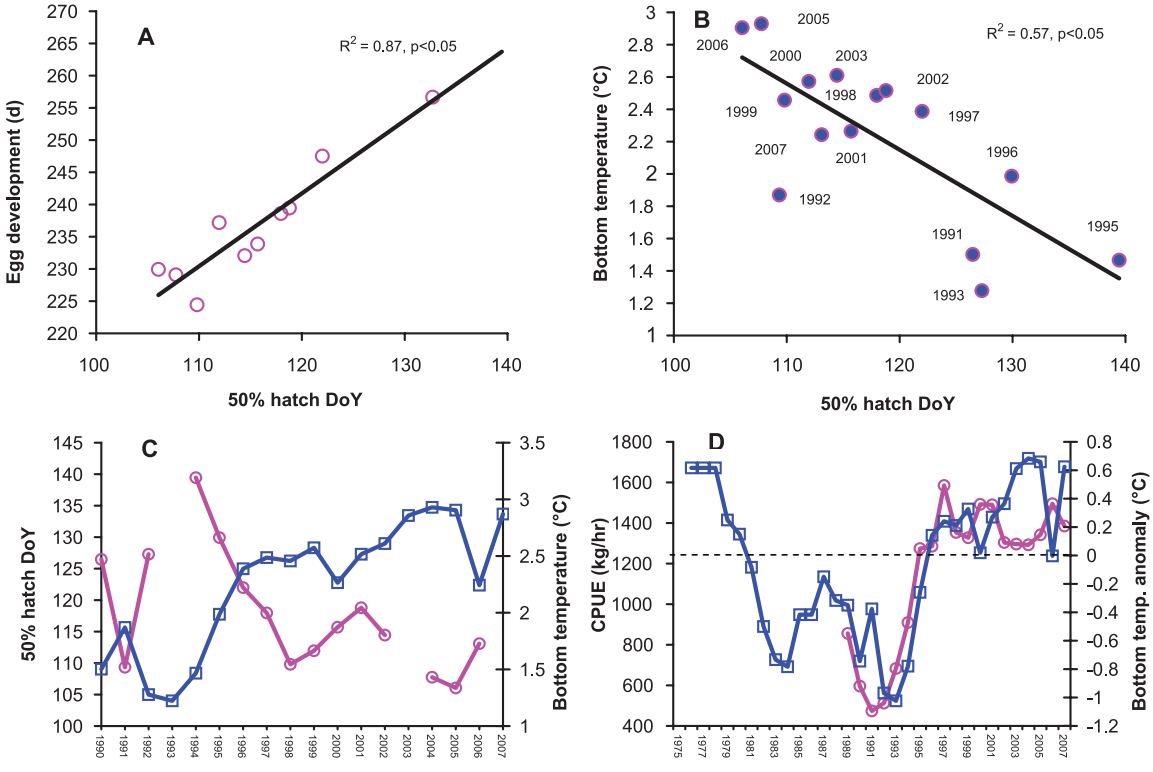

Fig. 3. Local influences on egg hatching times and population changes on the south Newfoundland Shelf. (**A**) Length of egg development from year y to y + 1 versus 50% hatching DoY in year y + 1. (**B**) Annual mean bottom temperatures measured in the fall of year y versus 50% hatching DoY in year y + 1. (**C**) Annual changes in 50% hatch DoY (pink circles) and bottom temperatures (blue squares) during and after the period of increasing abundances. (**D**) Bottom temperature anomalies (blue squares) and catch per unit of effort from commercial shrimp trawlers (pink circles). Survey bottom temperatures were not available before 1991; representative deep water (150 m) temperatures on Hamilton Bank were used for this period. Commercial shrimp trawls mainly catch larger, older (≥4 years) shrimp, hence increased larval survival would be reflected in data on catch per unit of effort only after several years.

the spring bloom and surface warming, resulting in less-frequent strong year classes. Shrimp abundance, however, remained high because of continued low predation pressure from depleted groundfish stocks.

The Gulf of St. Lawrence has the lowest annual minimum SSTs, and the bloom begins at relatively cool SSTs as compared with those in other areas, but its SSTs warm up most rapidly (Fig. 4). More rapid warming results in warmer SSTs during the phytoplankton bloom when food is most abundant, enhancing larval growth and survival. This explains the observed positive correlation between SST warming rates and larval survival (*9*). The longstanding but contradictory negative relationship between coastal spring SSTs measured at Boothbay Harbor, Maine, and larval survival reported in the Gulf of Maine (*4*, *15*), is likely to be a result of the Gulf of Maine's location at the southern end of the range of *P. borealis*, where both SSTs and bottom temperatures are warm. High bottom temperatures in the Gulf of Maine (Fig. 1) result in the earliest hatching dates and a long time lag between hatch and bloom (Figs. 2A and 4). It is also the only stock in which egg-bearing females migrate during winter from offshore waters into shallow, colder nearshore water (*4*, *15*). This migration may be a behavioral adaptation to warm bottom water temperatures that delays egg development and brings hatching closer to the spring bloom. This effect would be enhanced when coastal SSTs in Boothbay Harbor (representative of the well-mixed nearshore waters sought by egg-bearing females) were colder, leading to the observed negative correlation. The later bloom at Flemish Cap is probably a result of the oceanographic conditions prevailing at the front between the Labrador and North Atlantic Currents. It appears that the shrimp population at Flemish Cap established itself only recently through larval drift from the adjacent south Newfoundland shelf (*21*). The large offset in hatch and bloom timing at Flemish Cap (Figs. 2 and 4) may occur because the determinants of hatch timing have evolved under different conditions.

Decoupling a match between hatching and bloom to long-term average environmental conditions may arise if the interacting environmental factors are driven by different oceanographic processes; that is, for *P. borealis*, bottom temperatures determine egg development and hatch times (Fig. 1), and surface temperatures (Fig. 4) influence the timing of the spring bloom and larval growth rates. Specific conditions leading to a match or mismatch may differ between areas with different magnitudes of, and temporal relationships between, the factors associated with larval survival, as in the examples above for the Gulf of Maine, the Gulf of St. Lawrence, and Flemish Cap (Figs. 1 and 4). The collapse of the Gulf of Maine shrimp stock in the 1970s has been attributed to warmer temperatures or overfishing (*4*). More likely, both contributed. Further elucidation of area-specific recruitment mechanisms will help the development of management models that incorporate the important environmental factors influencing stock productivity. The confounding effects of top-down processes such as trophic cascades (*7*) further complicate this difficult task.

Our macroecological approach using satellite-sensed data has demonstrated the evolutionary plasticity of an important marine species adapting to distinct environmental conditions across its range and provides a framework for discussion of how shrimp stocks and possibly other economically and ecologically important species might respond to climate change. In the climate change context, we may anticipate that *P. borealis* will be affected by changes in both the timing of the spring bloom and bottom temperatures. A tendency to early stratification (for example, caused by increased melting of ice or faster warming of surface waters), which would favor early blooms, may be offset by higher winds (a higher frequency of storms). Furthermore, bottom temperatures are affected by quite different processes. Our understanding of how climate change may affect these processes is improving, but accurate prediction of how they in turn will affect living marine resources will require continued building of relevant environmental time series and further model studies that elucidate the coupling between the physics and biology of the oceans.

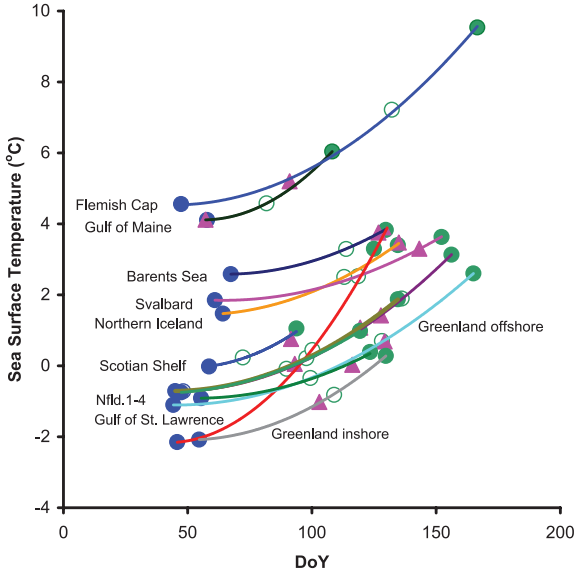

Fig. 4. SSTs for each study area at their annual minimum (solid blue circles), at phytoplankton bloom initiation (open green circles), at peak chlorophyll concentration (solid green circles), and at 50% hatch times (pink triangles).

References and Notes

1. B. Worm, R. A. Myers, *Ecology* **84**, 162 (2003).
2. D. G. Parsons, E. B. Colbourne, *J. Northwest Atl. Fish. Sci.* **27**, 11 (2000).
3. G. R. Lilly, D. G. Parsons, D. W. Kulka, *J. Northwest Atl. Fish. Sci.* **27**, 45 (2000).
4. S. H. Clark *et al.*, *Atl. Fish. Sci.* **27**, 193 (2000).
5. P. Koeller, *J. Northwest Atl. Fish. Sci.* **27**, 21 (2000).
6. K. Wieland, *ICES J. Mar. Sci.* **62**, 1454 (2005).
7. K. T. Frank, B. Petrie, J. Choi, W. C. Leggett, *Science* **308**, 1621 (2005).
8. C. H. Greene, A. J. Pershing, *Science* **315**, 1084 (2007).
9. P. Ouellet, L. Savard, P. Larouche, *Mar. Ecol. Prog. Ser.* **339**, 229 (2007).
10. H. U. Sverdrup, *J. Conseil Exp. Mer* **18**, 287 (1953).
11. T. Platt, C. Fuentes-Yaco, K. T. Frank, *Nature* **423**, 398 (2003).
12. T. Platt, S. Sathyendranath, C. Fuentes-Yaco, *ICES J. Mar. Sci.* **64**, 863 (2007).
13. D. H. Cushing, *Adv. Mar. Biol.* **26**, 249 (1990).
14. T. Platt, G. W. White III, L. Zhai, S. Sathyendranath, S. Roy, *Ecol. Model.*, 10.1016/j.ecolmodel.2008.11.022 (2009).
15. S. E. Shumway, H. C. Perkins, D. F. Schick, A. P. Stickney, *FAO Fish Synop.* **144**, 57 (1985).
16. B. I. Bergstrøm, *J. Shellfish Res.* **10**, 327 (1991).
17. B. I. Bergstrøm, in vol. 38 of *Advances in Marine Biology*, A. J. Southward, P. A. Tyler, C. M. Young, L. A. Fulman, Eds. (Academic Press, London, 2000), pp. 55–256.
18. Materials and methods are available as supporting material on *Science* Online.
19. Y. Wu, T. Platt, C. Tang, S. Sathyendranath, *Mar. Ecol. Prog. Ser.* **355**, 9 (2008).
20. C. H. Greene, A. J. Pershing, T. M. Cronin, N. Ceci, *Ecology* **89**, S24 (2008).
21. D. G. Parsons, E. B. Colbourne, G. R. Lilly, D. W. Kulka, *J. Northwest Atl. Fish. Sci.* **24**, 1 (1998).

22. This analysis was made possible by the satellite data provided by NASA and the efforts of the technical personnel in six countries whose efforts at sea and in the laboratory provided the biological and physical oceanographic data. We also thank G. White III for extensive data preparation. This work was supported by the Canadian Space Agency through the Government Related Initiatives Program and by the Natural Sciences and Engineering Research Council of Canada through research grants to T.P. and S.S. This work is a contribution to the National Centre for Earth Observation and the Oceans 2025 programs of the Natural Environment Research Council of the UK.

Supporting Online Material

www.sciencemag.org/cgi/content/full/324/5928/791/DC1
Materials and Methods
Figs. S1 to S6
Table S1
References

15 January 2009; accepted 23 March 2009
10.1126/science.1170987

Apicomplexan Parasites Co-Opt Host Calpains to Facilitate Their Escape from Infected Cells

Rajesh Chandramohanadas,[1] Paul H. Davis,[2] Daniel P. Beiting,[2] Michael B. Harbut,[1] Claire Darling,[1] Geetha Velmourougane,[1] Ming Yeh Lee,[2] Peter A. Greer,[3] David S. Roos,[2] Doron C. Greenbaum[1]*

Apicomplexan parasites, including *Plasmodium falciparum* and *Toxoplasma gondii* (the causative agents of malaria and toxoplasmosis, respectively), are responsible for considerable morbidity and mortality worldwide. These pathogenic protozoa replicate within an intracellular vacuole inside of infected host cells, from which they must escape to initiate a new lytic cycle. By integrating cell biological, pharmacological, and genetic approaches, we provide evidence that both *Plasmodium* and *Toxoplasma* hijack host cell calpain proteases to facilitate parasite egress. Immunodepletion or inhibition of calpain-1 in hypotonically lysed and resealed erythrocytes prevented the escape of *P. falciparum* parasites, which was restored by adding purified calpain-1. Similarly, efficient egress of *T. gondii* from mammalian fibroblasts was blocked by either small interfering RNA–mediated suppression or genetic deletion of calpain activity and could be restored by genetic complementation.

Apicomplexan parasites are obligate intracellular pathogens that exhibit complex life cycles involving distinct sexual and asexual stages of growth. The asexual phase is made up of a lytic cycle in which parasites establish an intracellular niche within the host: *Plasmodium* species infect erythrocytes, whereas *Toxoplasma gondii* infects nucleated animal cells. The process of schizogony in *Plasmodium* (endodyogeny in *Toxoplasma*) involves replication within a specialized "parasitophorous vacuole" to yield multiple daughter parasites (*1*, *2*). The resulting merozoites (tachzyoites in *Toxoplasma*) must escape from this vacuole and the host cell to invade uninfected cells and continue the infection. Egress from the infected cell is a rapid event, requiring only seconds at the end of the ~36- to 48-hour intracellular life cycle (*3*, *4*). Both calcium (*5*, *6*) and proteases (*4*, *7*–*10*) have been implicated in escape from the parasitophorous vacuole and/or host cell membranes.

In studies on *P. falciparum*, DCG04 (a biotinylated derivative of the nonspecific papain family protease inhibitor E64) labels multiple proteases in parasite lysates, including falcipain-1 (*11*). Although falcipain-1 is most abundant in extracellular merozoites, treatment of living *P. falciparum* cultures with DCG04 revealed a specific block in schizont-stage parasites (Fig. 1A). DCG04-treated merozoites developed normally (*12*) but became trapped within intact red blood cell (RBC) membranes. Cysteine proteases may play a role in host cell rupture (*3*, *4*), suggesting the feasibility of exploiting an activity-based probe such as DCG04 for affinity purification of the relevant enzyme(s).

To focus on those proteases most likely to be involved in parasite egress, infected cultures were labeled with DCG04, treated with saponin to permeabilize the RBC and parasitophorous vacuole membranes, centrifuged briefly to remove parasite cells (which are not permeabilized by saponin), and pelleted to produce soluble and membrane-associated fractions (*13*). The ability of saponin to lyse the RBC and parasitophorous vacuole membranes selectively, while sparing the parasite plasma membrane, was confirmed by assaying leakage of a cytoplasmic green fluorescent protein (GFP) marker. Immunoblotting with antibodies to GFP, the parasite plasma membrane marker MSP1, the digestive vacuole marker plasmepsin-II, and the erythrocyte membrane marker stomatin showed efficient separation of erythrocyte components from parasite material (fig. S1).

Biotinylated DCG04 detected a single reactive peak of ~80 kD specific to membranes isolated from erythrocytes infected with schizont-stage parasites and maximal at ~48 hours postinfection (Fig. 1B). Mass spectrometry of DCG04-labeled material purified from a streptavidin affinity column unequivocally identified human calpain-1, based on 27 peptides (42% coverage) (table S1). Failure to label other cysteine proteases such as SERAs, falcipains, or other digestive vacuole enzymes (despite their abundance in infected cultures) confirms the removal of parasites and that digestive vacuole contents were not released during egress. DCG04 also failed to label the parasite's endogenous calpain, an essential cytoplasmic protease required for early cell cycle progression, but not for egress (*14*).

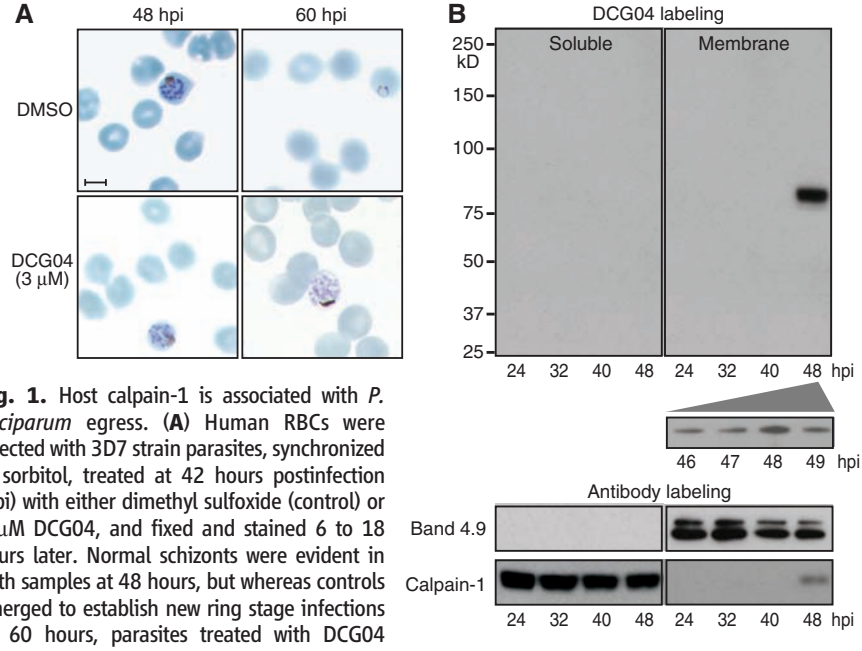

Fig. 1. Host calpain-1 is associated with *P. falciparum* egress. (**A**) Human RBCs were infected with 3D7 strain parasites, synchronized in sorbitol, treated at 42 hours postinfection (hpi) with either dimethyl sulfoxide (control) or 3 μM DCG04, and fixed and stained 6 to 18 hours later. Normal schizonts were evident in both samples at 48 hours, but whereas controls emerged to establish new ring stage infections by 60 hours, parasites treated with DCG04 appeared unable to egress, remaining arrested as schizonts. Scale bar, 5 μm. (**B**) Synchronized infected cultures were treated with 3 μM DCG04 for 2 hours beginning at various times throughout the intraerythrocytic life cycle, followed by incubation with 0.02% saponin to permeabilize the RBC and parasitophorous vacuole membrane (but not parasites). Parasites were removed by centrifugation, and the remaining material fractionated to yield a host + parasitophorous vacuole membrane pellet and a soluble fraction. Blotting identified proteins biotinylated by DCG04 (labeling any active cysteine protease), as well as the RBC membrane marker band 4.9, and calpain-1 (a cytoplasmic RBC protein when inactive). The single prominent ~80-kD band observed in membranes isolated from RBCs harboring schizont-stage parasites was identified as host cell calpain-1 (table S1).

[1]Department of Pharmacology, University of Pennsylvania, Philadelphia, PA 19104, USA. [2]Department of Biology and the Penn Genome Frontiers Institute, University of Pennsylvania, Philadelphia, PA 19104, USA. [3]Department of Pathology and Molecular Medicine, Queen's Cancer Research Institute, Queen's University, Kingston, ON K7L 3N6, Canada.

*To whom correspondence should be addressed. E-mail: dorong@upenn.edu

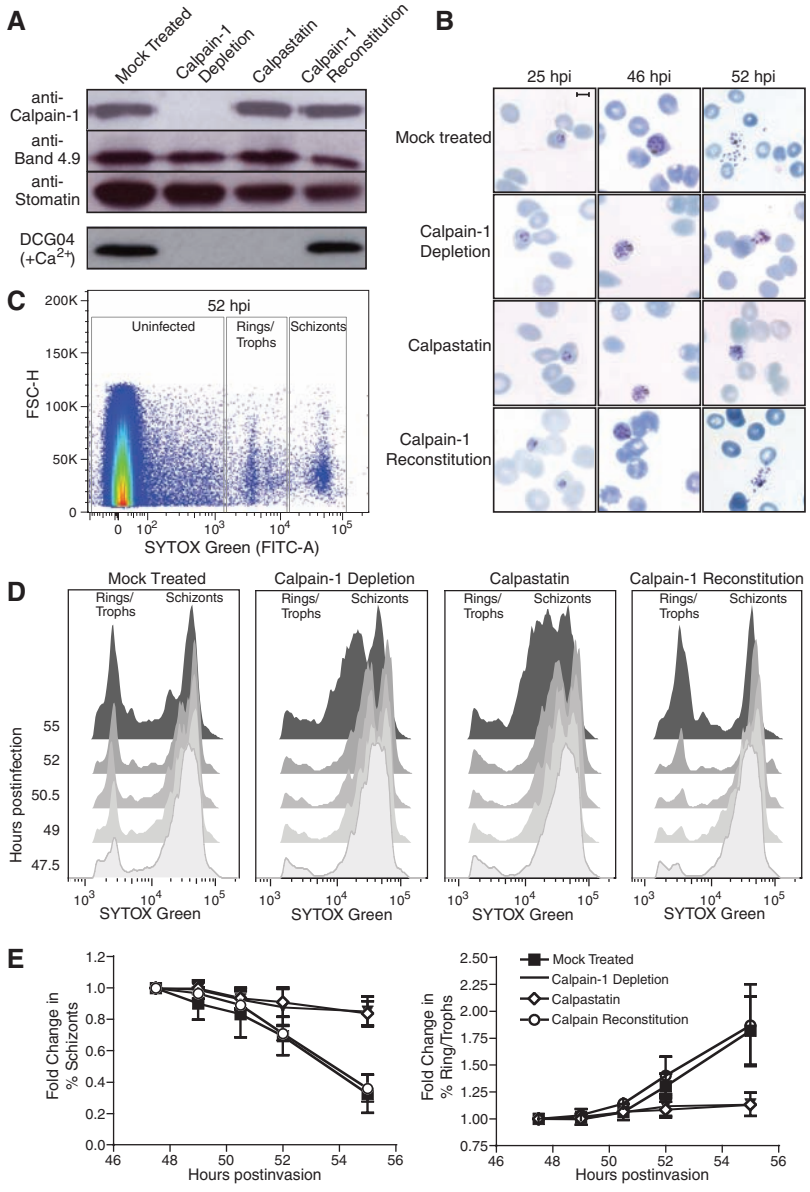

Fig. 2. Host calpain-1 is required for *P. falciparum* egress. Uninfected RBCs were hypotonically lysed, immunodepleted with monoclonal anti–calpain-1 conjugated to Sepharose (or mock-treated with Sepharose beads only), and resealed under hypotonic conditions in the presence of 1 μM calpastatin, purified calpain-1, or buffer alone. (**A**) Immunoblots showed specific removal of calpain-1 in immunodepleted RBCs and reconstitution with purified enzyme; equal loading was confirmed with the use of anti-band 4.9 and anti-stomatin. Labeling of resealed RBCs with 5 μM DCG04 in the presence of calcium demonstrated that calpain activity was eliminated by either immunodepletion or calpastatin loading; activity was restored by reconstitution with exogenous calpain-1. (**B**) Purified schizont-stage parasites were mixed with resealed RBCs and incubated for various times before fixation. Giemsa-stained smears showed incomplete egress from calpain-depleted or calpastatin-loaded cells, but proper egress from RBCs reconstituted with purified calpain-1. Scale bar = 5 μm. (**C**) During late schizogony, infected resealed RBCs were harvested at 90-min intervals, fixed, and stained for flow cytometry based on forward scatter (FSC-H) and parasite DNA content (SYTOX-Green). Boxes indicate gates defining uninfected cells, rings/trophozoites, and schizont-stage parasites (sample plot; see fig. S2B). (**D**) Flow cytometric data was gated to exclude uninfected erythrocytes and converted to a two-dimensional plot highlighting the progress of calpain-reconstituted cultures from schizonts to ring-stage infection as efficiently as mock treated controls, in contrast to the arrest of calpain-depleted and calpastatin-treated cells in schizogony, indicating an egress defect. (**E**) Quantitation of flow cytometric data (percentage of rings/trophozoites or schizonts relative to time $t = 0$, ± SE, from four independent experiments).

Of the two common calcium-regulated cysteine proteases in human cells, calpains 1 and 2, only the former is found in erythrocytes, where it is the most abundant cysteine protease (*15*) (erythrocytes lack the hydrolytic enzymes associated with lysosomes). Calpains are normally inactive cytosolic enzymes, but upon binding calcium they become proteolytically active and associate with membranes (*16*, *17*). Probing DCG04-labeled subcellular fractions of *P. falciparum*–infected erythrocytes with anti–calpain-1 antibody revealed abundant calpain-1 in the erythrocyte cytoplasm throughout the parasite growth cycle (Fig. 1B), but membrane-associated enzyme was found only during late schizogony. The observed pattern of membrane association coincides precisely with calpain activation as detected by the activity-based probe DCG04 (Fig. 1B).

As malaria parasites can replicate in hypotonically lysed and resealed erythrocytes (*18*), we employed a biochemical/cell biological approach to assess the role of calpains in *P. falciparum* egress. Lysed RBCs were incubated with anti–calpain-1 antibody conjugated to protein G Sepharose beads, allowing depletion of all detectable calpain-1 before resealing (Fig. 2A). Calpain-1 was also reconstituted into immunodepleted RBCs by resealing in the presence of purified, inactive calpain-1 (without calcium). Control samples were lysed and treated with unconjugated Sepharose (mock) or beads conjugated to anti-flotillin, and a mock-depleted sample was resealed in the presence of the 14-kD, non-cell permeable domain I of the highly specific calpain inhibitor calpastatin (*19*–*21*). DCG04 labeling of calcium-treated resealed erythrocytes confirmed that calpain-1 activity was removed by immunodepletion, that calpastatin loading blocked calpain-1 activity, and that reconstitution with calpain-1 restored activity to approximately wild-type (WT) levels (Fig. 2A).

Incubation of lysed and resealed erythrocytes with highly synchronized *P. falciparum* schizonts produced ~80% of the parasitemia levels observed during parallel infection of control erythrocytes (fig. S2A) (*18*). In calpain-1–depleted or calpastatin-loaded cells, however, development of intracellular parasites was arrested during late schizogony, and parasites failed to egress (Fig. 2B). Very few ring stage parasites were observed in calpain-1–depleted or calpastatin-loaded cells, even as late as 75 hours postinvasion. Flow cytometry of DNA content in infected RBCs was used as a quantitative measure of the intraerythrocytic *P. falciparum* life cycle (*22*), permitting the discrimination of schizonts from ring/trophozoite stages and uninfected RBCs (Fig. 2C and fig. S2B). Both resealed (mock treated) erythrocytes and erythrocytes immunodepleted by an antibody unrelated to calpain (anti-flotillin) (fig. S3) displayed normal kinetics of parasite growth and egress, progressing from ring stages (1 N) to multinucleated schizonts (~16 N), followed by egress and reinvasion to produce rings in fresh erythrocytes ~50 hours postinfection (Fig. 2, D

and E). Calpastatin-loaded and calpain-1 immunodepleted erythrocytes progressed to schizonts with normal kinetics but arrested in late schizogony, producing few new ring-stage infections (the broad "schizont" peak observed at late time points probably represents dying parasites). Erythrocyte ghosts reconstituted with purified calpain-1 after immunodepletion restored the transition from schizonts to rings.

Thus, calpain-1 activity is required for efficient egress of *P. falciparum* parasites from infected human erythrocytes in vitro, but it is difficult to assess the importance of calpain-mediated parasite egress in vivo because RBCs are not readily amenable to genetic manipulation. Calpain-1 deficiency has not been described in humans, and *P. falciparum* will not infect rodent erythrocytes. *P. yoelii* will infect calpain-1 knockout (KO) mice (*23*), but these parasites preferentially invade reticulocytes (*24*), which express both calpain-1 and calpain-2 (*25*) (National Center for Biotechnology Information GEO profile GDS2655), in contrast to human erythrocytes, which express calpain-1 only (*15*). Genetic deletion of either calpain-2 (*26*) or the CAPNS1 regulatory subunit required for activity of both calpains (*27*) produces embryonic lethality in mice.

To further explore the importance of calpains during parasite infection, we turned to the apicomplexan parasite *T. gondii*, which is related to *Plasmodium* but able to invade, establish its parasitophorous vacuole, and replicate in virtually any nucleated cell (*28*). WT fibroblasts are typically lysed by *T. gondii* parasites ~48- to 60-hours postinfection, releasing free tachyzoites into the medium, whereupon they invade new host cells. This process is readily visualized in living cultures using transgenic parasites expressing a fluorescent protein reporter (*29*). Although CAPNS1 KO mice die as embryos (*27*), KO cell lines and small interfering RNA (siRNA) approaches provide alternative experimental routes to assess the importance of calpain for *T. gondii* egress.

Most mammalian cells express both calpain-1 and 2, but targeting the regulatory subunit CAPNS1 permits the elimination of both. Two oligonucleotides were employed (independently) for siRNA studies in U2OS human host cells, both of which produced >20-fold reduction in CAPNS1 transcript levels and even greater protein depletion (Fig. 3B). Many extracellular *T. gondii* tachyzoites could be seen after infection of control cultures, but very few were observed after transfection with either of the CAPNS1 siRNAs (Fig. 3A). Rather, these cultures were character-

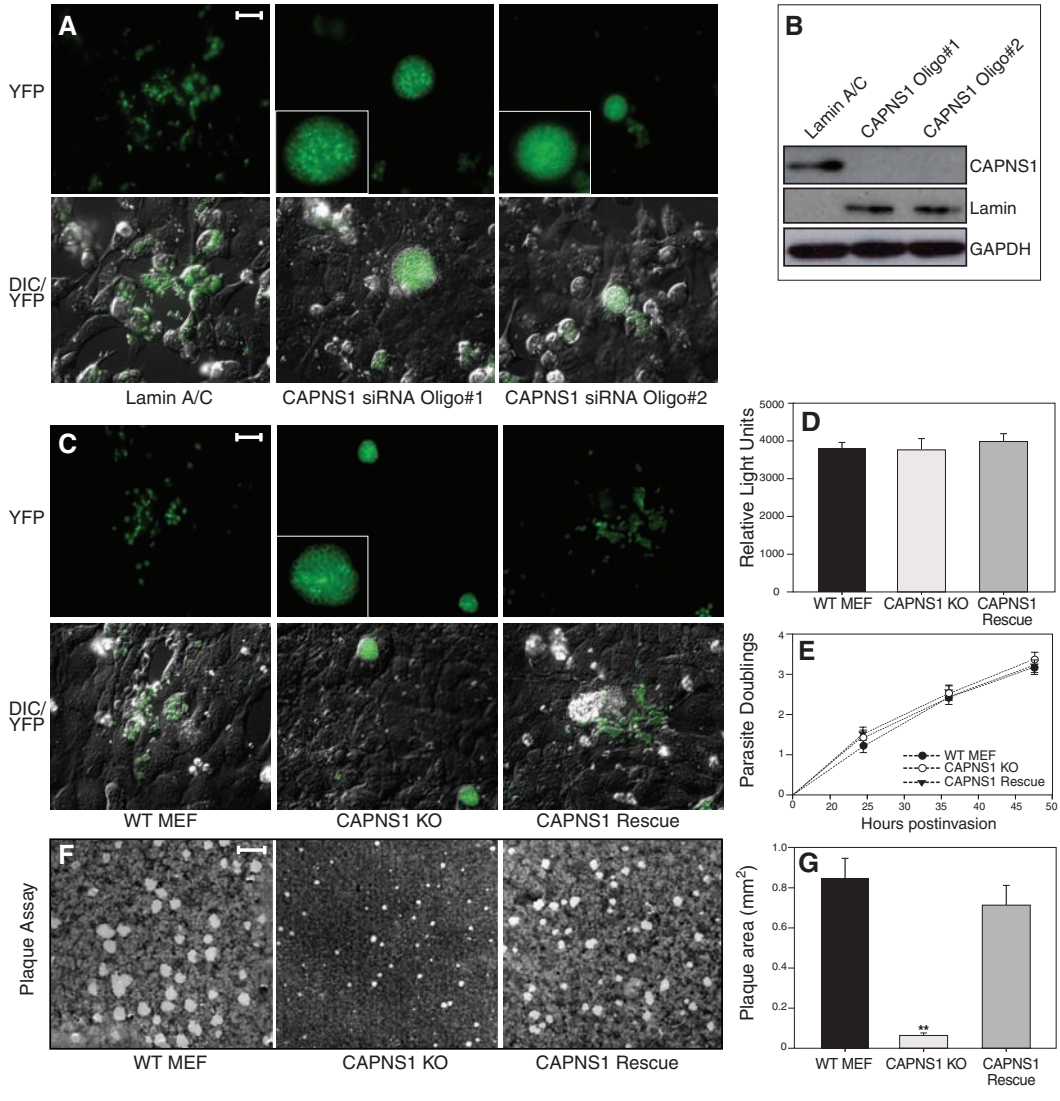

Fig. 3. Host calpain facilitates the egress of *T. gondii*. (**A**) U2OS cells were transfected with siRNAs targeting either the common calpain regulatory subunit CAPNS1 (two different siRNAs) or lamin A/C, infected 24 hours post-transfection with *T. gondii* parasites expressing yellow fluorescent protein (YFP), and examined by fluorescence microscopy 56 hours later. Parasites ruptured out of most infected cells in controls, but not the knockdown cultures, where infected cells were grossly swollen with intracellular parasites. Insets show enlarged images of parasite-containing vacuoles. Scale bar, 30 μm. (**B**) Suppression of CAPNS1 protein levels was assessed in uninfected cells 72 hours post transfection using antibodies to CAPNS1, lamin A/C, and glyceraldehyde phosphate dehydrogenase (GAPDH). (**C**) YFP parasites were used to follow replication and egress in CAPNS1 KO host cells. By 56 hours postinfection, parasites had ruptured out of most cells in the WT and CAPNS1 rescue cultures, whereas CAPNS1 KO cells were heavily infected but unlysed. Scale bar, 30 μm. (**D**) To follow infection, cells were inoculated with luciferase-expressing transgenic parasites, producing comparable numbers of intracellular tachyzoites 4 hours postinfection. (**E**) To assay intracellular replication, host cell monolayers were infected with parasites, and parasitophorous vacuoles were scored every 12 hours for the number of parasites per vacuole, demonstrating comparable growth rates throughout the intracellular growth cycle (represented as $\log_2$ parasite count). (**F**) Confluent fibroblast monolayers were infected with *T. gondii* tachyzoites, and plaques were stained with crystal violet at 7 days, demonstrating comparable rates of infection but very small plaques in the CAPNS1 KO cultures, as a consequence of the egress defect in this mutant host cell line. Scale bar, 2 mm. (**G**) Quantitation of plaque size revealed a substantial decrease in the CAPNS1 KOs versus WT and CAPNS1 rescued cells (average radius of 20 randomly selected plaques per sample ± SE). Asterisks indicate the statistical significance using a Student's two-tailed *t* test comparing CAPNS1 KO to WT, which yielded a *P* value of 1.91×10^{-7}.

ized by host cells packed full of fluorescent parasites unable to egress efficiently. These grossly swollen cells often detached from the monolayer and could be found floating in the culture medium giving the appearance of a hot air balloon convention.

Fibroblast cell lines derived from CAPNS1 KO mouse embryos lack both calpain-1 and -2 activity (*30*), and infection of these cells with *T. gondii* produced the same swollen cell phenotype observed in CAPNS1 knock-down experiments (Fig. 3C). Transgenic expression of CAPNS1 in the KO mutants restores calpain-1 and -2 activity (*30*) and also complemented the *T. gondii* egress defect. Parasite tachyzoites were readily able to invade (Fig. 3D) and replicate (Fig. 3E) in WT, CAPNS1 KOs, and CAPNS1-complemented fibroblasts, demonstrating that the impact of host cell calpains on *T. gondii* infection is specific to egress. Plaque assays showed a ~13-fold reduction in plaque size for *T. gondii* in CAPNS1 mutants versus parental MEF cells or CAPNS1-complemented KOs (Fig. 3, F and G). In contrast to *P. falciparum*, which rarely emerge from calpain-depleted erythrocytes (Fig. 2), some *T. gondii* parasites did eventually manage to escape from calpain-deficient fibroblasts, yielding a small plaque phenotype.

In summary, in addition to the many roles that parasite-encoded cysteine proteases play in the biology of infection and pathogenesis (*25*), the apicomplexans *Plasmodium falciparum* and *Toxoplasma gondii* both exploit host cell calpains to facilitate escape from the intracellular parasitophorous vacuole and/or host plasma membrane. The precise mechanism of calpain-mediated parasite egress is unknown, but calpains play a role in remodeling of the cytoskeleton and plasma membrane during the migration of mammalian cells (*31*), and activated calpain-1 can degrade erythrocyte cytoskeletal proteins in vitro and during *P. falciparum* infection in vivo (fig. S4). The calcium responsible for calpain activation during parasite infection may be supplied through the action of a parasite-encoded perforin recently implicated in *T. gondii* egress (*32*). The parasitophorous vacuole was labeled by the calcium-specific dye Fluo-4-AM during late schizogony, and depletion of internal calcium with the membrane-permeant chelator EGTA-AM blocked parasite egress, whereas removal of calcium from the culture medium did not (fig. S5). We suggest a model in which a calcium signal triggered late during parasite infection activates host cell calpain, which relocalizes to the host plasma membrane, cleaving cytoskeletal proteins to facilitate parasite egress (fig. S6). Because parasites that fail to escape from their host cells are unable to proliferate, this suggests an intriguing strategy for anti-parasitic therapeutics.

References and Notes

1. M. Nishi, K. Hu, J. M. Murray, D. S. Roos, *J. Cell Sci.* **121**, 1559 (2008).
2. K. Hu *et al.*, *Mol. Biol. Cell* **13**, 593 (2002).
3. S. Glushakova, D. Yin, T. Li, J. Zimmerberg, *Curr. Biol.* **15**, 1645 (2005).
4. B. L. Salmon, A. Oksman, D. E. Goldberg, *Proc. Natl. Acad. Sci. U.S.A.* **98**, 271 (2001).
5. M. W. Black, G. Arrizabalaga, J. C. Boothroyd, *Mol. Cell. Biol.* **20**, 9399 (2000).
6. K. Nagamune *et al.*, *Nature* **451**, 207 (2008).
7. T. Hadley, M. Aikawa, L. H. Miller, *Exp. Parasitol.* **55**, 306 (1983).
8. M. E. Wickham, J. G. Culvenor, A. F. Cowman, *J. Biol. Chem.* **278**, 37658 (2003).
9. S. Arastu-Kapur *et al.*, *Nat. Chem. Biol.* **4**, 203 (2008).
10. S. Yeoh *et al.*, *Cell* **131**, 1072 (2007).
11. D. C. Greenbaum *et al.*, *Science* **298**, 2002 (2002).
12. S. Glushakova, J. Mazar, M. F. Hohmann-Marriott, E. Hama, J. Zimmerberg, *Cell. Microbiol.* **11**, 95 (2009).
13. Materials and methods are available as supporting material on *Science* Online.
14. I. Russo, A. Oksman, B. Vaupel, D. E. Goldberg, *Proc. Natl. Acad. Sci. U.S.A.* **106**, 1554 (2009).
15. E. M. Pasini *et al.*, *Blood* **108**, 791 (2006).
16. D. E. Croall, K. Ersfeld, *Genome Biol.* **8**, 218 (2007).
17. D. E. Goll, V. F. Thompson, H. Li, W. Wei, J. Cong, *Physiol. Rev.* **83**, 731 (2003).
18. S. C. Murphy *et al.*, *PLoS Med.* **3**, e528 (2006).
19. R. A. Hanna, R. L. Campbell, P. L. Davies, *Nature* **456**, 409 (2008).
20. T. Moldoveanu, K. Gehring, D. R. Green, *Nature* **456**, 404 (2008).
21. S. Gil-Parrado *et al.*, *Biol. Chem.* **384**, 395 (2003).
22. A. E. Bianco, F. L. Battye, G. V. Brown, *Exp. Parasitol.* **62**, 275 (1986).
23. M. Hanspal, V. K. Goel, S. S. Oh, A. H. Chishti, *Mol. Biochem. Parasitol.* **122**, 227 (2002).
24. L. Weiss, J. Johnson, W. Weidanz, *Am. J. Trop. Med. Hyg.* **41**, 135 (1989).
25. P. J. Rosenthal, *Int. J. Parasitol.* **34**, 1489 (2004).
26. P. Dutt *et al.*, *BMC Dev. Biol.* **6**, 3 (2006).
27. J. S. Arthur, J. S. Elce, C. Hegadorn, K. Williams, P. A. Greer, *Mol. Cell. Biol.* **20**, 4474 (2000).
28. D. S. Roos, R. G. Donald, N. S. Morrissette, A. L. Moulton, *Methods Cell Biol.* **45**, 27 (1994).
29. K. A. Joiner, D. S. Roos, *J. Cell Biol.* **157**, 557 (2002).
30. N. Dourdin *et al.*, *J. Biol. Chem.* **276**, 48382 (2001).
31. A. Huttenlocher *et al.*, *J. Biol. Chem.* **272**, 32719 (1997).
32. B. F. C. Kafsack *et al.*, *Science* **323**, 530 (2009); published online 18 December 2008 (10.1126/science.1165740).

33. We thank R. W. Doms, M. Marti, and M. Klemba for critical discussions; the Penn Proteomics Core for mass spectrometry; and M. A. Lampson for help with imaging. *P. falciparum* expressing GFP were provided by O. S. Harb. P.H.D. and D.P.B. are funded by National Research Service Awards, and D.S.R. is an Ellison Medical Foundation Senior Scholar in Global Infectious Disease, supported by grants from NIH. D.C.G. was supported by the Ritter Foundation, the Penn Genome Frontiers Institute, and the Penn Institute for Translational Medicine and Therapeutics.

Supporting Online Material

www.sciencemag.org/cgi/content/full/1171085/DC1
Materials and Methods
Figs. S1 to S6
Table S1
References

20 January 2009; accepted 10 March 2009
Published online 2 April 2009;
10.1126/science.1171085
Include this information when citing this paper.

Human Induced Pluripotent Stem Cells Free of Vector and Transgene Sequences

Junying Yu,[1,2,3]* Kejin Hu,[3] Kim Smuga-Otto,[1,2,3] Shulan Tian,[1,2] Ron Stewart,[1,2] Igor I. Slukvin,[3,4] James A. Thomson[1,2,3,5]*

Reprogramming differentiated human cells to induced pluripotent stem (iPS) cells has applications in basic biology, drug development, and transplantation. Human iPS cell derivation previously required vectors that integrate into the genome, which can create mutations and limit the utility of the cells in both research and clinical applications. We describe the derivation of human iPS cells with the use of nonintegrating episomal vectors. After removal of the episome, iPS cells completely free of vector and transgene sequences are derived that are similar to human embryonic stem (ES) cells in proliferative and developmental potential. These results demonstrate that reprogramming human somatic cells does not require genomic integration or the continued presence of exogenous reprogramming factors and removes one obstacle to the clinical application of human iPS cells.

The proliferative and developmental potential of both human embryonic stem (ES) cells and human induced pluripotent stem (iPS) cells offers unprecedented access to the differentiated cells that make up the human body (*1*–*3*). In addition, iPS cells can be derived with a specific desired genetic background, including patient-specific iPS cells for disease models and for transplantation therapies, without the problems associated with immune rejection. Reprogramming of both mouse and human somatic cells into iPS cells has been achieved by expressing combinations of factors such as *OCT4*, *SOX2*, c-*Myc*, *KLF4, NANOG*, and *LIN28* (*2*–*4*). Initial methods used to derive human iPS cells used viral vectors, in which both the vector backbone and transgenes are permanently integrated into the genome (*2*, *3*). Such vectors can produce insertional mutations that interfere with the normal function of iPS cell derivatives, and residual transgene expression can influence differentiation into specific lineages (*2*), or even result in tumorigenesis (*5*). Vector integration–free mouse iPS cells have been derived from

liver cells with adenoviral vectors (*6*) and from embryonic fibroblasts with repeated plasmid transfections (*7*), but the low frequencies obtained make it unclear how practical these approaches will be for human cells, which generally require longer exposure to reprogramming factors (*2*, *3*).

While this manuscript was in review, two alternative approaches were described to remove transgenes from mouse or human iPS cells. In one approach, Cre/LoxP recombination was used to excise integrated transgenes (*8*, *9*). This approach successfully removes transgene sequences, but leaves behind residual vector sequences, which can still create insertional mutations. A second approach used seamless excision of piggyBac transposons to produce vector- and transgene-free mouse iPS cells (*10*). Although a promising approach, vector removal from human iPS cells produced by this method has not yet been reported, and removing multiple transposons is labor intensive. Here, we report that human iPS cells completely free of vector and transgene sequences can be derived from fibroblasts by a single transfection with oriP/EBNA1 (Epstein-Barr nuclear antigen-1)–based episomal vectors.

Derived from the Epstein-Barr virus, oriP/EBNA1 vectors are well suited for introducing reprogramming factors into human somatic cells, as these plasmids can be transfected without the need for viral packaging and can be subsequently removed from cells by culturing in the absence of drug selection. The stable extrachromosomal replication of oriP/EBNA1 vectors in mammalian cells requires only a cis-acting oriP element (*11*) and a trans-acting EBNA1 gene (*12*). The oriP/EBNA1 vectors replicate only once per cell cycle, and with drug selection can be established as stable episomes in about 1% of the initial transfected cells (*13*, *14*). If drug selection is subsequently removed, the episomes are lost at ~5% per cell generation owing to defects in plasmid synthesis and partitioning; thus, cells devoid of plasmids can be easily isolated (*15*).

OCT4, *SOX2*, *NANOG*, and *LIN28* are sufficient to reprogram human embryonic, neonatal, and adult fibroblasts to iPS cells (*2*, *16*), but the reprogramming efficiency is low (<0.01% for newborn foreskin fibroblasts) (*2*). Such low efficiency makes it difficult to reprogram with oriP/EBNA1-based vectors because the stable transfection efficiency is almost two orders of magnitude less than that of our lentiviral vectors (*2*). Thus, we first improved reprogramming efficiency with lentiviral vectors. By testing different linkers to coexpress *OCT4* and *SOX2*, we found that the internal ribosome entry site 2 (IRES2) supported higher reprogramming efficiency (fig. S1, A and B). Because linkers have less effect on reprogramming efficiency when used to coexpress *NANOG* and *LIN28* (fig. S1B), IRES2 was chosen to coexpress reprogramming factors. Using IRES2-mediated expression of OCT4, SOX2, NANOG, and LIN28, we improved the reprogramming efficiency for human foreskin fibroblasts by about 10-fold (~0.1%) over what we had previously reported (fig. S1C). The addition of c-Myc and KLF4 further improved the reprogramming efficiency to more than 1%, the highest efficiencies we have achieved for these cells (fig. S1C) (*17*). Thus, we cloned all six reprogramming factors (*OCT4*, *SOX2*, *NANOG*, *LIN28*, c-*Myc*, and *KLF4*) into an oriP/EBNA1 vector using IRES2 for coexpression. Because our previous experience suggested that both the balance between transgenes and their absolute expression levels are critically important to achieving reprogramming, we tested different transgene arrangements to achieve appropriate levels empirically (table S1).

Initial tests with the six reprogramming genes in the episomal vectors failed to yield human iPS cell colonies (table S2). With this combination of genes, substantial cell death was observed during the first week after transfection, possibly

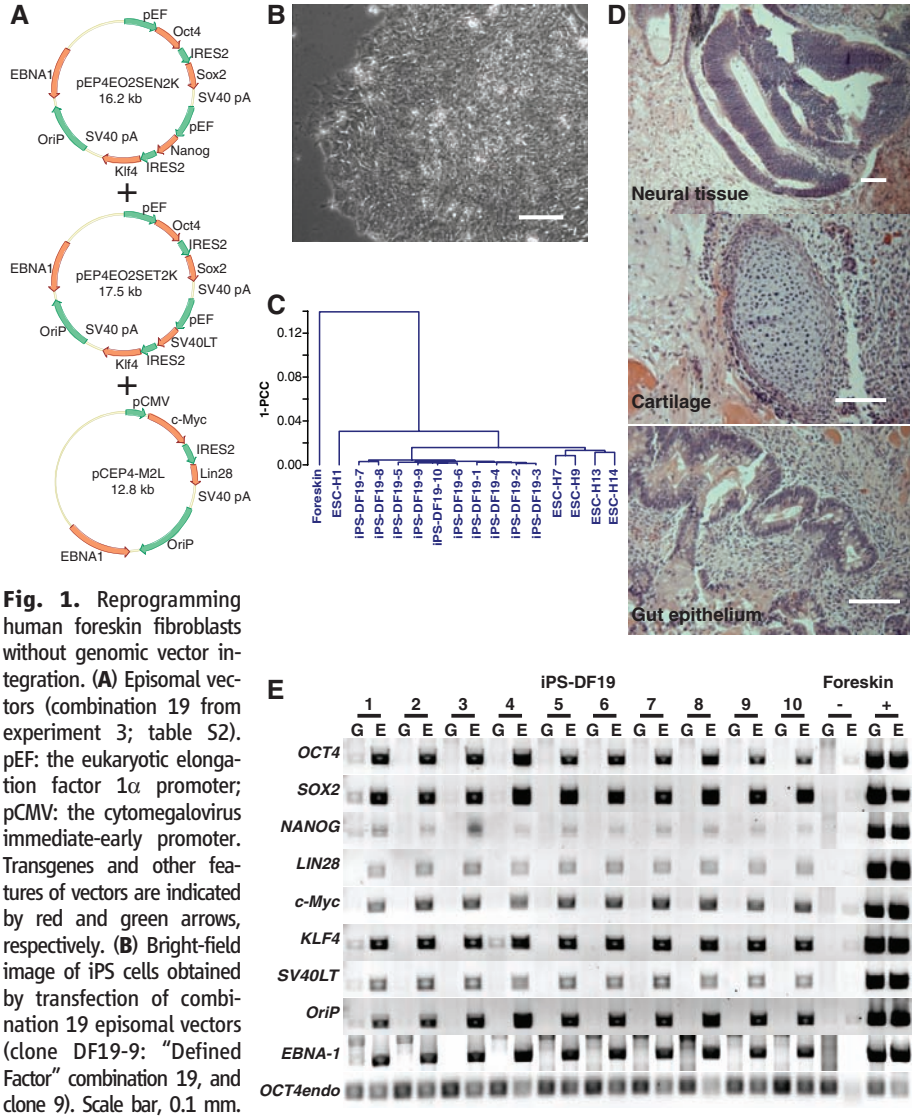

Fig. 1. Reprogramming human foreskin fibroblasts without genomic vector integration. (**A**) Episomal vectors (combination 19 from experiment 3; table S2). pEF: the eukaryotic elongation factor 1α promoter; pCMV: the cytomegalovirus immediate-early promoter. Transgenes and other features of vectors are indicated by red and green arrows, respectively. (**B**) Bright-field image of iPS cells obtained by transfection of combination 19 episomal vectors (clone DF19-9: "Defined Factor" combination 19, and clone 9). Scale bar, 0.1 mm. (**C**) Pearson correlation analyses of global gene expression (51,337 transcripts) in human fibroblast-derived iPS cell clones (combination 19). 1-PCC: Pearson correlation coefficient. (**D**) Hematoxylin and eosin staining of teratoma sections of iPS cell clone DF19-9 (53 days after injection). Teratomas were obtained from all 10 iPS-DF19 clones. Scale bars, 0.1 mm. (**E**) PCR analysis of episomal DNA in iPS-DF19 clone 1 to 10. G: genomic DNA template; E: episomal DNA template. Genomic and episomal DNA from nontransfected and combination 19 episomal vector-transfected (day 17 after transfection) fibroblasts were used as negative (–) and positive (+) controls, respectively. Thirty-two PCR cycles were used for all primer sets.

[1]Morgridge Institute for Research, Madison, WI 53707–7365, USA. [2]Genome Center of Wisconsin, Madison, WI 53706–1580, USA. [3]Wisconsin National Primate Research Center, University of Wisconsin-Madison, Madison, WI 53715–1299, USA. [4]Department of Pathology and Laboratory Medicine, University of Wisconsin-Madison, Madison, WI 53706, USA. [5]Department of Anatomy, University of Wisconsin-Madison, Madison, WI 53706–1509, USA.

*To whom correspondence should be addressed. E-mail: jyyu2008@gmail.com (J.Y.); thomson@primate.wisc.edu (J.A.T.)

owing to the toxic effects of high c-Myc expression (*18*). To counteract the possible toxic effects of c-Myc expression, we included the SV40 large T gene (*SV40LT*) in some of the combinations (*19*). Three of these combinations, all of which included *OCT4*, *SOX2*, *NANOG*, *LIN28*, c-*Myc*, *KLF4*, and *SV40LT*, were successful in producing iPS cell colonies from human foreskin fibroblasts with oriP/EBNA1-based vectors (Fig. 1A, fig. S2D, and table S2). At least two plasmids in each successful combination express OCT4 and SOX2, consistent with the observation that high expression of these transgenes improves reprogramming. Clones from two of these combinations (19 from experiment 3 and 6 from experiment 4; table S2) were chosen for expansion and analysis. These iPS cell colonies exhibited typical human ES cell morphology (e.g., compact colonies, high nucleus-to-cytoplasm ratios, and prominent nucleoli) (Fig. 1B) and exhibited gene expression profiles that were very similar to those of human ES cell lines, but dissimilar to those of the parental fibroblasts (Fig. 1C and table S3). Similar to human ES cells, when injected into immunocompromised mice, these iPS cells formed teratomas consisting of differentiated derivatives of all three primary

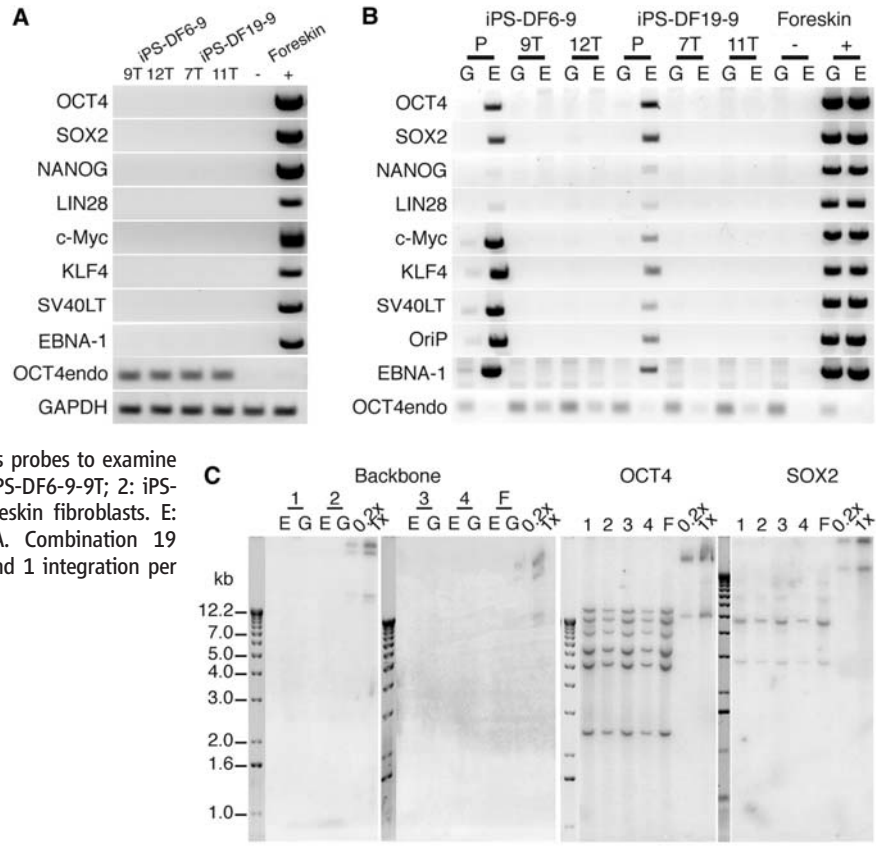

Fig. 2. Human foreskin fibroblast–derived iPS cells free of vectors and transgenes. (**A**) RT-PCR analysis of transgene expression in iPS-DF6-9 subclone 9T and 12T, and iPS-DF-19-9 subclone 7T and 11T. Negative control (–): fibroblasts; positive control (+): fibroblasts transfected with combination 19 episomal vectors (day 4 after transfection). Thirty-two PCR cycles were used for all primer sets. (**B**) PCR analysis of episomal DNA in iPS-DF6-9 (P: parental clone), iPS-DF6-9 subclone 9T and 12T, iPS-DF19-9 (P), and iPS-DF19-9 subclones 7T and 11T. G: genomic DNA template; E: episomal DNA template. Negative (–) and positive (+) controls were the same as in Fig. 1E. Thirty-two PCR cycles were used for all primer sets except *OCT4* endo (28 cycles). (**C**) Southern blot analysis of exogenous DNA in iPS-DF6-9 and iPS-DF-19-9 subclones. The pCEP4 vector was used as a probe to detect the presence of vector backbone, and the open reading frames of *OCT4* and *SOX2* were used as probes to examine both the endogenous gene and possible transgenes. 1: iPS-DF6-9-9T; 2: iPS-DF6-9-12T; 3: iPS-DF19-9-7T; 4: iPS-DF19-9-11T; F: foreskin fibroblasts. E: undigested episomal DNA; G: digested genomic DNA. Combination 19 episomal vector DNA diluted to the equivalents of 0.2 and 1 integration per genome was used as positive controls (0.2× and 1×).

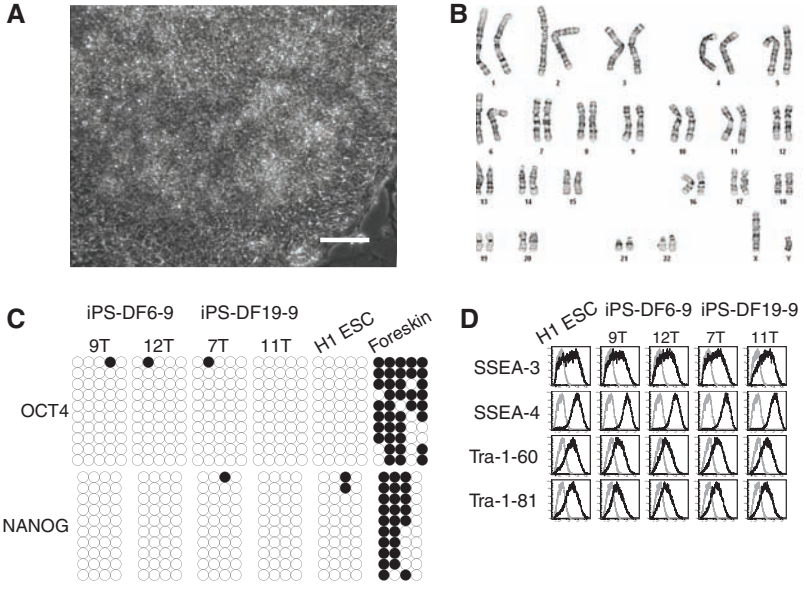

Fig. 3. Characterization of iPS cell subclones. (**A**) Bright-field image of iPS-DF6-9-12T. Scale bar, 0.1 mm. (**B**) G-banding chromosome analysis of iPS-DF6-9-12T. (**C**) Analysis of the methylation status of the *OCT4* and *NANOG* promoters in iPS cell subclones by means of bisulfite sequencing. Open circles indicate unmethylated, and filled circles indicate methylated CpG dinucleotides. (**D**) Flow cytometry expression analysis of human ES cell–specific cell surface markers. Gray line: isotype control; black line: antigen staining.

germ layers (Fig. 1D). Polymerase chain reaction (PCR) analysis failed to detect episomal vector integration in the genome, but did detect their persistence in the episomal fraction (Fig. 1E). The persistence of the episomal vectors suggests that prolonged transgene expression is required for successful reprogramming.

Because oriP/EBNA1 episomal vectors are gradually lost from proliferating cells in the absence of selection, we performed subcloning to derive iPS cell clones that had spontaneously lost the episomal vectors. We chose one iPS cell clone derived with combination 6 (iPS-DF6-9) and another one with combination 19 (iPS-DF19-9), and isolated 12 subclones from each. More than one-third of the subclones lost their episomal vectors (fig. S3A). We expanded two subclones from each vector combination for detailed analysis (iPS-DF6-9 subclone 9T and 12T, iPS-DF19-9 subclone 7T and 11T). Reverse transcription (RT)–PCR analysis with transgene-specific primers failed to detect any residual transgene expression in any of the four iPS cell subclones (Fig. 2A). In contrast to the parental iPS cell clones, PCR analysis demonstrated the absence of the vector and transgene sequences in both the genomic and the episomal fractions of all four iPS cell subclones (Fig. 2B), which was confirmed by Southern blot analysis (Fig. 2C and fig. S3B).

The iPS cell subclones were morphologically similar to human ES cells (Fig. 3A); had normal karyotypes (Fig. 3B); expressed human ES cell–specific cell surface markers (Fig. 3D) and genes (Fig. 4, A and B, fig. S4, and table S4); and differentiated into derivatives of all three germ layers in teratomas (Fig. 4C). Both the *OCT4* promoter and the *NANOG* promoter were demethylated in these iPS cells, similar to human ES cells and in contrast to the parental foreskin fibroblasts (Fig. 3C). As of this writing, combination 19 iPS cells have been in continuous culture for 7 months after the initial fibroblast transfection and have demonstrated no period of replicative crisis. DNA fingerprinting confirmed their origin from foreskin fibroblasts (table S5).

With oriP/EBNA1-based episomal vectors, exogenous DNA is not integrated into the human iPS cell genome, and owing to the gradual loss of cellular episomal vectors in the absence of drug selection, vector- and transgene-free human iPS cells can be isolated through subcloning without further genetic manipulation. Similar to mouse studies based on nonintegrating reprogramming methods (*6*, *7*), the current reprogramming efficiency of human fibroblasts with oriP/EBNA1 vectors is low (about three to six colonies per 10^6 input cells). These frequencies are, however, sufficient to recover iPS cells from a reasonable number of starting cells, and fibroblasts are easy to obtain and culture. Because different cell types have different reprogramming frequencies (*20*), and oriP/EBNA1-based vectors are established as stable episomes at different frequencies in different cell types (*13*), it might be possible to identify another accessible human cell type more easily reprogrammed with these episomal vectors. The addition of chemical compounds that increase reprogramming efficiency might also facilitate reprogramming by these episomal vectors (*21*, *22*).

Given the rapid pace of the iPS cell field, it is likely that reprogramming efficiencies will improve substantially and that it soon will be possible to derive vector- and transgene-free human iPS cells by several alternative methods. However, it will be essential to determine which of these methods most consistently produces iPS cells with the fewest genetic or epigenetic abnormalities, because any abnormalities would affect the application of these cells in basic research, drug development, and transplantation therapies much more than the initial reprogramming frequencies. Substantial challenges also remain in cell-specific differentiation and delivery, but the derivation of vector- and transgene-free human iPS cells is nonetheless an important advance toward the clinical application of these cells.

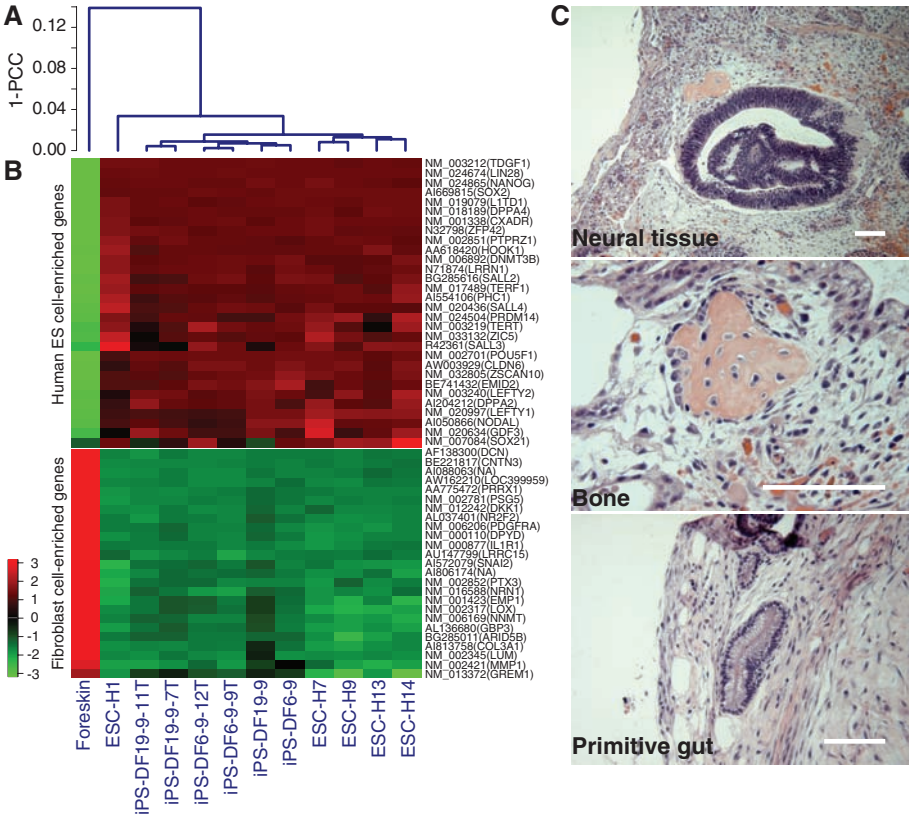

Fig. 4. Characterization of iPS cell subclones. (**A**) Pearson correlation analyses of global gene expression (51,337 transcripts) in iPS cell parental clone DF6-9 and DF19-9; iPS cell subclone DF6-9-9T, DF6-9-12T, DF19-9-7T, and DF19-9-11T; five human ES cell lines; foreskin fibroblasts. 1-PCC: Pearson correlation coefficient. (**B**) Expression of genes that are differentially expressed between human ES cells and foreskin fibroblasts. (Top) Thirty well-known human ES cell–enriched genes; (bottom) top 25 foreskin fibroblast-enriched genes. The color key is shown on the left. (**C**) Hematoxylin and eosin staining of teratoma sections of iPS-DF19-9-11T (7 weeks after injection). Teratomas were obtained from all four iPS cell subclones. Scale bars, 0.1 mm.

References and Notes

1. J. A. Thomson *et al.*, *Science* **282**, 1145 (1998).
2. J. Yu *et al.*, *Science* **318**, 1917 (2007).
3. K. Takahashi *et al.*, *Cell* **131**, 861 (2007).
4. K. Takahashi, S. Yamanaka, *Cell* **126**, 663 (2006).
5. K. Okita, T. Ichisaka, S. Yamanaka, *Nature* **448**, 313 (2007).
6. M. Stadtfeld, M. Nagaya, J. Utikal, G. Weir, K. Hochedlinger, *Science* **322**, 945 (2008).
7. K. Okita, M. Nakagawa, H. Hyenjong, T. Ichisaka, S. Yamanaka, *Science* **322**, 949 (2008).
8. K. Kaji *et al.*, *Nature* **458**, 771 (2009).
9. F. Soldner *et al.*, *Cell* **136**, 964 (2009).
10. K. Woltjen *et al.*, *Nature*, 10.1038/nature07863 (2009).
11. J. Yates, N. Warren, D. Reisman, B. Sugden, *Proc. Natl. Acad. Sci. U.S.A.* **81**, 3806 (1984).
12. J. L. Yates, N. Warren, B. Sugden, *Nature* **313**, 812 (1985).
13. E. R. Leight, B. Sugden, *Mol. Cell. Biol.* **21**, 4149 (2001).
14. J. L. Yates, N. Guan, *J. Virol.* **65**, 483 (1991).
15. A. Nanbo, A. Sugden, B. Sugden, *EMBO J.* **26**, 4252 (2007).
16. A. D. Ebert *et al.*, *Nature* **457**, 277 (2009).
17. J. Liao *et al.*, *Cell Res.* **18**, 600 (2008).
18. G. I. Evan *et al.*, *Cell* **69**, 119 (1992).
19. W. C. Hahn *et al.*, *Nature* **400**, 464 (1999).
20. T. Aasen *et al.*, *Nat. Biotechnol.* **26**, 1276 (2008).
21. Y. Shi *et al.*, *Cell Stem Cell* **3**, 568 (2008).
22. D. Huangfu *et al.*, *Nat. Biotechnol.* **26**, 795 (2008).

23. Funding was provided by the Charlotte Geyer Foundation and NIH (grants P51 RR000167 and P01 GM081629). We thank A. Griep, P. Powers, B. Sugden, M. Probasco, A. Elwell, C. Glennon, V. Ruotti, and D. J. Faupel for assistance and advice. The authors declare competing financial interests: J.A.T. is a founder, stock owner,

consultant, and board member of Cellular Dynamics International (CDI). He also serves as a scientific adviser to and has financial interests in Tactics II Stem Cell Ventures. I.I.S. is a founder, stock owner, and consultant for CDI. The authors are filing a patent based on the results reported in this paper. Combination 6 and 19 episomal vectors are deposited in Addgene (Cambridge, MA), and vector-free human iPS cell subclones are deposited in the WiCell International Stem Cell (WISC) Bank (Madison, WI). Microarray data are deposited in the Gene Expression Omnibus (GEO) database (accession number GSE15148).

Supporting Online Material
www.sciencemag.org/cgi/content/full/1172482/DC1
Materials and Methods
Figs. S1 to S4
Tables S1 to S8
References

18 February 2009; accepted 17 March 2009
Published online 26 March 2009;
10.1126/science.1172482
Include this information when citing this paper.

Benzothiazinones Kill *Mycobacterium tuberculosis* by Blocking Arabinan Synthesis

Vadim Makarov,[1,2]* Giulia Manina,[1,3]* Katarina Mikusova,[1,4]* Ute Möllmann,[1,5]* Olga Ryabova,[1,2] Brigitte Saint-Joanis,[1,6] Neeraj Dhar,[7] Maria Rosalia Pasca,[1,3] Silvia Buroni,[1,3] Anna Paola Lucarelli,[1,3] Anna Milano,[1,3] Edda De Rossi,[1,3] Martina Belanova,[1,4] Adela Bobovska,[1,4] Petronela Dianiskova,[1,4] Jana Kordulakova,[1,4] Claudia Sala,[1,7] Elizabeth Fullam,[1,7] Patricia Schneider,[1,7] John D. McKinney,[7] Priscille Brodin,[8] Thierry Christophe,[8] Simon Waddell,[1,9] Philip Butcher,[1,9] Jakob Albrethsen,[1,10] Ida Rosenkrands,[1,10] Roland Brosch,[1,6] Vrinda Nandi,[1,11] Sowmya Bharath,[1,11] Sheshagiri Gaonkar,[1,11] Radha K. Shandil,[1,11] Venkataraman Balasubramanian,[1,11] Tanjore Balganesh,[1,11] Sandeep Tyagi,[12] Jacques Grosset,[12] Giovanna Riccardi,[1,3] Stewart T. Cole[1,7]†

New drugs are required to counter the tuberculosis (TB) pandemic. Here, we describe the synthesis and characterization of 1,3-benzothiazin-4-ones (BTZs), a new class of antimycobacterial agents that kill *Mycobacterium tuberculosis* in vitro, ex vivo, and in mouse models of TB. Using genetics and biochemistry, we identified the enzyme decaprenylphosphoryl-β-D-ribose 2′-epimerase as a major BTZ target. Inhibition of this enzymatic activity abolishes the formation of decaprenylphosphoryl arabinose, a key precursor that is required for the synthesis of the cell-wall arabinans, thus provoking cell lysis and bacterial death. The most advanced compound, BTZ043, is a candidate for inclusion in combination therapies for both drug-sensitive and extensively drug-resistant TB.

The loss of human lives to tuberculosis (TB) continues essentially unabated as a result of poverty, synergy with the HIV/AIDS pandemic, and the emergence of multi- drug- and extensively drug-resistant strains of *Mycobacterium tuberculosis* (*1*–*3*). Despite some recent successes, such as the discovery of the diarylquinoline drug TMC207 (*4*) and the promise of the bicyclic nitroimidazole compounds (*5*–*8*), and because of the high attrition rate in drug development (*9*), much greater effort is required to find better drugs in order to meet the desired goals of killing persistent tubercle bacilli and reducing TB treatment duration from 6 to less than 3 months (*10*, *11*).

A series of sulfur-containing heterocycles was synthesized and tested for antibacterial and antifungal activity (*12*, *13*). Among their derivatives, compounds belonging to the nitrobenzothiazinone (BTZ) class showed particular promise in terms of their potency and specificity for mycobacteria. One of them, 2-[2-methyl-1,4-dioxa-8-azaspiro[4.5]dec-8-yl]-8-nitro-6-(trifluoromethyl)-4*H*-1,3-benzothiazin-4-one (BTZ038), was selected for further studies. This compound (series number 10526038; $C_{17}H_{16}F_3N_3O_5S$, with a molecular weight of 431.4; log$P$ = 2.84) (Fig. 1A) was synthesized in seven steps with a yield of 36%. Structure activity relationship work showed that the sulfur atom and the nitro group at positions 1 and 8, respectively, were critical for activity. BTZ038 has a single chiral center, and both enantiomers, BTZ043 (*S*) and BTZ044 (*R*), were found to be equipotent in vitro. Because early metabolic studies with bacteria or mice indicated that the nitro group could be reduced to an amino group, and because many TB drugs are prodrugs that require activation by *M. tuberculosis* (*14*), the *S* and *R* enantiomers of the amino derivatives and the likely hydroxylamine intermediate were synthesized and tested for antimycobacterial activity in vitro (table S1). The amino (BTZ045, *S* and *R*) and hydroxylamine (BTZ046) derivatives were substantially less active (500- to 5000-fold).

The minimal inhibitory concentrations (MICs) of a variety of BTZs against different mycobacteria were very low, ranging from ~0.1 to 80 ng/ml for fast growers and from 1 to 30 ng/ml for members of the *M. tuberculosis* complex (*13*). The MIC of BTZ043 against *M. tuberculosis* H37Rv and *Mycobacterium smegmatis* were 1 ng/ml (2.3 nM) and 4 ng/ml (9.2 nM), respectively (Table 1), which compares favorably with those of the existing TB drugs isoniazid (INH) (0.02 to 0.2 μg/ml) and ethambutol (EMB) (1 to 5 μg/ml) (*14*). From structure activity relationship studies, >30 different BTZ derivatives showed MICs of <50 ng/ml against tubercle

Table 1. MIC of BTZ043 against three different mycobacterial species and their resistant mutants.

Strain	MIC (ng/ml)	Codon	Amino acid
M. smegmatis mc^{2}155	4	TGC	Cysteine
M. smegmatis MN47	4000	GGC	Glycine
M. smegmatis MN84	>16,000	TCC	Serine
M. bovis BCG	2	TGC	Cysteine
M. bovis BCG BN2	>16,000	TCC	Serine
M. tuberculosis H37Rv	1	TGC	Cysteine
M. tuberculosis NTB9	250	GGC	Glycine
M. tuberculosis NTB1	10,000	TCC	Serine

[1]New Medicines for Tuberculosis (NM4TB) Consortium (www.nm4tb.org). [2]A. N. Bakh Institute of Biochemistry, Russian Academy of Science, 119071 Moscow, Russia. [3]Dipartimento di Genetica e Microbiologia, Università degli Studi di Pavia, via Ferrata, 1, 27100 Pavia, Italy. [4]Department of Biochemistry, Faculty of Natural Sciences, Comenius University, Mlynska dolina, 84215 Bratislava, Slovakia. [5]Department of Molecular and Applied Microbiology, Leibniz Institute for Natural Product Research and Infection Biology–Hans Knoell Institute, Beutenbergstrasse 11a, D-07745 Jena, Germany. [6]Institut Pasteur, Integrated Mycobacterial Pathogenomics, 25-28, Rue du Docteur Roux, 75724 Paris Cedex 15, France. [7]Global Health Institute, Ecole Polytechnique Fédérale de Lausanne, CH-1015 Lausanne, Switzerland. [8]Inserm Avenir Group, Institut Pasteur Korea, 39-1 Hawolgok-dong, Seongbuk-gu, 136-791 Seoul, Korea. [9]Division of Cellular and Molecular Medicine, St. George's Hospital, University of London, Cranmer Terrace, SW17 ORE London, UK. [10]Statens Serum Institut, Department of Infectious Disease Immunology, Artillerivej 5, DK-2300 Copenhagen S, Denmark. [11]AstraZeneca India, Bellary Road Hebbal, Bangalore, India. [12]Center for Tuberculosis Research, Johns Hopkins University School of Medicine, Baltimore, MD 21231, USA.

*These authors contributed equally to this work.
†To whom correspondence should be addressed. E-mail: stewart.cole@epfl.ch

bacilli (examples are shown in table S2). Crucially, BTZ043 displayed similar activity against all clinical isolates of *M. tuberculosis* that were tested, including multidrug-resistant and extensively drug-resistant strains, indicating that it targets a previously unknown biological function (table S3). BTZ043 is bactericidal, reducing viability in vitro by more than 1000-fold in under 72 hours (Fig. 1B), which is comparable to the killing effect seen with INH. In two different model systems (auxotrophy and starvation) involving metabolically inert *M. tuberculosis*, BTZ043 was less effective, which implies that it blocks a step in active metabolism, similar to INH (*14*).

Observation with time-lapse fluorescence microscopy of individual *M. smegmatis* cells [expressing green fluorescent protein (GFP)] growing in a microfluidic device (*15*) revealed that upon exposure to BTZ043, the growth rate decreased rapidly followed by a swelling of the poles and lysis of the cells after a few hours (movie S1). *M. tuberculosis* showed similar but delayed behavior (movie S2 and fig. S1).

Comparative transcriptome analysis of *M. tuberculosis* offered no evidence of mutagenic or nitrosative gene expression signatures after treatment with BTZ043, although expression of 60 genes was induced (table S4), and this was corroborated with proteomics. The transcriptional signature most resembled that generated by the cell wall inhibitors INH, isoxyl, and ethionamide, with the greatest overlap seen with the response to EMB treatment (*16*, *17*). This is consistent with cell lysis and indicated that BTZ targets cell wall biogenesis.

We then tested the uptake, intracellular killing, and potential cytotoxicity of BTZ compounds in an ex vivo model using a high-content screening approach (*18*, *19*) in order to monitor macrophages infected with *M. tuberculosis* expressing GFP. Macrophages treated with BTZ043 were protected (fig. S2) as compared with those treated with the amino derivative BTZ045 or the negative controls [dimethyl sulfoxide (DMSO)]. The deduced MIC of BTZ043 was <10 ng/ml, indicating that this compound is more potent than INH (100 ng/ml) and rifampin (>1 μg/ml) against intracellular bacteria (Fig. 1C). In contrast, the amino metabolite BTZ045 had an MIC of >1μg/ml, which is consistent with the in vitro findings (table S1). As a direct correlate of the antibacterial effect, there was extensive macrophage survival when all compounds were used at doses well above the MIC. BTZ043 was more cytotoxic than INH (Fig. 1C) at the highest concentration tested (10 μg/ml) but nonetheless has a favorable selectivity index of >100. Additional in vitro toxicology tests revealed no particularly unfavorable effects (table S4).

The in vivo efficacy of BTZ043 was assessed 4 weeks after a low-dose aerosol infection of BALB/c mice in the chronic model of TB. Four weeks of treatment with BTZ043 reduced the bacterial burden in the lungs and spleens by 1 and 2 logs, respectively, at the concentrations used (Fig. 1D). Additional results suggest that BTZ efficacy is time- rather than dose-dependent. Acute (5 g/kg) and chronic (25 and 250 mg/kg) toxicology studies in uninfected mice showed that, even at the highest dose tested, there were no adverse anatomical, behavioral, or physiological effects after one month (table S5).

To find the target for BTZ, we employed two independent genetic approaches. First, we identified cosmids bearing DNA from *M. smegmatis* that confer increased resistance on *M. smegmatis*, and we pinpointed the region responsible by subcloning. Second, we isolated and characterized mutants of *M. smegmatis*, *M. bovis* Bacille Calmette-Guérin (BCG), and *M. tuberculosis* displaying high-level BTZ resistance. The first approach revealed that the *MSMEG_6382* gene of *M. smegmatis* or its *M. tuberculosis* ortholog *rv3790* mediated increased resistance (Fig. 2A), whereas the second showed that drug-resistant mutants harbor missense mutations in the same gene (Table 1). Biochemical studies showed that *rv3790* and the neighboring gene *rv3791* code for proteins that act in concert to catalyze the epimerization of decaprenylphosphoryl ribose (DPR) to decaprenylphosphoryl arabinose (DPA) (*20*), a precursor for arabinan synthesis without which a complete mycobacterial cell wall cannot be produced. These essential membrane-associated enzymes (*20*–*23*) have been suggested to act as decaprenylphosphoryl-β-D-ribose oxidase and decaprenylphosphoryl-D-2-keto erythro pentose reductase, respectively, and we propose naming them DprE1 and DprE2. In all of the drug-resistant mutants we examined, the same

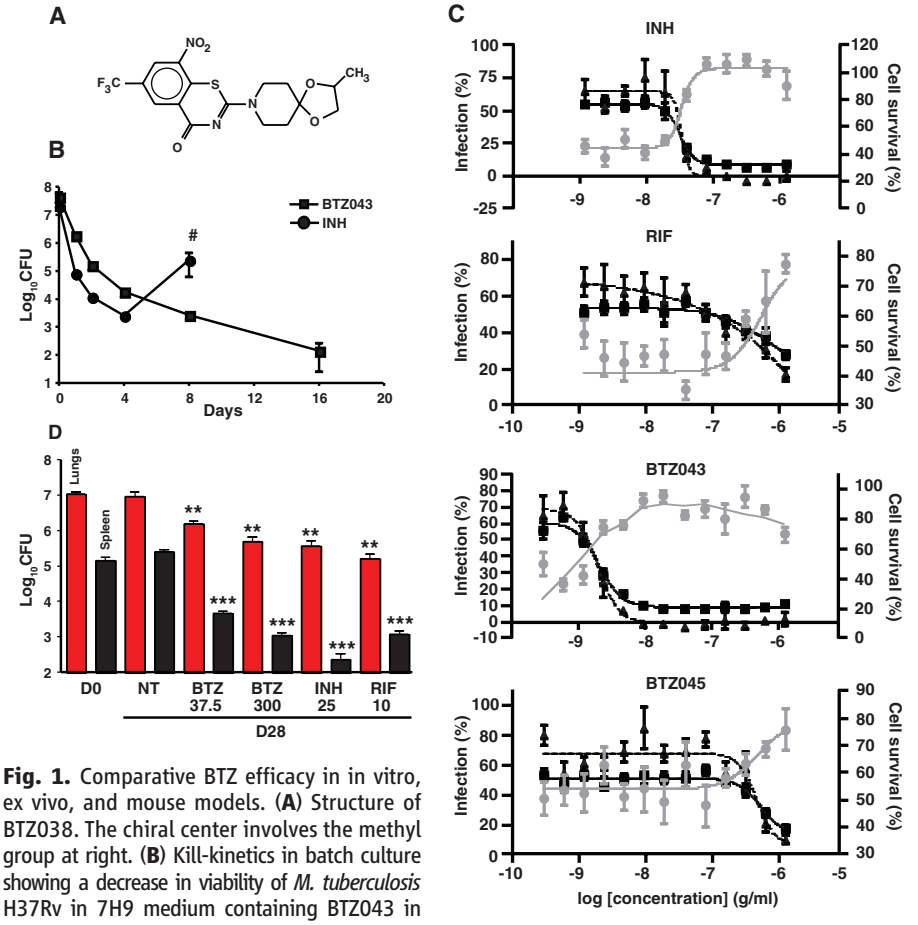

Fig. 1. Comparative BTZ efficacy in in vitro, ex vivo, and mouse models. (**A**) Structure of BTZ038. The chiral center involves the methyl group at right. (**B**) Kill-kinetics in batch culture showing a decrease in viability of *M. tuberculosis* H37Rv in 7H9 medium containing BTZ043 in comparison with INH (both at 200 ng/ml). The regrowth after treatment with INH (pound sign indicates the experiment was terminated because of resistance) is not seen with BTZ043. (**C**) Response of macrophages infected with GFP-labeled *M. tuberculosis* to treatment with different compounds, expressed in percent of bacterial load (triangles), cell survival (circles), and infected cells (squares) relative to compound concentration in grams per milliliter. Each percentage is based on DMSO and INH controls from the same experiments. For each concentration, the mean ± SEM of the quadruplicate are reported. For the original images, see fig. S2. (**D**) Efficacy of BTZ043 in a mouse model of chronic tuberculosis compared with INH, rifampin (RIF), and untreated controls. Red and black columns correspond to the bacterial load in the lungs and spleens, respectively, of chronically infected BALB/c mice (4 weeks after infection) at day 0 (D0), before treatment. The remaining columns show bacterial loads at day 28 in untreated animals (NT) (5 per group) or in mice treated with various drugs at the doses indicated (milligrams per kilogram of body weight per day). Bars represent the mean ± SEM; data are representative of two independent experiments from two different centers. $^{**}P = 0.001$; $^{***}P < 0.000001$.

codon of *rv3790* (*dprE1*) was affected, in which Cys387 was replaced by Ser or Gly codons, respectively (Table 1). Mutants, harboring alleles such as those in MN47 or MN84, were rare, arising at a frequency of $<10^{-8}$, and were dominant over the wild-type gene upon introduction into a BTZ-susceptible mycobacterium. Comparative genomics revealed that the BTZ resistance–determining region of *rv3790* was highly conserved in orthologous genes from various actinobacteria, except that in a few cases Cys387 was replaced by Ser or Ala (Fig. 2B). The corresponding bacteria, *M. avium* and *M. aurum*, were found to be naturally resistant to BTZ (table S3), thus supporting the identification of DprE1/Rv3790 as the target.

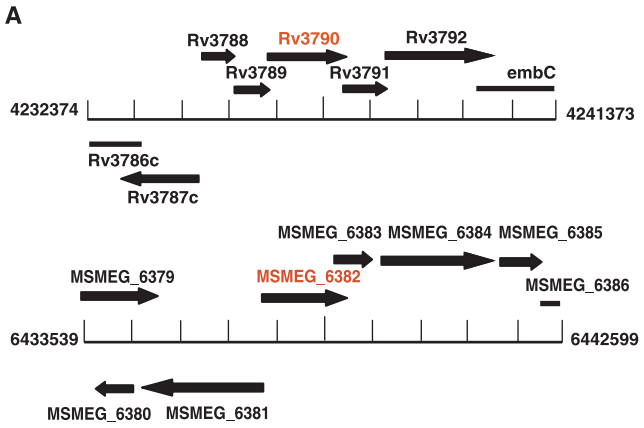

B

```
                                361                 381                 401                 420
                                 |                   |                   |                   |
M. tuberculosis (Rv3790)        SFLNVFKLFGPRNQAPLSFPIPGWNICVDFPIKDGLGKFVSELDRRVLEFGGRLYTAKDS
M. bovis                        SFLNVFKLFGPRNQAPLSFPIPGWNICVDFPIKDGLGKFVSELDRRVLEFGGRLYTAKDS
M. leprae                       SFLNVFKLFGPGNQAPLSFPIPGWNICVDFPIKSGLNEFVNKLDRRVMELGGRLYTAKDS
M. avium                        SALNVFKLFGPGNRAPLSFPMAGWNVAMDFPNKPGVNEFLNELDRRVLQFGGRVYTAKDS
M. avium paratuberculosis       SALNVFKLFGPGNRAPLSFPMAGWNVAMDFPNKPGVNEFLNELDRRVLQFGGRVYTAKDS
M. smegmatis                    SFLNVFKLFGPGNQAPLSFPIPGWNVCVDFPIKAGLHEFVTELDRRVLEFGGRLYTAKDS
M. aurum                        SFLNVFKLFGPRNQAPLSFPIPGWNISVDFPIKDGLGKFVSELDRRVLEFGGRLYTAKDS
M. gilvum                       SFLNVFKLFGPGNQAPLSFPIPGWNVCVDFPITAGLNEFLNGLDKRVLQFGGRLYTAKDS
M. vanbalenii                   SFLNVFKLFGPGNDAPLSFPIPGWNVCVDFQINPGLNEFLNGLDKRVLEFGGRLYTAKDS
M. marinum                      SFLNVFKLFGAGNQAPLSFPIPGWNICVDFPIKAGLNEFVSELDRRVMEFGGRLYTAKDS
Rhodococcus spp.                SFLNVFKLFGEGNQAPLSFPIPGWNICVDFRIKPGLNEFVTELDKRVLKFGGRLYTAKDS
Nocardia farcinica              SFLNVFKYFGQGNQAPLSFPMPGWNVCLDFPIKPGLNEFVTELDSRVLEFGGRLYTGKDS
Corynebacterium glutamicum      SALNVFKLFGEGNKAPLSYPMPGWNVCVDFPIKPGLGAFLDDLDKRVMEFGGRLYLAKES
                                * ***** **  * ****:*:.***:.:*:    *:  *:  ** **:::***:* .*:*
```

Fig. 2. Identification of the BTZ target. (**A**) Organization of genomic regions of *M. tuberculosis* and *M. smegmatis* associated with BTZ resistance. (**B**) Multiple alignment of the BTZ resistance–determining region in orthologs of Rv3790 from various actinobacteria.

Further corroboration was obtained biochemically (Fig. 3) by using membrane preparations from *M. smegmatis* to catalyze the epimerization reaction from radiolabeled DPR precursor, which was produced in situ from 5-phosphoribose diphosphate (*20*), in the presence or absence of BTZ. Addition of BTZ038, or its enantiomers BTZ043 and BTZ044, abolished the production of DPA from DPR. This reaction was scarcely affected by either the *S* or *R* forms of BTZ045 (Fig. 3A) or by BTZ046 (fig. S3). Using recombinant proteins, we found that the reaction requires both DprE1 and E2 (Rv3790 and Rv3791) (Fig. 3B), with neither enzyme alone capable of catalyzing DPA formation. Furthermore, when BN2, the highly BTZ-resistant mutant of *M. bovis* BCG, or *M. smegmatis* MN47 and MN84, with missense mutations in *MSMEG_6382* (*dprE1*) (Table 1), were used as sources of enzymes, epimerization was no longer subject to inhibition (Fig. 3C and fig. S3), thereby confirming identification of the BTZ target.

The point of BTZ inhibition in the biosynthetic pathway for arabinan precursors is shown in fig. S4, and as predicted by the gene expression profiling results, BTZ and EMB both target the same pathway, which is restricted to certain actinobacteria. The latter drug acts downstream on the EmbCAB arabinosyl transferases that use DPA, the sole arabinan donor in mycobacteria, to produce arabinogalactan or lipoarabinomannan (*24*, *25*). Consistent with DPA limitation, BTZ treatment also blocks the production of both of these species (fig. S3). Arabinogalactan plays a critical function in the mycobacterial cell envelope by acting as a covalent linker between peptidoglycan on the inside and the mycolic acids at the outer surface, thus playing a pivotal role in cellular integrity. A major difference between the two drugs lies in the potency of BTZ, which is 1000-fold more active than EMB against *M. tuberculosis*.

In conclusion, BTZ is a candidate for development into a sterilizing TB drug acting on the enzyme decaprenylphosphoryl-β-D-ribose 2′-epimerase. This target has been chemically validated in vivo and can now be used in screening for the identification of additional inhibitors.

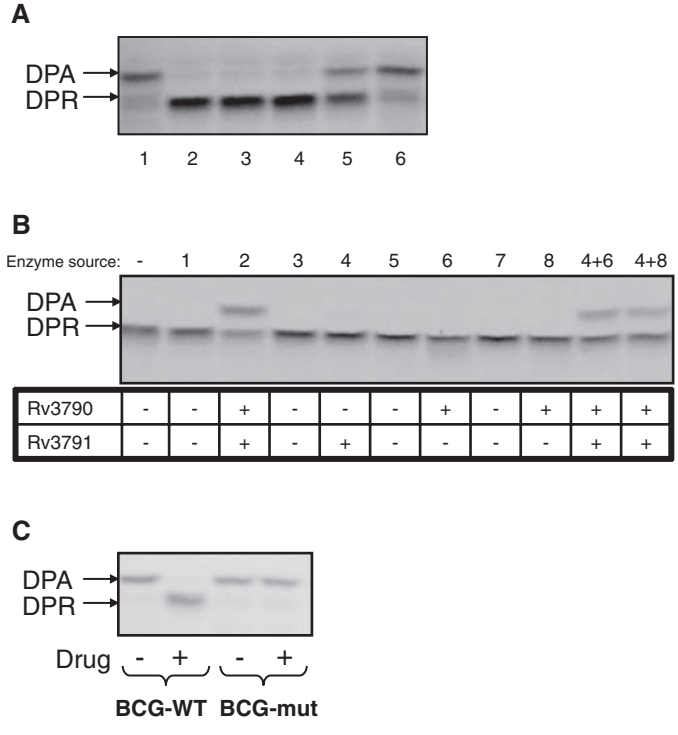

Fig. 3. Inhibition of decaprenylphosphoryl-β-D-ribose epimerization by BTZ. (**A**) Effect of different BTZ derivatives (table S1) on DPA production from DPR by using mycobacterial membranes in vitro. Lane 1, no drug control; lane 2, BTZ038; lane 3, BTZ043; lane 4, BTZ044; lane 5, BTZ045S; lane 6, BTZ045R. (**B**) Production of DPA from DPR requires both Rv3790 (DprE1) and Rv3791 (DprE2). *E. coli* strains that were used in the experiment (*26*) expressed the following *M. tuberculosis* proteins: lane 1, none; lane 2, Rv3790-Rv3791; lane 3, none; lane 4, Rv3791; lane 5, none; lane 6, Rv3790; lane 7, none; lane 8, Rv3790. (**C**) Effect of BTZ043 on DPA production by using cell wall fractions from BTZ-sensitive *M. bovis* BCG and its BTZ-resistant mutant, BN2 (Table 1).

References and Notes

1. C. Dye, *Lancet* **367**, 938 (2006).
2. N. R. Gandhi *et al.*, *Lancet* **368**, 1575 (2006).
3. M. Zignol *et al.*, *J. Infect. Dis.* **194**, 479 (2006).
4. K. Andries *et al.*, *Science* **307**, 223 (2005).
5. C. K. Stover *et al.*, *Nature* **405**, 962 (2000).

6. U. H. Manjunatha *et al.*, *Proc. Natl. Acad. Sci. U.S.A.* **103**, 431 (2006).
7. M. Matsumoto *et al.*, *PLoS Med.* **3**, e466 (2006).
8. R. Singh *et al.*, *Science* **322**, 1392 (2008).
9. T. S. Balganesh, P. M. Alzari, S. T. Cole, *Trends Pharmacol. Sci.* **29**, 576 (2008).
10. Global Alliance for TB, *Tuberculosis (Edinb.)* **81**, (suppl. 1), 1 (2001).
11. D. B. Young, M. D. Perkins, K. Duncan, C. E. Barry 3rd, *J. Clin. Invest.* **118**, 1255 (2008).
12. V. Makarov, U. Möllmann, S. T. Cole, Eurasian Patent Application EP2029583 (2007).
13. V. Makarov *et al.*, *J. Antimicrob. Chemother.* **57**, 1134 (2006).
14. Y. Zhang, C. Vilcheze, W. R. Jacobs Jr., in *Tuberculosis and the Tubercle Bacillus*, S. T. Cole, K. D. Eisenach, D. N. McMurray, W. R. Jacobs Jr., Eds. (American Society for Microbiology Press, Washington, DC, 2005), pp. 115–140.
15. N. Q. Balaban, J. Merrin, R. Chait, L. Kowalik, S. Leibler, *Science* **305**, 1622 (2004).
16. H. I. Boshoff *et al.*, *J. Biol. Chem.* **279**, 40174 (2004).
17. S. J. Waddell, P. D. Butcher, *Curr. Mol. Med.* **7**, 287 (2007).
18. V. C. Abraham, D. L. Taylor, J. R. Haskins, *Trends Biotechnol.* **22**, 15 (2004).
19. D. Fenistein, B. Lenseigne, T. Christophe, P. Brodin, A. Genovesio, *Cytometry A* **73**, 958 (2008).
20. K. Mikusova *et al.*, *J. Bacteriol.* **187**, 8020 (2005).
21. C. M. Sassetti, D. H. Boyd, E. J. Rubin, *Proc. Natl. Acad. Sci. U.S.A.* **98**, 12712 (2001).
22. B. A. Wolucka, *FEBS J.* **275**, 2691 (2008).
23. C. E. Barry, D. C. Crick, M. R. McNeil, *Infect. Disord. Drug Targets* **7**, 1 (2007).
24. K. Mikusova, R. A. Slayden, G. S. Besra, P. J. Brennan, *Antimicrob. Agents Chemother.* **39**, 2484 (1995).
25. L. J. Alderwick *et al.*, *J. Biol. Chem.* **280**, 32362 (2005).
26. Materials and methods are available as supporting material on *Science* Online.

27. We thank A. Deshpande, I. Heinemann, P. Højrup, K. Johnsson, M. K. N. Kumar, N. Kumar, L. Pagani, P. Marone, M. R. McNeil, I. Old, J. Reddy, S. Schmitt, P. Vachaspati, and C. Weigel for their help and support. Patents related to this work have been filed (WO/2007/134625, WO/2009/010163, and PCT/EP2008/001088). The NM4TB Consortium is funded by the European Commission (LHSP-CT-2005-018923), and microarray work at St George's Hospital, University of London, is supported by the Wellcome Trust (grant 062511). Microarray data are Minimum Information About a Microarray Experiment (MIAME)–compliant and deposited under accession number E-BUGS-80 at http://bugs.sgul.ac.uk/E-BUGS-80.

Supporting Online Material

www.sciencemag.org/cgi/content/full/1171583/DC1
Materials and Methods
Figs. S1 to S4
Tables S1 to S6
References
Movies S1 and S2

29 January 2009; accepted 13 March 2009
Published online 19 March 2009;
10.1126/science.1171583
Include this information when citing this paper.

Mammalian Expression of Infrared Fluorescent Proteins Engineered from a Bacterial Phytochrome

Xiaokun Shu,[1,2] Antoine Royant,[3] Michael Z. Lin,[2] Todd A. Aguilera,[2] Varda Lev-Ram,[2] Paul A. Steinbach,[1,2] Roger Y. Tsien[1,2,4]*

Visibly fluorescent proteins (FPs) from jellyfish and corals have revolutionized many areas of molecular and cell biology, but the use of FPs in intact animals, such as mice, has been handicapped by poor penetration of excitation light. We now show that a bacteriophytochrome from *Deinococcus radiodurans*, incorporating biliverdin as the chromophore, can be engineered into monomeric, infrared-fluorescent proteins (IFPs), with excitation and emission maxima of 684 and 708 nm, respectively; extinction coefficient >90,000 M^{-1} cm^{-1}; and quantum yield of 0.07. IFPs express well in mammalian cells and mice and spontaneously incorporate biliverdin, which is ubiquitous as the initial intermediate in heme catabolism but has negligible fluorescence by itself. Because their wavelengths penetrate tissue well, IFPs are suitable for whole-body imaging. The IFPs developed here provide a scaffold for further engineering.

In vivo optical imaging of deep tissues in animals is most feasible between 650 and 900 nm because such wavelengths minimize the absorbance by hemoglobin, water, and lipids, as well as light-scattering (*1*, *2*). Thus, genetically encoded IFPs would be particularly valuable for whole-body imaging in cancer and stem cell biology (*3*, *4*), gene therapy, and so on. However, excitation and emission maxima of FPs have not yet exceeded 598 and 655 nm, respectively (*5*–*7*). Somewhat longer wavelengths (644-nm excitation, 672-nm emission) have been observed in a phytochrome-based FP that incorporates phycocyanobilin (PCB) as the chromophore (*8*). However, neither incorporation of exogenous PCB nor transfer of its biosynthetic pathway into animal cells has yet been demonstrated. Bacterial phytochromes are more promising because they incorporate biliverdin IXα (BV) instead of PCB (*9*), and BV is the initial intermediate in heme catabolism by heme oxygenase (HO-1) in all aerobic organisms, including animals. For example, normal adult humans endogenously generate and metabolize 300 to 500 mg BV each day simply from routine heme breakdown (*10*). Recently, a full-length bacteriophytochrome (DrBphP) from *Deinococcus radiodurans* with a single mutation (D207H) (*11*) was reported to be red fluorescent at 622 nm upon excitation of the Soret band near 416 nm (*12*). Excitation of the Q band absorbing at 699 nm gave no fluorescence (*12*), which contradicted Kasha's rule that fluorescence occurs from the lowest excited state. Emission peaks at 710 to 725 nm have been observed from various forms of *Rhodopseudomonas palustris* (*13*) and *Pseudomonas aeruginosa* (*14*) bacteriophytochromes expressed in *Escherichia coli*, but fluorescence efficiencies have not been quantified, and reconstitution in nonbacterial systems has not yet been demonstrated.

To minimize the probability of nonradiative decay, we chose to limit DrBphP to its chromophore-binding domain (CBD), consisting of the PAS and GAF domains, which are

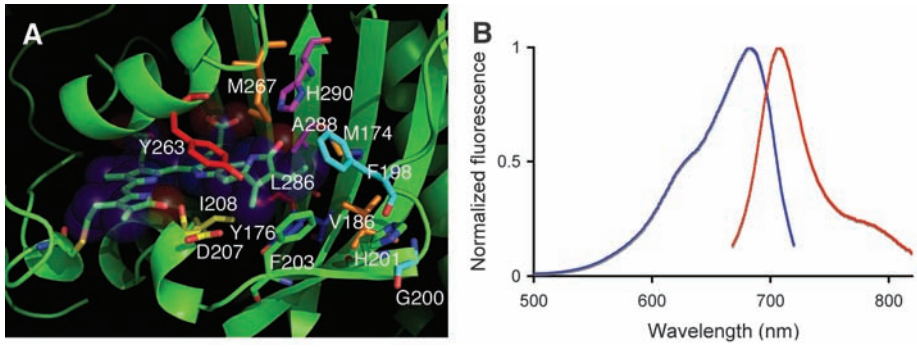

Fig. 1. Infrared fluorescent proteins created by structure-based engineering of a bacteriophytochrome. (**A**) Fourteen residues surrounding the biliverdin in DrCBD [Protein Data Bank (PDB) ID: 1ztu] (*16*) were divided into seven groups (shown in different colors) and targeted for mutagenesis. (**B**) Normalized excitation (blue) and emission (red) spectra of IFP1.4.

[1]Howard Hughes Medical Institute, University of California at San Diego, 9500 Gilman Drive, La Jolla, CA 92093–0647, USA. [2]Department of Pharmacology, University of California at San Diego, 9500 Gilman Drive, La Jolla, CA 92093–0647, USA. [3]Institut de Biologie Structurale 41, rue Jules Horowitz, 38027 Grenoble CEDEX 1, France. [4]Departments of Chemistry and Biochemistry, University of California at San Diego, 9500 Gilman Drive, La Jolla, CA 92093–0647, USA.

*To whom correspondence should be addressed. E-mail: rtsien@ucsd.edu

necessary and sufficient for covalent incorporation of BV (*15*, *16*). We discarded the PHY domain and the C-terminal histidine kinase–related domain (HKRD) (*9*), which transduce excited-state energy into conformational change and biochemical signaling (*16*). A gene encoding DrCBD (321 amino acids) with the D207H mutation (in which His replaces Asp at codon 207) was synthesized with codons optimized for *E. coli* (*17*). When coexpressed with cyanobacterial HO-1 in *E. coli* and excited near 700 nm, the truncated mutant fluoresced in the infrared with emission maximum of 722 nm. However, this mutant, dubbed IFP1.0, is weakly fluorescent (table S1), reversibly photofatiguable (fig. S1), and dimeric (fig. S2). The dimerization of IFP1.0 is due to at least four residues (Y307/L311/L314/V318) through hydrophobic interactions (fig. S3A).

On the basis of the crystal structure of DrCBD (*16*), nonradiative decay of the excited chromophore is probably promoted by rotation of the D pyrrole ring because of relatively sparse packing of surrounding residues. Multiple sequence alignment of >100 phytochromes revealed conserved residues, some of which may contribute to photoisomerization [see supporting online material (SOM) text]. In order to increase the brightness of IFP1.0, 14 residues near the D ring were chosen and divided into seven groups for saturation mutagenesis (Fig. 1A), followed by DNA shuffling, which generated IFP1.1, with excitation and emission maxima of 686 and 713 nm, respectively, and brightness greater than that of IFP1.0 by a factor of ~2.6 (table S1). Several more rounds of directed evolution of IFP1.1 led to IFP1.4 (fig. S4).

IFP1.4 is about four times brighter than IFP1.0 (table S1), and its fluorescence is stable over a wide pH range from 5 to 9 (fig. S5). IFP1.4 is monomeric (fig. S2) and no longer shows significant reversible photofatigue (fig. S1). At an excitation rate that initially produces 1000 emitted photons per s per molecule of IFP1.1 or 1.4, the time to photobleach by 50% ($t_{1/2}$) is 8.5 or 8.4 s, respectively. For comparison, $t_{1/2}$ of the popular yellow fluorescent protein Venus is 15 s (*18*). A rationally introduced mutation L311K replaced a hydrophobic group by a charged amino acid and disrupted the dimer interface in IFP1.2 (fig. S3B). Mutation A288V likely eliminated the residual photoconversion of IFP1.0, because two additional methyl groups of Val^{288} may limit the D-ring rotation. However, the excitation and emission maxima of IFP1.4, 684 and 708 nm, respectively, are slightly blue-shifted compared with IFP1.0 (Fig. 1B). The blue shift may have resulted from using 676-nm excitation, the longest-wavelength laser line available to us, to select for higher brightness during fluorescence-activated cell sorting.

Expression of IFP1.4 alone without exogenous BV leads to bright and homogeneous infrared fluorescence in human embryonic kidney cells (HEK293A) (Fig. 2A). Furthermore, exogenously added BV further increased infrared fluorescence of transfected cells including neurons (fig. S6), which demonstrated that BV is membrane-permeant and adds rapidly to fill

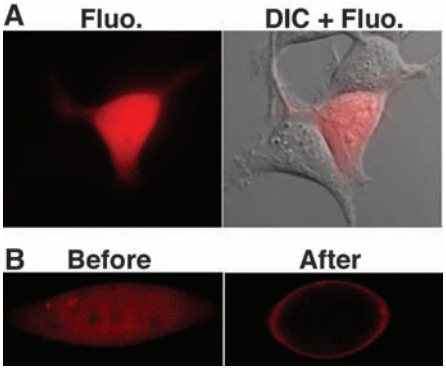

Fig. 2. Imaging of IFP1.4 and IFP1.4-PH^{AKT1} in HEK293A cells. (**A**) Fluorescence image of IFP1.4 taken with Cy5.5 filter set (665 ± 22.5 nm excitation, 725 ± 25 nm emission) with and without differential interference contrast (DIC). (**B**) Confocal laser-scanning microscopy of IFP1.4-PH^{AKT1} before and after insulin stimulation (excitation by 635-nm laser, emission by 650-nm long-pass filter).

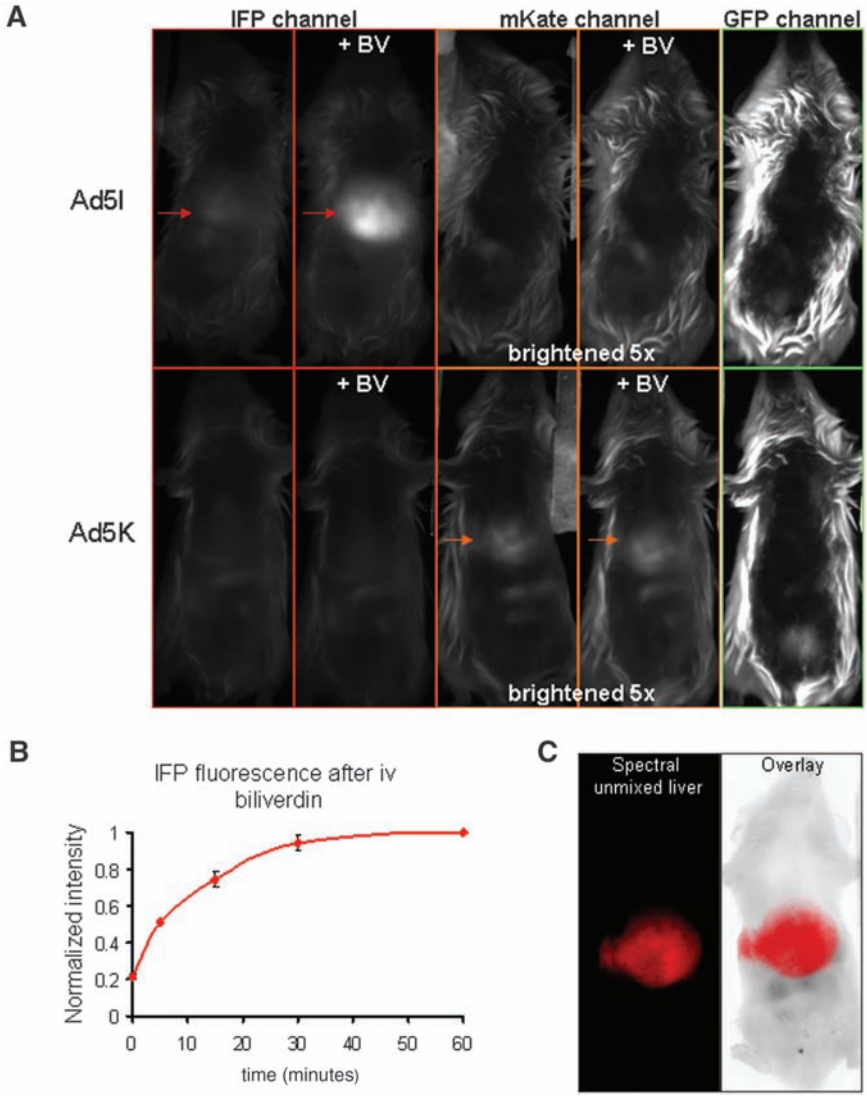

Fig. 3. Imaging of GFP, mKate, and IFP1.1 in living mice. (**A**) Liver fluorescence of living mice injected with Ad5I (top row) and Ad5K (bottom row), imaged in the IFP excitation and emission channel before and after BV administration, mKate channel before and after BV, and GFP channel (*17*). Images through the mKate channel have been 5× brightened in software to render them visible, so the relative gains of the IFP channel, mKate channel, and GFP channel were 1, 5, and 1, respectively. Arrows point to the liver. Note that the GFP images are dominated by autofluorescence, which renders the livers invisible. (**B**) Time course of averaged and normalized Ad5I liver fluorescence before and after BV injection. (**C**) Images of IFP-expressing mouse showing spectrally deconvoluted liver fluorescence (left, red) and its overlay (right) with autofluorescence (gray).

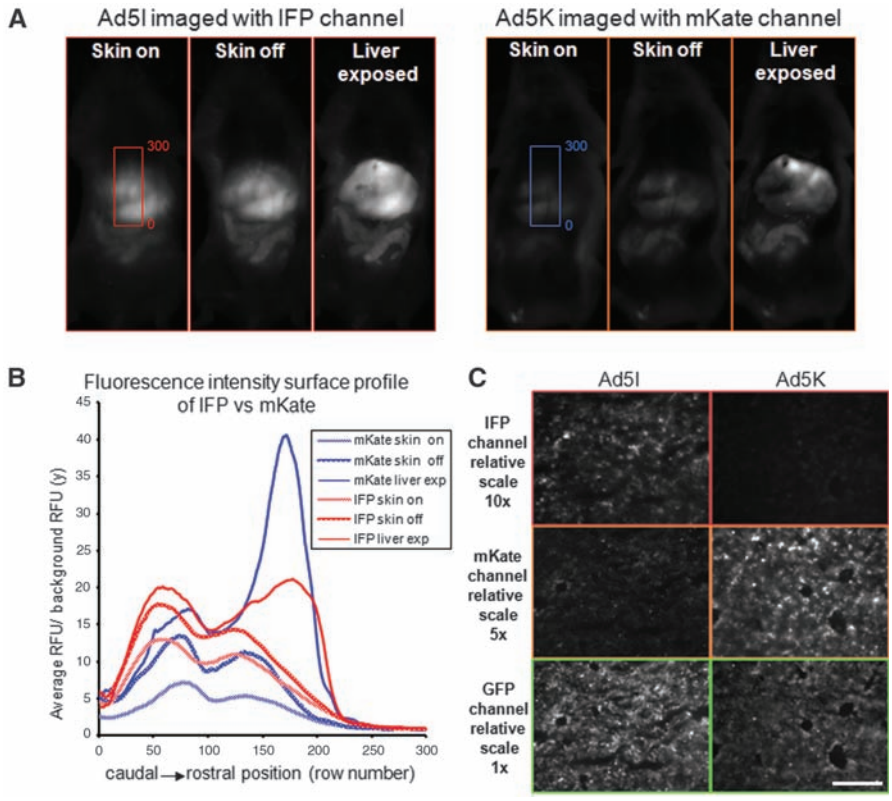

Fig. 4. Analysis of mKate and IFP1.1 visibility and expression levels in livers of mice infected with Ad5I and Ad5K. (**A**) IFP and mKate fluorescence images before dissection (skin on), after removal of skin (skin off), and after removal of overlying peritoneum and rib cage (liver exposed). mKate images were 2.5× brightened relative to IFP images. Note that the Ad5I-infected mouse was imaged after 250 nmol intravenous injection of BV. See bright-field images in fig. S9. (**B**) Fluorescence intensity (signal-to-noise ratio) analysis of livers from (**A**). Average of 80 pixels in the horizontal *x* axis divided by the average of the 30 most rostral horizontal lines from each of the images starting below the liver (i.e., signal-to-noise ratio), moving rostrally for 300 lines. (**C**) Frozen sections were imaged to show IFP, mKate, and GFP expression with a fluorescence stereomicroscope (Lumar, Zeiss) (*17*), displayed with relative intensity gains of 10, 5, and 1, respectively. Scale bar, 200 μm.

IFP1.4 when endogenous BV had not saturated the protein. The half-life of IFP1.4 is about 4 hours in HEK293A cells (figs. S7, S8).

As a simple demonstration that IFP1.4 fusions can be functional, IFP1.4 was fused to the pleckstrin homology (PH) domain of human AKT1 (*19*). This PH domain is known to bind to phosphatidylinositol 3,4,5-trisphosphate formed at the plasma membrane after growth factor stimulation. Serum-starved HEK293 cells expressing the IFP1.4-PH^{AKT1} fusion showed IR fluorescence diffusely distributed in the cytosol, but this signal translocated to the plasma membrane within 10 min after insulin stimulation (Fig. 2B), which illustrated that IFP1.4 can highlight the trafficking of fusion proteins.

Expression of IFPs in intact mice via adenovirus serotype 5 (Ad5) also produced infrared fluorescence. Ad5 is well known to infect mouse liver specifically (*20*). Two modified versions of Ad5 were generated: Ad5I and Ad5K. Ad5I contains the genes for IFP1.1 and green fluorescent protein (GFP), the latter controlled by an internal ribosome entry sequence (IRES) (*17*). Ad5K encodes mKate, a red fluorescent protein advocated for in vivo imaging (*5*), and IRES-GFP. Weak infrared fluorescence of liver was detected 5 days after intravenous injection of Ad5I through tail vein (Fig. 3A). The whole liver was easily detected after intravenous injection of 250 nmol (~7 mg/kg) BV (Fig. 3A). The increase in liver fluorescence was half-maximal in ~10 min and maximal (about fivefold) 1 hour after BV injection (Fig. 3B). Resolution of IFP fluorescence from background autofluorescence can be enhanced by spectral deconvolution (Fig. 3C). The three-dimensional distribution of IFP fluorescence in the mouse liver can be reconstructed tomographically (fig. S9). BV injection did not cause observable toxicity in mice (*21*). Furthermore, higher doses of BV (35 to 50 mg/kg) have been reported to give beneficial protection in vivo against reactive oxygen species (*22*) and transplantation-induced injury (*23*). As a control, intravenous injection of 250 nmol BV did not generate infrared fluorescence in either Ad5K-infected mice (Fig. 3A) or uninfected mice (not shown). The far-red fluorescence of mKate was observed in Ad5K-infected liver and was unaffected by BV. Neither Ad5I- nor Ad5K-infected intact mice displayed GFP fluorescence in their livers (Fig. 3A). Removal of the overlying skin, followed by complete exposure of the liver, increased the mKate fluorescence by a much greater factor than for the IFP signal (Fig. 4 and fig. S10), which showed how overlying tissues attenuate mKate's excitation and emission wavelengths to a greater extent than those for IFP.

The entire dissected liver was fluorescent for mice expressing IFP and mKate (fig. S11), which suggested virus infection of the whole liver. GFP fluorescence became visible only after complete extraction of the liver and was similar for Ad5I and Ad5K (fig. S11), which indicated similar efficiencies of viral infection. Fluorescence microscopy of frozen sections showed fluorescence increasing in the order IFP1.1 < mKate < GFP fluorescence (Fig. 4C), which confirmed that IFP remains detectable in histology and that its improved visibility in vivo is due not to higher expression levels but rather to superior penetration of longer excitation and emission wavelengths through bulk pigmented tissue.

IFPs can be imaged over spatial scales from subcellular resolution up to strongly pigmented organs within intact whole mammals, whereas luciferase-based bioluminescence is useful mainly for whole-body imaging (*24*). The wavelengths of IFPs are particularly well-suited to optical tomographic reconstruction (fig. S9) (*25*). Even for microscopic imaging where existing FPs are highly effective, IFPs should reduce the contribution of cellular autofluorescence; enable excitation by cheap laser diodes; add new wavelengths for multicolor labeling; and accept resonance energy transfer from other dyes, FPs, or bioluminescent proteins. BV is uniquely advantageous as a cofactor because it is spontaneously and irreversibly incorporated into bacteriophytochromes (*26*), nontoxic at appropriate doses (*21*–*23*), nonfluorescent by itself, endogenously produced, and can be further supplemented either by expression of HO-1 or by direct administration of commercially available material. HO-1 is an important enzyme in its own right and is involved in various diseases (*27*). Its cumulative activity could be monitored by IFP fluorescence if apoprotein expression were in excess over BV. More than 1500 bacteriophytochrome-like sequences are already available in the National Center for Biotechnology Information (NIH) and CAMERA databases (*28*). These genes should provide raw material for selection and directed evolution of photochemical transducers based on a scaffold completely independent of the 11-stranded β barrel of coelenterate FPs.

References and Notes

1. F. F. Jöbsis, *Science* **198**, 1264 (1977).
2. R. Weissleder, V. Ntziachristos, *Nat. Med.* **9**, 123 (2003).
3. T. Schroeder, *Nature* **453**, 345 (2008).
4. R. Weissleder, M. J. Pittet, *Nature* **452**, 580 (2008).
5. D. Shcherbo *et al.*, *Nat. Methods* **4**, 741 (2007).
6. M. A. Shkrob *et al.*, *Biochem. J.* **392**, 649 (2005).

7. L. Wang, W. C. Jackson, P. A. Steinbach, R. Y. Tsien, *Proc. Natl. Acad. Sci. U.S.A.* **101**, 16745 (2004).
8. A. J. Fischer, J. C. Lagarias, *Proc. Natl. Acad. Sci. U.S.A.* **101**, 17334 (2004).
9. S. J. Davis, A. V. Vener, R. D. Vierstra, *Science* **286**, 2517 (1999).
10. J. W. Harris, R. W. Kellermeyer, *The Red Cell* (Harvard Univ. Press, Cambridge, MA, 1970).
11. Single-letter abbreviations for the amino acid residues are as follows: A, Ala; C, Cys; D, Asp; E, Glu; F, Phe; G, Gly; H, His; I, Ile; K, Lys; L, Leu; M, Met; N, Asn; P, Pro; Q, Gln; R, Arg; S, Ser; T, Thr; V, Val; W, Trp; and Y, Tyr.
12. J. R. Wagner *et al.*, *J. Biol. Chem.* **283**, 12212 (2008).
13. E. Giraud *et al.*, *J. Biol. Chem.* **280**, 32389 (2005).
14. X. Yang, J. Kuk, K. Moffat, *Proc. Natl. Acad. Sci. U.S.A.* **105**, 14715 (2008).
15. N. C. Rockwell, Y. S. Su, J. C. Lagarias, *Annu. Rev. Plant Biol.* **57**, 837 (2006).
16. J. R. Wagner, J. S. Brunzelle, K. T. Forest, R. D. Vierstra, *Nature* **438**, 325 (2005).
17. Materials and methods are available as supporting material on *Science* Online.
18. N. C. Shaner, P. A. Steinbach, R. Y. Tsien, *Nat. Methods* **2**, 905 (2005).
19. A. Bellacosa, J. R. Testa, S. P. Staal, P. N. Tsichlis, *Science* **254**, 274 (1991).
20. S. N. Waddington *et al.*, *Cell* **132**, 397 (2008).
21. Six mice after BV injection were observed for 3 days (the maximum time that we could hold mice for imaging according to our university-approved animal protocol).
22. R. Ollinger *et al.*, *Antioxid. Redox Signal.* **9**, 2175 (2007).
23. A. Nakao *et al.*, *Gastroenterology* **127**, 595 (2004).
24. C. H. Contag, M. H. Bachmann, *Annu. Rev. Biomed. Eng.* **4**, 235 (2002).
25. V. Ntziachristos *et al.*, *Proc. Natl. Acad. Sci. U.S.A.* **101**, 12294 (2004).
26. Electrospray mass spectrometry of bacterially expressed IFP1.4 holoprotein in 5% acetonitrile, 0.05% trifluoroacetic acid reported an average relative molecular mass (M_r) of 36,342 daltons, within experimental error of the M_r (36,332 daltons) expected from covalent incorporation of BV (582.6 daltons) into the apoprotein (35,749.6 daltons) from Ala^2 to the C terminus.
27. N. G. Abraham, A. Kappas, *Pharmacol. Rev.* **60**, 79 (2008).
28. D. B. Rusch *et al.*, *PLoS Biol.* **5**, e77 (2007).

29. We thank J. C. Lagarias and S. Field for donation of cDNAs encoding HO-1 and AKT1's PH domain, respectively; J. M. Saathoff and G. Tran for help with plasmid purification; M. Timmers for help with tissue culture; S. Adams for help with light scattering measurements; L. Gross for mass spectrometry; and Q. Xiong for flow cytometry. This work was supported by NIGMS grant R01 GM086197 and the Howard Hughes Medical Institute.

Supporting Online Material

www.sciencemag.org/cgi/content/full/324/5928/804/DC1
Materials and Methods
SOM Text
Figs. S1 to S11
Table S1
References

18 November 2008; accepted 10 March 2009
10.1126/science.1168683

High-Throughput Sequencing of the Zebrafish Antibody Repertoire

Joshua A. Weinstein,[1]* Ning Jiang,[2]* Richard A. White III,[3] Daniel S. Fisher,[1,4,5] Stephen R. Quake[1,2,3,4]†

Despite tremendous progress in understanding the nature of the immune system, the full diversity of an organism's antibody repertoire is unknown. We used high-throughput sequencing of the variable domain of the antibody heavy chain from 14 zebrafish to analyze VDJ usage and antibody sequence. Zebrafish were found to use between 50 and 86% of all possible VDJ combinations and shared a similar frequency distribution, with some correlation of VDJ patterns between individuals. Zebrafish antibodies retained a few thousand unique heavy chains that also exhibited a shared frequency distribution. We found evidence of convergence, in which different individuals made the same antibody. This approach provides insight into the breadth of the expressed antibody repertoire and immunological diversity at the level of an individual organism.

The nature of the immune system's antibody repertoire has been a subject of fascination for more than a century. This repertoire is highly plastic and can be directed to create antibodies with broad chemical diversity and high selectivity (*1*, *2*). There is also a good understanding of the potential diversity available and the mechanistic aspects of how this diversity is generated. Antibodies are composed of two types of chains (heavy and light), each containing a highly diversified antigen-binding domain (variable). The V, D, and J gene segments of the antibody heavy-chain variable genes go through a series of recombination events to generate a new heavy-chain gene (Fig. 1). Antibodies are formed by a mixture of recombination among gene segments, sequence diversification at the junctions of these segments, and point mutations throughout the gene (*3*). Estimates of immune diversity for antibodies or the related T cell receptors either have attempted to extrapolate from small samples to entire systems or have been limited by coarse resolution of immune receptor genes (*4*). However, certain very elementary questions have remained open more than a half-century after being posed (*1*, *5*, *6*): It is still unclear what fraction of the potential repertoire is expressed in an individual at any point in time and how similar repertoires are between individuals who have lived in similar environments. Moreover, because each individual's immune system is an independent experiment in evolution by natural selection, these questions about repertoire similarity also inform our understanding of evolutionary diversity and convergence.

Zebrafish are an ideal model system for studying the adaptive immune system because in evolutionary terms they have the earliest recognizable adaptive immune system whose features match the essential human elements (*7*, *8*). Like humans, zebrafish have a recombination activating gene (RAG) and a combinatorial rearrangement of V, D, and J gene segments to create antibodies. They also have junctional diversity during recombination and somatic hypermutation of antibodies to improve specificity, and the organization of their immunoglobulin (Ig) gene loci approximates that of human (*9*). In addition, the zebrafish immune system has only ~300,000 antibody-producing B cells, making it three orders of magnitude simpler than mouse and five orders simpler than human in this regard.

We developed an approach to characterize the antibody repertoire of zebrafish by analyzing complimentarity-determining region 3 (CDR3) of the heavy chain, which contains the vast majority of immunoglobulin diversity (*10*, *11*) and can be captured in a single sequencing read (Fig. 1). Using the 454 GS FLX high-throughput pyrosequencing technology allowed sequencing of 640 million bases of zebrafish antibody cDNA from 14 zebrafish in four families (Fig. 1B). Zebrafish were raised in separate aquaria for each family and were allowed to have normal interactions with the environment, including the development of natural internal flora. We chose to investigate the quiescent state of the immune system, a state where the zebrafish had sampled a complex but fairly innocuous environment and had established an equilibrium of normal immune function. mRNA was prepared from whole fish, and we synthesized cDNA using primers designed to capture the entire variable region.

Between 28,000 and 112,000 useful sequencing reads were obtained per fish, and we focused our analysis on CDR3 sequences. Each read was assigned V and J by alignment to a reference with a 99.6% success rate (table S3); failures were due to similarity in some of the V gene segments. D was determined for each read by applying a clustering algorithm to all of the reads within a given

[1]Biophysics Program, Stanford University, Stanford, CA 94305, USA. [2]Department of Bioengineering, Stanford University, Stanford, CA 94305, USA. [3]Howard Hughes Medical Institute, Stanford University, Stanford, CA 94305, USA. [4]Department of Applied Physics, Stanford University, Stanford, CA 94305, USA. [5]Department of Biology, Stanford University, Stanford, CA 94305, USA.

*These authors contributed equally to this work.
†To whom correspondence may be addressed. E-mail: quake@stanford.edu

VJ and then aligning the consensus sequence from each cluster to a reference. D was assigned to 69.6% of reads; many of the unassignable cases had D regions mostly deleted. Both the isotypes that are known to exist in zebrafish (IgM and IgZ) were found, and their relative abundance agrees with previous studies (*12*). Our analysis focused on IgM, which is the most abundant species; IgZ data are presented in figs. S3 and S4 (*13*).

There are 975 possible VDJ combinations in zebrafish (39 V × 5 D × 5 J = 975 VDJ). In any given fish, the VDJ combination coverage was at least 50% and in some cases at least 86% (Fig. 2). By using subsets of the full data set to perform rarefaction studies, we demonstrated that our sampling of the VDJ repertoire was asymptoting toward saturation (Fig. 3A). Any VDJ classes that may be missing from the data are occurring at frequencies below 10^{-4} to 10^{-5}. There was a commonality to the frequency distributions of VDJ usage that was independent of the specific VDJ repertoire for individual fish (Fig. 3B). Specifically, the majority of VDJ combinations in each fish were of low abundance, but a similarly small fraction—although different combinations for different fish—were found at high frequencies. This distribution could be used to constrain theoretical models of repertoire development.

We next asked whether there is a quantitative relationship between the VDJ usage of different fish. The VDJ repertoire is a vector in which each element records the number of reads that map to a particular VDJ class. The dot product between VDJ repertoire vectors measures the degree of correlation between different fish (table S5 and Fig. 3C) [control experiments are described in (*13*)].

Most fish were uncorrelated in their VDJ repertoires; however, some fish were highly correlated, and three pairs of fish had correlation coefficients in the range 0.62 to 0.75. Some of these correlations appear to derive from the largest VDJ class in the repertoire (table S5A and Fig. 3C). When the fish-fish VDJ correlations were computed in the absence of the largest VDJ class, we discovered that although the largest correlations disappeared, a new set of correlations appeared between a larger fraction of the fish (table S5B and Fig. 3D). These correlations were mostly weaker than the previous correlations but still well above the statistical noise.

We were surprised to find measurable correlation in antibody repertoires between independent organisms. We created a model for random VDJ repertoire assembly, using simulated VDJ distributions that replicated the actual measured distributions and coverage fractions. The correlations in these simulated VDJ repertoires are all near zero, and the probability of two fish having a highly correlated random repertoire is less than 10^{-6} (Fig. 3, C and D). Thus, even though the VDJ repertoire is believed to be generated by a series of random molecular events within independent individual cells, in zebrafish the VDJ repertoire appears substantially structured and nonrandom on a global scale. It is possible that the source of this structure is simply convergent evolution, that the fish see a similar enough environment that selection in their quiescent immune systems converges to correlated VDJ usage. It is also possible that this distribution reflects bias in the VDJ recombination mechanisms, which would have important implications for antibody diversity space and would suggest that the number of solutions to a given antigen recognition problem, or at least the number that are readily evolvable, may be much smaller than previously assumed.

Summarizing the VDJ repertoire with a simple count of the number of different VDJ combinations neglects the variation in abundance of different VDJ species. Ecologists have the same problem in characterizing species diversity; they refer to the counting approach as species richness and have developed other methods to characterize variation of abundance, which they term "heterogeneity" (*14*). The most popular approach to characterize heterogeneity is based on information theory, specifically the Shannon-Weaver entropy, which summarizes the frequency distribution in a single number (*14*). The VDJ repertoire entropies generally varied between 3.1 and 7.7 bits for individual fish. Exponentiating the entropy indicates the effective size of the VDJ repertoire, and this varied between 9 and 200 with an average of 105, or an average effective VDJ repertoire coverage of about 9%. This can be interpreted as the fraction of highly expressed VDJ classes.

Whereas the VDJ repertoire provides a coarse view of immunological diversity, each VDJ class can contain a large number of distinct individual antibodies that differ as a result of hypermutations and junctional changes. We characterized the antibody repertoire by using quality threshold clustering of Smith-Waterman alignments to group similar reads together; each cluster defines an antibody. Performing this analysis on control data with well-defined sequence clones allowed us to calibrate the clustering algorithm and separate true hypermutation diversity from sequencing errors. Many VDJ combinations included a

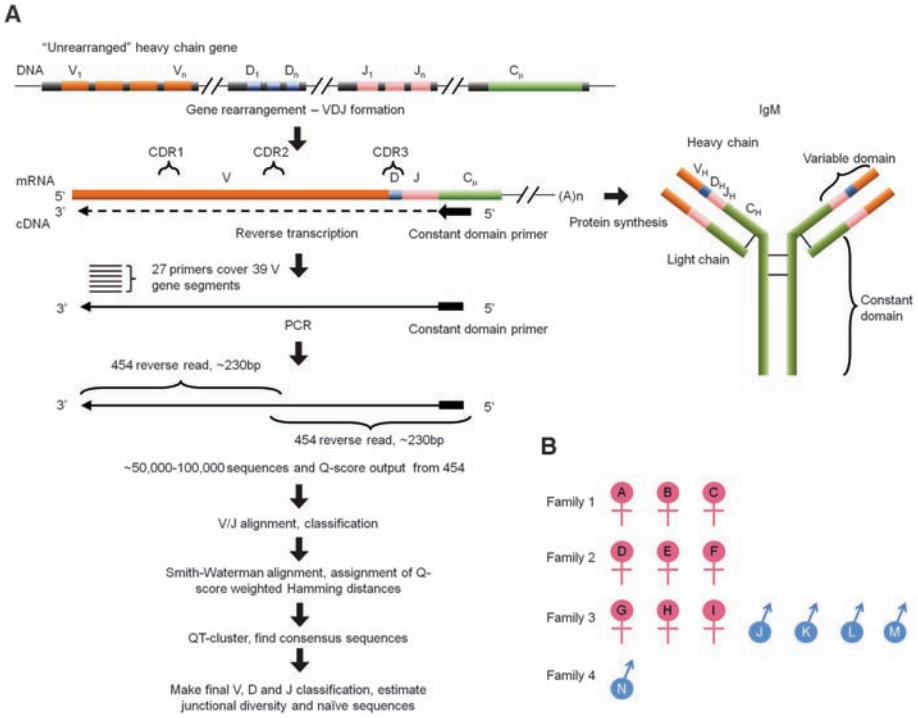

Fig. 1. (**A**) Schematic drawing of the VDJ recombination of an antibody heavy-chain gene, the cDNA amplicon library construction, and the infomatics pipeline. The heavy-chain VDJ segment of an antibody is created by recombination, junctional diversity, and hypermutation. We designed primer sets to amplify the expressed heavy-chain mRNA, which were then sequenced and analyzed as outlined. High-throughput sequencing allows determination of the identity of nearly all heavy-chain sequences. (**B**) Gender and family information for the 14 sequenced zebrafish.

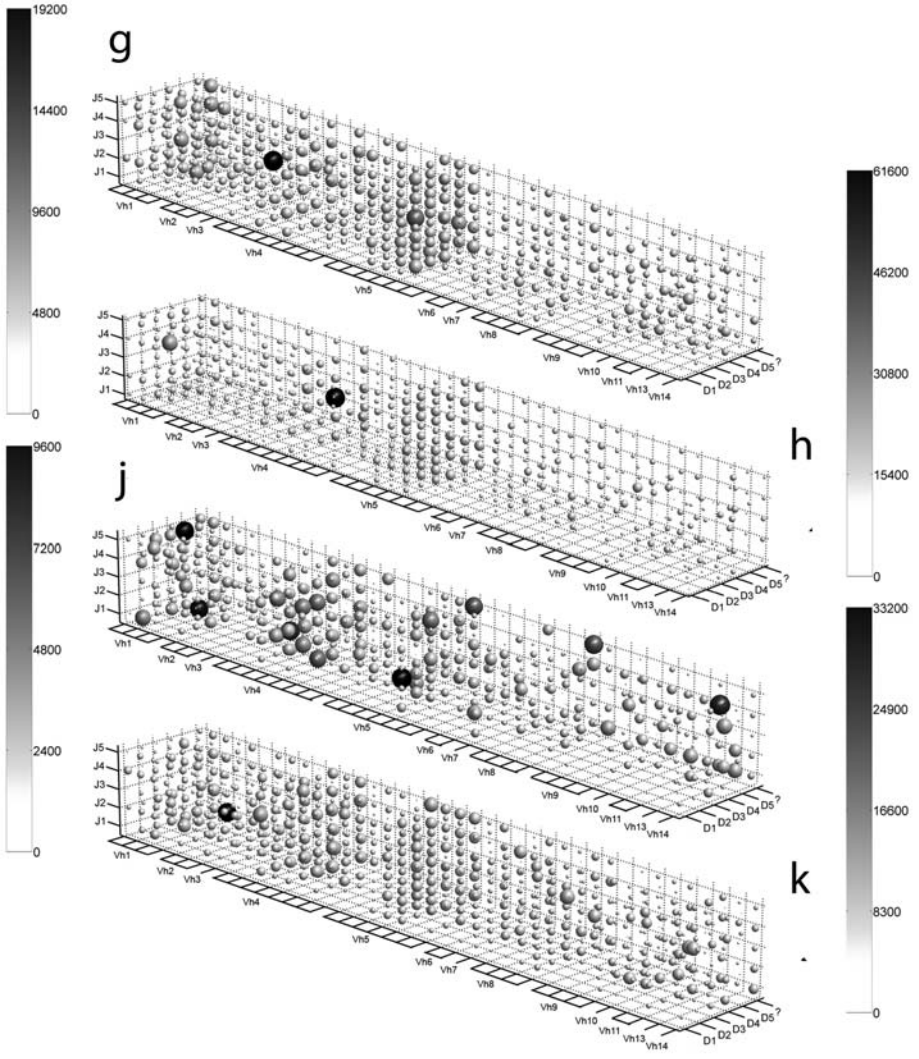

Fig. 2. The entire expressed VDJ repertoires for individual fish g, h, j, and k (top to bottom). The three axes enumerate all possible V, D, and J values, so each point in three-space is a unique VDJ combination. Both the size of the sphere at each point and the intensity correspond to the number of reads matching that particular VDJ combination. Gray scale is plotted on a linear scale, and the dot size is plotted on a log scale. The upper limits of the scales are set to the most populated VDJ combination for each fish, with PCR bias factored out.

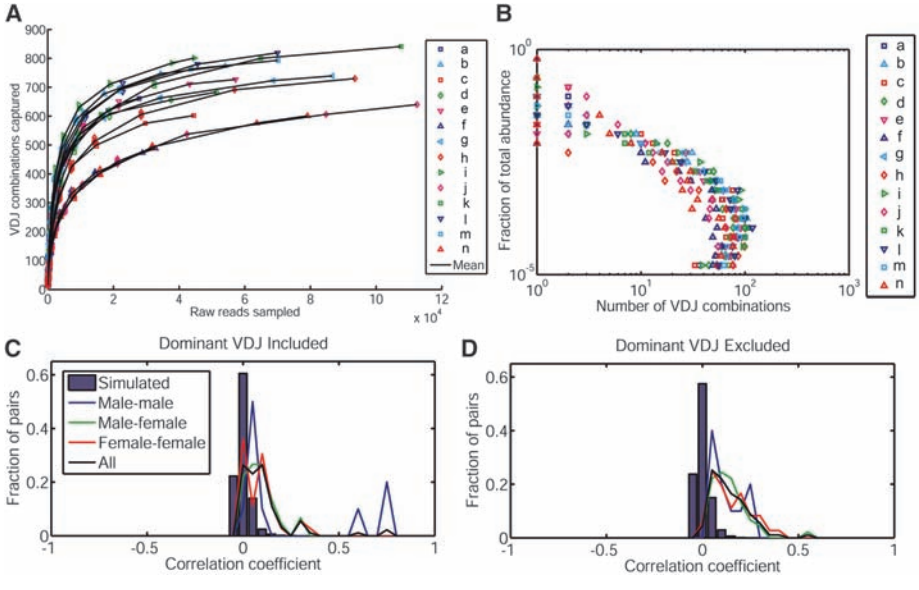

Fig. 3. VDJ repertoire analysis for all 14 fish. (**A**) Abundance distribution for each VDJ combination. A small number of VDJ combinations are highly represented in each fish, and most VDJ combinations are represented only at low abundance. The shape of the distribution is common among all of the fish sampled. This histogram is oriented sideways (from left to right) to emphasize that a small number of VDJ combinations are highly abundant, with a distribution that falls off rapidly. (**B**) Rarefaction analysis of VDJ diversity demonstrates that as one sequences more deeply into a fish, the number of new VDJ classes discovered saturates. (**C**) Histogram of correlations between VDJ repertoires. The data are collected as histograms and compared to simulated fish which have random VDJ repertoires. The simulated fish have no significant correlations, whereas some of the real fish have high correlations, representing 5 SD outliers of the random model. The highest correlations are from males in the same family (table S5A). (**D**) When the largest VDJ class in each fish is eliminated, the correlations are reduced and there is a larger proportion of moderate female correlations.

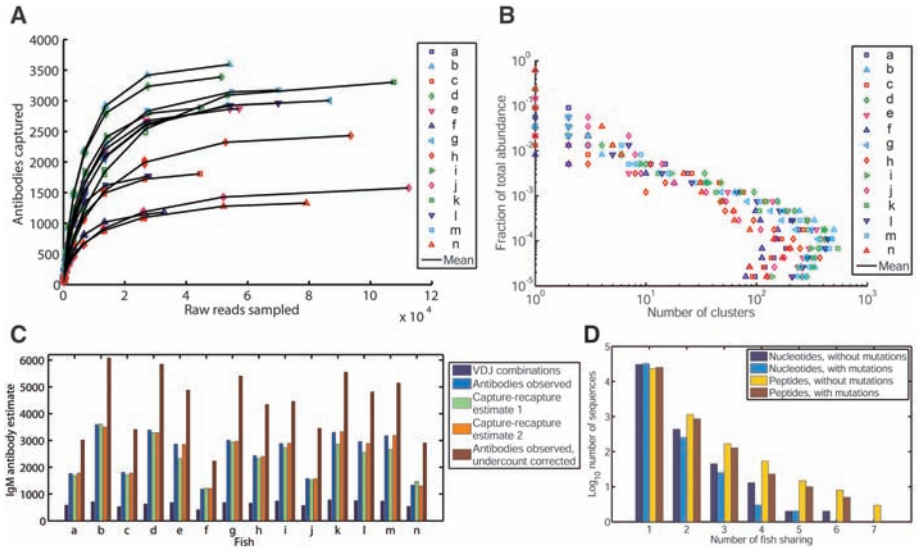

Fig. 4. Antibody heavy-chain repertoire diversity estimates for IgM in all 14 fish. (**A**) Rarefaction analysis of heavy-chain diversity demonstrates that as one sequences more deeply into a fish, the number of new antibodies discovered saturates at a few thousand. (**B**) Antibody abundance distributions for each fish. This histogram is oriented sideways (from left to right) to emphasize that a small number of antibodies (clusters) are highly abundant, with a distribution that falls off rapidly as a power law. The shape of the distribution is universal among all of the fish sampled. The bend at small abundance is caused by variability in the total reads sampled per fish and is not significant. (**C**) Total antibody diversity estimates for IgM using different criteria. VDJ diversity is the number of VDJ classes per fish, as described in Fig. 3A. Antibodies observed (>2 reads; VDJ classes composed only of antibody clusters with two or fewer reads are counted as one) is the number of unique antibodies per fish described in Fig. 4A. Capture-recapture estimate 1 refers to an estimate based on observed antibody abundances (*13*). Capture-recapture estimate 2 refers to an estimate using equal probability of all antibodies. Antibodies observed, undercount corrected refers to the upper bound. (**D**) Histogram of number of fish with shared IgM sequences. Hundreds of sequences are shared between pairs of fish, while a few tens of sequences are shared between three fish. Five sequences are shared between four or more fish, and none are shared among all fourteen fish. Sequence comparisons without mutations incorporate differences at the V/D and D/J junctions alone. Convergence on the amino acid level is also plotted.

large number of distinct antibodies. We found that the overall distribution of the abundances of the antibodies followed an apparent power law with scaling parameter 2.2, and this was consistent among all fish over two decades (Fig. 4B). This behavior may represent an important signature of the underlying dynamics of the adaptive immune system. It was not observed for either the control data or the VDJ distributions, and thus we ruled out the possibility that it is an artifact of polymerase chain reaction (PCR) bias.

There are several ways to use this data to estimate the number of unique antibodies per fish. The first is to perform rarefaction studies and determine whether the number of independent clusters tends to saturate. We did this and found that the saturation occurs at between ~1200 and 3500 unique antibodies per fish (Fig. 4A). Another way is by applying approaches used in ecology to estimate population sizes and diversity—sample and resample techniques (*15*). This yielded an estimate of between 1200 and 3700 unique antibodies per fish, whether applied blindly or using knowledge of the antibody abundance distributions (Fig. 4C). Both approaches are lower bounds on the true antibody diversity because antibodies that differ by only one or two mutations will be incorporated into the same cluster. We corrected for this effect by reanalyzing the data within each cluster with zero error tolerance, only matching exact reads. The largest clusters each had several subclusters with more than two reads each, and the control sequence data indicated that probably half of those clusters are real while the other half are artifacts due to sequencing error. By combining this stringent method of finding small differences in common sequences with the more permissive method of clustering rare sequences with less similarity together (thereby having tolerance to sequencing errors on rare transcripts), we estimated that the upper limit of heavy-chain antibody diversity is within 50% of the lower bound estimates, or between 5000 and 6000 antibodies in an individual fish.

To see how often repertoires converged to the same antibody, we searched for sequences that are shared between fish. Although there were no antibodies common to all fish, some antibodies were shared between smaller groups of fish (Fig. 4D). These cases of convergent evolution were more frequent than one would expect from a random usage model, with P values as low as 10^{-15}. Unexpectedly, different individuals shared heavy chains that were identical in the region we sequenced, even up to hypermutation. Specifically, there were 254 unique sequences shared between two fish and 2 unique sequences shared between five fish. These data illustrate the powerful forces of selection and perhaps can be used to estimate evolutionary dynamics in this system.

In conclusion, we have performed a comprehensive measurement of the heavy-chain antibody repertoire of zebrafish. We discovered that the abundance distributions of both the VDJ repertoire and antibody heavy-chain diversity were similar between individuals, that VDJ usage is not uniform, that individuals can have highly correlated VDJ repertoires, and that convergent evolution of identical heavy-chain sequences is unexpectedly common. With the rapid advance of sequencing throughput, it will soon be possible to make similar measurements on mice and humans. These organisms use the same molecular mechanisms for repertoire generation as fish; thus, we predict that they may also show similar distributions of antibody frequencies.

References and Notes

1. T. J. Kindt, J. D. Capra, *The Antibody Enigma* (Plenum Press, New York, 1984).
2. S. P. Singh, *Z. Allg. Mikrobiol.* **18**, 111 (1978).
3. C. A. Janeway, M. J. Shlomchik, M. Walport, P. Travers, *Immunobiology* (Garland Science Publishing, New York, ed. 6, 2004).
4. P. Boudinot *et al.*, *Mol. Immunol.* **45**, 2437 (2008).
5. E. S. Golub, *Cell* **48**, 723 (1987).
6. D. W. Talmage, *Science* **129**, 1643 (1959).
7. N. S. Trede, D. M. Langenau, D. Traver, A. T. Look, L. I. Zon, *Immunity* **20**, 367 (2004).
8. J. A. Yoder, M. E. Nielsen, C. T. Amemiya, G. W. Litman, *Microbes Infect.* **4**, 1469 (2002).
9. G. W. Litman, J. P. Cannon, L. J. Dishaw, *Nat. Rev. Immunol.* **5**, 866 (2005).
10. J. L. Xu, M. M. Davis, *Immunity* **13**, 37 (2000).
11. E. P. Rock, P. R. Sibbald, M. M. Davis, Y. H. Chien, *J. Exp. Med.* **179**, 323 (1994).
12. N. Danilova, J. Bussmann, K. Jekosch, L. A. Steiner, *Nat. Immunol.* **6**, 295 (2005).
13. Materials and methods are available as supporting material on *Science* Online.
14. R. K. Peet, *Annu. Rev. Ecol. Syst.* **5**, 285 (1974).
15. J. Bunge, M. Fitzpatrick, *J. Am. Stat. Assoc.* **88**, 364 (1993).
16. We thank W. Talbot for useful conversations and the generous loan of equipment and N. Neff for assistance with sequencing. IgM and IgZ sequence and quality-score files are available on the NIH short-read archive, with accession number SRA008134. This research was supported by the NIH Director's Pioneer award (S.R.Q.), the Arthritis Foundation Postdoctoral Fellowship (N.J.), and an NSF graduate fellowship (J.A.W.).

Supporting Online Material

www.sciencemag.org/cgi/content/full/324/5928/807/DC1
Materials and Methods
Figs. S1 to S7
Tables S1 to S6
References

19 December 2008; accepted 18 March 2009
10.1126/science.1170020

Movement Intention After Parietal Cortex Stimulation in Humans

Michel Desmurget,[1,2] Karen T. Reilly,[1,2] Nathalie Richard,[1,2] Alexandru Szathmari,[3] Carmine Mottolese,[3] Angela Sirigu[1,2]*

Parietal and premotor cortex regions are serious contenders for bringing motor intentions and motor responses into awareness. We used electrical stimulation in seven patients undergoing awake brain surgery. Stimulating the right inferior parietal regions triggered a strong intention and desire to move the contralateral hand, arm, or foot, whereas stimulating the left inferior parietal region provoked the intention to move the lips and to talk. When stimulation intensity was increased in parietal areas, participants believed they had really performed these movements, although no electromyographic activity was detected. Stimulation of the premotor region triggered overt mouth and contralateral limb movements. Yet, patients firmly denied that they had moved. Conscious intention and motor awareness thus arise from increased parietal activity before movement execution.

A central question in the study of human behavior concerns the origin of willed actions. Where in the brain are intentions formed? How do we become aware of these intentions? According to the dualist philosophy (*1*), our encephalon is just the recipient of conscious intentions formed elsewhere in a nonphysical realm. This implies that conscious intention comes first, as the leading cause of our actions. Although appealing from a spiritual point of view, this hypothesis was progressively challenged by a large set of studies (*2*–*4*). Results showing that the decision to move did not precede, but instead lagged, the onset of brain activity signaling motor preparedness were especially convincing (*5*–*7*). Thus, researchers suggested that conscious intention of a movement emerged as a consequence of increased neural activity in a premotor-parietal circuit, which elaborates motor plans before action (*2*). This cortical circuit has also been involved in motor awareness, that is, the awareness that we are actually executing the intended action (*7*–*10*).

However, the specific contribution of premotor and parietal regions to conscious intention and motor awareness remains unclear. We reasoned that, by directly stimulating parietal and premotor cortex regions, we should be able to evoke motor responses in specific body parts and that, in areas involved in carrying out advance computations related to conscious intention and motor awareness, these movements should be accompanied or preceded by the subjective experience of willed actions. We used direct electrical stimulation (DES) in seven individuals with brain tumors located anteriorly ($N = 4$, PM1 to PM4) or posteriorly ($N = 3$, PP1 to PP3) to the central sulcus. Patients were operated under local anesthesia by using DES as a functional mapping technique in order to minimize the risk of postoperative sequelae (*11*). DES was delivered with a bipolar electrode using standard increasing intensities (2, 5, and 8 mA) and durations (1, 2, and 4 s). Up to four replications were performed for each stimulation site. Replications were delivered nonconsecutively to avoid provoking seizures. Throughout the experiment, electromyographic (EMG) signals were collected in the contralesional hemibody in 12 muscles covering the face, hand, wrist, elbow, knee, and foot. Stimulation sites were localized with high resolution on individual magnetic resonance (MR) images by using a peri-operative neuronavigation system and reconstructed offline.

Fifty-seven sites were stimulated in the frontal, parietal, and temporal regions (fig. S2A). Posterior parietal stimulations were performed in Brodmann areas (BAs) 7, 39, and 40. Premotor stimulations were performed in the dorsal sector of BA 6, excluding the convexity and mesial structures involving the supplementary motor area (SMA). Of the stimulated sites, 46% were silent, meaning that DES did not produce any sensations or overt motor responses, and 20% were associated with somatic sensations such as tingling or itching. One participant (PP1) reported a robust visual illusion of background displacement when stimulated in the superior temporal gyrus (BA 22). Of the remaining sites (34%), 16% evoked responses related to motor awareness or movement intention, whereas 18% triggered actual movements. We will focus on these remaining sites, designated as responsive. The distribution of DES effects across brain areas is summarized in fig. S2B.

For the three patients with postcentral tumors, nine responsive sites were found in BAs 39 and 40 (Fig. 1). Stimulation of all these sites produced a pure intention, that is, a felt desire to move without any overt movement being produced or EMG activity recorded in the concerned muscles. In two of the patients (PP1 and PP2), the same sites were stimulated again later but at a higher intensity. Conscious motor intentions were replaced by a sensation that a movement had been accomplished, and yet, just as during the first stimulation trial, no actual movement or EMG activity was observed. Thus, these patients experienced awareness of an illusory movement (Fig. 2). For example, patient PP3 reported after low-intensity stimulation of one site (5 mA, 4 s;

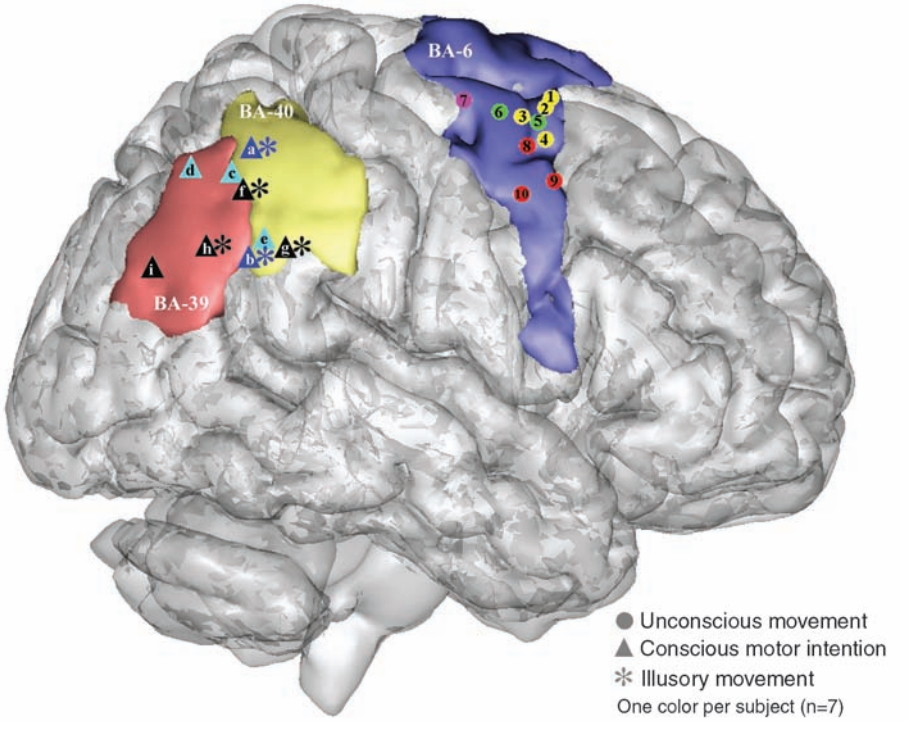

Fig. 1. Premotor and parietal responsive sites shown after registration of the individual MR image to the MNI template. Left stimulations have been reported on the right hemisphere. Colored areas define the anatomical boundaries of BA 40 (yellow), BA 39 (orange), and BA 6 (blue).

[1]Centre de Neuroscience Cognitive, CNRS, UMR 5229, 69500 Bron, France. [2]Université Lyon 1, 69100 Villeurbanne, France. [3]Neurosurgery Unit 500, Hôpital Pierre Wertheimer, Hospices Civils de Lyon, 69003 Lyon, France.

*To whom correspondence should be addressed. E-mail: sirigu@isc.cnrs.fr

site a in Fig. 1), "I felt a desire to lick my lips" and at a higher intensity (8 mA, 4 s), "I moved my mouth, I talked, what did I say?" Similar results were found in patient PP1 for hand (two sites, g and h, in Fig. 1) and foot (one site, f, in Fig. 1) movements. Patient PP2 reported, after stimulation in BA 40 (8 mA, 4 s; site e in Fig. 1), that she felt "like a will to move" her chest (*12*). The same words were later used for another site with respect to the arm (8 mA, 4 s; site c in Fig. 1). Without prompting by the examiner, all three patients spontaneously used terms such as "will," "desire," and "wanting to," which convey the voluntary character of the movement intention and its attribution to an internal source, that is, located within the self (movies S2 and S3).

Electrical stimulation in the frontal cortex contrasted sharply with the above descriptions (Fig. 3). For the four precentral patients, 10 responsive sites were found in the dorsal part of the premotor cortex (BA 6; Fig. 1). These sites triggered movements of various limb segments and the mouth (fig. S2C) (*13*) devoid of conscious intention and awareness. Patients never expressed the desire to move and never became aware that they produced a motor response. For example, during stimulation patient PM1 exhibited a large multijoint movement involving flexion of the left wrist, fingers, and elbow, as well as a rotation of the forearm (8 mA, 4 s; site 7 in Fig. 1). He did not spontaneously comment on this, and when asked whether he had felt a movement he responded negatively. The ability of patients to detect electrically evoked movements did not change with the intensity of the stimulation. Higher currents evoked larger movements and

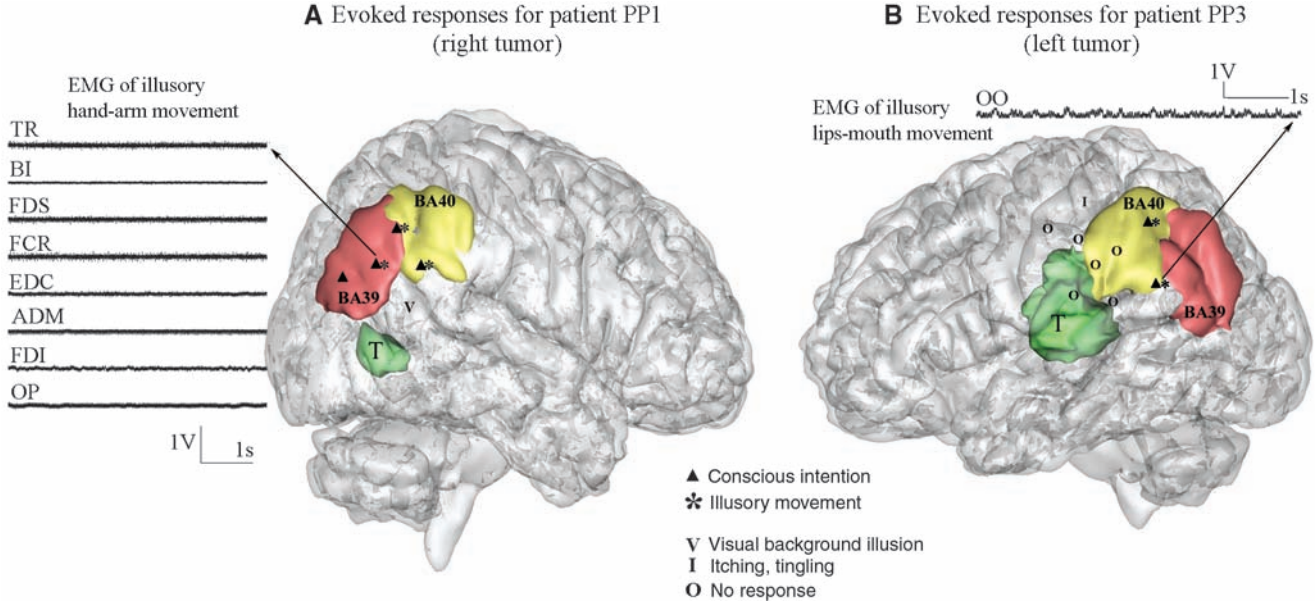

Fig. 2. (**A** and **B**) Individual brains and stimulation sites reconstructed for two patients harboring postcentral tumors. EMG signals are shown for the stimulation sites identified by arrows. T indicates tumor; TR, triceps; BI, biceps; FDS, flexor digitorium superficialis; FCR, flexor carpi radialis; EDC, extensor digitorium communis; ADM, abductor digiti minimi; FDI, first dorsal interosseous; OP, opponens pollicis; and OO, orbicularis oris. Colored areas define the anatomical boundaries of the tumor (green), BA 40 (yellow), and BA 39 (orange).

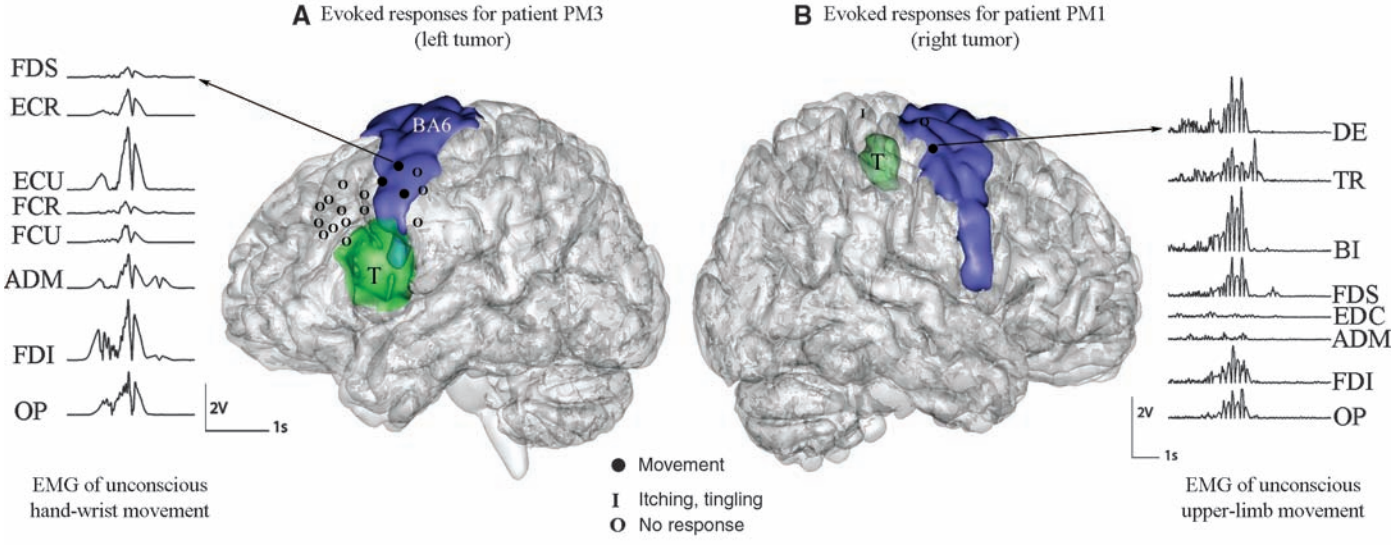

Fig. 3. (**A** and **B**) Individual brains and stimulation sites reconstructed for two patients harboring precentral tumors. EMG signals are shown for the stimulation sites identified by arrows. DE, deltoid; ECR, extensor carpi radialis; ECU, extensor carpi ulnaris; and FCU, flexor carpi ulnaris. Colored areas define the anatomical boundaries of the tumor (green) and BA 6 (blue).

recruited more muscles as compared with movements triggered by lower currents. Despite increasing stimulation intensity, patients remained completely unaware that a movement occurred (movies S1 and S4) (*14*).

We report two main contrasting findings: (i) Stimulation of the posterior parietal cortex caused human participants to intend to move and to report having moved, even in the absence of actual motor responses. (ii) Stimulation of the premotor cortex triggered limb and mouth movements that were not consciously detected by the patients.

Clinical observations of high-level movement deficits in patients with apraxia after parietal damage have led to the hypothesis that the posterior parietal cortex contains stored movement representations (*15*, *16*). It can be proposed that direct stimulation of the parietal cortex activates such representations. However, the fact that patients experienced a conscious desire to move indicates that stimulation did not merely evoke a mental image of a movement but also the intention to produce a movement, an internal state that resembles what Searle called "intention in action" (*17*). This finding is consistent with nonhuman primate results suggesting that the posterior parietal cortex harbors a "map of intentions," with different subregions dedicated to the planning of eye, reaching, and grasping movements (*18*), and that activity of parietal neurons is highly correlated to processes of motor planning and decision-making (*19*, *20*). It is tempting to propose that electrically induced intentions arise, in our study, from the activation of some nodes within this intentional map. Interestingly, when the stimulation intensity was increased, motor intentions were replaced by a form of illusory movement awareness. In the absence of any muscle contraction, the patients reported that they had actually performed the movement they previously intended to do. Although the nature of this phenomenon cannot be formally elucidated here, it may be hypothesized that motor intention arises from the activation of a limited subregion within the cortical network activated during movement execution. According to this view, higher intensities of stimulation would not simply prime a motor representation to consciousness (giving rise to intention) but also recruit the executive network responsible for movement monitoring through forward modeling. This process of forward modeling has been shown to rely on posterior parietal computations (*21*–*23*). It could form the basis of the illusory movement awareness experienced by our patients, assuming that the signal we are aware of when making a movement does not emerge from the movement itself but rather from the predictions we make about the movement in advance of action (*3*, *4*, *7*, *24*, *25*).

It has been reported that stimulation of the SMA triggers an urge to move that resembles an irrepressible desire to move going beyond patients' will (*26*). This suggests a potential role of SMA in generating motor intentions (*2*, *27*). However, intentions evoked by stimulation of SMA stand in contrast with what was described by our patients, who reported experiencing an endogenously generated wish to move. The imperative character of the motor intention with SMA stimulation is demonstrated by the fact that higher currents triggered movements (*26*), whereas none of the stimulated parietal sites ever evoked actual muscle contractions. It is possible that both the parietal cortex and the SMA are linked to motor intentions but that intentions processed in these two regions correspond to different stages of movement planning: Intentions in the parietal lobe may be processed in relation to sensory predictions, whereas in the SMA intentions may be more closely related to motor commands.

Regarding the dorsal premotor cortex, stimulations triggered complex multijoint movements, as already reported in awake monkeys (*28*). Stimulation intensities were comparable to those performed in the parietal cortex. Yet, patients remained unable to detect the limb and mouth movements evoked by electrical stimulations. This suggests that the proprioceptive volleys associated with the movement were disregarded or not decodable by the brain areas which normally receive these feedback signals. This finding strengthens the conclusion that awareness of initiating and executing a movement is not derived from afferent inputs but rather from the internal computations carried out in the posterior parietal cortex before action (*2*–*4*, *7*). Our data are compatible with behavioral studies showing that we are largely unaware of sensory feedback about the ongoing state of our motor system, as long as our intentions are achieved (*4*). Peripheral inputs probably intervene at a further stage for comparing expected and actual movements, that is, when we need to construct a veridical motor awareness (*2*, *24*, *25*). Recently, Berti *et al*. (*9*) have linked the comparative process leading to veridical awareness to the functioning of the dorsal premotor cortex (BA 6). As shown by the authors, this structure is the most commonly lesioned in hemiplegic patients who obstinately claim that they can move their paralyzed limbs. In our study, premotor stimulations did not evoke any form of conscious intention. As a consequence, the proprioceptive inputs could not be compared to any expected input to estimate movement state to construct a veridical motor awareness.

Our study suggests that motor intention and awareness are emerging consequences of increased parietal activity before movement execution. The subjective (and potentially illusory) feeling that we are executing a movement does not arise from movement itself, but it is generated by prior conscious intention and its predicted consequences.

References and Notes

1. R. Descartes, *Méditations Métaphysiques (1641)* (Flammarion, Paris, 1992).
2. P. Haggard, *Trends Cogn. Sci.* **9**, 290 (2005).
3. P. Haggard, *Nat. Rev. Neurosci.* **9**, 934 (2008).
4. C. D. Frith, S. J. Blakemore, D. M. Wolpert, *Philos. Trans. R. Soc. London Ser. B* **355**, 1771 (2000).
5. B. Libet, C. A. Gleason, E. W. Wright, D. K. Pearl, *Brain* **106**, 623 (1983).
6. P. Haggard, M. Eimer, *Exp. Brain Res.* **126**, 128 (1999).
7. A. Sirigu *et al*., *Nat. Neurosci.* **7**, 80 (2004).
8. A. Sirigu, E. Daprati, P. Pradat-Diehl, N. Franck, M. Jeannerod, *Brain* **122**, 1867 (1999).
9. A. Berti *et al*., *Science* **309**, 488 (2005).
10. P. Haggard, E. Magno, *Exp. Brain Res.* **127**, 102 (1999).
11. Materials and methods including stimulation protocol, EMG recording procedure, and reconstruction of stimulation sites are available as supporting material on *Science* Online.
12. This result is consistent with monkey studies showing that protrusion movements of the chest are represented in the posterior parietal cortex (*29*).
13. The movements observed in our premotor patients were similar to the movements reported in monkeys after long train stimulations (*28*). It is thought that these electrically induced movements are functionally meaningful (*30*, *31*).
14. The possibility can be ruled out that the absence of motor awareness in our patients was due to a low level of vigilance. The anesthetic and stimulation protocols were identical in premotor and in parietal patients who did report illusory movements. During peri-operative functional evaluation, premotor patients appeared well awake (see movies S1 to S4) and otherwise behaved as the parietal patients: They could talk, count, or move in response to verbal commands. Some of them reported sensory feelings of tingling or itching, indicating that they could introspect on stimulation-induced experiences. In one patient (PM4), we examined whether unseen passive movements of the forearm were perceived and reported. Indeed, this was the case.
15. L. J. Rothi, C. Ochipa, K. M. Heilman, in *Apraxia: The Neuropsychology of Action*, L. J. Rothi, K. M. Heilman, Eds. (Psychology Press, Hove, UK, 1997), pp. 29–49.
16. A. Sirigu *et al*., *Cortex* **31**, 41 (1995).
17. J. R. Searle, *Intentionality: An Essay in the Philosophy of Mind* (Cambridge Univ. Press, Cambridge, 1983).
18. R. A. Andersen, C. A. Buneo, *Annu. Rev. Neurosci.* **25**, 189 (2002).
19. L. H. Snyder, A. P. Batista, R. A. Andersen, *Vision Res.* **40**, 1433 (2000).
20. J. I. Gold, M. N. Shadlen, *Nature* **404**, 390 (2000).
21. J. R. Duhamel, C. L. Colby, M. E. Goldberg, *Science* **255**, 90 (1992).
22. M. Desmurget, S. Grafton, *Trends Cogn. Sci.* **4**, 423 (2000).
23. A. Sirigu *et al*., *Science* **273**, 1564 (1996).
24. A. Berti, L. Spinazzola, L. Pia, M. Rabuffeti, in *Sensorimotor Foundations of Higher Cognition Series: Attention and Performance XXII*, P. Haggard, Y. Rossetti, M. Kawato, Eds. (Oxford Univ. Press, New York, 2007), pp. 163–182.
25. A. Fotopoulou *et al*., *Brain* **131**, 3432 (2008).
26. I. Fried *et al*., *J. Neurosci.* **11**, 3656 (1991).
27. H. C. Lau, R. D. Rogers, P. Haggard, R. E. Passingham, *Science* **303**, 1208 (2004).
28. M. S. Graziano, C. S. Taylor, T. Moore, *Neuron* **34**, 841 (2002).
29. H. Gemba, K. Matsuura-Nakao, R. Matsuzaki, *Neurosci. Lett.* **357**, 68 (2004).
30. M. Graziano, *Annu. Rev. Neurosci.* **29**, 105 (2006).
31. E. Stark, I. Asher, M. Abeles, *J. Neurophysiol.* **97**, 3351 (2007).

32. This study was funded by Centre National de la Recherche Scientifique, Agence Nationale de la Recherche (Neuro-031-02), and by Human Frontiers Science Program (RGP0056/2005-C) to A.S. We thank J. R. Duhamel for helpful discussion. We thank patients for their cooperation and L. Pouga and the clinical staff for help during testing.

Supporting Online Material

www.sciencemag.org/cgi/content/full/324/5928/811/DC1
Materials and Methods
Figs. S1 and S2
References
Movies S1 to S4

17 December 2008; accepted 13 March 2009
10.1126/science.1169896

Do more with proven miRCURY LNA™ tools for microRNA research

miRCURY LNA™ tools from Exiqon give you the reliability and specificity you need to trust your results. And we've got the data to prove it.

Søren Møller, Ph.D., VP Research & Development

MicroRNA expression profiling

Exiqon's miRCURY LNA™ Arrays produce highly reliable microRNA profiles from just 30 ng total RNA.

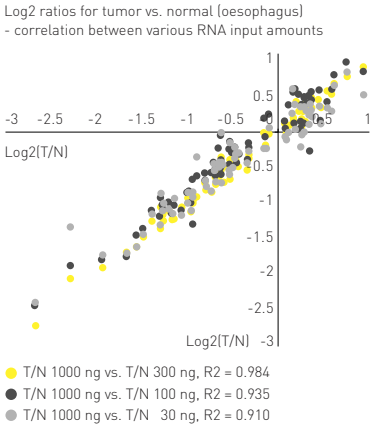

Learn more at:
exiqon.com/array

Determination of microRNA function

With Exiqon's miRCURY LNA™ Knockdown Probes, you can achieve comprehensive inhibition of microRNA activity.

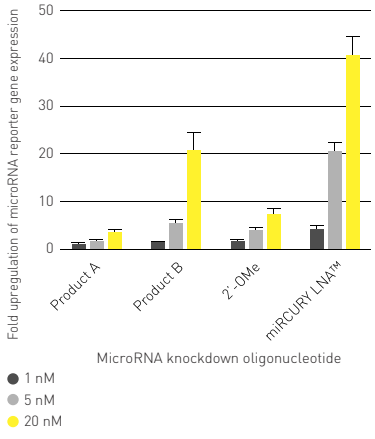

Learn more at:
exiqon.com/knockdown

Precise visualization of microRNAs in tissue

Exiqon's miRCURY LNA™ Detection Probes address the "when" and "where" a particular microRNA is expressed.

Visualization of miR-206 expression in the skeletal precursors of a Gallus Gallus embryo.

Learn more at:
exiqon.com/insitu

Sensitive real-time microRNA quantitation

With our new miRCURY LNA™ PCR System, your discovery starts from just 10 pg total RNA – you only need a single cell.

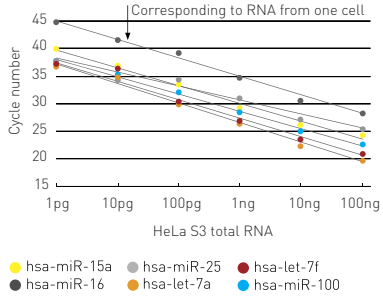

Dilution series of 6 different miRCURY LNA™ PCR assays showing accurate quantitation from total RNA amounts equivalent to a single cell.

Learn more at:
exiqon.com/pcr

Learn more
Visit exiqon.com
NEW! view a 3-D animation of LNA™ on exiqon.com

EXIQON
Seek Find Verify

MOLECULAR DIAGNOSTICS:

PERSONALIZING PERSONALIZED MEDICINE

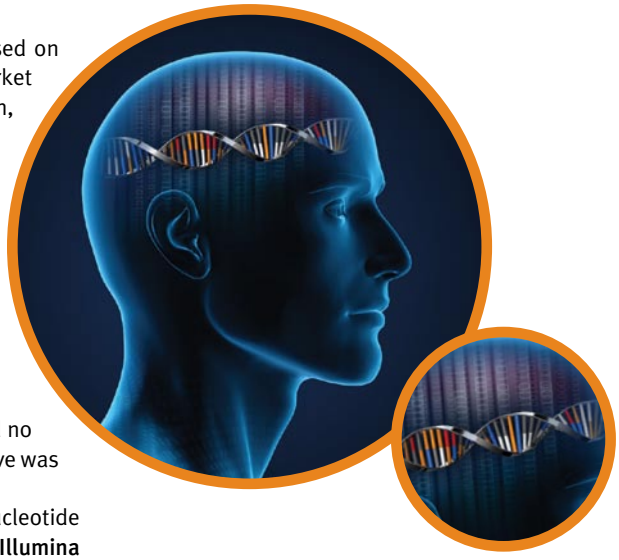

Thirteen years after Roche launched the industry with a test for HIV load based on transcript abundance, molecular diagnostics is in full flower. A $3.3 billion market growing at 17 percent annually, the field includes assays for disease predisposition, screening, diagnosis, prognosis, monitoring, and predicting treatment efficacy, using markers ranging from SNPs to methylcytosine, messenger RNA to microRNA. Bringing digital power to traditional analog medicine, the field "is absolutely going to revolutionize health care," says Harry Glorikian, managing partner at Scientia Advisors. "I believe it with every fiber in my being."

By Jeffrey M. Perkel

About a year ago, 48-year-old Jeff Gulcher's doctor called to say Jeff had cancer. His prostate was teeming with cells scored at Gleason-6, the high end of intermediate grade. The recommendation: radical prostatectomy.

The diagnosis was shocking. Gulcher wasn't at risk as far as he knew: he had no family history of early prostate cancer, and he had no symptoms. What he did have was a suspicious genotype.

Gulcher had paid $985 for the deCODEme test, a genome-scale single nucleotide polymorphism screening service from **deCODE Genetics.** The test uses **Illumina** microarrays to profile about a million loci, reporting back on the relatively small number of conditions that can be tied to the results. Scattered across 10 chromosomes, the test's 13 prostate cancer–related markers suggested that Gulcher's lifetime risk for the disease is about twice the average, or 32 percent. That's not a diagnosis, but a warning, like elevated cholesterol. It means, pay attention.

Gulcher's physician recommended a prostate specific antigen (PSA) test. Such screening typically doesn't begin until age 50. In this case, the test came back at 2.0 ng/mL, "in sort of the mid-normal range," Gulcher says. Normally harmless, that value plus the genotype data prompted his urologist to refer Jeff for a biopsy.

"I'm thinking, there's no way I have cancer," Gulcher recalls. "I'll go through the motions, have the biopsy. But just having this higher risk doesn't mean I'm going to get prostate cancer by any stretch of the imagination."

Fortunately, Gulcher didn't rely on his intuition, and the surgeon excised his tumor intact; postoperatively, it was reassessed at high grade. PSA score down to zero, Gulcher appears to have dodged a bullet, all thanks to a molecular diagnostic that he actually helped develop. Gulcher is deCODE's co-founder and chief scientific officer.

"This genetic test is reclassifying people who are thought to have average risk into somebody who really is at higher risk, and may benefit from extra surveillance," Gulcher says.

That, in a nutshell, is the promise of molecular diagnostics (MDx). Whether stratifying patients for heightened or diminished scrutiny, advising doctors on treatment decisions, or diagnosing disease, the field is redefining medicine.

From Analog to Digital

Every diagnostic is molecular, whether measuring cholesterol for heart disease, radiolabeled glucose for brain imaging, or mass spectrometric peaks for ovarian cancer. So just what, exactly, is a "molecular" diagnostic?

According to Harry Glorikian of **Scientia Advisors,** the term generally applies to assays that detect nucleic acids, whether single nucleotide polymorphisms, mutations, or RNAs, with a sprinkling of "certain very high-quality, high-value protein assays," as well.

They come in a variety of flavors. Besides predisposition tests like deCODEme, there are assays for diagnosis, prognosis, prediction of drug response, and disease continued >

"Whether stratifying patients for heightened or diminished scrutiny, advising doctors on treatment decisions, or diagnosing disease, the field is redefining medicine."

Look for these **Upcoming** Articles

Nucleic Acid Purification and Manipulation — May 15

Technologies for Gene Transfer — June 19

Label-free Technologies — Sept. 18

Inclusion of companies in this article does not indicate endorsement by either AAAS or Science, *nor is it meant to imply that their products or services are superior to those of other companies.*

Though many MDx probe single nucleic acids, a small but growing number profile panels of genes simultaneously.

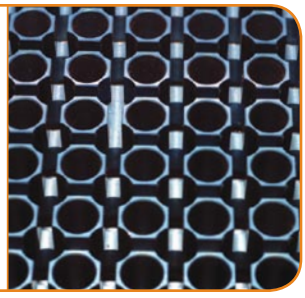

monitoring. Such tests, says Glorikian, represent a fundamental break from what he calls the traditional "gestalt" diagnostic approach. Blood pressure, temperature, and blood chemistry "are not digital indicators but analog indicators," Glorikian says, "where [the doctor] uses the computer between his/her ears, looks at all this stuff, bins it together, and says aha! This is what I think."

By contrast many MDx tests provide quantitized, digital data, as well as actionable results.

Take Down syndrome. Traditionally, a woman's likelihood of having a baby with trisomy-21 is first assessed by noninvasive screens based on maternal serum proteins and ultrasound. Yet these assays provide risk scores rather than absolute diagnoses, and must often be supplemented with more accurate, but also invasive tests such as amniocentesis, which literally count fetal chromosomes.

Sequenom's trisomy-21 MDx, set for launch later this year, blends these two approaches. Using mass spectrometry to count fetal chromosome 21–derived transcripts in maternal blood, the test is both noninvasive and quantitative—though not, per se, digital; the test measures the ratio of maternal and paternal alleles from chromosome 21.

"It's an absolute result," says Harry Stylli, **Sequenom's** president and CEO. "You're not dealing with a risk score." As a result, high-risk pregnancies may be properly managed, while the number of pregnancies unnecessarily subjected to invasive procedures—currently about 140,000 per year, Stylli estimates—"will dramatically decrease."

The Sequence Space

Perhaps no genes more starkly illustrate the actionable power of MDx than BRCA1 and BRCA2. Mutations in these genes carry such high risk of breast and ovarian cancer (about 82 percent) that some carriers opt for prophylactic radical mastectomy, using **Myriad Genetics'** BRAC*Analysis* blood test to help guide their decision.

Based on full-length Sanger dideoxy gene sequencing, BRAC*Analysis* is an unusual test; sequencing is more typically suited to research labs. Yet unlike proteins or transcripts, Gulcher notes, DNA "is the only stable molecule in your body." It enables Myriad to pick up novel mutations. "Unfortunately there are a very large number of mutations in the genes that we look at, so it is not a mutation-specific test, it is a full DNA sequence test," explains Pete Meldrum, Myriad's president and CEO.

Myriad offers the test as a lab-developed "home brew" assay available through the company's Clinical Laboratory Improvement Amendments (CLIA)–certified facility in Salt Lake City, Utah. Not yet vetted by the US Food and Drug Administration (FDA), such tests can only be offered by the lab that develops them.

In this case, results come back in about 10 days. That's not generally a problem for predisposition tests. But sometimes, and especially when confronting acute medical issues, patients don't have that kind of time.

"In general, the faster the results become available, the more likely it is that they are going to be actionable," says David Persing, executive vice president and chief medical and technology officer at **Cepheid.**

Testing on Demand

When speed is required, real-time or quantitative PCR (qPCR) delivers. Most labs have a PCR machine, and most lab techs are competent to run them.

"Real-time PCR is quite a forgiving technique," says Stephen Little, CEO of **DxS.** "You can put different levels and quantities of samples into the test and it will still give a good result."

Even so, clinical labs often delay crucial tests because they must process them in batches. Cepheid's GeneXpert system was built to circumvent this problem, says Persing. A modular, independently addressable real-time PCR system, the GeneXpert is "the first sample-in, answer-out machine for real-time PCR to hit the market," says Glorikian.

Anyone can use it, Persing says. In one study, nurses running the company's Group B *Streptococcus* test in the labor and delivery suite "delivered results that were highly accurate, and were as reliable and as good as the ones delivered by the lab."

In part, that's because there's no sample prep; the system processes raw samples straight to analysis. Results can arrive in as little as 31 minutes, fast enough to catch patients before they leave the doctor's office.

Cepheid's new Xpert MTB/RIF assay reports in less than two hours both if an individual has tuberculosis and whether it is resistant to rifampicin. Traditional culture methods take weeks to make that assessment, says Persing, during which time patients may unwittingly spread the infection.

Cepheid's assays are mostly based on **Applied Biosystems'** TaqMan reagents, modified oligonucleotides that contain a fluorescent dye on one end and a quencher on the other. During PCR, this oligo binds its target DNA between the two amplification primers, where it is chewed up by the polymerase's 5' to 3' exonuclease activity, separating dye from quencher in a burst of fluorescence.

DxS uses an alternative detection reagent, called a "scorpion" probe, for its TheraScreen assays.

A scorpion, says Little, is "a self-quenching molecule." A hairpin with a PCR primer at its 3' end, the scorpion serves as a 5' PCR primer. The hairpin is complementary to part of the amplified sequence, and like a TaqMan probe bears both a fluorophore and a quencher. In the absence of amplification, the closed hairpin keeps the two dyes in close proximity, dousing fluorescence. But after amplification, the probe can denature, unfold like a scorpion's tail, and hybridize to the amplified segment. In the process, the fluorophore and quencher dissociate.

"That's the signal that the reaction has taken place and we use it to signal the presence or absence of the mutations that we look for," says Little.

In the case of DxS's K-RAS and EGFR assays, the resulting data can guide treatment. Knowledge of a K-RAS mutation helps oncologists choose between cetuximab and panitumumab in colorectal cancer, while different mutations in EGFR affect which works better for nonsmall-cell lung cancer (NSCLC), gefitinib or erlotinib.

Multivariate Assays

Though many MDx probe single nucleic acids, a small but growing number profile panels of genes simultaneously.

"As our understanding of genetics increases, we are going to learn that most diseases are multigenic in nature," says Amit Kumar, president and CEO of **Combimatrix,** which develops MDx based on

array comparative genomic hybridization; "It's not just one gene that's causing a particular illness or disease; it's a combination of multiple genes functioning together."

Three such tests have been cleared under the FDA's "in vitro diagnostics–multivariate index assay" guidelines, all based on gene expression. **XDx's** 20-gene AlloMap test uses reverse transcriptase (RT) PCR to monitor heart transplant rejection; **Agendia's** 70-gene MammaPrint microarray assay predicts whether breast cancer patients are likely to relapse and benefit from chemotherapy; and **Pathwork Diagnostics'** Tissue of Origin test uses a 1,500-gene array to determine the source of a primary tumor in patients that present only with metastases.

"In order to effectively treat a metastasis, you have to treat it in the same way that you treat the primary tumor," explains Ronen Tamir, chief commercialization officer at **Rosetta Genomics,** whose "miRview mets" test addresses the same problem using a 48-gene RT-PCR assay. In other words, a breast tumor that metastasizes to the colon should be treated as breast cancer.

Such tests may be less digital, perhaps, than the Down syndrome or BRCA tests—they sometimes provide probabilities rather than certainties—yet they still can help doctors make smarter treatment choices.

According to Steve Shak, chief medical officer at **Genomic Health,** whose 21-gene RT-PCR–based Oncotype DX assay also predicts breast cancer relapse, the most common treatment for women with node-negative, estrogen receptor–positive breast cancer is chemotherapy. Yet only about 4 percent of patients benefit from that option; the rest would do just as well with surgery plus hormonal therapy alone.

Now, using Oncotype DX, about one-third of treatment decisions change, Shak says. "Some women with high recurrence scores who might have been treated with hormonal therapy alone are then given hormonal therapy plus chemotherapy," he says. Similarly, "there are many women who might have considered chemotherapy but based on the results will be confident in getting hormonal therapy alone." Agendia cites similar numbers for its MammaPrint diagnostic.

Yet when it comes to multivariate MDx, array-based assays like MammaPrint are relatively rare; frequently, developers use arrays for test development, reverting to RT-PCR once the hard work of biomarker identification is done. Such was the case for Oncotype DX and AlloMap.

"The thing with arrays is they are a little bit clunky to use, whereas RT-PCR, if you can use it, is a much easier technology to fit into a lab," says Little. "Ease of use and convenience are very important considerations when you move into diagnostics."

Of Methyl-C and microRNAs

Ease of use and convenience are especially important when it comes to more esoteric markers, such as DNA methylation or microRNAs.

LabCorp's ColoSure test measures methylation of the vimentin gene in stool samples. **Epigenomics** is developing a blood-based assay for *SEPT9* methylation. Both are early indicators of colon cancer, and both are based on qPCR detection of bisulfite-treated DNA (in which unmethylated cytosine is converted to uracil, while methyl-C remains unmodified).

"Having a very innovative test with a novel analyte [DNA methylation], we decided to be rather conservative when it comes to the assay technology," says Achim Plum, senior vice president for corporate development at Epigenomics.

Slated for European release this year, Epigenomics' assay won't be the first blood test–based colon cancer screen on the market; **GeneNews** beat them to the punch in 2008 with ColonSentry, based on microRNA expression.

Short, endogenous, regulatory RNAs that silence the translation of complementary mRNAs, microRNAs are relatively recent discoveries. Yet they have emerged as hot commodities in MDx, and Cepheid, Rosetta Genomics, **Exiqon,** and Combimatrix are all also pursuing them.

Exiqon's in-development assay for colorectal cancer prognosis is based on the detection of microRNAs with DNA analogs called Locked Nucleic Acids (LNA), because, says Søren Møller, Exiqon's vice president of research and development, standard nucleic acids just aren't specific enough.

"You don't have much sequence space," Møller explains. "microRNAs are 20–23 nucleotides long, and if you need to detect those in complex samples, you need very, very accurate detection techniques. LNA provides that advantage."

Rosetta's miRview squamous test uses RT-PCR of a single microRNA to help distinguish between squamous and nonsquamous NSCLC—an actionable result, says Tamir.

"Alimta is only labeled for nonsquamous NSCLC; Avastin is labeled for both," he says. But a "black box" warning on Avastin "warns against fatal hemorrhaging of 40 percent of the patients which are squamous."

A potentially life-saving decision based on a type of molecule researchers barely knew existed 10 years ago, it's just another example of putting the "personal" in personalized medicine. The MDx landscape continues to change as new technologies—like next-generation sequencing—come to the fore.

"There's a lot going on in this space, it's so exciting," says Glorikian. "Anybody who isn't in this space needs to ask themselves why."

Featured Participants

Agendia
www.agendia.com

Applied Biosystems
www.appliedbiosystems.com

Cepheid
www.cepheid.com

Combimatrix
www.combimatrix.com

deCODE Genetics
www.decode.com

DxS
www.dxsdiagnostics.com

Epigenomics
www.epigenomics.com

Exiqon
www.exiqon.com

GeneNews
www.genenews.com

Genomic Health
www.genomichealth.com

Illumina
www.illumina.com

LabCorp
www.labcorp.com

Myriad Genetics
www.myriad.com

Pathwork Diagnostics
www.pathworkdx.com

Rosetta Genomics
www.rosettagenomics.com

Scientia Advisors
www.scientiaadv.com

Sequenom
www.sequenom.com

XDx
www.xdx.com

Jeffrey M. Perkel is a freelance science writer based in Pocatello, Idaho.
DOI: 10.1126/science.opms.p0900034

New Products

Eppendorf
For information +49-40-53801-0
www.eppendorf.com

Automated Pipetting Systems

The epMotion 5075 TMX features an integrated Thermomixer to shake and heat or cool sample tubes and plates. The Thermomixer's orbital shaking and balance of speed and mixing radius optimize resuspension of bacteria pellets and beads. It prevents droplets from collecting on the side of tubes or plate wells, eliminating the need for additional centrifugation steps. It features a pipetting range from 1 to 1,000 µl, automated loading of the Thermomixer, and 12 worktable positions to provide walkaway automation. It saves time by automating all heating steps for lysis and incubation.

PCR Reagent

The SsoFast EvaGreen Supermix reduces the time needed to get quantitative polymerase chain reaction (qPCR) results from 40 minutes to 30 minutes. Part of a next-generation family of high-performance, real-time PCR reagents, the supermix speeds qPCR cycling protocols through instant polymerase activation, optimal primer binding, and rapid polymerization kinetics. The combination of Bio-Rad's patented hot-start Sso7d fusion protein technology, optimized buffer, and EvaGreen dye increases the product's reliability and sensitivity. Its reproducibility enables efficient and accurate quantification of gene targets over a broad range of expression levels.
Bio-Rad Laboratories
For information 800-424-6723
www.bio-rad.com/supermixes

Genetic Analysis System

The new EP1 system for genetic analysis provides the efficiency of integrated fluidic circuit (IFC)-based genotyping in a desktop-sized configuration at an affordable price. When used with Fluidigm Dynamic Arrays, the system provides superior data quality and a fast, easy workflow. It delivers high-quality single nucleotide polymorphism genotyping results, with better than 99 percent call rates and 99.75 percent accuracy. It can provide up to 9,216 data points per IFC chip with results in four hours. The EP1 system, which includes an IFC controller, standalone thermal cycler, and end-point reader, provides more than 27,000 genotypes a day. More IFC controllers and thermal cyclers can be used in conjunction with a single EP1 Reader to generate more than 200,000 genotypes in a day.
Fluidigm Europe
For information +33-44-259-3861
www.fluidigm.com

TaqSelect DNA Polymerase

TaqSelect is a high-purity, high-activity Taq polymerase that contains a specially formulated stabilizer and enhancer to provide outstanding performance in genotyping and routine polymerase chain reaction (PCR). It contains an optimal concentration of magnesium to enhance PCR results and allows direct gel-loading after PCR. Formulated as a 2X premix, it does not contain deoxynucleotides, allowing the user greater flexibility.
Lucigen Corp.
For information 608-831-9011
www.lucigen.com

DNA Isolation Kit

The BiOstic FFPE Tissue DNA Isolation Kit is for extraction of DNA from formalin-fixed paraffin-embedded (FFPE) tissue. The kit features a fast and safe method to directly melt the wax away from tissues without the use of solvents such as xylene to deparaffinize the tissue. This gentle method achieves high DNA yields. The recovered DNA is pure and free from contaminants that can have an adverse effect on detection sensitivity and amplification efficiency. Genomic DNA extracted with the kit can be used in real-time polymerase chain reaction, single nucleotide polymorphism genotyping, and other genetic analysis methods. The BiOstic Paraffin Removal Reagent is a nonhazardous, nontoxic alternative to xylene that can be used with the FFPE Tissue DNA Isolation Kit.
Mo Bio Laboratories
For information 800-606-6246
www.mobio.com

Genomic DNA Labeling Kit

The Genomic DNA labeling kit offers a fast, simple protocol for use in cytogenetic arrays. The kit contains Cy3 and Cy5 dyes for dual-color hybridizations and makes use of a unique buffer formulation to achieve more efficient use of reagents without loss of signal intensity. The kit contains everything required for the protocol, including nucleotide mix, random primers, enzymes, cleanup columns, and collection tubes. The manufacturer offers analysis software to allow easier interpretation of results with data exchange for comprehensive, state-of-the-art cytogenetic profiling and comprehensive customer training.
Oxford Gene Technology
For information +44-1865-856828
www.ogt.co.uk

Electronically submit your new product description or product literature information! Go to **www.sciencemag.org/products/newproducts.dtl** for more information.

Newly offered instrumentation, apparatus, and laboratory materials of interest to researchers in all disciplines in academic, industrial, and governmental organizations are featured in this space. Emphasis is given to purpose, chief characteristics, and availabilty of products and materials. Endorsement by *Science* or AAAS of any products or materials mentioned is not implied. Additional information may be obtained from the manufacturer or supplier.

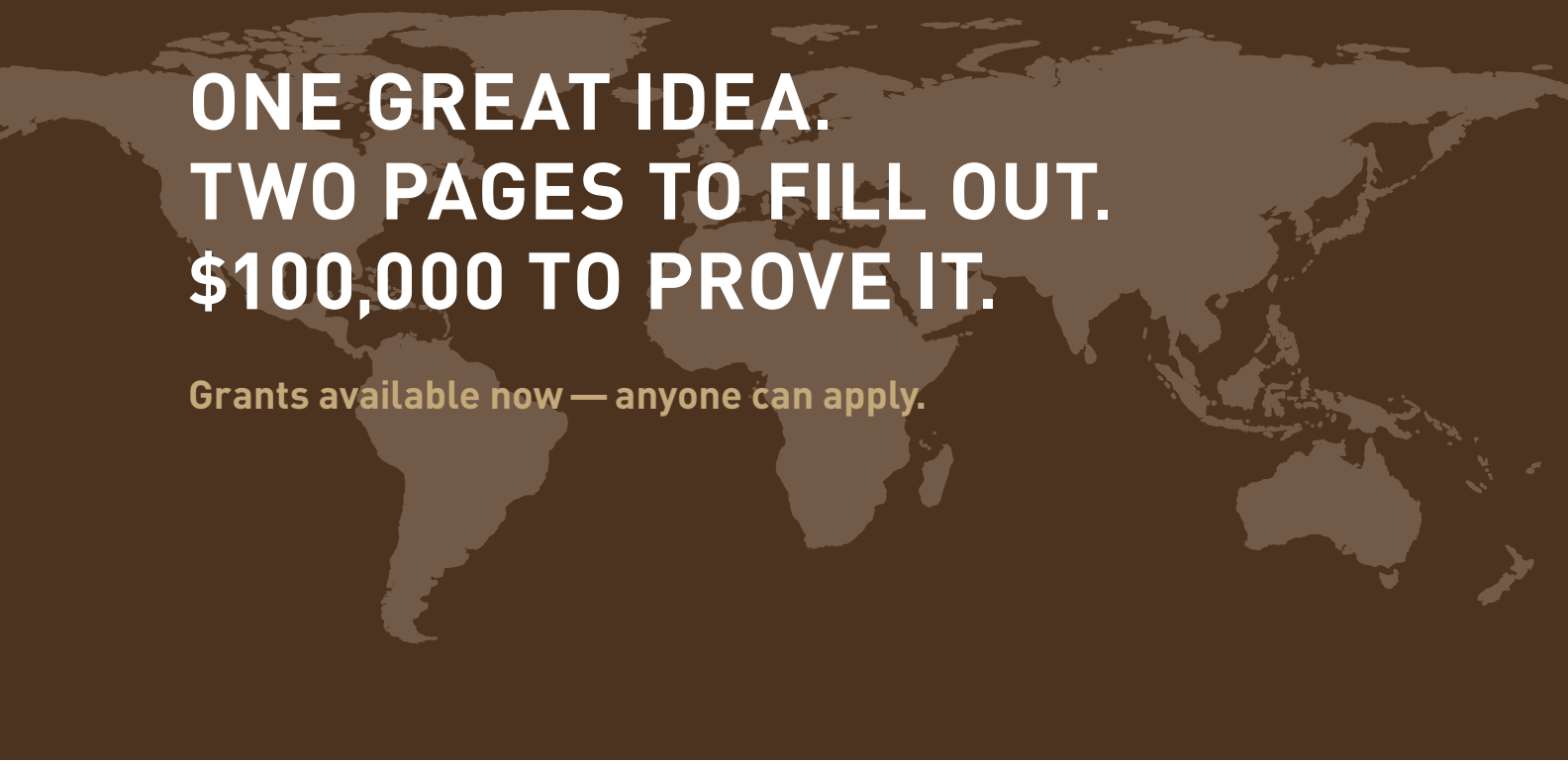

ONE GREAT IDEA.
TWO PAGES TO FILL OUT.
$100,000 TO PROVE IT.

Grants available now — anyone can apply.

The Bill & Melinda Gates Foundation seeks bold ideas from innovative thinkers to solve the greatest challenges in global health.

As part of our Grand Challenges Explorations initiative, grants of $100,000 are awarded two times a year. Projects that show great promise have the opportunity to receive a subsequent grant of $1 million or more.

Proposals will be accepted March 31 through May 28, 2009.

Please visit www.grandchallenges.org/explorations for Round 3 topics and complete application materials.

BILL & MELINDA GATES *foundation*

Grand Challenges | EXPLORATIONS

POSITIONS OPEN

UAB

The Department of Pathology invites applications for a nontenure-track **RESEARCH INSTRUCTOR** position in the Division of Molecular and Cellular Pathology. This individual will contribute to the discovery and molecular and biochemical characterization of metastasis suppressors. Since the project is focused on breast cancer metastasis suppression, expertise with breast cancer and/or mammary gland biology, chromatin remodeling complexes, and in vivo animal models of metastasis is required. The applicant must also have a solid track record of peer-reviewed research publications and preferably a record of successful federal funding. The successful candidate will be expected to initiate an active extramural funding program. Salary will be commensurate with experience. Self-motivated applicants must hold a Ph.D. in cell biology, biochemistry, or similar field and have a minimum of four years of relevant postdoctoral experience. Interested candidates should submit a letter of interest together with a comprehensive curriculum vitae that outlines research interests to: **Danny R. Welch, Ph.D., Division of Molecular and Cellular Pathology, Department of Pathology University of Alabama at Birmingham, 1670 University Boulevard VH-G019, Birmingham, AL 35294-0019.** *The University of Alabama at Birmingham is an Affirmative Action/Equal Opportunity Employer and welcomes applications from qualified women and minorities.*

DUCTUS ARTERIOSUS SCIENTIST

The Department of Medicine/Section of Cardiology is seeking qualified applicants for a full-time **RESEARCH ASSOCIATE** (**ASSISTANT/ASSOCIATE/PROFESSOR**) position to work with **Dr. Stephen Archer** on the physiology and O_2 sensing mechanisms of the human ductus arteriosus (DA). The successful applicant will join the Heart and Vascular Research Group, led by Dr. Archer.

The primary activity of the Research Associate (Assistant/Associate/Professor) is academic research to study mechanisms of O_2 constriction in human ductus arteriosus, in association with a faculty member or team. Qualified applicants are required to possess a doctorate degree in pathology and pathophysiology. Applicants should possess excellent knowledge and experience with patch clamp technique of whole cell and single channel recording and calcium imaging technique. Experience in small animal work (including small animal surgeries) and basic molecular biology skills such as RT PCR are required. Two to three years of postdoctoral training is required. Applicant should be familiar with physiologic assessment of the cardiopulmonary system, including the use of the isolated perfused lung model. A demonstrated track record of publication and the potential to apply for peer-reviewed funding is preferred. Compensation and level of appointment are dependent on qualifications. The University provides a generous package of fringe benefits. Screening of applications will continue until position is filled. Interested applicants should submit cover letter, curriculum vitae, and three letters of reference electronically to: **Dr. Stephen Archer, e-mail: sarcher@medicine.bsd.uchicago.edu.** *The University of Chicago is an Affirmative Action/Equal Opportunity Employer.*

Drexel University College of Medicine in Philadelphia, Pennsylvania, is seeking a full-time chemistry **ASSISTANT PROFESSOR** to teach graduate forensic toxicology, undergraduate chemistry I and II, and organic chemistry I and II starting in August 2009.

Educational requirement: Ph.D. in chemistry with college-level teaching experience required.

Please send curriculum vitae to **e-mail: medsci@drexelmed.edu.**

POSITIONS OPEN

HEAD, DEPARTMENT OF COMPARATIVE PATHOBIOLOGY

The Purdue University School of Veterinary Medicine (**website: http://www.vet.purdue.edu/**) invites applications for the position of Head of the Department of Comparative Pathobiology (**website: http://www.vet.purdue.edu/cpb/**). We seek an individual with strong leadership skills, an internationally recognized record of scholarship and research, and the ability to guide this Department of 33 faculty members in their continued development of excellence in learning, diagnostic engagement, and discovery. Departmental faculty members have expertise and research interests in pathology, microbiology, immunology, parasitology, epidemiology, public health, toxicology, and the human-animal bond. The Department has approximately 50 graduate students who participate with faculty members in multidisciplinary and multi-institutional research projects. The graduate program includes residency training in veterinary anatomic and clinical pathology and in laboratory animal medicine. Faculty members teach in the veterinary professional curriculum, the veterinary technology program, and the professional curriculum of the Indiana University School of Medicine at Lafayette. Some faculty members also have partial appointments in other units on campus. The School of Veterinary Medicine has a strong focus on comparative medicine and offers research support laboratories in the Medical Discovery Resource Unit (**website: http://www.vet.purdue.edu/mdru/**). Purdue University provides exciting opportunities for collaborative and interdisciplinary research through the National Cancer Iinstitute–funded Purdue Cancer Center, the Bindley Bioscience Center and Birck Nanotechnology Center in Discovery Park (**website: http://www.purdue.edu/discoverypark/**), the Department of Biomedical Engineering, and other academic departments and centers.

The successful candidate must have a D.V.M. (or equivalent) and/or Ph.D. degree, qualify for appointment as a tenured **FULL PROFESSOR** and have a record of extramurally funded research. Candidates must be familiar with modern molecular technology in the investigation of natural and experimental disease of infectious and noninfectious origins. Candidates must possess outstanding communication and interpersonal skills; administrative experience is desired. Commitment to the departmental missions of discovery, learning, and engagement and the promotion and implementation of the School's strategic plan (**website: http://www.vet.purdue.edu/strategic_plan/StrategicPlan2008-2014.pdf**) are essential. The Department Head must be dedicated to promoting the career development of others and to promoting an atmosphere of cultural diversity. The Department Head will work closely with the Director of the Animal Disease Diagnostic Laboratory (**website: http://www.addl.purdue.edu/**) and must value and support diagnostic activities. The Department Head serves on the Executive Committee and the Academic Leaders Group of the School.

The review of applications will begin on July 1, 2009, and will continue until the position is filled. Applications, including a statement of professional goals, curriculum vitae, and names and addresses of four references, should be sent as PDF files to **e-mail: whiteb@purdue.edu.** Applicants wishing more information are encouraged to contact **Dr. Steve Hooser,** Chair of the search committee, at **e-mail: shooser1@purdue.edu** or by **telephone: 765-494-7440.**

Purdue University is an Equal Opportunity/Equal Access/Affirmative Action Employer fully committed to achieving a diverse work force.

NIH-funded **POSTDOCTORAL POSITIONS** are available to study mechanism of human and bacterial DNA helicases for recent Ph.D.s with publications in molecular biology, enzymology, or biophysics. NIH scale salary. *Must be U.S. citizen or permanent resident.* Send curriculum vitae and references to: **Dr. Subhasis Biswas, e-mail: biswassb@umdnj.edu.**

CORPORATE CULTURE IN CURRENT TIMES -

SEEKING THE RIGHT FIT

Like it or not, each of us has only 168 hours a week to spend in whatever way we see fit, and most of us apply at least one-fourth of those hours—about half of our waking hours—engaged in some type of gainful employment. The "corporate culture" of where we work and whether our chosen employer represents an appropriate fit, therefore, will play a significant role in our day-to-day joie de vivre. **By Emma Hitt**

For scientists selecting a place to work in industry, several components of a company's corporate culture should be considered, some of them unique to a particular company (corporate philosophy, the extent to which employees are allowed to act upon their scientific thinking) and some of them standard for the industry (pay, benefits, dress code). Talking with people and networking are essential steps in determining a company's corporate culture, whereas a company's website is not always the best place to get a clear picture.

Components of Corporate Culture

Corporate culture is one of those nebulous terms that conjures up a variety of images. Some of them may be positive: a welcoming environment where people feel secure in their jobs, where independent thinking and work-life balance are encouraged. And some may be not so positive: excessive work hours or unexpected changes in job description. While no standard definition of corporate culture exists, the term typically refers to the overall philosophy and environment of a workplace: can you wear jeans or is a business suit the norm? Does a company focus on innovation or do they try to do what they already know? What would happen if you showed up 15 minutes late or told your direct supervisor that you disagreed with his/her ideas? The answers to these questions and others constitute the unique style and policies of a company.

Some of the key factors to consider with respect to corporate culture include diversity in leadership, philosophy about work-life balance, project range and scope, attitudes about employee development, the mission statement, and tolerance for diverse ideas, notes **Karen Habucky,** the 2008 president of the American Association of Pharmaceutical Scientists (AAPS), an educational and networking professional development society of about 13,000 scientists.

The Times They Are A-Changin'

With recent layoffs and restructuring at numerous companies, an important issue that directly affects corporate culture these days is job security. "The industry as a whole is going through a rather rigorous evolution," says **Michael Steiner,** leader of the Pharmaceutical Executive Services Group at RegentAtlantic Capital, LLC, and provider of wealth management services for pharmaceutical and biotech industry executives. Compared to some industries, the pharmaceutical industry is faring well, but at the same time, pharma and biotech companies are contending with unique pressures, such as patent expirations and changes in health care. In addition, layoffs in the thousands have been taking place at some of the bigger pharmaceutical companies. "Several forces are seemingly colluding," Steiner says, "and these forces are building upon one another to create a good deal of synergistic pressure." continued »

"Several forces are seemingly colluding, and these forces are building upon one another to create a good deal of synergistic pressure."

UPCOMING FEATURES

Diversity Feature: Asian American Scientists — May 29

Focus on Cambridge/Oxford/London — June 26

Bioentrepeneurship — July 17

"In a small company, more time is spent on science, whereas the established culture of a big company has the potential to stifle the creative spirit and take time away from doing science."
—Allen Sessions

According to Steiner, corporate culture has been influenced in a dramatic way by these changes. What used to be a "paternalistic" type culture—where an employee would start work right out of graduate school, stay for 30 years, and be "taken care of" by a company, is no longer the norm. "What we see is more of a shift towards an entrepreneurial-like atmosphere," he says. "People are encouraged to take more business risks, because ultimately this is where the rewards are to be found. In the past, employees have tended to get too complacent and comfortable in their positions at the expense of innovation."

"In tight economic times, we are all being asked how things can be done quicker and cheaper while maintaining high quality standards," Habucky says. "In the future, I feel there will be a greater emphasis on creative problem solving and more challenges to the status quo; this could lead to the development of innovative ideas that will help propel the industry through the tough times, and scientists may even feel a greater ownership in a company's success," she says.

Many companies are understaffed right now, given budget constraints and layoffs, according to **Shannon Peryea,** an executive recruiter for the pharmaceutical industry with Sheila Greco Associates. "Employees will be working longer hours, handling a larger workload, while being paid the same salary," she says. "Until things pick up and companies are given the green light to hire new employees or bring back laid-off workers, I think most corporate cultures will tend toward a 'roll up your sleeves and pitch in anywhere you are needed'–type mentality. This may cause some amount of worker burnout, but I think when things improve, the companies will not forget those who stayed and worked their hardest to ensure the company survived," Peryea notes.

Sizing Up Opportunity

Steiner suggests that a key question people need to ask themselves is whether they are more suited to working for a large or a small company. "Picking a big company simply because of perceived stability can be a mistake these days—you cannot apply safety in numbers any more," he says, "although picking a smaller company sometimes means even more risk, but a higher potential reward."

Genentech, which employs about 11,000 workers (and in January 2009 had 585 job openings), has been included on the Fortune "100 Best Companies to Work For" list for 11 consecutive years and has ranked in the top 10 in recent years (No. 1 in 2006, 2 in 2007, 5 in 2008, and 7 in 2009). The Fortune 100 list includes companies in any industry with more than a thousand employees and that have been in business for at least seven years. Rankings are based mainly on responses by employees to a 57-question survey and the findings of a "culture audit," which includes questions about demographics, pay scales, benefits, and other factors.

Featured Participants

American Association of Pharmaceutical Scientists
www.aapspharmaceutica.com

AstraZeneca
www.astrazeneca.com

Genentech
www.gene.com

GrassRoots Biotechnology
www.grassrootsbio.com

Massachusetts Biotechnology Council
www.massbio.org

RegentAtlantic Capital, LLC
www.regentatlantic.com

Sheila Greco Associates
www.sheilagreco.com

At Genentech, the CEO (Arthur D. Levinson) wears jeans and sneakers and "it is not unusual to walk into the research labs and hear music blaring while scientists conduct experiments in search of important discoveries," says **Robin Snyder,** with Genentech Corporate Relations. "We refer to this combination of gravity and informality as 'casual intensity,' and we believe it is part of what has made us successful." Genentech perks include free espresso and the use of a WiFi equipped "GenenBus" to neighborhoods throughout the greater San Francisco Bay Area. In addition, regular full-time employees get six paid weeks of sabbatical every six years.

Another large company, AstraZeneca, which has approximately 66,000 employees, ranked No. 5 in *Science* magazine's ranking of the world's most respected biopharmaceutical employers in 2008. Benefits include flextime, the opportunity to work a compressed work week and/or telecommute, and on-site services such as a hair and nail salon and DVD rentals. According to **Sarah J. Bolton,** a research scientist with Global Discovery at AstraZeneca, the best things about working at AstraZeneca include the flexible work arrangements and the opportunity for "work-life balance." Bolton also points out that many training opportunities are available. For instance, an e-learning module entitled "Working for Your Inner Boss," a worksheet called "Keeping Your Balance," as well as other personal and management development tools are available. "AstraZeneca encourages and challenges its scientists to come up with innovative ways of approaching disease targets and to better understand the wider implications for patients," she says. "There also seems to be an increasing openness and transparency, as well as an acceptance of employees challenging the status quo," she adds.

At the other end of the size spectrum, **Allen Sessions,** a senior scientist for GrassRoots Biotechnology, says he enjoys working at a "small, young" company. GrassRoots, located in Chapel Hill, North Carolina, currently has only seven employees and is developing crop lines for the biofuel, food, and industrial markets. "In a small company, more time is spent on science, whereas the established culture of a big company has the potential to stifle the continued »

Lead the next generation of pharmaceutical science.

Discover the Answers that Matter.

Eli Lilly and Company is a leading, innovation-driven pharmaceutical corporation with approximately 42,000 employees worldwide. Lilly is developing a growing portfolio of best-in-class, first-in-class pharmaceutical products. We achieve this by applying the latest research from our own worldwide laboratories, by collaborating with eminent scientific organisations and by making use of the most up-to-date technological tools.

Established in 2002, Lilly Singapore Centre for Drug Discovery (LSCDD) is now expanding its capabilities to discover and develop new medicines more productively, in the areas of cancer and metabolic disorders. We form a network of drug development partners, and through innovative data integration approaches, discover and apply biomarker and patient-tailoring solutions.

Located in the exciting Singapore Biopolis, LSCDD's multi-disciplinary and multi-cultural team is working to redefine the leading edge. We are looking for outstanding individuals with demonstrated industry experience in Biotech/Pharmaceutical/Drug Discovery to fill the following positions:

- **Group Leader, Diabetes Biology**
- **Senior Scientist, Diabetes Biology**
- **Group Leader, Cancer Biology**
- **Group Leader, Target Identification & Validation (Systems Biology)**
- **Bioinformatics Group Leader (Systems Biology)**
- **Bioinformatics Manager (Integrative Computational Sciences)**
- **Senior Statistical Geneticist (Integrative Computational Sciences)**
- **Senior Bioinformatics Scientist (Integrative Computational Sciences)**
- **Principal Statistician (Integrative Computational Sciences)**

Log on to **www.lscdd.lilly.com.sg** to find out more about this position and what a career at Eli Lilly and Company can offer you. Eli Lilly is an equal opportunity employer.

www.lscdd.lilly.com.sg

Lilly

Answers That Matter.

Research Associate/Scientist (CNS Research)

Who we are
At Roche, 80,000 people across 150 countries are pushing back the frontiers of healthcare. Working together, we've become one of the world's leading research-focused healthcare groups. Our success is built on innovation, curiosity and diversity, and on seeing each other's differences as an advantage. To innovate healthcare, Roche has ambitious plans to keep learning and growing – and is seeking people who have the same goals for themselves.

The headquarters in Basel is one of Roche's largest sites. It is home to the Corporate Executive Committee, the Pharmaceuticals and Diagnostics Divisions and the global business functions. Roche Basel also covers the entire business chain from research, development and production through to marketing. Over 8,000 people from more than 60 countries work at the site.

The Position
You will join a behavioural pharmacology section within the Neuroscience area. This section is responsible for providing the full range of expertise and technologies to profile molecules in animal models of psychiatric disorders throughout the course of drug discovery. The scientists of the behavioural pharmacology section are integrated members of drug discovery project teams and are responsible for the full characterisation of drug candidates and provide key information on in vivo activity in projects. In your role as research scientist you are expected to conduct laboratory research and to provide scientific input to ongoing and newly established drug discovery programs. As part of the project teams you will report directly to project leaders and senior level scientists.

Who you are
You're someone who wants to influence your own development. You're looking for a company where you have the opportunity to pursue your interests across functions and geographies, and where a job title is not considered the final definition of who you are, but the starting point.

You have a PhD in psychopharmacology or a related discipline, with experience in model development and statistical analysis. Knowledge of neuropharmacology and neuroanatomy are considered a plus. You have a strong technical troubleshooting skill and you are driven by quality. You have practical knowledge of the drug discovery process gained in an industrial environment, in particular active and successful participation in CNS drug discovery programs. You will have provided high quality data and reports and you will have contributed to documentation preparation (company presentations, patent applications, IB, and due diligence). You will also have published your data in peer-reviewed scientific journals. You will be responsible for the development and implementation of a battery of behavioural tests and for the supervision of testing drug candidates.

In your role as research scientist you will continuously support our discovery programs with your expertise and with high quality data. You will communicate your data to project teams and senior management, and will propose and execute in vivo experiments for the continued progression of the project, for patent exemplification and Investigator Brochure documentation. You are flexible, have strong team skills and are used to paying attention to detail and adjusting to new challenges. You have an excellent command of spoken and written English and good presentation skills.

Job ID No.: 15051
Contact HR: M. Ceroni, +41 61 687 34 58
Contact Line: J. Wettstein, +41 61 688 81 13

The next step is yours. To apply online today or learn about other exciting positions, please visit http://careers.roche.com

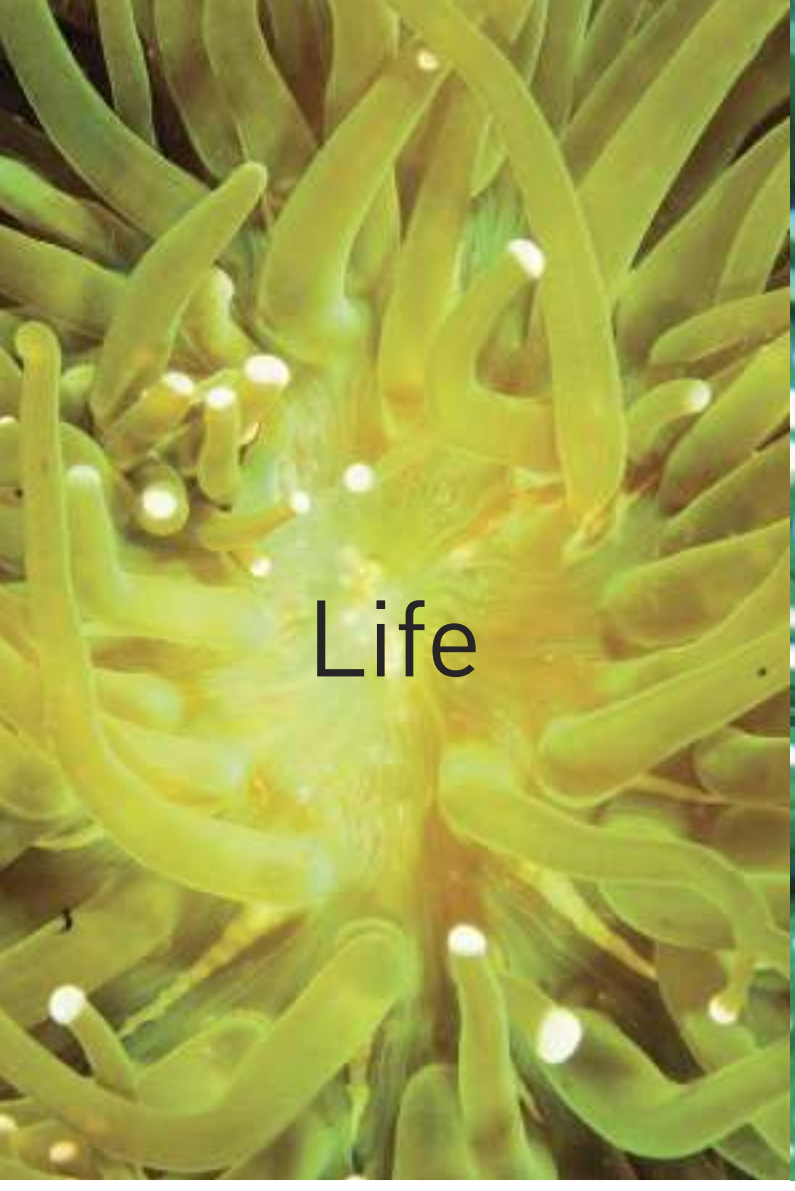

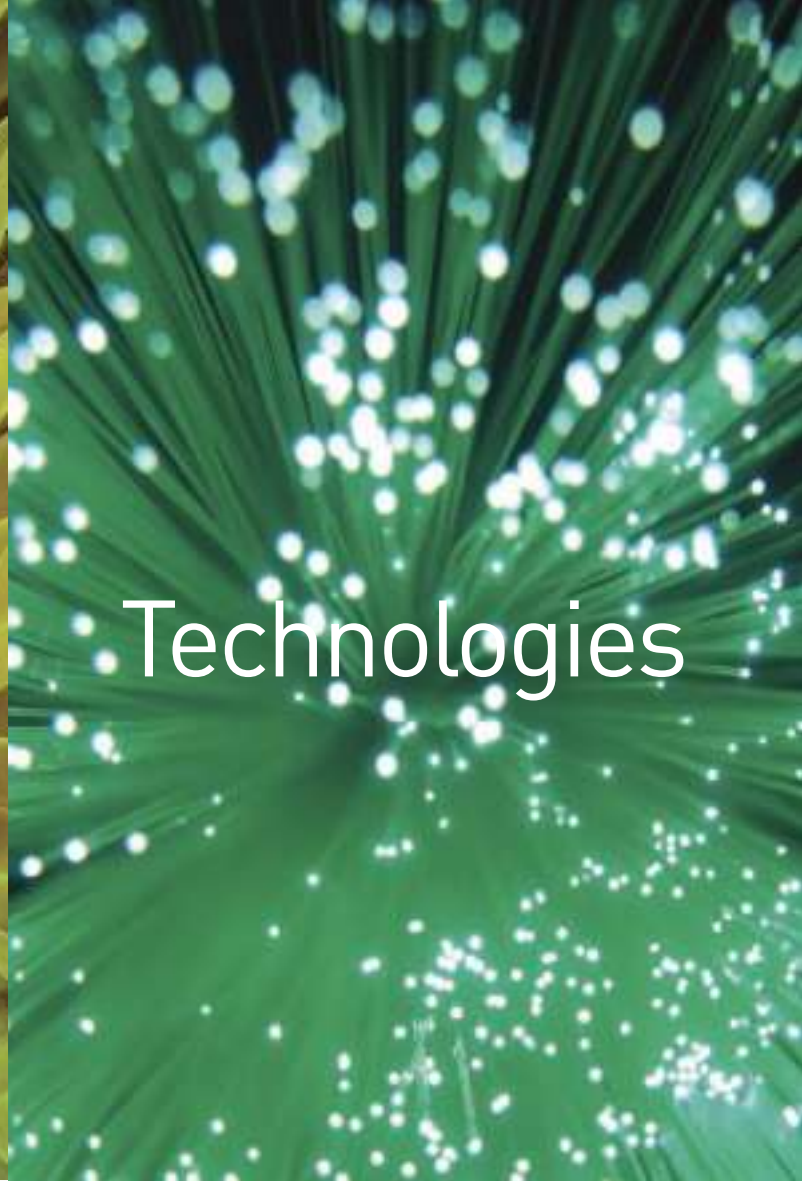

Life Technologies, created through the combination of Invitrogen Corporation and Applied Biosystems, Inc., is a global biotechnology tools company dedicated to improving the human condition.

Life Technologies gives you the opportunity to apply your expertise, develop your skills and play an active role in making an impact in the world. Whether it's in scientific research, product sales or many other areas that support improving the human condition, at Life Technologies, a career here means not only transforming yourself, but transforming life.

Life Technologies values and promotes a diverse workplace that allows each individual to succeed. Visit: www.lifetechnologies.com today to learn how you can make Life Even Better.

Come visit our booth at the BIO Career Fair in Atlanta, GA on May 18th, 2009.

life technologies™

Life Even Better™

www.lifetechnologies.com

"The industry as a whole is going through a rather rigorous evolution."
—Michael Steiner

creative spirit and take time away from doing science," Sessions believes. According to Sessions, in this phase of the company's development, every type of idea is encouraged. "We make decisions as a group and there is a feeling that the sky is the limit if our creative juices can get it all right," he says.

Seeking the Right Fit

Most information about a company's culture can be gained by talking to people, and networking with recruiters and members of industry associations, Habucky says. An important question to ask that is particularly relevant in science is whether a given job will be intellectually challenging and stimulating and will present opportunities for growth. "Your career is a commodity and you need to develop a 'business plan' to make it flourish," she advises. "The plan needs to include short- and long-term goals that incorporate continual learning and the diversification of your skill set."

Another important aspect to consider, especially in the current market, is the financials of a given company and whether that company is stable, says Steiner. "This is especially important if you are seeking a job at a smaller, venture-backed, or private-equity–backed company," he says. "You want to find out whether they have three months or three years worth of cash on hand. Take a look through the company's financial reports to the extent they are available. In many instances you may find that the income statement is really an expense statement. At that point you should look at their assets to find out whether they have enough cash to sustain the company." If there is still concern about the financial viability, ask what the plan and likelihood is of obtaining additional capital. This can give a sense of how much potential there is with a company and whether investors believe in that potential.

Then there's the pay, which isn't everything, but certainly counts toward job satisfaction. The average salary in the biotech industry in Massachusetts is over $100,000, says **Bob Coughlin,** president and CEO of the Massachusetts Biotechnology Council, which has a membership of close to 650 biotechnology companies, universities, and academic institutions in the area. Likewise the AAPS Annual Salary Survey reported that the median base annual income for its members who responded to the survey was $115,000, with a total median compensation of $131,000. The survey also indicated that the typical (median) US full-time employee has been with the current principal employer for five years; only 8 percent indicated 20 years or more, while 17 percent indicated fewer than two years.

Think Not What Your Company Can Do for You...

In summary, it is important to think about what you have to offer to companies more than what they can offer you. In this current economic climate, turnover at many companies is high, particularly at the larger companies and at the upper levels of management. "Changes in upper-level management are made as a cost-savings move," Steiner says. "A company can lay off a person with 30 years of experience and bring in someone with 20 years of experience, with a resulting salary and benefit savings." As a result of these changes, there will really be two types of people that will thrive in the current and future pharmaceutical and biotech industry, says Steiner, and they can be classified as either "athletes" or "specialists." The athletes are people who can deal with adversity and complex challenges, and who can marry the science and business aspects of industry. These individuals may not be highly technical, but are able to see the big picture. They will continue to be much sought-after for upper management positions. By contrast, the specialists are people who have highly technical skills, with more depth than breadth. Those people can exploit their individual talents and continue to build on them, and will survive no matter what the corporate culture.

Six Future High-Growth Areas in Industry

1. Commercialization of Dormant Compounds
Companies often have a reservoir of compounds that they abandoned prior to FDA approval, or that they did not commercialize. Finding ways to reposition or repurpose these compounds is a high-growth opportunity due to the relatively low cost compared to developing new compounds. Repurposing a compound also extends the life of patent protection.

2. Generic or Biosimilar Versions of Biologics
Biosimilar versions of a treatment are not identical but have enough similarity to produce comparable results. This is likely to be a high-growth area, given the upcoming expiration of patents on some high-revenue biologics.

3. Improved Research and Development Efficiency
As R&D costs increase, a focus of industry will be to identify ways in which to improve efficiency while decreasing costs. Efforts will also be made to reduce the time from discovery to regulatory approval so as to maximize the life of a patent.

4. Oncology and Central Nervous System Disorders Research
These areas of research are especially important as the global population ages, with increasing burdens of Alzheimer's disease and cancer. These trends will increase the need for new drugs in these areas.

5. Stratified Medicine and Diagnostics
Finding ways to tailor and personalize medicine, especially in the realm of diagnostic tests, presents a high-growth opportunity. Diagnostic tests are often cheaper and easier to develop than new therapies and are used by a larger segment of the population than actual therapies.

6. Fusion of Pharmaceuticals and Consumer Goods
Due to stricter regulation of consumer goods, companies specializing in these products are likely to increasingly seek individuals with experience in the pharmaceutical industry because of their ability to manage highly regulated businesses and to ensure product safety and efficacy.

Adapted from: RegentAtlantic Capital, LLC, The Continuing Evolution of the Pharmaceutical Industry: Career Challenges and Opportunities, December 2007.

Emma Hitt is a freelance medical and science writer residing in Marietta, Georgia.

DOI: 10.1126/science.opms.r0900071

The world, re-imagined

At Monsanto, our talented employees are contributing to our success as a global leader in biotechnology. By delivering exceptional results in one of the world's most important industries – agriculture – we are creating solutions that improve productivity in farming while reducing the impact on our environment.

The life of the plants we depend upon most begins in a small seed. Within the right environment it grows to become something amazing. At Monsanto, our philosophy is the same – we are committed to helping individuals progress in careers with unlimited potential. We are looking for talented scientists who can work in dynamic, cross functional teams with specialization in one or more of the following fields:

All Positions Located in China

Bioinformatics Scientist
Collaboration Manager
Communication Lead
Computational Biologist
Data Manager and Database Administrator
Lead Computational Biologist
Lead Bioinformatics Scientist
Patent Scientist
Project and Relationship Manager
Technology Alliance Manager

Imagine your world at Monsanto by visiting us on our website,
http://www.monsanto.com.cn/

Monsanto is an equal opportunity employer who values diversity.

MONSANTO imagine®

BBSRC bioscience for the future

Rothamsted Research
World-Class Science for Sustainable Land-Management

DIRECTOR & CHIEF EXECUTIVE

ROTHAMSTED RESEARCH

An outstanding opportunity to lead an internationally renowned centre for research in Food Security and Bioenergy.

The Biotechnology and Biological Sciences Research Council (BBSRC) is seeking to appoint an individual combining strong personal research credibility in the area of sustainable land-management with excellent strategic management skills, to lead the Institute in the next stage of its development.

You will provide inspirational leadership and vision to a team of over 500 staff, plus PhD students and visiting scientists, ensuring that the Institute both maintains and develops its reputation as a world-renowned research institute of international standing delivering both significant outputs to a range of stakeholders and blue-sky science of the highest quality.

The post will be based at Rothamsted Research in Harpenden, Hertfordshire.

An attractive salary plus performance related bonus is available commensurate with the level and the strategic importance of the post.

Further information, including instructions on how to apply, may be obtained from BBSRC's recruitment consultants, Carbon-NfP, who would be happy to provide further written information and/or to have an informal and confidential telephone discussion. Please contact Sharon Taylor by email sharon.taylor@carbon-nfp.com in the first instance.

The closing date for applications is Friday, 6 June 2009.

Carbon-NfP, 17 Russell Court, Woburn Place, London WC1H 0LL.

BBSRC welcomes applications from all sections of the community irrespective of race, ethnic origin, religion or belief, sexual orientation, disability, age or gender. As users of the disability symbol, we guarantee to interview all disabled applicants who meet the minimum criteria for the vacancy.

POSITIVE ABOUT DISABLED PEOPLE

www.carbon-nfprecruit.com

CARBON-NfP

Seattle Children's
HOSPITAL · RESEARCH · FOUNDATION

Neurological Surgery
Associate Professor / Professor

The recently established Center for Neuroscience at the Seattle Children's Research Institute invites applications for a full-time faculty position, with the University of Washington School of Medicine Department of Neurological Surgery, at the rank of Associate Professor or full Professor, without tenure. Qualified applicants should be established investigators who are applying techniques of molecular, genetic or cellular biology to study mechanisms underlying hydrocephalus. The Center for Neuroscience at the Seattle Children's Research Institute's research vision is to restore children's health through a mechanistic understanding. The applicant's area of research interest should be complementary to the interests of current faculty working on various areas of neuroscience and bioengineering. Researchers interested in understanding CSF hydrodynamics, choroid plexus function, neuroendocrinology, brain metabolism, blood brain barrier function, brainstem neurobiology and proteomics research are particularly encouraged to apply. The successful candidate must have a M.D. and/or Ph.D. degree and have active nationally funded research grants. Level and salary will be based on applicant's qualifications and experience. Responsibilities of the position include development of an independent, extramurally funded research program, establishing a hydrocephalus section within the Center for Neuroscience and mentoring graduate and post-doctoral students and junior faculty investigators.

This position is open until filled. Address any inquiries to **Dr. Jan-Marino Ramirez, Center Director**, at **nino.ramirez@seattlechildrens.org**. Please send CV, a statement of current and future research interests and the names and contact information of three references to: **Wendy Kramer, Seattle Children's Research Institute, 1900 Ninth Avenue, M/S C9S-9, Seattle, WA 98101**.

For more information about Seattle Children's Research Institute, please visit:
http://research.seattlechildrens.org.

All University of Washington faculty engage in teaching, research, and service.
The University of Washington is an Equal Opportunity/Affirmative Action Employer.
Women and minorities are encouraged to apply.

UW Medicine
SCHOOL OF MEDICINE

POSTDOCTORAL POSITION,

Hematology and Medical Oncology-
Institute for Computational Biomedicine

Weill Cornell Medical College seeks a highly motivated professional PhD for a Postdoctoral position to explore the dynamics of the B-cell transcriptome during differentiation and malignant transformation, using the tools of high throughput analysis of chromatin and gene expression and function. The work will be performed under the supervision of Dr. Ari Melnick, Associate Professor of Medicine and Biochemistry and Dr. Olivier Elemento, from the Institute for Computational Biomedicine. The applicant would join a thriving and highly interactive research team including cancer biologists, immunologists, hematopathologists, and computational biologists.

Requirements: PhD degree and experience in QPCR, ChIP assays, microarray assays, a basic understanding of microarray analytical statistical considerations, and ideally with experience in high throughput sequencing (e.g. Solexa, 454).

Appointments are for one year, with renewal based upon satisfactory performance and funding availability.

Excellent benefits package (includes tuition reimbursement).

Please send cover letter and resume to:
ATTN: ARI MELNICK, M.D.
E-MAIL: amm2014@med.cornell.edu

WEILL CORNELL MEDICAL COLLEGE

EOE/M/F/D/V

www.med.cornell.edu/jobs

3M Harry Heltzer Multidisciplinary Chair in Science and Technology

University of Minnesota, Minneapolis, MN USA

The Graduate School and the Institute of Technology at the University of Minnesota—Twin Cities invites applications and nominations for the position of 3M Harry Heltzer Multidisciplinary Chair in Science and Technology. This is a tenured and endowed position at the rank of associate or full professor (dependent upon qualifications and experience) in the area of physical and biological structures characterization using microscopy and imaging. Candidates must have outstanding academic and research records, with several years of successful research and teaching experience. A Ph.D. degree and dedication to teaching, graduate student advising, and regular and sustained interaction with industry are required. Candidates are sought whose research agenda will contribute to building cross-disciplinary and cross-college collaboration in one or more areas of strategic importance university-wide, including within the Institute of Technology and with other units at the University of Minnesota. This endowed chair is intended to foster industry-university research interaction and collaboration while advancing scientific and technological expertise in new frontiers of knowledge relevant to the Institute of Technology and 3M. Candidates with a background in any relevant areas of science or engineering are encouraged to apply. Department affiliation will depend on the candidate's area of expertise, with the possibility of a joint appointment with one or more units in the Institute of Technology or elsewhere in the University.

Applications should be submitted online at: **https://employment.umn.edu**, under Req. **# 154636**, and include a cover letter, curriculum vitae (including list of publications), research description/plan, statement of teaching interest, and contact information for three references. Review of applications will begin immediately and continue until the position is filled. For further information, contact **Douglas Ernie** at **ernie@umn.edu**.

The University of Minnesota is an
Equal Opportunity Educator and Employer.

CIN
Werner Reichardt
Centrum für Integrative Neurowissenschaften

Eberhard Karls
Universität
Tübingen

Postdoc Position in Systems Neuroscience

The Werner Reichardt Center for Integrative Neuroscience (CIN, http://www.neuroscience-tuebingen.de/cin/) invites applications for a postdoctoral position in systems neuroscience. Applicants should have a Ph.D. or M.D. degree. The successful candidate will work in the field of tactile perception and its underlying neuronal basis in the rodent whisker system. The project will combine tactile psychophysics in awake behaving rodents with *in vivo* imaging techniques, and will be jointly supervised by two researchers within the CIN, Dr. Cornelius Schwarz (Hertie Institute for Clinical Brain Research, http://www.hih-tuebingen.de/en/kn/forschung0/active-perception-lab/) and Dr. Jason Kerr (Max Planck Institute for Biological Cybernetics, http://www.kyb.mpg.de/kerrgroup/index.html). Experience in one of the following *in vivo* techniques is welcome, 2-photon microscopy, behavioral training, and/or electrophysiology - but other backgrounds are no criterion for exclusion. We are looking for someone who can work independently and is highly motivated. The salary is TV-L E13 (German, public employee salary scale). According to German law, disabled persons with equal occupational aptitude will be given preferred consideration. The University of Tübingen strives to promote equal opportunities in science and is committed to increasing the percentage of female scientists in teaching and research. Qualified female candidates are thus strongly encouraged to apply. Interested applicants should submit their curriculum vitae, a letter of interest with a statement of career objectives, and the names and contact information of three individuals qualified to comment on the candidate's prior achievements. Please send applications in electronic form to **cornelius.schwarz@uni-tuebingen.de.**

Please indicate **code number Zx53**

Executive Director

Virginia Bioinformatics Institute at Virginia Tech

www.vbi.vt.edu

Nominations and applications are invited for the position of Executive Director of the Virginia Bioinformatics Institute at Virginia Tech. The Executive Director will lead and direct the promotion and positioning of the Virginia Bioinformatics Institute as a premier trandisciplinary life sciences institute with research strengths in computational, molecular and systems biology, structural biology, infectious disease and cancer research, cyberinfrastructure for the life sciences, physics, complexity research, and policy informatics. The Institute was founded in 2000 and has quickly grown to 240 research and administrative personnel occupying more than 140,000 square feet of state-of-the-art research facilities at three sites: on the Virginia Tech campus, at the Virginia Tech Corporate Research Center (off-campus) and in Alexandria, Virginia, in the National Capital Region. The Institute has a combined annual operating and extramural research budget of more than $27 million, and is an organizational unit of Virginia Tech.

The Executive Director will represent the Institute's interests at the executive level within the university, with key directors or division officers at leading federal funding agencies, with corporate partners, and with private foundations. The Executive Director will report to the university president or designee; will interact with, respond to, and support the Institute's Policy Advisory Board and Scientific Advisory Board; and will be responsible for overseeing the development and execution of the Institute's strategic plan in support of the university's strategic plan.

Responsibilities

- Oversees the development of a recruiting strategy for executive personnel and key researchers.
- Secures private, federal, state and corporate funding and support for the furtherance of the Institute's research, education, and outreach missions, consistent with the university's and the Institute's long range plans.
- Develops internal research resources that enable successful competition for high visibility, large-scale and highly complex research proposals in key research areas.
- Enables a creative research environment responsive to key granting agency research directions and to further collaborative research goals on campus.
- Advises university executive leaders of future research directions that will impact the university's research goals.
- Ultimately responsible for budget and operations.

Qualifications

- Experience in leading and managing a research organization in a collegial or institutional environment as a scientific program director, project director, or principal investigator.
- Significant post-doctoral or professional research experience in relevant scientific field(s).
- Credentials consistent for appointment to rank of Professor.
- Record of high-quality peer-reviewed publications and excellent track record of extramural funding from federal and state agencies, private foundations and/or corporations.
- Creativity, high motivation, and leadership capabilities.
- Excellent communication and collaboration skills.
- Sound project management and laboratory management skills, if appropriate.
- Excellent leadership in grantsmanship at an institutional level.

Preferences

- Experience in leading and developing a collaborative environment or culture in transdisciplinary research.
- Ph.D. in Biology, Biochemistry or other Life Sciences discipline; Physics, Computer Science, Mathematics or other computational science discipline; with recognition of advanced scientific achievement.

For further information

VIRGINIA BIOINFORMATICS INSTITUTE AT VIRGINIA TECH

VirginiaTech *Invent the Future*

Dr. Paul Knox
Interim Director,
Virginia Bioinformatics Institute
University Distinguished Professor
phone: (540) 231-2582; email: knox@vt.edu

To apply, visit www.jobs.vt.edu and search by posting number 090199
To learn more about VBI, please visit www.vbi.vt.edu

Kumamoto University

Location: Kumamoto, Japan

Open Recruitment of Young Researchers (2nd Stage)

1. **Open Recruitment of Researchers (2nd stage)**
   • Special project researchers (all given the title of "specially appointed assistant professor")
   • A maximum of 3 researchers
2. **Qualification Requirements**
   (1) Academic degree, etc.: Young researchers who have obtained a PhD degree within approximately the past 10 years (as of April 1, 2009)
   (2) Achievements/ability: Has outstanding research capabilities and/or research achievements in one of the specialty areas outlined at the following website: **http://sendou.kuma-u.jp/**.
3. **Arrival:** As soon as possible between September 2009 and October 2009
4. **Period of Employment**
   • Those hired in stage 2 will be employed through March 2014. (Contracts will be for one year each and will be renewed once a year through March 31, 2014.)
   (Note: After having gone through career advancement evaluations and after the end of one's term of employment, it is possible for one to be promoted to the position of "Associate Professor" in the Kumamoto University Priority Organization for Innovation and Excellence. A total of approximately 8 people from stages 1 and 2 will be chosen for these positions.)
5. **Application Deadline:** Applications must reach the university by no later than **May 29, 2009** (Friday).
6. **Inquiries:** Any inquiries should be made by e-mail to the Research Cooperation Section (person in charge of research strategy) of Kumamoto University at the e-mail address written below: **k-senryaku@jimu.kumamoto-u.ac.jp**.

Please be sure to allow enough time before the application deadline for a response to be made to you.

For details on applying, please visit the following website: http://sendou.kuma-u.jp/

Applications will not be accepted through our website.

Shanghai Jiao Tong University
Med-X-Renji Hospital
Clinical Stem Cell Research Center
P. R. China

The newly established **Med-X-Renji Hospital Clinical Stem Cell Research Center** at Shanghai Jiao Tong University, P.R. China invites applications for the Director of the Center at the rank of **Senior Research Scientist / Full Professor**. Applicants should have a Ph.D. and/or M.D degree, and a strong record of experience in stem cell research with clinical application preferred. The candidate will be expected to help build the research center. Review of applications will begin May 15, 2009, and be continued until the position is filled. Startup fund and salary package will be determined based upon experience and qualification. A cover letter, curriculum vitae, a statement of research interests and visions for the center development, and a list of 5 references with addresses, e-mail addresses, and telephone numbers must be included in the application, and mailed to: Prof. Jiufu Luo, Associate Dean for Human Resource at Med-X Research Institute, Shanghai Jiao Tong University, Shanghai 200030, P.R. China. Telephone: 86-21-62932359; Fax: 86-21-62932302; E-mail: **jfluo@sjtu.edu.cn**.

SJTU is an Equal Opportunity/Affirmative Action Employer.

DALIAN INSTITUTE OF CHEMICAL PHYSICS, CHINESE ACADEMY OF SCIENCES

Lab Director and Division Directors, Dalian National Laboratory for Clean Energy

Dalian National Laboratory for Clean Energy (DNL), based mainly in Dalian Institute of Chemical Physics (DICP), Chinese Academy of Sciences (CAS), is looking for outstanding candidates for **DNL director and directors for its nine research divisions: optimized utilization of fossil energy, low carbon catalysis and engineering, energy saving & energy environment, fuel cell & energy storage, hydrogen energy, biomass energy, solar energy, maritime renewable energy, basic & strategic studies on energy, and service center for energy researches**. More details about DICP can be found at **http://www.dicp.ac.cn/.**

Successful candidates for these positions should have a Ph. D. degree and are expected to be an accomplished scientist in his or her academic field, who has demonstrated a strong record of scientific publications in leading scientific journals. Candidates for the DNL director should be under age of 55 and at the rank of full professor or equivalent position with a track record of management in universities or research institutions; while candidates, applying from abroad, for the DNL division directors should be at the rank of associate professor or above, and under age of 50.

Successful candidates will be provided with competitive salary and benefits. A generous start-up research fund for each successful candidate will also be provided.

Candidates, who are interested in these positions, should send a complete CV and publication list to Dr. Hua'an Zhang, Department of Personnel (86-411-84379556, **talents@dicp.ac.cn**), Mr. Zhiyuan Mao (**maozy@dicp.ac.cn**), Prof. Can Li (**canli@dicp.ac.cn**) and Prof. Tao Zhang (**taozhang@dicp.ac.cn**).

INSTITUT DE PHYSIQUE DU GLOBE DE PARIS
Earth - Planets - Environnement - Natural Hazards

DIRECTOR

The Institut de Physique du Globe de Paris (IPGP) is seeking applications for the position of Director of IPGP, which will begin October 1, 2010.

The IPGP is the largest institute of Earth Sciences in France and also one of the largest in Europe. The Institute conducts research and education in geology, geophysics, geochemistry and the environmental sciences. It is in charge of monitoring the three active French volcanoes (Guadeloupe, Martinique, La Réunion) through its volcanic and seismologic observatories. It is also in charge of the magnetic observatory of Chambon-la-Foret (international INTERMAGNET network) and the global seismological network GEOSCOPE. IPGP currently employs about 300 permanent researchers and staff. There are in addition some 200 MSc and PhD students, post-docs and visitors.
The Director will be responsible for supervising the Institute's research and teaching activities, including general administrative tasks, and conducting negotiations with national and European funding agencies. The Director is also the chair of the Institute's scientific Council, whereas the IPGP Board is chaired by a scientist from outside IPGP.
Candidates are expected to be highly accomplished scientists. They will be evaluated on the basis of their academic record in research and teaching, their experience in management, and their vision for the future of IPGP. Interested candidates should submit a two-page vision statement, their Curriculum Vitae and names of three individuals who are willing to be contacted references.

Applications must be received by June 15, 2009.

Application materials should be sent to:
Lydia Zerbib - IPGP General Secretary, Institut de Physique du Globe
4 Place Jussieu, 75252 Paris Cedex 5, France
E-mail: zerbib@ipgp.fr - www.ipgp.fr




Nontraditional Careers:
Opportunities Away From the Bench

Webinar

Want to learn more about exciting and rewarding careers outside of academic/industrial research? View a roundtable discussion that looks at the various career options open to scientists across different sectors and strategies you can use to pursue a nonresearch career.

Now Available
On Demand
www.sciencecareers.org/webinar

Participating Experts:

Dr. Lori Conlan
Director of Postdoc Services,
Office of Intramural Training and Education
National Institutes of Health

Pearl Freier
President
Cambridge BioPartners

Dr. Marion Müller
Director, DFG Office North America
Deutsche Forschungsgemeinschaft
(German Research Foundation)

Richard Weibl
Director, Center for Careers in Science and Technology
American Association for the Advancement of Science

Produced by the
Science/AAAS Business Office.

Science Careers
From the journal *Science* AAAS

A neurochemistry postdoctoral position is available immediately in the laboratories of Dr. Nicholas E. Goeders in the Department of Pharmacology, Toxicology & Neuroscience at the LSU Health Sciences Center in Shreveport. This position will be part of a team investigating the neurobiology of stress and addiction, with special emphasis on the brain mechanisms involved in drug craving and drug seeking. Applicants should have training in the operation and maintenance of commercial mass spectrometers and HPLC. Salary will be $28,000-$51,036 depending on experience. Applications should include a CV, a list of publications and the names of references familiar with the applicant's work. The LSU Health Sciences Center in Shreveport, located in northwest Louisiana, is the largest medical facility in the Tri-State area and has a reputation for excellence in medical and graduate student education and research. Excellent core facilities exist within the LSU Health Sciences Center and the adjoining Biomedical Research Institute.

Nicholas E. Goeders, Ph.D.
Professor and Head
Department of Pharmacology, Toxicology, & Neuroscience
LSU Health Sciences Center
P.O. Box 33932
Shreveport, LA 71130-3932
NGOEDE@LSUHSC.EDU
www.sh.lsuhsc.edu

Louisiana State University is an Equal Opportunity/Affirmative Action Employer.

DNA Sequencing and Computational Biology Core Facility Director
Health and Human Services (HHS)
National Institutes of Health (NIH)
National Heart, Lung and Blood Institute (NHLBI)

An expert is sought in the area of **Computational Biology with an emphasis on next-generation DNA sequence analysis** to direct the DNA Sequencing and Computational Biology (DSCB) Core Facility, Division of Intramural Research (DIR), National Heart, Lung and Blood Institute (NHLBI), NIH in Bethesda, Maryland USA. The successful applicant will interact with DIR Principal Investigators in the design and interpretation of experiments involving all applications of the Illlumina/Solexa DNA sequencing platform, including chromatin immunoprecipitation, RNA expression profiling, and both targeted and whole-genome DNA sequence determination. He/she will oversee DSCB Core Facility personnel in the maintenance and operation of Core sequencing instruments, in the introduction of standard operating procedures and QA/QC measures, in establishing a comprehensive sequence analysis pipeline, in basic bioinformatics studies for the presentation of sequence output to end users, and in original collaborative research at the interface between genomics and proteomics. State-of-the-art IT infrastructure and support will be provided.

The DSCB Core Facility is part of an NHLBI DIR Initiative in Systems Biology, and the DSCB Core Director is expected to interact closely with the Director and staff of an independently operated DIR Proteomics Facility. Although the DSCB Core Facility is oriented toward providing service and conducting collaborative research, the Director will have the opportunity to devote up to 20% of his/her time to undertaking a personal research program in the area of integrative computational biology. The mission of the DIR is to improve the health of all Americans through basic and clinical research, research training, and translation of discoveries to new tools to be applied directly to the field of medicine.

We are seeking an experienced scientist (with Ph.D. or equivalent) with an outstanding track record in computational biology research. Wet laboratory skills relevant to next-generation DNA sequencing technology would be advantageous but are not essential. Salary will be commensurate with qualifications and experience. More detailed information about the NHLBI Division of Intramural Research may be found at: **http://dir.nhlbi.nih.gov/** .

Applicants should submit the following: cover letter highlighting key qualifications; current curriculum vitae with complete bibliography; names and addresses of four references; a one-page summary of the applicant's philosophy of core facility operation; and a one-page description of current and future research interests.

Applications must be received by **June 15, 2009**. PDF versions of documents sent by electronic mail are strongly preferred. Materials should be sent to Dr. Alan M. Michelson c/o: Trina Gregory, Administrative Officer, NHLBI, by email: **gregoryp@nhlbi.nih.gov**; or by regular mail: Building 10, Room 7N220, 10 Center Drive MSC 1670, Bethesda, MD 20892-1670.

HHS and NIH are Equal Opportunity Employers

Eastern Illinois University invites applications for **Chair, Department of Biological Sciences**, 12 month position beginning July 1, 2010. The Chair is responsible for administration of all instructional programs in Biological Sciences. The Department includes 25 tenured/tenure track faculty and large undergraduate and graduate programs. Qualifications include a Ph.D. in Biological Sciences or a related field with a teaching, research and service record commensurate for tenure and the rank of full professor. Candidates must have a strong commitment to undergraduate and graduate programs and the advancement of faculty/student mentoring and research programs.

For more information on this position and application instructions, see the website at: **http://www.eiu.edu/~colsci/biochair.php**.

AA/EOE

Employment Opportunities

Professor and Chair
Department of Basic Pharmaceutical Sciences

The School of Pharmacy is seeking an accomplished academic leader and scientist to serve as Professor and Chair of the Department of Basic Pharmaceutical Sciences. The position is a fully funded, 12-month appointment at the rank of professor or associate professor with tenure. Faculty rank and salary are commensurate with qualifications. The successful candidate will have the leadership skills and vision required to achieve the research, education, and service missions of the department and to promote collaborative research efforts.

Excellent opportunities exist for collaborations with faculty involved in drug discovery and therapeutics, as well as translational and population-based research. Recent Health Sciences Center research infrastructure additions include two research buildings that collectively provide approximately 200,000 sq. ft. of research space and a new Library Learning Center. The School of Pharmacy has active research collaborations with scientists in the campus-based NIOSH research facility, the Mary Babb Randolph Cancer Center, the WVU Center for Neuroscience, and the WVNano Initiative in nanoscience. WVU offers interdisciplinary Ph.D. research training programs in the biomedical sciences as well as a professional Pharm.D. degree.

Qualifications: Doctoral degree in a pharmaceutical science or related discipline, an active federally-funded research program, experience in program administration and planning, and experience in graduate and professional student education.

West Virginia University is a land grant Carnegie-designated Doctoral Research/Extensive institution, with approximately 27,000 undergraduate and 5,500 graduate/professional students. The WVU Health Sciences Center includes the Schools of Pharmacy, Medicine, Dentistry, and Nursing. Morgantown has 55,000 residents and is rated as one of the best small towns in the U.S., with affordable housing, excellent schools, a picturesque countryside and many outdoor activities.

The position is available immediately, and applications will be accepted until an appointment is made. Applications must include a formal letter of application; curriculum vitae; and the names, addresses (including e-mail), and phone numbers of three references. Please submit all application materials to: **Dr. Terry Schwinghammer, West Virginia University School of Pharmacy, P.O. Box 9520, Morgantown, WV 26506**; telephone (304) 293-2573; fax (304) 293-7672. Electronic submissions are encouraged: **tschwinghammer@hsc.wvu.edu**.

For more information, please visit

www.hsc.wvu.edu

WVU is an AA/EOE Employer. Minorities, persons with disabilities and women are encouraged to apply.

Center for Immunology and Microbial Disease
Albany Medical College
Faculty Position

The Center for Immunology and Microbial Disease at Albany Medical College invites applications for a tenure-track faculty position from individuals who have a doctoral degree, postdoctoral experience, and demonstrated research productivity. Those with an interest in host-pathogen interactions are particularly encouraged to apply. The successful candidate will be expected to establish an independent, extramurally funded research program and participate in the teaching of medical and graduate students. The basic science departments at Albany Medical College are organized as interdisciplinary research centers and the Center for Immunology and Microbial Disease has a focus on microbial pathogenesis and immune defense, particularly as related to biothreat agents and emerging infections. Faculty at the Albany Medical College receive competitive salaries, attractive start-up packages, and access to the Center's ABSL-3/BSL-3, Microbiology and Immunology Core Labs. In addition, we have established a close relationship with the New York State Department of Health Wadsworth Laboratories, providing a diverse environment that is rich in infectious disease expertise. Albany Medical College is located in a mid-sized city within the upstate New York Capital Region, and has easy access to Boston, New York City, and the Adirondack Mountains.

Applicants should send their curriculum vitae, a statement of research plans, and three letters of reference to: **Dennis W. Metzger, Ph.D., Professor, Theobald Smith Alumni Chair and Director, Center for Immunology and Microbial Disease, Albany Medical College, 47 New Scotland Avenue, MC-151, Albany, NY 12208.**

For further information about the Center, visit **www.amc.edu/Academic/Research/imd.htm**.

An Equal Opportunity/Affirmative Action Employer.
Women and minorities are encouraged to apply.

ASSISTANT/ASSOCIATE PROFESSOR OF BIOCHEMISTRY

The Department of Biochemistry, University of Missouri, invites applications for a tenure-track Assistant or Associate Professor position from scientists applying biochemical and molecular approaches to the study of fundamental biological processes related to health and disease. We are particularly interested in individuals who would complement existing research strengths in neurodegenerative diseases, inflammation, radiopharmaceuticals, molecular nutrition, diabetes/cardiovascular disease, cancer and ageing. The University is noted for interdisciplinary research programs including a multidisciplinary Life Sciences Center, a NIH-funded Imaging Center that complements a productive institutional nuclear reactor and an International Institute for Nano and Molecular Medicine. Position qualifications include a Ph.D. and/or M.D. in biochemistry or related field and postdoctoral experience. The successful applicant will develop or continue an outstanding research program and contribute to Departmental teaching activities.

Submit a curriculum vitae and descriptions of current and planned research activities, and have three letters of reference sent to: **Chair Biochemistry Search Committee, Department of Biochemistry, 117 Schweitzer Hall, University of Missouri, Columbia, MO 65211**. Electronic submission to **biochemsearch@missouri.edu** is encouraged. Review of applications will begin **July 1, 2009**.

MU is an EEO/AA/ADA Employer, and encourages applications from women and minorities. For ADA accommodations, please contact our ADA Coordinator at (573) 884-7278 (V/TTY).

Associate or Full Professor

Thomas Jefferson University, Department of Pathology, Anatomy & Cell Biology invites applicants for research faculty positions at the level of Associate Professor or Full Professor (tenure track) with scientific interests in neuroscience, cardiovascular biology and pathology, or tumor development and metastasis. Successful candidates will interact and develop collaborations with well-established investigators in these and related areas, with the goal of developing effective, multi-investigator groups in focused research themes.

Applications from individuals with MD, MD/PhD, PhD or equivalent degrees, investigative backgrounds and active grant funding are welcome. Preference will be accorded to federally funded investigators with vigorous research programs in the target areas listed, and to those with established capabilities of collaborating effectively with others. Training in Pathology, and the ability to participate in clinical activities relevant to the research focus is optional.

Applicant qualifications will determine the level of appointment, faculty track, including tenure or tenure-track, and the availability of additional positions as part of the recruitment package.

Thomas Jefferson University is home to one of the largest and most active groups of investigators in a Department of Pathology in the United States. Key areas of interest include neurodegenerative diseases and neuroAIDS, cellular signaling pathways, alcohol-induced tissue and cellular injury, computational and systems biology, tumor invasion and metastasis, matrix biology, and gene therapy. The University has identified four strategic areas for research growth: oncology, neurosciences, cardiovascular biology and infection and immunity. Active transdepartmental centers, including the Kimmel Cancer Center, the Farber Institute for Neurosciences and the Wills Eye Institute provide a framework for programmatic development. Important collaborations both among departmental investigators and between departmental scientists and others on campus encompass the areas of concentration for which we currently seek applicants.

All correspondence should include the following: curriculum vitae; names and contact information for at least three professional references; summary of current and pending grant support; and an introductory letter emphasizing professional and investigative goals, active collaborations and anticipated career development.

Please address all correspondence to: **David S. Strayer, MD, PhD, Professor, Head, Faculty Search Committee, c/o Ms. Jennifer Jackson, 279 Jefferson Alumni Hall, Department of Pathology, Jefferson Medical College, Thomas Jefferson University, 1020 Locust Street, Philadelphia, Pennsylvania 19107.** Apply at our website www.jefferson.edu/careers reference #52657. Also send by email to **Kathleen.welsh@jefferson.edu** and cc: **Jennifer.jackson@jefferson.edu.** EOE

Jefferson™

ETH

Eidgenössische Technische Hochschule Zürich
Swiss Federal Institute of Technology Zurich

Professor of Crop Science

The Department of Agricultural and Food Sciences (www.agrl.ethz.ch) at ETH Zurich invites applications for a professorship of Crop Science.

The new professor is expected to develop an internationally recognized research program in plant breeding with an emphasis on the development of crops adapted to abiotic and/or biotic stresses for increased sustainable plant production or on the development of crops with improved quality for human nutrition. The research will focus on the field level and comprise investigations from the single plant trait level to the landscape level and will be relevant both for industrialized and developing countries.

The successful candidate will be expected to teach undergraduate level courses (German or English) and graduate level courses (English) in the field of crop science and plant breeding. Collaboration in research and teaching is expected within the Institute of Plant Science and with other groups of the ETH domain and related institutions.

Please submit your application together with a curriculum vitae, a list of publications, a statement of research and teaching interests, and the names and contact information of three possible referees **to the President of ETH Zurich, Prof. Dr. Ralph Eichler, Raemistrasse 101, 8092 Zurich, Switzerland, no later than June 30, 2009.** With a view toward increasing the number of female professors, ETH Zurich specifically encourages female candidates to apply.

POSITIONS OPEN

ASSOCIATE PROFESSOR
University of California, Irvine
Department of Pharmaceutical Sciences

The Department of Pharmaceutical Sciences at University of California, Irvine invites applications for a 50 percent time, tenured faculty position in the area of drug design and development, with a particular emphasis on translational research and the treatment of cancer. The appointment will be made at the Associate or Full Professor level, commensurate with the applicant's qualifications and experience. The successful candidate will be expected to have active basic and clinical research programs in the area of targeted drug action, and in addition, experience translating basic research results expeditiously into clinical applications.

Interested applicants should submit curriculum vitae, the names of three prominent references, and a brief outline of future research plans. Application instructions can be found at **website: https://recruit.ap.uci.edu.** Review of applications will begin immediately. To ensure full consideration, applications and all supporting materials should be received by May 22, 2009. The position will remain open until filled.

UCI is an Equal Opportunity Employer committed to excellence through diversity and strongly encourages applications from all qualified applicants, including women and minorities.

POSTDOCTORAL POSITION, BOSTON
in TUBEROUS SCLEROSIS AND LAM

The Henske laboratory at Harvard Medical School and the Brigham and Women's Hospital is seeking a highly motivated Postdoctoral Fellow with training in genetics, biochemistry, or cell biology to study tuberous sclerosis complex (TSC) and/or lymphangioleiomyomatosis (LAM). Please send curriculum vitae, cover letter, and names of three references to: **Dr. Elizabeth Petri Henske, Brigham and Women's Hospital, One Blackfan Circle, 6th Floor, Boston, MA 02115. Or e-mail: henskelab@gmail.com**. *BWH is an Affirmative Action/Equal Opportunity Employer.*

POSITIONS OPEN

UNIVERSITY OF WASHINGTON

POSTDOCTORAL POSITION: NIH T32 training grant is available at the University of Washington, Division of Rheumatology, July 2009. Research includes: the role of B cells in autoimmunity (**Jeff Ledbetter**); targeting of costimulatory molecules in autoimmunity, how defects in apoptosis lead to inflammation and autoimmunity (**Keith Elkon**). Candidates must have an M.D., Ph.D., or M.D.-Ph.D. and *must be a U.S. citizen or green card holder* and should have experience in immunology and/or molecular biology. Submit a cover letter with interests and goals, curriculum vitae, and three reference letters to: **Cathy Johnson, e-mail: pingpong@u.washington.edu.**

The University of Washington is an Affirmative Action, Equal Opportunity Employer.

POSTDOCTORAL POSITION

NIH-funded Postdoctoral position in cellular and molecular immunology to study mechanisms contributing to Th2 memory cell development and associated host protective effects on helminth parasites. Highly motivated researchers having experience using mouse models to investigate the immunology of infectious disease and/or study immune regulatory mechanisms are preferred. Please submit curriculum vitae and three letters of reference to **e-mail: gausewc@umdnj.edu. William C. Gause, Ph.D.,** University Professor, University of Medicine and Dentistry of New Jersey–New Jersey Medical School, Department of Medicine. *UMDNJ is an Affirmative Action/Equal Opportunity Employer, Minorities/Females/Persons with Disabilities/Veterans, and is a member of the University Health Systems of New Jersey.*

CAREER OPPORTUNITY

Doctor of Optometry (O.D.) degree in 27 months for Ph.D.s in science and M.D.s. Excellent career opportunities for O.D./Ph.D.s and O.D./M.D.s in research, education, industry, and clinical practice. This unique program starts in March 2009, and features small classes and 12 months devoted to clinical care.

Contact the **Admissions Office, telephone: 800-824-5526** at the **New England College of Optometry, 424 Beacon Street, Boston, MA 02115.** Additional information at **website: http://www.neco.edu, e-mail: admissions@neco.edu.**

MARKETPLACE

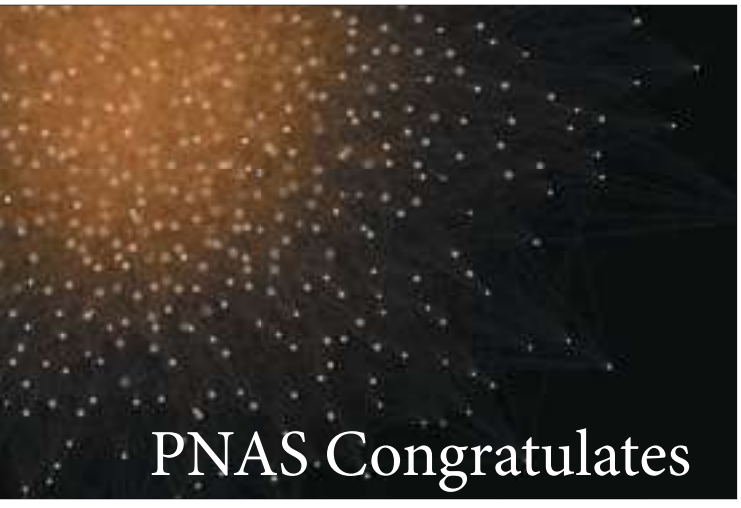

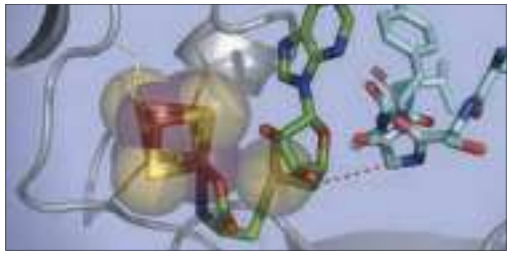

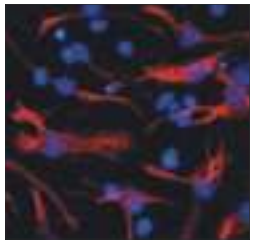

PNAS Congratulates

2008 Cozzarelli Prize Recipients

The *Proceedings of the National Academy of Sciences* (PNAS) has selected 6 outstanding articles for the 2008 Cozzarelli Prize, in recognition of their scientific excellence and originality. Winners were selected from the 3,500 research articles published online in PNAS in 2008 and represent exceptional contributions to the 6 broadly defined classes under which the National Academy of Sciences is organized.

2008 COZZARELLI PRIZE RECIPIENTS

Class I: Physical And Mathematical Sciences
Fluid helium at conditions of giant planetary interiors
Lars Stixrude and Raymond Jeanloz
(2008) PNAS 105:11071–11075

Class II: Biological Sciences
MicroRNA-directed transcriptional gene silencing in mammalian cells
Daniel H. Kim, Pål Sætrom, Ola Snøve, Jr., and John J. Rossi
(2008) PNAS 105:16230–16235

Class III: Engineering and Applied Sciences
The implications of human metabolic network topology for disease comorbidity
D.-S. Lee, J. Park, K. A. Kay, N. A. Christakis, Z. N. Oltvai, and A.-L. Barabási
(2008) PNAS 105:9880–9885

Class IV: Biomedical Sciences
Neurons derived from reprogrammed fibroblasts functionally integrate into the fetal brain and improve symptoms of rats with Parkinson's disease
Marius Wernig, Jian-Ping Zhao, Jan Pruszak, Eva Hedlund, Dongdong Fu, Frank Soldner, Vania Broccoli, Martha Constantine-Paton, Ole Isacson, and Rudolf Jaenisch
(2008) PNAS 105:5856–5861

Class V: Behavioral and Social Sciences
Cross-modal individual recognition in domestic horses (*Equus caballus*)
Leanne Proops, Karen McComb, and David Reby
(2009) PNAS 106:947–951

Class VI: Applied Biological, Agricultural, and Environmental Sciences
Decreases in dengue transmission may act to increase the incidence of dengue hemorrhagic fever
Yoshiro Nagao and Katia Koelle
(2008) PNAS 105:2238–2243

Podcast interviews with the authors will be available at www.pnas.org/site/misc/podcasts.shtml

PNAS
www.pnas.org

R&D Systems
High Performance Antibodies.

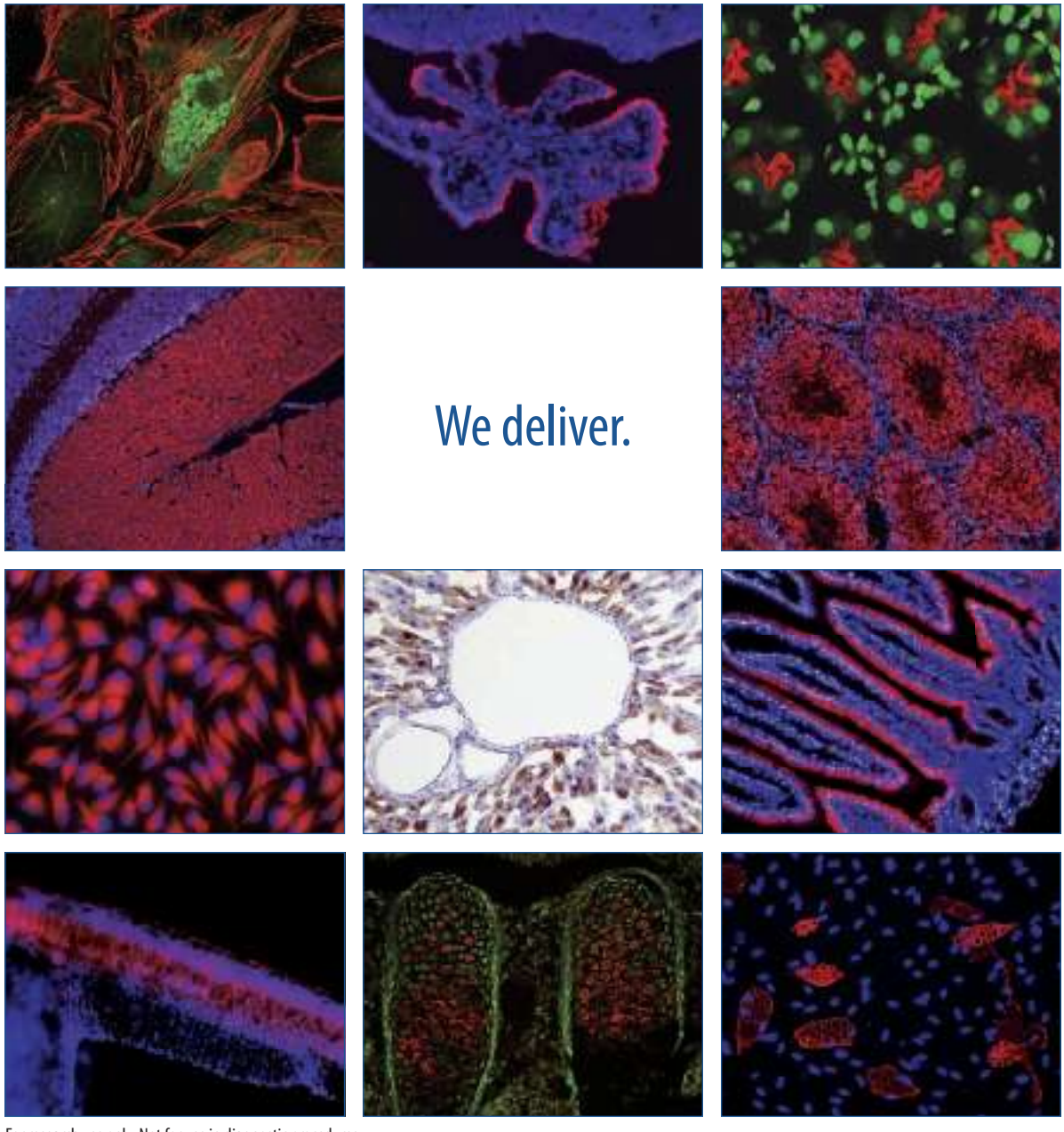

We deliver.

For research use only. Not for use in diagnostic procedures.

For details about the images above, please visit our website at www.RnDSystems.com/go/AntibodyAd

R&D Systems Tools for Cell Biology Research™

USA & Canada **R&D Systems, Inc.** Tel: (800) 343-7475 info@RnDSystems.com

Europe **R&D Systems Europe, Ltd.** Tel: +44 (0)1235 529449 info@RnDSystems.co.uk

Selection expanding weekly—visit **www.RnDSystems.com/go/request** to sign up for weekly new product updates.

R&D SYSTEMS®